

Pacific National University

**NUCLEAR THEORY
IN THE SUPERCOMPUTING ERA – 2016
(NTSE-2016)**

International Conference

Khabarovsk, Russia, September 19–23, 2016

PROCEEDINGS

Editors A. M. Shirokov and A. I. Mazur

Khabarovsk, Russia
Pacific National University
2018

УДК 539.14
ББК В38я431

N 91

N 91

Nuclear Theory in the Supercomputing Era – 2016 (NTSE-2016): International Conference. Khabarovsk, Russia, September 19–23, 2016. Proceedings. Eds. A. M. Shirokov and A. I. Mazur. — Khabarovsk, Russia: Pacific National University, 2018. — 294 p.

ISBN 978-5-7389-2475-0

The primary motivation for the series of International Conference “Nuclear Theory in the Supercomputing Era (NTSE)” (<http://ntse.khb.ru>) was the rapid growth of supercomputers and the impact they, along with theoretical and algorithmic developments, are having on nuclear theory. The first conferences in this series, “Horizons of Innovative Theories, Experiments, and Supercomputing in Nuclear Physics” (HITES-2012) and NTSE-2012, were hosted respectively by the Louisiana State University in New Orleans, Louisiana, USA in June 4–7, 2012 (<http://www.phys.lsu.edu/hites2012>) and by the Pacific National University, Khabarovsk, Russia in June 18–22, 2012 (<http://www.ntse-2012.khb.ru>). These conferences were proceeded later under the common title NTSE. The NTSE-2013 (<http://ntse.khb.ru/2013>) was hosted by the Iowa State University, Ames, Iowa, USA in May 13–17, 2013 and celebrated the 70th birthday of Professor James Vary. The NTSE-2014 (<http://www.ntse-2014.khb.ru>) was hosted by the Pacific National University, Khabarovsk, Russia in June 23–27, 2014.

These proceedings includes talks presented at the NTSE-2016 Conference hosted by the Pacific National University, Khabarovsk, Russia in September 19–23, 2016. The Conference was sponsored by the Pacific National University, Khabarovsk, Russia and by the Russian Foundation for Basic Research.

The contributions to the NTSE-2016 Proceedings published here, are also available online at <http://www.ntse.khb.ru/2016/Proc/>.

УДК 539.14
ББК В38я431

ISBN 978-5-7389-2475-0

©Pacific National University, 2018

Preface

The International Conference on Nuclear Theory in the Supercomputing Era — 2016 (NTSE-2016) brought together experts in nuclear theory and high-performance computing in Khabarovsk, Russia, from September 19 to September, 2016. This conference series was started in 2012 by the NTSE-2012 and HITES-2012 conferences which were proceeded later under the common title NTSE. The NTSE conferences focus on forefront challenges in physics, namely the fundamentals of nuclear structure and reactions, the origin of the strong inter-nucleon interactions from QCD, and computational nuclear physics with leadership class supercomputer facilities to provide forefront simulations leading to new discoveries.

The conference welcomed many young scientists, including graduate students in nuclear physics, computational science and applied mathematics. All participants together made the conference a great success.

The conference topics,

- (1) *Ab initio* nuclear structure;
- (2) Microscopic approaches to nuclear reactions;
- (3) Origin and properties of the strong interactions; and
- (4) Computational science and applied mathematics,

reflect current world-wide research interests and encompass a broad area of fundamental physics and high-performance computing.

We would like to express our appreciation to all participants of the NTSE-2016 conference, to all contributors to these proceedings, to all members of the Scientific Advisory Committee and to the NTSE-2016 sponsors including Pacific National University and the Russian Foundation for Basic Research.

The organizing committee:

Sergey Ivanchenko (Chair), Pacific National University, Russia

Sergey Burkov, Pacific National University, Russia

Alexander Mazur (Scientific secretary), Pacific National University, Russia

Igor Mazur, Pacific National University, Russia

Vladimir Rimlyand, Pacific National University, Russia

Andrey Shirokov (Vice Chair), Moscow State University, Russia

Tatiana Sytnikova, Pacific National University, Russia

Yurii Tchuvil'sky (Vice Chair), Moscow State University, Russia

James Vary (Vice Chair), Iowa State University, USA

NTSE-2016 Scientific Advisory Committee:

- **James Vary (Chair)**, Iowa State University, USA
- **Bruce Barrett**, University of Arizona, USA
- **Leonid Blokhintsev**, Moscow State University, Russia
- **Stanley J. Brodsky**, SLAC-Stanford, USA
- **Ümit Çatalyürek**, The Ohio State University, USA
- **Mark Caprio**, University of Notre Dame, USA
- **David Dean**, Oak Ridge National Laboratory, USA
- **Jerry Draayer**, Louisiana State University, USA
- **Victor Efros**, Russian Research Centre Kurchatov Institute, Russia
- **Charlotte Elster**, Ohio University, USA
- **Evgeny Epelbaum**, University of Bochum, Germany
- **Morten Hjorth-Jensen**, University of Oslo, Norway and Michigan State University, USA
- **Sergey Ivanchenko**, Pacific National University, Russia
- **Youngman Kim**, Institute for Basic Science, South Korea
- **Ruprecht Machleidt**, University of Idaho, USA
- **Alexander Mazur**, Pacific National University, Russia
- **Alexander Motovilov**, Joint Institute for Nuclear Research, Russia
- **Petr Navrátil**, TRIUMF, Canada
- **Esmond Ng**, Lawrence Berkeley National Laboratory, USA
- **W. Erich Ormand**, Lawrence Livermore National Laboratory, USA
- **Takaharu Otsuka**, University of Tokyo, Japan
- **Wayne Polyzou**, University of Iowa, USA
- **Jianwei Qiu**, Brookhaven National Laboratory, USA
- **Sophia Quaglioni**, Lawrence Livermore National Laboratory, USA
- **Kimiko Sekiguchi**, Tohoku University, Japan
- **Andrey Shirokov**, Moscow State University, Russia

- **Masha Sosonkina**, Old Dominion University, USA
- **Yurii Tchuvil'sky**, Moscow State University, Russia
- **Furong Xu**, Peking University, China
- **Xingbo Zhao**, Institute of Modern Physics, China

NTSE-2016 Organizing Committee:

- **Sergey Ivanchenko (Chair)**, Pacific National University, Russia
- **Sergey Burkov**, Pacific National University, Russia
- **Alexander Mazur (Scientific secretary)**, Pacific National University, Russia
- **Igor Mazur**, Pacific National University, Russia
- **Vladimir Rimyand**, Pacific National University, Russia
- **Andrey Shirokov (Vice Chair)**, Moscow State University, Russia
- **Tatiana Sytnikova**, Pacific National University, Russia
- **Yurii Tchuvil'sky (Vice-Chair)**, Moscow State University, Russia
- **James Vary (Vice Chair)**, Iowa State University, USA

Program of International Conference on Nuclear Theory in the Supercomputing Era — 2016 (NTSE-2016)

Sunday, September 18

Arrival

Monday, September 19

Conference Hall

9:00–9:40am	<i>Registration</i>
9:40–10:00am	<i>Conference opening</i> Sergey N. Ivanchenko, president PNU Welcome from Pacific National University
10:00–11:00am	James Vary <i>Ab initio</i> No-Core Shell Model with Leadership Class Supercomputers

11:00–11:20am	<i>Coffee break</i>
---------------	---------------------

Chair: Charlotte Elster

11:20–12:20pm	Carlo Barbieri Self-Consistent Green's Function Theory Computations of Medium Mass Isotopes
12:20–1:20pm	Furong Xu CGSM and MBPT Calculations with Realistic Nuclear Forces

1:20–2:20pm	<i>Lunch break</i>
-------------	--------------------

Chair: Roman Skibiński

2:20–3:20pm	Andrey Shirokov <i>NN</i> Interaction Daejeon16
3:20–4:20pm	Kimiko Sekiguchi Approach to Three Nucleon Forces from Experiment

4:20–4:40pm	<i>Coffee break</i>
-------------	---------------------

Room 201

Discussion leader: Viktor Efros

4:40–6:00pm	Discussions, additional questions to speakers
-------------	---

6:30 pm	<i>Welcome party</i>
---------	----------------------

Tuesday, September 20*Conference Hall***Chair: Andrey Shirokov**

9:00–10:00am	Viktor Efros An Approach to the Computation of Few/Many-Body Multichannel Reactions
10:00–11:00am	Charlotte Elster Reactions with Light Nuclei

11:00–11:20am	<i>Coffee break</i>
---------------	---------------------

Chair: Kimiko Sekiguchi

11:20–12:20pm	Alexander Motovilov Structure of T -Matrices on Unphysical Energy Sheets and Few- Body Resonances
12:20–1:20pm	Roman Skibiński Modern two-nucleon forces in three-nucleon reactions

1:20–2:20pm	<i>Lunch break</i>
-------------	--------------------

Chair: Noritaka Shimizu

2:20–3:20pm	Xingbo Zhao Time-dependent Basis Function Approach to Nuclear Scattering
3:20–4:20pm	Kai Wen The Inertial Mass and Collective Path in Nuclear Fusion/Fission Reactions
4:20–5:10pm	Nikolay Khokhlov Deuteron Wave Function and Elastic eD Scattering

5:10–5:30pm	<i>Coffee break</i>
-------------	---------------------

*Room 201***Discussion leader: James Vary**

5:30–6:50pm	Discussions, additional questions to speakers
-------------	---

Wednesday, September 21*Conference Hall***Chair: John Hill**

9:00–10:00am	Joel Lynn Quantum Monte Carlo Calculations with Chiral Effective Field Theory Interactions
10:00–11:00am	Youngman Kim QCD Fossils in Nuclei?

11:00–11:20am	<i>Coffee break</i>
---------------	---------------------

Chair: Sergey Yakovlev

11:20–12:20pm	Shan-Gui Zhou Nuclear Tetrahedral Shapes from MDC-CDFT
12:20–1:20pm	Junchen Pei Continuum DFT Studies of Exotic Nuclei and Dynamics

1:20–2:20pm	<i>Lunch break</i>
-------------	--------------------

Chair: Yuri Tshuvil'sky

2:20–3:20pm	Noritaka Shimizu Large-Scale Shell-Model Studies for Exotic Nuclei and Nuclear Level Densities
3:20–4:20pm	Alexander Mazur Analysis of Resonant States within the SS-HORSE Method
4:20–4:50pm	Myeong-Hvan Mun Study of Low-Energy Phase Shift using NCSM with Three Different NN Interactions

4:50–5:10pm	<i>Coffee break</i>
-------------	---------------------

*Room 201***Discussion leader: Luigi Coraggio**

5:10–6:30pm	Discussions, additional questions to speakers
-------------	---

Thursday, September 22

Conference Hall

Chair: Alexander Motovilov

9:00–10:00am	Olga Rubtsova Solution of Few-Body Scattering Problems in a Discrete Representation by Using GPU
10:00–11:00am	Luigi Coraggio Large-Scale Shell-Model Challenges within the RIB Era

11:00–11:20am	<i>Coffee break</i>
---------------	---------------------

Chair: Carlo Barbieri

11:20–12:20am	Sergey Yakovlev Scattering in the System of Three Charged Particles
12:20–1:00pm	Sergey Zaytsev Electron Correlations in the Framework of Quasi Sturmian Functions Approach

1:00–2:00pm	<i>Lunch break</i>
-------------	--------------------

Room 201

Discussion leader: Furong Xu

2:00–3:10pm	Discussions, additional questions to speakers
-------------	---

3:10–7:30pm	<i>Excursion</i>
7:30pm	<i>Conference dinner</i>

Friday, September 23*Conference Hall***Chair: Youngman Kim**

9:00–10:00am	John Hill Highlights from the 15 Year Heavy Ion Program at the PHENIX Experiment
10:00–11:00am	Yurii Tchuviľ'sky Asymptotic Properties of Resonance and Weakly-Bound States in the Shell-Model Calculations

11:00–11:20am	<i>Coffee break</i>
---------------	---------------------

Chair: Shan-Gui Zhou

11:20–12:10pm	Alexander Soloviev The Algebraic Versions of the Resonating Group Model and the Orthogonality Conditions Model as Fundamentals of Theoretical Approaches for Describing Nuclear Reactions
12:10–12:50pm	Igor Mazur Energy and Width of the Resonance in the $4n$ System
12:50–1:20pm	Vasily Kulikov S -matrix Method for Extrapolation of the Results of No-Core Shell Model Calculations

1:20–2:20pm	<i>Lunch break</i>
-------------	--------------------

Public Lectures

2:20–3:20pm	James Vary Role of Supercomputers in Basic Science Simulations
3:20–4:20pm	Victor Efros Quantum Mechanics of Reactions with Many Open Channels (in Russian)

4:20–4:40pm	<i>Coffee break</i>
-------------	---------------------

*Room 201***Discussion leader: Andrey Shirokov**

4:40–6:00pm	Discussions, additional questions to speakers
6:00pm	<i>Conference closing</i>

Saturday, September 24**Public Lectures**

10:00–11:00am	Yurii Tchuviľ'sky Current Status and Prospects of Nuclear Physics Research (in Russian)
---------------	---

Contents

<i>Preface</i>	3
<i>NTSE-2016 Scientific Advisory Committee</i>	4
<i>NTSE-2016 Organizing Committee</i>	5
<i>Program of International Conference on Nuclear Theory in the Supercomputing Era — 2016 (NTSE-2016)</i>	6
Invited talks:	
<u>James P. Vary</u> , Robert Basili, Weijie Du, Matthew Lockner, Pieter Maris, Dossay Oryspayev, Soham Pal, Shiplu Sarker, Hasan Metin Aktulga, Esmond Ng, Meiyue Shao and Chao Yang, <i>Ab initio No Core Shell Model with Leadership-class supercomputers</i>	15
F. Raimondi and <u>C. Barbieri</u> , <i>Irreducible 3-body force contributions to the self-energy</i>	36
Zhonghao Sun, Qiang Wu and <u>Furong Xu</u> , <i>Green's function calculations of light nuclei</i>	52
<u>Kimiko Sekiguchi</u> , <i>Experiments of few-nucleon scattering and three-nucleon forces</i>	60
<u>V. D. Efros</u> , <i>Approach to computation of few/many-body multichannel reactions</i> ..	66
L. Hlophe and <u>Ch. Elster</u> , <i>Energy dependent separable optical potentials for (d, p) reactions</i>	76
<u>R. Skibiński</u> , J. Golak, A. M. Shirokov, K. Topolnicki, Y. Volkotrub and H. Witała, <i>Three-nucleon reactions with recently derived nuclear potentials</i>	90
W. Du, P. Yin, G. Chen, <u>X. Zhao</u> and J. P. Vary, <i>Deuteron Coulomb excitation in peripheral collisions with a heavy ion</i>	102
<u>Kai Wen</u> and Takashi Nakatsukasa, <i>Self-consistent collective motion path for nuclear fusion/fission reactions</i>	115
<u>N. A. Khokhlov</u> , <i>Deuteron wave function and neutron form factors from elastic electron-deuteron scattering</i>	124
<u>Joel E. Lynn</u> , <i>Quantum Monte Carlo calculations with chiral effective field theory interactions: developments and a recent application</i>	140
<u>Youngman Kim</u> , <i>QCD Fossils in Nuclei?</i>	154
Jie Zhao, Bing-Nan Lu, En-Guang Zhao and <u>Shan-Gui Zhou</u> , <i>Nuclear tetrahedral shapes from multidimensionally-constrained covariant density functional theories</i>	159
Kai Wang and <u>Junchen Pei</u> , <i>Pygmy dipole modes in shape-coexisting ⁴⁰Mg</i>	174

<u>Noritaka Shimizu</u> , <i>Large-scale shell-model studies of exotic nuclei and nuclear level densities</i>	179
<u>A. I. Mazur</u> , A. M. Shirokov, I. A. Mazur, E. A. Mazur, Y. Kim, I. J. Shin, L.D. Blokhintsev and J.P. Vary, <i>Resonant states in ^5He and ^5Li and nucleon-α scattering</i>	185
<u>O. A. Rubtsova</u> , V. N. Pomerantsev and V. I. Kukulin, <i>Solving few-body scattering problems in a discrete representation by using GPU</i>	205
<u>L. Coraggio</u> , A. Gargano and N. Itaco, <i>Large-scale shell-model challenges within the RIB era</i>	226
A. S. Zaytsev, M. S. Aleshin, L. U. Ancarani and <u>S. A. Zaytsev</u> , <i>Electron correlations in the framework of the quasi Sturmian approach</i>	236
<u>John C. Hill</u> for the PHENIX Collaboration, <i>Highlights from the 17-year heavy ion program at the PHENIX experiment at RHIC</i>	246
<u>A. S. Solovyeu</u> , S. Yu. Igashov and Yu. M. Tchuvil'sky, <i>Algebraic versions of resonating group and orthogonality condition models as fundamentals of theoretical approaches to the description of radiative capture</i>	267
<u>I. A. Mazur</u> , A. M. Shirokov, A. I. Mazur, I. J. Shin, Y. Kim and J. P. Vary, <i>Ab initio description of the tetra-neutron with realistic NN interactions within the NCSM-SS-HORSE approach</i>	280
Alphabetic list of the NTSE-2016 speakers	293

International Conference
NUCLEAR THEORY
IN THE SUPERCOMPUTING ERA – 2016
(NTSE-2016)

INVITED TALKS

Ab Initio No Core Shell Model with Leadership-Class Supercomputers

James P. Vary^a, Robert Basili^a, Weijie Du^a,
Matthew Lockner^a, Pieter Maris^a, Dossay Oryspayev^b,
Soham Pal^a, Shiplu Sarker^a, Hasan Metin Aktulga^c,
Esmond Ng^d, Meiyue Shao^d, Chao Yang^d

^a*Department of Physics and Astronomy, Iowa State University, Ames, IA 50011, USA*

^b*Department of Computer Science, Iowa State University, Ames, IA, 50011, USA*

^c*Department of Computer Science, Michigan State University, East Lansing, MI 48824, USA*

^d*Lawrence Berkeley National Laboratory, Berkeley, CA 94720, USA*

Abstract

Nuclear structure and reaction theory is undergoing a major renaissance with advances in many-body methods, strong interactions with greatly improved links to Quantum Chromodynamics (QCD), the advent of high performance computing, and improved computational algorithms. Predictive power, with well-quantified uncertainty, is emerging from non-perturbative approaches along with the potential for guiding experiments to new discoveries. We present an overview of some of our recent developments and discuss challenges that lie ahead. Our foci include: (1) strong interactions derived from chiral effective field theory; (2) advances in solving the large sparse matrix eigenvalue problem on leadership-class supercomputers; (3) selected observables in light nuclei with the JISP16 interaction; (4) effective electroweak operators consistent with the Hamiltonian; and (5) discussion of $A = 48$ system as an opportunity for the no-core approach with the reintroduction of the core.

Keywords: *No Core Shell Model; chiral Hamiltonians; LENPIC interaction; JISP16 interaction; Petascale computers; Exascale computers*

1 Introduction

With continuing advances in leadership-class supercomputers and plans for further developments leading to Exascale systems [defined as having capabilities for 10^{18} floating-point operations per second (flops)], theoreticians are developing quantum many-body approaches that portend a new era of research and discovery in physics as well as in other disciplines. In particular, the nuclear physics quantum many-body problem presents unique challenges that include the need to simultaneously develop (1) strong inter-nucleon interactions with ties to QCD in order to control

Proceedings of the International Conference ‘Nuclear Theory in the Supercomputing Era — 2016’ (NTSE-2016), Khabarovsk, Russia, September 19–23, 2016. Eds. A. M. Shirokov and A. I. Mazur. Pacific National University, Khabarovsk, Russia, 2018, p. 15.

<http://www.ntse-2016.khb.ru/Proc/Vary.pdf>.

the concomitant freedoms; (2) non-perturbative methods that respect all the underlying symmetries such as translational invariance; and (3) new algorithms that prove efficient in solving the quantum many-body problem on leadership-class supercomputers. This triad of forefront requirements impels multi-disciplinary collaborations that include physicists, applied mathematicians and computer scientists.

While the physics goals for computational nuclear structure and reactions may seem obvious — i. e., retaining predictive power and quantifying the uncertainties — the opportunities and challenges presented with the continuing rapid development of supercomputer architectures is less obvious to the broader community; so we will introduce some of these issues in this work. With the need to develop and apply fully microscopic approaches to heavier nuclei as well as to include multi-nucleon interactions and coupling to the continuum, even Exascale computers will be insufficient to meet all our plans. We therefore must also work to develop renormalization schemes that reduce the computational burden without loss of fidelity to the underlying theory.

2 Strong inter-nucleon interactions linked to QCD

Major theoretical advances have been made in the last few years in developing the theory of nuclear strong interaction Hamiltonians from the underlying theory QCD using chiral effective field theory (EFT) [1, 2]. The chiral EFT provides a hierarchy of two-nucleon (NN), three-nucleon ($3N$), four-nucleon ($4N$) interactions, etc., with increasing chiral order where chiral order is defined in terms of a dimensionless parameter Q/Λ . Here Q represents a characteristic low-momentum scale, which is frequently taken to be the mass of the pion or the momentum transfer in the case of scattering, and Λ is the confinement (symmetry breaking) scale of QCD which is usually in the range of 4–7 times the mass of the pion. Most recently, a new generation of chiral interactions is becoming available [3, 4] that aims for improved consistency of the NN and multi- N interactions. These developments motivate us to adopt chiral EFT Hamiltonians in our current and planned applications.

One hallmark of the development of the newest generation of chiral Hamiltonians is the close collaboration of the few-body teams traditionally leading the Hamiltonian developments and the many-body applications teams that have traditionally been on the receiving end of the Hamiltonians once they are released. This teamwork is exemplified by the Low Energy Nuclear Physics International Collaboration (LENPIC) [4, 5] which has a workflow portrayed in Fig. 1. In this new paradigm, there is a close interplay between the Hamiltonian developers and the many-nucleon applicators so that there is now feedback on important issues such as the choice of regulators and the determination of the low-energy constants (LECs) that cannot yet be determined directly from QCD. In principle, this will lead to a selection of the ingredients in the chiral EFT that are more harmonious with improved convergence rates, predictive power and quantified uncertainties.

At the present time, only the new chiral NN interactions are available [6] and the consistent chiral $3N$ and $4N$ interactions are under development with an expected release in 2018. The results with the new chiral NN interactions are very encouraging yet still indicate the need for consistent $3N$ interactions to accurately describe the properties of light nuclei [3, 4]. In order to reach such a conclusion, new methods of uncertainty quantification were developed and applied [3, 4, 6]. For the purposes of this work we will adopt alternative state-of-the-art NN interactions to illustrate

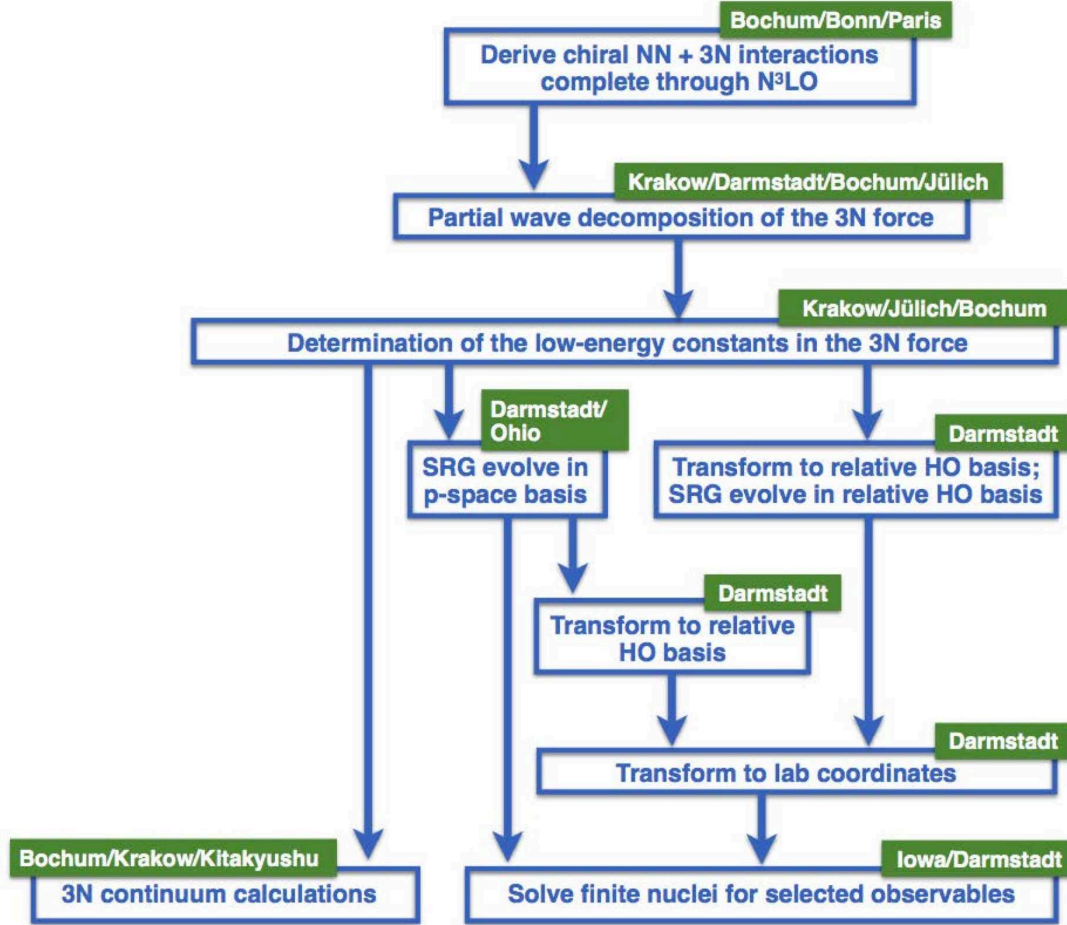


Figure 1: Workflow of the Low Energy Nuclear Physics International Collaboration (LENPIC) depicting a one-pass effort [5]. Multiple passes through the entire workflow and/or subareas of the workflow are performed in order to arrive at a final regulated chiral EFT interaction with quantified uncertainties in the LECs.

calculated nuclear properties and uncertainty quantification with leadership-class supercomputers.

3 *Ab initio* No Core Shell Model

The *ab initio* No Core Shell Model (NCSM) formulates the nuclear quantum many-body problem as a non-relativistic Hamiltonian eigenvalue problem in an adopted basis space [most frequently a harmonic oscillator (HO) basis] where all nucleons in the nucleus are treated on the same footing [7–14]. This representation of the Hamiltonian in a basis, using NN , $3N$ and $4N$ interactions, generates a large sparse matrix eigenvalue problem for which we seek the low-lying eigenvalues and eigenvectors in order to compare with experimental data and to make testable predictions.

Since the interactions are strong, inducing short-range correlations, the challenge is to perform the calculations in a sufficiently large basis to obtain convergence. Alternatively, one may perform a sequence of calculations in ever-increasing basis spaces and extrapolate the eigenvalues, as well as other observables, to the infinite matrix limit. We refer to this approach for obtaining the converged results and quantified uncertainties as the No-Core Full Configuration (NCFC) method.

The reach of the NCFC method with fixed uncertainty is limited by the available computational resources. To minimize uncertainties while increasing the range of accessible atomic numbers A , we seek to efficiently use the largest and fastest available supercomputers.

To achieve this goal within a constantly evolving leadership-class supercomputing environment (see the following section) requires collaborations of physicists, computer scientists and applied mathematicians. Such collaborations have resulted in a string of successes in the areas of eigensolver algorithms, memory management and communications [15–30].

In order to characterize the level of effort required to achieve a target level of uncertainty, we can take the example of the NCSM/NCFC application to light nuclei within a HO basis where we employ a many-body cutoff parameter N_{\max} . N_{\max} is defined as the maximum number of HO quanta (summed over the single-particle states in each basis state) allowed above the minimum needed to satisfy the Pauli principle. The basis is also constrained by total parity and total angular momentum projection M . The latter constraint is available since we work in an M -scheme basis rather than in a basis of good total angular momentum J . With a given choice of M , all states of good $J \geq |M|$ are accessible in the same calculation and we evaluate J in a post-analysis using the produced eigenfunctions. Once N_{\max} and the other constraints are determined, the matrix dimension is known. The left panel of Fig. 2 shows a semi-log plot of the rapid rise of matrix dimension with N_{\max} at $M = 0$ for natural parity states in a selection of nuclei. In order to obtain convergence for bound states with realistic interactions (those that accurately describe NN scattering) and achieve a reasonable uncertainty, we find it highly desirable to have results at $N_{\max} = 10$ or above as indicated by the vertical line in the left panel of Fig. 2.

The right panel of Fig. 2 illustrates a useful measure of the computational effort — the number of non-zero (NNZ) many-body matrix elements as a function of the matrix dimension. Here we adopt the same cases shown in the left panel and present the NNZs for both NN -only calculations and calculations with $3N$ interactions. Note that the NNZs rise with nearly linear trajectories on this log-log plot and they are tightly bunched so as to suggest a reasonable independence of A for each trajectory. Since the computational effort (consisting of both the time to evaluate and store the many-body Hamiltonian, and the amount of memory needed) is based primarily on the NNZs, we can estimate the computational resources needed once the matrix dimension is known (as in the left panel of Fig. 2) and the interaction is specified. This process is illustrated by the arrows reaching from the left panel to the right panel of Fig. 2 for the case of ^{12}C at $N_{\max} = 10$ for either a pure NN or a $3N$ interaction. With the NNZs fixed, we know whether a given calculation fits within the memory of the chosen leadership-class supercomputer as indicated by the labels on the two arrows. With the requirement to store the many-body Hamiltonian in core and to use it for the diagonalization process on Titan or Mira, we determine that we can solve for the low-lying spectra of ^{12}C at $N_{\max} = 10$ with an NN -only interaction but not

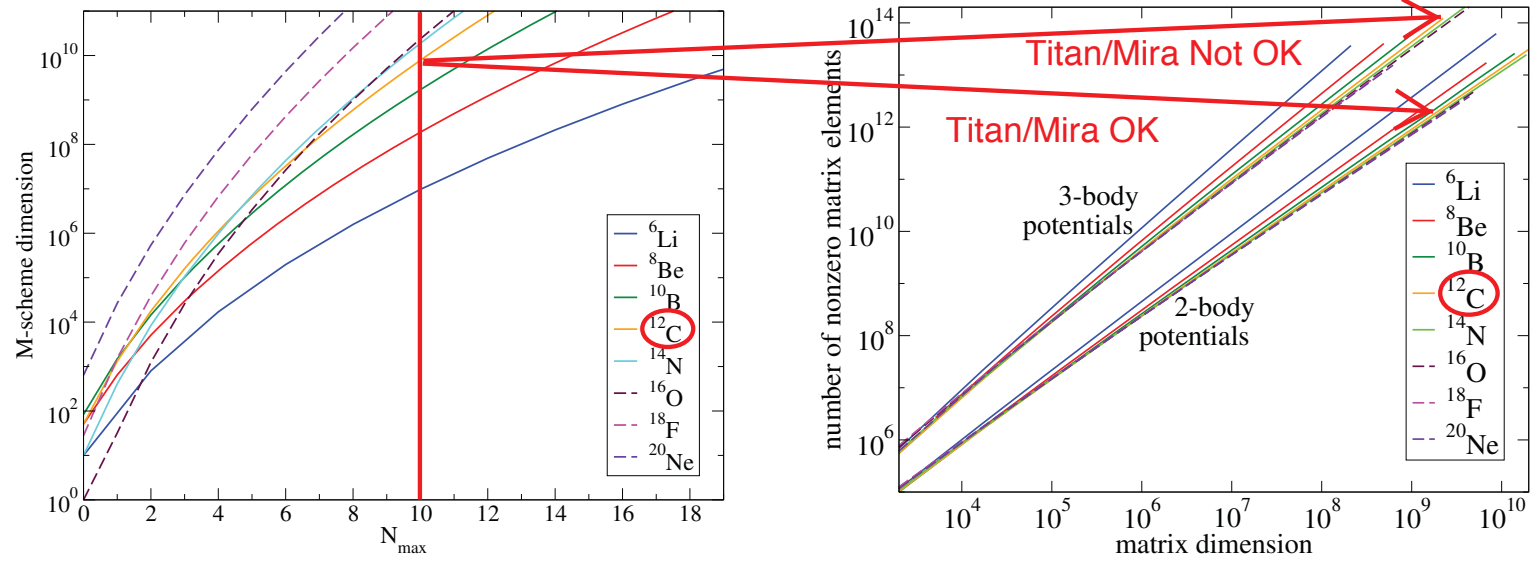


Figure 2: Left panel presents the Hamiltonian matrix dimension for a basis with total angular momentum projection $M = 0$ as a function of N_{\max} for a selection of even- A nuclei. Right panel displays the number of non-zero matrix elements as a function of $M = 0$ matrix dimension for the same cases as the left panel with either NN -only (“2-body potentials”) or $3N$ interactions (“3-body potentials”). The arrows stretching from the left panel to the right panel indicate the supercomputers on which that case will not fit (“Not OK”) or will fit (“OK”) within available memory. Mira is located at Argonne National Laboratory and Titan is located at Oak Ridge National Laboratory.

with $3N$ interactions. A simple functional form relating the matrix dimension D to the NNZs for 2-body interactions is [16]

$$\text{NNZ} = D + D^{1 + \frac{12}{14 + \ln D}}. \quad (1)$$

It should be noted that these NCSM/NCFC successes in low-energy nuclear physics have applications in other areas of strong-interaction physics. For example, Hamiltonian methods are gaining popularity in non-perturbative solutions of quantum field theory [31–41] motivated, in part, by the advances being made by our teams in solving the *ab initio* NCSM/NCFC. Recent applications, in what is called the Basis Light-Front Quantization (BLFQ) approach [31–33], include non-perturbative solutions of positronium at strong coupling [38, 42–46] and solutions for the mass spectra, decay constants, form factors and vector meson production rates for heavy quarkonia [47–54]. Remarkably, results for QED in the BLFQ approach have been achieved with Hamiltonian matrix dimensions exceeding 18 billion basis states [40, 41].

In addition to the use of relativistic Hamiltonian methods for static properties of strongly-interacting systems, time-dependent scattering with strong fields in quantum field theory has been introduced and successfully applied using the interaction picture. This is referred to as the time-dependent BLFQ (tBLFQ) approach [55–58]. In the tBLFQ approach, one first solves the relevant bound state problems in BLFQ and then evolves the system in light-front time with the possible addition of strong time-dependent external fields. This quantum time evolution approach leads to the total scattering amplitude from which projections to specific final channels can be performed and relativistic observables evaluated. Analogous development and applications of a time-dependent NCSM approach to non-relativistic strong interaction problems is underway [59] adapting techniques from tBLFQ.

Following the next two sections devoted to a perspective on supercomputer resources (Section 4) and algorithm improvements (Section 5), we present a selection of recent results and outline challenges that lie ahead. Our aim with this limited choice of applications is to complement other presentations at this meeting that cover closely-related topics. We note especially the papers at this meeting related to the NCSM/NCFC, new Hamiltonians and NCSM extensions to scattering theory by Shirokov, by Skibinski [60], by Zhao [59], by A. Mazur [61], by I. Mazur [62], and by Kulikov. We therefore focus here on the following recent results: (1) nuclear binding energies, excitation energies and magnetic moments of light nuclei with a realistic NN interaction; (2) construction of effective electroweak interactions for nuclear moments and transitions; and (3) outline of an approach for calculating $A = 48$ nuclei for evaluating nuclear double beta-decay matrix elements both with and without neutrinos.

4 Leadership-class supercomputers

The list of the world’s top 500 supercomputers is updated every six months [63] where one observes that China’s TaihuLight has topped the list for the past few cycles. TaihuLight has more than 10 million cores and is rated at 93 PetaFlops or nearly 10^{17} floating point operations per second. In the United States, we currently refer to leadership-class supercomputers as those rated at about one-tenth of the TaihuLight rating. For the United States, this includes facilities available for general scientific computing such as Titan at Oak Ridge National Laboratory (rated number 4 with 17.6 PetaFlops), Cori at Lawrence Berkeley National Laboratory/NERSC

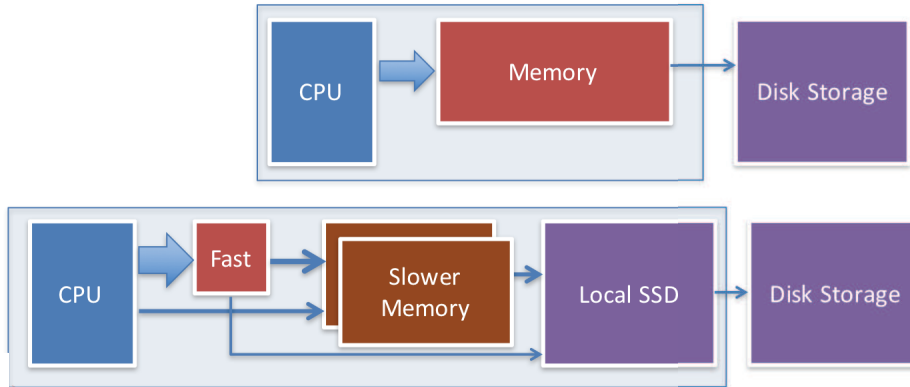


Figure 3: Sketch of the change in computer architecture providing new levels of challenges for algorithms and software. The traditional single-level of random-access memory (RAM) is replaced by a memory hierarchy that, to be used efficiently, requires careful analysis of data locality and usage intensity.

(rated number 6 with 14 PetaFlops) and Mira at Argonne National Laboratory (rated number 9 with 8.6 PetaFlops). Researchers using other leadership-class supercomputers are also attending this meeting and will likely credit their own facilities while the results that we present have most frequently been produced on these three above-mentioned US facilities by our group at Iowa State University and by our collaborators.

Here, we would also like to mention that each facility has a different architecture and that each architecture requires extensive efforts by physicists, applied mathematicians and computer scientists to enable forefront research with efficient algorithms and finely-tuned parallel computing codes. For these purposes, we have benefitted greatly from more than ten years of support from the US Department of Energy’s SciDAC program [64] that supports the collaborative research on the *ab initio* NCSM/NCFC algorithms and codes keeping them competitive over cycles in disruptive architecture changes. As an illustration of some of the newer architectures, Fig. 3 sketches the move into hierarchical memories. Multiple communication topologies within nodes and among nodes further increase the complexities.

While today’s leadership-class supercomputers are certainly impressive technological achievements empowering forefront discoveries, there is a race to design, fund and build even larger machines to reach the Exascale capability level of 10^{18} floating point operations per second, more than an order of magnitude increase over the current top supercomputer, TaihuLight, in China. Policies have been announced to achieve this goal within 5 years. Past experience supports the belief that the technology will be further disruptive and will require major efforts by the same teams at work today in order to achieve forefront physics results with algorithms and codes that run efficiently at Exascale. Those efforts have to begin years before the machine comes into operation in order to fully capitalize on the major investments to design, build and operate it. Fortunately, the US Department of Energy is continuing its support through SciDAC and we can remain optimistic that theoretical nuclear physics will benefit greatly from the Exascale machine when it is delivered. In the interim, leadership-class supercomputers with capabilities in the hundreds of PetaFlops are

under construction now and will become available in 2018–19 to provide an intermediate step from the current machines to the Exascale machines and we plan to fully utilize these new facilities for *ab initio* nuclear structure and nuclear reactions.

5 Algorithmic improvements for the NCSM/NCFC

Efficient methods to construct and diagonalize the sparse nuclear Hamiltonian of the *ab initio* NCSM on leadership-class supercomputers have been implemented in the software package MFDn (Many Fermion Dynamics for nuclear structure) [19, 21, 28]. MFDn uses the Lanczos algorithm [65, 66] to compute the desired eigenvalues and eigenvectors. Using the eigenvectors, MFDn then produces additional experimental observables such as electromagnetic and weak interaction transition rates. There is flexibility to use only NN interactions or NN plus $3N$ interactions as an input.

Over the last several years, we have developed a number of techniques to improve the computational efficiency of MFDn including:

- an efficient scalable parallel scheme for constructing the Hamiltonian matrix [15],
- efficient data distribution schemes that take into account the topology of the interconnect [20],
- techniques to overlap communication with computation in a hybrid MPI/OpenMP programming model [23, 24],
- an efficient scheme to multiply the sparse matrix Hamiltonian with a number of vectors [29],
- introduction of an accelerated eigensolver that employs a preconditioned block iterative method [30].

As the number of cores has been increasing dramatically during the past decade, one faces an increasing challenge to minimize the time spent on inter-processor communications. Among our accomplishments, we developed distribution schemes for the computations that reduce communication times as illustrated in the left panel of Fig. 4 where we sketch the distribution of unique partitions of the symmetric matrix among processors P_{ij} . This distribution achieves a balance of the MPI reduce (and subsequent broadcast) operations for rows and columns of processors that perform the matrix–vector multiplies for both the Hamiltonian matrix and its transpose.

The most recent development [30] introduces a new eigensolver into MFDn, the Locally Optimal Block Preconditioned Conjugate Gradient (LOBPCG) algorithm [67]. The use of a block iterative method allows us to improve the memory access pattern of the computation and make use of approximations to several eigenvectors at the same time. To make this algorithm efficient, as shown in the right panel of Fig. 4, we identified an effective preconditioner coupled with techniques to generate good initial guesses that significantly accelerate the convergence of the LOBPCG algorithm on large-scale distributed-memory clusters.

Further efforts are underway to speed up communications among nodes and to develop a post processor for efficiently evaluating transitions between nuclear systems.

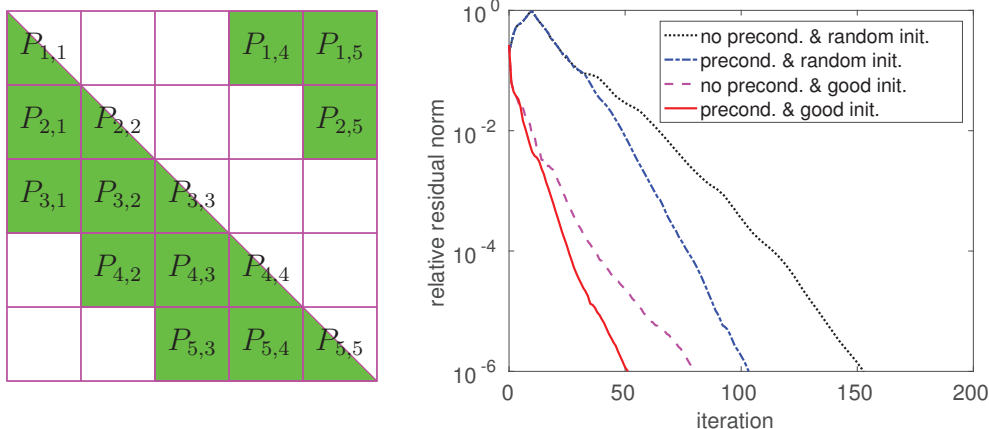


Figure 4: Left panel displays the assignment of matrix elements of a symmetric matrix (green shaded regions) among MPI ranks (squares) that achieves a balance in communications during the Lanczos process. Right panel shows improved convergence rates of the LOBPCG algorithm achieved by preconditioning and by good initialization [30].

The latter is needed for planned calculations of the nuclear matrix elements for double-beta decay, both with and without neutrinos. Additional efforts are underway to develop scripts for a broad set of standard applications that facilitate conversion from one architecture to another.

6 Results for light nuclei with JISP16

In this section, we briefly review selected results for light nuclei using the realistic JISP16 NN interaction [68, 69] within the NCFC approach [10, 11, 13, 14]. Fig. 5 presents ground state energies for 24 light nuclei in the left panel. While JISP16 was tuned with phase-equivalent transformations to the properties of nuclei up to $A = 7$, it was only approximately tuned to the ground state energy of ^{16}O . It is therefore not surprising that JISP16 overbinds nuclei at the upper end of the p -shell beginning with $A = 10$. We note that the recently-developed Daejeon16 NN interaction succeeds in improving the agreement between theory and experiment for the ground state energies of the p -shell nuclei as well as other properties of light nuclei [70].

Applications of JISP16 to the Lithium isotopes and the Beryllium isotopes already have an extensive track record due both to experimental interests and to NCFC advances that provide results with increasing precision over time. An earlier detailed investigation of the Lithium isotopes with JISP16 [71] provides NCFC results that serve as a baseline for recent extensive investigations of ^6Li [72] as well as ^7Li and ^7Be [73]. Among other improvements, these recent works achieve spectral and electroweak properties in larger model spaces than previously feasible. That is, they provide results closer to convergence which, upon extrapolation, provide NCFC observables with diminished uncertainties.

We accumulate a sample of the results for the ^6Li extrapolated ground state (g.s.) energy with the JISP16 interaction in Table 1. Results from both the NCFC and

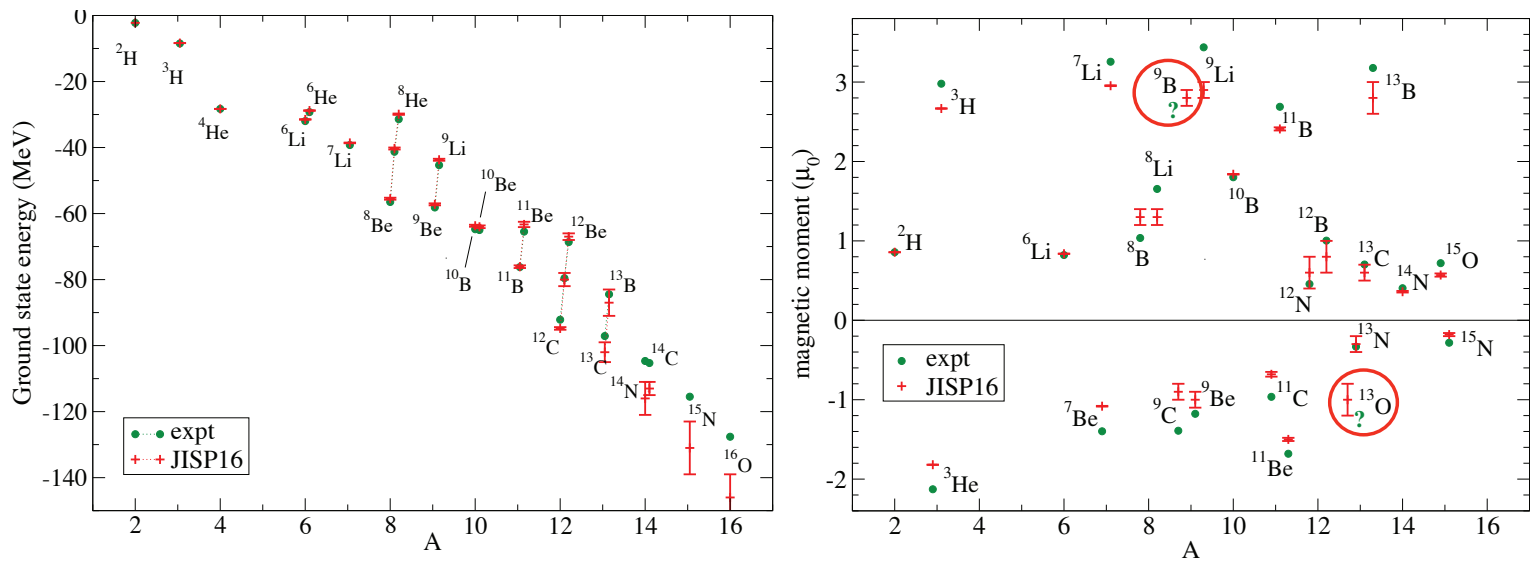


Figure 5: NCFC results for the ground states of light nuclei obtained with the JISP16 interaction (red points) compared with experiment (green points) where available [13]. Uncertainties in NCFC extrapolations are indicated by the red error bars. Left panel displays ground state energies while the right panel shows magnetic moments. Note that two cases are circled to indicate that they represent predictions awaiting experimental results for comparison.

Table 1: Dependence on the many-body method, on the extrapolation method, and on the model space cutoff of the theoretical g. s. energy (in MeV) of ${}^6\text{Li}$ with JISP16. The results are arranged vertically in chronological order from earliest to most recent. The N_{max} cutoff of the NCFC method and the K_{max} of the Hyperspherical Harmonics (HH) method are not directly related except that both should be taken to infinity to obtain the exact result. For comparison, the experimental ${}^6\text{Li}$ g.s. energy is -31.995 MeV and the NCFC result with Daejeon16 using results up through $N_{\text{max}} = 14$ is $-31.98(2)$ MeV [70]. For completeness, we note that Ref. [72] quotes an extrapolated RMS charge radius of $2.28(3)$ fm for ${}^6\text{Li}$ which is to be compared with the experimental result of $2.38(3)$ fm.

NCFC	N_{max}	Ref.	HH	K_{max}	Ref.
$-31.00(31)$	12	[69]	$-31.46(5)$	14	[74]
$-31.47(9)$	16	[10]	$-31.67(3)$	12	[75]
$-31.49(3)$	16	[71]			
$-31.49(6)$	16	[13]			
$-31.42(5)$	16	[14]			
$-31.46(3)$	14	[72]			
$-31.51(3)$	16	[72]			
$-31.53(2)$	18	[72]			

the Hyperspherical Harmonics (HH) method are included with the reference for each result quoted. In general, there is a consistency among these results with the possible exception of the earliest NCFC result extrapolating from the smallest basis space. Another exception may be the HH result of Ref. [75] that extrapolated results obtained with the OLS renormalization (second entry in the HH column). It is interesting to note that the NCFC results have tended to drift towards increased binding and towards the experimental result as results from larger basis spaces have become available over time. The difference between the experimental and theoretical g. s. energy is now at $470(20)$ keV. It is also interesting to note that the extrapolated root-mean-square (RMS) radius is tending in the direction of the experimental result (from below) as the use of larger basis spaces become available [72].

In the right panel of Fig. 5, we present a comparison between theory and experiment for 23 magnetic moments of states in light nuclei, where such a comparison is feasible. In two cases, we present predictions for comparison with possible future experiments. We evaluate these magnetic moments using only the bare operator. Overall, the agreement is good considering the level of the approximation for the magnetic dipole operator. In the future, we plan to incorporate 2-body current corrections. We anticipate that these corrections will be of the order of a few percent and will further improve the agreement between theory and experiment. We base these estimations on the results presented in Ref. [76] where similar differences between theory and experiment are obtained before 2-body currents are introduced. Those 2-body currents are found to further improve the agreement between theory and experiment.

In the previous conference in this series, we reviewed [28] NCFC results for the Beryllium isotopes with JISP16 where emergent collective motion is evident in the spectra, magnetic dipole moments, $M1$ transitions, quadrupole moments and $E2$ transitions. Recent efforts further support and extend the claims of emergent collec-

tive rotational behavior in the Beryllium isotopes [77–79]. Multiple rotational bands have been identified in the NCFC calculations for both natural and unnatural parity. It is interesting to note that some of the bands are not observed to terminate at the angular momentum naively expected from nucleons populating the p -shell orbits. Analysis of extrapolations of the NCFC results provides rotational model parameters in good agreement with the corresponding parameters extracted from the experimental data [77–79].

Emergent collective motion also provides inspiration for optimized basis spaces, basis spaces that offer the promise of accelerating convergence [80–82]. With JISP16 we have investigated truncation schemes based on $SU(3)$ symmetry in p -shell nuclei. We have found that basis space dimensions can indeed be reduced while incurring additional computational cost for evaluating the many-body matrix elements in the $SU(3)$ basis. Developments are ongoing so it will be some time before we know definitively the net gains achievable with selected $SU(3)$ basis spaces. In the meantime, the more compact $SU(3)$ representation of eigenfunctions promotes our physical intuition and knowledge of the nuclear underlying symmetries predicted by the *ab initio* NCFC.

7 Effective electroweak interactions for the NCSM

We now turn attention to the effects that arise when consistent effective electroweak operators are included. By consistent, we mean that the electroweak operators are evaluated in the same formalism as the strong interactions employed in the Hamiltonian. In the case of interactions from chiral EFT, this implies that the electroweak operators are also evaluated in chiral EFT to the same chiral order as the strong interaction.

Here we will provide demonstration cases using only the two-nucleon system for the present purposes. Specifically, we study the simple case of the g. s. of the deuteron solved as a matrix eigenvalue problem in the HO basis as a function of the N_{\max} truncation. Using the LENPIC NN interaction at chiral N2LO with the regulator fixed at 1.0 fm [5], we present the deuteron g. s. energy in the upper-left quadrant of Fig. 6 as a function of N_{\max} at $\hbar\Omega = 20$ MeV. As expected the g. s. energy converges uniformly from above with increasing N_{\max} . In the same panel we show the g. s. energy results in the N_{\max} -truncated spaces following renormalization with the Okubo–Lee–Suzuki (OLS) method [12, 83–85]. The OLS procedure produces the exact ground state energy to within numerical precision for every truncated model space. This confirms the method is working as it should and we have numerical stability in our procedures.

Next, we apply the derived OLS transformation to additional deuteron ground state observables and display the results in the remaining three panels of Fig. 6. In each case, we employ only the bare operator in the present demonstration in order to gauge the size of the effects of truncation without OLS renormalization. For r_{RMS} a very small basis space results in about a 30% reduction which slowly falls to about 1% at about $N_{\max} = 40$. We stress that these results, as well as those for the other observables, are dependent on the chosen value of $\hbar\Omega$ which we have taken arbitrarily to be 20 MeV in the present demonstration.

The quadrupole moment appears to fluctuate in the truncated model spaces which can be attributed to a sensitivity to having an odd versus an even number of $L = 2$

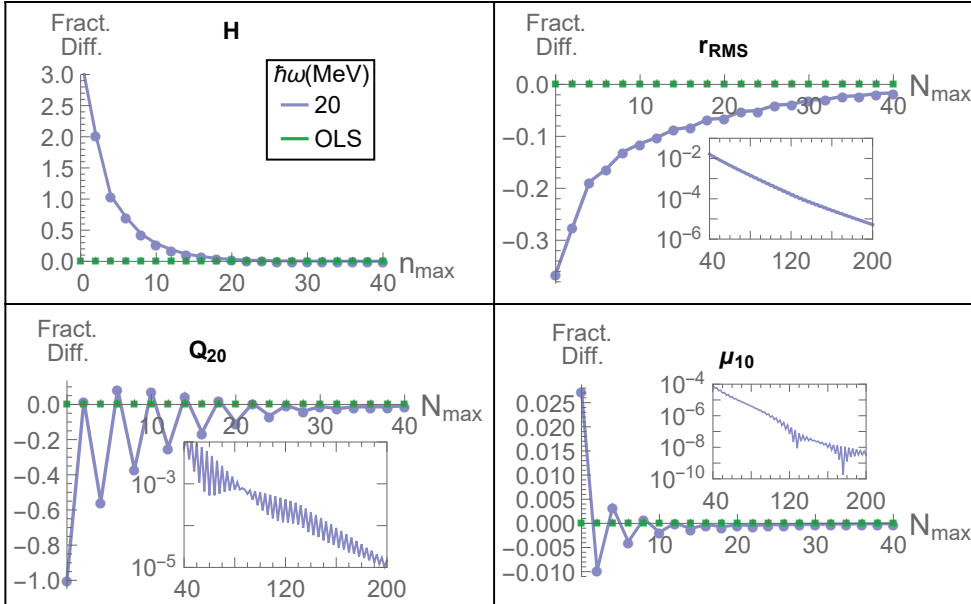


Figure 6: Comparisons of bare operators (solid dots) and OLS-renormalized operators (green squares) for the g.s. of the deuteron obtained with the LENPIC chiral N2LO interaction [4] as a function of N_{\max} in a HO basis with $\hbar\Omega = 20$ MeV. These basis parameters define the model space in which the calculation is performed. The observables include the g.s. energy (upper left panel), RMS radius r_{RMS} (upper right panel), quadrupole moment Q_{20} (lower left panel) and magnetic moment μ_{10} (lower right panel). All results are plotted as a fractional difference “Fract. Diff.” defined as $(model - exact)/exact$. We take the results at $N_{\max} = 400$ as the exact results since they are converged to at least 8 significant digits. The insets present the magnitude of the fractional difference on a log scale for an extended range of N_{\max} .

orbitals in the basis space. An even number of $L = 2$ orbitals produce a larger Q_{20} result with the bare operator in the truncated basis. This signals that the mixing generated by the g.s. eigenvector in the truncated basis has favorable phases for contributions to Q_{20} with an even number of $L = 2$ orbitals.

On the other hand, the magnetic dipole operator shown in Fig. 6 reflects minimal renormalization effects. Note that the scale for these results is only a couple of percent in the smallest model spaces. This is consistent with a number of many-body applications that, with increasing model spaces, show the magnetic moments are well converged in contrast to other long-range observables such as the r_{RMS} , Q_{20} and $B(E2)$ operators.

For each observable in Fig. 6, the size of the effects in smaller model spaces may, at first, appear large compared with the systematic study conducted in Ref. [86] showing long-range operators receive only minor renormalization effects from the OLS procedure. However, it is important to note that our test two-nucleon problem is special in that we can treat the OLS renormalization exactly for all observables in all model spaces. This contrasts the cases studied in Ref. [86] where the OLS renormalization was performed at the two-nucleon level but then applied in many-nucleon systems so

that the induced many-nucleon correlation contributions to the effective electroweak operators were neglected. Thus, as was emphasized in Ref. [86], one must be cautious when drawing conclusions from many-body applications using OLS renormalization limited to the two-nucleon level.

8 $A = 48$ in the NCSM with a core approach

There is considerable interest in pushing *ab initio* nuclear structure and nuclear reaction methods to heavier nuclei and a number of approaches are under development. For the NCSM, the path forward has been defined in a series of efforts [87, 88]. Schematically, the approach adopts the NCSM for a chosen core such as ^{16}O or ^{40}Ca in as large a basis as feasible and uses the OLS renormalization for that basis. An alternative would be to use the Similarity Renormalization Group (SRG) method [89–92] for the NCSM treatment of the adopted A_c nucleon “core” system. In like manner, one solves the $A_c + 1$ nucleon and $A_c + 2$ nucleon systems to obtain the eigenvalues and eigenfunctions. With the resulting eigenvalues and eigenfunctions, one then performs another OLS treatment for the $N_{\text{max}} = 0$ space or valence space with 2 nucleons beyond the core to derive an effective 2-valence nucleon interaction. This valence-only interaction is guaranteed to generate the same results in the $N_{\text{max}} = 0$ space as the original NCSM calculation for the $A_c + 2$ nucleon system as demonstrated in Refs. [87, 88]. This logic is straightforwardly extended to derive a 3-valence nucleon effective interaction or even 4-valence nucleon effective interaction. This process is illustrated schematically in Fig. 7.

For an application in the *pf*-shell, such as the $A = 48$ nuclei, we envision solving for ^{40}Ca (the core), ^{41}Ca (core + 1) and ^{42}Ca (core + 2) systems in the NCSM with $N_{\text{max}} = 4$. Later, we would include the ^{43}Ca (core + 3) system to obtain a valence 3-neutron effective interaction. Once the second OLS transformation is performed we would have the valence single-particle-energies and valence effective two-body interactions suitable for a standard shell model calculation of ^{48}Ca . Next, we would seek to confirm that this provides a reasonable description of the properties of ^{48}Ca . Following that, we would proceed with additional calculations needed to evaluate the double beta-decays of ^{48}Ca , both with neutrinos and without neutrinos. Such studies will be valuable for benchmarking other nuclear structure approaches that are currently in use for evaluating nuclear matrix elements for double-beta decays in heavier nuclei.

Let us examine a few more of the specifics of the double OLS approach to the $A = 48$ nuclei with a particular selection of ingredients. Let us select an $NN + NNN$ interaction case for the NCSM treatment of ^{40}Ca and the $A = 41$ and $A = 42$ nuclei in the $N_{\text{max}} = 4$ space with OLS renormalization. The largest matrix encountered is that of ^{42}Sc with M -scheme dimension 1, 211, 160, 184 and 54×10^{12} nonzero many-body matrix elements. We would need to converge a minimum of 60 eigenvalues and eigenvectors to perform the second OLS transformation needed for the 195 valence NN interaction matrix elements with good J, T . The reason for the minimum of 60 is that we should obtain those eigenvalues whose eigenvectors have significant overlap with the *pf*-space and have the requisite number for each J, T combination. These calculations seem likely to be feasible with current technologies.

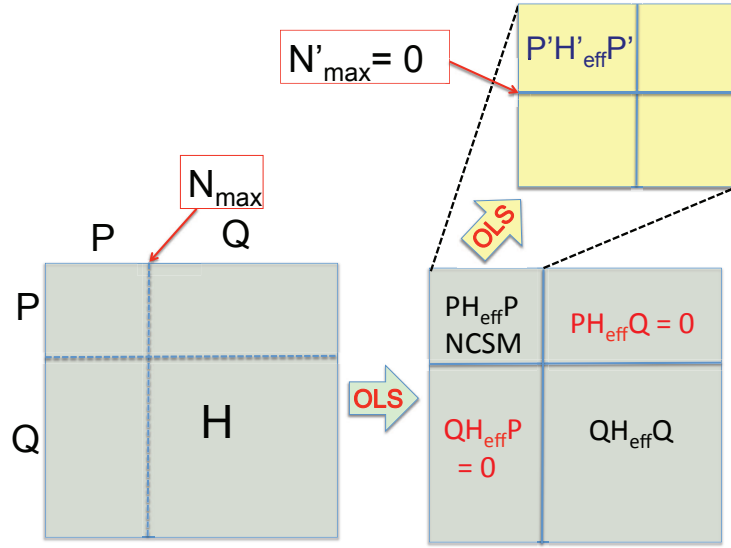


Figure 7: Schematic of the “double OLS” procedure that first takes results from a NCSM calculation for a core system, using an OLS procedure for a model space defined by N_{\max} , as input to generate an effective interaction among valence nucleons in the $N'_{\max} = 0$ model space as described in Refs. [87,88]. That is, the OLS procedure is first applied to derive a NCSM effective interaction for the full A -nucleon system resulting in the “primary” effective Hamiltonian $PH_{\text{eff}}P$ for the chosen no-core basis space (the “ P -space”) indicated on the large square on the right of the figure in its upper left corner. The OLS procedure is applied again by using the NCSM results to derive the “secondary” effective Hamiltonian $P'H'_{\text{eff}}P'$ for the valence space (the P' -space with the smaller many-body cutoff N'_{\max}) indicated on the square in the upper right of the figure.

9 Future prospects

Most of our applications have focused on light nuclei with atomic number $A \leq 16$ where our theoretical many-body methods have achieved successes with leadership-class facilities. However, the frontiers of our field include applications to heavier nuclei and utilizing new and improved interactions from chiral EFT. At the same time, we aim to evaluate observables with increasing sophistication using their operators also derived within chiral effective field theory. We sketched a near-term project for the $A = 48$ nuclei. Our approach, which aims to make contact with experimental and other theoretical efforts in double-beta decay, is but one exciting example of frontier research with *ab initio* nuclear theory. Others are also addressed at this same meeting.

We continue to face the dual challenge of advancing the underlying theoretical physics at the same time as advancing the algorithms to keep pace with the growth in the size and complexity of leadership-class computers. Recent history of these efforts, with the substantial support of the funding agencies, indicates we are experiencing a “Double Moore’s Law” rate of improvement — i. e. the Moore’s Law for hardware improvements and a simultaneous Moore’s Law improvement in the algorithms/software. We value this continued support of the funding agencies which has

been and continues to be critical for our multi-disciplinary collaborations as well as their support of the growth in leadership-class facilities. This continued support will allow us to achieve the full discovery potential of computational fundamental physics.

Acknowledgments

This work was supported in part by the US Department of Energy (DOE) under Grant Nos. DE-FG02-87ER40371, DESC0008485 (SciDAC-3/NUCLEI), DE-SC0018223 (SciDAC-4/NUCLEI) and DE-SC0015376 (DOE Topical Collaboration in Nuclear Theory for Double-Beta Decay and Fundamental Symmetries). A portion of the computational resources were provided by the National Energy Research Scientific Computing Center (NERSC), which is supported by the US DOE Office of Science, and by an INCITE award, “Nuclear Structure and Nuclear Reactions”, from the US DOE Office of Advanced Scientific Computing. This research also used resources of the Argonne Leadership Computing Facility, which is a DOE Office of Science User Facility supported under Contract DE-AC02-06CH11357.

References

- [1] E. Epelbaum, H.-W. Hammer and U.-G. Meißner, *Rev. Mod. Phys.* **81**, 1773 (2009).
- [2] R. Machleidt and D. R. Entem, *Phys. Rep.* **503**, 1 (2011).
- [3] P. Maris *et al.*, *EPJ Web Conf.* **113**, 04015 (2016).
- [4] S. Binder *et al.* (LENPIC Collaboration), *Phys. Rev. C* **93**, 044002 (2016).
- [5] Low energy nuclear physics international collaboration (LENPIC), <http://www.lenpic.org>.
- [6] E. Epelbaum, H. Krebs and U. G. Meißner, *Phys. Rev. Lett.* **115**, 122301 (2015), arXiv:1412.4623 [nucl-th] (2014).
- [7] P. Navrátil, J. P. Vary and B. R. Barrett, *Phys. Rev. Lett.* **84**, 5728 (2000).
- [8] P. Navrátil, J. P. Vary and B. R. Barrett, *Phys. Rev. C* **62**, 054311 (2000).
- [9] P. Navrátil, V. G. Gueorguiev, J. P. Vary, W. E. Ormand and A. Nogga, *Phys. Rev. Lett.* **99**, 042501 (2007).
- [10] P. Maris, J. P. Vary and A. M. Shirokov, *Phys. Rev. C* **79**, 014308 (2009).
- [11] P. Maris, A. M. Shirokov and J. P. Vary, *Phys. Rev. C* **81**, 021301 (2010).
- [12] B. R. Barrett, P. Navrátil and J. P. Vary, *Prog. Part. Nucl. Phys.* **69**, 131 (2013) *and references therein*.
- [13] P. Maris and J. P. Vary, *Int. J. Mod. Phys. E* **22**, 1330016 (2013).
- [14] A. M. Shirokov, V. A. Kulikov, P. Maris and J. P. Vary, in *NN and 3N interactions*, eds. L. D. Blokhintsev and I. I. Strakovsky. Nova Science, Hauppauge, NY, 2014, Chap. 8, p. 231, http://www.novapublishers.com/catalog/product_info.php?products_id=50945.

-
- [15] P. Sternberg, E. G. Ng, C. Yang, P. Maris, J. P. Vary, M. Sosonkina and H. V. Le, in *Proc. 2008 ACM/IEEE Conf. on Supercomputing, Austin, November 15–21, 2008*. IEEE Press, Piscataway, NJ, 2008, p. 15:1, <http://doi.acm.org/10.1145/1413370.1413386>.
- [16] J. P. Vary, P. Maris, E. Ng, C. Yang and M. Sosonkina, *J. Phys. Conf. Ser.* **180**, 012083 (2009), arXiv:0907.0209 [nucl-th] (2009).
- [17] P. Maris, M. Sosonkina, J. P. Vary, E. G. Ng and C. Yang, *Proc. Comput. Sci.* **1**, 97 (2010).
- [18] H. M. Aktulga, C. Yang, E. G. Ng, P. Maris and J. P. Vary, in *Proc. 2011 Int. Conf. on High Performance Computing and Simulation (HPCS 2011), July 4–July 8, 2011, Istanbul, Turkey*. IEEE Press, 2011, p. 176.
- [19] P. Maris, H. M. Aktulga, M. A. Caprio, Ü. Çatalyürek, E. G. Ng, D. Oryspayev, H. Potter, E. Saule, M. Sosonkina, J. P. Vary, C. Yang and Z. Zhou, *J. Phys. Conf. Ser.* **403**, 012019 (2012).
- [20] H. M. Aktulga, C. Yang, E. N. Ng, P. Maris and J. P. Vary, in *Euro-Par*, eds. C. Kaklamanis, T. S. Papatheodorou and P. G. Spirakis. *Lecture Notes Comp. Sci.* **7484**, 830 (2012).
- [21] P. Maris, H. M. Aktulga, S. Binder, A. Calci, Ü. V. Çatalyürek, J. Langhammer, E. Ng, E. Saule, R. Roth, J. P. Vary and C. Yang, *J. Phys. Conf. Ser.* **454**, 012063 (2013).
- [22] D. Oryspayev, H. Potter, P. Maris, M. Sosonkina, J. P. Vary, S. Binder, A. Calci, J. Langhammer and R. Roth, in *Proc. IEEE 27th Int. Parallel and Distrib. Processing Symp. Workshops & PhD Forum, Boston, MA, USA, 20–24 May, 2013*. 2013, p. 1365, DOI:10.1109/IPDPSW.2013.253.
- [23] H. M. Aktulga, C. Yang, E. N. Ng, P. Maris and J. P. Vary, *Concurrency Computat.: Pract. Exper.* **26**, 2631 (2014).
- [24] D. Oryspayev, H. M. Aktulga, M. Sosonkina, P. Maris and J. P. Vary, *Concurrency Computat.: Pract. Exper.*, **27**, 5019 (2015).
- [25] H. Potter, D. Oryspayev, P. Maris, M. Sosonkina, J. Vary, S. Binder, A. Calci, J. Langhammer, R. Roth, Ü. Çatalyürek and E. Saule, in *Proc. Int. Conf. Nucl. Theor. Supercomputing Era (NTSE-2013), Ames, IA, USA, May 13–17, 2013*, eds. A. M. Shirokov and A. I. Mazur. Pacific National University, Khabarovsk, 2014, p. 263, <http://ntse-2013.khb.ru/Proc/Sosonkina.pdf>.
- [26] H. D. Potter, S. Fischer, P. Maris, J. P. Vary, S. Binder, A. Calci, J. Langhammer and R. Roth, *Phys. Lett. B* **739**, 445 (2014).
- [27] C. Yang, H. M. Aktulga, P. Maris, E. Ng and J. Vary, in *Proc. Int. Conf. Nucl. Theor. Supercomputing Era (NTSE-2013), Ames, IA, USA, May 13–17, 2013*, eds. A. M. Shirokov and A. I. Mazur. Pacific National University, Khabarovsk, 2014, p. 272, <http://ntse-2013.khb.ru/Proc/Yang.pdf>.

- [28] J. P. Vary, P. Maris, H. Potter, M. A. Caprio, R. Smith, S. Binder, A. Calci, S. Fischer, J. Langhammer, R. Roth, H. M. Aktulga, E. Ng, C. Yang, D. Oryspayev, M. Sosonkina, E. Saule and Ü. Çatalyürek, in *Proc. Int. Conf. Nucl. Theor. Supercomputing Era (NTSE-2014), Khabarovsk, Russia, June 23–27, 2014*, eds. A. M. Shirokov and A. I. Mazur. Pacific National University, Khabarovsk, 2016, p. 154, <http://www.ntse-2014.khb.ru/Proc/Vary.pdf>.
- [29] H. M. Aktulga, Md. Afibuzzaman, S. Williams, A. Buluc, M. Shao, C. Yang, E. G. Ng, P. Maris and J. P. Vary, *IEEE Trans. Parall. Distrib. Syst.* **28**, 1550 (2016).
- [30] M. Shao, H. M. Aktulga, C. Yang, E. G. Ng, P. Maris and J. P. Vary, arXiv:1609.01689 [cs.NA] (2016), *accepted for publications in Comp. Phys. Comm.*, <https://doi.org/10.1016/j.cpc.2017.09.004>.
- [31] J. P. Vary, H. Honkanen, J. Li, P. Maris, S. J. Brodsky, P. Sternberg, E. G. Ng and C. Yang, *PoS LC2008*, 040 (2008), arXiv:0812.1819 [nucl-th] (2008).
- [32] J. P. Vary, P. Maris, A. M. Shirokov, H. Honkanen, J. Li, S. J. Brodsky, A. Harindranath and G. F. de Teramond, *AIP Conf. Proc.* **1182**, 917 (2009).
- [33] J. P. Vary, H. Honkanen, J. Li, P. Maris, S. J. Brodsky, A. Harindranath, G. F. de Teramond, P. Sternberg, E. G. Ng and C. Yang, *Phys. Rev. C* **81**, 035205 (2010), arXiv:0905.1411 [nucl-th] (2009).
- [34] J. P. Vary, H. Honkanen, J. Li, P. Maris, S. J. Brodsky, A. Harindranath, G. F. de Teramond, P. Sternberg, E. G. Ng and C. Yang, *Nucl. Phys. B Proc. Suppl.* **199**, 64 (2010), arXiv:0911.2929 [nucl-th] (2009).
- [35] J. P. Vary *et al.*, *Pramana* **75**, 39 (2010).
- [36] H. Honkanen, P. Maris, J. P. Vary and S. J. Brodsky, *Phys. Rev. Lett.* **106**, 061603 (2011), arXiv:1008.0068 [hep-ph] (2010).
- [37] X. Zhao, H. Honkanen, P. Maris, J. P. Vary and S. J. Brodsky, *Few-Body Syst.* **52**, 339 (2012), arXiv:1110.0553 [hep-ph] (2011).
- [38] P. Maris, P. Wiecki, Y. Li, X. Zhao and J. P. Vary, *Acta Phys. Polon. Suppl.* **6**, 321 (2013).
- [39] J. P. Vary, X. Zhao, A. Ilderton, H. Honkanen, P. Maris and S. J. Brodsky, *Nucl. Phys. B Proc. Suppl.* **251-252**, 10 (2014), arXiv:1406.1838 [nucl-th] (2014).
- [40] X. Zhao, H. Honkanen, P. Maris, J. P. Vary and S. J. Brodsky, *Phys. Lett. B* **737**, 65 (2014), arXiv:1402.4195 [nucl-th] (2014).
- [41] D. Chakrabarti, X. Zhao, H. Honkanen, R. Manohar, P. Maris and J. P. Vary, *Phys. Rev. D* **89**, 116004 (2014), arXiv:1403.0704 [hep-ph] (2014).
- [42] Y. Li, P. W. Wiecki, X. Zhao, P. Maris and J. P. Vary, in *Proc. Int. Conf. Nucl. Theor. Supercomputing Era (NTSE-2013), Ames, IA, USA, May 13–17, 2013*, eds. A. M. Shirokov and A. I. Mazur. Pacific National University, Khabarovsk, 2014, p. 136, <http://ntse-2013.khb.ru/Proc/YLi.pdf>, arXiv:1311.2980 [nucl-th] (2013).

- [43] P. W. Wiecki, Y. Li, X. Zhao, P. Maris and J. P. Vary, in *Proc. Int. Conf. Nucl. Theor. Supercomputing Era (NTSE-2013), Ames, IA, USA, May 13–17, 2013*, eds. A. M. Shirokov and A. I. Mazur. Pacific National University, Khabarovsk, 2014, p. 146, <http://ntse-2013.khb.ru/Proc/Wiecki.pdf>, arXiv:1311.2908 [nucl-th] (2013).
- [44] P. Wiecki, Y. Li, X. Zhao, P. Maris and J. P. Vary, *Few-Body Syst.* **56**, 489 (2015), arXiv:1502.02993 [nucl-th] (2015).
- [45] P. Wiecki, Y. Li, X. Zhao, P. Maris and J. P. Vary, *Phys. Rev. D* **91**, 105009 (2015), arXiv:1404.6234 [nucl-th] (2014).
- [46] L. Adhikari, Y. Li, X. Zhao, P. Maris, J. P. Vary and A. Abd El-Hady, *Phys. Rev. C* **93**, 055202 (2016), arXiv:1602.06027 [nucl-th] (2016).
- [47] Y. Li, P. Maris, X. Zhao and J. P. Vary, *Phys. Lett. B* **758**, 118 (2016), arXiv:1509.07212 [hep-ph] (2015).
- [48] J. P. Vary, L. Adhikari, G. Chen, Y. Li, P. Maris and X. Zhao, *Few-Body Syst.* **57**, 695 (2016).
- [49] J. P. Vary, L. Adhikari, G. Chen, M. Li, Y. Li, P. Maris, W. Qian, J. R. Spence, S. Tang, K. Tuchin and X. Zhao, *Few-Body Syst.* **58**, 56 (2017), arXiv:1612.03963 [nucl-th] (2016).
- [50] G. Chen, Y. Li, P. Maris, K. Tuchin and J. P. Vary, *Phys. Letts. B* **769**, 477 (2017), arXiv:1610.04945 [nucl-th] (2016).
- [51] G. Chen, Y. Li, P. Maris, K. Tuchin and J. P. Vary, *Nucl. Part. Phys. Proc.* **289–290**, 409 (2017), arXiv:1701.02279 [nucl-th] (2017).
- [52] Y. Li, *Few-Body Syst.* **58**, 109 (2017), arXiv:1612.01259 [nucl-th] (2016).
- [53] Y. Li, P. Maris and J. P. Vary, *Phys. Rev. D* **96**, 016022 (2017), arXiv:1704.06968 [hep-ph] (2017).
- [54] S. Leitão, Y. Li, P. Maris, M. T. Peña, A. Stadler, J. P. Vary and E. P. Biernat, arXiv:1705.06178 [hep-ph] (2017).
- [55] X. Zhao, A. Ilderton, P. Maris and J. P. Vary, *Phys. Rev. D* **88**, 065014 (2013), arXiv:1303.3273 [nucl-th] (2013).
- [56] J. P. Vary, X. Zhao, A. Ilderton, H. Honkanen, P. Maris and S. J. Brodsky, *Acta Phys. Polon. Suppl.* **6**, 257 (2013).
- [57] X. Zhao, A. Ilderton, P. Maris and J. P. Vary, *Phys. Lett. B* **726**, 856 (2013), arXiv:1309.5338 [nucl-th] (2013).
- [58] G. Chen, X. Zhao, Y. Li, K. Tuchin and J. P. Vary, *Phys. Rev. D* **95**, 096012 (2017), arXiv:1702.06932 [nucl-th] (2017).
- [59] W. Du, P. Yin, G. Chen, X. Zhao and J. P. Vary, *see these Proceedings*, p. 102, <http://www.ntse-2016.khb.ru/Proc/Zhao.pdf>, arXiv 1704:05520 [nucl-th] (2017).

-
- [60] R. Skibiński, J. Golak, A. M. Shirokov, K. Topolnicki, Y. Volkotrub and H. Witała, *see these Proceedings*, p. 90, <http://www.ntse-2016.khb.ru/Proc/Skibinski.pdf>.
- [61] A. I. Mazur, A. M. Shirokov, I. A. Mazur, E. A. Mazur, Y. Kim, I. J. Shin, L. D. Blokhintsev and J. P. Vary *see these Proceedings*, p. 185, <http://www.ntse-2016.khb.ru/Proc/AMazur.pdf>.
- [62] I. A. Mazur, A. M. Shirokov, A. I. Mazur, I. J. Shin, Y. Kim and J. P. Vary, *see these Proceedings*, p. 280, <http://www.ntse-2016.khb.ru/Proc/IMazur.pdf>.
- [63] <https://www.top500.org/lists/2017/06/>.
- [64] <http://www.scidac.gov/>.
- [65] C. Lanczos, *J. Res. Nat'l Bur. Std.* **45**, 255(1950).
- [66] Y. Saad, *Numerical methods for large eigenvalue problems, 2nd ed.* SIAM, Philadelphia, 2011.
- [67] A. V. Knyazev, *SIAM J. Sci. Comput.* **23**(2), 517 (2001).
- [68] A. M. Shirokov, J. P. Vary, A. I. Mazur, S. A. Zaytsev and T. A. Weber, *Phys. Lett. B* **621**, 96 (2005).
- [69] A. M. Shirokov, J. P. Vary, A. I. Mazur and T. A. Weber, *Phys. Lett. B* **644**, 33 (2007); fortran subroutines to generate the JISP16 interaction in the HO basis are available at <http://nuclear.physics.iastate.edu>.
- [70] A. M. Shirokov, I. J. Shin, Y. Kim, M. Sosonkina, P. Maris and J. P. Vary, *Phys. Lett. B* **761**, 87 (2016), arXiv:1605.00413 [nucl-th] (2016); fortran subroutines to generate the Daejeon16 interaction in the HO basis are available at http://lib.dr.iastate.edu/energy_datasets/1/.
- [71] C. Cockrell, J. P. Vary and P. Maris, *Phys. Rev. C* **86**, 034325 (2012), arXiv:1201.0724 [nucl-th] (2012).
- [72] I. J. Shin, Y. Kim, P. Maris, J. P. Vary, C. Forssén, J. Rotureau and N. Michel, arXiv:1605.02819 [nucl-th] (2016).
- [73] T. Heng, J. P. Vary and P. Maris, *Phys. Rev. C* **95**, 014306 (2017), arXiv:1602.00156 [nucl-th] (2016).
- [74] S. Vaintraub, N. Barnea and D. Gazit, *Phys. Rev. C* **79**, 065501 (2009), arXiv:0903.1048 [nucl-th] (2009).
- [75] N. Barnea, W. Leidemann and G. Orlandini, *Phys. Rev. C* **81**, 064001 (2010).
- [76] S. Pastore, S. C. Pieper, R. Schiavilla and R. B. Wiringa, *Phys. Rev. C* **87**, 035503 (2013), arXiv:1212.3375 [nucl-th] (2012).
- [77] P. Maris, M. A. Caprio and J. P. Vary, *Phys. Rev. C* **91**, 014310 (2015).
- [78] M. A. Caprio, P. Maris, J. P. Vary and R. Smith, *Rom. J. Phys.* **60**, 738 (2015), arXiv:1502.01083 [nucl-th] (2015).

-
- [79] M. A. Caprio, P. Maris, J. P. Vary and R. Smith, *Int. J. Mod. Phys. E* **24**, 1541002 (2015), arXiv:1509.00102 [nucl-th] (2015).
- [80] T. Dytrych *et al.*, *Phys. Rev. Lett.* **111**, 252501 (2013), arXiv:1312.0969 [nucl-th] (2013).
- [81] T. Dytrych, A. C. Hayes, K. D. Launey, J. P. Draayer, P. Maris, J. P. Vary, D. Langr and T. Oberhuber, *Phys. Rev. C* **91**, 024326 (2015), arXiv:1502.03066 [nucl-th] (2015).
- [82] T. Dytrych *et al.*, *Comput. Phys. Commun.* **207**, 202 (2016), arXiv:1602.02965 [nucl-th] (2016).
- [83] S. Okubo, *Progr. Theor. Phys.* **12**, 603 (1954).
- [84] K. Suzuki and S. Y. Lee, *Progr. Theor. Phys.* **64**, 2091 (1980).
- [85] K. Suzuki, *Progr. Theor. Phys.* **68**, 246 (1982).
- [86] I. Stetcu, B. R. Barrett, P. Navratil and J. P. Vary, *Phys. Rev. C* **71**, 044325 (2005), nucl-th/0412004 (2004).
- [87] A. F. Lisetskiy, B. R. Barrett, M. K. G. Kruse, P. Navratil, I. Stetcu and J. P. Vary, *Phys. Rev. C* **78**, 044302 (2008), arXiv:0808.2187 [nucl-th] (2008).
- [88] E. Dikmen, A. F. Lisetskiy, B. R. Barrett, P. Maris, A. M. Shirokov and J. P. Vary, *Phys. Rev. C* **91**, 064301 (2015), arXiv:1502.00700 [nucl-th] (2015).
- [89] S. D. Glazek and K. G. Wilson, *Phys. Rev. D* **48**, 5863 (1993).
- [90] F. Wegner, *Ann. Phys. (Berl.)* **506**, 77 (1994).
- [91] S. K. Bogner, R. J. Furnstahl, P. Maris, R. J. Perry, A. Schwenk and J. P. Vary, *Nucl. Phys. A* **801**, 21 (2008).
- [92] H. Hergert and R. Roth, *Phys. Rev. C* **75**, 051001 (2007).

Irreducible 3-body Force Contributions to the Self-Energy

F. Raimondi and C. Barbieri

Department of Physics, University of Surrey, Guildford GU2 7XH, United Kingdom

Abstract

The inclusion of three-nucleon forces (3NFs) in *ab initio* many-body approaches is a formidable task, due to the computational load implied by the treatment of their matrix elements. For this reason, practical applications have mostly been limited to contributions where 3NFs enter as effective two-nucleon interactions. In this contribution, we derive the algebraic diagrammatic construction (ADC) working equations for a specific Feynman diagram of the self-energy that contains a fully irreducible three-nucleon force. This diagram is expected to be the most important among those previously neglected, because it connects dominant excited intermediate state configurations.

Keywords: *Self-consistent Green's function; algebraic diagrammatic construction; three-nucleon forces; computational physics; ab initio nuclear theory*

1 Introduction

The strong connection between advances in theoretical frameworks and empowering of the computational resources has emerged as one of the pillars for the future development of the nuclear theory [1]. Different methods, such as the no-core shell model [2], coupled cluster [3], in-medium similarity renormalization group [4] and self-consistent Green's function (SCGF) formalism [5, 6], have been extended in recent years by finding efficient algorithms capable to handle the dimensionality of the nuclear many-body problem. Most of these efforts involved novel developments of many-body formalism. In the context of the SCGF theory applied to nuclei, different applications are currently explored. For instance, the extension of the SCGF to encompass the concept of quasiparticle in the sense of the Bogoliubov formalism, opens the possibility to study the open shell nuclei via the solution of the Gorkov equation [7]. Another possibility is a description of nuclear states in the continuum, such as electromagnetic excitations and one-nucleon elastic scattering [8]. Also the impact of three-nucleon forces (3NFs) on the mechanism of the saturation in nuclear matter [9] and on the correlations of finite nuclei [10, 11] has been extensively studied.

The formalism required for the inclusion of the 3NFs in the SCGF has been laid down in Ref. [12], where the treatment of the 3NFs in terms of effective (i. e., averaged) one- and two-nucleon forces (2NFs) is described, along with the corresponding

Proceedings of the International Conference 'Nuclear Theory in the Supercomputing Era — 2016' (NTSE-2016), Khabarovsk, Russia, September 19–23, 2016. Eds. A. M. Shirokov and A. I. Mazur. Pacific National University, Khabarovsk, Russia, 2018, p. 36.

<http://www.ntse-2016.khb.ru/Proc/Barbieri.pdf>.

Feynman rules for the perturbative expansion of the single-particle (s.p.) propagator. However, the working equations for interaction-irreducible 3NFs (i. e., those diagrams that cannot simplify into effective forces) have not been investigated to date. In this work we derive the working equations of one such self-energy Feynman diagram that contains a 3NF insertion not implicitly included in the effective 2NFs. Among the diagrams featuring interaction-irreducible 3NFs, we focus here on the one which is believed to be dominant, according to the energy required to excite the intermediate particle-hole configurations in the diagram. The equations are cast according to the algebraic diagrammatic construction (ADC) method, a scheme devised in quantum chemistry and applied for the first time to the perturbative expansions of the two-particle (polarization) propagator [13] and one-body propagator [14] of finite Fermi systems. The ADC allows for an efficient organization of different correlation terms in the description of the self-energy, corresponding to Feynman diagrams with different topologies such as ladder and ring series. Within this scheme, the nuclear Dyson equation is reformulated as an energy-independent Hermitian eigenvalue problem. This simplifies the numerical solution, without resorting to the time-consuming algorithms that scan the entire energy spectrum in search for each pole separately. The increased dimensionality of the eigenvalue problem can be kept under control with the help of large-scale diagonalization algorithms, such as Lanczos or Arnoldi.

We present a brief overview of the SCGF formalism in Section 2, covering the expressions of the Dyson equation and the irreducible self-energy. In Section 3 we review the ADC(n) formalism up to orders $n = 2$ and 3, and we outline the procedure to find the working equations for the elements for the Dyson matrix [see Eq. (19) below]. These working equations are given in Section 4.1 for $n = 2$ and Section 4.2 for $n = 3$. The formalism at the second order is worked out in full, while at the third order we limit ourselves to the set of diagrams that involve two-particle–one-hole ($2p1h$) and two-hole–one-particle ($2h1p$) intermediate configurations to illustrate the approach. In particular, we focus on the interaction-irreducible 3NF Feynman diagram that was neglected in previous works. Finally, the conclusions are given in Section 5.

2 Basic concepts of Green’s function theory

In a microscopic approach, the description of the dynamics of nucleus is based on a realistic interaction among the nucleons, which in principle contains different components, from the 2NF sector until the full N -body interaction. Here, we consider up to 3NFs and start from the nuclear Hamiltonian

$$\hat{H} = \hat{T} + \hat{V} + \hat{W}, \quad (1)$$

with \hat{T} the kinetic energy part, \hat{V} the 2NF and \hat{W} the 3NF.

In order to treat the interaction perturbatively, we introduce the first approximation, based on the concept of the mean field felt by the nucleons as an effective external potential produced by the nuclear medium itself. Accordingly, the Hamiltonian

is written as

$$\hat{H} = \sum_{\alpha\beta} h_{\alpha\beta}^{(0)} a_{\alpha}^{\dagger} a_{\beta} - \sum_{\alpha\beta} U_{\alpha\beta} a_{\alpha}^{\dagger} a_{\beta} + \frac{1}{4} \sum_{\substack{\alpha\gamma \\ \beta\delta}} V_{\alpha\gamma,\beta\delta} a_{\alpha}^{\dagger} a_{\gamma}^{\dagger} a_{\delta} a_{\beta} + \frac{1}{36} \sum_{\substack{\alpha\gamma\epsilon \\ \beta\delta\eta}} W_{\alpha\gamma\epsilon,\beta\delta\eta} a_{\alpha}^{\dagger} a_{\gamma}^{\dagger} a_{\epsilon}^{\dagger} a_{\eta} a_{\delta} a_{\beta}, \quad (2)$$

with $\hat{h}^{(0)} \equiv \hat{T} + \hat{U}$ being the mean field part, while the remaining terms give the residual interaction, which is treated in a perturbative way. The mean field part is given by the sum of the kinetic energy T and the auxiliary potential U , defining the dynamics of the zeroth-order propagator $g^{(0)}$ introduced below, which is referred to as a mean-field reference state. In Eq. (2), $V_{\alpha\gamma,\beta\delta}$ and $W_{\alpha\gamma\epsilon,\beta\delta\eta}$ are the *antisymmetrized* matrix elements of the $2N$ and $3N$ forces respectively, with the Greek indices $\alpha, \beta, \gamma, \dots$ labeling a complete set of s. p. states defining the model space used in the computation.

The peculiarity of the self-consistent Green's functions approach consists in including the solution of the dynamics of the A and $A \pm 1$ nucleons systems from the start and on the same footing. This information is conveyed by the one-body propagator, or two-point Green's function. The latter is defined as the matrix element of the time-ordered product (\mathcal{T}) of an annihilation and creation field operators $a(t)$ and $a^{\dagger}(t)$ with respect to the fully correlated A -body wave function $|\Psi_0^A\rangle$ in the ground state, i. e.,

$$g_{\alpha\beta}(t-t') = -\frac{i}{\hbar} \langle \Psi_0^A | \mathcal{T} [a_{\alpha}(t) a_{\beta}^{\dagger}(t')] | \Psi_0^A \rangle. \quad (3)$$

The function in Eq. (3) is describing both the propagation of a particle created at time t' in the quantum state β and destroyed at a later time t in the quantum state α , and the propagation of a hole moving in the opposite time direction for $t' > t$. This is why $g(\tau)$ also takes the name of one-body propagator.

The time-coordinate representation in Eq. (3) can be Fourier-transformed to the energy domain in order to obtain the Lehmann representation of the Green's function,

$$g_{\alpha\beta}(\omega) = \sum_n \frac{\langle \Psi_0^A | a_{\alpha} | \Psi_n^{A+1} \rangle \langle \Psi_n^{A+1} | a_{\beta}^{\dagger} | \Psi_0^A \rangle}{\hbar\omega - (E_n^{A+1} - E_0^A) + i\eta} + \sum_k \frac{\langle \Psi_0^A | a_{\beta}^{\dagger} | \Psi_k^{A-1} \rangle \langle \Psi_k^{A-1} | a_{\alpha} | \Psi_0^A \rangle}{\hbar\omega - (E_0^A - E_k^{A-1}) - i\eta}, \quad (4)$$

which contains the relevant spectroscopic informations of the A - and $(A \pm 1)$ -body systems, contained in the transition amplitudes,

$$\mathcal{X}_{\beta}^n \equiv \langle \Psi_n^{A+1} | a_{\beta}^{\dagger} | \Psi_0^A \rangle \quad (5)$$

and

$$\mathcal{Y}_{\alpha}^k \equiv \langle \Psi_k^{A-1} | a_{\alpha} | \Psi_0^A \rangle, \quad (6)$$

which are the overlap integrals related to the probability of adding a particle to an orbital β or removing it from an orbital α in a system with A particles. In the following, we will use the common notation,

$$\mathcal{Z}_{\alpha}^{i=n,k} \equiv \begin{cases} (\mathcal{X}_{\alpha}^n)^* \\ \mathcal{Y}_{\alpha}^k, \end{cases} \quad (7)$$

with the index i valid for both forward-in-time (particle attachment) and backward-in-time (nucleon removal) processes. Note that we use n to denote particle states and k for hole states. The denominators in Eq. (4) contain also the one-nucleon addition and removal energies

$$\varepsilon_n^+ \equiv (E_n^{A+1} - E_0^A) \quad (8)$$

and

$$\varepsilon_k^- \equiv (E_0^A - E_k^{A-1}), \quad (9)$$

from which one can derive the eigenvalues corresponding to the correlated wave functions $|\Psi_n^{A\pm 1}\rangle$, once the ground state energy E_0^A of $|\Psi_0^A\rangle$ is known. In the following, we will use the compact notations of Eqs. (5)–(9) to present our equations.

The s. p. Green's function (4) is completely determined by solving the Dyson equation,

$$g_{\alpha\beta}(\omega) = g_{\alpha\beta}^{(0)}(\omega) + \sum_{\gamma\delta} g_{\alpha\gamma}^{(0)}(\omega) \Sigma_{\gamma\delta}^*(\omega) g_{\delta\beta}(\omega), \quad (10)$$

which is a non-linear equation for the correlated propagator, $g(\omega)$. The unperturbed propagator $g^{(0)}(\omega)$ is the propagator corresponding to the Hamiltonian $h^{(0)}$ defining the reference state. The irreducible self-energy $\Sigma^*(\omega)$ encodes the effects of the nuclear medium on the propagation and is equivalent to the optical potential for the states in the continuum [8, 15].

The irreducible self-energy can be separated in a term which is time-independent, Σ^∞ , and an energy-dependent part $\tilde{\Sigma}(\omega)$ containing contributions from the dynamical excitations given by the intermediate state configurations (ISCs) within the system:

$$\Sigma_{\alpha\beta}^*(\omega) = \Sigma_{\alpha\beta}^\infty + \tilde{\Sigma}_{\alpha\beta}(\omega). \quad (11)$$

An inspection of the Dyson equation (10) shows that the self-energy contains all the effects on the propagation of the s. p. that go beyond the mean-field description: for this reason the self-energy can be regarded as an effective potential enriching the unperturbed propagator with many-body correlations and turning it into the “dressed” propagator. If the exact $\Sigma^*(\omega)$ is known, Eq. (10) yields the equivalent of the exact solution of the Schrödinger equation.

3 ADC formalism as matrix eigenvalue problem

In the following we apply the algebraic diagrammatic construction to the dynamic (i. e., energy-dependent) part of the irreducible self-energy of Eq. (11). For this purpose, we write $\tilde{\Sigma}(\omega)$ in the most general form of its spectral representation,

$$\begin{aligned} \tilde{\Sigma}_{\alpha\beta}(\omega) &= \sum_{jj'} \mathbf{M}_{\alpha j}^\dagger \left[\frac{1}{\hbar\omega\mathbb{1} - (E\mathbb{1} + \mathbf{C}) + i\eta\mathbb{1}} \right]_{jj'} \mathbf{M}_{j'\beta} \\ &+ \sum_{kk'} \mathbf{N}_{\alpha k} \left[\frac{1}{\hbar\omega\mathbb{1} - (E\mathbb{1} + \mathbf{D}) - i\eta\mathbb{1}} \right]_{kk'} \mathbf{N}_{k'\beta}^\dagger. \end{aligned} \quad (12)$$

At this stage, the expression in Eq. (12) is a formal decomposition defining two types of matrices with respect to the ISCs j, j' (k, k'): the coupling matrix $\mathbf{M}_{j\alpha}$ ($\mathbf{N}_{\alpha k}$),

and the interaction matrix $\mathbf{C}_{jj'}$ ($\mathbf{D}_{kk'}$) for the forward-in-time (backward-in-time) part of the self-energy. The coupling matrices couple the initial and final s. p. states of the propagator to the ISCs, while the interaction matrices \mathbf{C} and \mathbf{D} contain the matrix elements of the residual interactions (up to 3NFs) among the ISCs themselves. In general, ISCs are multiparticle-multihole excitations resulting from the same-time propagation of fermion lines within Feynman diagrams. For nucleon addition, with $M + 1$ particles and M holes, $(M + 1)pMh$, their unperturbed energies are

$$E_j = \varepsilon_{n_1}^+ + \varepsilon_{n_2}^+ + \dots + \varepsilon_{n_M}^+ + \varepsilon_{n_{M+1}}^+ - \varepsilon_{k_1}^- - \varepsilon_{k_2}^- - \dots - \varepsilon_{k_M}^-, \quad (13)$$

and similarly for nucleon removal. In the following we will make use of the shorthand notation for the forward-in-time terms (corresponding to particle attachment)

$$\left. \begin{array}{l} r, r' \equiv (n_1, n_2, k_3) \\ q, q' \equiv (n_1, n_2, n_3, k_4, k_5) \end{array} \right\} j \ j' \quad (14)$$

and

$$\left. \begin{array}{l} s, s' \equiv (k_1, k_2, n_3) \\ u, u' \equiv (k_1, k_2, k_3, n_4, n_5) \end{array} \right\} k \ k' \quad (15)$$

for the backward-in-time terms (i. e., for particle removal). For instance, $j \equiv (n_1, n_2, k_3)$ in the coupling matrix $\mathbf{M}_{(n_1, n_2, k_3)\alpha}$ connects a s. p. state α to an intermediate state composed by a $2p1h$ configuration. Each ISC gives a different term in Eq. (12), with the configurations $3p2h$, $4p3h$ and so on pertaining to more complicated, but also energetically less important, intermediate states.

While the energy-dependence in the self-energy is a direct consequence of the underlying dynamics in the many-body system, it gives rise to a major computational bottleneck. In order to find all the poles of the propagator in Eq. (10), one should scan the energy plane with an extremely fine mesh, therefore the direct search of the s. p. energies in this way would be costly, with the possibility to leave some solutions undetected. For this reason it is convenient to rearrange the Dyson equation in a matrix form independent of energy. This is achieved by introducing the eigenvector

$$\mathbf{z}^{i\dagger} \equiv (\mathcal{Z}_\delta^{i\dagger} \quad \mathcal{W}_r^{i\dagger} \quad \mathcal{W}_s^{i\dagger} \quad \mathcal{W}_q^{i\dagger} \quad \mathcal{W}_u^{i\dagger} \quad \dots) \quad (16)$$

with the first component given by the transition amplitudes of Eq. (7). The other components contain the information on the ISCs propagated through $\Sigma(\omega)$ but evaluated at the specific quasiparticle energy ε_i^\pm of each solution,

$$\mathcal{W}_j^i \equiv \mathcal{W}_j(\omega)|_{\hbar\omega=\varepsilon_i} = \sum_{j'} \left[\frac{1}{\hbar\omega\mathbb{1} - (E\mathbb{1} + \mathbf{C})} \right]_{jj'} \mathbf{M}_{j'\delta} \mathcal{Z}_\delta^i \Big|_{\hbar\omega=\varepsilon_i}, \quad (17)$$

and

$$\mathcal{W}_k^i \equiv \mathcal{W}_k(\omega)|_{\hbar\omega=\varepsilon_i} = \sum_{k'} \left[\frac{1}{\hbar\omega\mathbb{1} - (E\mathbb{1} + \mathbf{D})} \right]_{kk'} \mathbf{N}_{k'\delta}^\dagger \mathcal{Z}_\delta^i \Big|_{\hbar\omega=\varepsilon_i}. \quad (18)$$

The task now is to diagonalize the following matrix, being equivalent to the original

eigenvalue problem [16],

$$\epsilon_i \mathbf{Z}^i = \begin{pmatrix} \varepsilon^{(0)} + \Sigma_{\alpha\delta}^\infty & \mathbf{M}_{\alpha r}^\dagger & \mathbf{N}_{\alpha s} & \mathbf{M}_{\alpha q}^\dagger & \mathbf{N}_{\alpha u} & \cdots \\ \mathbf{M}_{r'\alpha} & E_r \delta_{rr'} + \mathbf{C}_{rr'} & & \mathbf{C}_{r'q} & & \cdots \\ \mathbf{N}_{s'\alpha}^\dagger & & E_s \delta_{ss'} + \mathbf{D}_{ss'} & & \mathbf{D}_{s'u} & \cdots \\ \mathbf{M}_{q'\alpha} & \mathbf{C}_{q'r} & & E_q \delta_{qq'} + \mathbf{C}_{q'q} & & \cdots \\ \mathbf{N}_{u'\alpha}^\dagger & & \mathbf{D}_{u's} & & E_u \delta_{uu'} + \mathbf{D}_{u'u} & \cdots \\ \vdots & \vdots & \vdots & \ddots & & \ddots \end{pmatrix} \mathbf{Z}^i, \quad (19)$$

with the normalization condition

$$\sum_{\alpha\beta} (\mathbf{Z}_\alpha^i)^\dagger \mathbf{Z}_\beta^i + (\mathcal{W}_j^i)^\dagger \mathcal{W}_j^i + (\mathcal{W}_k^i)^\dagger \mathcal{W}_k^i + \dots = 1. \quad (20)$$

With the procedure outlined above and the introduction of the eigenvector \mathbf{Z}^i of Eq. (16), each energy eigenvalue is now related to an eigenvector of larger dimension. Once Eq. (19) is diagonalized, its eigenvalues and the first portions of their eigenvectors \mathbf{Z}^i yield the one-body propagator according to Eq. (4). The severe growth in the dimension of the Dyson matrix can be handled by projecting the set of the energies configurations to a smaller Krylov subspace, and then a multi-pivot Lanczos-type algorithm can be applied as illustrated in Ref. [17].

The ADC is a systematic approach to find expressions for the coupling and interaction matrices appearing in Eq. (19) that include the correlations due to 2NFs, 3NFs, and so on. This is achieved by expanding Eq. (12) in powers of the residual interaction \hat{U} , the 2NF \hat{V} and 3NF \hat{W} and then by comparing the result with the Goldstone–Feynman perturbative expressions for the self-energy. Formally, we have:

$$\mathbf{M}_{j\alpha} = \mathbf{M}_{j\alpha}^{(I)} + \mathbf{M}_{j\alpha}^{(II)} + \mathbf{M}_{j\alpha}^{(III)} + \dots, \quad (21)$$

where the term $\mathbf{M}_{j\alpha}^{(n)}$ is of the n^{th} order in the residual interaction. For the backward-in-time coupling matrices we have:

$$\mathbf{N}_{\alpha k} = \mathbf{N}_{\alpha k}^{(I)} + \mathbf{N}_{\alpha k}^{(II)} + \mathbf{N}_{\alpha k}^{(III)} + \dots. \quad (22)$$

The matrices \mathbf{C} and \mathbf{D} can only be at first order in the residual interaction, but they appear also at the denominators in the spectral representation (12). Thus, they give rise to a geometrical series according to the identity

$$\frac{1}{A-B} = \frac{1}{A} + \frac{1}{A} B \frac{1}{A-B} = \frac{1}{A} + \frac{1}{A} B \frac{1}{A} + \frac{1}{A} B \frac{1}{A} B \frac{1}{A} + \dots \quad (23)$$

for $A = \hbar\omega - E$ and $B = \mathbf{C}, \mathbf{D}$.

Using the expressions (21)–(23) in Eq. (12) gives rise to the following expansion

for the energy-dependent irreducible self-energy,

$$\begin{aligned}
\tilde{\Sigma}_{\alpha\beta}(\omega) = & \sum_j \mathbf{M}_{\alpha j}^{(I)\dagger} \left[\frac{1}{\hbar\omega - E_j + i\eta} \right] \mathbf{M}_{j\beta}^{(I)} \\
& + \sum_j \mathbf{M}_{\alpha j}^{(II)\dagger} \left[\frac{1}{\hbar\omega - E_j + i\eta} \right] \mathbf{M}_{j\beta}^{(I)} + \sum_j \mathbf{M}_{\alpha j}^{(I)\dagger} \left[\frac{1}{\hbar\omega - E_j + i\eta} \right] \mathbf{M}_{j\beta}^{(II)} \\
& + \sum_{jj'} \mathbf{M}_{\alpha j}^{(I)\dagger} \left[\frac{1}{\hbar\omega - E_j + i\eta} \right] \mathbf{C}_{jj'} \left[\frac{1}{\hbar\omega - E_{j'} + i\eta} \right] \mathbf{M}_{j'\beta}^{(I)} + \dots \\
& + \sum_k \mathbf{N}_{\alpha k}^{(I)} \left[\frac{1}{\hbar\omega - E_k - i\eta} \right] \mathbf{N}_{k\beta}^{(I)\dagger} \\
& + \sum_k \mathbf{N}_{\alpha k}^{(II)} \left[\frac{1}{\hbar\omega - E_k - i\eta} \right] \mathbf{N}_{k\beta}^{(I)\dagger} + \sum_k \mathbf{N}_{\alpha k}^{(I)} \left[\frac{1}{\hbar\omega - E_k - i\eta} \right] \mathbf{N}_{k\beta}^{(II)\dagger} \\
& + \sum_{kk'} \mathbf{N}_{\alpha k}^{(I)} \left[\frac{1}{\hbar\omega - E_k - i\eta} \right] \mathbf{D}_{kk'} \left[\frac{1}{\hbar\omega - E_{k'} - i\eta} \right] \mathbf{N}_{k'\beta}^{(I)\dagger} + \dots, \tag{24}
\end{aligned}$$

where we show all contributions up to the second and third order. The procedure is to compare term by term the formal expansion (24) with the calculated Goldstone-type diagrams. One then extracts the minimal expressions for the matrices \mathbf{M} , \mathbf{N} , \mathbf{C} and \mathbf{D} given in terms of the transitions amplitudes of Eqs. (5)–(6) and the quasiparticle energies of Eqs. (8)–(9), that ensure consistency with the standard perturbative expansion up to order n . The content of the $\text{ADC}(n)$ expansion is far from trivial when one moves from the second to the third order: in fact the structure of the third-order terms in Eq. (24) as analytic functions in the energy plane, does not match the general spectral representation of Eq. (12) which is required for the correct self-energy. However, once \mathbf{M} , \mathbf{N} , \mathbf{C} and \mathbf{D} are found one can insert them in the correct analytical representation of Eqs. (12) and (19). As a result, the $\text{ADC}(n)$ approach will include selected contributions at order higher than n , as well as all-order non-perturbative resummations as shown by Eq. (23).

4 ADC equations up to the third order

In this section we collect the building blocks of the ADC at the second order and present a selected set of coupling and interaction matrices that play a dominant role at the third order in a sense to be specified in the following discussion.

All diagrams discussed in this work are one-particle irreducible, skeleton and interaction-irreducible diagrams. When limiting oneself to interaction-irreducible diagrams only, one needs to substitute the original one- and two-nucleon residual interactions, $-\hat{U}$ and \hat{V} , by corresponding effective interactions which we label respectively \tilde{U} and \tilde{V} and represent diagrammatically as wavy lines. The latter contain averaged contributions from 3NFs that account for the discarded interaction-reducible diagrams. Hence, one reduces the number of perturbative terms (i. e., diagrams) that need to be dealt with. A detailed exposition of these aspects and the extension of Feynman rules to the case of many-nucleon interactions is beyond the scope of the present work. The interested reader is referred to the thorough discussion in Ref. [12]. For the present discussion, we only need to keep in mind that the 2NFs in Figs. 1a

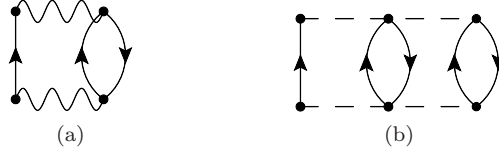


Figure 1: One-particle irreducible, skeleton and interaction-irreducible self-energy diagrams appearing at second order in the perturbative expansion of the self-energy. The wiggly lines represent the effective 2NF \tilde{V} containing averaged 3NF components, while the long-dashed lines represent the interaction-irreducible 3NF, \hat{W} .

are effective interactions which contain the most ‘trivial’ contributions of \hat{W} in the sense that they do not require any extension of the formalism and computer codes previously developed for pure two-body interactions.

4.1 ADC(2) building blocks

At the second order and with 3NFs, the dynamic self-energy is composed by the two diagrams depicted in Fig. 1. The main topological difference between them is given by the fact that Fig. 1a propagates $2p1h$ and $2h1p$ as intermediate states, whereas the diagram of Fig. 1b contains irreducible 3NFs that generate $3p2h$ and $3h2p$ ISCs. Since the latter are energetically less favorable, they are expected to play a minor role at the Fermi surface and to contribute weakly to the total ground state energy. Following the same argument, we can expect that the third-order diagrams containing $2p1h$ and $2h1p$ ISCs discussed in Section 4.2 (see Fig. 3), are more important than those with $3p2h$ and $3h2p$ configurations at the same order.

To define the ADC(2) approximation scheme, we present the explicit expressions of the coupling and interaction matrices contained in the diagrams of Fig. 1. Unless otherwise stated, in this section and in the rest of the paper, we adopt the Einstein’s convention of summing over repeated indexes for both model-space s. p. states (α, β, \dots) and the particle and hole orbits ($n_1, n_2, \dots, k_1, k_2, \dots$). We also use collective indexes for ISCs according to the notation set in Eqs. (14)–(15) where appropriate.

We show first the expressions for the energy-dependent self-energy of Fig. 1a,

$$\tilde{\Sigma}_{\alpha\beta}^{(1a)}(\omega) = \frac{1}{2} \tilde{V}_{\alpha\epsilon, \gamma\rho} \left(\sum_{n_1, n_2, k_3} \frac{(\mathcal{X}_\gamma^{n_1} \mathcal{X}_\rho^{n_2} \mathcal{Y}_\epsilon^{k_3})^* \mathcal{X}_\mu^{n_1} \mathcal{X}_\nu^{n_2} \mathcal{Y}_\lambda^{k_3}}{\hbar\omega - (\varepsilon_{n_1}^+ + \varepsilon_{n_2}^+ - \varepsilon_{k_3}^-) + i\eta} + \sum_{k_1, k_2, n_3} \frac{\mathcal{Y}_\gamma^{k_1} \mathcal{Y}_\rho^{k_2} \mathcal{X}_\epsilon^{n_3} (\mathcal{Y}_\mu^{k_1} \mathcal{Y}_\nu^{k_2} \mathcal{X}_\lambda^{n_3})^*}{\hbar\omega - (\varepsilon_{k_1}^- + \varepsilon_{k_2}^- - \varepsilon_{n_3}^+) - i\eta} \right) \tilde{V}_{\mu\nu, \beta\lambda}. \quad (25)$$

and in Fig. 1b,

$$\begin{aligned} \tilde{\Sigma}_{\alpha\beta}^{(1b)}(\omega) = & \frac{1}{12} W_{\alpha\gamma\delta,\xi\tau\sigma} \left(\sum_{\substack{n_1, n_2, n_3 \\ k_4, k_5}} \frac{(\mathcal{X}_\xi^{n_1} \mathcal{X}_\tau^{n_2} \mathcal{X}_\sigma^{n_3} \mathcal{Y}_\delta^{k_4} \mathcal{Y}_\gamma^{k_5})^* \mathcal{X}_\mu^{n_1} \mathcal{X}_\nu^{n_2} \mathcal{X}_\lambda^{n_3} \mathcal{Y}_\rho^{k_4} \mathcal{Y}_\eta^{k_5}}{\hbar\omega - (\varepsilon_{n_1}^+ + \varepsilon_{n_2}^+ + \varepsilon_{n_3}^+ - \varepsilon_{k_4}^- - \varepsilon_{k_5}^-) + i\eta} \right. \\ & \left. + \sum_{\substack{k_1, k_2, k_3 \\ n_4, n_5}} \frac{\mathcal{Y}_\xi^{k_1} \mathcal{Y}_\tau^{k_2} \mathcal{Y}_\sigma^{k_3} \mathcal{X}_\delta^{n_4} \mathcal{X}_\gamma^{n_5} (\mathcal{Y}_\mu^{k_1} \mathcal{Y}_\nu^{k_2} \mathcal{Y}_\lambda^{k_3} \mathcal{X}_\rho^{n_4} \mathcal{X}_\eta^{n_5})^*}{\hbar\omega - (\varepsilon_{k_1}^- + \varepsilon_{k_2}^- + \varepsilon_{k_3}^- - \varepsilon_{n_4}^+ - \varepsilon_{n_5}^+) - i\eta} \right) W_{\mu\nu\lambda,\beta\eta\rho}. \end{aligned} \quad (26)$$

These expressions at the second order in the Feynman–Goldstone perturbative expansion, already match the second-order terms in the analogous expansion of the self-energy [the first and fourth lines in Eq. (24)]. Since they are already in the correct form of the spectral representation, Eq. (12), it is easy to read the coupling matrices at the ADC(2) level directly from them. In the first line of Eq. (25), we find the coupling matrix

$$\mathbf{M}_{(n_1 n_2 k_3)\alpha}^{(I-2N)} \equiv \frac{1}{\sqrt{2}} \mathcal{X}_\mu^{n_1} \mathcal{X}_\nu^{n_2} \mathcal{Y}_\lambda^{k_3} \tilde{V}_{\mu\nu,\alpha\lambda}, \quad (27)$$

while in the backward-in-time part [the second line of Eq. (25)] we have

$$\mathbf{N}_{\alpha(k_1 k_2 n_3)}^{(I-2N)} \equiv \frac{1}{\sqrt{2}} \tilde{V}_{\alpha\lambda,\mu\nu} \mathcal{Y}_\mu^{k_1} \mathcal{Y}_\nu^{k_2} \mathcal{X}_\lambda^{n_3}, \quad (28)$$

that couples the s. p. states to the $2h1p$ propagator through an effective $2NF$. Both these coupling matrices can be depicted as fragments of Goldstone diagrams, as shown in Figs. 2a and 2c.

The matrix coupling to $3p2h$ ISCs is found from Eq. (26) and comes from the diagram of Fig. 1b,

$$\mathbf{M}_{(n_1 n_2 n_3 k_4 k_5)\alpha}^{(I-3N)} \equiv \frac{1}{\sqrt{12}} \mathcal{X}_\mu^{n_1} \mathcal{X}_\nu^{n_2} \mathcal{X}_\lambda^{n_3} \mathcal{Y}_\rho^{k_4} \mathcal{Y}_\eta^{k_5} W_{\mu\nu\lambda,\alpha\eta\rho}, \quad (29)$$

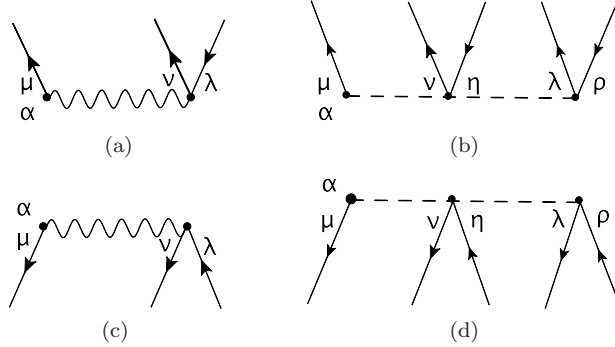


Figure 2: Diagrams of the ADC(2) coupling matrices containing effective $2N$ interaction \tilde{V} (left column) and interaction-irreducible $3NF$ \tilde{W} (right column). The coupling matrices (a) and (c) connect with $2p1h$ and $2h1p$ ISCs respectively (see Eqs. (27,28)), while the coupling matrices (b) and (d) connect with $3p2h$ and $3h2p$ ISCs respectively [see Eqs. (29)–(30)]. The diagrams 2a and 2b contribute to $\mathbf{M}^{(I)}$, while 2c and 2d contribute to $\mathbf{N}^{(I)}$.

while the coupling matrix to $3h2p$ ISCs has the following expression:

$$\mathbf{N}_{\alpha(k_1 k_2 k_3 n_4 n_5)}^{(I-3N)} \equiv \frac{1}{\sqrt{12}} W_{\alpha\eta\rho,\mu\nu\lambda} \mathcal{Y}_{\mu}^{k_1} \mathcal{Y}_{\nu}^{k_2} \mathcal{Y}_{\lambda}^{k_3} \mathcal{X}_{\rho}^{n_4} \mathcal{X}_{\eta}^{n_5}. \quad (30)$$

Their representation as fragments of Goldstone diagrams is given in Figs. 2b and 2d, respectively.

All four expressions of Eqs. (27)–(30) are building blocks of the ADC(2). These complete the set of coupling matrices needed to reproduce the second order terms (the first and fourth rows) in Eq. (24) and no interaction matrix is needed at this order. Hence, the ADC(2) working equations are finally summarized by Eq. (13) and the following expressions:

$$\mathbf{M}_{j\alpha}^{(I)} = \begin{cases} \mathbf{M}_{r\alpha}^{(I-2N)} & \text{for } j = r = (n_1 n_2 k_3), \\ \mathbf{M}_{q\alpha}^{(I-3N)} & \text{for } j = q = (n_1 n_2 n_3 k_4 k_5), \end{cases} \quad (31)$$

$$\mathbf{N}_{\alpha k}^{(I)} = \begin{cases} \mathbf{N}_{\alpha s}^{(I-2N)} & \text{for } k = s = (k_1 k_2 n_3), \\ \mathbf{N}_{\alpha u}^{(I-3N)} & \text{for } k = u = (k_1 k_2 k_3 n_4 n_5), \end{cases} \quad (32)$$

$$\mathbf{C}_{jj'} = 0, \quad (33)$$

$$\mathbf{D}_{kk'} = 0. \quad (34)$$

In ADC(2), the coupling matrices are linked directly without any intermediate interaction insertion, therefore the interaction matrices \mathbf{C} and \mathbf{D} in Eqs. (33)–(34) are set to zero. As we show below, this is not anymore true for ADC(3), where the interaction matrices \mathbf{C} and \mathbf{D} no longer vanish and give rise to infinite (and non-perturbative) resummations of diagrams.

4.2 ADC(3) building blocks with $2p1h$ and $2h1p$ ISCs

The perturbative expansion of the self-energy generates 17 interaction-irreducible Feynman diagrams at the third order [12]. Of these, only the three shown in Fig. 3 propagate at most $2p1h$ and $2h1p$ ISCs, whereas the remaining diagrams (not shown here) entail at least some contribution from the $3p2h$ or $3h2p$ configurations. Moreover, Figs. 3a and 3b are the sole diagrams that do not involve any interaction-irreducible $3N$ term. Given that the three-body forces are weaker for most systems than the corresponding two-body ones¹, we expect that the contributions of Fig. 3a and 3b are the most important and that the diagram 3c is the next in order of relevance, while the remaining 14 diagrams will not be dominant. In this section, we present the explicit expressions of the coupling and interaction matrices entering the ADC(3) formalism at the third order, as derived from the three aforementioned diagrams.

As for the second order, a set of expressions for the matrices \mathbf{M} , \mathbf{N} , \mathbf{C} , \mathbf{D} and E at ADC(3) is obtained from the direct comparison between the equations of the Feynman diagrams of Fig. 3, with the general form of the self-energy in Eq. (24). The different terms can be organized according to the kind of interactions appearing in their contribution. For instance, the diagrams 3a and 3b give contributions to the coupling matrices $\mathbf{M}^{(II)}$ and $\mathbf{N}^{(II)}$ that involve two effective $2N$ interactions and will be labelled with a “ $2N\ 2N$ ” superscript.

¹For nuclear physics, one may estimate that $\langle \hat{W} \rangle \approx \frac{1}{10} \langle \hat{V} \rangle$ [18, 19].

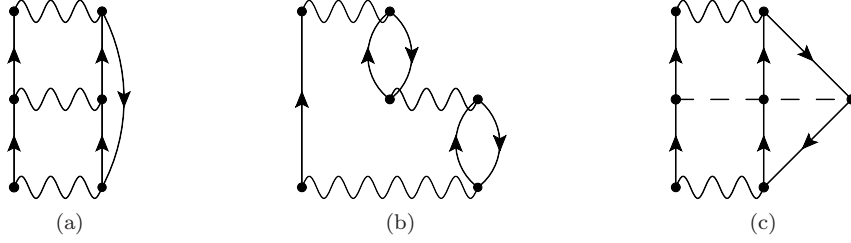


Figure 3: Three one-particle irreducible, skeleton and interaction-irreducible self-energy diagrams appearing at third order in the perturbative expansion of $\tilde{\Sigma}(\omega)$. Only the third-order diagrams with at most $2p1h$ and $2h1p$ intermediate states are shown.

Figures 3a and 3b generate all order summations of ladder and ring diagrams, respectively. These contain *only* effective $2NF$ s and their ADC(3) equations are well known [14, 16]. Hence, we simply state the results here. The forward-in-time coupling matrix arising from Fig. 3a is given by

$$\mathbf{M}_{(n_1 n_2 k_3)\alpha}^{(2N \ 2N \ a)} \equiv \frac{1}{2\sqrt{2}} \frac{\mathcal{X}_\rho^{n_1} \mathcal{X}_\sigma^{n_2} \tilde{V}_{\rho\sigma,\gamma\delta} \mathcal{Y}_\gamma^{k_4} \mathcal{Y}_\delta^{k_5}}{\varepsilon_{k_4}^- + \varepsilon_{k_5}^- - \varepsilon_{n_1}^+ - \varepsilon_{n_2}^+} (\mathcal{Y}_\mu^{k_4} \mathcal{Y}_\nu^{k_5})^* \mathcal{Y}_\lambda^{k_3} \tilde{V}_{\mu\nu,\alpha\lambda}. \quad (35)$$

The ring diagram of Fig. 3b gives rise to the forward-in-time coupling matrix,

$$\mathbf{M}_{(n_1 n_2 k_3)\alpha}^{(2N \ 2N \ b)} = \frac{1}{\sqrt{2}} \left(\frac{\mathcal{X}_\sigma^{n_2} \mathcal{Y}_\delta^{k_3} \tilde{V}_{\sigma\rho,\delta\gamma} \mathcal{Y}_\gamma^{k_5} \mathcal{X}_\rho^{n_4}}{\varepsilon_{k_3}^- - \varepsilon_{n_2}^+ + \varepsilon_{k_5}^- - \varepsilon_{n_4}^+} \mathcal{X}_\mu^{n_1} (\mathcal{Y}_\nu^{k_5} \mathcal{X}_\lambda^{n_4})^* \tilde{V}_{\mu\nu,\alpha\lambda} \right. \\ \left. - \frac{\mathcal{X}_\sigma^{n_1} \mathcal{Y}_\delta^{k_3} \tilde{V}_{\sigma\rho,\delta\gamma} \mathcal{Y}_\gamma^{k_5} \mathcal{X}_\rho^{n_4}}{\varepsilon_{k_3}^- - \varepsilon_{n_1}^+ + \varepsilon_{k_5}^- - \varepsilon_{n_4}^+} \mathcal{X}_\mu^{n_2} (\mathcal{Y}_\nu^{k_5} \mathcal{X}_\lambda^{n_4})^* \tilde{V}_{\mu\nu,\alpha\lambda} \right), \quad (36)$$

which is explicitly antisymmetrized with respect to the n_1 and n_2 fermion lines. The diagrammatic representations of the two coupling matrices of Eqs. (35) and (36) are depicted in Figs. 4a and 4b, respectively.

For the same self-energy diagrams of Figs. 3a and 3b but from the backward-in-time Goldstone diagrams, we find the coupling matrices

$$\mathbf{N}_{\alpha(k_1 k_2 n_3)}^{(2N \ 2N \ a)} \equiv \frac{1}{2\sqrt{2}} \tilde{V}_{\alpha\lambda,\mu\nu} \mathcal{X}_\lambda^{n_3} (\mathcal{X}_\mu^{n_4} \mathcal{X}_\nu^{n_5})^* \frac{\mathcal{X}_\rho^{n_4} \mathcal{X}_\sigma^{n_5} \tilde{V}_{\rho\sigma,\gamma\delta} \mathcal{Y}_\gamma^{k_1} \mathcal{Y}_\delta^{k_2}}{\varepsilon_{k_1}^- + \varepsilon_{k_2}^- - \varepsilon_{n_4}^+ - \varepsilon_{n_5}^+} \quad (37)$$

and

$$\mathbf{N}_{\alpha(k_1 k_2 n_3)}^{(2N \ 2N \ b)} \equiv \frac{1}{\sqrt{2}} \left(\tilde{V}_{\alpha\lambda,\mu\nu} (\mathcal{Y}_\lambda^{k_5})^* \mathcal{Y}_\mu^{k_1} (\mathcal{X}_\nu^{n_4})^* \frac{\mathcal{X}_\sigma^{n_4} \mathcal{Y}_\delta^{k_5} \tilde{V}_{\sigma\rho,\delta\gamma} \mathcal{Y}_\gamma^{k_2} \mathcal{X}_\rho^{n_3}}{\varepsilon_{k_2}^- - \varepsilon_{n_3}^+ + \varepsilon_{k_5}^- - \varepsilon_{n_4}^+} \right. \\ \left. - \tilde{V}_{\alpha\lambda,\mu\nu} (\mathcal{Y}_\lambda^{k_5})^* \mathcal{Y}_\mu^{k_2} (\mathcal{X}_\nu^{n_4})^* \frac{\mathcal{X}_\sigma^{n_4} \mathcal{Y}_\delta^{k_5} \tilde{V}_{\sigma\rho,\delta\gamma} \mathcal{Y}_\gamma^{k_1} \mathcal{X}_\rho^{n_3}}{\varepsilon_{k_1}^- - \varepsilon_{n_3}^+ + \varepsilon_{k_5}^- - \varepsilon_{n_4}^+} \right). \quad (38)$$

Their diagrammatic representation is displayed in Figs. 4c and 4d respectively, where it is clear that they are linked to the $2h1p$ propagators.

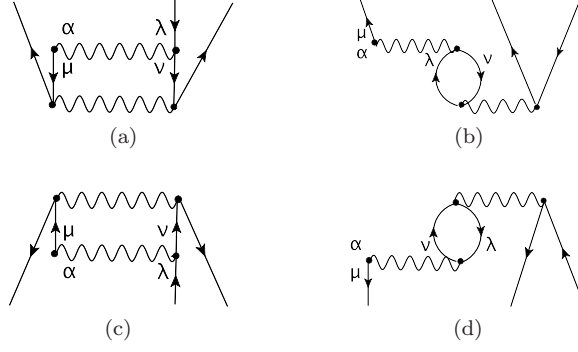


Figure 4: Diagrams of the ADC(3) coupling matrices with two effective $2NFs$ \tilde{V} that link to $2p1h$ ISCs (first row) and $2h1p$ ISCs (second row). The coupling matrices (a) and (b) correspond to Eqs. (35), (36), while the coupling matrices (c) and (d) correspond to Eqs. (37), (38).

The interaction matrices are found by comparing the third order Goldstone diagrams with double poles to the third and sixth lines of Eq. (24). The interaction matrix connecting $2p1h$ propagators through a particle-particle (pp), ladder interaction is

$$\mathbf{C}_{(n_1 n_2 k_3), (n_4 n_5 k_6)}^{pp} \equiv \frac{1}{2} \mathcal{X}_\mu^{n_1} \mathcal{X}_\nu^{n_2} \tilde{V}_{\mu\nu, \lambda\rho} (\mathcal{X}_\lambda^{n_4} \mathcal{X}_\rho^{n_5})^* \delta_{k_3 k_6}, \quad (39)$$

while the one connecting through particle-hole (ph) rings is composed by four terms that arise from the antisymmetrization with respect to the n_1 and n_2 particles to the left and the n_4 and n_5 ones to the right,

$$\begin{aligned} \mathbf{C}_{(n_1 n_2 k_3), (n_4 n_5 k_6)}^{ph} = & \frac{1}{2} \left(\mathcal{X}_\nu^{n_2} \mathcal{Y}_\rho^{k_3} \tilde{V}_{\mu\nu, \lambda\rho} (\mathcal{X}_\lambda^{n_5} \mathcal{Y}_\mu^{k_6})^* \delta_{n_1 n_4} \right. \\ & - \mathcal{X}_\nu^{n_2} \mathcal{Y}_\rho^{k_3} \tilde{V}_{\mu\nu, \lambda\rho} (\mathcal{X}_\lambda^{n_4} \mathcal{Y}_\mu^{k_6})^* \delta_{n_1 n_5} \\ & - \mathcal{X}_\nu^{n_1} \mathcal{Y}_\rho^{k_3} \tilde{V}_{\mu\nu, \lambda\rho} (\mathcal{X}_\lambda^{n_5} \mathcal{Y}_\mu^{k_6})^* \delta_{n_2 n_4} \\ & \left. + \mathcal{X}_\nu^{n_1} \mathcal{Y}_\rho^{k_3} \tilde{V}_{\mu\nu, \lambda\rho} (\mathcal{X}_\lambda^{n_4} \mathcal{Y}_\mu^{k_6})^* \delta_{n_2 n_5} \right). \end{aligned} \quad (40)$$

In the backward-in-time self-energy Goldstone diagrams, the interaction matrices connecting $2h1p$ propagators through a hole-hole (hh) interaction lead to

$$\mathbf{D}_{(k_1 k_2 n_3), (k_4 k_5 n_6)}^{hh} \equiv -\frac{1}{2} (\mathcal{Y}_\mu^{k_1} \mathcal{Y}_\nu^{k_2})^* \tilde{V}_{\mu\nu, \lambda\rho} \mathcal{Y}_\lambda^{k_4} \mathcal{Y}_\rho^{k_5} \delta_{n_3 n_6}, \quad (41)$$

while the one connecting through a hole-particle (hp) interaction gives

$$\begin{aligned} \mathbf{D}_{(k_1 k_2 n_3), (k_4 k_5 n_6)}^{hp} = & \frac{1}{2} \left((\mathcal{Y}_\mu^{k_2} \mathcal{X}_\rho^{n_3})^* \tilde{V}_{\mu\nu, \lambda\rho} \mathcal{Y}_\lambda^{k_5} \mathcal{X}_\nu^{n_6} \delta_{k_1 k_4} \right. \\ & - (\mathcal{Y}_\mu^{k_2} \mathcal{X}_\rho^{n_3})^* \tilde{V}_{\mu\nu, \lambda\rho} \mathcal{Y}_\lambda^{k_4} \mathcal{X}_\nu^{n_6} \delta_{k_1 k_5} \\ & - (\mathcal{Y}_\mu^{k_1} \mathcal{X}_\rho^{n_3})^* \tilde{V}_{\mu\nu, \lambda\rho} \mathcal{Y}_\lambda^{k_5} \mathcal{X}_\nu^{n_6} \delta_{k_2 k_4} \\ & \left. + (\mathcal{Y}_\mu^{k_1} \mathcal{X}_\rho^{n_3})^* \tilde{V}_{\mu\nu, \lambda\rho} \mathcal{Y}_\lambda^{k_4} \mathcal{X}_\nu^{n_6} \delta_{k_2 k_5} \right). \end{aligned} \quad (42)$$

We now turn to the Feynman diagram of Fig. 3c, which is the focus of the present work. To our knowledge, the ADC formulas arising from this term have not been presented before. The Feynman rules give the following expression for it:

$$\begin{aligned} \Sigma_{\alpha\beta}^{(3c)}(\omega) = & -\frac{(\hbar)^4}{4} \int \frac{d\omega_1}{2\pi i} \int \frac{d\omega_2}{2\pi i} \int \frac{d\omega_3}{2\pi i} \int \frac{d\omega_4}{2\pi i} \sum_{\substack{\gamma\delta\nu\mu\epsilon\lambda \\ \xi\eta\theta\sigma\tau\chi}} \tilde{V}_{\alpha\gamma,\delta\nu} g_{\xi\gamma}(\omega_3) g_{\nu\lambda}(\omega - \omega_1 + \omega_3) \\ & \times g_{\delta\epsilon}(\omega_1) W_{\mu\epsilon\lambda,\xi\eta\theta} g_{\theta\tau}(\omega - \omega_2 + \omega_4) g_{\eta\sigma}(\omega_2) g_{\chi\mu}(\omega_4) \tilde{V}_{\sigma\tau,\beta\chi}. \quad (43) \end{aligned}$$

By performing the four integrals in the complex plane, we find six terms corresponding to the different time orderings of three interactions. Altogether we obtain

$$\begin{aligned} \Sigma_{\alpha\beta}^{(3c)}(\omega) = & \frac{1}{4} \sum_{\substack{\gamma\delta\nu\mu\epsilon\lambda \\ \xi\eta\theta\sigma\tau\chi}} \tilde{V}_{\alpha\gamma,\delta\nu} W_{\epsilon\lambda\mu,\eta\theta\xi} \tilde{V}_{\sigma\tau,\beta\chi} \\ & \times \left(- \sum_{\substack{n_1 n_2 k_3 \\ n_4 n_5 k_6}} \frac{(\mathcal{X}_\delta^{n_1} \mathcal{X}_\nu^{n_2} \mathcal{Y}_\gamma^{k_3})^* \mathcal{X}_\epsilon^{n_1} \mathcal{X}_\lambda^{n_2} \mathcal{Y}_\xi^{k_3} (\mathcal{X}_\eta^{n_4} \mathcal{X}_\theta^{n_5} \mathcal{Y}_\mu^{k_6})^* \mathcal{X}_\sigma^{n_4} \mathcal{X}_\tau^{n_5} \mathcal{Y}_\chi^{k_6}}{(\hbar\omega - (\varepsilon_{n_1}^+ + \varepsilon_{n_2}^+ - \varepsilon_{k_3}^-) + i\eta) (\hbar\omega - (\varepsilon_{n_4}^+ + \varepsilon_{n_5}^+ - \varepsilon_{k_6}^-) + i\eta)} \right. \\ & + \sum_{\substack{k_1 k_2 n_3 \\ n_4 n_5 k_6}} \frac{\mathcal{Y}_\delta^{k_1} \mathcal{Y}_\nu^{k_2} \mathcal{X}_\gamma^{n_3} (\mathcal{Y}_\epsilon^{k_1} \mathcal{Y}_\lambda^{k_2} \mathcal{Y}_\mu^{k_6} \mathcal{X}_\eta^{n_4} \mathcal{X}_\theta^{n_5} \mathcal{X}_\xi^{n_3})^* \mathcal{X}_\sigma^{n_4} \mathcal{X}_\tau^{n_5} \mathcal{Y}_\chi^{k_6}}{(\varepsilon_{k_1}^- + \varepsilon_{k_2}^- + \varepsilon_{k_6}^- - \varepsilon_{n_3}^+ - \varepsilon_{n_4}^+ - \varepsilon_{n_5}^+) (\hbar\omega - (\varepsilon_{n_4}^+ + \varepsilon_{n_5}^+ - \varepsilon_{k_6}^+) + i\eta)} \\ & + \sum_{\substack{k_1 k_2 n_3 \\ n_4 n_5 k_6}} \frac{(\mathcal{X}_\delta^{n_4} \mathcal{X}_\nu^{n_5} \mathcal{Y}_\gamma^{k_6})^* \mathcal{X}_\epsilon^{n_4} \mathcal{X}_\lambda^{n_5} \mathcal{X}_\mu^{n_3} \mathcal{Y}_\eta^{k_1} \mathcal{Y}_\theta^{k_2} \mathcal{Y}_\xi^{k_6} (\mathcal{Y}_\sigma^{k_1} \mathcal{Y}_\tau^{k_2} \mathcal{X}_\chi^{n_3})^*}{(\hbar\omega - (\varepsilon_{n_4}^+ + \varepsilon_{n_5}^+ - \varepsilon_{k_6}^-) + i\eta) (\varepsilon_{k_1}^- + \varepsilon_{k_2}^- + \varepsilon_{k_6}^- - \varepsilon_{n_3}^+ - \varepsilon_{n_4}^+ - \varepsilon_{n_5}^+)} \\ & - \sum_{\substack{k_1 k_2 n_3 \\ k_4 k_5 n_6}} \frac{\mathcal{Y}_\delta^{k_1} \mathcal{Y}_\nu^{k_2} \mathcal{X}_\gamma^{n_3} (\mathcal{Y}_\epsilon^{k_1} \mathcal{Y}_\lambda^{k_2} \mathcal{X}_\xi^{n_3})^* \mathcal{Y}_\eta^{k_4} \mathcal{Y}_\theta^{k_5} \mathcal{X}_\mu^{n_6} (\mathcal{Y}_\sigma^{k_4} \mathcal{Y}_\tau^{k_5} \mathcal{X}_\chi^{n_6})^*}{(\hbar\omega - (\varepsilon_{k_1}^- + \varepsilon_{k_2}^- - \varepsilon_{n_3}^+) - i\eta) (\hbar\omega - (\varepsilon_{k_4}^- + \varepsilon_{k_5}^- - \varepsilon_{n_6}^+) - i\eta)} \\ & - \sum_{\substack{k_1 k_2 n_3 \\ n_4 n_5 k_6}} \frac{\mathcal{Y}_\delta^{k_1} \mathcal{Y}_\nu^{k_2} \mathcal{X}_\gamma^{n_3} (\mathcal{Y}_\epsilon^{k_1} \mathcal{Y}_\lambda^{k_2} \mathcal{Y}_\mu^{k_6} \mathcal{X}_\eta^{n_4} \mathcal{X}_\theta^{n_5} \mathcal{X}_\xi^{n_3})^* \mathcal{X}_\sigma^{n_4} \mathcal{X}_\tau^{n_5} \mathcal{Y}_\chi^{k_6}}{(\hbar\omega - (\varepsilon_{k_1}^- + \varepsilon_{k_2}^- - \varepsilon_{n_3}^+) - i\eta) (\varepsilon_{k_1}^- + \varepsilon_{k_2}^- + \varepsilon_{k_6}^- - \varepsilon_{n_3}^+ - \varepsilon_{n_4}^+ - \varepsilon_{n_5}^+)} \\ & \left. - \sum_{\substack{k_1 k_2 n_3 \\ n_4 n_5 k_6}} \frac{(\mathcal{X}_\delta^{n_4} \mathcal{X}_\nu^{n_5} \mathcal{Y}_\gamma^{k_6})^* \mathcal{X}_\epsilon^{n_4} \mathcal{X}_\lambda^{n_5} \mathcal{X}_\mu^{n_3} \mathcal{Y}_\eta^{k_1} \mathcal{Y}_\theta^{k_2} \mathcal{Y}_\xi^{k_6} (\mathcal{Y}_\sigma^{k_1} \mathcal{Y}_\tau^{k_2} \mathcal{X}_\chi^{n_3})^*}{(\varepsilon_{k_1}^- + \varepsilon_{k_2}^- + \varepsilon_{k_6}^- - \varepsilon_{n_3}^+ - \varepsilon_{n_4}^+ - \varepsilon_{n_5}^+) (\hbar\omega - (\varepsilon_{k_1}^- + \varepsilon_{k_2}^- - \varepsilon_{n_3}^-) - i\eta)} \right), \quad (44) \end{aligned}$$

where the first (last) three terms correspond to forward-in-time (backward-in-time) Goldstone diagrams.

By comparing to the third order terms in Eq. (24), one sees that the new contributions to the coupling matrices contain one effective 2NF and one interaction-irreducible 3NF. The following forward-in-time matrix can be singled out from either the second or third line of Eq. (44),

$$\mathbf{M}_{(n_1 n_2 k_3)\alpha}^{(2N \ 3N \ a)} \equiv \frac{1}{2\sqrt{2}} \frac{\mathcal{X}_\xi^{n_4} \mathcal{X}_\rho^{n_1} \mathcal{X}_\sigma^{n_2} W_{\xi\rho\sigma,\zeta\eta\theta} \mathcal{Y}_\zeta^{k_3} \mathcal{Y}_\eta^{k_5} \mathcal{Y}_\theta^{k_6}}{\varepsilon_{k_3}^- + \varepsilon_{k_5}^- + \varepsilon_{k_6}^- - \varepsilon_{n_1}^+ - \varepsilon_{n_2}^+ - \varepsilon_{n_4}^+} (\mathcal{Y}_\mu^{k_5} \mathcal{Y}_\nu^{k_6} \mathcal{X}_\lambda^{n_4})^* \tilde{V}_{\mu\nu,\alpha\lambda}, \quad (45)$$

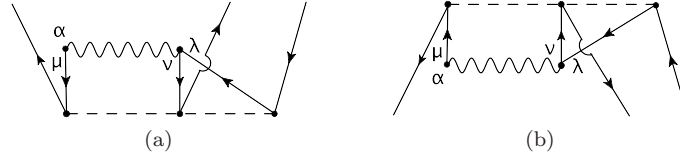


Figure 5: Diagrams of the ADC(3) coupling matrices with one effective 2NF \tilde{V} and one interaction-irreducible 3NF \tilde{W} . The coupling matrix (a) is linked to $2p1h$ ISCs and corresponds to Eq. (45), while (b) is linked to $2h1p$ ISCs and corresponds to Eq. (46).

while in the last two lines of Eq. (44) we read the backward-in-time coupling matrix:

$$\mathbf{N}_{\alpha(k_1 k_2 n_3)}^{(2N \ 3N \ a)} \equiv -\frac{1}{2\sqrt{2}} \tilde{V}_{\alpha\lambda, \mu\nu} (\mathcal{Y}_\lambda^{k_4} \mathcal{X}_\mu^{n_5} \mathcal{X}_\nu^{n_6})^* \frac{\mathcal{X}_\rho^{n_3} \mathcal{X}_\sigma^{n_5} \mathcal{X}_\xi^{n_6} W_{\rho\sigma\xi, \theta\zeta\eta} \mathcal{Y}_\theta^{k_4} \mathcal{Y}_\zeta^{k_1} \mathcal{Y}_\eta^{k_2}}{\varepsilon_{k_1}^- + \varepsilon_{k_2}^- + \varepsilon_{k_4}^- - \varepsilon_{n_3}^+ - \varepsilon_{n_5}^+ - \varepsilon_{n_6}^+}. \quad (46)$$

The diagrammatic representations of Eqs. (45) and (46) are displayed in Fig. 5.

The only interaction matrix that connects $2p1h$ ISCs through a 3NF is found from the first term of Eq. (44),

$$\mathbf{C}_{(n_1 n_2 k_3), (n_4 n_5 k_6)}^{3N} \equiv -\frac{1}{2} \mathcal{X}_\nu^{n_1} \mathcal{X}_\mu^{n_2} \mathcal{Y}_\rho^{k_3} W_{\nu\mu\lambda, \epsilon\eta\rho} (\mathcal{X}_\epsilon^{n_4} \mathcal{X}_\eta^{n_5} \mathcal{Y}_\lambda^{k_6})^*, \quad (47)$$

which is explicitly antisymmetric in the particle indexes. With Eqs. (47) and (27) we can rewrite the first term of Eq. (44) as

$$\mathbf{M}_{\alpha r}^{\dagger(I-2N)} \frac{1}{\hbar\omega - E_r} \mathbf{C}_{r r'}^{3N} \frac{1}{\hbar\omega - E_{r'}} \mathbf{M}_{r' \beta}^{(I-2N)}. \quad (48)$$

The expression (48) contains only the first order contribution in the interaction matrix expansion corresponding to the second term in the r. h. s. of Eq. (23) for $B = \mathbf{C}^{3N}$. This is resummed to all order by diagonalizing the Dyson matrix (19), which will automatically include *all* the higher order terms in the expansion.

From the fourth term of Eq. (44), we single out the only backward-in-time interaction matrix connecting two $2h1p$ configurations through the $3N$ interaction, that is

$$\mathbf{D}_{(k_1 k_2 n_3), (k_4 k_5 n_6)}^{3N} \equiv -\frac{1}{2} (\mathcal{Y}_\nu^{k_1} \mathcal{Y}_\mu^{k_2} \mathcal{X}_\rho^{n_3})^* W_{\nu\mu\lambda, \epsilon\eta\rho} \mathcal{Y}_\epsilon^{k_4} \mathcal{Y}_\eta^{k_5} \mathcal{X}_\lambda^{n_6}, \quad (49)$$

which is also explicitly antisymmetric in the hole indexes. With Eqs. (49) and (28) we associate the fourth term of Eq. (44) to rewrite it as

$$\mathbf{N}_{\alpha s}^{(I-2N)} \frac{1}{\hbar\omega - E_s} \mathbf{D}_{s s'}^{3N} \frac{1}{\hbar\omega - E_{s'}} \mathbf{N}_{s' \beta}^{\dagger(I-2N)}. \quad (50)$$

We stress again the fact that Eq. (50), being a first-order term in \mathbf{D}^{3N} , is resummed with *all* other higher order contributions when solving the Dyson equation.

Finally, the ADC(3) working equations for the set of Feynman diagrams in Fig. 3

is summarized by the following expressions:

$$\mathbf{M}_{j\alpha}^{(\text{II})} = \mathbf{M}_{(n_1 n_2 k_3)\alpha}^{(2N \ 2N \ \text{a})} + \mathbf{M}_{(n_1 n_2 k_3)\alpha}^{(2N \ 2N \ \text{b})} + \mathbf{M}_{(n_1 n_2 k_3)\alpha}^{(2N \ 3N \ \text{a})}, \quad (51)$$

$$\mathbf{N}_{\alpha k}^{(\text{II})} = \mathbf{N}_{\alpha(k_1 k_2 n_3)}^{(2N \ 2N \ \text{a})} + \mathbf{N}_{\alpha(k_1 k_2 n_3)}^{(2N \ 2N \ \text{b})} + \mathbf{N}_{\alpha(k_1 k_2 n_3)}^{(2N \ 3N \ \text{a})}, \quad (52)$$

$$\mathbf{C}_{jj'} = \mathbf{C}_{(n_1 n_2 k_3), (n_4 n_5 k_6)}^{pp} + \mathbf{C}_{(n_1 n_2 k_3), (n_4 n_5 k_6)}^{ph} + \mathbf{C}_{(n_1 n_2 k_3), (n_4 n_5 k_6)}^{3N}, \quad (53)$$

$$\mathbf{D}_{kk'} = \mathbf{D}_{(k_1 k_2 n_3), (k_4 k_5 n_6)}^{hh} + \mathbf{D}_{(k_1 k_2 n_3), (k_4 k_5 n_6)}^{hp} + \mathbf{D}_{(k_1 k_2 n_3), (k_4 k_5 n_6)}^{3N}. \quad (54)$$

At the third order, besides the equations summarized above, there are the coupling and interaction matrices imposed by the remaining 14 one-particle irreducible, skeleton and interaction-irreducible self-energy diagrams, which are topologically distinct from Fig. 3 [12]. The expressions of the coupling and interaction matrices derived from all these diagrams contribute to the $3p2h$ and $3h2p$ sectors of Eq. (19) [20].

5 Summary and outlook

We have shown the working equations for the ADC(3) formalism applied to the irreducible self-energy in the SCGF formalism with 2NFs and 3NFs. This formalism allows an efficient and accurate numerical implementation for the solution of the Dyson equation, which is recast as an energy eigenvalue problem. Moreover, within a given order, the matrix form of the Dyson equation allows the infinite resummation of certain classes of diagrams, specifically ladder and ring diagrams, preserving the non-perturbative nature of the SCGF approach.

The minimal expressions for both coupling and interaction matrices required to conform to the structure of the self-energy as analytic function in the energy plane, have been revisited completely at the ADC(2) level. We have displayed the most important terms at the third order, and we derived for the first time the coupling and interaction matrices of the Feynman diagram in Fig. 3c containing one interaction-irreducible 3NF. This term is relevant because it is the only irreducible 3NF insertion that links to the dominant ISCs in the self-energy, that is $2p1h$ and $2h1p$ intermediate excitations. The complete ADC(3) working equations for the Dyson SCGF approach will be presented in a forthcoming publication [20], while the extension of the Gorkov SCGF formalism of Ref. [7] to ADC(3) is a part of future plans.

References

- [1] J. P. Vary, in *Proc. Int. Conf. Nucl. Theor. Supercomputing Era (NTSE-2013)*, Ames, IA, USA, May 13–17, 2013, eds. A. M. Shirokov and A. I. Mazur. Pacific National University, Khabarovsk, Russia, 2014, p. 15, <http://ntse-2013.khb.ru/Proc/JPVary.pdf>.
- [2] B. R. Barrett, P. Navrátil and J. P. Vary, *Rep. Prog. Phys.* **69**, 131 (2013).
- [3] G. Hagen, T. Papenbrock, M. Hjorth-Jensen and D. J. Dean, *Rep. Prog. Phys.* **77**, 096302 (2014).

-
- [4] H. Hergert, S. Bogner, T. Morris, A. Schwenk and K. Tsukiyama, Phys. Rep. **621**, 165 (2016).
- [5] W. Dickhoff and D. Van Neck, *Many-body theory exposed! Propagator description of quantum mechanics in many-body systems*. World Scientific, Singapore, 2005.
- [6] W. Dickhoff and C. Barbieri, Prog. Part. Nucl. Phys. **52**, 377 (2004).
- [7] V. Somà, T. Duguet and C. Barbieri, Phys. Rev. C **84**, 064317, (2011).
- [8] A. Idini, C. Barbieri and P. Navrátil, arXiv:1612.01478 [nucl-th] (2016).
- [9] A. Carbone, A. Polls and A. Rios, Phys. Rev. C **88**, 044302 (2013).
- [10] A. Cipollone, C. Barbieri and P. Navrátil, Phys. Rev. Lett. **111**, 062501 (2013).
- [11] A. Cipollone, C. Barbieri and P. Navrátil, Phys. Rev. C **92**, 014306 (2015).
- [12] A. Carbone, A. Cipollone, C. Barbieri, A. Rios and A. Polls, Phys. Rev. C **88**, 054326 (2013).
- [13] J. Schirmer, Phys. Rev. A **26**, 2395 (1982).
- [14] J. Schirmer, L. S. Cederbaum and O. Walter, Phys. Rev. A **28**, 1237 (1983).
- [15] F. Capuzzi and C. Mahaux, Ann. Phys. (NY) **245**, 147 (1996).
- [16] C. Barbieri and A. Carbone, arXiv:1611.03923 [nucl-th] (2016).
- [17] V. Somà, C. Barbieri and T. Duguet, Phys. Rev. C **89**, 024323 (2014).
- [18] P. Grangé, A. Lejeune, M. Martzolff and J.-F. Mathiot, Phys. Rev. C **40**, 1040 (1989).
- [19] E. Epelbaum, H.-W. Hammer and U.-G. Meisner, Rev. Mod. Phys. **81**, 1773 (2009).
- [20] F. Raimondi and C. Barbieri, *Algebraic diagrammatic construction formalism with three-body interactions, to be published*.

Green's Function Calculations of Light Nuclei

Zhonghao Sun, Qiang Wu and Furong Xu

School of Physics, Peking University, Beijing 100871, China

Abstract

An influence of short-range correlations in nuclei is investigated with realistic nuclear force. The nucleon-nucleon interaction is renormalized with $V_{\text{low-}k}$ technique and applied to Green's function calculations. The Dyson equation is reformulated using algebraic diagrammatic constructions. We also analyze the ${}^4\text{He}$ binding energy calculated with chiral and CD-Bonn potentials. The properties of Green's function with realistic nuclear forces are also discussed.

Keywords: *Green's function, ab initio calculations, realistic nuclear forces*

1 Introduction

A recent research on theoretical descriptions of nuclear structure has shown that correlations beyond Hartree–Fock (HF) play a significant role. High-resolution nucleon knockout reaction ($e, e'p$) experiments indicate a probability of a dilution phenomenon in particle occupancy around the Fermi surface. The HF approach is a mean-field method in which the ground state of the system is described with a single Slater determinant and particles occupy only the orbitals below the Fermi surface. Many attempts to account for correlations beyond HF have been made, such as the Jastrow method, configuration interaction methods including the random phase approximation (RPA), the many-body perturbation theory (MBPT), the Bruckner Hartree–Fock (BHF), and the Green's function method.

A development of modern nuclear forces makes it possible to investigate nuclear structure from first principles and perform microscopic calculations with realistic nuclear forces [1]. Although we already have many theoretical methods to study exotic nuclear structures, such as the projected shell model [2] and other phenomenological models [3–6], a microscopic description of nucleus is of great importance for studying fundamental problems in nuclear structure and nuclear forces. The nature of the inter-nucleon force is determined by symmetries of the two-nucleon system; the parameters such as coupling constants and other physical parameters, are fitted to reproduce low-energy phase shifts. Usually, however, realistic nuclear forces cannot be exploited directly in nuclear structure calculations because of their strong short-range repulsive nature. Various methods have been tried to make realistic forces better adjusted for many-body calculations, such as the energy-dependent Bloch–Horowitz method, the

Proceedings of the International Conference 'Nuclear Theory in the Supercomputing Era — 2016' (NTSE-2016), Khabarovsk, Russia, September 19–23, 2016. Eds. A. M. Shirokov and A. I. Mazur. Pacific National University, Khabarovsk, Russia, 2018, p. 52.

<http://www.ntse-2016.khb.ru/Proc/Xu.pdf>.

Lee–Suzuki transformation [7], the unitary model operator approach (UMOA) [8], and the G -matrix method. In the present study we use realistic nuclear forces for the Green's function calculation of ${}^4\text{He}$. The difference between the calculations with the CD-Bonn and chiral nuclear N^3LO forces is discussed herein.

2 Green's function method

Ab initio self-consistent calculations within the Green's function method have made a great progress since the late 1990s [9]. A brief review of the Green's function theory for many-body systems follows.

Suppose that one has the ground state of a N -particle system, $|\Phi_0\rangle$. The one-particle Green's function is defined as

$$S_{\alpha\beta}(t_1 - t_2) = \langle \Phi_0 | T [a_\alpha(t_2) a_\beta^\dagger(t_1)] | \Phi_0 \rangle, \quad (1)$$

where T is the time ordering operator and $a_\alpha(t)$ is an operator in the Heisenberg picture:

$$a_\alpha(t) = \exp(iHt) a_\alpha \exp(-iHt). \quad (2)$$

The single-particle propagator can be written as

$$G_{\alpha\beta}(t_1 - t_2) = \begin{cases} \langle \Phi_0 | a_\alpha e^{i(\hat{H}-E_0)(t_1-t_2)} a_\beta^\dagger | \Phi_0 \rangle, & t_1 \geq t_2 \\ -\langle \Phi_0 | a_\beta^\dagger e^{-i(\hat{H}-E_0)(t_1-t_2)} a_\alpha | \Phi_0 \rangle, & t_1 < t_2 \end{cases} \quad (3)$$

One can calculate an expectation value of a single-particle operator by the single-particle propagator,

$$\langle n_\alpha \rangle = - \lim_{t \rightarrow +0} G_{\alpha\beta}(t). \quad (4)$$

We use an energy representation of the Green's function $G_{\alpha\beta}(\omega)$ which is the Fourier transformation of $G_{\alpha\beta}(t)$. If we choose the Hartree–Fock basis as a starting point, the Green's function is given by the Dyson equation

$$G_{\alpha\beta}(\omega) = G_{\alpha\beta}^{HF}(\omega) + G_{\alpha\gamma_1}^{HF}(\omega) \Sigma_{\gamma_1\gamma_2}(\omega) G_{\gamma_2\beta}(\omega) \quad (5)$$

with

$$G_{\alpha\beta}^{HF} = \left[\frac{\Theta(\alpha - F)}{\omega - \epsilon_\alpha + i\eta} + \frac{\Theta(F - \alpha)}{\omega - \epsilon_\alpha - i\eta} \right] \delta_{\alpha\beta}, \quad (6)$$

where G^{HF} is a free Green's function built with Hartree–Fock single-particle energies, and the self-energies $\Sigma(\omega)$ are defined as sums of all one-particle irreducible diagrams (which account for all corrections from other particles [10]). In self-consistent Green's function calculations, the self-energies constructed using fully dressed Green's functions, are defined as

$$\Sigma(\omega)_{ab} = \frac{1}{2} \sum_{\gamma\delta\mu} \int \frac{d\omega_1}{2\pi i} \int \frac{d\omega_2}{2\pi i} \langle a\delta | V | \gamma\mu \rangle \langle \gamma\mu | V | b\delta \rangle g_\gamma(\omega - \omega_1 + \omega_2) g_\delta(\omega_1) g_\mu(\omega_2). \quad (7)$$

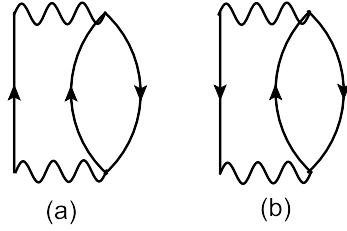


Figure 1: Second order self-energy: a) $2p1h$ and b) $2h1p$ contributions. The wavy line represents the interaction vertex and the solid line is the Green's function.

In the Lehmann representation, the Green's function can be written as

$$\begin{aligned}
 G_{\alpha\beta}(\omega) &= \int d(t-t') e^{i\omega(t-t')} G(t, t') \\
 &= \sum_n \frac{\langle \Phi_0 | c_\alpha | \Phi_n^{N+1} \rangle \langle \Phi_n^{N+1} | c_\beta^\dagger | \Phi_0 \rangle}{\omega + E_0^N - E_n^{N+1} + i\eta} + \sum_m \frac{\langle \Phi_0 | c_\alpha^\dagger | \Phi_m^{N-1} \rangle \langle \Phi_m^{N-1} | c_\beta | \Phi_0 \rangle}{\omega + E_0^{N-1} - E_m^N - i\eta} \\
 &= \sum_n \frac{X_\alpha^n X_\beta^{n*}}{\omega - \omega^+ + i\eta} + \sum_m \frac{X_\alpha^m X_\beta^{m*}}{\omega - \omega^- - i\eta}. \quad (8)
 \end{aligned}$$

The first term includes a spectroscopic factor indicating the transition from $(A+1)$ to A , and the second term corresponds to the transition from A to $A-1$. The inner structure of the self-energy contains all one-body irreducible diagrams and cannot be calculated exactly; the self-energy is calculated perturbatively using the HF propagator (see Fig. 1). Hereon the Dyson equation can be solved.

The expectation values of single-particle operators can be calculated as

$$\langle \Psi_0 | \hat{O} | \Psi_0 \rangle = \int_C \frac{d\omega}{2\pi i} \sum_{\alpha\beta} \langle \alpha | \hat{O} | \beta \rangle G_{\alpha\beta}(\omega), \quad (9)$$

where the integration contour encompasses all poles of the Green's function below the Fermi surface (Fig. 2). The particle number conservation is not guaranteed since the self-energy is not calculated with the fully-dressed Green's function.

We calculate the self-energy to the second order and use the algebraic diagrammatic construction (ADC) method to transform the Dyson equation to an eigenvalue problem (details can be found in Ref. [11]),

$$\begin{pmatrix} H_0 & a^T & A^T \\ a & e & 0 \\ A & 0 & E \end{pmatrix} \begin{pmatrix} X \\ X_P \\ X_Q \end{pmatrix} = \omega_n \begin{pmatrix} X \\ X_P \\ X_Q \end{pmatrix}, \quad (10)$$

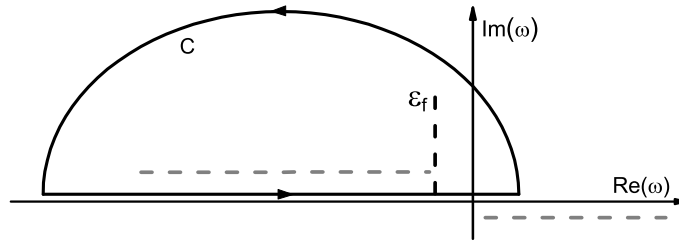


Figure 2: Integration contour for one-body operators wraps the upper half plain encompassing all poles below the Fermi surface ε_f .

where H_0 is the diagonal matrix of Hartree–Fock energies, a is the coupling between single particles,

$$a_{i\alpha} = \langle \alpha h | V | p_1 p_2 \rangle, \quad (11)$$

P is the space spanned by all $2p1h$ states $|p_1 p_2 h\rangle_i$, and A is the coupling to the Q space spanned with all $2h1p$ states $|h_1 h_2 p\rangle_j$,

$$A_{j\alpha} = \langle \alpha p | V | h_1 h_2 \rangle. \quad (12)$$

Respectively, $e = \text{diag}\{e_i^{(p_1, p_2, h)}\}$ and $E = \text{diag}\{e_i^{(h_1, h_2, p)}\}$ are the unperturbed energies in the P and Q spaces. By solving the secular equation (10), one obtains the pole ω_n and corresponding spectroscopic amplitudes X^n defined in Eq. (8)

3 Renormalization of bare nuclear forces

Since 1980s, several modern nuclear forces have been developed based on the fundamental symmetries of nuclear interaction. The local potential Argonne V_{18} [12] is established with all two-body operators that obey the symmetries of angular momentum, parity, and isospin. The parameters are fitted to reproduce low-energy phase shifts and the deuteron binding energy. The CD-Bonn potential [13] is defined in the momentum space and based on the one-boson-exchange mechanism. Chiral interactions are built upon the chiral symmetry breaking of low-energy QCD [14,15]. The soft potential JISP is based on the inverse scattering method [16,17]. All realistic nuclear forces have a similar long-range behavior as they are fitted to low-energy phase shifts (typically up to 350 MeV). The short-range parts of nuclear forces can be however different. A nuclear system is typically dominated by the long-range and intermediate-range parts of nuclear forces. However the couplings between different energy scales of the nuclear force need to be treated properly in order to preserve the symmetries and favour a better perturbation behavior in the system. Some bare forces can be considered as already renormalized [18] and therefore can be directly applied to nuclear structure calculations.

Advanced computer resources make it possible to use bare NN forces in *ab initio* calculations within large model spaces. However the computational burden is remarkably reduced by using renormalization procedures without losing the low-energy physics. Several renormalizing techniques are available. The G -matrix [19,20] sums up the ladder diagrams to infinite orders. The similarity renormalization group (SRG) [21] uses a series of similarity transformations to reduce off-diagonal matrix elements that are responsible for the coupling between the low-energy and high-energy components of nuclear forces. The unitary correlation operator method (UCOM) [22,23] introduces short-range central and tensor correlations into the uncorrelated many-body states by a unitary transformation. The $V_{\text{low-}k}$ approach uses the Lee–Suzuki transformation to decouple the high and low momenta in nuclear forces. By utilizing the similarity transformation, the effective interaction can be decoupled into low- and high-momentum parts thus leading to a faster convergence of calculations. However, the reduction of the model space always generates many-body forces originating from the high-momentum contributions of nuclear force. It has been found that the effects of induced many-body forces are dependent on the model space cutoff. One may find an optimal truncation to neglect the many-body forces. In the present study,

we use the N³LO and CD-Bonn forces. The NN potential is renormalized with the Okamoto–Lee–Suzuki transformation in momentum space [24].

Let H be a full Hamiltonian H with a set of eigenvalues E_k and eigenvectors $|k\rangle$,

$$H|k\rangle = E_k|k\rangle. \quad (13)$$

In practice, H is the Hamiltonian of a certain channel in momentum space or center-of-mass harmonic oscillator basis. The main purpose is to choose a model space P spanned with d vectors $|\alpha_P\rangle$ and the complementary space Q spanned by $|\alpha_Q\rangle$, $P + Q = 1$. We seek for a unitary transformation $\mathcal{H} = e^{-\omega} H e^{\omega}$ resulting in zero coupling between P and Q spaces, i. e.,

$$Q e^{-\omega} H e^{\omega} P = 0. \quad (14)$$

Equation (14) is the decoupling condition; the transformation operator ω is known as a correlation operator which is determined by solving Eq. (14). According to the definition of ω that recovers the Q -space component from the projected wave function, one has

$$P\omega P = Q\omega Q = P\omega Q = 0, \quad \omega^2 = 0, \quad (15)$$

and a linear form of the transformation is $e^{\omega} = 1 + \omega$. Due to the decoupling equation, the effective low-energy interaction which reproduces the d states of the full Hamiltonian, can be written as

$$\begin{aligned} P\mathcal{H}P &= E_k P|k\rangle, \\ \omega P|k\rangle &= Q|k\rangle. \end{aligned} \quad (16)$$

To obtain ω explicitly, one can use

$$\langle\alpha_Q|k\rangle = \sum_{\alpha_P} \langle\alpha_Q|\omega|\alpha_P\rangle \langle\alpha_P|k\rangle. \quad (17)$$

One can find that ω is just a wave operator and corresponds to infinite order corrections to the projected wave function in perturbation. In matrix form, one can rewrite ω in terms of vector components generated by a diagonalization of the full Hamiltonian,

$$\langle\alpha_Q|\omega|\alpha_P\rangle = \sum_{k \in \mathcal{K}} \langle\alpha_Q|k\rangle \langle\tilde{k}|\alpha_P\rangle, \quad (18)$$

where $\langle\tilde{k}|\alpha_P\rangle$ is the biorthogonal vector to a projected P -space state vector, i. e., $\sum_{\alpha_P} \langle\tilde{k}|\alpha_P\rangle \langle\alpha_P|k'\rangle = \delta_{kk'}$. Once the transformation operator ω is constructed, a Hermitian effective Hamiltonian can be found as [24]

$$H_{eff} = \frac{P + P\omega^\dagger Q}{\sqrt{P(1 + \omega^\dagger\omega)P}} H \frac{Q\omega P + P}{\sqrt{P(1 + \omega^\dagger\omega)P}}. \quad (19)$$

The unitary transformation is not unique. A detailed discussion can be found in Ref. [25].

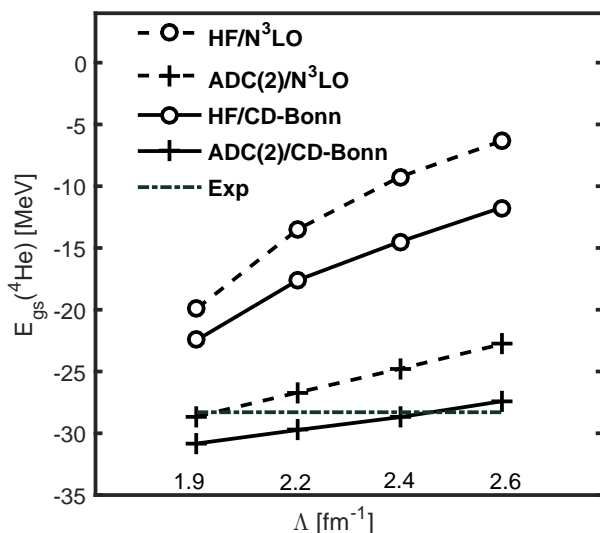


Figure 3: Hartree-Fock and Green's function calculations of ${}^4\text{He}$ with N³LO and CD-Bonn NN potentials. The Green's function approach utilizes the ADC method for solving the Dyson equation.

4 Calculations and discussion

In order to investigate high-momentum contributions in the N³LO and CD-Bonn NN potentials, we renormalize the bare forces with $V_{\text{low-}k}$ procedure with the momentum space cutoff Λ varying from 1.9 fm^{-1} to 2.6 fm^{-1} . The N³LO interaction should be accompanied by a generic three-body force which contains counter-terms in renormalization of the two-body part. An additional three-body force originates due to the $V_{\text{low-}k}$ procedure used for the further reduction of model space. In our calculations the induced three-body force is neglected. However, as we increase the momentum cutoff, the Hartree-Fock calculations of ${}^4\text{He}$ result in decrease of the binding energy (Fig. 3). This result stems from the fact that the short-range repulsive part of the nuclear forces becomes stronger. As discussed above, by including configuration interaction in the Green's function, we can obtain the correct binding energy. We see that the Green's function calculations provide a much better convergence than the HF calculations. Figure 4 displays the convergence of HF and Green's function calculations with respect to $\hbar\omega$. A good convergence is obtained in both the HF and Green's function methods, but the Green's function provides a much better binding energy as compared with the experimental data. This result implies that high-order contributions which are beyond the HF are important.

5 Conclusion

Starting with realistic nucleon-nucleon interactions and modern renormalization technique, we performed *ab initio* calculations of ${}^4\text{He}$ with the Green's function method. High-order correlations can be well described by including the $2p1h$ and $2h1p$ configurations. In order to consider short-range correlations, one has to include higher-order terms in the self-energy calculations. In addition, the induced three-body force has to be treated exactly.

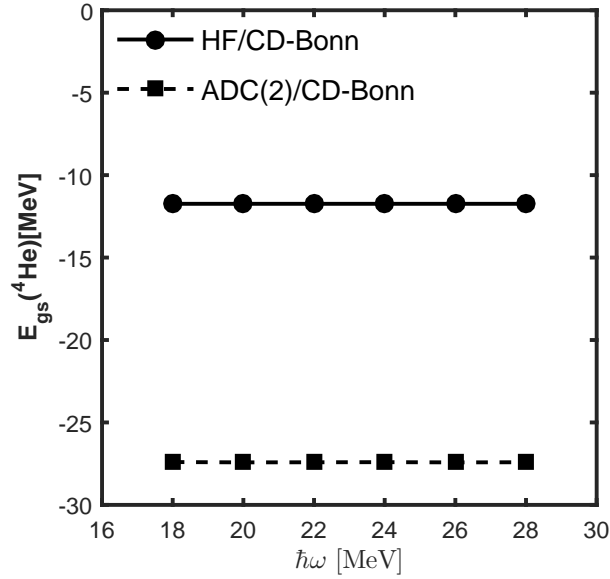


Figure 4: Hartree–Fock and Green’s function calculations of ^4He with CD-Bonn NN potential with various $\hbar\omega$ values and $\Lambda = 2.6 \text{ fm}^{-1}$.

References

- [1] X. B. Wang and G. X. Dong, *Sci. China Phys. Mech. Astron.* **58**(10), 102001 (2015).
- [2] Y. X. Liu, S. Y. Yu and C. W. Shen, *Sci. China Phys. Mech. Astron.* **58**(1), 012001 (2015).
- [3] Q. H. Mo, M. Liu, L. C. Cheng, N. Wang, *Sci. China Phys. Mech. Astron.* **58**(8), 082001 (2015).
- [4] X. H. Fan, J. M. Dong and W. Zuo, *Sci. China Phys. Mech. Astron.* **58**(6), 062002 (2015).
- [5] G. X. Dong, X. B. Wang and S. Y. Yu, *Sci. China Phys. Mech. Astron.* **58**(11), 112004 (2015).
- [6] K. P. Xie, W. Y. Ke, W. Y. Liang, X. M. Fu, C. F. Jiao, J. C. Pei and F. R. Xu, *Sci. China Phys. Mech. Astron.* **57**(2), 189 (2014).
- [7] P. Navrátil, J. P. Vary and B. R. Barrett, *Phys. Rev. C* **62**, 054311 (2000).
- [8] S. Fujii, R. Okamoto and K. Suzuki, *J. Phys. Conf. Ser.* **20**, 83 (2005).
- [9] A. Carbone, A. Cipollone, C. Barbieri, A. Rios and A. Polls, *Phys. Rev. C* **88**, 054326 (2013).
- [10] K. Amir-Azimi-Nili, H. Mütter, L. D. Skouras and A. Polls, *Nucl. Phys. A* **604**, 245 (1996).
- [11] H. Mütter and L.D. Skouras, *Nucl. Phys. A* **555**, 541 (1993).
- [12] R. B. Wiringa, V. G. J. Stoks and R. Schiavilla, *Phys. Rev. C* **51**, 38 (1995).

-
- [13] R. Machleidt, Phys. Rev. C **63**, 024001 (2001).
 - [14] D. R. Entem and R. Machleidt, Phys. Rev. C **68**, 041001 (2003).
 - [15] R. Machleidt and D. Entem, Phys. Rep. **503**, 1 (2011).
 - [16] A. M. Shirokov, A. I. Mazur, S. A. Zaytsev, J. P. Vary and T. A. Weber, Phys. Rev. C **70**, 044005 (2004).
 - [17] A. M. Shirokov, J. P. Vary, A. I. Mazur, S. A. Zaytsev and T. A. Weber, Phys. Lett. B **621**, 96 (2005).
 - [18] I. Stetcu, J. Rotureau, B. R. Barrett and U. van Kolck, J. Phys. G **37**, 064033 (2010).
 - [19] M. Borromeo, D. Bonatsos, H. Müther and A. Polls, Nucl. Phys. A **539**, 189 (1992).
 - [20] M. Hjorth-Jensen, T. T. Kuo and E. Osnes, Phys. Rep. **261**, 125 (1995).
 - [21] S. K. Bogner, R. J. Furnstahl and R. J. Perry, Phys. Rev. C **75**, 061001 (2007).
 - [22] R. Roth, H. Hergert, P. Papakonstantinou, T. Neff and H. Feldmeier, Phys. Rev. C **72**, 034002 (2005).
 - [23] R. Roth, T. Neff and H. Feldmeier, Prog. Part. Nucl. Phys., **65**, 50 (2010).
 - [24] K. Suzuki and R. Okamoto, Progr. Theor. Phys. **70**, 439 (1983).
 - [25] J. D. Holt, T. T. S. Kuo and G. E. Brown, Phys. Rev. C **69**, 034329 (2004).

Experiments of Few-Nucleon Scattering and Three-Nucleon Forces

Kimiko Sekiguchi

Department of Physics, Tohoku University, Sendai, 980-8578, Japan

Abstract

We have measured a complete set of deuteron analyzing powers in deuteron-proton elastic scattering at 190, 250, and 294 MeV/nucleon. The obtained data are compared with Faddeev calculations based on modern nucleon-nucleon forces together with the Tucson–Melbourne’99 and UrbanaIX three-nucleon forces. The data are also presented with the calculations based on the N4LO NN potentials of the chiral effective field theory.

Keywords: *Three-nucleon force, $^1\text{H}(d, d)^1\text{H}$ reaction, iT_{11} , T_{20} , T_{21} , T_{22}*

1 Introduction

One of the main interests in nuclear physics is understanding of forces acting between nuclear constituents. A hot topic in the study of nuclear forces is to clarify the roles of three-nucleon forces (3NFs) in nuclei, and to describe various phenomena of nuclei by explicitly taking into account nucleon-nucleon (NN) interactions combined with 3NFs. The 3NFs arise naturally in the standard meson exchange picture [1] as well as in the framework of chiral effective field theory (χ EFT) which has a link to QCD [2, 3].

The first evidence for a 3NF was found in the three-nucleon bound states, ^3H and ^3He [4, 5]. The binding energies of these nuclei are not reproduced by exact solutions of three-nucleon Faddeev equations employing modern NN forces only, i. e., AV18 [6], CD-Bonn [7], Nijmegen I, II [8]. The underbinding of ^3H and ^3He is removed by adding a 3NF, mostly based on 2π -exchange, acting between three nucleons [4, 5, 9]. The importance of 3NFs is further supported by the binding energies of light-mass nuclei, and by the empirical saturation point of symmetric nuclear matter. *Ab initio* microscopic calculations of light mass nuclei, such as Green’s Function Monte Carlo [10] and no-core shell model calculations [11], highlight the necessity of including 3NFs to explain the binding energies and low-lying levels of these nuclei. As for the density of symmetric nuclear matter, it has been reported that all NN potentials provide saturation at too high density, and the inclusion of a short-range repulsive 3NF is a possibility to shift the theoretical results to the empirical point [12]. In the past decade, low energy scattering, binding energies of light [13] and medium mass nuclei [14, 15] and nuclear matter [16] have been extensively studied also in

Proceedings of the International Conference ‘Nuclear Theory in the Supercomputing Era — 2016’ (NTSE-2016), Khabarovsk, Russia, September 19–23, 2016. Eds. A. M. Shirokov and A. I. Mazur. Pacific National University, Khabarovsk, Russia, 2018, p. 60.

<http://www.ntse-2016.khb.ru/Proc/Sekiguchi.pdf>.

the framework of chiral effective field theory (χ EFT). In all these investigations, it became evident that 3NFs are taken as the key element to understand various nuclear phenomena. Therefore, they should be investigated in a wide momentum region to understand their properties in detail.

In order to study the dynamical aspects of 3NFs, such as momentum, spin, and isospin dependences, the three-nucleon scattering system is an attractive probe because various kinematical conditions allow to measure not only differential cross sections but also a rich set of polarization observables. The importance of 3NFs in three-nucleon scattering has been shown in the Nd elastic scattering for the first time in Ref. [17]. Clear signals from 3NFs has been found around the cross section minimum occurring at c. m. angle $\theta_{c.m.} \approx 120^\circ$ for incident energies above 60 MeV/nucleon. Since then the pd/nd scattering experiments at 60–200 MeV/nucleon were performed at various facilities, e. g., RIKEN, RCNP, KVI, and IUCF, providing precise data of the cross sections as well as various types of spin observables [18]. At RIKEN we performed the measurements of the cross sections and spin observables with the polarized deuteron beams at the incident energies up to 135 MeV/nucleon [19]. Recently we extended the measurements at the RIKEN RI Beam Factory (RIBF) with the polarized deuteron beams to the energies of 250 and 300 MeV/nucleon which are slightly above the pion emission threshold energy of 210 MeV [20, 21].

In the following sections the recent achievements in the study of 3NFs via measurements of the dp scattering at the RIKEN RIBF are discussed.

2 Experiment at RIKEN

At the RIBF the vector and tensor polarized deuteron beam was provided by the polarized ion source and was accelerated by the AVF, RRC and SRC. The measurement for elastic dp scattering was performed with the detector system BigDpol which was installed at the extraction beam line of the SRC. A polyethylene (CH_2) target with a thickness of 330 mg/cm² was used as a hydrogen target. In the BigDpol four pairs of plastic scintillators coupled with photo-multiplier tubes were placed symmetrically in the directions of azimuthal angles to left, right, up and down. Scattered deuterons and recoil protons were detected in a kinematical coincidence condition by each pair of the detectors. The measured angles in the center of mass system are $\theta_{c.m.} = 40^\circ - 160^\circ$. In the experiment the deuteron beams were stopped in the Faraday cup which was installed at the focal plane F0 of the BigRIPS spectrometer.

The beam polarizations were monitored continuously with a beam line polarimeter Dpol prior to acceleration by the SRC using the reaction of elastic dp scattering at 70, 90 and 100 MeV/nucleon. At the RIKEN RIBF the single-turn extractions were available for all cyclotrons used for the experiments. Therefore depolarizations were expected to be small during beam acceleration. In the measurement, typical values of the beam polarizations were 80% of the theoretical maximum values.

3 Results

The obtained data of the deuteron analyzing powers iT_{11} and T_{22} at 190 and 250 MeV/nucleon are shown in Fig. 1 with open circles together with the previously reported data at 135 MeV/nucleon [19]. Statistical errors are only shown. The data

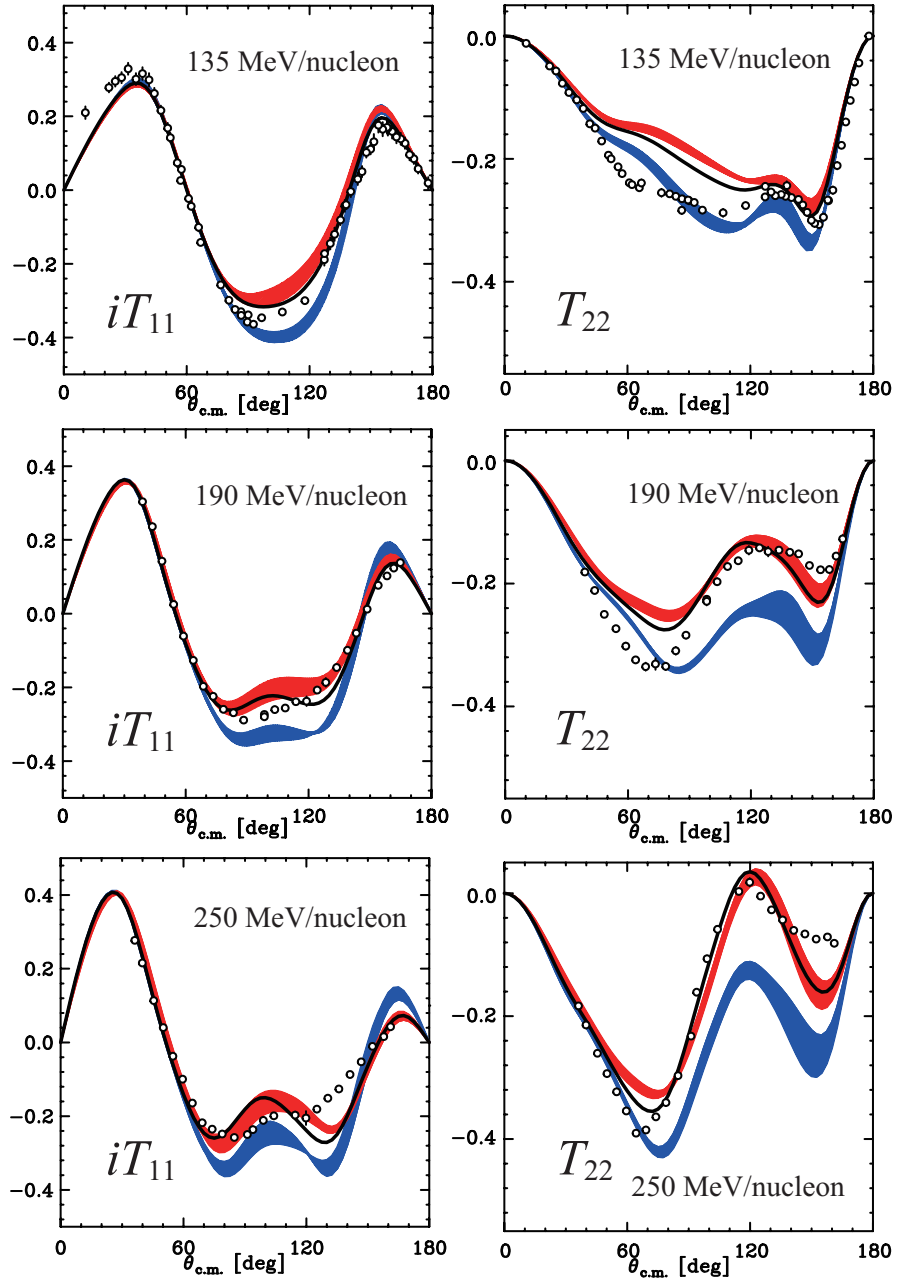


Figure 1: Deuteron analyzing powers iT_{11} , T_{22} for elastic Nd scattering at 135, 190 and 250 MeV/nucleon. See the text for the descriptions of calculations.

are compared with the Faddeev calculations based on the modern nucleon-nucleon forces combined with the three-nucleon forces. The red (blue) bands in the figure are the Faddeev calculations with (w/o) Tucson–Melbourne’99 (TM99) 3NF [22] based on the modern NN potentials, namely CDBonn [7], AV18 [23], Nijmegen I and II [8].

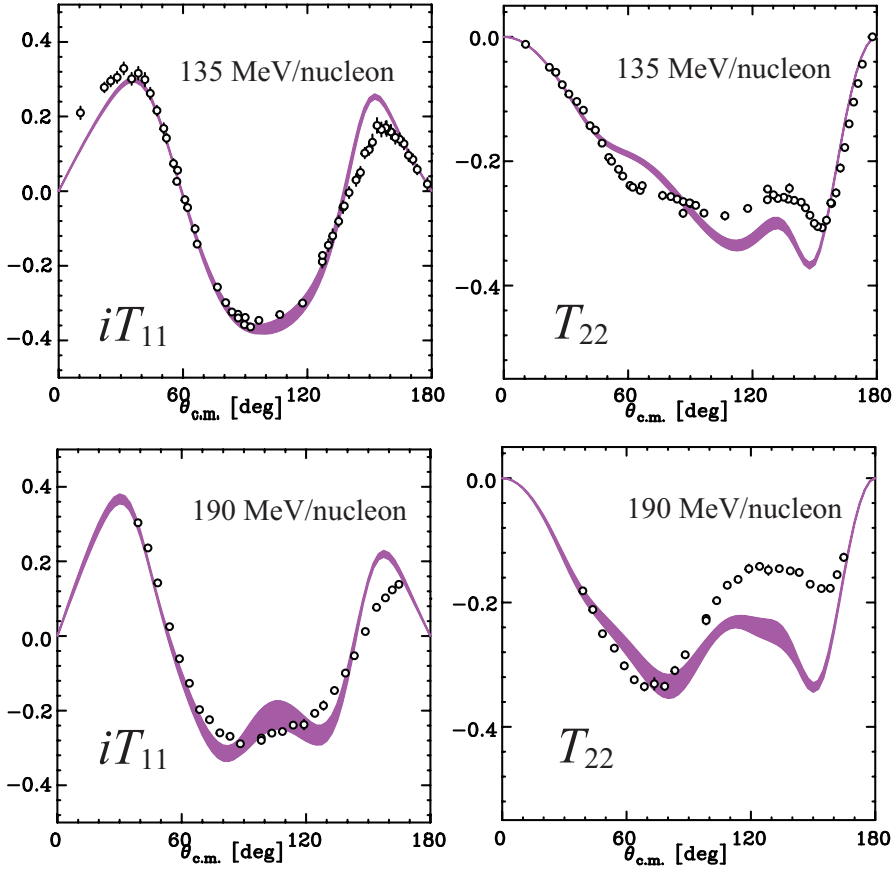


Figure 2: Deuteron analyzing powers iT_{11} , T_{22} for elastic Nd scattering at 135 and 190 MeV/nucleon. See the text for the descriptions of calculations.

The solid lines are the calculations with the Urbana IX 3NF [24] and the AV18 NN potential.

For the vector analyzing power iT_{11} the discrepancies between the data and the predictions based on 2NFs (blue bands) are seen at the angles $\theta_{c.m.} \sim 120^\circ$. At 135 and 190 MeV/nucleon, the data have good agreements to the predictions with the 3NFs while at 250 MeV/nucleon a discrepancy exists at backward angles $\theta_{c.m.} \gtrsim 120^\circ$. The tensor analyzing power T_{22} reveals a different energy dependence from that of iT_{11} . At 135 MeV/nucleon adding the 3NFs worsens the description of data in a large angular region. It is contrary to what happens at 190 and 250 MeV/nucleon, where large 3NF effects are supported by the measured data. The results of comparison shows that the 3NF is definitely needed in Nd elastic scattering. However the spin dependent parts of the 3NF may be deficient.

It is interesting to see how the potential of the chiral effective field theory (χ EFT) describes the deuteron analyzing powers for the dp elastic scattering. In Fig. 2 the data are compared with the calculations based on the χ EFT N4LO NN potentials [25]. The vector analyzing power iT_{11} data are well described by the χ EFT N4LO NN potential, while large discrepancies are found for the tensor analyzing power T_{22} . In

order to see how χ^{EFT} 3NFs describe the data, the theoretical treatments are now in progress [26].

4 Summary and Outlook

3NFs are now accepted as the key elements in understanding various nuclear phenomena, e. g., properties of light mass nuclei and equation of state for nuclear matter. The Nd scattering data provide rich sources to explore the properties of 3NFs such as momentum and spin dependence. In this talk, the experiments performed with polarized deuteron beams at RIKEN are presented and the recent achievements of the study of 3NFs via dp scattering at 100–300 MeV/nucleon are discussed. The energy and angular dependent results of the cross sections as well as the polarization observables show that (1) clear signatures of the 3NF effects are found in the cross section, (2) the spin dependent parts of the 3NFs may be deficient, and (3) shorter-range components of the 3NFs are probably required for the description of the cross sections as well as of the spin observables at backward angles with contributions increasing with incident energies.

As the next step of 3NF study in the few nucleon scattering it would be interesting to see new theoretical approaches, e. g., an inclusion of 3NFs other than of the 2π -exchange type. Recently the calculations based on the χ EFT potentials become available for the Nd scattering up to 200 MeV/nucleon in which the NN forces up to the next-to-next-to-next-to-next-to leading order are taken into account [25]. The results show possible signatures of 3NF effects at backward angles. Theoretical analyses with 3NFs which include not only the 2π -exchange type but also other various diagrams of the 3NFs, are now in progress. Together with this, it should be also mentioned that careful treatments for the effects of π -emission might be necessary for Nd scattering around and above the π -creation threshold energy. So far we have expected that the cross sections for the π emission are quite small in analogy with the total cross section of the pp scattering [27].

Experimentally, it is interesting to measure spin correlation coefficients as well as polarization transfer coefficients for elastic dp scattering at higher energies 200–400 MeV/nucleon. Various kinematic configurations of the exclusive pd breakup reactions should also be measured in order to study the properties of 3NFs as well as relativistic effects. As a first step from few- to many-body systems it is interesting to extend the measurements to $4N$ scattering systems, e. g., $p + {}^3\text{He}$ scattering, which would provide a valuable source of information on 3NFs including their isospin dependences.

Acknowledgments

The author would like to thank the collaborators for the experiments performed with the polarized deuteron beams at RIKEN RI Beam Factory. She is also grateful to the strong supports from the theorists, H. Witała, W. Glöckle, H. Kamada, J. Golak, A. Nogga, R. Skibiński, P. U. Sauer, A. Deltuva, and A. C. Fonseca.

References

- [1] J. Fujita and H. Miyazawa, *Progr. Theor. Phys.* **17**, 360 (1957).
- [2] U. van Kolck, *Phys. Rev. C* **49**, 2932 (1994).
- [3] E. Epelbaum, H.-W. Hammer and U.-G. Meißner, *Rev. Mod. Phys.* **81**, 1773 (2009).
- [4] C. R. Chen *et al.*, *Phys. Rev. C* **33**, 1740 (1986).
- [5] T. Sasakawa and S. Ishikawa, *Few-Body Syst.* **1**, 3 (1986).
- [6] R. B. Wiringa *et al.*, *Phys. Rev. C* **51**, 38 (1995).
- [7] R. Machleidt, *Phys. Rev. C* **63**, 024001 (2001).
- [8] V. G. J. Stoks *et al.*, *Phys. Rev. C* **49**, 2950 (1994).
- [9] A. Nogga *et al.*, *Phys. Rev. C* **65**, 054003 (2002).
- [10] S. C. Pieper *et al.*, *Phys. Rev. C* **64**, 014001 (2001).
- [11] P. Navrátil and W. E. Ormand, *Phys. Rev. C* **68**, 034305 (2003).
- [12] See, for example, A. Akmal *et al.*, *Phys. Rev. C* **58**, 1804 (1998).
- [13] E. Epelbaum *et al.*, *Phys. Rev. C* **66**, 064001 (2002).
- [14] S. Binder *et al.*, *Phys. Rev. C* **87**, 021303 (2013).
- [15] T. A. Lähde *et al.*, arXv.1311.0477 [nucl-th] (2013).
- [16] K. Hebeler *et al.*, *Phys. Rev. C* **83**, 031301 (2011).
- [17] H. Witala *et al.*, *Phys. Rev. Lett.* **81**, 1183 (1998).
- [18] See references in N. Kalantar-Nayestanaki *et al.*, *Rep. Prog. Phys.* **75**, 016301 (2012).
- [19] N. Sakamoto *et al.*, *Phys. Lett. B* **367**, 60 (1996); H. Sakai *et al.*, *Phys. Rev. Lett.* **84**, 5288 (2000); K. Sekiguchi *et al.*, *Phys. Rev. C* **65**, 034003 (2002); K. Sekiguchi *et al.*, *Phys. Rev. C* **70**, 014001 (2004); K. Sekiguchi *et al.*, *Phys. Rev. Lett* **95**, 162301 (2005).
- [20] K. Sekiguchi *et al.*, *Phys. Rev. C* **83**, 061001 (2011).
- [21] K. Sekiguchi *et al.*, *Phys. Rev. C* **89**, 064007 (2014).
- [22] S. A. Coon and H. K. Han, *Few Body Syst.*, **30**, 131 (2001).
- [23] R. B. Wiringa *et al.*, *Phys. Rev. C* **51**, 38 (1995).
- [24] B. S. Pudliner *et al.*, *Phys. Rev. C* **56**, 1720 (1997).
- [25] S. Binder *et al.*, *Phys. Rev. C* **93**, 044002 (2016).
- [26] E. Epelbaum, private communications.
- [27] See, for example, K. A. Olive *et al.* (Particle Data Group), *Chin. Phys. C* **38**, 090001 (2014).

Approach to Computation of Few/Many-Body Multichannel Reactions

V. D. Efros

*National Research Centre “Kurchatov Institute”, 123182 Moscow, Russia
National Research Nuclear University MEPhI, Moscow, Russia*

Abstract

A method to calculate reactions in quantum mechanics is outlined. It is advantageous, in particular, in problems with many open channels of various nature, i. e., when the energy is not low. Within this method, there is no need to specify reaction channels in a dynamics calculation. These channels come into play at merely the kinematics level and only after the dynamics calculation is done. Such a calculation is of a bound-state type and continuum spectrum states never enter the game.

Keywords: *Multichannel reactions; microscopic calculations; method of integral transforms*

1 Overview

An approach reviewed in this paper is advantageous, in particular, in problems with many open channels of various nature, i. e., when the energy is not low. Conventional approaches dealing with continuum wave functions are impractical in such problems at least at $A > 3$. The approach was successfully applied in nuclear reaction problems with $3 \leq A \leq 7$ and also recently for $A = 12$ and 16 proceeding from NN or $NN + NNN$ forces. Many cases of reactions induced by a perturbation, i. e., electromagnetic or weak interaction, were considered. Both inclusive (mostly) and exclusive processes were studied. Reactions induced by strong interaction still were not considered although this can be done in a similar way, see below.

The main features of the approach are the following. In a dynamics calculation within its framework there is no need to specify reaction channels at all. These come into play at merely the kinematics level and only after the dynamics calculation is done. Such a calculation is of a bound-state type.

Correspondingly, continuum spectrum states never enter the game. In place of them, “response-like” functions of the type of Eq. (1) below, are the basic ingredients of the approach. Reaction observables are expressed in terms of these functions as quadratures, see Eqs. (3)–(6) below. It should also be noted that, in some problems of importance, the quantities of the form of Eq. (1) are of interest themselves representing observable response functions for inclusive perturbation-induced reactions.

Proceedings of the International Conference ‘Nuclear Theory in the Supercomputing Era — 2016’ (NTSE-2016), Khabarovsk, Russia, September 19–23, 2016. Eds. A. M. Shirokov and A. I. Mazur. Pacific National University, Khabarovsk, Russia, 2018, p. 66.

<http://www.ntse-2016.khb.ru/Proc/Efros.pdf>

The “response-like” functions of the form of Eq. (1) are obtained not in terms of complicated continuum spectrum states entering their definition but via a bound-state type calculation. As the first step, an integral transform of such a function is performed. This transform is expressed in a closed form and represents a “continuum sum rule” depending on a σ parameter, see Eq. (12). It is evaluated via a bound-state type calculation. As the next step, this sum rule is considered as an equation determining the “response-like” function, i. e., its inversion is performed. Once this is done, the above mentioned quadratures giving the reaction observables are readily obtained.

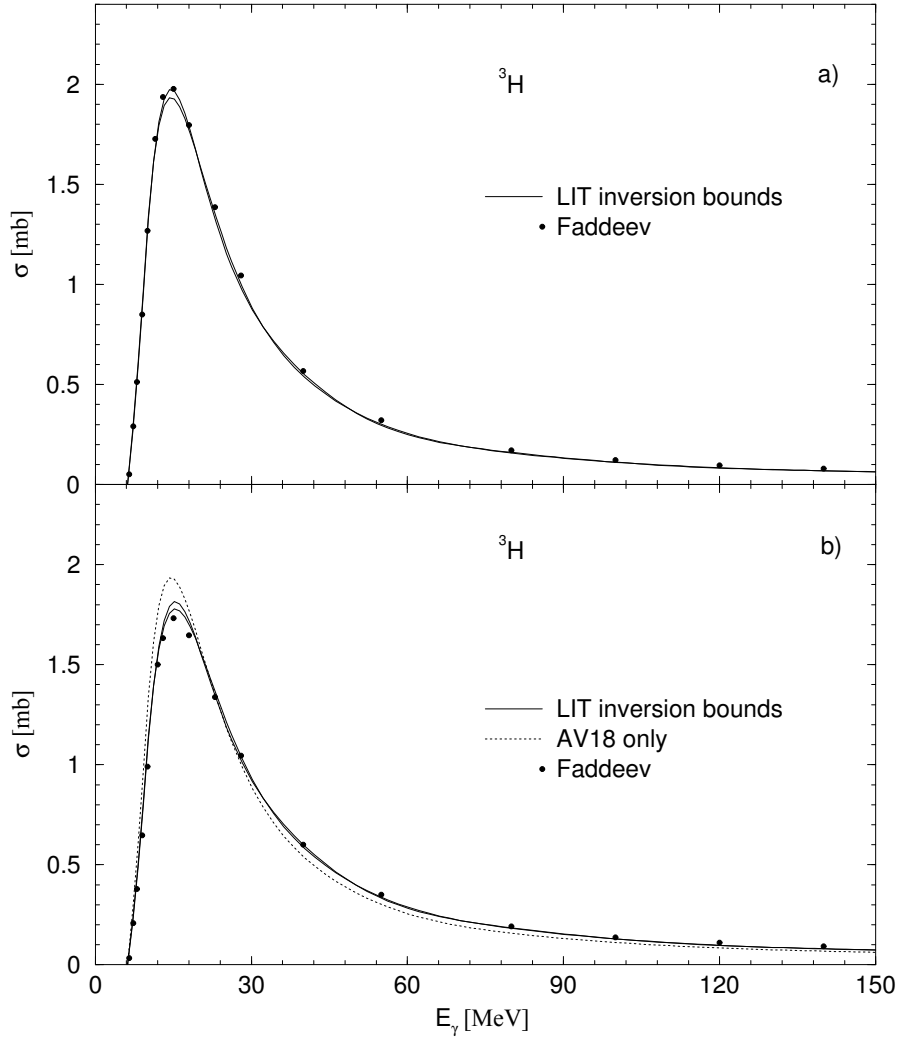


Figure 1: Comparison of Faddeev and LIT results for the total ^3H photoabsorption cross section in unretarded dipole approximation a) with NN (AV18) force only and b) with NN (AV18) + NNN (UrbIX) force. Dots are the Faddeev results and two curves represent the bounds for the LIT inversion. Dotted curve in b) is the result with AV18 only.

Thus, as claimed above, a specification of reaction channels in the dynamics calculation and dealing with continuum wave functions are avoided in this approach. A criterion of accuracy is the stability of the response-like function obtained.

In addition to the stability checks, comparisons with more conventional calculations that deal with continuum wave functions, have been performed. In the benchmark paper [1], the Faddeev results for the ${}^3\text{H}$ photoabsorption total cross section are compared with the results [2] obtained via the above described approach. In the framework of this approach, the Lorentz integral transform (LIT), see the next section, was used. The Argonne V18 NN interaction and the Urbana IX NNN potential have been employed. The results are shown in Fig. 1.

A complete agreement is observed in the case when only the NN force is retained, while in the case when the NNN force is added, such an agreement is observed everywhere except for the peak region where a slight difference is present. In Ref. [3] the LIT results in the same problem have been obtained employing expansions over two different bases at solving the dynamics equation, the correlated hyperspherical basis (CHH) and the effective interaction hyperspherical basis (EIHH). The results are shown in Fig. 2.

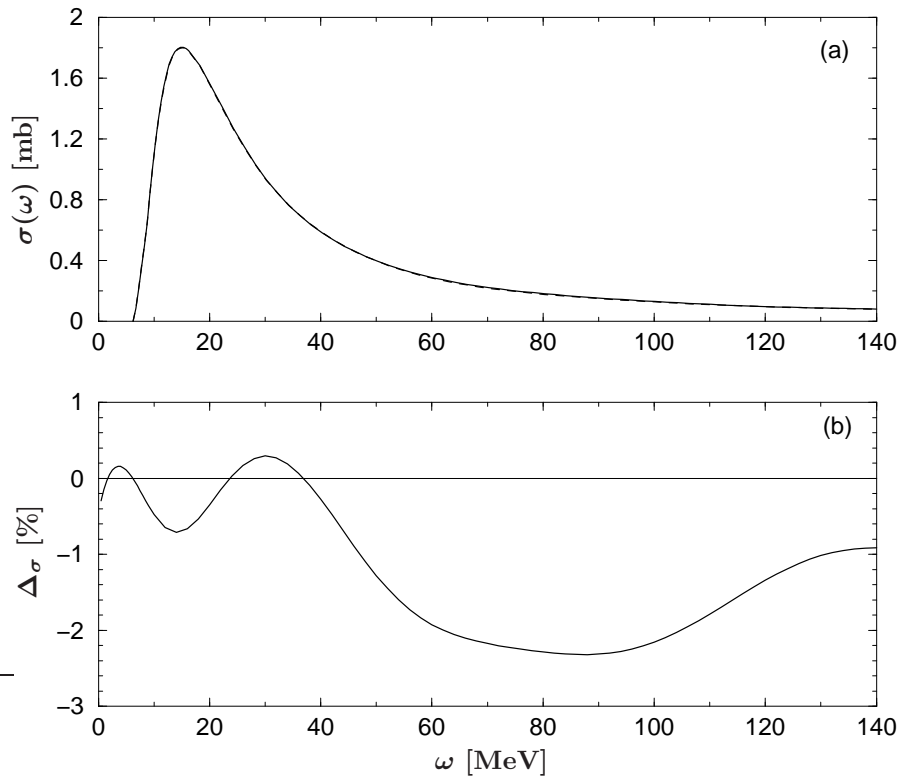


Figure 2: (a) The same cross section calculated with the same $NN + NNN$ force as in Fig. 1(b) ($E_\gamma \rightarrow \omega$). It is obtained with the help of LIT at solving the dynamics equation in two ways. Full and dashed curves represent the results gained using the CHH and EIHH expansions, respectively. (b) Relative difference $\Delta_\sigma = [\sigma(\text{CHH}) - \sigma(\text{EIHH})]/\sigma(\text{CHH})$ between these cross sections.

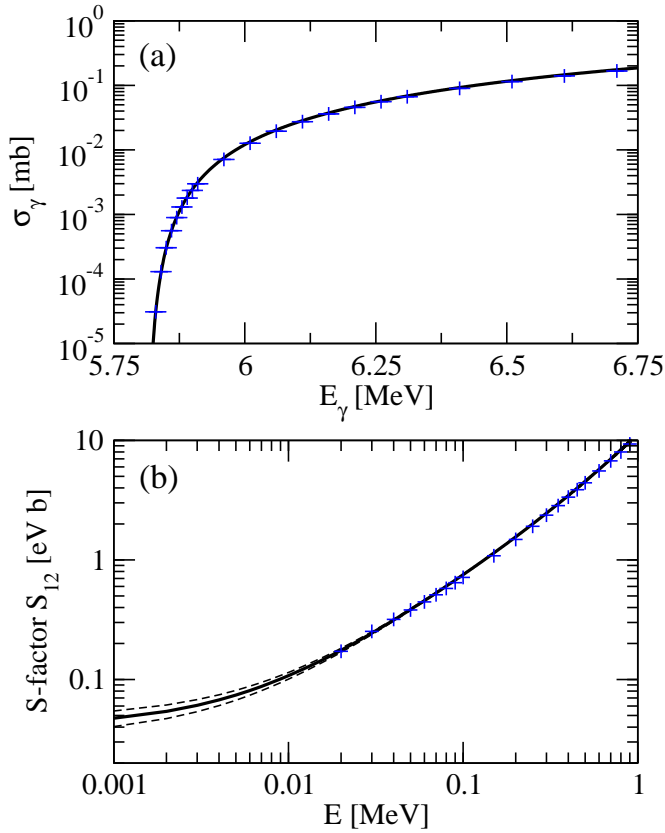


Figure 3: (a) Total ${}^3\text{He}$ photoabsorption cross section in the threshold region calculated with the MT NN potential. Full curve — LIT results; plus signs — direct calculation utilizing explicit continuum wave functions. (b) The same as (a) but rescaled in order to determine the S -factor. The inversion error bounds are shown by dashed lines. E denotes the p - d relative motion energy.

These results practically coincide with each other which testifies to that the LIT results in Fig. 1(b) are accurate.

One more test [4] is presented in Fig. 3. The total cross section of the ${}^3\text{He}(\gamma, p)d$ reaction in the threshold region is calculated in two ways, by means of the LIT as discussed above, and via a direct calculation of the pd continuum wave functions. In this case, there is no real need to use the method of integral transforms since the problem is single-channel. Another point is that the problem considered is unfavorable for this method since the cross section at the threshold is tiny, and the values of the response function at such energies contribute extremely little to the integral pertaining to the corresponding integral equation (12) and therefore to the input to solving this equation. Despite this, a complete agreement of the results of two methods is observed. This is most clearly seen from Fig. 3(b) where the quickly varying Gamow factor is factored out from the cross section, and the remaining astrophysical S -factor is presented. The central Malfliet–Tjon NN potential was employed in this calculation. Let us also mention that the pd continuum wave functions that have led to the results in Fig. 3, provide the phase shifts practically indistinguishable from those of another group [5].

The basic points of the approach are presented in the next Section, and Section 3 contains further comments.

2 Basics of the method

As said above, “response-like” quantities of the type

$$R(E) = \sum_n \langle Q' | \Psi_n \rangle \langle \Psi_n | Q \rangle \delta(E - E_n) + \int d\gamma \langle Q' | \Psi_\gamma \rangle \langle \Psi_\gamma | Q \rangle \delta(E - E_\gamma) \quad (1)$$

are the basic ingredients of the approach. Here Ψ_n are bound states and Ψ_γ are continuum spectrum states. They represent a complete set of eigenstates of the Hamiltonian of a problem. The subscript γ denotes collectively a set of continuous and discrete variables labeling the states which is symbolized in the summation over integration notation. The normalizations $\langle \Psi_n | \Psi_{n'} \rangle = \delta_{n,n'}$ and $\langle \Psi_\gamma | \Psi_{\gamma'} \rangle = \delta(\gamma - \gamma')$ are adopted, so that

$$\sum_n |\Psi_n\rangle \langle \Psi_n| + \int d\gamma |\Psi_\gamma\rangle \langle \Psi_\gamma| = I, \quad (2)$$

I being the identity operator.

In the method discussed, the quantities $R(E)$ of Eq. (1) are obtained not in terms of complicated states Ψ_γ entering their definition but via a bound-state type calculation. Reaction observables are expressed in terms of $R(E)$ as quadratures.

Let us first explain the latter of these points. Consider a strong interaction induced reaction. Denote $\mathcal{A}\phi_i(E)$ and $\mathcal{A}\phi_f(E)$ the antisymmetrized “channel free-motion states”. Here the subscript i (f) refers to the initial (final) state of the reaction, $\phi_{i,f}(E)$ are products of fragment bound states and of factors describing their free relative motion [6], and \mathcal{A} denotes the operator realizing antisymmetrization with respect to identical particles ($\mathcal{A}^2 = \mathcal{A}$) [6]. Denote $\bar{\phi}_i(E) = \mathcal{A}(H - E)\phi_i(E)$ and $\bar{\phi}_f(E) = \mathcal{A}(H - E)\phi_f(E)$ where H is the Hamiltonian. One has $\bar{\phi}_i = \mathcal{A}V_i^{res}\phi_i$ and $\bar{\phi}_f = \mathcal{A}V_f^{res}\phi_f$, where $V_{i,f}^{res}$ are interactions between fragments in the initial and final states. Here it is assumed that these interactions are of a short range so that the outer parts of the long-range inter-fragment Coulomb interaction are disregarded. This point is reconsidered below.

The T matrix determining the reaction rates is [6]

$$T_{fi} = T_{fi}^{Born} + \langle \bar{\phi}_f(E) | (E - H + i\epsilon)^{-1} | \bar{\phi}_i(E) \rangle, \quad \epsilon \rightarrow +0. \quad (3)$$

Here T_{fi}^{Born} is the simple Born contribution,

$$T_{fi}^{Born} = \langle \phi_f | \bar{\phi}_i \rangle = \langle \bar{\phi}_f | \phi_i \rangle,$$

and the main problem is a calculation of the second term in Eq. (3) that includes the Green function $(E - H + i\epsilon)^{-1}$. This contribution may be presented as

$$\int dE' R_E(E') (E - E' + i\epsilon)^{-1} \equiv -i\pi R_E(E) + P \int dE' R_E(E') (E - E')^{-1}, \quad (4)$$

where

$$R_E(E') = \sum_n \langle \bar{\phi}_f(E) | \Psi_n \rangle \langle \Psi_n | \bar{\phi}_i(E) \rangle \delta(E' - E_n) + \int d\gamma \langle \bar{\phi}_f(E) | \Psi_\gamma \rangle \langle \Psi_\gamma | \bar{\phi}_i(E) \rangle \delta(E' - E_\gamma). \quad (5)$$

The quantity (5) is just of the structure of Eq. (1) (with the $E \rightarrow E'$ replacement). Thus, indeed, to calculate matrix elements of the T matrix it is sufficient to have the quantities of this structure. Once they are available, the integrations in Eq. (4) are readily done.

The amplitude of a perturbation-induced reaction is $\langle \Psi_f^- | \hat{O} | \Psi_0 \rangle$ where \hat{O} is a perturbation, Ψ_0 is an unperturbed initial bound state, and Ψ_f^- is a continuum spectrum state. To calculate this amplitude, let us substitute $\langle \Psi_f^- |$ in it by the expression [6]

$$\langle \Psi_f^- | = \langle \phi_f | + \langle \bar{\phi}_f | (E - H + i\epsilon)^{-1}.$$

Then

$$\langle \Psi_f^- | \hat{O} | \Psi_0 \rangle = \langle \phi_f | \hat{O} | \Psi_0 \rangle + \langle \bar{\phi}_f | (E - H + i\epsilon)^{-1} | \hat{O} | \Psi_0 \rangle, \quad (6)$$

and one may proceed as above with the replacement $\bar{\phi}_i \rightarrow \hat{O} \Psi_0$.

Modifications of the above relations required to incorporate the long-range inter-fragment Coulomb interaction are outlined in Ref. [7]. (If the response function itself is the objective of the calculation, the Coulomb interaction does not require a special consideration as will be seen below.) These modifications consist in changes of the Q and Q' states which include the Coulomb functions in the inner region of the relative motion of fragments. Of course, it is very easy to obtain such Coulomb functions in the case of two-fragment reaction channels.

Now let us explain the above mentioned point by calculating the quantities expressed by Eq. (1). Let us rewrite Eq. (1) as

$$R(E) = \sum_n R_n \delta(E - E_n) + f(E), \quad R_n = \langle Q' | \Psi_n \rangle \langle \Psi_n | Q \rangle, \quad (7)$$

$$f(E) = \int d\gamma \langle Q' | \Psi_\gamma \rangle \langle \Psi_\gamma | Q \rangle \delta(E - E_\gamma). \quad (8)$$

The contribution (8) includes an integration over few- or many-body continuum states Ψ_γ that are very complicated except for low energies, and the main problem is just the calculation of this contribution. If E_{thr} denotes the threshold value for the continuum state energies then $f(E)$ is different from zero at $E_{thr} \leq E < \infty$.

An easy task is the sum rule calculation. Using Eq. (2) one gets

$$\int_{E_{thr}}^{\infty} f(E) dE + \sum_n R_n = \langle Q' | Q \rangle. \quad (9)$$

Obviously, knowing the quantity (9) is not enough to reconstruct the $R(E)$ itself. To achieve this goal, let us consider "generalized sums" of the form

$$\int K(\sigma, E) R(E) dE. \quad (10)$$

These sums are equal to

$$\int d\gamma \langle Q' | \Psi_\gamma \rangle K(\sigma, E_\gamma) \langle \Psi_\gamma | Q \rangle + \sum_n \langle Q' | \Psi_n \rangle K(\sigma, E_n) \langle \Psi_n | Q \rangle. \quad (11)$$

Since Eq. (2) is valid, this quantity is equal to $\langle Q' | K(\sigma, H) | Q \rangle$ where, as above, H is the Hamiltonian of a problem. Thus one comes to the relation

$$\int_{E_{thr}}^{\infty} K(\sigma, E) f(E) dE + \sum_n K(\sigma, E_n) R_n = \Phi(\sigma), \quad \Phi(\sigma) \equiv \langle Q' | K(\sigma, H) | Q \rangle, \quad (12)$$

where $f(E)$ and R_n are the continuous part and discrete contributions to the response-like function $R(E)$, see Eqs. (8) and (7). Since this relation is valid for any σ , it may be considered as an equation to determine $R(E)$, i. e., $f(E)$ and R_n , provided that one is able to calculate the quantity $\langle Q' | K(\sigma, H) | Q \rangle$.

3 Further comments

Thus an equation of the form given by Eq. (12) is to be solved. First, one needs to calculate the right-hand side input. If one is able to diagonalize the Hamiltonian on a sufficiently big subspace of basis functions this can be readily done. In this case, one can use an approximation of the type

$$\langle Q' | K(\sigma, H) | Q \rangle \simeq \sum_{n=1}^N \langle Q' | \varphi_n^N \rangle K(\sigma, E_n^N) \langle \varphi_n^N | Q \rangle. \quad (13)$$

Here N is the dimensionality of the subspace and other notations are obvious. Suppose, for example, that the kernel $K(\sigma, E) = \exp[-(\sigma - E)^2/\sigma_0^2]$ is employed. At a given accuracy of the input $\Phi(\sigma)$, smaller σ_0 values would lead to a better reproduction of details of $f(E)$ at solving Eq. (12). Indeed, at large σ_0 values, contributions to $\Phi(\sigma)$ from peculiarities of $f(E)$ are spread over large σ intervals, and sizes of these contributions may be comparable with sizes of inaccuracies in calculated $\Phi(\sigma)$. At the same time, smaller σ_0 values require use of subspaces of basis functions of higher dimensionality. Indeed, accurate $\Phi(\sigma)$ values emerge only at such sizes of these subspaces that (at σ values of significance) the energy ranges $\sigma - \sigma_0 \leq E \leq \sigma + \sigma_0$ contain sufficiently large numbers of E_n^N eigenvalues.

The right-hand side of Eq. (13) represents the result of smoothing the pseudo-response

$$\sum_{n=1}^N \langle Q' | \varphi_n^N \rangle \langle \varphi_n^N | Q \rangle \delta(E - E_n^N)$$

with the help of the smoothing function $K(\sigma, E)$. Such type smoothings were performed in the literature and their results were considered as approximations to true responses for perturbation-induced inclusive reactions. Contrary to this, within the present approach such results are not adopted as approximations to the true responses. Here they play the role of an input to the integral equation which solution provides the final true responses. This refinement makes it possible to obtain more accurate and consistent results.

At some choices of the kernel K , it is possible to calculate the input $\Phi(\sigma)$ to Eq. (12) without the diagonalization of the Hamiltonian. The simplest example is the Stieltjes kernel $K(\sigma, E) = (\sigma + E)^{-1}$ where σ is real and lies apart from the spectrum of the Hamiltonian. In this case one has

$$\Phi(\sigma) = \langle Q' | \tilde{\psi} \rangle, \quad \tilde{\psi} = (H + \sigma)^{-1} Q, \quad (14)$$

i. e., $\tilde{\psi}$ is a solution of the inhomogeneous Schrödinger-like equation

$$(H + \sigma)\tilde{\psi} = Q. \quad (15)$$

From the fact that $\langle Q|Q \rangle$ is finite it follows that the solution is localized, and such a solution is unique. Another example is the so-called Lorentz kernel,

$$K(\sigma = \sigma_R + i\sigma_I, E) = 1/[(\sigma_R - E)^2 + \sigma_I^2]. \quad (16)$$

By writing

$$\frac{1}{(\sigma_R - E)^2 + \sigma_I^2} = \frac{1}{2i\sigma_I} \left(\frac{1}{\sigma_R - E - i\sigma_I} - \frac{1}{\sigma_R - E + i\sigma_I} \right), \quad (17)$$

one reduces the calculation in this case to that with the Stieltjes complex kernels. The solutions of respective equations of the type of Eq. (15) are also localized and unique.

Since the Lorentz kernel has a limited range, the inversion of the transform is more accurate than in the case of the Stieltjes kernel at the same accuracy in the input, cf. the reasoning above. Still, if an expansion over a basis is applied to solve Eq. (15), the convergence of $\Phi(\sigma)$ in the Stieltjes case is faster than that in the Lorentz case with a small σ_I . Indeed, at $\sigma_I \rightarrow 0$, the continuum spectrum regime is recovered at σ_R values of interest belonging to the scattering line.

One more example is the Laplace kernel $K(\sigma, E) = \exp(-\sigma E)$. The corresponding input $\langle Q'|e^{-\sigma H}|Q \rangle$ may be calculated with the Green's Function Monte Carlo method.

We shall not discuss here methods of solving Eq. (12), i. e., the inversion of the transform, referring for this to the literature. Let us mention only that such an equation represents a classical "ill-posed problem" (this does not mean at all that the problem is a very difficult one!). A standard regularization procedure was applied in practical calculations and convergent results have been obtained. Still, with such a procedure, a sufficient accuracy of the input $\Phi(\sigma)$ may be harder to achieve in problems with not a small number of particles. A new method to solve Eq. (12) has been proposed recently [8]. In this method, the number of maxima and minima of the desired solution is imposed as an additional constraint. The method does not require a regularization. It has been proved that the method is convergent at least everywhere except for the points of maxima and minima of $f(E)$. Thus, apart from this restriction, the problem becomes a well-posed one with the constraint imposed. With the same approximate inputs, the method provides much more accurate results than the standard regularization procedure in simple examples considered. However its further study is still required.

The discrete contributions R_n in Eq. (12) may be calculated separately. A convenient way to do this in the cases of the Lorentz or Stieltjes transforms can be found in Ref. [7]. Another option is the following. A general algorithm for solving Eq. (12) suggests to express $f(E)$ through some parameters and to fit these parameters to $\Phi(\sigma)$. The R_n amplitudes may be included in the set of such parameters.

A limitation of the present approach is that in order to reproduce very fine details of spectra of reactions, such as widths of narrow resonances, an increased accuracy in the input $\Phi(\sigma)$ is required. The reason is the same as the discussed above in connection with Eq. (13). This feature is similar to the situation with extracting, say, widths of narrow resonances from experiments measuring scattering or reaction cross sections. However narrow resonances are usually located at low energies whereas the present method is designed for calculations of reactions with many open channels, i. e., not at low energies. Furthermore, the information on the widths of narrow resonances taken from experiment or from alternative calculations may be readily incorporated

in the algorithm of solving Eq. (12). Anyway, the inaccuracies in widths of resonances at low energies in the present method would not lead to inaccuracies at reproducing reaction spectra at higher energy. In addition, the widths of resonances in light nuclei are normally not so narrow. The width about 200 KeV of such a resonance in ${}^4\text{He}$ was reproduced in Ref. [9] with a reasonable accuracy in the framework of the present approach; see also Fig. 3 in this respect.

In conclusion, the relevant literature is listed in addition to the references above. The approach to calculate reactions described in Sec. 2 has been introduced in Ref. [10]. Its presentation here is close to Ref. [7]. The bound-state type, i. e., the sum rule calculation of the integral transforms of observable responses $R(E)$, i. e., pertaining to the inclusive perturbation-induced reactions, has been suggested in Ref. [11] in the case of the Stieltjes transform and in Ref. [12] in the case of the Laplace transform. Inversions of the transforms were not considered in those works. An alternative approach [13] in which an observable $R(E)$ is reconstructed from its moments of the type $\langle E^{-n} \rangle$, $n = 0, \dots, N$, has been also developed. The quantity of Eq. (9) represents in this case the zero moment. The subsequent moments are calculated recursively. Contrary to the above described method [10] of treatment of general type reactions, i. e., exclusive perturbation- and strong interaction-induced ones, the approach of Ref. [13] is applicable only to the inclusive perturbation-induced reactions. The described way to calculate $\Phi(\sigma)$ involving Eq. (13) was suggested in Ref. [7] (although at too restrictive conditions imposed on Q and Q'). The Lorentz transform has been introduced in the present context in Ref. [14]. Its evaluation in the form listed above was given in Ref. [7]. In Ref. [15] an efficient algorithm to calculate $\Phi(\sigma)$ by solving Eq. (15) with the help of an expansion in a series of basis functions, has been developed. In the review papers [7] and [16] the transform inversion in the framework of a conventional approach is considered. In Ref. [16] earlier applications performed with the help of the Lorentz transform are reviewed as well. Among later applications, advances in studies of heavier nuclei [17, 18] are to be mentioned.

References

- [1] J. Golak, W. Glöckle, H. Kamada, A. Nogga, R. Skibiński, H. Witała, V. D. Efros, W. Leidemann, G. Orlandini and E. L. Tomusiak, Nucl. Phys. A **707**, 365 (2002).
- [2] V. D. Efros, W. Leidemann, G. Orlandini and E. L. Tomusiak, Nucl. Phys. A **689**, 421c (2001).
- [3] N. Barnea, W. Leidemann, G. Orlandini, V. D. Efros and E. L. Tomusiak, Few-Body Syst. **39**, 1 (2006).
- [4] S. Deflorian, V. D. Efros and W. Leidemann, Few-Body Syst. **58**: 3 (2017).
- [5] A. Kievsky, *private communication* (2016).
- [6] M. Goldberger and K. Watson, *Collision theory*. Dover, New York, 2004.
- [7] V. D. Efros, Yad. Fiz. **62**, 1975 (1999) [Phys. At. Nucl. **62**, 1833 (1999)], arXiv:nucl-th/9903024 (1999).
- [8] V. D. Efros, Phys. Rev. E **86**, 016704 (2012).

-
- [9] W. Leidemann, Phys. Rev. C **91**, 054001 (2015).
- [10] V. D. Efros, Yad. Fiz. **41**, 1498 (1985) [Sov. J. Nucl. Phys **41**, 949 (1985)].
- [11] V. D. Efros, Ukr. Fiz. Zh. **25**, 907 (1980).
- [12] D. Thirumalai and B. J. Berne, J. Chem. Phys. **79**, 5029 (1983).
- [13] W. P. Reinhardt, in *Theory of applications of moment methods in many-fermion systems*, eds. B. J. Dalton *et al.* Plenum, New York, 1980, p. 129; P. W. Langhoff, *ibid.*, p. 191.
- [14] V. D. Efros, W. Leidemann and G. Orlandini, Phys. Lett. B **338**, 130 (1994).
- [15] M. A. Marchisio, N. Barnea, W. Leidemann and G. Orlandini, Few-Body Syst. **33**, 259 (2003).
- [16] V. D. Efros, W. Leidemann, G. Orlandini and N. Barnea, J. Phys. G **34**, R459 (2007).
- [17] S. Bacca, N. Barnea, G. Hagen, G. Orlandini and T. Papenbrock, Phys. Rev. Lett. **111**, 122502 (2013).
- [18] A. Lovato, S. Gandolfi, J. Carlson, S. C. Pieper and R. Schiavilla, Phys. Rev. Lett. **117**, 082501 (2016).

Energy Dependent Separable Optical Potentials for (d, p) Reactions

L. Hlophe^{a,b} and Ch. Elster^a

^a*Institute of Nuclear and Particle Physics and Department of Physics and Astronomy,
Ohio University, Athens, OH 45701, USA*

^b*National Superconducting Cyclotron Laboratory and Department of Physics and Astronomy,
Michigan State University, East Lansing, MI 48824, USA*

Abstract

An important ingredient for applications of nuclear physics to, e. g., astrophysics or nuclear energy are the cross sections for reactions of neutrons with rare isotopes. Since direct measurements are often not possible, indirect methods like (d, p) reactions must be used instead. Those (d, p) reactions may be viewed as effective three-body reactions and described with Faddeev techniques. An additional challenge posed by (d, p) reactions involving heavier nuclei is the treatment of the Coulomb force. To avoid numerical complications in dealing with the screening of the Coulomb force, recently a new approach using the Coulomb distorted basis in momentum space was suggested. In order to implement this suggestion separable representations of neutron- and proton-nucleus optical potentials, which are not only complex but also energy dependent, need to be introduced. Including excitations of the nucleus in the calculation requires a multichannel optical potential, and thus separable representations thereof.

Keywords: *Energy dependent separable representation of optical potentials, multi-channel optical potentials, nonlocal optical potentials, (d, p) reactions*

1 Introduction

Nuclear reactions are an important probe to learn about the structure of unstable nuclei. Due to the short lifetimes involved, direct measurements are usually not possible. Therefore indirect measurements using (d, p) reactions have been proposed (see, e. g., Refs. [1–3]). Deuteron induced reactions are particularly attractive from an experimental perspective since deuterated targets are readily available. From a theoretical perspective they are equally attractive because the scattering problem can be reduced to an effective three-body problem [4]. Traditionally deuteron-induced single-neutron transfer (d, p) reactions have been used to study the shell structure in stable nuclei, nowadays experimental techniques are available to apply the same approaches to exotic beams (see, e. g., Ref. [5]). Deuteron induced (d, p) or (d, n) reactions in inverse kinematics are also useful to extract neutron or proton capture

Proceedings of the International Conference ‘Nuclear Theory in the Supercomputing Era — 2016’ (NTSE-2016), Khabarovsk, Russia, September 19–23, 2016. Eds. A. M. Shirokov and A. I. Mazur. Pacific National University, Khabarovsk, Russia, 2018, p. 76.

<http://www.ntse-2016.khb.ru/Proc/Elster.pdf>

rates on unstable nuclei of astrophysical relevance. Given the many ongoing experimental programs worldwide using these reactions, a reliable reaction theory for (d, p) reactions is critical.

One of the most challenging aspects of solving the three-body problem for nuclear reactions is the repulsive Coulomb interaction. While for very light nuclei, exact calculations of (d, p) reactions based on momentum-space Faddeev equations in the Alt–Grassberger–Sandhas (AGS) [6] formulation can be carried out [7] by using a screening and renormalization procedure [8,9], this technique leads to increasing technical difficulties when moving to computing (d, p) reactions with heavier nuclei [10]. Therefore, a new formulation of the Faddeev–AGS equations which does not rely on the screening procedure, was presented in Ref. [11]. Here the Faddeev–AGS equations are cast in the momentum-space Coulomb-distorted partial-wave representation instead of the plane-wave basis. Thus all operators, specifically the interactions in the two-body subsystems, must be evaluated in the Coulomb basis, which is a nontrivial task (performed recently for the neutron-nucleus interaction [12]). The formulation of Ref. [11] requires the interactions in the subsystems to be of separable form.

Separable representations of the forces between constituents forming the subsystems in the Faddeev approach have a long tradition, specifically when considering the nucleon-nucleon (NN) interaction (see, e. g., Ref. [13–15]) or meson-nucleon interactions [16,17]. Here the underlying potentials are Hermitian, and a scheme for deriving separable representations suggested by Ernst–Shakin–Thaler [18] (EST) is well suited, specifically when working in momentum space. It has a nice property that the on-shell and half-off-shell transition matrix elements of the separable representation are exact at predetermined energies, the so-called EST support points. However, when dealing with neutron-nucleus (nA) or proton-nucleus (pA) phenomenological optical potentials, which are in general complex to account for absorptive channels that are not explicitly treated, as well as energy-dependent, extensions of the EST scheme have to be made.

2 Separable representation of single channel energy dependent optical potentials

The pioneering work by Ernst, Shakin and Thaler [18] constructed separable representations of Hermitian potentials. To apply this formalism to optical potentials, it needs to be extended to handle complex potentials [19]. We briefly recall the most important features, namely that a separable representation for a complex, energy-independent potential U_l in a fixed partial wave of orbital angular momentum l is given by [19]

$$u_l = \sum_{ij} U_l |\psi_{l,i}^+\rangle \lambda_{ij}^{(l)} \langle \psi_{l,j}^- | U_l, \quad (1)$$

where $|\psi_{l,i}^+\rangle$ is a solution of the Hamiltonian $H = H_0 + U_l$ with outgoing boundary conditions at energy E_i , and $|\psi_{l,i}^-\rangle$ is a solution of the Hamiltonian $H = H_0 + U_l^*$ with incoming boundary conditions. The energies E_i are referred to as EST support points. The free Hamiltonian H_0 has eigenstates $|k_i\rangle$ with $k_i^2 = 2\mu E_i$, μ being the reduced mass of the neutron-nucleus system. The EST scheme constrains the matrix

$\lambda_{ij}^{(l)}$ with the conditions

$$\begin{aligned}\delta_{kj} &= \sum_i \langle \psi_{l,k}^- | U_l | \psi_{l,i}^+ \rangle \lambda_{ij}^{(l)}, \\ \delta_{ik} &= \sum_j \lambda_{ij}^{(l)} \langle \psi_{l,j}^- | U_l | \psi_{l,k}^+ \rangle,\end{aligned}\tag{2}$$

where the subscript $i = 1, \dots, N$ and N indicates the rank of the separable potential. Those two constraints of Eq. (2) on $\lambda_{ij}^{(l)}$ are an essential feature of the EST scheme and ensure that at the EST support points E_i both, the original U and the separable potential u , have identical wave functions or half-shell t -matrices. The corresponding separable t -matrix takes the form

$$t_l(E) = \sum_{ij} U_l | \psi_{l,i}^+ \rangle \tau_{ij}^{(l)}(E) \langle \psi_{l,j}^- | U_l,\tag{3}$$

with

$$\left(\tau_{ij}^{(l)}(E) \right)^{-1} = \langle \psi_{l,i}^- | U_l - U_l g_0(E) U_l | \psi_{l,j}^+ \rangle.\tag{4}$$

Here $g_0(E) = (E - H_0 + i\varepsilon)^{-1}$ is the free propagator. The form factors are given as half-shell t -matrices

$$T_l(E_i) | k_i \rangle \equiv U_l | \psi_{l,i}^+ \rangle,\tag{5}$$

and are obtained through solving a momentum space Lippmann–Schwinger (LS) equation. However, when applying the same formulation to an energy-dependent complex potential $U(E)$, one obtains

$$u_l = \sum_{ij} U_l(E_i) | \psi_{l,i}^+ \rangle \lambda_{ij}^{(l)} \langle \psi_{l,j}^- | U_l(E_j),\tag{6}$$

with the constraints

$$\begin{aligned}\delta_{kj} &= \sum_i \langle \psi_{l,k}^- | U_l(E_i) | \psi_{l,i}^+ \rangle \lambda_{ij}^{(l)}, \\ \delta_{ik} &= \sum_j \lambda_{ij}^{(l)} \langle \psi_{l,j}^- | U_l(E_j) | \psi_{l,k}^+ \rangle.\end{aligned}\tag{7}$$

Omitting the partial wave index l , the two constraints on λ can be written in matrix form as

$$\mathcal{U}^t \lambda = \mathbf{1} = \lambda \mathcal{U},\tag{8}$$

with

$$\mathcal{U}_{ij} = \langle \psi_i^- | U(E_i) | \psi_j^+ \rangle.\tag{9}$$

For a separable potential of rank $N > 1$ it is obvious that the matrix \mathcal{U}_{ij} is not symmetric in the indices i and j . This leads to an asymmetric matrix λ and thus a t -matrix which violates reciprocity. Therefore, a different approach must be taken in order to construct separable representations for energy-dependent potentials. Here we note that although the potential u contains some of the energy dependence of $U(E)$ through the form factors calculated at the different fixed energy support points E_i , it has no explicit energy dependence. Thus, this separable construction needs to be considered as energy-independent EST representation.

A separable expansion for energy-dependent Hermitian potentials was suggested by Pearce [20]. It is straightforward to apply this suggestion to complex potentials by using the insights previously gained in Ref. [19]. In analogy, we define the EST separable representation for complex, energy-dependent potentials (eEST) by allowing an explicit energy dependence of the coupling matrix elements λ_{ij} .

$$u(E) = \sum_{ij} U(E_i) |\psi_i^+\rangle \lambda_{ij}(E) \langle \psi_j^- | U(E_j), \quad (10)$$

where the partial wave index l has been omitted for simplicity. In order to obtain a constraint on the matrix $\lambda(E)$, we require that the matrix elements of the potential $U(E)$ and its separable form $u(E)$ between the states $|\psi_i^+\rangle$ be the same at all energies E . This condition ensures that the potentials $U(E)$ and $u(E)$ lead to identical wave functions at the EST support points, just like in the energy-independent EST scheme.

The constraints on $\lambda_{ij}(E)$ become

$$\langle \psi_m^- | U(E) | \psi_n^+ \rangle = \langle \psi_m^- | u(E) | \psi_n^+ \rangle = \sum_i \langle \psi_m^- | U(E_i) | \psi_i^+ \rangle \lambda_{ij}(E) \langle \psi_j^- | U(E_j) | \psi_n^+ \rangle. \quad (11)$$

The corresponding separable t -matrix then takes the form

$$t(E) = \sum_{ij} U(E_i) |\psi_i^+\rangle \tau_{ij}(E) \langle \psi_j^- | U(E_j). \quad (12)$$

Substituting Eqs. (10)–(12) into the LS equation leads to constraint for the matrix $\tau(E)$ such that

$$R(E) \cdot \tau(E) \equiv \mathcal{M}(E), \quad (13)$$

where

$$R_{ij}(E) = \langle \psi_i^- | U(E_i) | \psi_j^+ \rangle - \sum_n \mathcal{M}_{in}(E) \langle \psi_n^- | U(E_n) g_0(E) U(E_j) | \psi_j^+ \rangle, \quad (14)$$

with

$$\mathcal{M}_{in}(E) \equiv [\mathcal{U}^e(E) \cdot \mathcal{U}^{-1}]_{in}. \quad (15)$$

The matrix elements of \mathcal{U} are defined in Eq. (9), and

$$\mathcal{U}_{ij}^e(E) \equiv \langle \psi_i^- | U(E) | \psi_j^+ \rangle. \quad (16)$$

For energy-independent potentials, $\mathcal{U}^e(E)$ becomes \mathcal{U} and the matrix $\mathcal{M}(E)$ is the unit matrix. The matrix element $\mathcal{U}_{ij}^e(E)$ is explicitly given as

$$\begin{aligned} \mathcal{U}_{ij}^e(E) &= U(k_i, k_j, E) + \int_0^\infty dp p^2 T(p, k_i; E_i) g_0(E_i, p) U(p, k_j, E) \\ &\quad + \int_0^\infty dp p^2 U(k_i, p, E) g_0(E_j, p) T(p, k_j; E_j) \\ &\quad + \int_0^\infty dp p^2 \int_0^\infty dp' p'^2 T(p, k_i; E_i) g_0(E_i, p) U(p, p', E) g_0(E_j, p') T(p', k_j; E_j), \quad (17) \end{aligned}$$

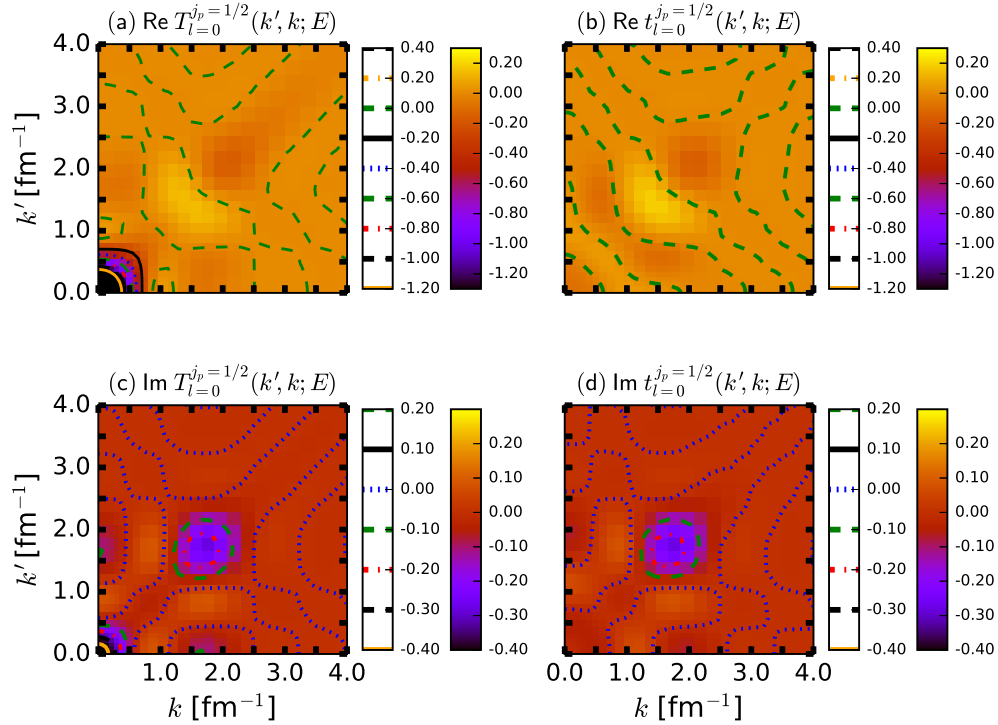


Figure 1: s -wave off-shell t -matrix for the $n + {}^{48}\text{Ca}$ system calculated from the CH89 optical potential [23] as a function of the off-shell momenta k and k' at 20 MeV incident neutron laboratory kinetic energy. (a) and (c) — real and imaginary t -matrix elements corresponding to the CH89 global optical potential; (b) and (d) — real and imaginary parts of the eEST separable representation of the off-shell t -matrix. The on-shell momentum is $k = 0.978 \text{ fm}^{-1}$.

where $g_0(E, p) = [E - p^2/2\mu + i\varepsilon]^{-1}$. For the evaluation of $U_{ij}^e(E)$ for all energies E within the relevant energy regime, the form factors $T(p', k_j; E_j)$ are needed at the specified EST support points and the matrix elements of the potential $U(p', p, E)$ at all energies. The explicit derivation of the above expressions is given in Refs. [21, 22] together with suggestions to simplify the calculation of $U(p', p, E)$. The difference between the energy-dependent separable representation and its energy-independent counterpart is illustrated in Fig. 1 for the s -wave off-shell t -matrix for the $n + {}^{48}\text{Ca}$ system.

To apply the formulation to proton-nucleus scattering, one first realizes that the proton-nucleus potential consists of the point Coulomb force V^c together with a short-ranged nuclear as well as a short-ranged Coulomb interaction representing the charge distribution of the nucleus which we refer to as $U^s(E)$. While the point Coulomb potential has a simple analytical form, an optical potential is employed to model the short-range nuclear potential. The extension of the energy-independent EST separable representation to proton-nucleus optical potentials was carried out in Ref. [24]. In that work it was shown that the form factors of the separable representation are solutions of the LS equation in the Coulomb basis, and that they are obtained using

methods introduced in Refs. [25, 26]. It was also demonstrated that the extension of the energy-independent EST separable representation scheme to proton-nucleus scattering involves two steps. First, the nuclear wave functions $|\psi_{l,i}^{(+)}\rangle$ are replaced by Coulomb-distorted nuclear wavefunctions $|\psi_{l,i}^{sc(+)}\rangle$. Second, the free resolvent $g_0(E)$ is replaced by the Coulomb Green's function, $g_c(E) = (E - H_0 - V^c + i\varepsilon)^{-1}$, and third, the energy-dependent scheme must be generalized.

Upon suppressing the index l we obtain a constraint similar to Eq. (13),

$$R^c(E) \cdot \tau^c(E) = \mathcal{M}_{ij}^c(E), \quad (18)$$

with the matrix elements of $R^c(E)$ satisfying

$$R_{ij}^c(E) = \langle \psi_i^{sc(-)} | U^s(E_i) | \psi_j^{sc(+)} \rangle - \sum_i \mathcal{M}_{in}^c(E) \langle \psi_n^{sc(-)} | U^s(E_n) g_c(E) U^s(E_j) | \psi_j^{sc(+)} \rangle. \quad (19)$$

The matrix $\mathcal{M}^c(E)$ is the Coulomb distorted counterpart of $\mathcal{M}(E)$ of Eq. (15), and is defined as

$$\mathcal{M}_{in}^c(E) = [\mathcal{U}^{e,sc}(E) \cdot (\mathcal{U}^{sc})^{-1}]_{in}, \quad (20)$$

with

$$\begin{aligned} \mathcal{U}_{ij}^{sc} &\equiv \langle \psi_i^{sc(-)} | U^s(E_i) | \psi_j^{sc(+)} \rangle, \\ \mathcal{U}_{ij}^{e,sc}(E) &\equiv \langle \psi_{k_i}^{sc(-)} | U^s(E) | \psi_{k_j}^{sc(+)} \rangle. \end{aligned} \quad (21)$$

If the potential is energy-independent the matrix $\mathcal{M}^c(E)$ becomes a unit matrix just like $\mathcal{M}(E)$. Further details for the explicit evaluation are given in Refs. [21, 22].

In order to illustrate the quality of the separable representation of energy-dependent optical potentials for neutron as well as proton elastic scattering, the differential cross sections for proton scattering off ^{48}Ca at laboratory kinetic energy 38 MeV and ^{208}Pb at 45 MeV are shown in Fig. 2 and compared to the equivalent coordinate space calculations. We observe that the separable representation provides an excellent description on both cases. The power of a separable representation based on the EST scheme lies in the choice of the basis, namely here the half-shell t -matrices calculated at specific energies. This basis contains a lot of information about the system considered, and thus only a small number of basis states, represented by the rank of the separable potential, are needed to have this excellent representation.

3 Coordinate space separable representation of single channel optical potentials

A formal scheme for deriving separable representations for Hermitian potentials was given by Ernst, Shakin, and Thaler in Ref. [18], and an application of the scheme to a two-body coordinate space potential representing an s-wave bound and scattering state in can be found in Ref. [28]. The authors chose to carry out their construction of the separable representation in the coordinate space, which makes the procedure more cumbersome compared to the momentum space construction we employ, leading

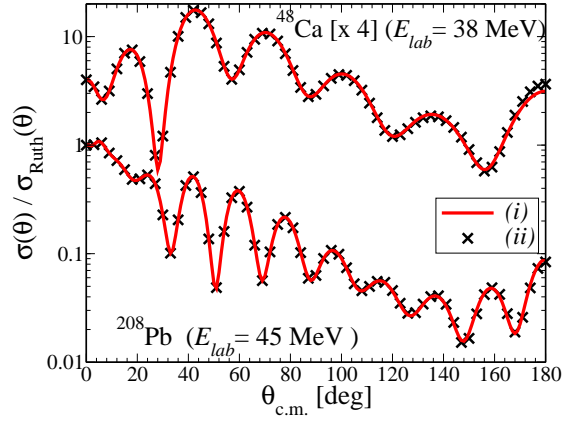


Figure 2: Unpolarized differential cross section for elastic scattering of protons by ^{48}Ca (upper) and ^{208}Pb (lower) as a function of the c. m. angle. For ^{48}Ca the cross section is calculated at a laboratory kinetic energy of 38 MeV and is scaled by a factor of 4. The calculation for ^{208}Pb is carried out at $E_{lab} = 45$ MeV. Solid curves (i) — the cross section calculated in momentum space based on the rank-5 separable representation of the phenomenological optical potential CH89 [23], crosses (ii) — the corresponding coordinate space calculations [27].

to a momentum space separable representation of either the transition matrix or the potential.

Since coordinate space techniques have long tradition in nuclear physics, it can be useful to consider an EST based separable representation of potentials in coordinate space. Separable potentials are inherently nonlocal. Using the EST formulation leads to a well defined behavior of this non-locality. However, instead of implementing the EST construction in the coordinate space, one can carry out the entire scheme in the momentum space and then Fourier transform the momentum space result to the coordinate space. This is quite simple since it involves only a one-dimensional Fourier transform of the form factors.

To illustrate the coordinate space realization of the EST separable representation, we show in Fig. 3 the form factors $h_{l,i}$ as a function of the momentum p for the $n + ^{48}\text{Ca}$ system in panel (a) together with their Fourier transformed counterparts in the coordinate space in panel (b). The index i refers to the EST support points used. The form factors are well behaved functions in the momentum space as well as in the coordinate space. In Fig. 4 the s -wave form factors for the $n + ^{208}\text{Pb}$ system are shown, and we note that for the heavier nucleus ^{208}Pb they extend to larger values of r as should be expected considering the larger size of the heavier nucleus.

The separable representation of the coordinate space potential in a given partial wave is obtained by summing over the rank of the potential according to Eq. (1). The resulting nonlocal separable coordinate space representation of the CH89 optical potential is shown in Fig. 5 for the $n + ^{48}\text{Ca}$ system for the $s_{1/2}$ and $p_{3/2}$ channels. The non-locality is symmetric in r and r' as required by reciprocity and its extension in r and r' is given by the fall-off behavior of the form factors. It also shows a more intricate behavior than the often employed Perey–Buck Gaussian-type [29] non-

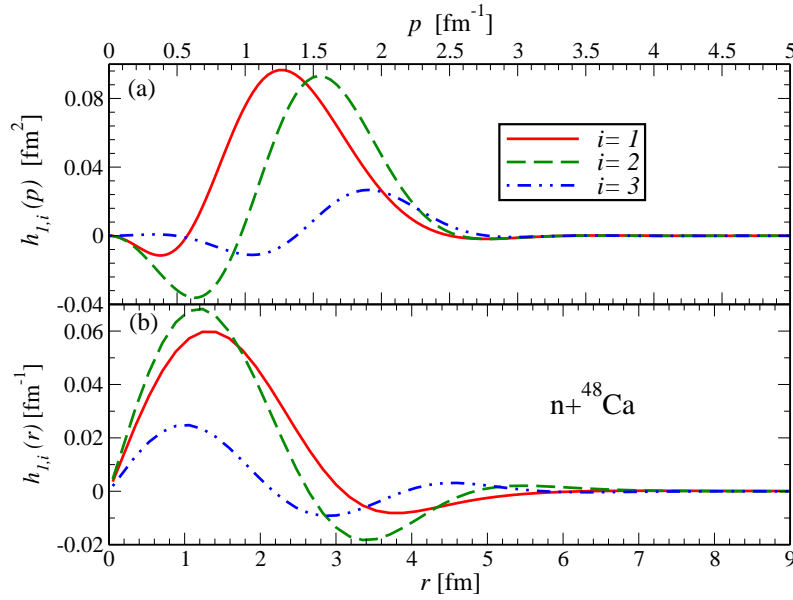


Figure 3: $p_{3/2}$ form factors $h_{1,i}$ for the $n+^{48}\text{Ca}$ system obtained from the CH89 optical potential [23]. Panel (a) illustrates the form factors as a function of the momentum p while panel (b) depicts its Fourier transform as a function of the position coordinate r . The indices $i = 1, 2$, and 3 correspond to the support points 5, 21, and 47 MeV.

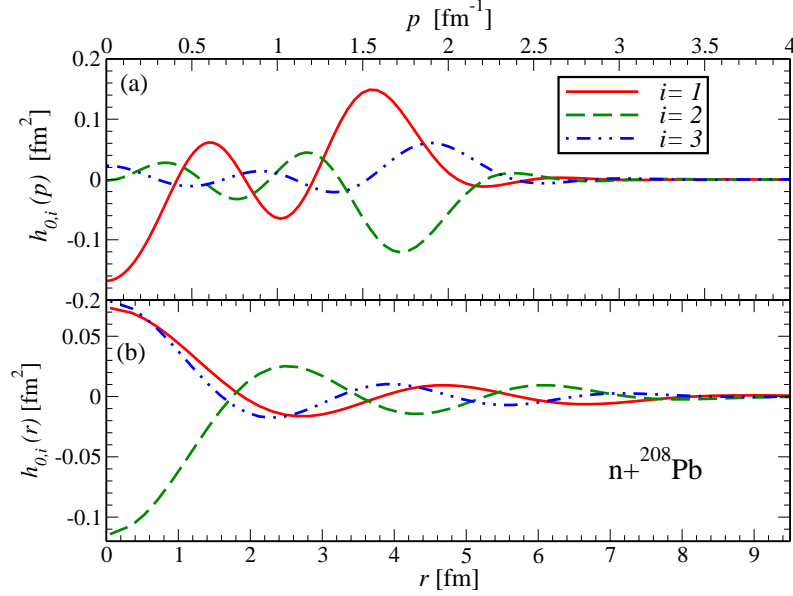


Figure 4: s -wave form factors $h_{0,i}$ for the $n+^{208}\text{Pb}$ system obtained from the CH89 optical potential [23]. See Fig. 3 for details.

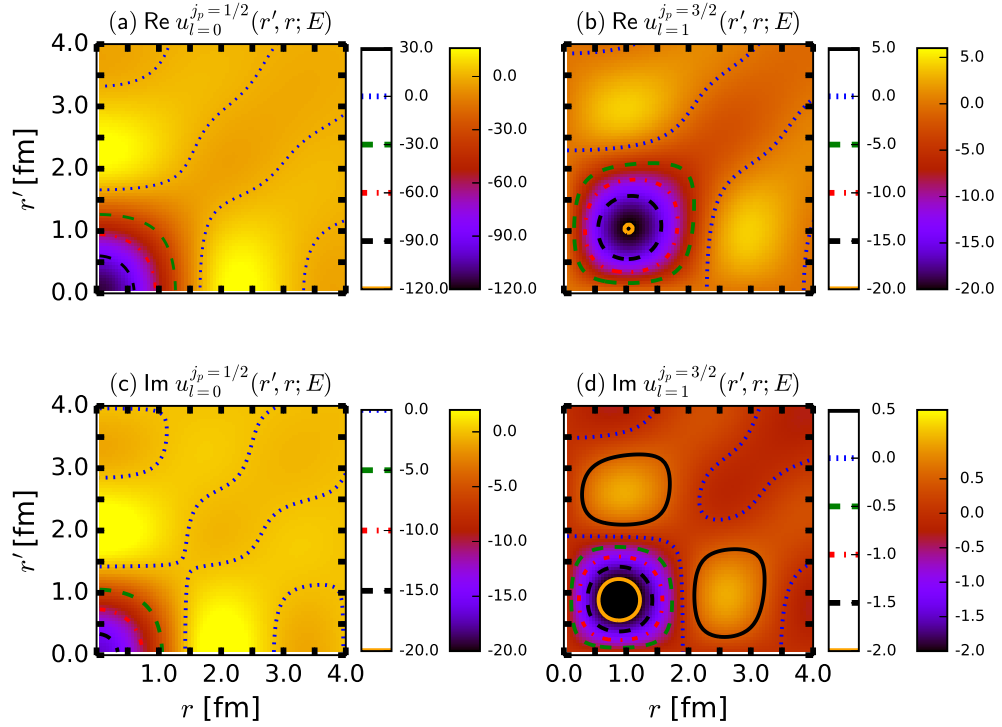


Figure 5: Off-shell potential elements $u_l^{j_p}(r', r, E)$ of the separable representation of the CH89 optical potential [23] for the $n + {}^{48}\text{Ca}$ system as a function of the coordinates r and r' at $E = 20$ MeV incident neutron laboratory kinetic energy. (a) and (c) — real and imaginary potential matrix elements for the $s_{1/2}$ partial wave; (b) and (d) — real and imaginary parts of the $p_{3/2}$ separable potential.

locality construct. Employing the nonlocal separable representation in solving the integro-differential Schrödinger equation [30] reveals that the resulting coordinate space wave function exactly agree with the wavefunctions obtained from solving the Schrödinger equation with the local CH89 optical potential [31].

4 Separable representation of multi-channel energy dependent optical potentials

To generalize the energy-dependent EST (eEST) scheme to multichannel potentials, we proceed analogously to Ref. [32] and replace the single-channel scattering wavefunctions with their multichannel counterparts, leading to a multichannel separable potential

$$u(E) = \sum_{\rho\sigma} \sum_{ij} \left(\sum_{\gamma JM} U(E_i) |\gamma JM \Psi_{\gamma\rho,i}^{J(+)}\rangle \right) \lambda_{ij}^{\rho\sigma}(E) \left(\sum_{\gamma JM} \langle \Psi_{\gamma\sigma,j}^{J(-)} | \gamma JM | U(E_j) \right). \quad (22)$$

The indices i and j stand for the EST support points. Using the definition of the multichannel half-shell t -matrix [33],

$$T(E_i)|\rho JM k_i^\rho\rangle = \sum_{\gamma} U(E_i)|\gamma JM \Psi_{\gamma\rho}^{J(+)}\rangle, \quad (23)$$

Eq. (22) can be recasted as

$$u(E) = \sum_{JM} \sum_{J'M'} \sum_{\rho\sigma} \sum_{ij} T(E_i)|\rho JM k_i^\rho\rangle \lambda_{ij}^{\rho\sigma}(E) \langle k_j^\sigma \sigma J' M' | T(E_j). \quad (24)$$

To determine the constraint on $u(E)$, we first generalize the matrices $\mathcal{U}^e(E)$ and \mathcal{U} to multichannel potentials. This is accomplished by replacing the single-channel scattering states by the multichannel scattering states so that

$$\mathcal{U}_{mn}^{e,\alpha\beta}(E) \equiv \sum_{\gamma\nu} \langle \Psi_{\gamma\alpha,m}^{J(-)} \gamma JM | U(E) | \nu JM \Psi_{\nu\beta,n}^{J(+)} \rangle = \sum_{\gamma\nu} \langle \Psi_{\gamma\alpha,m}^{J(-)} | U_{\gamma\nu}^J(E) | \Psi_{\nu\beta,n}^{J(+)} \rangle, \quad (25)$$

and

$$\mathcal{U}_{mn}^{\alpha\beta} \equiv \mathcal{U}_{mn}^{e,\alpha\beta}(E_m) = \sum_{\gamma\nu} \langle \Psi_{\gamma\alpha,m}^{J(-)} | U_{\gamma\nu}^J(E_m) | \Psi_{\nu\beta,n}^{J(+)} \rangle. \quad (26)$$

The J dependence of matrix elements $\mathcal{U}_{mn}^{e,\alpha\beta}(E)$ and $\mathcal{U}_{mn}^{\alpha\beta}$ is omitted for simplicity. On one hand, Eq. (26) shows that the matrix \mathcal{U} depends only on the support energies E_m and E_n . On the other hand, we see from Eq. (25) that $\mathcal{U}^e(E)$ depends on the projectile energy E as well as the support energies. The constraint on the separable potential is obtained by substituting the multichannel matrices \mathcal{U}^e and \mathcal{U} into Eq. (11) leading to

$$\mathcal{U}_{mn}^{e,\alpha\beta}(E) = \sum_{\rho\sigma} \sum_{ij} (\mathcal{U}^t)_{mi}^{\alpha\rho} \lambda_{ij}^{\rho\sigma}(E) \mathcal{U}_{jn}^{\sigma\beta} = [\mathcal{U}^t \cdot \lambda(E) \cdot \mathcal{U}]_{mn}^{\alpha\beta}. \quad (27)$$

To evaluate the separable multichannel t -matrix, we insert Eqs. (24)–(27) into a multichannel LS equation and obtain

$$\begin{aligned} t(E) &= \sum_{\rho\sigma} \sum_{ij} \left(\sum_{\gamma JM} U(E_i) |\gamma JM \Psi_{\gamma\rho,i}^{J(+)}\rangle \right) \tau_{ij}^{\rho\sigma}(E) \left(\sum_{\gamma JM} \langle \Psi_{\gamma\sigma,j}^{J(-)} \gamma JM | U(E_j) \right) \\ &= \sum_{JM} \sum_{J'M'} \sum_{\rho\sigma} \sum_{ij} T(E_i) |\rho JM k_i^\rho\rangle \tau_{ij}^{\rho\sigma}(E) \langle k_j^\sigma \sigma J' M' | T(E_j). \end{aligned} \quad (28)$$

The coupling matrix elements $\tau_{ij}^{\rho\sigma}(E)$ fit the equation

$$R(E) \cdot \tau(E) = \mathcal{M}(E), \quad (29)$$

where

$$\begin{aligned} R_{ij}^{\rho\sigma}(E) &= \langle k_i^\rho | T_{\rho\sigma}^J(E_i) + \sum_{\beta} T_{\rho\beta}^J(E_i) G_{\beta}(E_j) T_{\beta\sigma}^J(E_j) | k_j^\sigma \rangle \\ &\quad - \sum_{\beta\beta'} \sum_n \mathcal{M}_{in}^{\rho\beta}(k_n^\beta) | T_{\beta\beta'}^J(E_n) G_{\beta'}(E) T_{\beta'\sigma}^J(E_j) | k_j^\sigma \rangle, \end{aligned} \quad (30)$$

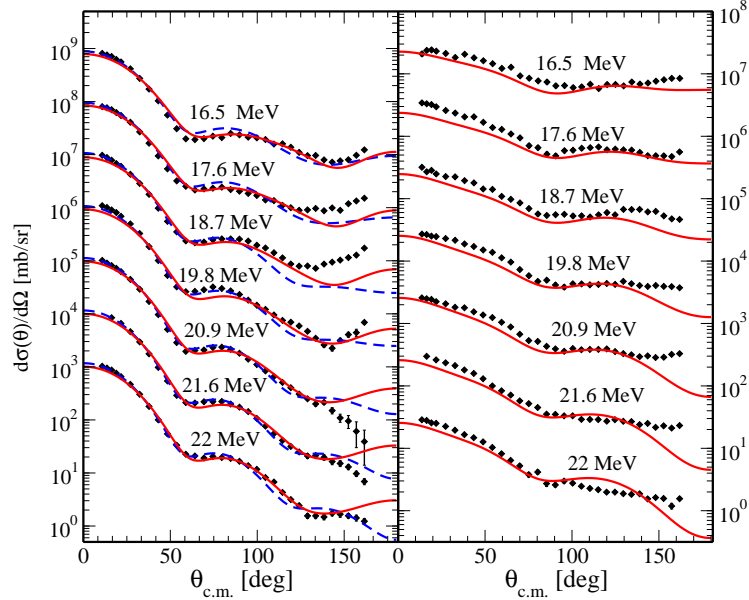


Figure 6: Differential cross sections for scattering in the $n + {}^{12}\text{C}$ system computed at various incident neutron energies with the eEST separable representation of the Olsson *et al.* DOMP [34] (solid curves). Left (right) panel shows the results for the elastic scattering (inelastic scattering to the 2^+ state of ${}^{12}\text{C}$). Dashed curves indicate the cross sections computed with the spherical OMP of Olsson *et al.* [34]. Filled diamonds are the data taken from Ref. [34]. The cross sections are scaled up by the multiples of 10, e. g., the results at 21.6 MeV are multiplied by 10, those at 20.9 MeV are multiplied by 100, etc.

and

$$\mathcal{M}_{ij}^{\rho\sigma}(E) = [\mathcal{U}^e(E) \cdot \mathcal{U}^{-1}]_{ij}^{\rho\sigma}. \quad (31)$$

The expression for the matrix $R_{ij}^{\rho\sigma}(E)$ is analogous to the one for the single-channel case except for the extra channel indices.

To illustrate the implementation of the multichannel eEST separable representation scheme, we consider the scattering of neutrons by the ${}^{12}\text{C}$ nucleus. The ${}^{12}\text{C}$ nucleus possesses selected excited states, with the first and second levels having $I^\pi = 2^+$ and $I^\pi = 4^+$ and located at 4.43 and 14.08 MeV above the 0^+ ground state. The collective rotational model [35] is assumed to describe the coupling between the ground state and these excited states. We consider here the elastic scattering and the inelastic scattering to the 2^+ rotational state. To test the multichannel eEST separable representation, we use the deformed optical potential model (DOMP) derived by Olsson *et al.* [34] and fitted to elastic and inelastic scattering data at laboratory kinetic energies between 16 and 22 MeV. In Fig. 6, the differential cross sections for the elastic and inelastic scattering in the $n + {}^{12}\text{C}$ system are shown at various incident neutron energies. The left hand panel shows the differential cross section of the elastic scattering, and the right hand panel presents the differential cross section of the inelastic scattering to the 2^+ state of ${}^{12}\text{C}$. The support points are at $E_{lab} = 6$ and 40 MeV. The

separable representation describes both differential cross sections very well. In addition, it is in good agreement with the coupled-channel calculations shown in Fig. 1 of Ref. [34]. The dashed curves indicate the cross sections computed with the spherical OMP of Olsson *et al.* [34].

5 Summary and outlook

In a series of steps we developed the input that will serve as a basis for Faddeev-AGS three-body calculations of (d,p) reactions which will not rely on the screening of the Coulomb force. To achieve this, Ref. [11] formulated the Faddeev-AGS equations in the Coulomb basis using separable interactions in the two-body subsystems. We developed separable representations of phenomenological optical potentials of the Woods-Saxon type for neutrons and protons. First we concentrated on the neutron-nucleus optical potentials and generalized the EST scheme [18] so that it can be applied to complex and energy-dependent optical potentials [19,21]. In order to consider the proton-nucleus optical potentials, we further extended the EST scheme so that it can be applied to the scattering of charged particles with a repulsive Coulomb force [24]. Finally we extended the EST formulation to incorporate multi-channel optical potentials [36].

The results demonstrate that separable representations based on a generalized EST scheme reproduce the standard coordinate space calculations of neutron and proton scattering cross sections very well. We also showed that the coordinate space separable representations can be obtained from the corresponding momentum space representations using Fourier transforms of the form factors. From those solutions, observables for (d,p) transfer reactions using the Faddeev-AGS formulation should be readily calculated. Work along these lines is in progress.

Acknowledgments

This material is based on work in part supported by the U. S. Department of Energy, Office of Science of Nuclear Physics under the contract No. DE-FG02-93ER40756 with Ohio University. The authors thank F. M. Nunes and A. Ross for fruitful discussions.

References

- [1] J. E. Escher *et al.*, Rev. Mod. Phys. **84**, 353 (2012).
- [2] J. Cizewski *et al.*, J. Phys. Conf. Ser. **420**, 012058 (2013).
- [3] R. Kozub *et al.*, Phys. Rev. Lett. **109**, 172501 (2012).
- [4] F. Nunes and A. Deltuva, Phys. Rev. C **84**, 034607 (2011).
- [5] K. Schmitt *et al.*, Phys. Rev. Lett. **108**, 192701 (2012).
- [6] E. Alt, P. Grassberger and W. Sandhas, Nucl. Phys. B **2**, 167 (1967).
- [7] A. Deltuva and A. Fonseca, Phys. Rev. C **79**, 014606 (2009).
- [8] A. Deltuva, A. Fonseca and P. Sauer, Phys. Rev. C **71**, 054005 (2005).

-
- [9] A. Deltuva, A. Fonseca and P. Sauer, Phys. Rev. C **72**, 054004 (2005).
- [10] F. Nunes and N. Upadhyay, J. Phys. Conf. Ser. **403**, 012029 (2012).
- [11] A. Mukhamedzhanov, V. Eremenko and A. Sattarov, Phys. Rev. C **86**, 034001 (2012).
- [12] N. Upadhyay *et al.* (TORUS Collaboration), Phys. Rev. C **90**, 014615 (2014).
- [13] J. Haidenbauer and W. Plessas, Phys. Rev. C **27**, 63 (1983).
- [14] J. Haidenbauer, Y. Koike and W. Plessas, Phys. Rev. C **33**, 439 (1986).
- [15] D. Entem, F. Fernandez and A. Valcarce, J. Phys. G **27**, 1537 (2001).
- [16] T. Ueda and Y. Ikegami, Progr. Theor. Phys. **91**, 85 (1994).
- [17] A. Gal and H. Garcilazo, Nucl. Phys. A **864**, 153 (2011).
- [18] D. J. Ernst, C. M. Shakin and R. M. Thaler, Phys. Rev. C **8**, 46 (1973).
- [19] L. Hlophe *et al.* (TORUS Collaboration), Phys. Rev. C **88**, 064608 (2013).
- [20] B. Pearce, Phys. Rev. C **36**, 471 (1987).
- [21] L. Hlophe and C. Elster, Phys. Rev. C **93**, 034601 (2016).
- [22] L. Hlophe, *Separable representation of nucleon-nucleus optical potentials as input to (d,p) reaction calculations* (PhD dissertation). Ohio University, 2016.
- [23] R. Varner, W. Thompson, T. McAbee, E. Ludwig and T. Clegg, Phys. Rep. **201**, 57 (1991).
- [24] L. Hlophe *et al.*, Phys. Rev. C **90**, 061602 (2014).
- [25] C. Elster, L. C. Liu and R. M. Thaler, J. Phys. G **19**, 2123 (1993).
- [26] C. R. Chinn, C. Elster and R. M. Thaler, Phys. Rev. C **44**, 1569 (1991).
- [27] F. Nunes, *private communication* (2014).
- [28] D. J. Ernst, C. M. Shakin, R. M. Thaler and D. Weiss, Phys. Rev. C **8**, 2056 (1973).
- [29] F. Perey and B. Buck, Nucl. Phys. **32**, 353 (1962).
- [30] L. J. Titus, A. Ross and F. M. Nunes, Comput. Phys. Commun. **207**, 499 (2016), arXiv:1606.07341 [nucl-th] (2016).
- [31] A. Ross, *private communication* (2016).
- [32] S. C. Pieper, Phys. Rev. C **9**, 883 (1974).
- [33] W. Glöckle, *The quantum mechanical few-body problem*. Springer-Verlag, Berlin, Heidelberg, 1983.
- [34] B. Olsson, B. Trostell and E. Ramstrom, Nucl. Phys. A **469**, 505 (1989).

- [35] I. J. Thompson and F. M. Nunes, *Nuclear reactions for astrophysics: Principles, calculation and applications of low-energy reactions*. Cambridge University Press, New York, 2009.
- [36] L. Hlophe and C. Elster, Phys. Rev. C **95**, 054617 (2017), arXiv:1611.05734 [nucl-th] (2016).

Three-Nucleon Reactions with Recently Derived Nuclear Potentials

R. Skibiński^a, J. Gólaś^a, A. M. Shirokov^b, K. Topolnicki^a,
Y. Volkotrub^a and H. Witała^a

^a*M. Smoluchowski Institute of Physics, Jagiellonian University, PL-30348 Kraków, Poland*

^b*Skobeltsyn Institute of Nuclear Physics, Moscow State University, Moscow 119991, Russia*

Abstract

Elastic nucleon-deuteron scattering is investigated at low and medium energies within the formalism of the Faddeev equations. We present various observables for this process obtained using the recently developed JISP16 nucleon-nucleon interaction and the chiral two-nucleon N^4 LO force with the semi-local regularization. Comparison with data demonstrates, in general, good behavior of these two interactions at low energies but also reveals inadequacies of the JISP16 force for some observables. The origin of the observed problems lies in drawbacks of the P -wave interactions implemented in the JISP16 model.

Keywords: *Elastic nucleon-deuteron scattering, nucleon-nucleon force, few-body systems*

1 Introduction

The complex structure of nuclear interactions is one of the reasons why nuclear physics is still a significant intellectual challenge. Unfortunately, a derivation of nuclear system properties directly from Quantum Chromodynamics is still beyond the realms of possibility, despite the first ongoing attempts [1, 2]. This situation implies that the effective models of nuclear interactions are considered and used in practical *ab initio* calculations. Most of such models are semi-phenomenological and among the most advanced ones let us mention the Nijmegen [3, 4], the Argonne V18 (AV18) [5] and the Charge-Dependent Bonn (CD Bonn) [6, 7] forces. These potentials depend on several dozens of free parameters to be fixed from experimental data in the two-nucleon sector. These semi-phenomenological models describe experimental data for proton-proton (pp) and neutron-proton (np) scattering up to the two-nucleon energy of about 350 MeV very well, yielding $\chi^2/data'99 = 1.01$ in the case of the CD Bonn [8] and $\chi^2/data'99 = 1.35$ for the AV18 [8].

The nucleon-nucleon potential JISP16 [9] is one of the newest semi-phenomenological forces. This force is a successor of the J -matrix Inverse Scattering Potential [10] which in turn follows the Inverse Scattering Tridiagonal Potential (ISTP) developed within the inverse scattering methods in [11]. The free parameters of the JISP6 force

Proceedings of the International Conference 'Nuclear Theory in the Supercomputing Era — 2016' (NTSE-2016), Khabarovsk, Russia, September 19–23, 2016. Eds. A. M. Shirokov and A. I. Mazur. Pacific National University, Khabarovsk, Russia, 2018, p. 90.

<http://www.ntse-2016.khb.ru/Proc/Skibinski.pdf>.

have been fixed from the bound and resonance states of nuclei up to $A = 6$ [10]. Correspondingly, bound and resonance states of nuclei up to ^{16}O have been used to determine the JISP16 parameters [9]. The JISP forces also describe two-nucleon scattering data with a precision comparable to other modern potentials, reaching $\chi^2=1.03(1.05)$ for the JISP6 with the neutron-proton data'1992(1999). The main motivation behind developing the JISP16 model was a derivation of the two-body interaction which, at least partially, accommodates effects of many-body forces. This should result in a substantial improvement of the convergence of the nuclear structure calculations, especially ones performed within the No-Core Shell Model [12]. This aim has been achieved and indeed the JISP16 force works very well in investigations of bound and resonant states, as was documented for example in Refs. [13–15]. In this contribution we use the JISP16 interaction to study the elastic nucleon-deuteron scattering performing the first test of this force in few-body reactions.

The chiral approach to the nuclear forces has been developed simultaneously with the semi-phenomenological methods described above. The nuclear interaction is constructed in a framework of the effective field theory for nucleon and pion fields with incorporated chiral symmetry, see, e. g., Ref. [16] for a detailed review. Within this approach, it is possible to derive the nuclear interaction perturbatively by expanding the Lagrangian in powers ν of the parameter $(\frac{Q}{\Lambda_\chi})$, where Q is the scale of typical values of nucleon momenta in the initial and final states, and $\Lambda_\chi \approx 1$ GeV is the scale of chiral symmetry breaking. The ν parameter can be related to geometrical properties (like the number of vertices, number of loops, etc.) of the graphs representing a given contribution to the potential. The resulting dominant contribution to the nucleon-nucleon interaction comes from the one-pion exchange force. On top of that also two-nucleon contact terms are present. They describe a short-ranged nucleon-nucleon interaction which in the semi-phenomenological models is represented by heavier meson (like σ , ρ or ω) exchanges.

The chiral potentials, starting from the smallest possible value of $\nu = 0$ [the leading order (LO)], $\nu = 2$ [the next-to-leading order (NLO)], have been completely constructed up to $\nu = 5$ (N^4LO). Moreover, some dominant contributions arising at N^5LO have been also derived [17]. The most advanced two- and consistent three-nucleon chiral forces have been derived by the Bochum/Jülich group [18–22]. The newest version of the two-body force presented in Refs. [21, 22] includes all terms of the chiral expansion up to N^4LO and benefits from an improved way in which values of the low-energy constants in the long-range part of the interaction are established. Namely, in Refs. [21, 22] the values of these constants are taken directly from the pion-nucleon scattering without additional fine tuning applied in the previous model. Secondly, an improved regularization method has been used. In the older model, matrix elements of the potential V , $\langle \vec{p}' | V | \vec{p} \rangle$, were multiplied by the exponential factor $\exp[-(p'^6 + p^6)/\Lambda^6]$, where \vec{p}' and \vec{p} are the relative momenta of nucleons in the initial and final states, respectively, $p' = |\vec{p}'|$, $p = |\vec{p}|$ and $\Lambda \approx 550$ MeV is the regularization parameter. Such a non-local regularization implemented in the same way for all partial waves, leads to unwelcome artifacts in the long-range part of the nucleon-nucleon force and does not completely eliminate unwanted short-range components of the two-pion exchange. The same non-local regularization has been also utilized for the three-nucleon ($3N$) force [23] affecting the description of observables in the $3N$ sector, see Refs. [24] and [25] for applications in the nucleon-deuteron elastic scattering and in the neutron induced deuteron breakup, respectively. The extensive tests

of electroweak processes using the older chiral models, can be found in Refs. [26–28]. These works have revealed that the cut-off dependence of the nuclear forces employed there is too strong (especially at N³LO) and precludes precise conclusions about the investigated processes.

Within the improved model of Refs. [21,22], the semi-local regularization has been applied. It means that the long-range component of the interaction in the coordinate space is multiplied by the function $f(r) = [1 - \exp(-r^2/R^2)]^6$ while the contact interactions are regularized using a non-local Gaussian regulator in the momentum space. The values of the cut-off parameter R are chosen in the 0.8–1.2 fm range, however they do not describe the two-nucleon phase shifts equally well — the best description (up to $E_{\text{lab}} = 300$ MeV) is obtained for R of 0.9 and 1.0 fm. The first applications of this newest two-body chiral force to the studies of the elastic nucleon-deuteron scattering have been announced in Ref. [29] and investigations of various electroweak processes have been described in Ref. [30]. These first tests demonstrate a good quality of the chiral interaction, a weak regulator dependence, a fast chiral convergence and a good behavior at high energies. In this paper we present results which are based on the N⁴LO chiral nucleon-nucleon force [21, 22] with semi-local regularization and choose the regulator $R = 0.9$ fm.

A transition from the two- to the three-nucleon system entails substantial complications of theoretical and numerical methods required for a precise analysis of scattering processes. Even the simplest three-nucleon reaction, the elastic nucleon-deuteron scattering, reveals the differences between various models of the nucleon-nucleon force. A review of numerous observables and their sensitivity to the interaction details can be found in Refs. [31] and [32]. In the case of the chiral forces an additional uncertainty of theoretical predictions stems from the regularization methods which employ unknown *a priori* regularization parameters. However, as demonstrated in Ref. [29], the model of Refs. [21,22] shows at N⁴LO only a weak dependence on the regulator values from the range suggested by the two-body phase shift analysis.

The elastic nucleon-deuteron scattering process has been also intensively investigated experimentally, see, e. g., Refs. [33–35] for recent reviews. The comparison of theoretical predictions for the elastic nucleon-deuteron scattering obtained within various theoretical approaches [31, 32, 36–38], shows that the three-nucleon force is important for this process at energies above approx 30 MeV. However, in this work, we restrict ourselves only to the nucleon-nucleon interactions and present just a single set of predictions obtained with the Urbana IX three-nucleon force combined with the AV18 nucleon-nucleon interaction to give the reader an idea about a magnitude of expected three-nucleon force effects. The lack of some contributions in the present-day models of the three-nucleon force is considered as a probable source of remaining discrepancies observed in the nucleon-deuteron scattering at low and medium energies.

The elastic nucleon-deuteron scattering process can also be used to study relativistic effects observed in the cross section at energies around 200 MeV. Inclusion of such relativistic features as the relativistic correction to the nucleon-nucleon force, the boost of the potential and Wigner spin rotations, leads to noticeable effects, especially at backward scattering angles [39]. However up to now, the existing models of the three-nucleon force even combined with the relativistic ingredients are not fully able to explain the data. A comparison with the proton-deuteron data also indicates that neglecting the Coulomb force in the theoretical analysis increases the observed discrepancies, especially at low energies. The differential cross section for

the proton-deuteron elastic scattering at very forward angles at energies below approximately 20 MeV is a good example. The inclusion of the Coulomb force improves the description of the proton-deuteron data in that region of angles [40].

The paper is organized as follows: we briefly summarize our theoretical approach in Section 2 and present the results for the elastic nucleon-deuteron scattering in Section 3. We summarize in Section 4.

2 Formalism

Working in momentum space, in the nonrelativistic regime, and assuming only two-body interactions, we obtain observables for the elastic nucleon-deuteron scattering from an auxiliary state $T|\psi\rangle$ which fits a Faddeev-like equation [31]

$$T|\psi\rangle = tP|\psi\rangle + tPG_0T|\psi\rangle. \quad (1)$$

Allowing also for the three-body potential, leads to a more complicated Faddeev equation [32] with two additional terms involving the three-nucleon force:

$$T|\psi\rangle = tP|\psi\rangle + tPG_0T|\psi\rangle + (1+tG_0)V_4^{(1)}(1+P)|\psi\rangle + (1+tG_0)V_4^{(1)}(1+P)T|\psi\rangle. \quad (2)$$

In Eqs. (1) and (2), the initial state $|\psi\rangle$ is composed of a deuteron and a momentum eigenstate of the projectile nucleon, P is a permutation operator which takes into account the identity of the nucleons and G_0 is the free three-nucleon propagator. The $2N$ interaction V together with the two-nucleon free propagator \tilde{G}_0 enters Eqs. (1) and (2) through a solution of the Lippmann–Schwinger equation for the t-matrix:

$$t = V + V\tilde{G}_0t. \quad (3)$$

In Eq. (2), the $V_4^{(1)}$ is a part of the three-nucleon force which is symmetric under the exchange of nucleons 2 and 3.

We solve Eqs. (1) and (2) in the partial wave scheme. We use the $|p, q, \alpha\rangle$ basis states with $p = |\vec{p}|$ and $q = |\vec{q}|$ being the magnitudes of the relative Jacobi momenta \vec{p} and \vec{q} . Further, α represents the set of discrete quantum numbers for three-nucleon system in the jI -coupling:

$$\alpha = \left((l, s)j; \left(\lambda, \frac{1}{2}\right)I; (j, I)JM_J; \left(t, \frac{1}{2}\right)TM_T \right). \quad (4)$$

Here l , s , j and t denote the orbital angular momentum, total spin, total angular momentum and total isospin of the 2-3 subsystem. Further, λ and I are the orbital and total angular momenta of particle 1 with respect to the centre of mass of the 2-3 subsystem. Finally, J , M_J , T and M_T are the the total angular momentum of the $3N$ system, its projection on the quantization axis, the total $3N$ isospin and its projection, respectively.

Using the completeness relation for the $|p, q, \alpha\rangle$ states,

$$\sum_{\alpha} \int dp p^2 \int dq q^2 |p, q, \alpha\rangle \langle p, q, \alpha| = 1, \quad (5)$$

Eq. (1) can be rewritten as

$$\begin{aligned} \langle p, q, \alpha | T | \psi \rangle &= \sum_{\alpha'} \int dp' p'^2 \int dq' q'^2 \langle p, q, \alpha | t | p', q', \alpha' \rangle \langle p', q', \alpha' | P | \psi \rangle \\ &+ \sum_{\alpha'} \int dp' p'^2 \int dq' q'^2 \langle p, q, \alpha | t | p', q', \alpha' \rangle \langle p', q', \alpha' | P G_0 T | \psi \rangle. \end{aligned} \quad (6)$$

This form reveals that while solving Eq. (6), the two-nucleon force matrix elements present in the t -operator, clearly interfere which can significantly affect the observables. We solve Eq. (6) by generating its Neumann series and summing it up using the Padé method [31]. In the results presented here we use all partial waves with $j \leq 4$ and $J \leq \frac{25}{2}$. These values are sufficient to obtain fully converged solutions at the energies considered here. More details about our numerical performance can be found in Ref. [31]. Results presented in the next Section have been obtained using, in the case of all interaction models, only the neutron-proton force (including the neutron-neutron subsystem). The reason for this is that the JISP16 model assumes charge independence. This assumption has only a small influence on the magnitudes of the observables presented here.

3 Results

In the following we discuss results for various observables in the neutron-deuteron elastic scattering process at two laboratory energies of the incoming neutron: $E = 5$ MeV and $E = 65$ MeV. We present our predictions for the differential cross section $\frac{d\sigma}{d\Omega}$, neutron analyzing power $A_Y(N)$, deuteron vector analyzing power iT_{11} and deuteron tensor analyzing power T_{21} in Figs. 1–4. In all figures, the black solid, red dashed, blue

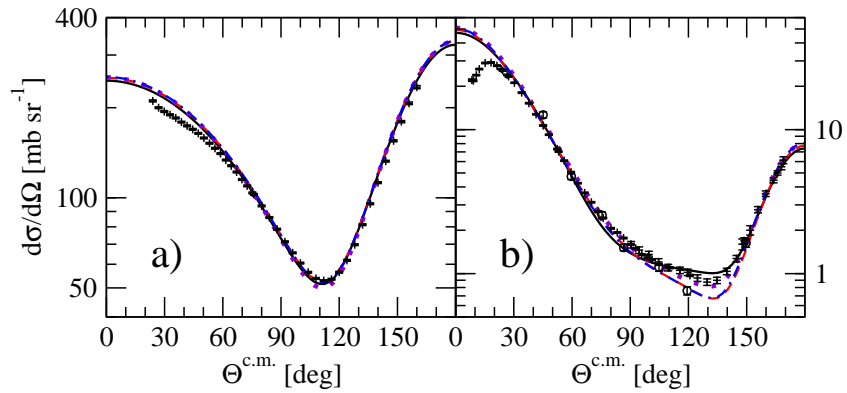


Figure 1: Differential cross section $d\sigma/d\Omega$ of elastic neutron-deuteron scattering at initial neutron laboratory energy $E = 5$ MeV (left) and $E = 65$ MeV (right). The black solid, red dashed, violet dotted and blue dash-dotted curves represent predictions based on the JISP16, AV18, AV18 + Urbana IX and chiral N^4 LO (with regularization parameter $R=0.9$ fm) forces, respectively. The data at $E = 5$ MeV are from Ref. [41] and the data at $E = 65$ MeV are from Ref. [42] (pd crosses) and [43] (nd circles).

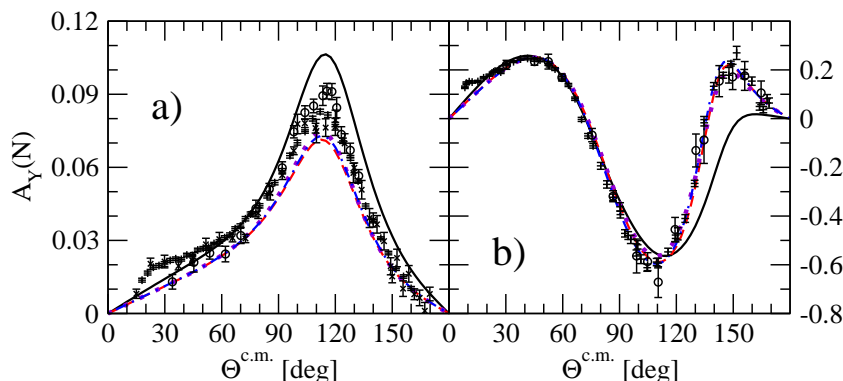


Figure 2: Nucleon analyzing power $A_Y(N)$ at the same energies as in Fig. 1. Curves are the same as in Fig. 1. Data at $E = 5$ MeV are from Ref. [41] (pd crosses), [44] (nd circles) and [45] (x-es). Data at $E = 65$ MeV are from Ref. [42] (pd crosses) and Ref. [43] (nd circles).

dash-dotted and violet dotted curves represent the predictions obtained with JISP16, AV18, chiral N^4 LO with $R=0.9$ fm and AV18 + Urbana IX forces, respectively.

All these interaction models lead to very similar results for the differential cross section at $E = 5$ MeV delivering excellent data description, as is documented in Fig. 1. Note, the discrepancy between the predictions and the proton-deuteron data clearly visible at very forward scattering angles, originates from neglecting the Coulomb force in our theoretical calculations. A deviation among various predictions is seen at $E = 65$ MeV. While the chiral and the AV18 results are practically indistinguishable and underestimate the data, the JISP16 results are on the opposite side of the data. Only the AV18 + Urbana IX predictions correctly describe the data.

The polarization observables are more sensitive to the details of nuclear interactions. In the case of the neutron analyzing power $A_Y(N)$ shown in Fig. 2, the difference between the JISP16 predictions and those based on the AV18 or the chiral interactions appears already at $E = 5$ MeV. At the maximum of the $A_Y(N)$, the JISP16 overpredicts the experimental data while the AV18 and the chiral results are below the data. At small scattering angles all theoretical models underestimate the experimental results. At $E = 65$ MeV all models of nuclear forces give very similar results, in agreement with the data, for the scattering angles below approximately $\theta^{c.m.} = 110^\circ$. At larger angles, the JISP16 predictions differ from the remaining ones suggesting a poor data description. For this observable, at both energies, the three-nucleon force effects are negligible, thus the AV18 + Urbana IX predictions practically overlap with those employing the AV18 nucleon-nucleon force alone.

A big difference between the JISP16 results and those based on the other models used here can be observed in the case of the deuteron vector analyzing power iT_{11} at $E = 5$ MeV (see Fig. 3). At the maximum of the iT_{11} , the JISP16 predictions are twice as big as the others. This picture changes when moving to $E = 65$ MeV where all predictions are much closer to each other although some difference between predictions based on the JISP16 model and other results remains, especially in the $90^\circ < \theta^{c.m.} < 150^\circ$ range. The three-nucleon force effects are small at both energies and the AV18 and chiral predictions follow the data at $E = 65$ MeV. The

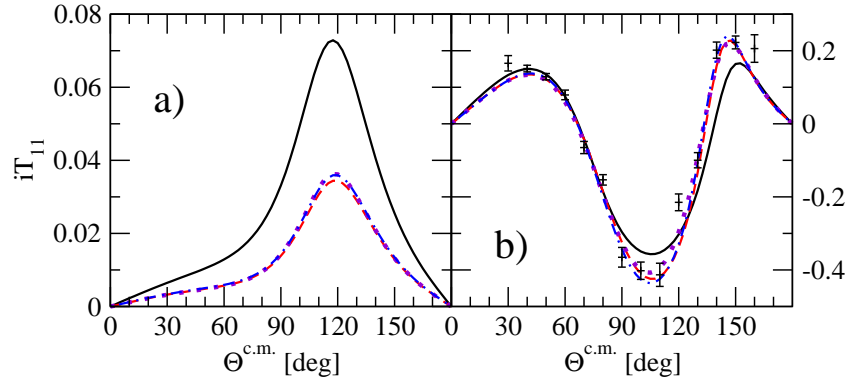


Figure 3: Deuteron analyzing power iT_{11} at the same energies as in Fig. 1. Curves are the same as in Fig. 1. Data at $E = 65$ MeV are from Ref. [46].

explanation of the puzzling behavior of the JISP16 potential at the lower energy has required a more detailed study and is discussed below.

Finally, in Fig. 4, T_{21} is shown as an example of the deuteron tensor analyzing powers. At both energies all interaction models predict qualitatively similar values of T_{21} and are in agreement with the data at $E = 65$ MeV. A closer look at Fig. 4b reveals that the JISP16 results are closer to the data at forward and at the very backward scattering angles while at medium angles the chiral N^4 LO model delivers the best data description. The three-nucleon force effects are again small and the AV18 + Urbana IX predictions usually overlap with those for the N^4 LO force.

The puzzling behavior of the JISP16 model in the case of the deuteron vector analyzing power iT_{11} has encouraged us to study this case in more detail. We present in Fig. 5 (in a restricted range of scattering angles) the results of calculations performed in such a way that for solving Eq. (6) the individual t -matrix elements for the JISP16 force in the two-nucleon subspace are replaced in given channels (defined by the l, s and j quantum numbers) by the same matrix elements taken from the chiral N^4 LO interaction. Thus the mixed interaction is used: in all partial waves the JISP16 force

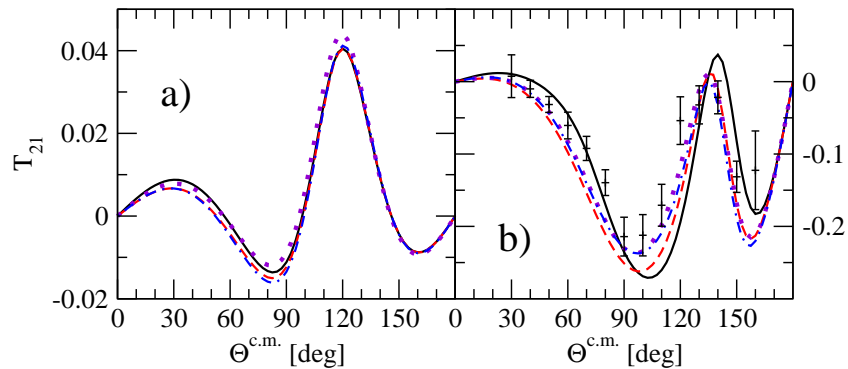


Figure 4: Deuteron tensor analyzing power T_{21} at the same energies as in Fig. 1. Curves are the same as in Fig. 1. Data at $E = 65$ MeV are from Ref. [46].

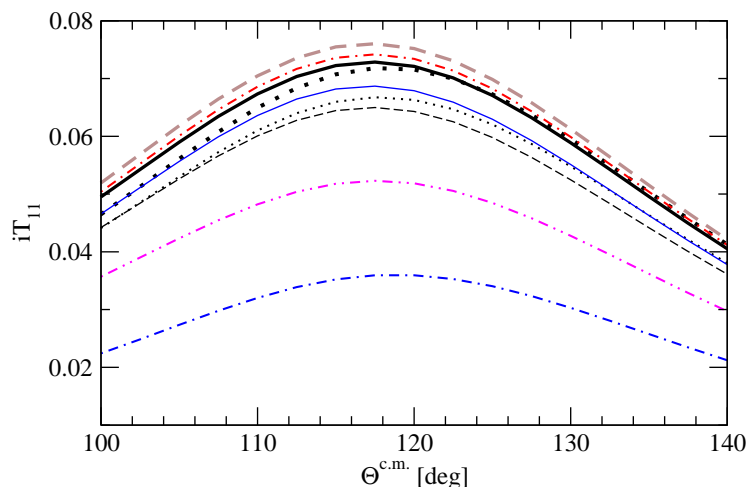


Figure 5: Deuteron vector analyzing power iT_{11} at $E = 5$ MeV. Predictions have been obtained with the JISP16 t -matrix with replacing its individual elements by the chiral N^4 LO ones (see text for more details) in 3P_0 (thin black dashed curve), 1S_0 and ${}^3S_1-{}^3D_1$ (thick black dotted curve), 1P_1 (thin black dotted curve), 3P_1 (thick brown dashed curve), 1D_2 (red dash-dotted curve), ${}^3P_2-{}^3F_2$ (magenta dash-double-dotted curve) or 3D_2 (thin blue solid curve) partial wave. The thick black solid curve represents the JISP16 results and the thick blue dash-dotted curve shows the chiral N^4 LO predictions.

is taken except for the one where it is replaced by the N^4 LO force. The results given in Fig. 5 demonstrate that different partial waves contribute to the iT_{11} with different strengths. The biggest change is caused by replacing the ${}^3P_2-{}^3F_2$ t -matrix which reduces the difference between the JISP16 and the chiral N^4 LO predictions by more than 50%. The 3P_0 and the 1P_1 channels are the next to produce the biggest changes in the iT_{11} values.

However, none of the exchanges of the individual partial wave in the t -matrix is able to explain completely the discrepancy between the JISP16 and the chiral N^4 LO predictions. Thus, in Fig. 6, we show what happens when not only a single individual partial wave is swapped but when a pair or more channels are replaced at the same time. We start from the simultaneous replacement of the ${}^3P_2-{}^3F_2$ and 3P_0 partial waves (the orange dashed curve). This reduces further the observed discrepancy by approximately 75%. A consecutive replacing of also the 3P_1 t -matrix does not introduce any visible shift but the interchanging in the 1P_1 partial wave on top of the ${}^3P_2-{}^3F_2$ and 3P_0 channels (the red dash-dotted curve) shifts the predictions in the proximity to the chiral results. Finally, exchanging all partial waves with $j \leq 2$ gives predictions overlapping with the pure N^4 LO results. This shows trivially that at this energy the higher partial waves can be neglected, but it demonstrates also that the difference in the deuteron wave function supported by the JISP16 and N^4 LO potentials, is unimportant in this case.

It is needed to check how the replacement of the P -waves influences predictions for other observables. In Fig. 7 we give an example of the nucleon analyzing power $A_Y(N)$ and the deuteron tensor analyzing power T_{21} at $E = 5$ MeV. In both cases we observe

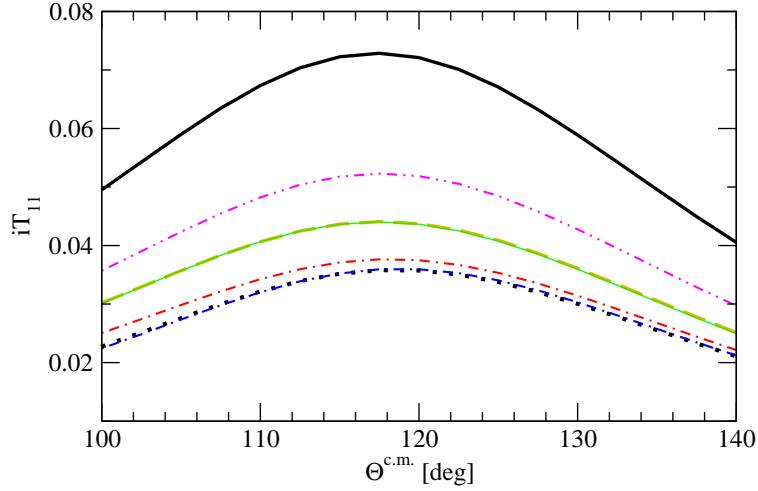


Figure 6: Deuteron vector analyzing power iT_{11} at $E = 5$ MeV. The thick black solid, thick blue dash-dotted and magenta dash-double-dotted curves are the same as in Fig. 5. Other curves present the predictions obtained with the JISP16 t -matrix with replacing some combinations of its matrix elements by the chiral N^4 LO ones: in the 3P_0 and ${}^3P_2-{}^3F_2$ partial waves (orange dashed), in the 3P_0 , 3P_1 and ${}^3P_2-{}^3F_2$ partial waves (thick green solid) and in the 1P_1 , 3P_0 and ${}^3P_2-{}^3F_2$ partial waves (red dash-dotted). The thick dotted curve shows the results obtained with the JISP16 t -matrix replaced by the chiral N^4 LO one in all partial waves with $j \leq 2$.

the anticipated behavior: when more partial waves are replaced, the predictions are shifted closer to the N^4 LO ones. This is also true for the differential cross section (not shown here), however the changes are practically negligible for this observable.

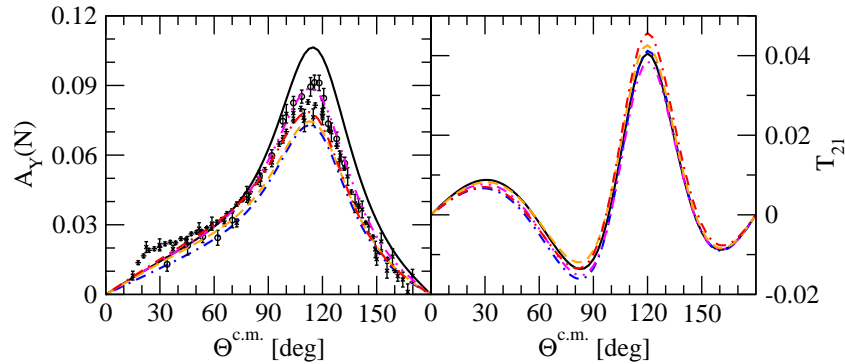


Figure 7: Nucleon analyzing power $A_Y(N)$ (left) and deuteron tensor analyzing power T_{21} (right) at $E = 5$ MeV. Curves are the same as in Fig. 6. Experimental data are the same as in Fig. 2.

4 Summary

In this contribution we present the first application of the JISP16 nucleon-nucleon interaction to the elastic nucleon-deuteron scattering process at incoming nucleon laboratory energies $E = 5$ MeV and $E = 65$ MeV. In addition to JISP16, the chiral N⁴LO interaction with a semi-local regularization using the regulator value of $R = 0.9$ fm and the semi-phenomenological AV18 nucleon-nucleon force are used. We present also the results obtained with the AV18 two-body force supplemented by the three-nucleon Urbana IX interaction.

For most of the observables, the N⁴LO predictions agree with those obtained using the AV18 interaction. The picture is more complicated for the JISP16 model. For some observables like the differential cross section or the deuteron tensor analyzing power T_{21} , the JISP16 results, in general, follow the data and predictions based on the remaining potentials. However, for other observables like the deuteron vector analyzing power iT_{11} , even at the lower energy, an essential discrepancy between the JISP16 results and predictions based on other applied interactions exists. The description of the three-nucleon scattering data obtained with the JISP16 model is not as good as the description of energy levels in nuclei observed for this force.

Comparing the AV18 + Urbana IX results with those based on the two-body JISP16 force only, we cannot conclude that the JISP16 results are closer to the predictions based on the two- and three-body potentials than the predictions obtained with other models of the nucleon-nucleon interaction.

We have found that the observed discrepancies originate from the off-shell behavior of the t -matrix operator for different P -waves derived from the JISP16 force. This in turn leads to the conclusion that in the future models of nuclear forces derived within the inverse scattering methods, the polarization observables should also be included into the set of observables used to fix parameters of the potential. Such an investigation is planned.

Acknowledgments

R. S. would like to thank the organizers of the NTSE-2016 conference for their hospitality and excellent organization of the conference. We would also like to thank Prof. Hiroyuki Kamada for helpful discussions. This work is a part of the LENPIC project. It was supported from the resources of the National Science Center (Poland) under the grants DEC-2013/10/M/ST2/00420 and DEC-2013/11/N/ST2/03733 and by the Russian Foundation for Basic Research under the grant No. 15-02-06604-a. The numerical calculations were done on the computers of the JSC in Jülich, Germany.

References

- [1] S. R. Beane, W. Detmold, K. Orginos and M. J. Savage, *Prog. Part. Nucl. Phys.* **66**, 1 (2011).
- [2] S. Aoki, *Prog. Part. Nucl. Phys.* **66**, 687 (2011).
- [3] V. Stoks, R. Klomp, M. Rentmeester and J. de Swart, *Phys. Rev. C* **48**, 792 (1993).

-
- [4] V. Stoks, R. Klomp, C. Terheggen and J. de Swart, *Phys. Rev. C* **49**, 2950 (1994).
- [5] R. Wiringa, V. Stoks and R. Schiavilla, *Phys. Rev. C* **51**, 38 (1995).
- [6] R. Machleidt, F. Sammarruca and Y. Song, *Phys. Rev. C* **53**, R1483 (1996).
- [7] R. Machleidt, *Phys. Rev. C* **63**, 024001 (2001).
- [8] R. Machleidt, *Nucl. Phys. A* **689**, 11c (2001).
- [9] A. M. Shirokov, J. P. Vary, A. I. Mazur and T. A. Weber, *Phys. Lett. B* **644**, 33 (2007).
- [10] A. M. Shirokov, J. P. Vary, A. I. Mazur, S. A. Zaytsev and T. A. Weber, *Phys. Lett. B* **621**, 96 (2005).
- [11] A. M. Shirokov, A. I. Mazur, S. A. Zaytsev, J. P. Vary and T. A. Weber, *Phys. Rev. C* **70**, 044005 (2004).
- [12] B. R. Barrett, P. Navrátil and J. P. Vary, *Prog. Part. Nucl. Phys.* **69**, 131 (2013).
- [13] T. Heng, J. P. Vary and P. Maris, *Phys. Rev. C* **95**, 014306 (2017).
- [14] A. M. Shirokov, A. G. Negoita, J. P. Vary, S. K. Bogner, A. I. Mazur, E. A. Mazur and D. Gogny, *Phys. Rev. C* **90**, 024324 (2014).
- [15] A. M. Shirokov, V. A. Kulikov, P. Maris and J. P. Vary, in *NN and 3N interactions*, eds. L. D. Blokhintsev and I. I. Strakovsky. Nova Science, Hauppauge, NY, 2014, Chap. 8, p. 231,
http://www.novapublishers.com/catalog/product_info.php?products_id=50945.
- [16] E. Epelbaum, *Prog. Part. Nucl. Phys.* **57**, 654 (2006).
- [17] D. R. Entem, N. Kaiser, R. Machleidt and Y. Nosyk, *Phys. Rev. C* **92**, 064001 (2015).
- [18] E. Epelbaum, W. Glöckle and U.-G. Meißner, *Nucl. Phys. A* **637**, 107 (1998).
- [19] E. Epelbaum, W. Glöckle and U.-G. Meißner, *Nucl. Phys. A* **671**, 295 (2000).
- [20] E. Epelbaum, W. Glöckle and U.-G. Meißner, *Nucl. Phys. A* **747**, 362 (2005).
- [21] E. Epelbaum, H. Krebs and U.-G. Meißner, *Eur. Phys. J. A* **51**, 53 (2015).
- [22] E. Epelbaum, H. Krebs and U.-G. Meißner, *Phys. Rev. Lett.* **115**, 12, 122301 (2015).
- [23] E. Epelbaum, A. Nogga, W. Glöckle, H. Kamada, U.-G. Meißner and H. Witała, *Phys. Rev. C* **66**, 064001 (2002).
- [24] H. Witała, J. Golak, R. Skibiński and K. Topolnicki, *J. Phys. G* **41**, 094011 (2014).
- [25] J. Golak *et al.*, *Eur. Phys. J. A* **50**, 177 (2014).
- [26] R. Skibiński, J. Golak, H. Witała, W. Glöckle, A. Nogga and E. Epelbaum, *Acta Phys. Polon. B* **37**, 2905 (2006).

- [27] R. Skibiński, J. Golak, D. Rozpędzik, K. Topolnicki and H. Witała, *Acta Phys. Polon. B* **46**, 159 (2015).
- [28] D. Rozpędzik, J. Golak, S. Kölling, E. Epelbaum, R. Skibiński, H. Witała and H. Krebs, *Phys. Rev. C* **83**, 064004 (2011).
- [29] S. Binder *et al.* (LENPIC Collaboration), *Phys. Rev. C* **93**, 044002 (2016).
- [30] R. Skibiński *et al.*, *Phys. Rev. C* **93**, 064002 (2016).
- [31] W. Glöckle, H. Witała, D. Hüber, H. Kamada and J. Golak, *Phys. Rep.* **274**, 107 (1996).
- [32] H. Witała, W. Glöckle, J. Golak, A. Nogga, H. Kamada, R. Skibiński and J. Kuroś-Zohmierzuk, *Phys. Rev. C* **63**, 024007 (2001).
- [33] K. Sagara, *Few-Body Syst.* **48**, 59 (2010).
- [34] N. Kalantar-Nayestanaki, E. Epelbaum, J. G. Messchendorp and A. Nogga, *Rep. Prog. Phys.* **75**, 016301 (2012).
- [35] K. Sekiguchi, *see these Proceedings*, p. 60,
<http://www.ntse-2016.khb.ru/Proc/Sekiguchi.pdf>.
- [36] A. Deltuva, A. C. Fonseca and P. U. Sauer, *Phys. Rev. C* **73**, 057001 (2006).
- [37] A. Kievsky, M. Viviani and S. Rosati, *Phys. Rev. C* **52**, R15(R) (1995).
- [38] O. Rubtsova, V. N. Pomerantsev and V. I. Kukulin, *see these Proceedings*, p. 205,
<http://www.ntse-2016.khb.ru/Proc/Rubtsova.pdf> and references therein.
- [39] H. Witała, J. Golak, R. Skibiński, W. Glöckle, H. Kamada and W. N. Polyzou, *Phys. Rev. C* **83**, 044001 (2011); *ibid.* **88**, 069904 (2013).
- [40] H. Witała, R. Skibiński, J. Golak and W. Glöckle, *Eur. Phys. J. A* **41**, 369 (2009).
- [41] K. Sagara, H. Oguri, S. Shimizu, K. Maeda, H. Nakamura, T. Nakashima and S. Morinobu, *Phys. Rev. C* **50**, 576 (1994).
- [42] S. Shimizu, K. Sagara, H. Nakamura, K. Maeda, T. Miwa, N. Nishimori, S. Ueno, T. Nakashima and S. Morinobu, *Phys. Rev. C* **52**, 1193 (1995).
- [43] H. Rühl *et al.*, *Nucl. Phys. A* **524**, 377 (1991).
- [44] W. Tornow *et al.*, *Phys. Lett. B* **257**, 273 (1991).
- [45] R. E. White, W. Grüebler, B. Jenny, V. König, P. A. Schmelzbach and H. R. Bürgi, *Nucl. Phys. A* **321**, 1 (1979).
- [46] H. Witała *et al.*, *Few-Body Syst.* **15**, 67 (1993).

Deuteron Coulomb Excitation in Peripheral Collisions with a Heavy Ion

W. Du^a, P. Yin^b, G. Chen^a, X. Zhao^b and J. P. Vary^a

^a*Department of Physics and Astronomy, Iowa State University, Ames, IA 50011, USA*

^b*Institute of Modern Physics, Chinese Academy of Sciences, Lanzhou, 730000, China*

Abstract

We develop and test an *ab initio* time-dependent Basis Function (tBF) method to solve non-perturbative and time-dependent problems in quantum mechanics. For our test problem, we apply this method to the Coulomb excitation of the deuteron by an impinging heavy ion. In the tBF method applied to deuterium, we employ wave functions for its bound and excited states to calculate its transition probabilities and the r.m.s. radius during the scattering process. For comparison, corresponding results based on first-order perturbation theory are also provided. For the Coulomb excitation process in a weak and time-varying Coulomb field, where higher-order effects are negligible, we obtain a good agreement of the results based on these two methods. The tBF method is then applied to the Coulomb excitation process with stronger external field. The higher-order effects, such as those appearing in the reorientation of the polarization of the deuteron system, are analyzed.

Keywords: *Coulomb excitation; non-perturbative; ab initio method*

1 Introduction

The importance of Coulomb excitation and its application in nuclear physics are well known (see, e. g., Ref. [1] and references therein). A target nucleus transitions to excited states when scattered by the electromagnetic (E&M) field produced by a projectile heavy ion. First order perturbation theory works well when the field is weak. When the field is strong (from, e. g., a highly charged ion), higher order effects, such as reorientation, become important. For a precise description, the numerical solution obtained from direct treatment of the time-dependent Schrödinger equation is necessary [2]. In this work, we present a non-perturbative method to solve the time-dependent Schrödinger equation, called the time-dependent basis function (tBF) method. It is closely related to our previous work on time-dependent Basis Light-Front Quantization (tBLFQ) [3, 4]. It enables tracking the evolution of quantum states as a function of time. The dynamics of the quantum system is revealed at the amplitude level. The tBF method will be especially useful when the interactions are strong, in which cases the perturbative calculations are not reliable.

Proceedings of the International Conference ‘Nuclear Theory in the Supercomputing Era — 2016’ (NTSE-2016), Khabarovsk, Russia, September 19–23, 2016. Eds. A. M. Shirokov and A. I. Mazur. Pacific National University, Khabarovsk, Russia, 2018, p. 102.

<http://www.ntse-2016.khb.ru/Proc/Zhao.pdf>.

In this paper, the deuteron Coulomb excitation problem is studied as a first test. The heavy ion impinges along a fixed impact parameter so the center of mass of the deuteron is held fixed during the collision process. The impact parameter is set to be sufficiently large such that the strong nuclear force does not affect the scattering. The projectile ion generates both time-varying electric (Coulomb) field and magnetic field. While both the neutron and the proton interact with the magnetic field, only the proton gets repelled by the Coulomb field. After the scattering, the polarization of the deuteron system has been reoriented. For our initial test application, we will consider only the Coulomb excitation effects modeled through the electric dipole transition operator.

2 Theory and properties of the test application

For the purposes of introducing our tBF approach, we will take the specific example of a peripheral heavy-ion collision with a deuteron and consider only its Coulomb excitation. The target can easily be generalized to other systems such as ${}^6\text{Li}$ or ${}^{12}\text{C}$. Each of the simplifications will be lifted in future efforts as our main purpose here is to introduce the method and provide initial tests. A main feature of our approach is that we employ *ab initio* solutions for the ground and excited states of the target system based on a realistic inter-nucleon interaction. Of course, phenomenological target wave functions may also be employed and may be necessary for heavier targets.

2.1 Target properties

Within our application of the tBF method, the state wave functions of the target, the neutron-proton (np) system, are solved with JISP16 NN interaction [5–7]. A multipole expansion is conducted for the Coulomb field [8] produced by the heavy ion and only the $E1$ multipole component is taken into account. The interaction between the field and the np system can be expressed in terms of the nuclear matrix elements that determine the radiative transitions. The time-dependent state wave functions of the np system are solved numerically and then applied to calculate the transition probabilities between states as well as the r.m.s. radius of the np system. We demonstrate how the tBF method provides a complete dynamic picture of the evolution of the np system, where all the higher-order effects are taken into account.

2.2 Peripheral scattering setup

The scattering plane is set to be the x - z plane, as shown in Fig. 1. The heavy ion, with charge Ze , moves straight with a constant velocity parallel to the \hat{z} -axis. The speed is taken as 0.1 (note we adopt the natural units and set $\hbar = c = 1$ throughout the paper) for our numerical results. The impact parameter is sufficiently large (taken as 7.5 fm for our numerical application) such that the strong nuclear force does not play a role. The nucleon mass is taken to be 938.92 MeV and the unit charge of the deuteron target is carried by the proton. No meson exchange current is evaluated. As an approximation, we consider the case where the impact parameter is constant throughout the collision process so that the center of mass of the target is always fixed at the origin. In this work, we consider only the $E1$ multipole contribution for the Coulomb excitation, though other multipole components, e. g., $E0$, $M1$, $E2$,

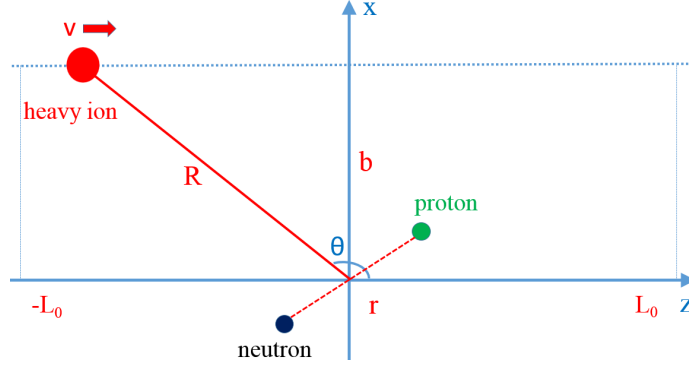


Figure 1: Schematic view of the scattering between the heavy ion and the deuteron target. The scattering plane is set to be in the x - z plane. The heavy ion moves in a straight trajectory parallel to the \hat{z} -axis. The center of mass of the target is fixed at the origin. No recoil of the target is considered when the heavy ion skims over. b is the impact parameter, v is the constant speed of the heavy ion projectile (along the \hat{z} -axis), L_0 is the horizontal distance to cut off the Coulomb interaction between the np system and the heavy ion, θ is the polar angle of the position of the heavy ion, R is the distance from the center of heavy ion to the origin, r is the separation between the proton and the neutron.

etc., contribute to the full problem. A cut-off distance is introduced for the Coulomb interaction, beyond which no significant transition takes place.

2.3 Hamiltonian

In the relative coordinates of the np system, the full Hamiltonian H_{full} (for the target interacting with external E&M field generated by the moving heavy ion) consists of two parts

$$H_{full} = H_0 + V_{int}, \quad (1)$$

where

$$H_0 = H_{KE} + V_{NN} + H_{ext} \quad (2)$$

is the time-independent Hamiltonian for the np system. The H_{KE} is the intrinsic kinetic energy of the np system. The V_{NN} describes the realistic nucleon-nucleon (NN) interaction. In this work, it is taken to be the JISP16 NN interaction [5–7]. Since the np system is weakly bound, a small external harmonic oscillator (HO) trap H_{ext} with $\omega = 5$ MeV is introduced to regulate the continuum states and produce a discretized representation of the continuum. In future works, we will employ a basis space regulator that does not affect the ground state while discretizing the continuum without an external field.

All the eigenstates of H_0 are obtained by diagonalization in a sufficiently large model space

$$H_0|\beta_j\rangle = E_j|\beta_j\rangle. \quad (3)$$

These energy eigenstates form the complete basis set $\{|\beta_j\rangle\}$ of the np system in our test problem. The time-dependent background field V_{int} induces transitions between eigenstates of the np system in the trap.

2.4 Background field

V_{int} is the time-dependent part of the full Hamiltonian. It is evaluated locally through the coupling between the four potential $A^\mu = (\varphi, \vec{A})$ from the moving charge and the four current of the np system $J^\mu = (\rho, \vec{j})$,

$$V_{int}(t) = \int A_\mu J^\mu d\vec{r} = \int \rho(\vec{r}, t) \varphi(\vec{r}, t) d\vec{r} - \int \vec{j}(\vec{r}, t) \cdot \vec{A}(\vec{r}, t) d\vec{r}, \quad (4)$$

where the relative coordinates relate to the single-particle coordinates of the np system as $\vec{r} = \vec{r}_p - \vec{r}_n$. The second term in Eq. (4) is neglected since the heavy ion is moving with low velocity in our initial application. Only the interaction between the Coulomb field of the incident heavy ion and the charge of the np system is evaluated. Moreover, the multipole expansion of the Coulomb field [8] is performed and only the $E1$ term is kept.

2.5 Interaction picture

The basis set is formed by the eigenstates of the free Hamiltonian H_0 . The transitions between these eigenstates are described in the interaction picture, in which the equation of motion (EOM) of the np system is

$$i \frac{\partial}{\partial t} |\psi; t\rangle_I = e^{iH_0 t} V_{int}(t) e^{-iH_0 t} |\psi; t\rangle_I \equiv V_I(t) |\psi; t\rangle_I, \quad (5)$$

where $V_I(t)$ is the interaction part of Hamiltonian in the interaction picture. The subscript ‘‘I’’ is adopted to distinguish the quantities in the interaction picture from those in the Schrödinger picture. The above EOM can be solved by integration

$$|\psi; t\rangle_I = \hat{T} \left\{ \exp \left[-i \int_{t_0}^t V_I(t') dt' \right] \right\} |\psi; t_0\rangle_I, \quad (6)$$

where \hat{T} is the time ordering operator towards the future. Instead of functional expansion in perturbation theory, the above equation is evaluated numerically in the tBF approach. For this purpose, we divide the time interval $[-T, T]$ into n segments, each segment with step length $\delta t = \frac{2T}{n}$. The integration in the exponent is then replaced as

$$\hat{T} \left\{ \exp \left[-i \int_{-T}^T V_I(t) dt \right] \right\} \xrightarrow{\sum \delta t} \left[1 - iV_I(t_n) \delta t \right] \left[1 - iV_I(t_{n-1}) \delta t \right] \cdots \left[1 - iV_I(t_1) \delta t \right]. \quad (7)$$

By multiple insertions of the projection operator defined from this complete basis set in Eq. (3),

$$\mathbf{1} = \sum_j |\beta_j\rangle \langle \beta_j|, \quad (8)$$

the right hand side of Eq. (7) reduces to matrix multiplications. The final state after evolution $|\psi; t\rangle_I$ in Eq. (6) is therefore obtained.

2.6 Interaction matrix

Taking only the $E1$ multipole component of the Coulomb field, the transition matrix element [1, 2] is

$$\langle \beta_j | V_I(t) | \beta_k \rangle = \frac{4\pi}{3} Z \alpha e^{i(E_j - E_k)t} \sum_{\mu} \frac{Y_{1\mu}^*(\Omega_{\vec{R}})}{|\vec{R}(t)|^2} \langle \beta_j | \frac{r}{2} Y_{1\mu}(\Omega_{\vec{r}}) | \beta_k \rangle, \quad (9)$$

where E_j and E_k are respective eigenenergies of eigenvectors $|\beta_j\rangle$ and $|\beta_k\rangle$ of the Hamiltonian H_0 , $Y_{\lambda\mu}(\Omega)$ ($\lambda = 1$ for the $E1$ multipole contribution) denotes the spherical harmonics following the Condon–Shortley convention [9], and α is the coupling constant for the E&M interaction. In the relative coordinates of the np system, r is the distance from the proton to the neutron, while $\vec{R}(t)$ is the position of the heavy ion projectile. The kernel in Eq. (9) is the matrix element for the $E1$ transition between eigenstates of the np system.

To compute the interaction matrix, the three dimensional harmonic oscillator (3DHO) representation is adopted. We adopt a model space truncation parameter $2n + l \leq N_{\max} = 60$ to define our approximation to the full basis space which leads to our definition of the complete 3DHO basis set $\{|nlsJM\rangle\}$ for each eigenvector in the basis set $\{|\beta_j\rangle\}$ of the np system (specified by good quantum numbers s , J and M):

$$\mathbf{1} = \sum_{nl} |nlsJM\rangle \langle nlsJM|. \quad (10)$$

Here, for each 3DHO basis wave function, n is the radial quantum number which denotes the number of nodes of the radial part of the wave function, l is the quantum number of orbital angular momentum \vec{l} , s is the quantum number for spin \vec{s} , \vec{l} and \vec{s} couple to the total angular momentum \vec{J} , which is a conserved quantity of the Hamiltonian H_0 . M is the magnetic quantum number of \vec{J} along the quantization axis (\hat{z} -axis in this case). The $E1$ matrix element in Eq. (9) becomes

$$\begin{aligned} & \langle \beta_j | \frac{r}{2} Y_{1\mu}(\hat{r}) | \beta_k \rangle \\ &= \sum_{nl} \sum_{n'l'} \langle \xi_j J_j M_j | nls J_j M_j \rangle \langle nls J_j M_j | \frac{r}{2} Y_{1\mu}(\hat{r}) | n'l' s' J_k M_k \rangle \langle n'l' s' J_k M_k | \xi_k J_k M_k \rangle, \end{aligned} \quad (11)$$

where

$$|\beta_j\rangle = \sum_{nl} \langle nls J_j M_j | \xi_j J_j M_j \rangle |nls J_j M_j\rangle \equiv \sum_{nl} a_{j;nl} |nls J_j M_j\rangle, \quad (12)$$

$$|\beta_k\rangle = \sum_{n'l'} \langle n'l' s' J_k M_k | \xi_k J_k M_k \rangle |n'l' s' J_k M_k\rangle \equiv \sum_{n'l'} a_{k;n'l'} |n'l' s' J_k M_k\rangle, \quad (13)$$

and ξ_j and ξ_k denote additional quantum numbers necessary to describe $|\beta_j\rangle$ and $|\beta_k\rangle$, respectively. In this work, the amplitudes $\{a_{j;nl}\}$ and $\{a_{k;n'l'}\}$ are solved by diagonalization of H_0 in the 3DHO representation. The middle kernel in Eq. (11) is the $E1$ matrix element $(r/2)Y_{1\mu}(\hat{r})$ in the 3DHO representation. It can be solved by

converting into the coordinate representation,

$$\begin{aligned} & \langle nlsJ_j M_j | \frac{r}{2} Y_{1\mu}(\hat{r}) | n'l's' J_k M_k \rangle \\ &= \sum_{m_l m_s} \sum_{m'_l m'_s} \delta_{ss'} \delta_{m_s m'_s} (lm_l s m_s | J_j M_j) (l' m'_l s' m'_s | J_k M_k) \int R_{nl}^*(r) \frac{r}{2} R_{n'l'}(r) r^2 dr \\ & \quad \times (-1)^{m_l} \sqrt{\frac{3(2l+1)(2l'+1)}{4\pi}} \begin{pmatrix} l & 1 & l' \\ -m_l & \mu & m'_l \end{pmatrix} \begin{pmatrix} l & 1 & l' \\ 0 & 0 & 0 \end{pmatrix}, \end{aligned} \quad (14)$$

where $R_{nl}(r)$ is the radial part of 3DHO wave function in the coordinate representation,

$$R_{nl}(r) = \sqrt{\frac{2n!}{r_0^3 \Gamma(n+l+\frac{3}{2})}} \left(\frac{r}{r_0}\right)^l \exp\left(-\frac{r^2}{2r_0^2}\right) L_n^{l+\frac{1}{2}}\left(\frac{r^2}{r_0^2}\right), \quad (15)$$

with $L_n^\alpha(r^2/r_0^2)$ the associated Laguerre polynomial. $r_0 = \sqrt{1/m\omega}$ is the oscillator length with m the reduced mass of the np system and the HO frequency ω taken to be the same as the frequency of the trap. This definition ensures that $R_{nl}(r)$ starts positive at the origin. The radial integral in Eq. (14) is evaluated to be

$$\begin{aligned} & \int R_{nl}^*(r) \frac{r}{2} R_{n'l'}(r) r^2 dr \\ &= \frac{r_0}{2} \begin{cases} \sqrt{n+l+\frac{3}{2}} \delta_{nn'} - \sqrt{n} \delta_{n,n'+1} & \text{for } l' = l+1; \\ \sqrt{n'+l'+\frac{3}{2}} \delta_{nn'} - \sqrt{n'} \delta_{n',n+1} & \text{for } l = l'+1; \\ 0 & \text{else.} \end{cases} \end{aligned} \quad (16)$$

$(lm_l s m_s | J_j M_j)$ in Eq. (14) is the CG-coefficient and

$$\begin{pmatrix} l & 1 & l' \\ -m_l & \mu & m'_l \end{pmatrix}$$

is the $3j$ -symbol following the Condon–Shortley convention [9]. The angular part determines the selection rule of the $E1$ transition.

2.7 Evolution of states

The method described in Eq. (7) is known as the Euler scheme. This approach is not stable because it is not symmetric in time. The norm of the state vector $|\psi; t\rangle_I$ may not be conserved under time evolution [10], which violates the conservation of probability. We therefore adopt the MSD2 [11] scheme

$$|\psi; t + \delta t\rangle_I \approx |\psi; t - \delta t\rangle_I - 2iV_I(t) \delta t |\psi; t\rangle_I. \quad (17)$$

For comparison with results from the MSD2 scheme, we also present the evolution calculated from the first-order perturbation theory. From Eq. (7), the evolution of state vector is evaluated to the leading order in the interaction V_I ,

$$|\psi; t_n\rangle_I \rightarrow \left[1 - i \delta t (V_I(t_n) + V_I(t_{n-1}) + \dots + V_I(t_1)) \right] |\psi; 0\rangle_I. \quad (18)$$

2.8 Observables

During the evolution, the wave function of the np system at a certain moment in terms of the basis set $\{|\beta_j\rangle\}$ is

$$|\psi; t\rangle = \sum_j A_j(t) |\beta_j\rangle, \quad (19)$$

where $|\beta_j\rangle$ denotes the tBF basis solved from Eq. (3). The amplitudes $A_j(t)$ are tracked for each basis state during evolution. Applying the time-dependent np wave function Eq. (19), we can track the r.m.s. radius of the np system as

$$\langle r^2(t) \rangle^{\frac{1}{2}} = \frac{1}{2} \sqrt{\langle \psi; t | r^2 | \psi; t \rangle}. \quad (20)$$

3 Results and discussion

For our test problem, we consider 3 interaction channels for the np system. They are $({}^3S_1, {}^3D_1)$, 3P_0 and 3P_1 . For each channel, the lowest states (degenerate in magnetic quantum numbers M) of H_0 are considered. The eigenenergy of each state is also shown in Fig. 2.

The heavy ion projectile is chosen to be fully stripped (all electrons removed) ${}^{124}\text{Sn}$, with $Z = 50$. It moves in a straight trajectory parallel to the \hat{z} -axis with a constant velocity which magnitude is set to 0.1 in our test problem. The center of mass of the np system is fixed at the origin. The impact parameter is fixed to be 7.5 fm. The exposure duration is 10 MeV $^{-1}$ (6.582×10^{-21} sec), during which time the projectile travels approximately 200 fm (100 fm before distance of closest approach and 100 fm after that). The initial state is prepared to be polarized along the negative \hat{z} -axis. That is, the initial state is selected to be the $({}^3S_1, {}^3D_1)$, $M = -1$ state.

Applying either the tBF method or the first-order perturbation theory, we will calculate the wave functions of the np system at selected moments during evolution. The wave functions are then applied to calculate the transition probabilities as well as the r.m.s. radius of the np system as a function of time. The dependence of these properties on the strength of external Coulomb field is also investigated by altering the coupling constant. We note that our discussion of properties at intermediate times is allowed in quantum mechanics but only the results at asymptotic times correspond to experimental observables.

$({}^3S_1, {}^3D_1)$	$M = -1$	-0.65289 MeV
$({}^3S_1, {}^3D_1)$	$M = 0$	-0.65289 MeV
$({}^3S_1, {}^3D_1)$	$M = +1$	-0.65289 MeV
3P_0	$M = 0$	12.0733 MeV
3P_1	$M = -1$	12.7585 MeV
3P_1	$M = 0$	12.7585 MeV
3P_1	$M = +1$	12.7585 MeV

Figure 2: Basis set of the np system for evolution.

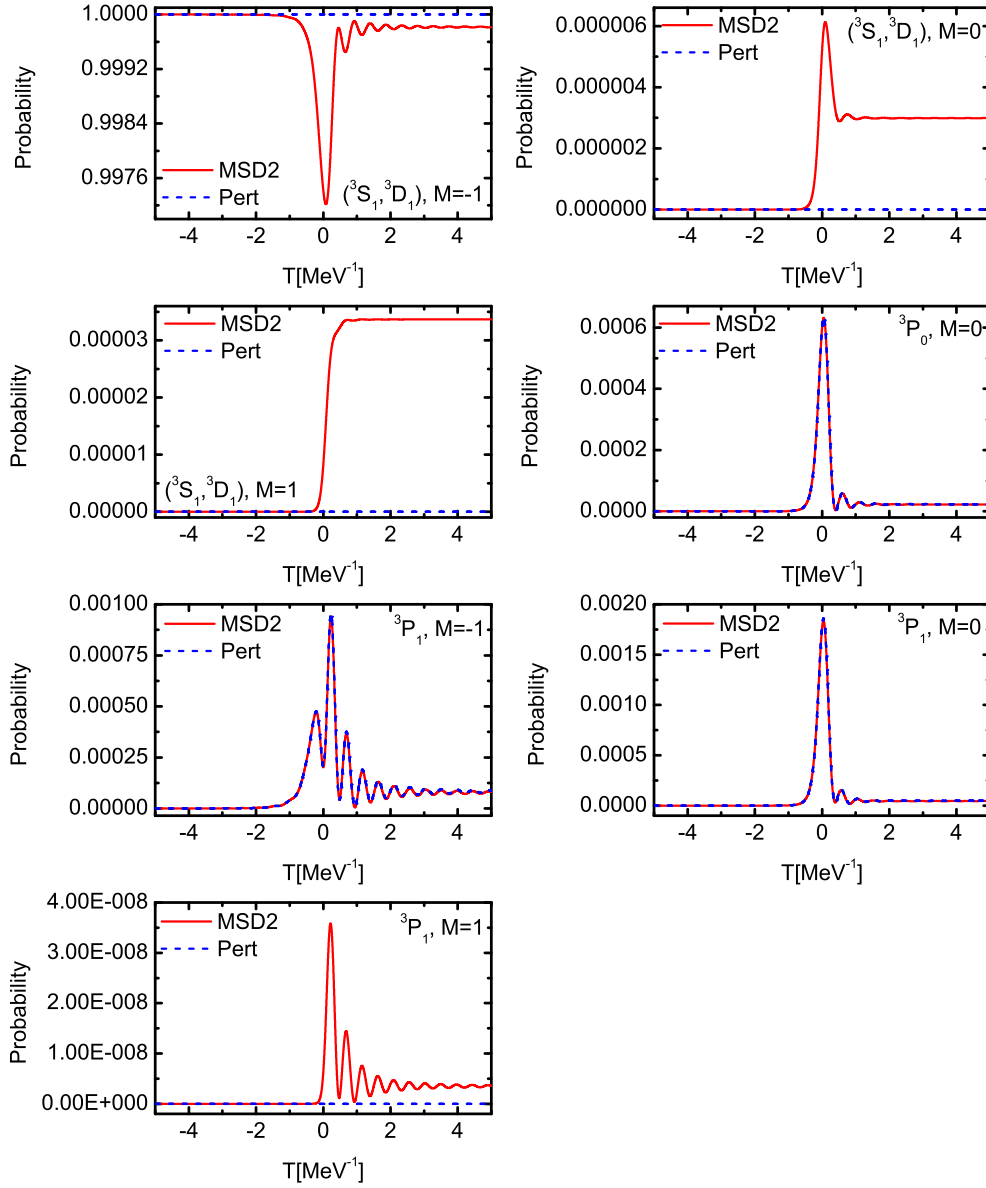


Figure 3: Time evolution of the np system (characterized by 7 basis states) in the weak and time-varying Coulomb field. The initial deuteron system is polarized along the negative \hat{z} -axis. The duration is 10 MeV^{-1} and the coupling constant is $1/137.04$. The charge of the heavy ion projectile is $Z = 50$ and it moves parallel to the \hat{z} -axis with a constant speed 0.1 . The impact parameter is 7.5 fm . The initial state is prepared to be the $({}^3S_1, {}^3D_1)$, $M = -1$ ground state (the lowest basis state in our eigenbasis). For each basis state, the red solid curve represents the probability calculated by the MSD2 scheme during evolution, while the blue dashed curve is the result from first-order perturbation theory.

3.1 Results with the physical coupling constant

In Fig. 3, we plot the time evolution of the probabilities of the np system when it is exposed to a weak, time-varying Coulomb field. The coupling constant is set to be $\alpha = 1/137.04$.

Intense probability fluctuations are found for some states at the middle of the scattering process, when the heavy ion is close to the np system. Such fluctuations are transient and they are signs of the virtual quantum processes. The probabilities converge to stable values when the Coulomb field fades away. The distance for the Coulomb field to be effective is related to the external interaction energy V_{int} and internal energy gaps of the np system.

For levels that obey the $E1$ selection rule, good agreement for the transition probabilities is obtained between calculations from the tBF method (red solid lines) and calculations from first-order perturbation theory (blue dashed lines). This shows that the tBF method is consistent with first-order perturbation theory when the interaction field is weak. For states that violate the $E1$ selection rule, however, differences are found between the results from the tBF method and those from first-order perturbation theory. For example, the forbidden states, (${}^3S_1, {}^3D_1$), $M = 0$ state, (${}^3S_1, {}^3D_1$), $M = 1$ state and 3P_1 , $M = 1$ state are excited at the end of evolution, though with relatively small probabilities. These “forbidden transitions” result from the higher-order processes which are excluded from first-order perturbation theory.

In Fig. 4, we present the r.m.s. radius for the np system during evolution. Due to the external HO potential trap H_{ext} in Eq. (2) introduced for constraining the np system, its r.m.s. radius before evolution, 1.472 fm, is approximately 25% smaller than the physical r.m.s. radius, 1.975(3) fm, of the natural deuteron [12, 13]. The r.m.s. radius expands when the np system gets excited to high-lying levels. The tiny difference in the r.m.s. radii given by the two approaches is due to the “forbidden transitions” to high-lying levels, which are the higher-order effects included by the tBF method. In general, the r.m.s. radius given by the tBF method (red solid line) agrees with that based on the perturbation theory (blue dashed line). At the end of evolution, both methods predict the net expansion of the order of 10^{-4} fm.

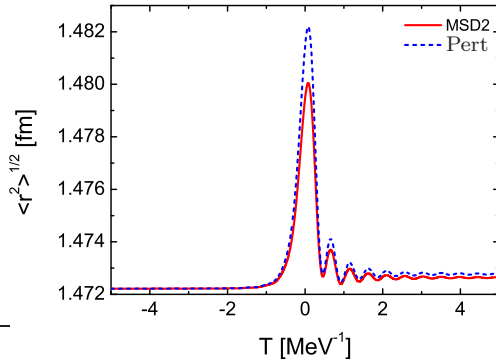


Figure 4: The r.m.s. radius of the np system during evolution. The simulation conditions for the intermediate np wave functions are the same as those described in Fig. 3. The red solid curve represents the r.m.s. radius calculated from the wave function obtained via the tBF method, while the blue dashed curve is the r.m.s. radius based on the wave function from first-order perturbation theory.

3.2 Results with an enlarged coupling constant

We test the tBF method for the evolution of the np system in the presence of a stronger and time-varying Coulomb field, where the coupling constant is set to $\alpha = 1/13.704$. We perform this calculation in order to enhance the visibility of the non-perturbative quantum effects that may become more evident with closer encounters and/or with relativistic heavy ions.

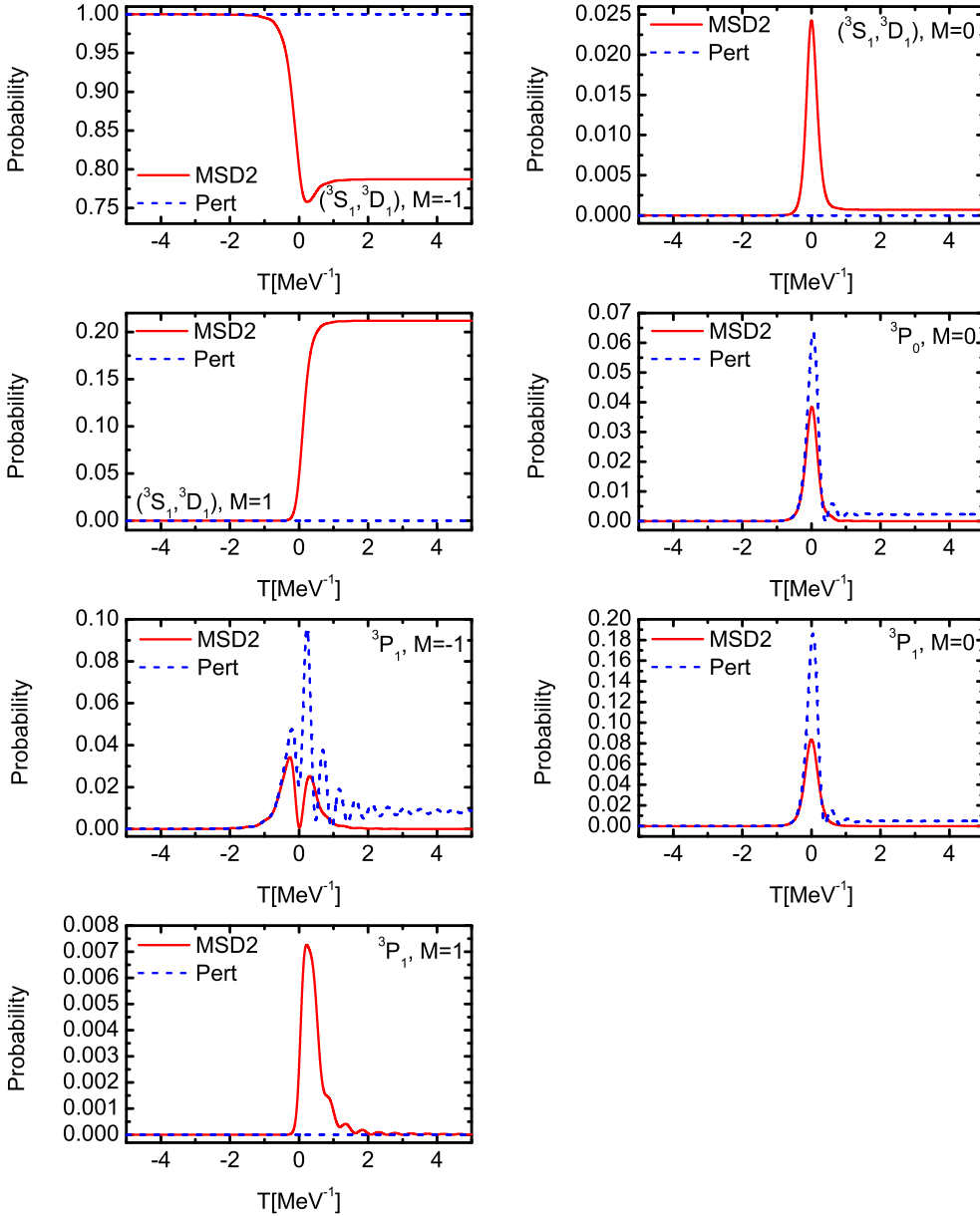


Figure 5: The same as in Fig. 3. However, the coupling constant is set to $1/13.704$.

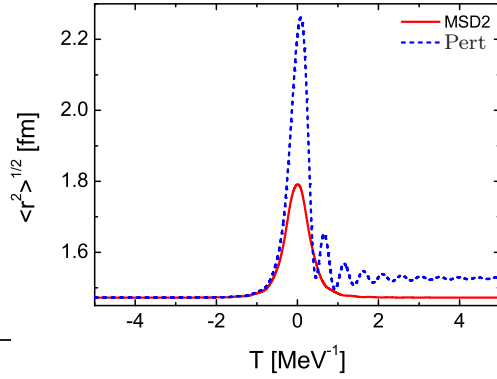


Figure 6: The same as in Fig. 4. However, the coupling constant is set to $1/13.704$.

For the np system, the non-perturbative tBF calculation for the transition probabilities during evolution (red solid lines) are shown in Fig. 5. The transition probabilities based on first-order perturbation theory are again provided (blue dashed lines) for comparison. However, it is easily anticipated, and observed, that first-order perturbation theory is not sufficient in this case.

The evident difference on transition probabilities is found between the calculation based on the tBF method and that on first-order perturbation theory. This difference shows that the higher-order effects are crucial for the precise calculation of the Coulomb excitation process in a strong field. Such higher order effects result in a significant reorientation of the polarization of the np system. This is observed from the large transition probabilities to levels that are forbidden by the first order $E1$ selection rule, e. g., to the $({}^3S_1, {}^3D_1)$, $M = 1$ state.

We observe that the np system is not significantly excited at the end of evolution. Though re-distributed, almost all of the population are still resident in the $({}^3S_1, {}^3D_1)$ levels. This results in a negligible expansion of the np system after the scattering process (Fig. 6), which is at the order of 10^{-4} fm. Note that the r.m.s. radius is a simple characteristic of the full final state distribution. Population of the excited states would be expected to lead to breakup or gamma emission back to the ground state but we do not incorporate those final state effects in our current calculations.

4 Conclusions and outlook

We have developed and applied a non-perturbative method, the time-dependent Basis Function (tBF) method, to study scattering problems in strong and time-dependent external fields. Since the tBF method enables calculations of intermediate state wave functions, it enables a detailed investigation on the dynamics of a system during evolution. As a test problem, we study the Coulomb excitation of the deuteron target when a heavy ion projectile impinges. The target deuteron is placed in a weak external harmonic oscillator potential trap and its center of mass is fixed. The energy eigenfunctions of the target (np) system are calculated with the JISP16 NN -interaction, from which only seven of them are kept as basis states for this test problem. For simplicity, only the $E1$ component of the Coulomb field is considered. Due to the Coulomb excitation, the np system gets excited during the scattering process. We calculate the np wave functions at selected moments during evolution

based on the tBF method. The wave functions are then applied to calculate the transition probabilities as well as the r.m.s. radius of the np system. For comparison, we also provide corresponding calculations which are based on first-order perturbation theory.

We first study the Coulomb excitation problem in a weak, time-varying external field. For those states that obey the $E1$ selection rule, we obtain agreement for the transition probability between these two approaches. This confirms that the tBF method is consistent with first-order perturbation theory in the limit of the weak interaction field. However, for the other states that violate the $E1$ selection rule, deviations from zero are obtained in the tBF approach. These deviations signify the higher-order effects missing in first-order perturbation theory.

In scattering problems with a stronger interaction field, the higher-order effects are expected to be important. To show this, we investigate the same Coulomb excitation problem but with a strong, time-varying external field. We achieve this by tuning the coupling constant to $1/13.704$, while all the remaining parameters are kept the same as those in the previous simulation. In this case, it is found that the higher-order effects largely reorient the polarization of the deuteron system, while the r.m.s. radius changes minimally after the evolution. At later times, differences in the level distribution and r.m.s. radius of the np system are observed between predictions based on the tBF method and first-order perturbation theory. This justifies a full non-perturbative treatment in the presence of strong interaction field.

In the next step, with the validity of the tBF method confirmed, we will apply this method to simulate the scattering process of the deuteron in the presence of both the electromagnetic interaction and the strong interaction due to an impinging heavy ion. In such cases, both the Coulomb interaction and the strong interaction can modify the polarization of the deuteron system [14–16]. Specific attention will be paid to the time-evolution of the charge and momentum distribution of the np system. These studies will be very important for understanding the dynamics of the deuteron breakup reaction [17, 18] and would serve as a precursor for investigating the internal structures of larger nuclei.

Acknowledgments

We acknowledge valuable discussions and help from Y. Li, L. Ou and Z. Xiao. This work was supported in part by the U. S. Department of Energy (DOE) under grants No. DESC0008485 (SciDAC/NUCLEI) and DE-FG02-87ER40371. X. Zhao is supported by new faculty startup funding from the Institute of Modern Physics, Chinese Academy of Sciences.

References

- [1] K. Alder, A. Bohr, T. Huus, B. Mottelson and A. Winther, *Rev. Mod. Phys.* **28**, 4 (1956).
- [2] J. M. Eisenberg and W. Greiner, *Nuclear theory: Excitation mechanisms of the nucleus*, 3rd. ed. North-Holland, 1988, p. 235.
- [3] X. Zhao, A. Ilderton, P. Maris and J. P. Vary, *Phys. Rev. D* **88**, 065014 (2013).

-
- [4] G. Chen, X. Zhao, Y. Li, K. Tuchin and J. P. Vary, arXiv:1702.06932 [nucl-th] (2017).
 - [5] A. M. Shirokov, J. P. Vary, A. I. Mazur, S. A. Zaytsev and T. A. Weber, Phys. Lett. B **621**, 96 (2005).
 - [6] A. M. Shirokov, J. P. Vary, A. I. Mazur and T. A. Weber, Phys. Lett. B **644**, 33 (2007).
 - [7] A. M. Shirokov, A. I. Mazur, S. A. Zaytsev, J. P. Vary and T. A. Weber, Phys. Rev. C **70**, 044005 (2004).
 - [8] A. Bohr and B. Mottelson, *Nuclear structure. Vol 1.* World Scientific, 1998, p. 92.
 - [9] J. Suhonen, *From nucleons to nucleus: Concepts of microscopic nuclear theory.* Springer-Verlag, Berlin, Heidelberg, 2007.
 - [10] A. Askar and A. S. Cakmak, J. Chem. Phys. **68**, 2794 (1978).
 - [11] T. Iitaka, Phys. Rev. E **49**, 4684 (1994).
 - [12] A. Huber, T. Udem, B. Gross, J. Reichert, M. Kourogi, K. Pachucki, M. Weitz and T. W. Hansch, Phys. Rev. Lett. **80**, 468 (1998).
 - [13] J. Martorell, D. W. L. Sprung and D. C. Zheng, Phys. Rev. C **51**, 1127 (1995).
 - [14] L. Ou , Z. Xiao, H. Yi, N. Wang, M. Liu and J. Tian, Phys. Rev. Lett. **115**, 212501 (2015).
 - [15] V. Baryshevsky and A. Rouba, Phys. Lett. B **683**, 299 (2010).
 - [16] H. Seyfarth, R. Engels, F. Rathmann, H. Ströher, V. Baryshevsky, A. Rouba, C. Düweke, R. Emmerich, A. Imig, K. Grigoryev, M. Mikirtychiants and A. Vasilyev, Phys. Rev. Lett. **104**, 222501 (2010).
 - [17] C. A. Bertulani and L. F. Canto, Nucl. Phys. A **539**, 163 (1992).
 - [18] L. F. Canto, R. Donangelo, A. Romanelli, M. S. Hussein and A. F. R. de Toledo Piza, Phys. Rev. C **55**, 570(R) (1997).

Self-Consistent Collective Motion Path for Nuclear Fusion/Fission Reactions

Kai Wen and Takashi Nakatsukasa

Center for Computational Sciences, University of Tsukuba, Tsukuba 305-8577, Japan

Abstract

The adiabatic self-consistent collective coordinate (ASCC) method is a microscopic theoretical framework to extract an optimal form of collective coordinate for the large amplitude nuclear collective motion. It also enables us to calculate the inertial mass for the nuclear collective motion. Based on this theoretical framework, we develop a numerical method to realize a calculation of the self-consistent collective motion path and inertial mass parameter for the nuclear fusion/fission reactions. We apply our method to the reaction ${}^8\text{Be} \leftrightarrow \alpha + \alpha$. The collective motion paths, collective potentials, and inertial masses for the relative motion are presented and discussed.

Keywords: *Nuclear fission; collective motion; collective path*

1 Introduction

The time-dependent density functional theory (TDDFT) [1–5] is a general microscopic theoretical framework to study low-energy nuclear fusion and fission reactions. Based on the TDDFT, a microscopic mechanism of nuclear collective dynamics has been extensively studied for many years. The linear approximation of TDDFT leads to the random-phase approximation (RPA) [5–7], which is capable of nuclear response calculations and provides an unified description for both the nuclear structure and collective dynamics. Despite a rich microscopic information embedded in the TDDFT calculations, it is difficult to give a full theoretical description for the nuclear collective dynamics. For instance, it cannot describe the sub-barrier fusion and spontaneous fission properly, due to its semiclassical nature [1, 5, 6].

For the study of large amplitude nuclear collective dynamics in the “macroscopic” collective level, it is of high interest to obtain an optimal form of collective variables maximally decoupled from other intrinsic degrees of freedom, so that equations of motion for these collective canonical variables become of closed form. The adiabatic self-consistent collective coordinate (ASCC) method [8–11] aims at determining such canonical variables by solving self-consistent equations. The ASCC method has been applied to many nuclear structure problems associated with large-amplitude oscillations described by Hamiltonians with separable interactions [10–13].

Proceedings of the International Conference ‘Nuclear Theory in the Supercomputing Era — 2016’ (NTSE-2016), Khabarovsk, Russia, September 19–23, 2016. Eds. A. M. Shirokov and A. I. Mazur. Pacific National University, Khabarovsk, Russia, 2018, p. 115.

<http://www.ntse-2016.khb.ru/Proc/Wen.pdf>.

The inertial mass of nuclear collective motion is another long-standing problem in nuclear structure physics [6, 14]. Apparently, it is very important for nuclear reaction dynamics. Especially, the derivation of the mass after a touch of two nuclei is a highly non-trivial problem. The calculation of the mass parameter requires properly extracted collective coordinates and conjugate momenta, which can be provided by the ASCC method. Thus the ASCC method is also capable of microscopic calculation of the inertial masses for the collective motion.

Recently, by combining the imaginary-time evolution [15] and the finite amplitude method [16–18], we proposed a numerical method to solve the ASCC equations and to determine a collective path for the nuclear collective motion [19]. The collective coordinate and momentum are obtained self-consistently. In this article we will introduce our method and present the first applications to simplest systems, the translational motion of a single alpha particle and the fission of ^8Be .

In Section 2, we give the formulation of the basic ASCC equations in the case of one-dimensional collective motion, introduce the method of constructing the collective path and the coordinate transformation procedure for calculating the mass parameter. In Section 3, we apply the method to the translational motion of a single alpha particle and to the reaction $^8\text{Be} \leftrightarrow \alpha + \alpha$. Summary and concluding remarks are given in Section 4.

2 Formulation of the ASCC method

To determine an optimal collective path in the high-dimensional space of Slater determinants, we first label the states on the collective path by a couple of canonical variables (p, q) , whose equation of motion can be maximally decoupled from other intrinsic degrees of freedom. Thus q and p represent the collective coordinate and the conjugate momentum respectively.

In the adiabatic limit, expanding the wave function $\psi(q, p)$ in powers of p up to the second order, the invariance principle of the SCC equation [8] leads to the equations of the ASCC method [5, 9]. Neglecting the curvature terms, it reduces to the following set of equations:

$$\delta\langle\Psi(q)|\hat{H}_{\text{mv}}|\Psi(q)\rangle = 0, \quad (1)$$

$$\delta\langle\Psi(q)|[\hat{H}_{\text{mv}}, \frac{1}{i}\hat{P}(q)] - \frac{\partial^2 V(q)}{\partial q^2}\hat{Q}(q)|\Psi(q)\rangle = 0, \quad (2)$$

$$\delta\langle\Psi(q)|[\hat{H}_{\text{mv}}, i\hat{Q}(q)] - \frac{1}{M(q)}\hat{P}(q)|\Psi(q)\rangle = 0, \quad (3)$$

with the moving mean-field Hamiltonian \hat{H}_{mv} defined as

$$\hat{H}_{\text{mv}} = \hat{H} - \frac{\partial V(q)}{\partial q}\hat{Q}(q), \quad (4)$$

where the potential $V(q)$ is the expectation value of the Hamiltonian,

$$V(q) = \langle\psi(q)|\hat{H}|\psi(q)\rangle, \quad (5)$$

$M(q)$ is the mass parameter of collective motion. $\hat{Q}(q)$ and $\hat{P}(q)$ correspond to the local generators of the variables p and q . Note that the collective motion path is

expressed by $\Psi(q)$, which represents the state $\Psi(q, p)$ with $p = 0$. Here we consider the one-dimensional description of collective motion without taking the pairing correlation into account. Equation (1) is similar to a constrained Hartree–Fock (HF) problem, however, the constraint operator $\hat{Q}(q)$ depends on the coordinate q , which is self-consistently determined by the RPA-like Eqs. (2) and (3) called moving RPA equations. The conventional RPA forward and backward amplitudes X and Y are linear combinations of $\hat{P}(q)$ and $\hat{Q}(q)$ which matrix elements X_{ni} , Y_{ni} and P_{ni} , Q_{ni} satisfy the relations

$$X_{nj} = \sqrt{\frac{\omega}{2}} Q_{nj} + \frac{1}{\sqrt{2\omega}} P_{nj}, \quad (6)$$

$$Y_{nj} = \sqrt{\frac{\omega}{2}} Q_{nj} - \frac{1}{\sqrt{2\omega}} P_{nj}. \quad (7)$$

Hereafter, indices i, j and n, m refer to the hole and particle states respectively. The RPA eigenfrequency ω is related to the mass parameter and the second derivative of the potential,

$$\omega^2 = \frac{1}{M(q)} \frac{\partial^2 V(q)}{\partial q^2}. \quad (8)$$

The operators of collective momentum $\hat{P}(q)$ and coordinate $\hat{Q}(q)$, as a pair of canonical variables, are imposed a weak canonicity condition,

$$\langle \Psi(q) | [i\hat{P}(q), \hat{Q}(q)] | \Psi(q) \rangle = 1, \quad (9)$$

which is equivalent to the RPA normalization condition,

$$\sum_{n,j} (X_{nj}^2 - Y_{nj}^2) = 1. \quad (10)$$

The collective path $\Psi(q)$ as well as $V(q)$ and $M(q)$ are determined self-consistently by Eqs. (1)–(3) and no *a priori* assumption is used.

The scale of the collective coordinate q in the ASCC equation set is arbitrary. It is easy to determine the scale by mapping the coordinate q onto any other collective quantity R as far as the one-to-one correspondence exists. For the study of nuclear scattering and nuclear fission, we define R as the relative distance between ions. The operator form of R can be expressed as

$$\hat{R} \equiv \int d\vec{r} \hat{\psi}^\dagger(\vec{r}) \hat{\psi}(\vec{r}) z \left[\frac{\theta(z - z_s)}{M_{\text{pro}}} - \frac{\theta(z_s - z)}{M_{\text{tar}}} \right], \quad (11)$$

where θ is the step function, and z_s is an artificially introduced section plane dividing the total system of mass $A = M_{\text{pro}} + M_{\text{tar}}$ into the left part with mass M_{pro} and the right part with mass M_{tar} . The relation between $M(R)$ and $M(q)$ reads

$$M(R) = M(q) \left(\frac{dq}{dR} \right)^2. \quad (12)$$

The calculation of the derivative dq/dR is straightforward once the collective path $\Psi(q)$ and the local generator $\hat{P}(q)$ are obtained. With this equation we can calculate the mass parameter with respect to R .

We solve the moving RPA equations (2) and (3) by taking advantage of the finite amplitude method (FAM) [16–18], especially of the matrix FAM prescription [18]. To solve the ASCC equations (1)–(3) self-consistently and to construct the collective motion path $\Psi(q)$, we adopt the following procedures: First, we calculate the HF ground state of the nucleus before fission $\Psi(q=0)$; based on $\Psi(q=0)$, we solve the moving RPA equations to obtain $\hat{Q}(q=0)$ and $\hat{P}(q=0)$. When $\Psi(q)$, $\hat{Q}(q)$, and $\hat{P}(q)$ are provided, we solve the moving HF equation to obtain the state $\Psi(q+\delta q)$ by using the constraint condition

$$\langle \Psi(q+\delta q) | \hat{Q}(q) | \Psi(q+\delta q) \rangle = \delta q. \quad (13)$$

With the new state $\Psi(q+\delta q)$, we may update the generators and get $\hat{Q}(q+\delta q)$ and $\hat{P}(q+\delta q)$; with the updated generators, we can obtain the new state by Eq. (13) again. Carrying on this iterative procedure, we can determine series of states $\Psi(0)$, $\Psi(\delta q)$, $\Psi(2\delta q)$, $\Psi(3\delta q)$, ... and obtain the ASCC collective path. The assumption adopted here is that $\Psi(q+\delta q) \simeq e^{-i\delta q \hat{P}(q)} \Psi(q)$.

3 Applications

3.1 Solution for the translational motion

The HF ground state is a trivial solution that satisfies the ASCC equations. Based on the ground state, we can calculate the translational mass as a test calculation. The calculation is done in the 3-dimensional coordinate space in a sphere with radius equal to 7 fm. The BKN energy density functional [20] is adopted in numerical calculation. The upper panel in Fig. 1 shows the eigenfrequency ω of several lowest RPA states for the ground state of alpha particle. Three translational modes along x , y , z axes are degenerate with an energy of about 1 MeV. The model space is discretized with the mesh size of 0.8 fm. Using a finer mesh size, the eigenfrequencies of these three modes approaches to zero. Due to a compact nature of alpha particle, the lowest physical excited state above the translational zero-modes, is 20 MeV higher representing a monopole vibration.

Below those three degenerated translational modes, there exists a mode with the energy equal to zero, this solution appears due to a numerical treatment of the particle states, namely, the particle state $|m\rangle$ is expressed through the coordinate $|\vec{r}\rangle$ in the whole model space. This redundancy in the representation of particle states results in additional solutions that are unphysical. This unphysical state does not affect the physical results and we may simply neglect it. Using Eq. (12), we calculate the translational mass parameter of the alpha particle. The model space is chosen to be a sphere with different mesh sizes. The lower panel in Fig. 1 shows the mass parameters of alpha particle in the translational motion along x , y and z axes and their dependence on the mesh size. As the mesh size decrease, the results approach the value of 4 in the units of nucleon mass, which is the correct mass number of the alpha particle.

3.2 ASCC motion path for ${}^8\text{Be} \leftrightarrow \alpha + \alpha$

A numerical application of the ASCC method to establishing a collective path for the nuclear fusion or fission reactions is a complicated computational problem. We

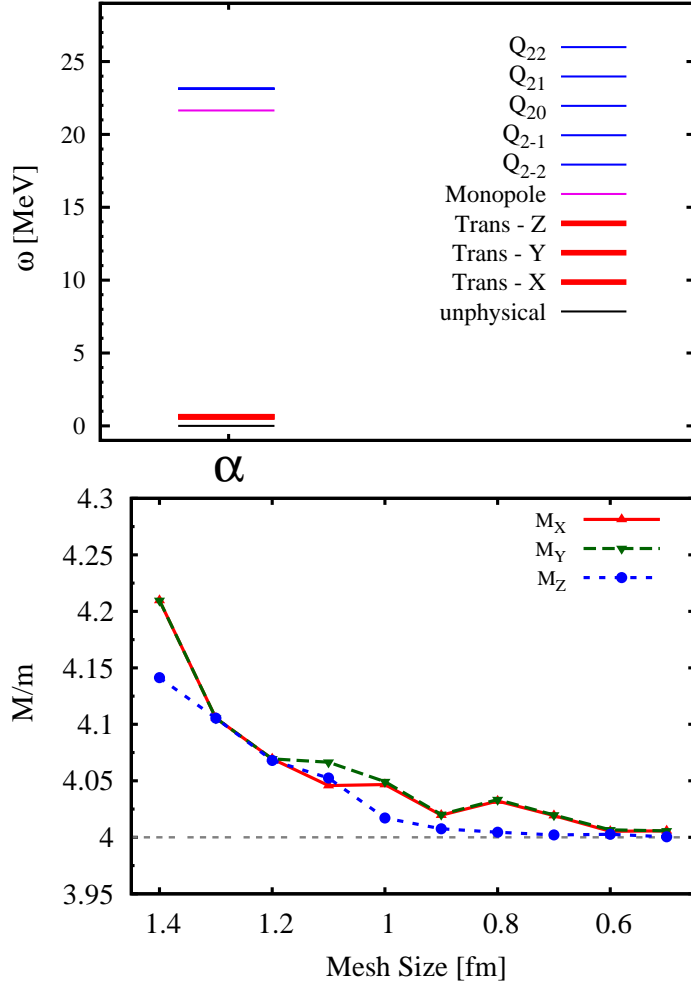


Figure 1: Top: calculated eigenfrequencies for the ground state of alpha particle. Three translational motion modes along x , y and z axis are shown by thick red lines. These three translational modes are degenerate, five quadrupole modes are also degenerate. Bottom: calculated translational mass of the alpha particle in units of nucleon's mass as a function of the mesh size.

show here our first result for the spontaneous fission path of ^8Be , that may be also regarded as the fusion path of two alpha particles at low incident energy. The model space is the three-dimensional grid space of the rectangular box size $10 \times 10 \times 18 \text{ fm}^3$ with the mesh size of 0.8 fm. The BKN energy density functional [20] is adopted in numerical calculation.

Starting from the ground state of ^8Be and carrying out the iterative procedure introduced in Section 2, we obtain the ASCC fission path of ^8Be demonstrating a smooth transformation of ^8Be into two well separated alpha particles. In Fig. 2, we show the calculated density distribution at four points on this collective path. The inset (a) shows the density distribution of the ground state of ^8Be at $R = 3.55 \text{ fm}$ while the inset (d) shows the density distribution of two alpha particle at $R = 6.40 \text{ fm}$. The insets (b) and (c) show the intermediate density distributions at $R = 4.10 \text{ fm}$ and 5.10 fm , respectively.

In the upper panel of Fig. 3, we plot the frequency ω of Eq. (8) for the solution of the moving RPA equations on the ASCC path compared with the binding energy of the last filled orbit as a function of R . The lower panel of Fig. 3 shows the potential

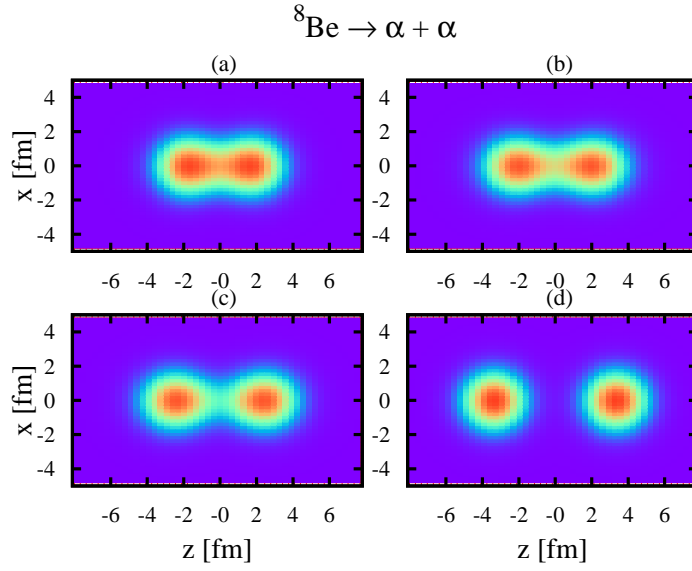


Figure 2: Calculated density distribution at four points on the ASCC collective fission path of ${}^8\text{Be}$. Insets (a), (b), (c), and (d) show the density distribution in the y - z plane of the ground state of ${}^8\text{Be}$ at $R = 3.55, 4.10, 5.10,$ and 6.40 fm, respectively.

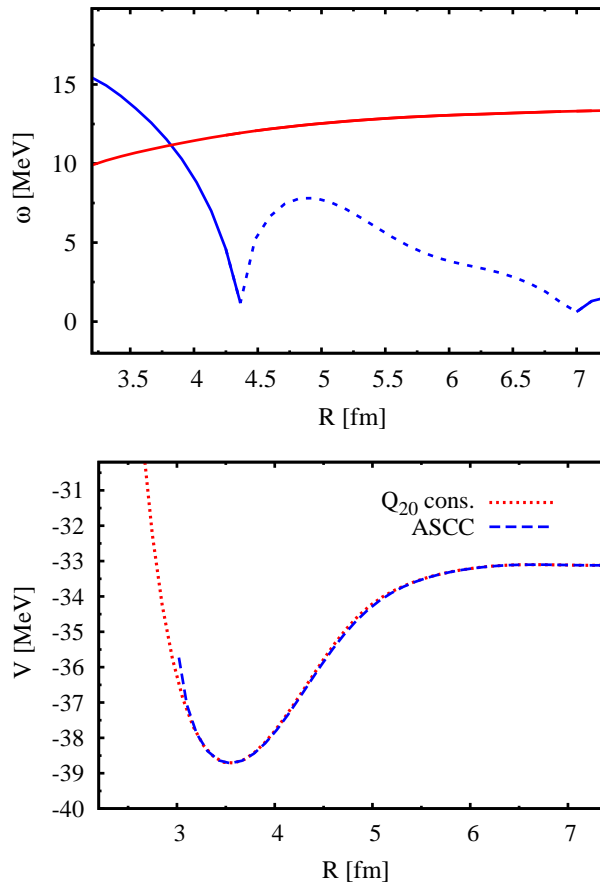


Figure 3: Top: RPA eigenfrequency ω on the ASCC collective fission path of ${}^8\text{Be}$ as a function of R . Solid (dashed) blue curve shows real (imaginary) ω , red curve demonstrates an absolute value of the single particle energy of the last filled orbit in ${}^8\text{Be}$. Bottom: potential energy as a function of R . Blue curve presents the potential on the ASCC collective path while the red curve is the potential of the constrained HF states with the constraint on Q_{20} .

energy as a function of R . The ground state of ${}^8\text{Be}$ is at $R = 3.55$ fm, the Coulomb barrier top is at $R = 6.6$ fm.

According to Eq. (8), ω^2 is proportional to the second order derivative of the collective potential $V(q)$ which can be negative. In the upper panel of Fig. 3, the imaginary ω is plotted by the dashed curve while the real one is plotted by the solid curve. In the region $4.4 \text{ fm} < R < 6.9 \text{ fm}$, the imaginary ω appears, where the state is not in the minimum but on the saddle point of the energy surface corresponding to the moving Hamiltonian H_{mv} . At a larger distance, ω should approach zero. As a general trend, the frequency ω for the relative motion increases as the nuclei approach each other. Inside the HF ground state at $R < 3.6$ fm, ω increases drastically and becomes larger than the binding energy of the last filled orbit, the RPA excitation here is above the bound threshold and in the continuum region. In this case the unbound RPA state features depend on the choice of model space, therefore we should not take the result in this region seriously.

3.3 Inertial mass for ${}^8\text{Be} \leftrightarrow \alpha + \alpha$

With the collective fission path obtained, the ASCC inertial mass $M_{\text{ASCC}}(R)$ for this fission path is calculated using Eq. (12) and shown in Fig. 4 in comparison with the cranking mass $M_{\text{cr}}(R)$.

The cranking inertial mass is derived by assuming a separable interaction and taking the adiabatic limit of the RPA inertial mass. In the case of one-dimensional motion, the widely used formula for the cranking mass reads [21]

$$M_{\text{cr}}(R) = \frac{1}{2} \left\{ S^{(1)}(R) \right\}^{-1} S^{(3)}(R) \left\{ S^{(1)}(R) \right\}^{-1}, \quad (14)$$

where

$$S^{(k)}(R) = \sum_{m,i} \frac{|\langle \varphi_m(R) | \hat{R} | \varphi_i(R) \rangle|^2}{\{e_m(R) - e_i(R)\}^k}. \quad (15)$$

Here the single-particle states $\phi(R)$ and energies $e(R)$ are defined with respect

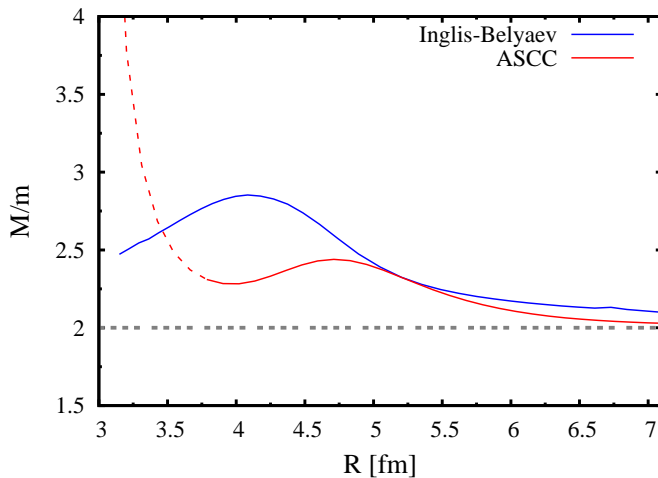


Figure 4: Inertial mass for the fission path of ${}^8\text{Be}$ as a function of relative distance R in the units of nucleon mass. Red (blue) curve is the ASCC (cranking) mass, the cranking mass is obtained with the CHF states with the constraint on R .

to $h_{\text{CHF}}(R) = h_{\text{HF}}[\rho] - \lambda(R)\hat{R}$ as

$$h_{\text{CHF}}(R) \varphi_{\mu}(R) = e_{\mu}(R) \varphi_{\mu}(R), \quad \mu = i, m. \quad (16)$$

Residual fields induced by the density fluctuations are neglected in the cranking formula. The calculation of the cranking mass is based on the CHF states with the constraint on R . The model space is the same as that for the ASCC.

As is seen in Fig. 4, the ASCC mass $M_{\text{ASCC}}(R)$ is smaller than the cranking mass. At large distance, both produce the reduced mass of 2 in the units of nucleon mass, which is just the reduced mass for the relative motion of two alpha particles; the precision of cranking mass is a little worse as compared with the ASCC mass. In the interior region after the touch of two nuclei, these masses have very different values. The cranking mass is found to be larger than the ASCC mass, especially at around $R = 4$ fm, the cranking mass has an about 40 percent larger value. This fact shows that the residual field arising from the density fluctuations makes a significant contribution. Compared with the cranking mass, the ASCC mass has an advantage that the collective coordinate as well as the wave functions are not assumed artificially but calculated self-consistently. As mentioned in the previous Subsection, we should not take seriously the results for the ASCC mass at $R < 3.6$ fm, the ASCC mass is plotted in this region by a dashed curve.

4 Summary

Based on the ASCC theory, we presented a method to determine the collective motion path for the large amplitude nuclear collective motion, and applied this method to the nuclear fusion/fission reaction ${}^8\text{Be} \leftrightarrow \alpha + \alpha$. In the 3D coordinate space representation, the reaction path, the collective potential and the inertial mass are calculated. Since the system under consideration presents one of the simplest cases, there is no significant difference in the reaction path as compared with that for the CHF states. The ASCC collective potential is similar to the potential of the CHF states. A comparison of the ASCC mass with the cranking mass is presented. The ASCC mass improves the cranking mass by taking into account the residual interaction caused by the density fluctuations. By using this method it is feasible to calculate the mass parameter for any collective coordinate. As our first application, we use a schematic BKN interaction, it is desired to use more realistic interactions accounting for pairing in our future study.

References

- [1] J. W. Negele, Rev. Mod. Phys. **54**, 913 (1982).
- [2] C. Simenel, Eur. Phys. J. A **48**, 1 (2012).
- [3] T. Nakatsukasa, Progr. Theor. Exp. Phys. **2012**, 01A207 (2012).
- [4] J. A. Maruhn, P.-G. Reinhard, P. D. Stevenson and A. S. Umar, Comput. Phys. Commun. **185**, 2195 (2014).
- [5] T. Nakatsukasa, K. Matsuyanagi, M. Matsuo and K. Yabana, Rev. Mod. Phys. **88**, 045004 (2016).

- [6] P. Ring and P. Schuck, *The nuclear many-body problem*. Springer-Verlag, Berlin, Heidelberg, 1980.
- [7] J.-P. Blaizot and G. Ripka, *Quantum theory of finite systems*. MIT Press, Cambridge, 1986.
- [8] T. Marumori, T. Maskawa, F. Sakata and A. Kuriyama, *Progr. Theor. Phys.* **64**, 1294 (1980).
- [9] M. Matsuo, T. Nakatsukasa and K. Matsuyanagi, *Progr. Theor. Phys.* **103**, 959 (2000).
- [10] N. Hinohara, T. Nakatsukasa, M. Matsuo and K. Matsuyanagi, *Progr. Theor. Phys.* **117**, 451 (2007).
- [11] N. Hinohara, T. Nakatsukasa, M. Matsuo and K. Matsuyanagi, *Phys. Rev. C* **80**, 014305 (2009).
- [12] N. Hinohara, Z. P. Li, T. Nakatsukasa, T. Nikšić and D. Vretenar, *Phys. Rev. C* **85**, 024323 (2012).
- [13] K. Sato, N. Hinohara, K. Yoshida, T. Nakatsukasa, M. Matsuo and K. Matsuyanagi, *Phys. Rev. C* **86**, 024316 (2012).
- [14] A. Bohr and B. R. Mottelson, *Nuclear structure. Vol. 2*. Benjamin, New York, 1975.
- [15] K. T. R. Davies, H. Flocard, S. Krieger and M. S. Weiss, *Nucl. Phys. A* **342**, 111 (1980).
- [16] T. Nakatsukasa, T. Inakura and K. Yabana, *Phys. Rev. C* **76**, 024318 (2007).
- [17] P. Avogadro and T. Nakatsukasa, *Phys. Rev. C* **84**, 014314 (2011).
- [18] P. Avogadro and T. Nakatsukasa, *Phys. Rev. C* **87**, 014331 (2013). *C* **76**, 024318 (2007).
- [19] K. Wen and T. Nakatsukasa, *Phys. Rev. C* **96**, 014610 (2017).
- [20] P. Bonche, S. Koonin and J. W. Negele, *Phys. Rev. C* **13**, 1226 (1976).
- [21] A. Baran, J. A. Sheikh, J. Dobaczewski, W. Nazarewicz and A. Staszczak, *Phys. Rev. C* **84**, 054321 (2011).

Deuteron Wave Function and Neutron Form Factors from Elastic Electron-Deuteron Scattering

N. A. Khokhlov

*Komsomolsk-on-Amur State Technical University, Komsomolsk-on-Amur, Russia
Southwest State University, Kursk, Russia*

Abstract

A study of the deuteron structure in the framework of relativistic quantum mechanics is presented. The point-form (PF) relativistic quantum mechanics (RQM) is applied to elastic eD scattering. The deuteron wave function and neutron form factors are fitted to electromagnetic deuteron form factors. We also compare results obtained with various realistic deuteron wave functions stemming from Nijmegen-I, Nijmegen-II, JISP16, CD-Bonn, Paris, Argonne, Idaho and Moscow (with forbidden states) potentials. It is shown that the electromagnetic deuteron form factors may be described without exchange currents.

Keywords: *Nucleon; potential; deuteron; eD elastic scattering; electromagnetic form factors; relativistic quantum mechanics; point-form dynamics*

1 Introduction

Being the simplest nucleus, the deuteron provides the most direct test of various nucleon-nucleon interaction models and relevant degrees of freedom. In this context, the deuteron electromagnetic studies with electron or photon probes are the simplest in theoretical and experimental aspects. These studies provide a picture of deuteron electromagnetic structure in terms of deuteron electromagnetic (EM) form factors (FFs). These FFs are functions of the square of the four-momentum transferred by a probe ($q^2 = -Q^2$).

During the last two decades a considerable advance has been made in the experimental knowledge of deuteron electromagnetic structure. On the other hand, there is a substantial diversity of opinions regarding an appropriate general theoretical approach. Anyhow, it seems natural as well as confirmed by a general data analysis [1] that in the space-like region of Q^2 (corresponding to the elastic scattering) a successful theory may be obtained from a relativistic description of the NN channel only which is supplemented by minor modifications of the short-range structure of the deuteron EM current operator. Here, again, there are various approaches to the relativistic description as well as to the EM current operator structure [1, 2].

A conventional assumption is that a majority of the existing data of eD elastic scattering are described to high precision within a single-photon exchange approximation and by three electromagnetic deuteron FFs [1, 3–5]. The deuteron FFs are

Proceedings of the International Conference ‘Nuclear Theory in the Supercomputing Era — 2016’ (NTSE-2016), Khabarovsk, Russia, September 19–23, 2016. Eds. A. M. Shirokov and A. I. Mazur. Pacific National University, Khabarovsk, Russia, 2018, p. 124.

<http://www.ntse-2016.khb.ru/Proc/Khokhlov.pdf>.

calculated in the conventional model using the deuteron wave function (S and D components) and nucleon FFs. FFs may be chosen so as to be equal in the $Q^2 = 0$ (static) limit to the deuteron charge, magnetic and quadrupole moments. The first two FFs are described within the conventional nuclear model in terms of nucleon degrees of freedom only. However the deuteron static electric quadrupole moment is not reproduced well enough in modern NN potential calculations. It is generally accepted that meson exchange contributions should be accounted for to get an agreement with the data.

The single-photon exchange approximation assumes that the electron and deuteron exchange a single virtual photon. It is believed that this approximation should be valid to a high precision due to a small value of the fine-structure constant. Therefore the elastic eD scattering allows to extract the deuteron EM FF dependencies on the transferred 4-momentum Q in the space-like region. To extract these dependencies, it is required to measure three independent observables of the eD elastic scattering in this region. Two of them (structure functions A and B) are extracted from the unpolarized differential cross section and the third one is extracted from polarization measurements.

Simple non-relativistic calculations with various realistic NN potentials (NN channel only) at low $Q \lesssim 0.7 \text{ GeV}/c \approx 3.5 \text{ Fm}^{-1}$ are in close harmony and agree well enough with the eD elastic scattering data [1, 2]. A disagreement between calculations increases with the rise of $Q > 3.5 \text{ Fm}^{-1}$. None of the calculations describes data for $Q \gtrsim 3.5 \text{ Fm}^{-1}$. This disagreement indicates that relativistic effects and contributions of other channels may be essential at $Q > 3.5 \text{ Fm}^{-1}$ [1, 2]. Indeed, an inclusion of relativistic and meson exchange corrections results in a good description of the data [6, 7]. However there is another problem that is not emphasized usually. Important ingredients of the calculations are the nucleon FF dependencies on the Q_i^2 transferred to an individual nucleon. These dependencies are extracted experimentally. The proton FFs are extracted from direct measurements with proton targets. Nevertheless, even in this case, there is a notable discrepancy between the values of the proton FF ratio, G_{Ep}/G_{Mp} , extracted from polarization and cross section experiments. The cross sections are necessary to extract the absolute values of G_{Ep} and G_{Mp} while the polarization transfer measurements provide information only about the ration G_{Ep}/G_{Mp} . The discrepancy begins at $Q \approx 1 \text{ GeV}/c \approx 5 \text{ Fm}^{-1}$. It may be explained by the hard two-photon exchange process (TPE), and the data reveal some evidence for this explanation [8]. It also should be noted that model calculations and analyses demonstrate that the TPE significantly changes G_{Ep} while the G_{Mp} alteration is at a few percent ($\sim 3\%$) level [9, 10]. The latest analytical fit to the proton FFs is a simultaneous fit to the polarization and cross section data. The cross section data are corrected by an additive term assuming some phenomenological TPE corrections [11].

A free neutron target is not available. The neutron FFs are extracted from the measurements of eD or $e^3\text{He}$ scattering. Therefore the data analysis is affected by uncertainties stemming from an assumed nuclear theoretical model describing the target nucleus and reaction.

A conventional procedure for the neutron FF extraction may be exemplified as follows. The electric neutron FF was measured in Ref. [12] up to $Q^2 = 3.4 \text{ GeV}^2/c^2$ using the $\overrightarrow{^3\text{He}}(\vec{e}, e'n)pp$ reaction. The extraction includes calculations of the asymmetries in the quasi-elastic processes $\overrightarrow{^3\text{He}}(\vec{e}, e'n)pp$ and $\overrightarrow{^3\text{He}}(\vec{e}, e'p)np$. These calculations were

performed using the generalized eikonal approximation and included spin-dependent final-state interactions (FSI), meson-exchange currents and the ${}^3\text{He}$ wave function resulting from the AV18 potential. Finally, to extract the G_{En} , a linearly interpolated G_{Mn} from Ref. [13] was used. The procedure of Ref. [13] is a measurement of the ratio R of the cross sections of the quasielastic ${}^2\text{H}(e, e'n)p$ and ${}^2\text{H}(e, e'p)n$ reactions. To extract the G_{Mn} from R , the authors use: 1) Cross section calculations within the Plane Wave Impulse Approximation (PWIA) for $Q^2 > 1.0 \text{ GeV}^2/c^2$, the AV18 deuteron wave function, and the Glauber theory for FSI; 2) Calculations of a nuclear correction factor which is the ratio of the results of the full calculation and those within the PWIA but without FSI; 3) The proton cross section (a parameterization of Ref. [10]); 4) Parameterizations of G_{En} of Ref. [14,15]. Obviously, it looks like a vicious circle. There is a model-insensitive technique for the G_{En} extraction of Ref. [16] but it is applicable only to the $d(\vec{e}, e'\vec{n})p$ reaction in the quasi-free kinematics. This technique was utilized to extract the G_{En} at $Q^2 = 0.255 \text{ GeV}^2$ ($Q \approx 2.6 \text{ Fm}^{-1}$) [17] resulting in $G_{En} = 0.066 \pm 0.036 \pm 0.009$. The “scale” uncertainty (± 0.009) was estimated using independent measurements of G_{Mn} and the so-called “Arenhövel’s model”. That sounds convincing and may mean that the Argonne V14 or other contemporary phenomenological potentials were used in the estimation. However there is no an estimation of the model systematic error and the whole procedure is again an obvious vicious circle.

There are various relativistic models [6,18–21] for calculations of the deuteron EM FFs. All of them look reasonable but they may produce different results. That is not a contradiction. This issue is discussed in the last part of the paper. In this paper, we extend our previous investigations where we described the elastic NN scattering up to laboratory energy of 3 GeV [22] and electromagnetic reactions with two nucleons: a bremsstrahlung in the pp scattering $pp \rightarrow pp\gamma$ [23], the deuteron photodisintegration $\gamma D \rightarrow np$ [24–26], the exclusive deuteron electrodisintegration [27] and the eD elastic scattering [28,29]. We apply manifestly covariant relativistic quantum mechanics (RQM) [30] in the point-form (PF). The PF is one of three forms of the RQM proposed by Dirac [31]. The other two forms in common use are the instant and the front forms. Each form is associated with a subgroup of the Poincaré group. This subgroup is considered to be free of interactions. All these forms are unitary equivalent [32], however each form has particular advantages. For example, the PF has some simplifying features [33]. Only in the PF all generators of the homogeneous Lorentz group are free of interactions. That means a manifest covariance that clearly simplifies the boost transformations. Therefore the spectator approximation (SA) of an electromagnetic process preserves its spectator character in any reference frame (r. f.) [34–36]. There are two equivalent SAs of the EM current operator in composite systems within the PF RQM [33,34]. The PF RQM SA has been applied to calculations of EM FFs of composite systems [20,37–41] with satisfactory results.

2 Potential model in PF RQM

A general method of allowing for interactions in generators of the Poincaré group was proposed by Bakamjian and Thomas [42]. We present here only the results of PF RQM necessary for our eD calculations. We use formalism and notation of Ref. [34] for calculation of matrix elements of the EM current operator.

Let p_i be the 4-momentum of nucleon i , $P \equiv (P^0, \mathbf{P}) = p_1 + p_2$ is the system

4-momentum, M is the system mass and $G = P/M$ is the system 4-velocity. The wave function of two particles with 4-momentum P is expressed through a tensor product of external and internal parts

$$|P, \chi\rangle = U_{12} |P\rangle \otimes |\chi\rangle, \quad (1)$$

where the internal wave function $|\chi\rangle$ satisfies Eqs. (7)–(8). The unitary operator

$$U_{12} = U_{12}(G, \mathbf{q}) = \prod_{i=1}^2 D[\mathbf{s}_i; \alpha(p_i/m)^{-1} \alpha(G) \alpha(q_i/m)] \quad (2)$$

relates the “internal” Hilbert space with the Hilbert space of two-particle states [34]. $D[\mathbf{s}; u]$ is a SU(2) operator corresponding to the element $u \in \text{SU}(2)$, \mathbf{s} are the SU(2) generators. In our case of spin $s = 1/2$ particles, we deal with the fundamental representation, i. e., $\mathbf{s}_i \equiv \frac{1}{2} \boldsymbol{\sigma}_i$ [$\boldsymbol{\sigma} = (\sigma_x, \sigma_y, \sigma_z)$ are the Pauli matrices] and $D[\mathbf{s}; u] \equiv u$. The momenta of the particles in their c. m. frame are

$$q_i = L[\alpha(G)]^{-1} p_i, \quad (3)$$

where $L[\alpha(G)]$ is the Lorentz boost to the frame moving with the 4-velocity G . The matrix

$$\alpha(g) = (g^0 + 1 + \boldsymbol{\sigma} \cdot \mathbf{g}) / \sqrt{2(g^0 + 1)} \quad (4)$$

corresponds to a 4-velocity $g \equiv (g^0, \mathbf{g})$.

The external part of the wave function is defined as

$$\langle G|P'\rangle \equiv \frac{2}{M'} G'^0 \delta^3(\mathbf{G} - \mathbf{G}'). \quad (5)$$

Its scalar product is

$$\langle P''|P'\rangle = \int \frac{d^3 \mathbf{G}}{2G^0} \langle P''|G\rangle \langle G|P'\rangle = 2\sqrt{M'^2 + \mathbf{P}'^2} \delta^3(\mathbf{P}'' - \mathbf{P}'), \quad (6)$$

where $G^0(\mathbf{G}) \equiv \sqrt{1 + \mathbf{G}^2}$. The internal part $|\chi\rangle$ is characterized by the total angular momentum J of the system and by momentum $\mathbf{q} = \mathbf{q}_1 = -\mathbf{q}_2$ of one of the particles in the c. m. frame.

The 4-momentum $\hat{P} = \hat{G}\hat{M}$ incorporates the interaction V_{int} , where \hat{M} is sum of the free mass operator M_{free} and the interaction, $\hat{M} = M_{free} + V_{int}$. The wave function is an eigenfunction of the system mass operator \hat{M} . We represent this wave function as a product of the external and internal parts. The internal wave function $|\chi\rangle$ is also an eigenfunction of the mass operator and for the system of two nucleons with masses $m_1 \approx m_2 \approx m = 2m_1 m_2 / (m_1 + m_2)$ satisfies the following equation:

$$\hat{M}|\chi\rangle \equiv \left[2\sqrt{\mathbf{q}^2 + m^2} + V_{int} \right] |\chi\rangle = M|\chi\rangle. \quad (7)$$

This equation can be rewritten as

$$[\mathbf{q}^2 + mV] |\chi\rangle = q^2 |\chi\rangle, \quad (8)$$

where V acts on internal variables only, and

$$q^2 = \frac{M^2}{4} - m^2. \quad (9)$$

The operators V_{int} and V (and therefore \hat{M} and M_{free}) commute with the spin operator J and with the 4-velocity operator \hat{G} . The generators of space-time rotations are interaction-free. Most of formal results of non-relativistic scattering theory are valid in the case of two relativistic particles [30]. For example, the relative orbital angular momentum and spins are coupled in the c.m. frame in the same manner as in the non-relativistic case. Equation (8) is identical in form to the Schrödinger equation. Relativistic corrections affect the deuteron binding energy only and may be easily accounted for by replacing the experimental deuteron binding of 2.2246 MeV by an effective value of 2.2233 MeV. The origin of this relativistic correction is the following. Let ε be the deuteron binding energy. Then $M = 2m - \varepsilon$ and $q^2 = \frac{M^2}{4} - m^2 = -m\varepsilon(1 - \frac{\varepsilon}{4m})$. Comparing with the non-relativistic relationship $q^2 = -m\varepsilon$, we identify the factor $(1 - \frac{\varepsilon}{4m})$ as a relativistic correction. There is no similar correction in the scattering domain since $q^2 = mE_{lab}/2$ is an exact relativistic relationship (E_{lab} is the laboratory energy) used in the partial wave analysis. The above correction is negligible for our problem.

The deuteron wave function $|P_i, \chi_i\rangle$ is normalized,

$$\langle P_f, \chi_f | P_i, \chi_i \rangle = 2P_i^0 \delta^3(\mathbf{P}_i - \mathbf{P}_f) \langle \chi_f | \chi_i \rangle. \quad (10)$$

3 eD elastic scattering

There is a convenient r. f. for calculation of current operator matrix elements in PF RQM introduced by F. Lev [34] (it coincides with the Breit r. f. in the case of elastic ed scattering). The Lev's r. f. is defined by the following condition for all EM reactions with two nucleons:

$$\mathbf{G}_f + \mathbf{G}_i = 0, \quad (11)$$

where $\mathbf{G}_f = \mathbf{P}_f/M_D$, $\mathbf{G}_i = \mathbf{P}_i/M_D$ are the final and initial 4-velocities of the deuteron and M_D is its mass. The matrix element of the current operator is [34]:

$$\langle P_f, \chi_f | \hat{J}^\mu(x) | P_i, \chi_i \rangle = 2(M_f M_i)^{1/2} \exp(i(P_f - P_i)x) \langle \chi_f | \hat{j}^\mu(\mathbf{h}) | \chi_i \rangle, \quad (12)$$

where the internal current operator $\hat{j}^\mu(\mathbf{h})$ defines an action of current operator in the internal space of the NN system,

$$\mathbf{h} = \frac{2(M_i M_f)^{1/2}}{(M_i + M_f)^2} \mathbf{k} = \frac{\mathbf{k}}{2M_D} \quad (13)$$

is a vector-parameter [34] ($0 \leq h \leq 1$), \mathbf{k} is the momentum of photon in the Lev's r. f., $M_i = M_f = M_D$ are the masses of the initial and final NN systems (deuteron).

The internal deuteron wave function

$$|\chi_i\rangle = \frac{1}{r} \sum_{l=0,2} u_l(r) |l, 1; J = 1M_J\rangle_{\mathbf{r}} \quad (14)$$

is normalized: $\langle \chi_i | \chi_i \rangle = 1$. This configuration space wave function has a physical sense only in the non-relativistic limit. In our calculations we use the momentum space wave function:

$$|\chi_i\rangle = \frac{1}{q} \sum_{l=0,2} u_l(q) |l, 1; 1M_J\rangle_{\mathbf{q}}, \quad (15)$$

where

$$u(q) \equiv u_0(q) = \sqrt{\frac{2}{\pi}} \int dr \sin(qr) u(r), \quad (16)$$

$$w(q) \equiv u_2(q) = \sqrt{\frac{2}{\pi}} \int dr \left[\left(\frac{3}{(qr)^2} - 1 \right) \sin(qr) - \frac{3}{qr} \cos(qr) \right] w(r). \quad (17)$$

A transformation of the Breit r. f. (11) into the final (initial) c. m. frame of the NN system is the boost along (in the backward direction than) vector \mathbf{h} (axis z). The projection of the total deuteron angular momentum onto the z is unaffected by these boosts. The initial deuteron in the Breit r. f. moves in the direction opposite to \mathbf{h} . Its internal wave function with the spirality Λ_i is

$$|\Lambda_i\rangle = \frac{1}{q} \sum_{l=0,2} u_l(q) |l, 1; 1, M_J = -\Lambda_i\rangle. \quad (18)$$

The wave function of the final deuteron with the spirality Λ_f is

$$|\Lambda_f\rangle = \frac{1}{q} \sum_{l=0,2} u_l(q) |l, 1; 1, M_J = \Lambda_f\rangle. \quad (19)$$

A conventional parametrization of the EM current operator matrix element for a spin-1 particle (deuteron) is [1, 2, 43]

$$\begin{aligned} & (4P_i^0 P_f^0)^{1/2} \langle P_f, \chi_f | J^\mu | P_i, \chi_i \rangle \\ &= - \left\{ G_1(Q^2) (\boldsymbol{\xi}_f^* \cdot \boldsymbol{\xi}_i) - G_3(Q^2) \frac{(\boldsymbol{\xi}_f^* \cdot \Delta P)(\boldsymbol{\xi}_i \cdot \Delta P)}{2M_D^2} \right\} (P_i^\mu + P_f^\mu) \\ & \quad - G_2(Q^2) [\xi_i^\mu (\boldsymbol{\xi}_f^* \cdot \Delta \mathbf{P}) - \xi_f^{*\mu} (\boldsymbol{\xi}_i \cdot \Delta \mathbf{P})], \quad (20) \end{aligned}$$

where $(a \cdot b) = a^0 b^0 - \mathbf{a} \cdot \mathbf{b}$, EM FFs $G_i(Q^2)$, $i = 1, 2, 3$ are functions of $Q^2 = -\Delta P^2$, $\Delta P = P_f - P_i$. In the Breit r. f. $\mathbf{P}_f = -\mathbf{P}_i$, $P_i^0 = P_f^0 \equiv P^0 = M_D/\sqrt{1-h^2}$, $\Delta P = (0, 2\mathbf{P}_f)$, $P_i^\mu + P_f^\mu = (2P^0, \mathbf{0})$, $\mathbf{P}_f/P^0 = \mathbf{h}$, $\mathbf{P}_f = \mathbf{h}M_D/\sqrt{1-h^2}$, $Q^2 \equiv -\Delta P^2$, $\Delta P^2 = -4h^2 M_D^2/(1-h^2)$, $h^2 = (\mathbf{h} \cdot \mathbf{h})$. Matrix elements of the internal current operator are

$$\begin{aligned} \langle \chi_f | j^0(\mathbf{h}) | \chi_i \rangle &= -G_1(Q^2) (\boldsymbol{\xi}_f^* \cdot \boldsymbol{\xi}_i) + 2G_3(Q^2) \frac{(\boldsymbol{\xi}_f^* \cdot \mathbf{h})(\boldsymbol{\xi}_i \cdot \mathbf{h})}{1-h^2} \\ & \quad + G_2(Q^2) [\xi_i^0 (\boldsymbol{\xi}_f^* \cdot \mathbf{h}) - \xi_f^{*0} (\boldsymbol{\xi}_i \cdot \mathbf{h})], \quad (21) \end{aligned}$$

$$\langle \chi_f | \mathbf{j}(\mathbf{h}) | \chi_i \rangle = G_2(Q^2) [\xi_i (\boldsymbol{\xi}_f^* \cdot \mathbf{h}) - \xi_f^* (\boldsymbol{\xi}_i \cdot \mathbf{h})] = G_2(Q^2) [\mathbf{h} \times [\boldsymbol{\xi}_i \times \boldsymbol{\xi}_f^*]]. \quad (22)$$

It has been shown [34] that these expressions are equivalent to choosing j^ν as

$$j^0(\mathbf{h}) = G_C(Q^2) + \frac{2G_Q(Q^2)}{(1-h^2)} \left[\frac{2}{3} h^2 - (\mathbf{h} \cdot \mathbf{J})^2 \right], \quad (23)$$

$$\mathbf{j}(\mathbf{h}) = -\frac{i}{\sqrt{1-h^2}} G_M(Q^2) (\mathbf{h} \times \mathbf{J}), \quad (24)$$

where \mathbf{J} is the total angular momentum (spin) of the deuteron; G_C , G_Q and G_M are its charge monopole, charge quadruple and magnetic dipole FFs.

Spiral polarizations of the deuteron in the initial and final states are

$$\xi_i^\Lambda = \begin{cases} (0, \pm 1, -\iota, 0)/\sqrt{2} & (\Lambda = \pm) \\ (-h, 0, 0, 1)/\sqrt{1-h^2} & (\Lambda = 0), \end{cases} \quad (25)$$

$$\xi_f^\Lambda = \begin{cases} (0, \mp 1, -\iota, 0)/\sqrt{2} & (\Lambda = \pm) \\ (h, 0, 0, 1)/\sqrt{1-h^2} & (\Lambda = 0). \end{cases} \quad (26)$$

A virtual photon polarization is

$$\epsilon^\lambda = \begin{cases} (0, \mp 1, -\iota, 0)/\sqrt{2} & (\lambda = \pm) \\ (1, 0, 0, 0) & (\lambda = 0). \end{cases} \quad (27)$$

The deuteron FFs G_i are expressed as

$$\begin{aligned} G_C &= G_1 + \frac{2}{3}\eta G_Q, \\ G_Q &= G_1 - G_M + (1 + \eta)G_3, \\ G_1 &= G_C - \frac{2h^2}{3(1-h^2)}G_Q, \\ G_3 &= G_Q \left(1 - \frac{h^2}{3}\right) - G_C(1-h^2) + G_M(1-h^2), \end{aligned} \quad (28)$$

where $\eta = Q^2/4M_D^2 = h^2/(1-h^2)$. The form factors $G_C(0) = e$, $G_M(0) = \mu_{De}/2M_D$ and $G_Q(0) = Q_{De}/M_D^2$ provide the deuteron charge, magnetic and quadruple moments respectively.

Denoting the helicity amplitudes as $j_{\Lambda_f \Lambda_i}^\lambda \equiv \langle \Lambda_f | (\epsilon_\mu^\lambda \cdot j^\mu(\mathbf{h})) | \Lambda_i \rangle$, we have:

$$j_{00}^0(Q^2) = G_C + \frac{4}{3} \frac{h^2}{1-h^2} G_Q, \quad (29)$$

$$j_{+-}^0(Q^2) = j_{-+}^0(Q^2) = G_C - \frac{2}{3} \frac{h^2}{1-h^2} G_Q, \quad (30)$$

$$\frac{j_{+0}^+(Q^2) + j_{0-}^+(Q^2)}{2} = -\frac{h}{\sqrt{1-h^2}} G_M \quad (31)$$

and

$$j_{+0}^+(Q^2) = j_{-0}^-(Q^2) \approx j_{0-}^+(Q^2) = j_{0+}^-(Q^2). \quad (32)$$

The squares of deuteron FFs are extracted from the elastic eD scattering with unpolarized particles and an additional polarization observable (usually $t_{20}(Q^2, \theta)$).

In the present paper we use the SA of EM current operator of Ref. [34] without expanding it in powers of h and calculate its matrix elements in the momentum space. Therefore we use the following expansion of $\hat{j}^\mu(\mathbf{h}) \approx \hat{j}_{SA}^\mu(\mathbf{h})$ [27] in calculations:

$$\begin{aligned} \hat{j}_{SA}^\mu(\mathbf{h}) &= (1 + (\mathbf{A}_2 \cdot \mathbf{s}_2)) (B_1^\mu + (\mathbf{C}_1^\mu \cdot \mathbf{s}_1)) \mathbf{I}_1(\mathbf{h}) \\ &\quad + (1 + (\mathbf{A}_1 \cdot \mathbf{s}_1)) (B_2^\mu + (\mathbf{C}_2^\mu \cdot \mathbf{s}_2)) \mathbf{I}_2(\mathbf{h}), \end{aligned} \quad (33)$$

where \mathbf{A}_i , B_i^μ , \mathbf{C}_i^μ are some cumbersome vector functions of \mathbf{h} and $\mathbf{q}(q, \theta, \phi)$. In the spherical coordinate system (q, θ, ϕ) , the ϕ dependence of these functions is $e^{\pm im\phi}$ ($m = 0, 1, 2$). The analytical integration with respect to ϕ results in trivial equalities (32).

4 Results and Conclusions

We study the eD elastic scattering within the simplest model supposing that the NN channel is described in the PF RQM and using the SA for the NN EM current operator. Therefore we assume that the exchange current effects are negligible within the NN deuteron models at least for this reaction. The momentum space deuteron wave functions are transformed into the configuration space using Eqs. (16)–(17). We assume that the configuration space wave functions of Eq. (14) have a physical sense only in the non-relativistic limit. The deuteron wave functions stemming from Nijmegen-I (NijmI), Nijmegen-I (NijmII) [44], JISP16 [45], CD-Bonn [46], Paris [47], Argonne18 [48] (for this momentum space deuteron wave function we use a parametrization of Ref. [49]), Idaho [50] (thanks to Prof. David R. Entem for the respective computer code) and Moscow (with forbidden states) [22] potentials are shown in Figs. 1 and 2. The Moscow potential parameters and computer code generating Moscow potentials are available upon a request from the author (e-mail: nikolakhokhlov@yandex.ru).

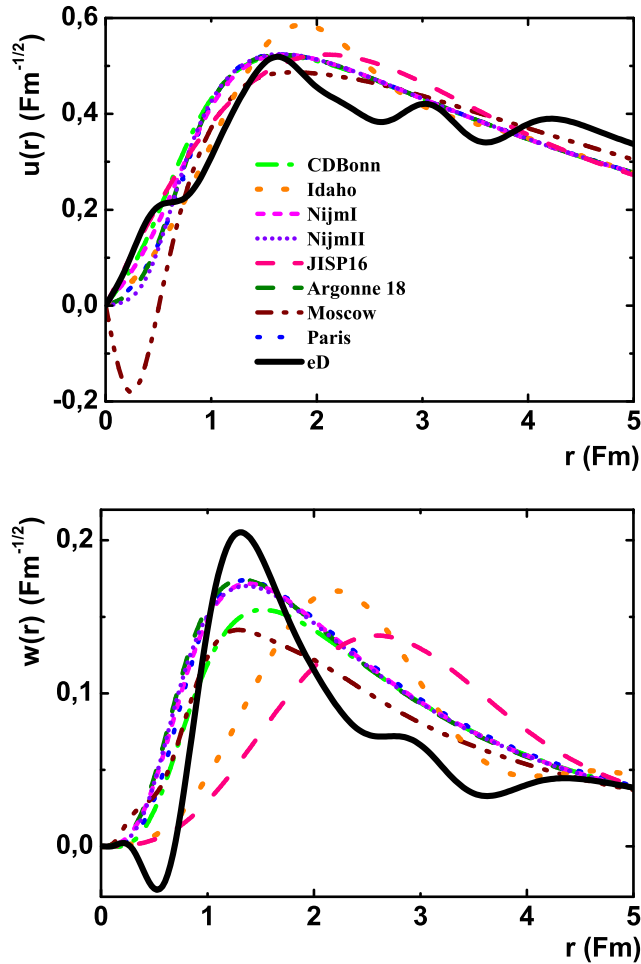


Figure 1: Configuration space deuteron wave functions used in calculations.

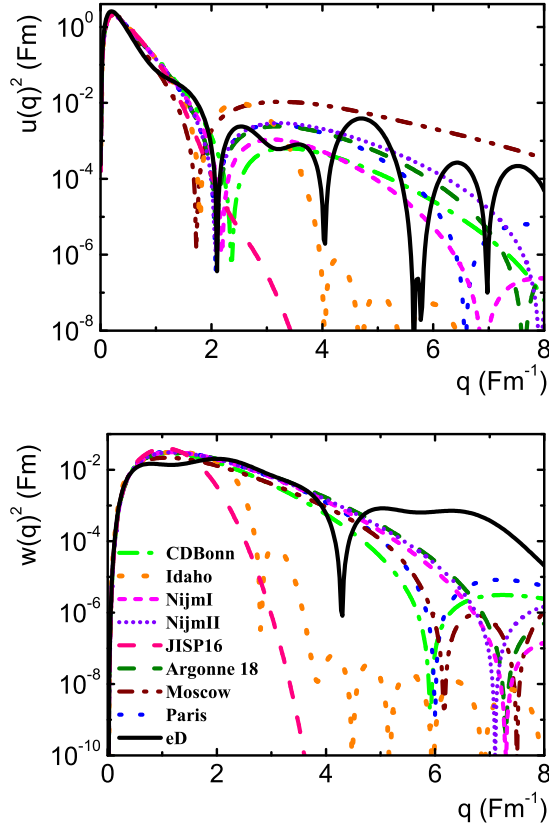


Figure 2: Momentum space deuteron wave functions used in the calculations.

In our previous studies [28, 29] we concentrated on the deuteron FF dependence on the nucleon FFs which was found to be considerable for $Q > 5 \text{ Fm}^{-1}$. Now we examine a possibility of extracting the deuteron wave function and neutron EM FFs from the elastic eD scattering. Therefore we perform a fit of the deuteron wave function and nucleons EM FFs. We use the nucleon FF functional dependence on Q^2 of Ref. [10] and fit the parameters. The deuteron wave function parametrization is described below. Results of the fit denoted as eD are presented in Table 1 and figures.

We use the deuteron wave functions in the analytic form of Ref. [47] modified by a short range addend. The ansatz for the configuration space wave functions is

$$u(r) = \sum_{i=0}^m a_i^0 R_{i,0}(r) + \sum_{j=1}^n C_j \exp(-m_j r), \quad (34)$$

$$w(r) = \sum_{i=0}^k a_i^2 R_{i,2}(r) + \sum_{j=1}^n D_j \exp(-m_j r) \left[1 + \frac{3}{m_j r} + \frac{3}{(m_j r)^2} \right], \quad (35)$$

where the oscillator functions

$$R_{n,l}(r) = (-1)^n \sqrt{\frac{2n!}{r_0 \Gamma(n+l+3/2)}} \left(\frac{r}{r_0} \right)^{l+1} \exp\left(-\frac{r^2}{2r_0^2}\right) L_n^{l+\frac{1}{2}}\left(\frac{r^2}{r_0^2}\right), \quad (36)$$

L_n^α is the associated Laguerre polynomial, the oscillator radius $r_0 = 0.4 \text{ fm}$.

Table 1: Static deuteron form factors. The slash-separated values are the results of relativistic/non-relativistic calculations.

	$G_M(0) = \frac{M_d}{m_p} \mu_d$	$G_Q(0) = M_d^2 Q_d$
Exp	1.7148	25.83
NijmI	1.697/1.695	24.8/24.6
NijmII	1.700/1.695	24.7/24.5
Paris	1.696/1.694	25.6/25.2
CD-Bonn	1.708/1.704	24.8/24.4
Argonne18	1.696/1.694	24.7/24.4
JISP16	1.720/1.714	26.3/26.1
Moscow06	1.711/1.699	24.5/24.2
Moscow14	1.716/1.700	26.0/25.8
Idaho	1.714/1.700	26.22/25.98
eD	1.715/1.700	25.83/25.54

The momentum space wave functions can be easily obtained analytically by the Fourier transform. The boundary condition at $r = 0$ leads to the constraints

$$C_n = - \sum_{j=1}^{n-1} C_j, \quad (37)$$

$$D_{n-2} = \frac{m_{n-2}^2}{(m_n^2 - m_{n-2}^2)(m_{n-1}^2 - m_{n-2}^2)} \times \left[-m_{n-1}^2 m_n^2 \sum_{j=1}^{n-3} \frac{D_j}{m_j^2} + (m_{n-1}^2 + m_n^2) \sum_{j=1}^{j=n-3} D_j - \sum_{j=1}^{n-3} D_j m_j^2 \right], \quad (38)$$

and two additional relations obtained by circular permutations of $n-2$, $n-1$, n . All parameters are available from the author upon a request.

Results of our calculations are presented in Figs. 1–5. We see a very good general agreement between the theory and experiment for $Q < 3 \text{ Fm}^{-1}$. Discrepancies at larger Q values are comparable with discrepancies between results obtained with different interaction models (potentials). Some model calculations [69] demonstrate that the meson exchange currents may contribute significantly to EM processes in the np -system. The meson exchange currents are not accounted for in our calculations. It is not clear how to correlate these currents with the short-range behavior of NN interaction of the QCD origin. We have a number of deuteron models (Figs. 1 and 2) that obviously require different meson exchange currents. The nucleon EM FFs are not described by meson degrees of freedom at intermediate and high energies [70]; moreover, the neutron EM FFs cannot be measured directly. As discussed in the Introduction, all available data on the neutron EM FFs are model dependent. Any conclusion about the meson exchange current contribution looks unjustified without having solid data on the neutron EM FFs.

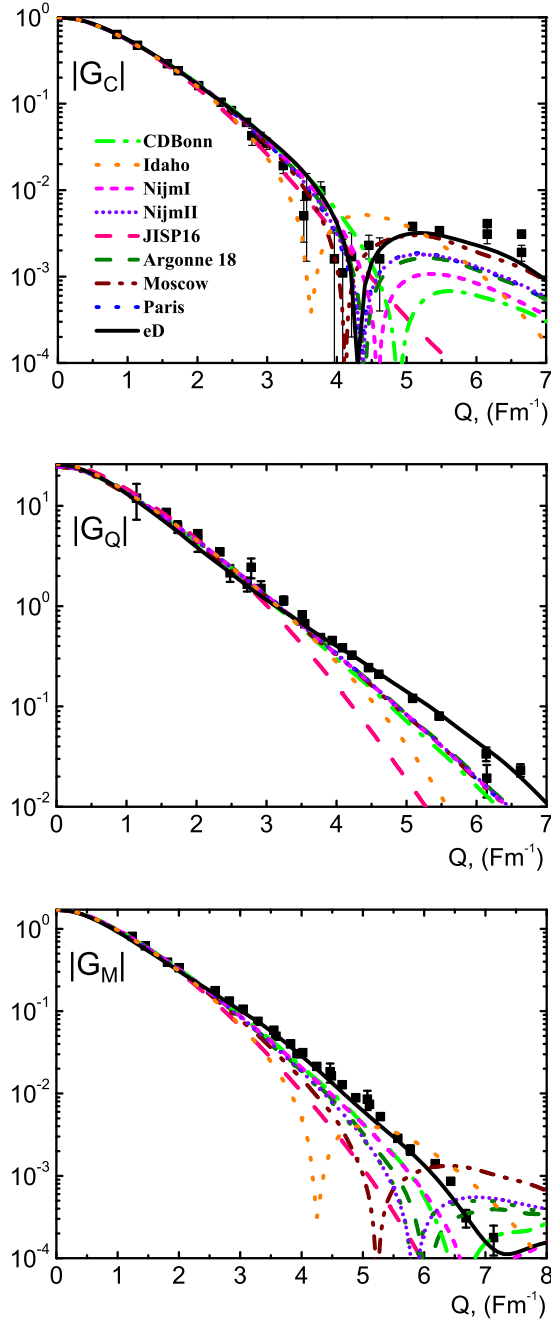


Figure 3: Deuteron form factors as a function of Q . Experimental data are the compilation of Ref. [2] where the results of experiments of Refs. [51–67] were analyzed.

Our calculations show that modest modifications of the deuteron wave function and nucleon FF parameterizations may simulate the effects of meson exchange currents in the eD elastic scattering. An analysis of Plachkov *et al.* [71] demonstrated that extracting the neutron electric FF is extremely model dependent (see Fig. 6). This analysis has been performed when the data on polarization experiments were

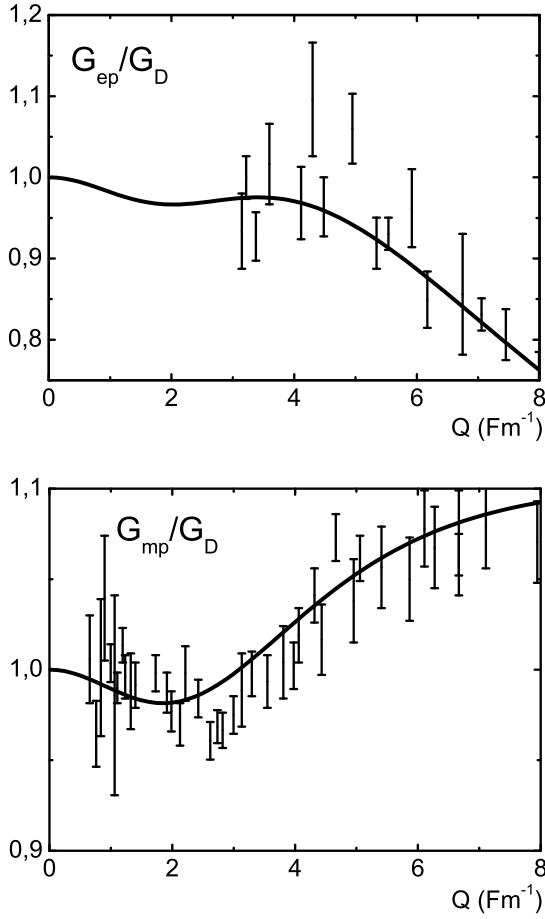


Figure 4: Proton EM FFs as a function of Q . Experimental data are the compilation of Ref. [68] of analyses of polarization experiments. Solid curves are proton FFs extracted from deuteron FFs by our fitting procedure.

scarce. Unfortunately, there is no a similar recent analysis of the neutron FFs based on the up-to-date experimental information. Such an analysis is complicated due to a large number of nuclear models and exchange currents used in modern literature. In addition, while extracting the neutron FFs, one faces the same difficulties as are inherent in the the proton FF extraction — their effect was never accurately estimated too. Therefore it is very possible that the error bars in the experimental data on the neutron FF presented in Fig. 5 are underestimated considerably, systematic errors of the NN interaction uncertainties are not properly accounted for. Our results for the nucleon FFs show that the extracted proton FFs are inside the experimental bars (Fig. 4), but the electric neutron FF (Fig. 5) may be 2–3 times larger than the results extracted using the so-called “Arenhövel’s model” [12]. In this case the magnetic neutron FF also changes (Fig. 5) but not drastically.

We plan to calculate the deuteron electrodisintegration to show that this reaction can be described in the “only NN channel” relativistic model, and our preliminary estimates are encouraging.

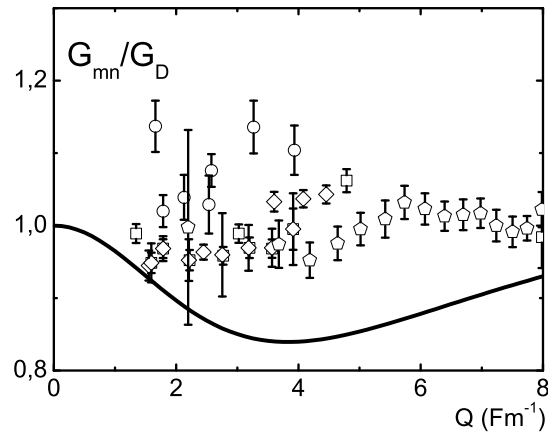
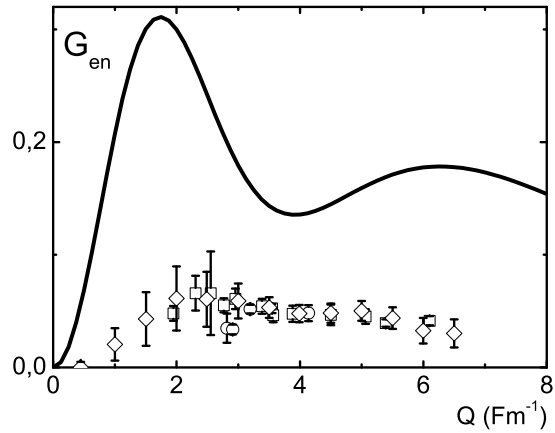


Figure 5: Neutron FFs as a function of Q . Experimental data are the compilation of Ref. [68] of model-dependent analyses of polarization experiments. Solid curves are neutron FFs extracted from deuteron FFs by our fitting procedure.

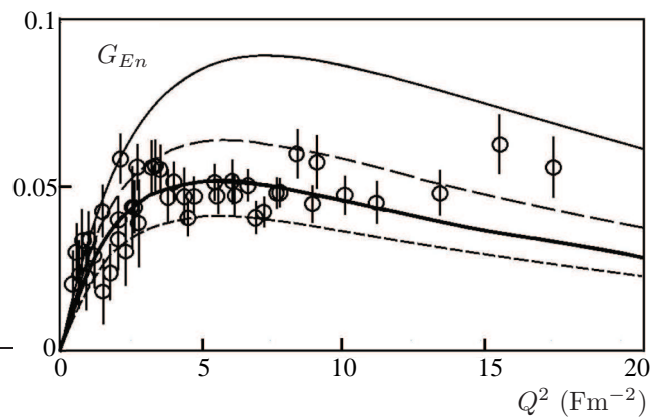


Figure 6: Data of Platchkov *et al.* [71] extracted from experiment using Paris potential. Curves are the fits to the same data extracted using Paris (thick solid), Reid soft core (short-dashed), Argonne V14 (long-dashed), and Nijmegen [72] (solid) potentials. The figure is grabbed from Ref. [71].

References

- [1] R. Gilman and F. Gross, *J. Phys. G* **28**, R37 (2002).
- [2] M. Garçon and J. W. Van Orden, *Adv. Nucl. Phys.* **26**, 293 (2001).
- [3] R. G. Arnold, C. E. Carlson and F. Gross, *Phys. Rev. C* **21**, 293 (1980).
- [4] T. W. Donnelly and A. S. Raskin, *Ann. Phys. (NY)* **169**, 247 (1986).
- [5] A. I. Akhiezer, A. G. Sitenko and V. K. Tartakovskii, *Nuclear Electrodynamics*. Springer, Berlin, 1994.
- [6] H. Arenhövel, F. Ritz and T. Wilbois, *Phys. Rev. C* **61**, 034002 (2000).
- [7] R. Schiavilla and V. R. Pandharipande, *Phys. Rev. C* **65**, 064009 (2002).
- [8] V. Punjabi, C. F. Perdrisat, M. K. Jones, E. J. Brash and C. E. Carlson, *Eur. Phys. J. A* **51**, 79 (2015).
- [9] E. J. Brash, A. Kozlov, S. Li and G. M. Huber, *Phys. Rev. C* **65**, 051001(R) (2002).
- [10] J. Arrington, *Phys. Rev. C* **68**, 034325 (2003).
- [11] W. M. Alberico, S. M. Bilenky, C. Giunti and K. M. Graczyk, *Phys. Rev. C* **79**, 065204 (2009).
- [12] S. Riordan *et al.*, *Phys. Rev. Lett.* **105**, 262302 (2010).
- [13] J. Lachniet *et al.*, *Phys. Rev. Lett.* **102**, 192001 (2009).
- [14] S. Galster, H. Klein, J. Moritz, K. Schmidt, D. Wegener and J. Bleckwenn, *Nucl. Phys. B* **32**, 221 (1971).
- [15] E. Lomon, *Phys. Rev. C* **66**, 045501 (2002).
- [16] H. Arenhövel, *Phys. Lett. B* **199**, 13 (1987).
- [17] T. Eden *et al.*, *Phys. Rev. C* **50**, R1749 (1994).
- [18] J. Adam, Jr. and H. Arenhövel, *Nucl. Phys. A* **614**, 289 (1997).
- [19] K. Tamura, T. Niwa, T. Sato and H. Ohtsubo, *Nucl. Phys. A* **536**, 597 (1992).
- [20] T. W. Allen, W. H. Klink and W. N. Polyzou, *Phys. Rev. C* **63**, 034002 (2001).
- [21] F. M. Lev, E. Pace and G. Salmè, *Phys. Rev. C* **62** 064004 (2000); *Nucl. Phys. A* **663**, 365c (2000).
- [22] N. A. Khokhlov and V. A. Knyr, *Phys. Rev. C* **73**, 024004 (2006).
- [23] N. A. Khokhlov, V. A. Knyr and V. G. Neudatchin, *Phys. Rev. C* **68**, 054002 (2003).
- [24] V. A. Knyr, V. G. Neudatchin and N. A. Khokhlov, *Phys. Atom. Nucl.* **70**, 879 (2007).

- [25] N. A. Khokhlov, V. A. Knyr and V. G. Neudatchin, *Phys. Rev. C* **75**, 064001 (2007).
- [26] V. A. Knyr, V. G. Neudatchin and N. A. Khokhlov, *Phys. Atom. Nucl.* **70**, 2152 (2007); V. A. Knyr and N. A. Khokhlov, *Phys. Atom. Nucl.* **66**, 1994 (2008).
- [27] V. A. Knyr and N. A. Khokhlov, *Phys. Atom. Nucl.* **70**, 2066 (2007).
- [28] N. A. Khokhlov and A. A. Vakulyuk, *Phys. Atom. Nucl.* **78**, 92 (2015).
- [29] N. A. Khokhlov, in *Proc. Int. Conf. Nucl. Theor. Supercomputing Era (NTSE-2014), Khabarovsk, Russia, June 23–27, 2014*, eds. A. M. Shirokov and A. I. Mazur. Pacific National University, Khabarovsk, 2016, p. 230, <http://www.ntse-2014.khb.ru/Proc/Khokhlov.pdf>.
- [30] B. D. Keister and W. Polyzou, *Adv. Nucl. Phys.* **20**, 325 (1991).
- [31] P. A. M. Dirac, *Rev. Mod. Phys.* **21**, 392 (1949).
- [32] S. N. Sokolov and A. M. Shatny, *Theor. Math. Phys.* **37**, 1029 (1978).
- [33] W. H. Klink, *Phys. Rev. C* **58**, 3587 (1998).
- [34] F. M. Lev, *Ann. Phys. (NY)* **237**, 355 (1995); arXiv:hep-ph/9403222 (1994).
- [35] T. Melde, L. Canton, W. Plessas and R. F. Wagenbrunn, *Eur. Phys. J. A* **25**, 97 (2005).
- [36] B. Desplanques and L. Theußl, *Eur. Phys. J. A* **13**, 461 (2002).
- [37] T. W. Allen and W. H. Klink, *Phys. Rev. C* **58**, 3670 (1998).
- [38] F. Coester and D. O. Riska, *Few-Body Syst.* **25**, 29 (1998).
- [39] R. F. Wagenbrunn, S. Boffi, W. Klink, W. Plessas and M. Radici, *Phys. Lett. B* **511**, 33 (2001).
- [40] A. Amghar, B. Desplanques and L. Theußl, *Phys. Lett. B* **574**, 201 (2003).
- [41] F. Coester and D. O. Riska, *Nucl. Phys. A* **728**, 439 (2003).
- [42] B. Bakamjian and L. H. Thomas, *Phys. Rev.* **92**, 1300 (1953).
- [43] R. G. Arnold, C. E. Carlson and F. Gross, *Phys. Rev. C* **23**, 363 (1981).
- [44] V. G. J. Stoks, R. A. M. Klomp, C. P. F. Terheggen and J. J. de Swart, *Phys. Rev. C* **49**, 2950 (1994).
- [45] A. M. Shirokov, J. P. Vary, A. I. Mazur and T. A. Weber, *Phys. Lett. B* **644**, 33 (2007).
- [46] R. Machleidt, *Phys. Rev. C* **63**, 024001 (2001).
- [47] M. Lacombe, B. Loiseau, R. Vinh Mau, J. Côté, P. Pirés and R. de Tournell, *Phys. Lett. B* **101**, 139 (1981).
- [48] R. B. Wiringa, V. G. J. Stoks and R. Schiavilla, *Phys. Rev. C* **51**, 38 (1995).

- [49] S. Veerasamy and W. N. Polyzou, Phys. Rev. C **84**, 034003 (2011).
- [50] D. R. Entem and R. Machleidt, Phys. Rev. C **68**, 041001 (2003).
- [51] J. E. Elias, J. I. Friedman, G. C. Hartmann, H. W. Kendall, P. N. Kirk, M. R. Sogard, L. P. Van Speybroeck and J. K. De Pagter, Phys. Rev. **177**, 2075 (1969).
- [52] R. G. Arnold, B. T. Chertok, E. B. Dally, A. Grigorian, C. L. Jordan, W. P. Schütz, R. Zdarko, F. Martin and B. A. Mecking, Phys. Rev. Lett. **35**, 776 (1975).
- [53] R. Cramer *et al.*, Z. Phys. C **29**, 513 (1985).
- [54] S. Platchkov, A. Amroun, S. Auffret, J.M. Cavedon, P. Dreux, J. Duclos, B. Frois, D. Goutte, H. Hachemi, J. Martino and X. H. Phan, Nucl. Phys. A **510**, 740 (1990).
- [55] L. C. Alexa *et al.*, Phys. Rev. Lett. **82**, 1374 (1999).
- [56] D. Abbott *et al.*, Phys. Rev. Lett. **82**, 1379 (1999).
- [57] S. Auffret *et al.*, Phys. Rev. Lett. **54**, 649 (1985).
- [58] P. E. Bosted *et al.*, Phys. Rev. C **42**, 38 (1990).
- [59] M. E. Schulze *et al.*, Phys. Rev. Lett. **52**, 597 (1984).
- [60] M. Garçon *et al.*, Phys. Rev. C **49**, 2516 (1994); I. The *et al.*, Phys. Rev. Lett. **67**, 173 (1991).
- [61] D. Abbott *et al.*, Phys. Rev. Lett. **84**, 5053 (2000).
- [62] V. F. Dmitriev *et al.*, Phys. Lett. B **157**, 143 (1985).
- [63] B. B. Voitsekhovskii, D. M. Nikolenko, K. T. Ospanov, S. G. Popov, I. A. Rachek, D. K. Toporkov, E. P. Tsentalovich and Yu. M. Shatunov, JETP Lett. **43**, 733 (1986).
- [64] R. Gilman *et al.*, Phys. Rev. Lett. **65**, 1733 (1990).
- [65] M. Ferro-Luzzi *et al.*, Phys. Rev. Lett. **77**, 2630 (1996).
- [66] M. Bouwhuis *et al.*, Phys. Rev. Lett. **82**, 3755 (1999).
- [67] D. Abbott *et al.*, Eur. Phys. J. A **7**, 421 (2000).
- [68] M. Kohl, Nucl. Phys. A **805**, 361c (2008).
- [69] H. Arenhoevel, E. M. Darwish, A. Fix and M. Schwamb, Mod. Phys. Lett. A **18**, 190 (2003).
- [70] C. F. Perdrisat, V. Punjabi and M. Vanderhaeghen, Prog. Part. Nucl. Phys. **59**, 694 (2007).
- [71] S. Platchkov *et al.*, Nucl. Phys. A **508**, 343 (1990).
- [72] M. M. Nagels, T. A. Rijken and J. de Swaart, Phys. Rev. D **17**, 769 (1978).

Quantum Monte Carlo Calculations with Chiral Effective Field Theory Interactions: Developments and a Recent Application

Joel E. Lynn

*Institut für Kernphysik, Technische Universität Darmstadt, 64289, Darmstadt, Germany
ExtreMe Matter Institute EMMI, GSI Helmholtzzentrum für Schwerionenforschung GmbH,
64291 Darmstadt, Germany*

Abstract

Quantum Monte Carlo methods are among the most accurate nuclear many-body methods available. Chiral effective field theory presents a systematic way to derive nuclear Hamiltonians from effective field theory with the same symmetries as low-energy quantum chromodynamics. Here we describe the developments that have led to the combination of these two powerful approaches, a recent application, and prospects for the future.

Keywords: *Nuclear interactions; ab initio methods*

1 Introduction

Low-energy nuclear physics sits in a privileged position, connecting many different research areas including (among others) nuclear structure, fundamental symmetries, and nuclear astrophysics. In each of these areas of inquiry, there are large open questions. For example, in nuclear structure, we might ask: What are the limits of existence of the nuclear chart? How far can *ab initio* calculations be pushed? How can we build a coherent framework for describing nuclei, nuclear matter, and nuclear reactions?

While quantum chromodynamics (QCD) is ultimately responsible for strong interactions, at low energies most applicable to many phenomenon in nuclear physics, the most relevant degrees of freedom are baryons and mesons, specifically nucleons and pions. But even choosing to work with these simplified degrees of freedom over the fundamental degrees of freedom (quarks and gluons), nuclear systems still present a significant challenge because they are strongly interacting many-body systems.

Two questions must be addressed: 1) How do we solve the many-body Schrödinger equation,

$$H|\Psi_0\rangle = E_0|\Psi_0\rangle? \quad (1)$$

and 2) Where should we take the Hamiltonian H ? There are, of course, many answers possible to both questions. In this brief overview, we will discuss one possible answer

Proceedings of the International Conference ‘Nuclear Theory in the Supercomputing Era — 2016’ (NTSE-2016), Khabarovsk, Russia, September 19–23, 2016. Eds. A. M. Shirokov and A. I. Mazur. Pacific National University, Khabarovsk, Russia, 2018, p. 140.

<http://www.ntse-2016.khb.ru/Proc/Lynn.pdf>

set: 1) Quantum Monte Carlo (QMC) methods, and 2) Chiral effective field theory (EFT). Low-energy nuclear theory can make significant contributions to many areas of research and the combination of QMC methods and chiral EFT interactions is an important piece of the puzzle.

2 Quantum Monte Carlo methods

Quantum Monte Carlo methods are among the most accurate many-body methods in use in nuclear physics. They include the Variational Monte Carlo (VMC) method, the Green's Function Monte Carlo (GFMC) method, and the Auxiliary-Field Diffusion Monte Carlo (AFDMC) method.

The first method relies on the Rayleigh–Ritz variational principle to establish an upper bound for the ground-state energy. In a few sentences, the idea is as follows. One makes an educated guess for the many-body wave function $|\Psi_T(\{c_i\})\rangle$, which is known as the trial wave function and which depends on some set of adjustable parameters $\{c_i\}$. A set of random configurations is generated $\{\mathbf{R}_i\}$, with $\mathbf{R}_i = \{\mathbf{r}_1, \mathbf{r}_2, \dots, \mathbf{r}_A\}_i$, a set of $3A$ coordinates for the A nucleons. Then, the Metropolis algorithm is used to generate new configurations $\{\mathbf{R}'_i\}$ based on the probability $P = \frac{|\Psi_T(\mathbf{R}')|^2}{|\Psi_T(\mathbf{R})|^2}$, suppressing the dependence on the variational parameters. Ultimately, what this yields is a set of configurations (often called “walkers”), which are distributed according to the square of the trial wave function. At this point, the variational principle is invoked and the expectation value of the Hamiltonian in this state is an upper bound to the ground-state energy:

$$\frac{\langle \Psi_T | H | \Psi_T \rangle}{\langle \Psi_T | \Psi_T \rangle} > E_0. \quad (2)$$

Searches are performed over parameter sets $\{c_i\}$ minimizing the energy.

In addition to the intrinsic value of VMC calculations, they also serve as the starting point for the latter two QMC methods, which belong to a class of so-called “diffusion” Monte Carlo methods. These solve the many-body Schrödinger equation,

$$H|\Psi_0\rangle = E_0|\Psi_0\rangle, \quad (3)$$

for a system described by a Hamiltonian H , with ground state $|\Psi_0\rangle$ and energy E_0 , by using the deceptively simple-looking evolution operator

$$\lim_{\tau \rightarrow \infty} e^{-H\tau} |\Psi_T\rangle \rightarrow |\Psi_0\rangle, \quad (4)$$

for an initial “trial” state $|\Psi_T\rangle$. (The operator $e^{-H\tau}$ is known by many names including the imaginary-time diffusion operator, the Euclidean-time projection operator, and the imaginary-time propagator.) To see how this works, expand the trial state in a complete set of eigenstates of the Hamiltonian:

$$|\Psi_T\rangle = \sum_{n=0}^{\infty} |\Psi_n\rangle \langle \Psi_n | \Psi_T \rangle = \sum_{n=0}^{\infty} \alpha_n |\Psi_n\rangle. \quad (5)$$

One tries to ensure that the overlap with the ground state is maximal: $\alpha_0 \gg \alpha_{n \neq 0}$, but inevitably, there is some contamination in the trial state from higher excited

states. Now propagate in imaginary time:

$$\begin{aligned} \lim_{\tau \rightarrow \infty} e^{-(H-E_T)\tau} \sum_{n=0}^{\infty} \alpha_n |\Psi_n\rangle &= \lim_{\tau \rightarrow \infty} e^{-(H-E_T)\tau} \sum_{n=0}^{\infty} \alpha_n e^{-(E_n-E_T)\tau} |\Psi_n\rangle \\ &= \lim_{\tau \rightarrow \infty} e^{-(E_0-E_T)\tau} \left(\alpha_0 |\Psi_0\rangle + \sum_{n>0}^{\infty} \alpha_n e^{-(E_n-E_0)\tau} |\Psi_n\rangle \right). \end{aligned} \quad (6)$$

Eq. (6) introduces the trial energy E_T , which controls the normalization, and makes the remainder of the argument clearer. It is typically chosen equal to the ground-state energy (though it need not be). In the second line, an overall exponential has been factored out. Now, given that $E_T \sim E_0$ and $E_n > E_0$, under the limit, the only term that remains is the ground state:

$$\lim_{\tau \rightarrow \infty} e^{-(H-E_T)\tau} |\Psi_T\rangle = \alpha_0 |\Psi_0\rangle. \quad (7)$$

3 Chiral effective field theory

Ultimately QCD is responsible for the properties of strongly interacting nuclear matter. The Lagrangian of QCD for the two lightest quarks, u and d , can be written as

$$\mathcal{L}_{\text{QCD}} = -\frac{1}{2g^2} \text{tr}\{G_{\mu\nu}G^{\mu\nu}\} + i\bar{q}\gamma^\mu D_\mu q - \bar{q}\mathcal{M}q, \quad (8)$$

where q (\bar{q}) collects the quark (antiquark) fields, $G_{\mu\nu}$ is the nonabelian gluon field strength tensor, g the coupling constant, D_μ a gauge covariant derivative, and \mathcal{M} the mass matrix. In the massless limit $\mathcal{M} \rightarrow 0$, the Lagrangian exhibits a chiral symmetry where the fields transform independently under left- and right-handed SU(2) rotations. This is the chiral symmetry of low-energy QCD. Now one can follow the Weinberg's prescription to write down the most general Lagrangian in the low-energy degrees of freedom (pions and nucleons) consistent with the important symmetries of the underlying theory (chiral symmetry),

$$\mathcal{L}_{\text{eff}} = \mathcal{L}_{\pi\pi} + \mathcal{L}_{\pi N} + \mathcal{L}_{NN}. \quad (9)$$

Once a power-counting method is specified, then one can order the Lagrangians in powers of a small parameter Q/Λ , where Q is some typical momentum scale in low-energy nuclear physics, e. g., the pion mass, and Λ is some hard scale naively of the order of the chiral symmetry breaking scale $\Lambda \sim 1$ GeV. For example, the nucleon-nucleon Lagrangian can be written as a sum of terms $\mathcal{L}_{NN}^{(n)}$ with n signifying the order $(Q/\Lambda)^n$:

$$\mathcal{L}_{NN} = \mathcal{L}_{NN}^{(0)} + \mathcal{L}_{NN}^{(2)} + \mathcal{L}_{NN}^{(3)} + \dots \quad (10)$$

From such an effective Lagrangian, a nuclear potential can be extracted, which also obeys the same ordering:

$$V_{NN} = V_{NN}^{(0)} + V_{NN}^{(2)} + V_{NN}^{(3)} + \dots \quad (11)$$

The advantages of this approach are several. All of the long-range physics is governed explicitly by one- and multi-pion exchanges. The short-range physics is captured in

contact operators multiplied by unknown low-energy constants (LECs) that must be fitted to data. And importantly, many-body forces and electroweak currents enter in a systematic way. For example, the three-nucleon interaction enters first at the order $(Q/\Lambda)^3$ (also known as next-to-next-to-leading order or $N^2\text{LO}$). For more details see Refs. [1, 2].

An important detail from the point of view of QMC methods, is that most chiral EFT interactions are nonlocal: $\langle \mathbf{r}|V|\mathbf{r}'\rangle = V(\mathbf{r}, \mathbf{r}')$. While some work has been done to include nonlocal potentials in QMC methods [3, 4], in practice, QMC methods require local potentials with $\langle \mathbf{r}|V|\mathbf{r}'\rangle = V(\mathbf{r})\delta^{(3)}(\mathbf{r} - \mathbf{r}')$. However, recently an equivalent formulation has been derived that allows for the construction of local interactions from chiral EFT up to $N^2\text{LO}$ [5, 6], which has been implemented and tested in GFMC calculations of light nuclei and AFDMC calculations of neutron matter [7, 8]. References [5–8] contain the detailed derivation of the local two- and three-nucleon interactions from chiral EFT, here we briefly summarize the underlying ideas.

If $\mathbf{q} \equiv \mathbf{p} - \mathbf{p}'$ is the momentum transfer in terms of the incoming and outgoing relative momenta \mathbf{p} and \mathbf{p}' , and $\mathbf{k} \equiv \frac{1}{2}(\mathbf{p} + \mathbf{p}')$ is the momentum transfer in the exchange channel, then any functional dependence on \mathbf{k} will lead to a nonlocal interaction, whereas the \mathbf{q} dependence Fourier transforms to a local interaction. Then, the two sources of nonlocality come from 1) the regulator function (used to regulate high-momentum components of the interaction) and 2) the choice of operators in the contact sector of the interaction. 1) The typical regulator function used in momentum space is $f(p) = e^{-(p/\Lambda)^n}$, with Λ being a cutoff scale, and $n > 2$ is some appropriate power. Then,

$$V(\mathbf{p}, \mathbf{p}') \rightarrow V(\mathbf{p}, \mathbf{p}') f(p) f(p'). \quad (12)$$

In short, even if $V(\mathbf{p}, \mathbf{p}')$ were such that it would Fourier transform to a local interaction, the regulation scheme of Eq. (12) spoils this. The solution is to regulate in the coordinate space in a local way: $f(r) \propto e^{-(r/R_0)^4}$, where $R_0 = 1.0\text{--}1.2$ fm serves as the coordinate-space cutoff (approximately equivalent to 500–400 MeV, respectively). 2) At leading order (LO) in Weinberg power counting, the nuclear interaction consists of the one-pion-exchange potential, and (in principle) four possible momentum-independent contact operators: $\{\mathbb{1}, \boldsymbol{\tau}_1 \cdot \boldsymbol{\tau}_2, \boldsymbol{\sigma}_1 \cdot \boldsymbol{\sigma}_2, \boldsymbol{\sigma}_1 \cdot \boldsymbol{\sigma}_2 \boldsymbol{\tau}_1 \cdot \boldsymbol{\tau}_2\}$. However, nucleons are fermions and obey the Pauli exclusion principle. This means that we will ultimately be taking matrix elements between antisymmetric states, and an antisymmetrized potential $V \rightarrow \mathcal{A}V$ will give equivalent results. Under this antisymmetrization operation, it can be shown that at LO, only two of four contact operators are linearly independent. This same freedom exists at the next-to-leading order (NLO) where out of fourteen possible momentum-dependent operators only seven are linearly independent under the antisymmetrization operation. This ‘‘Fierz’’ freedom can be exploited to choose a set of (mostly) local operators. (The exception comes from one operator proportional to $\mathbf{q} \times \mathbf{k}$, but this is none other than the spin-orbit operator, which has long been included explicitly in QMC methods and causes no significant difficulty.) At the next-to-next-to-next-to-leading order ($N^3\text{LO}$), this Fierz freedom is insufficient to remove all \mathbf{k} -dependent operators, and so a maximally local set will have to be selected. See Ref. [9] for a similar approach. It is possible that the remaining nonlocal operators are ‘‘small’’ and can be included perturbatively in QMC methods.

3.1 Three-nucleon interactions

An important consideration, both from the point of view of agreement with experimental nuclear structure and from the point of view of consistency in the power counting, is the inclusion of three-nucleon interactions that appear at N²LO. Again, we refer the interested reader to details provided in Refs. [6,8], but briefly summarize the important points here. There are three Feynman diagrams contributing to the three-nucleon interaction at N²LO in Weinberg power counting, pictured in Fig. 1.

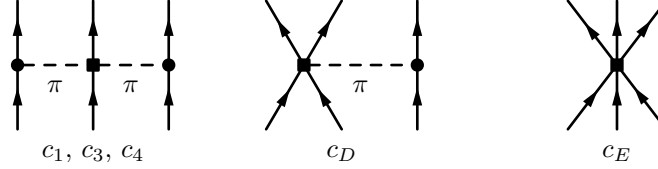


Figure 1: Feynman diagrams contributing to the three-nucleon interaction at N²LO. Solid lines are nucleons, dashed lines are pions.

The Fourier transform of the first diagram has two parts. The first, which depends on the LEC c_1 , is an s -wave two-pion exchange, which bears resemblance to the a' term of the Tucson–Melbourne interaction [10]. The second, which depends on the LECs c_3 and c_4 , is a p -wave two-pion exchange, which bears resemblance to the Fujita–Miyazawa interaction [11]. (There are short-range structures that arise in the Fourier transforms of the c_3 and c_4 interactions, which we retain explicitly.)

The second diagram proportional to the LEC c_D leads, under Fourier transform with a finite regulator, to two possible interactions, which in the infinite momentum-space cutoff limit would be identical. These two interactions differ in their short-distance structure:

$$V_{D1} \propto \sum_{i < j < k} \sum_{\text{cyc}} (\boldsymbol{\tau}_i \cdot \boldsymbol{\tau}_k) \times \left[X_{ik}(\mathbf{r}_{kj}) \delta_{R_{3N}}(\mathbf{r}_{ij}) + X_{ik}(\mathbf{r}_{ij}) \delta_{R_{3N}}(\mathbf{r}_{kj}) - \frac{8\pi}{m_\pi^2} \boldsymbol{\sigma}_i \cdot \boldsymbol{\sigma}_k \delta_{R_{3N}}(\mathbf{r}_{ij}) \delta_{R_{3N}}(\mathbf{r}_{kj}) \right]; \quad (13)$$

$$V_{D2} \propto \sum_{i < j < k} \sum_{\text{cyc}} (\boldsymbol{\tau}_i \cdot \boldsymbol{\tau}_k) \times \left[X_{ik}(\mathbf{r}_{ik}) - \frac{4\pi}{m_\pi^2} \boldsymbol{\sigma}_i \cdot \boldsymbol{\sigma}_k \delta_{R_{3N}}(\mathbf{r}_{ik}) \right] (\delta_{R_{3N}}(\mathbf{r}_{ij}) + \delta_{R_{3N}}(\mathbf{r}_{kj})). \quad (14)$$

Here, $\boldsymbol{\sigma}$ ($\boldsymbol{\tau}$) is a Pauli spin (isospin) matrix, m_π is the pion mass, $X_{ij}(\mathbf{r}) = [S_{ij}(\mathbf{r})T(r) + \boldsymbol{\sigma}_i \cdot \boldsymbol{\sigma}_j]Y(r)$ is the coordinate-space pion propagator with $S_{ij}(\mathbf{r}) = 3\boldsymbol{\sigma}_i \cdot \hat{\mathbf{r}} \boldsymbol{\sigma}_j \cdot \hat{\mathbf{r}} - \boldsymbol{\sigma}_i \cdot \boldsymbol{\sigma}_j$ being the tensor operator, the tensor and Yukawa functions are $T(r) = 1 + 3/(m_\pi r) + 3/(m_\pi r)^2$ and $Y(r) = e^{-m_\pi r}/r$, and $\delta_{R_{3N}}(\mathbf{r}) \propto e^{-(r/R_{3N})^4}$ is the short-range regulated delta function with cutoff R_{3N} . In the above expressions, the pion-exchange-range interactions ($\propto Y$) are multiplied by a long-range regulator of the form $1 - e^{-(r/R_{3N})^4}$. We take $R_{3N} = R_0$, where R_0 is the cutoff used in the two-nucleon interaction. The sums $\sum_{i < j < k}$ and \sum_{cyc} are taken over all triples in a nucleus and over all cyclic permutations of the labels i, j, k , respectively. It is straightforward

to see that in the limit of $R_{3N} \rightarrow 0$, that is, the limit where $\delta_{R_{3N}}(\mathbf{r}) \rightarrow \delta(\mathbf{r})$, equations (13) and (14) agree.

The third diagram proportional to the LEC c_E leads to an interaction of the following form:

$$V_E \propto \sum_{i < j < k} \sum_{\text{cyc}} O_{ijk} \delta_{R_{3N}}(\mathbf{r}_{ij}) \delta_{R_{3N}}(\mathbf{r}_{kj}), \quad (15)$$

where, in principle, the Fierz freedom as in the two-nucleon sector allows the choice of the operator O_{ijk} as one from the set

$$\{\mathbb{1}, \boldsymbol{\sigma}_i \cdot \boldsymbol{\sigma}_j, \boldsymbol{\tau}_i \cdot \boldsymbol{\tau}_j, \boldsymbol{\sigma}_i \cdot \boldsymbol{\sigma}_j \boldsymbol{\tau}_i \cdot \boldsymbol{\tau}_j, \boldsymbol{\sigma}_i \cdot \boldsymbol{\sigma}_j \boldsymbol{\tau}_i \cdot \boldsymbol{\tau}_k, [(\boldsymbol{\sigma}_i \times \boldsymbol{\sigma}_k) \cdot \boldsymbol{\sigma}_j][(\boldsymbol{\tau}_i \times \boldsymbol{\tau}_k) \cdot \boldsymbol{\tau}_j]\}. \quad (16)$$

However, with the particular choice of regulator we make, $\delta(\mathbf{r}) \rightarrow \delta_{R_{3N}}(\mathbf{r}) \propto e^{-(r/R_{3N})^4}$, this freedom is broken, and some sensitivity to the choice of operator in Eq. (16) remains. We have explored three options:

$$V_{E\tau} \propto \sum_{i < j < k} \sum_{\text{cyc}} \boldsymbol{\tau}_i \cdot \boldsymbol{\tau}_k \delta_{R_{3N}}(\mathbf{r}_{ij}) \delta_{R_{3N}}(\mathbf{r}_{kj}), \quad (17)$$

$$V_{E1} \propto \sum_{i < j < k} \sum_{\text{cyc}} \delta_{R_{3N}}(\mathbf{r}_{ij}) \delta_{R_{3N}}(\mathbf{r}_{kj}), \quad (18)$$

$$V_{EP} \propto \sum_{i < j < k} \sum_{\text{cyc}} \mathcal{P} \delta_{R_{3N}}(\mathbf{r}_{ij}) \delta_{R_{3N}}(\mathbf{r}_{kj}), \quad (19)$$

with the projector

$$\mathcal{P} = \frac{1}{36} \left(3 - \sum_{i < j} \boldsymbol{\sigma}_i \cdot \boldsymbol{\sigma}_j \right) \left(3 - \sum_{k < l} \boldsymbol{\tau}_k \cdot \boldsymbol{\tau}_l \right) \quad (20)$$

onto triples with total spin $S = \frac{1}{2}$ and total isospin $T = \frac{1}{2}$. These are the triples that would survive in the infinite momentum-space cutoff limit.

3.2 Fits and results

The LECs appearing in Fig. 1, c_1 , c_3 , and c_4 , are already set in the pion-nucleon sector. However, the LECs c_D and c_E first appear in the three-nucleon sector at N²LO and must be fitted to some three- (or more-) body observables. An important consideration is to fit to uncorrelated observables. In the past, properties of $A = 3$ and $A = 4$ nuclei have been used to fix c_D and c_E . The shortcoming of this approach, however, is that largely, if one obtains reasonable properties of $A = 3$ nuclei, then the properties of the $A = 4$ nucleus are typically reproduced well: the two systems are highly correlated. In addition, we have two other motivations for our choices. The first motivation is to probe properties of light nuclei. For this reason, we choose the ⁴He binding energy as one observable. The second motivation is to probe the $T = 3/2$ physics. For this reason, we choose to reproduce n - α elastic scattering P -wave phase shifts. See Ref. [12] for details on the scattering calculations. The n - α system is the lightest known nuclear system where three neutrons may interact and therefore probes the $T = 3/2$ physics. Figure 2 shows the fits we performed. The top panel shows contours of c_E vs c_D . Each point in this panel corresponds to values of c_D and c_E for a given operator combination (e. g., V_{D2} and $V_{E\tau}$), for a given cutoff R_0 which gives

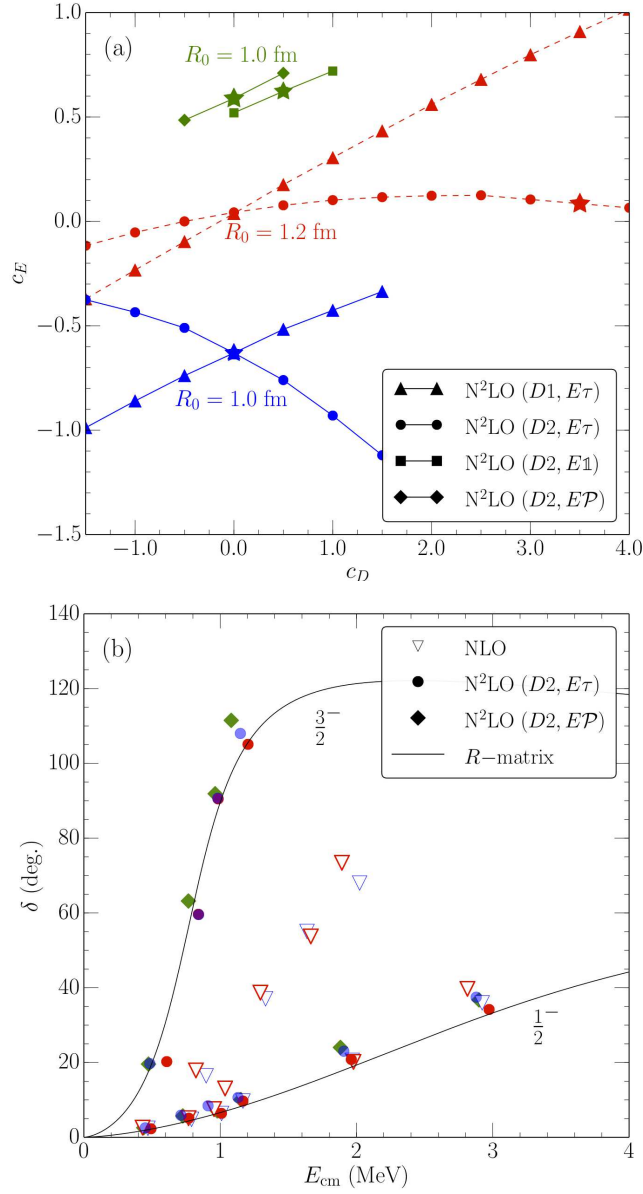


Figure 2: Top panel: Couplings c_E vs c_D obtained by fitting the ${}^4\text{He}$ binding energy for different $3N$ -operator forms. Triangles are obtained by using V_{D1} and $V_{E\tau}$, other symbols are obtained for V_{D2} and three different V_E -operator structures. The blue and green curves correspond to $R_0 = 1.0$ fm, the red curves correspond to $R_0 = 1.2$ fm. The GFMC statistical errors are smaller than the symbols. The stars correspond to the c_D and c_E values which simultaneously fit the $n-\alpha$ P -wave phase shifts. No fit to both observables can be obtained for the case with $R_0 = 1.2$ fm and V_{D1} . Bottom panel: P -wave $n-\alpha$ elastic scattering phase shifts compared with R -matrix analysis of experimental data. The same colors and symbols are used to distinguish the operator combinations. We include also the phase shifts calculated at NLO clearly indicating the necessity of $3N$ interactions to fit the P -wave splitting.

the experimental binding energy of ${}^4\text{He}$ in GFMC calculations. The stars in the left panel indicate values of c_D and c_E which simultaneously fit the ${}^4\text{He}$ binding energy and the P -wave elastic n - α scattering phase shifts shown in the bottom panel. A good description of both systems is obtained for both cutoffs ($R_0 = 1.0$ fm and $R_0 = 1.2$ fm) for the operator combinations V_{D2} and any of V_{E1} , $V_{E\tau}$, or V_{EP} (though only the cases with $V_{E\tau}$ and V_{EP} are shown in Fig. 2). Whereas for the operator combinations with V_{D1} and the softer cutoff $R_0 = 1.2$ fm, no fit to the P -wave n - α elastic scattering phase shifts could be obtained.

The interactions fit as just described, were used in GFMC calculations of light nuclei (top panel of Fig. 3) and in AFDMC calculations of the equation of state of neutron matter (bottom panel of Fig. 3). The uncertainties shown in Fig. 3 are obtained as a sum in quadrature of the QMC statistical uncertainties and a systematic estimate of the uncertainty induced by truncating the chiral expansion as in Ref. [13]. In short, taken together, Fig. 2 and Fig. 3 imply that our local N^2LO interactions have the freedom to simultaneously describe three benchmark nuclear systems: light nuclei, n - α elastic scattering phase shifts, and the neutron matter equation of state.

4 Application: neutrons in finite volume

Though QCD is the correct theory underlying the strong interactions, the only *ab initio* method to solve it directly at low energies is lattice QCD. Significant progress has been made in these simulations in the last two decades; however, even optimistically the simulation of ${}^{12}\text{C}$ in terms of quark and gluon degrees of freedom at physical pion masses is likely in a distant future. Therefore, some connection between the lattice QCD and *ab initio* calculations of nuclear systems in terms of nucleon and pion degrees of freedom is desirable. For example, it is conceivable that in the near future, matching of lattice QCD calculations to chiral Hamiltonians will allow for the extraction of LECs needed for chiral Hamiltonians from lattice QCD simulations. To help facilitate the construction of such a bridge, we have used the AFDMC method to calculate properties of two neutrons in a box with periodic boundary conditions and used the Lüscher formula to extract scattering properties (the scattering length a and effective range r_e) from our finite-volume calculations. For details, see Ref. [14]; here we summarize the main findings.

This work takes advantage of the formalism first introduced by Lüscher [15, 16] relating scattering phase shifts in infinite volume directly to the energy levels in finite volume. The relationship has some remarkable implications. For example, take a simple scattering problem, such as $np \rightarrow d\gamma$ radiative capture in the 1S_0 channel. One might naively expect that in order to simulate this problem in finite volume it would require cubic volumes with side lengths $L \gg |a^{1S_0}|, |a^{3S_1}|$, with, e. g., $a^{1S_0} = -23.71$ fm. However, this is not so. The Lüscher relationship

$$p \cot \delta_0(p) = \frac{1}{\pi L} S \left[\left(\frac{Lp}{2\pi} \right)^2 \right], \quad (21)$$

with the regulated sum

$$S(\eta) \equiv \lim_{\Lambda_j \rightarrow \infty} \left(\sum_j^{\Lambda_j} \frac{1}{|\mathbf{j}|^2 - \eta} - 4\pi\Lambda_j \right), \quad (22)$$

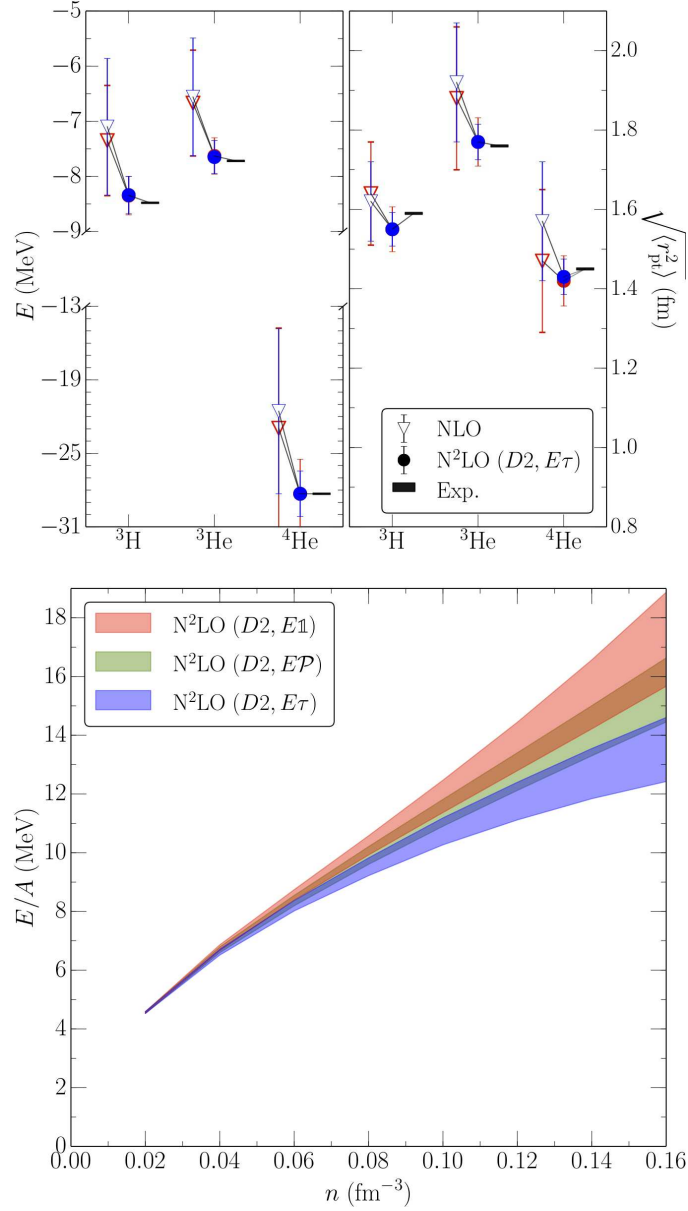


Figure 3: Top panel: Ground-state energies and point proton radii of $A = 3, 4$ nuclei calculated at NLO and N²LO (with V_{D_2} and $V_{E\tau}$) compared with experiment. Blue (red) symbols correspond to $R_0 = 1.0$ fm ($R_0 = 1.2$ fm). The errors are obtained as described in the text and include also the GFMC statistical uncertainties. Bottom panel: The energy per particle in neutron matter as a function of density for the NN and full $3N$ interactions at N²LO with $R_0 = 1.0$ fm. We use V_{D_2} and different $3N$ contact structures: the blue band corresponds to $V_{E\tau}$, the red band corresponds to V_{E1} , and the green band corresponds to V_{EP} . The green band coincides with the $NN + 2\pi$ -exchange-only result because both V_D and V_E vanish in this case. The bands are calculated as described in the text.

(with some caveats) relates the phase shifts $\delta_0(p)$ to the finite-volume spectrum (given by the discrete values of p) even for $L < |a^{1S_0}|$ or other relevant scales. In the above, \mathbf{j} is a vector of integers, and Λ_j is a cutoff such that $|\mathbf{j}| < \Lambda_j$. In particular, for low-energy S -wave scattering, one can expand the left-hand side of Eq. (21) to obtain a relationship between the scattering parameters of the two-neutron system and the finite-volume spectrum:

$$-\frac{1}{a^{1S_0}} + \frac{1}{2}r_e^{1S_0}p^2 = \frac{1}{\pi L} S \left[\left(\frac{Lp}{2\pi} \right)^2 \right]. \quad (23)$$

We first consider only a contact interaction (smeared out),

$$V(r) = C_0 e^{-(r/R_0)^4}, \quad (24)$$

which purposely has the same form as the regulated contact interactions we use in our chiral EFT interactions. We introduce a dimensionless variable $q \equiv pL/2\pi$, and calculate the finite-volume ground state for two values of C_0 . The first value reproduces the physical scattering length in the infinite volume, and the second produces a large scattering length $a = -101.7$ fm. In addition, we calculate the first excited state for the case which gives the physical scattering length, see Fig. 4. From these calculations, we can verify via Eq. (23) that our finite-volume spectra lie along the line predicted by the Lüscher formula with the appropriate scattering length and effective range (calculated in the infinite volume), and in kind, we can take the finite-volume spectra and fit them via Eq. (23) to make a prediction of the scattering length and effective range. In the case of the large scattering length, this fitting procedure gives $a = -98(4)$ fm compared with the value of $a = -101.7$ fm from the infinite volume. In the case of the physical scattering length, we find $a = -19.0(1)$ fm compared with $a = -18.9$ fm from the infinite volume calculations.

The bottom panel of Fig. 4 shows the first AFDMC calculations of an excited state of a nuclear system. The details are described in Ref. [14]; briefly, we first considered the possibility of introducing a purely spherical node in the Jastrow wave function (points given as red circles in the bottom panel of Fig. 4). However, we also diagonalized the system exactly and from this diagonalization extracted the nodal surface of the first excited state. This nodal surface showed itself to be a linear combination of cubical harmonics with a large spherical component, but with a non-negligible $Y_{l=4}^c$ component as well (Y_l^c is a cubical harmonic). To account for this discrepancy, we estimated the contribution from the non-spherical part of the wave function to contribute an additional 1% uncertainty in the energies we calculated. These are the larger error bars on the red circles in the bottom panel of Fig. 4. When we take this deformed nature of the nodal surface into account in our wave function (yellow squares in the right panel of Fig. 4), a significantly better agreement with the diagonalization and Lüscher formula is obtained.

We then included our local chiral EFT interactions up to N²LO. One caveat to this procedure is that Lüscher's derivation was in terms of a pionless EFT with contact-only interactions. Once the interaction involves the exchange of pions and a larger range, one needs to restrict the momenta used in the comparison to the radius of convergence of pionless EFT $|p| < m_\pi/2$. This excluded region is indicated in Fig. 5 and Fig. 6 by the gray shading, and furthermore, points in this region are not used in the subsequent fitting procedure to determine the scattering lengths and effective ranges.

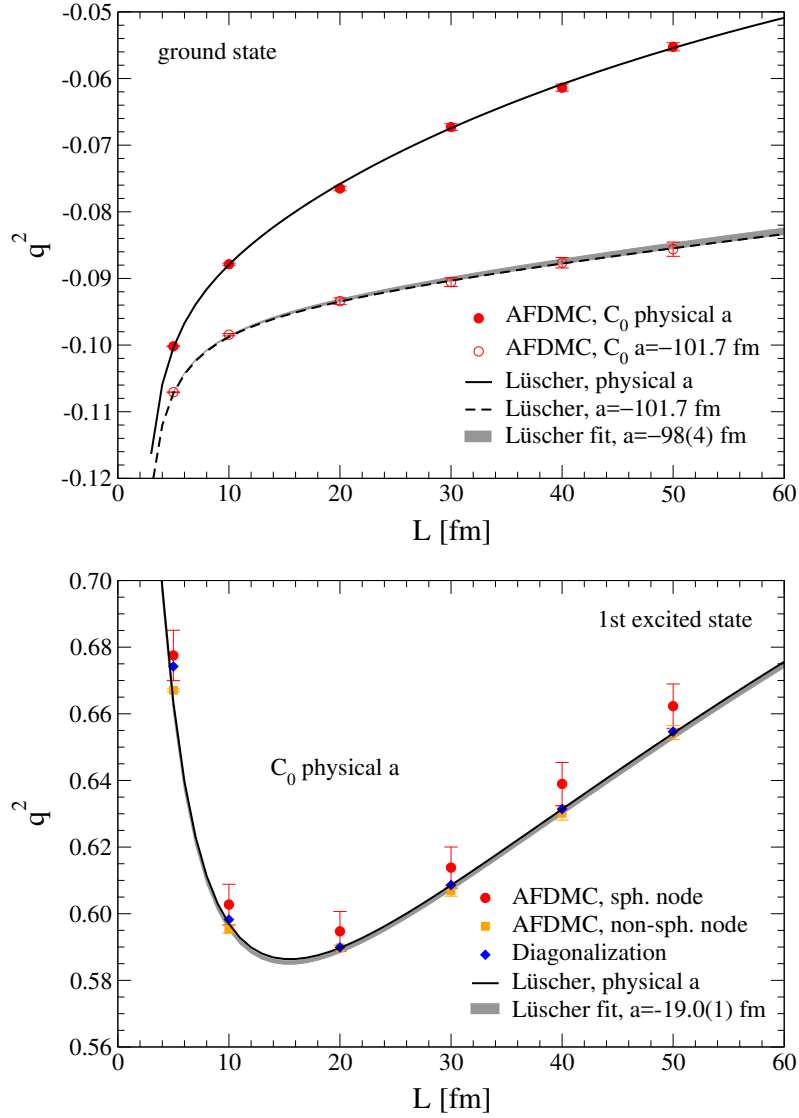


Figure 4: Top panel: AFDMC results for the energy of two neutrons in the ground state in finite volume with the contact potential Eq. (24) for different box sizes L compared with the Lüscher formula. C_0 is adjusted to give the physical nn scattering length $a = -18.9$ fm (closed circles/solid line) and to give a very large scattering length $a = -101.7$ fm (open circles/dashed line). The gray band shows a fit (as described in the text) to the AFDMC results for $a = -101.7$ fm. The energies are given in terms of the dimensionless quantity $q^2 = EML^2/(4\pi^2)$. Bottom panel: AFDMC results for the energy of two neutrons in the first excited state in finite volume with the contact potential for different box sizes L (red circles) compared with the Lüscher formula (solid line). The error bars of the AFDMC results with a spherical nodal surface include both statistical uncertainties and a systematic uncertainty of 1% discussed in the text. C_0 is adjusted to give the physical nn scattering length $a = -18.9$ fm. Also shown are the energies calculated by exact diagonalization (blue diamonds).

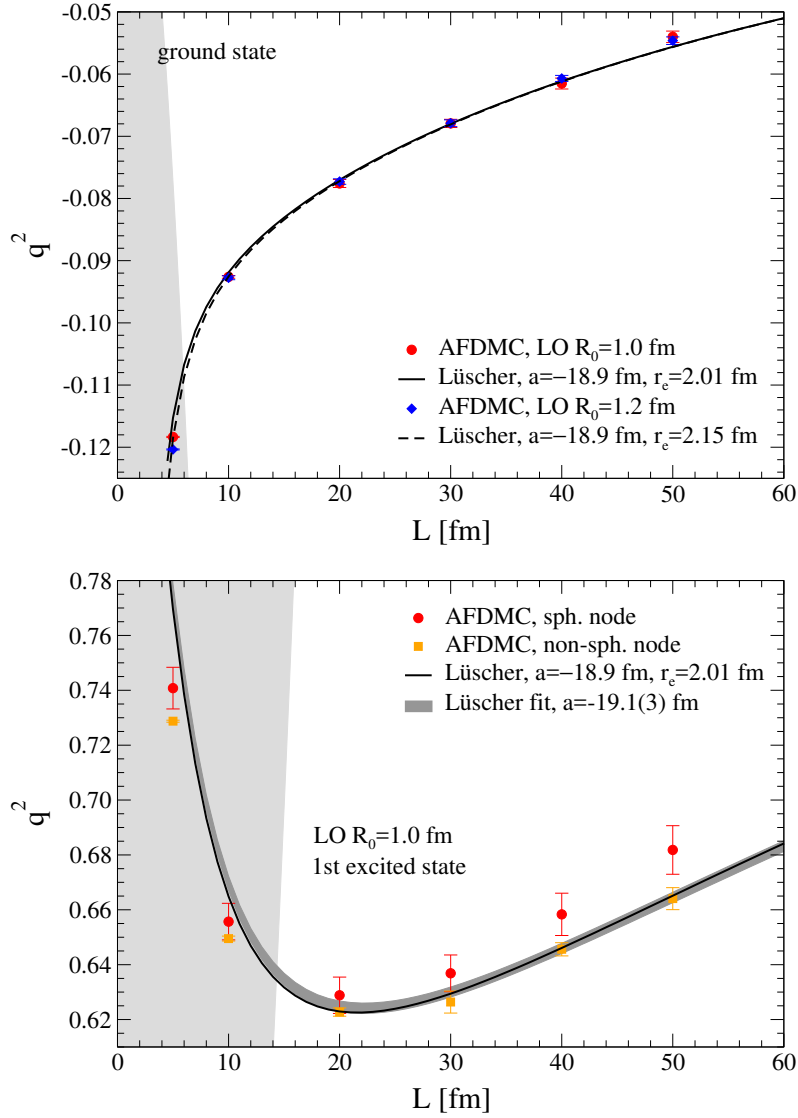


Figure 5: Top panel: AFDMC results for the energy of two neutrons in the ground state in finite volume with the LO chiral EFT interaction compared with the Lüscher formula for different box sizes L . The cutoffs $R_0 = 1.0$ fm (red circles/solid line) and $R_0 = 1.2$ fm (blue diamonds/dashed line) are used. The energies are given in terms of the dimensionless quantity $q^2 = EML^2/(4\pi^2)$. The region where $|p| > m_\pi/2$ is indicated by the gray band. Bottom panel: AFDMC results for the energy of two neutrons in the first excited state in finite volume with the LO chiral EFT interaction with cutoff $R_0 = 1.0$ fm (red circles) compared with the Lüscher formula (solid line) for different box sizes L . The error bars on the AFDMC results with a spherical nodal surface include both statistical uncertainties and a systematic uncertainty of 1% discussed in the text. The dark gray band shows a combined fit (as described in the text) to the ground and first excited state AFDMC results for the LO chiral potential. Points in the region $|p| > m_\pi/2$ indicated by the gray band are not included in the fit.

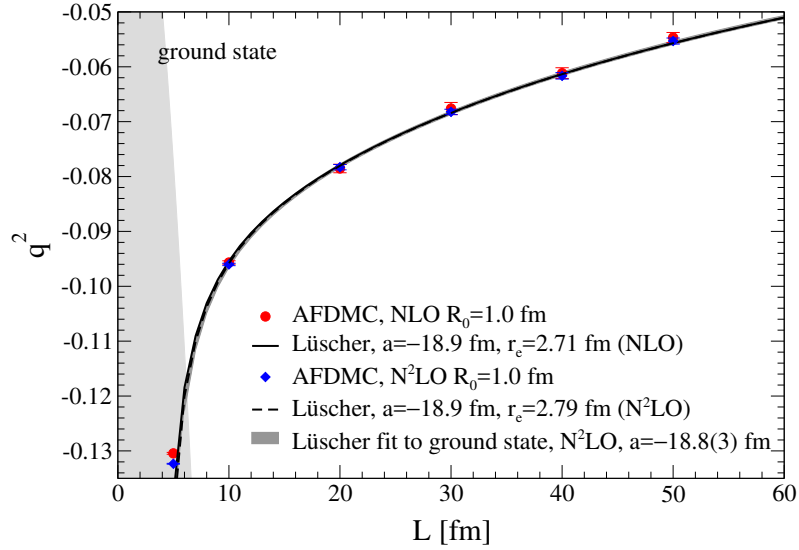


Figure 6: AFDMC results for the energy of two neutrons in the ground state in finite volume with the NLO and N^2 LO chiral EFT interactions with cutoff $R_0 = 1.0$ fm compared with the Lüscher formula for different box sizes L . The results at NLO (N^2 LO) are given as the red circles/solid line (blue diamonds/dashed line). The dark gray band shows a fit (as described in the text) to the AFDMC results for the N^2 LO chiral potential. The energies are given in terms of the dimensionless quantity $q^2 = EML^2/(4\pi^2)$. Points in the region $|p| > m_\pi/2$ indicated by the gray band are not included in the fit.

In summary, this application establishes the AFDMC method as a powerful way to match lattice QCD results to finite-volume calculations using chiral Hamiltonians. This procedure has several advantages, including the fact that it circumvents the small-volume and multi-body difficulties of direct Lüscher extensions. In the future, we hope to collaborate directly with the lattice QCD community and extract LECs directly from lattice simulations of few-nucleon systems.

5 Conclusion

The advent of QMC calculations combined with chiral EFT interactions is a significant advancement, which can yield new insights into both nuclear interactions and nuclear systems. Our results suggest that more investigation of regulator choices and effects are necessary. Our results also affirm that chiral two- and three-nucleon interactions at N^2 LO have sufficient freedom to give a good description of light nuclei, n - α scattering, and neutron matter. The application shown above demonstrates the exciting connections to diverse other fields that are now possible. The future includes many interesting directions including calculations of larger nuclear systems up to $A = 12$ with the GFMC method, and perhaps beyond with the AFDMC method. One important extension will be to apply our n - α scattering framework to other reactions in light nuclei. Low-energy nuclear theory can make significant contributions to many

areas of physics and the combination of chiral EFT in QMC calculations can play an important role.

References

- [1] E. Epelbaum, H.-W. Hammer and U.-G. Meißner, *Rev. Mod. Phys.* **81**, 1773 (2009).
- [2] R. Machleidt and D. R. Entem, *Phys. Rep.* **503**, 1 (2011).
- [3] J. E. Lynn and K. E. Schmidt, *Phys. Rev. C* **86**, 014324 (2012).
- [4] A. Roggero, A. Mukherjee and F. Pederiva, *Phys. Rev. Lett.* **112**, 221103 (2014).
- [5] A. Gezerlis, I. Tews, E. Epelbaum, M. Freunek, S. Gandolfi, K. Hebeler, A. Nogga and A. Schwenk, *Phys. Rev. C* **90**, 054323 (2014).
- [6] I. Tews, S. Gandolfi, A. Gezerlis and A. Schwenk, *Phys. Rev. C* **93**, 024305 (2016).
- [7] J. E. Lynn, J. Carlson, E. Epelbaum, S. Gandolfi, A. Gezerlis, and A. Schwenk, *Phys. Rev. Lett.* **113** 192501 (2014).
- [8] J. E. Lynn, I. Tews, J. Carlson, S. Gandolfi, A. Gezerlis, K. E. Schmidt and A. Schwenk, *Phys. Rev. Lett.* **116** 062501 (2016).
- [9] M. Piarulli, L. Girlanda, R. Schiavilla, R. Navarro Pérez, J. E. Amaro and E. Ruiz Arriola, *Phys. Rev. C* **91**, 024003 (2015).
- [10] S. A. Coon and H. K. Han, *Few-Body Syst.* **30**, 131 (2001).
- [11] J. Fujita and H. Miyazawa, *Progr. Theor. Phys.* **17**, 360 (1957).
- [12] K. M. Nollett, S. C. Pieper, R. B. Wiringa, J. Carlson and G. M. Hale, *Phys. Rev. Lett.* **99**, 022502 (2007).
- [13] E. Epelbaum, H. Krebs and U. G. Meißner, *Eur. Phys. J. A* **51**, 53 (2015).
- [14] P. Klos, J. E. Lynn, I. Tews, S. Gandolfi, A. Gezerlis, H.-W. Hammer, M. Hoferichter and A. Schwenk, *Phys. Rev. C* **94**, 054005 (2016).
- [15] M. Lüscher, *Commun. Math. Phys.* **105**, 153 (1986).
- [16] M. Lüscher, *Nucl. Phys. B* **354**, 531 (1991).

QCD Fossils in Nuclei?

Youngman Kim

Rare Isotope Science Project, Institute for Basic Science, Daejeon 34047, Korea

Abstract

It will be a dream of many nuclear physicists, or theoretical physicists in general, to understand nuclear physics in terms of quarks and gluons using quantum chromodynamics or its low-energy effective theories. Thanks to advancement in theory, in experiments and in supercomputers, we could now dream such a happy dream. We study asymmetric dense matter and finite nuclei in the framework of an effective theory of QCD. We show that the model can reproduce nuclear matter properties reasonably well. We find that the spin-orbit interaction is sensitive to the chiral invariant nucleon mass and can be used as litmus paper to study the origin of nucleon mass in nuclei.

Keywords: *Rare isotopes; QCD; nuclear matter*

1 Introduction

It is widely believed that quantum chromodynamics (QCD) is the fundamental theory of strong interactions. As it is well-recognized, however, we are still far away from describing nuclei in terms of quarks and gluons using QCD since nucleons and mesons are the degrees of freedom at low energies relevant to nuclear physics. However, thanks to developments in theory, i. e., effective field theories and many-body methods, in experiments and in supercomputers, we have now a good chance to understand nuclear physics in terms of QCD or its low-energy effective theories. This sort of efforts is important and timely not only for scientific amusement but also for challenges and opportunities to be posed and to be offered by forthcoming rare isotope facilities.

The nucleus is an interesting and intriguing quantum finite many-body system and provides convenient laboratory to test our understanding of strong interactions and many-body techniques. Since the nucleus consists of protons and neutrons, it is natural to model the nucleus as a collection of interacting protons and neutrons. Therefore, it will be highly nontrivial to understand nuclei in the context of QCD.

Nevertheless, one may ask a question whose answer might come with the next generation rare isotope (RI) facilities and supercomputers: *are there any remnants of non-perturbative QCD in nuclei?* Since the question “*what are the QCD fossils in nuclei?*” is too broad, we narrow it down to “*what is the origin of nucleon mass and how to study it with rare isotopes?*”

As it is well-said, the Higgs particle could explain the origin of a fraction of the mass of visible matter, roughly only 2% of them. If you address a question about

Proceedings of the International Conference ‘Nuclear Theory in the Supercomputing Era — 2016’ (NTSE-2016), Khabarovsk, Russia, September 19–23, 2016. Eds. A. M. Shirokov and A. I. Mazur. Pacific National University, Khabarovsk, Russia, 2018, p. 154.

<http://www.ntse-2016.khb.ru/Proc/Kim.pdf>.

the rest 98% to particle physicists, they would say that quarks and gluons moving around inside the hadrons with high velocity will explain the rest. If you ask the same question to nuclear physicists, they will propose something interesting which is related to QCD vacuum, i. e., quark-antiquark condensates.

It is out of questions that *ab initio* approaches in nuclear physics will reveal some aspect of the origin of nucleon mass in connection with rare isotopes, but in this article, we will discuss how such a question can be addressed in nuclei based on a chiral effective approach of QCD. In Section 2, we summarize two distinctive pictures on the origin of the nucleon mass in QCD effective approaches. Also, an extended parity doublet model will be introduced and a possibility to tell different pictures in nuclei will be discussed. We then present a brief summary of our discussion in Section 3.

2 Nucleon mass in a parity doublet model

In this section we present two distinctive pictures on the origin of nucleon mass, except the one from current quark masses.

As it is well-known, the nucleon mass (in the chiral limit) in the linear sigma model is given by

$$m_N = g_\pi \sigma_0, \quad (1)$$

where g_π is a coupling constant and σ_0 is the vacuum expectation value of the sigma field. As it is manifested, the nucleon mass in the chiral limit will be zero when $\sigma_0 = 0$, i. e., in the case of chiral symmetry restoration.

In the parity doublet model [1], two nucleon fields transform in a mirror way under the chiral $SU(2)_L \times SU(2)_R$ transformations,

$$\begin{aligned} \psi_{1R} &\rightarrow \mathcal{R}\psi_{1R}, & \psi_{1L} &\rightarrow \mathcal{L}\psi_{1L}, \\ \psi_{2R} &\rightarrow \mathcal{L}\psi_{2R}, & \psi_{2L} &\rightarrow \mathcal{R}\psi_{2L}. \end{aligned} \quad (2)$$

Now, one can easily show that $m_0(\bar{\psi}_2 \gamma_5 \psi_1 - \bar{\psi}_1 \gamma_5 \psi_2)$ is invariant under the chiral transformations; m_0 is called chiral invariant nucleon mass. Then, the nucleon part of the parity doublet model Lagrangian reads

$$\begin{aligned} \mathcal{L} = & \bar{\psi}_1 i \not{\partial} \psi_1 + \bar{\psi}_2 i \not{\partial} \psi_2 + m_0(\bar{\psi}_2 \gamma_5 \psi_1 - \bar{\psi}_1 \gamma_5 \psi_2) \\ & + a \bar{\psi}_1(\sigma + i\gamma_5 \vec{\tau} \cdot \vec{\pi})\psi_1 + b \bar{\psi}_2(\sigma - i\gamma_5 \vec{\tau} \cdot \vec{\pi})\psi_2. \end{aligned} \quad (3)$$

To obtain the mass of the nucleon $N(938)$ and its parity partner $N(1500)$, we diagonalize the kinetic and mass terms

$$m_{N\pm} = \frac{1}{2} \left(\sqrt{(a+b)^2 \sigma_0^2 + 4m_0^2} \mp (a-b)\sigma_0 \right). \quad (4)$$

Here, one can see that even if we assume the chiral symmetry restoration $\sigma_0 = 0$, the mass of the nucleon and its parity partner remains finite and degenerate as $m_{N\pm} = m_0$ to realize the chiral symmetry restoration. In Ref. [1] the value of the chiral invariant mass was determined as $m_0 = 270$ MeV from the decay width of $N^*(1535) \rightarrow N + \pi$. The model is then extended by including vector mesons to study the nuclear matter [2], where $m_0 \sim 800$ MeV to account for (symmetric) nuclear matter incompressibility.

If $m_0 \sim 800$ MeV is true, then the role of spontaneous symmetry breaking characterized by the non-zero value of σ_0 is quite minor when it comes to the origin of the nucleon mass and the value is too different from the one determined in free space. To understand this discrepancy and to study asymmetric dense nuclear matter, we further extended the model by including an additional potential term of σ and by considering the hidden local symmetry [3].¹

It was shown in Ref. [3] that the extended parity doublet model reasonably reproduces the properties of normal nuclear matter with the chiral invariant nucleon mass m_0 in the range from 500 to 900 MeV. It was also found that the first-order phase transition for the liquid-gas phase transition disappears in asymmetric matter and that the critical density for the chiral phase transition at nonzero density becomes smaller for larger asymmetry. The m_0 dependence of the slope parameter L was also investigated, where L is defined by

$$L = 3\rho_0 \left(\frac{\partial S}{\partial \rho} \right)_{\rho_0}. \quad (5)$$

Here ρ_0 denotes the saturation density and S is the nuclear symmetry energy. It was shown that the slope parameter is independent of m_0 [3].

2.1 Chiral invariant mass and nuclei

Since the nucleus is a quantum finite many-body system, physics in free space or in infinite nuclear matter can change in nuclei. For instance, the internal quark structure of a nucleon bound in nuclei differs from that of a free nucleon, see Ref. [4] for a recent review. It was observed in Ref. [5] that the confinement scale (or the intrinsic energy scale of QCD) might change from ~ 300 MeV in the free nucleon to ~ 100 MeV in a nucleus.

Now, we study the properties of nuclei in the extended parity doublet model with the relativistic Thomas–Fermi approximation to find any nuclear structure observables that are sensitive to the value of the chiral invariant mass [6]. As an example, we choose ^{40}Ca and focus on the spin-orbit interaction. The spin-orbit interaction $\alpha(r)$ is defined by

$$V_{SO}(r) = \frac{1}{2m_{N+r}} \left(g_\omega \frac{d\omega_0}{dr} - \frac{dm_{N+}}{dr} \right) \vec{s} \cdot \vec{L} \equiv \alpha(r) \vec{s} \cdot \vec{L}, \quad (6)$$

where ω_0 is the time component of the omega meson field. Referring to Ref. [6] for details, we here show a result which demonstrates m_0 dependence of the spin-orbit interaction. In Fig. 1 we plot the maximum value of the spin-orbit interaction α_{so}^{max} as a function of the chiral invariant mass with various values of the incompressibility K . Note that the empirical value of α_{so}^{max} is around 2 [7]. From Fig. 1 we can see that the spin-orbit interaction is sensitive to the value of the chiral invariant mass and prefers smaller m_0 .

¹Here, we briefly introduce the hidden local symmetry. In the non-linear sigma model, the basic building block to construct the Lagrangian is given in terms of $U = e^{2i\pi/f_\pi}$ and U transforms as $U \rightarrow \mathcal{L}U\mathcal{R}^\dagger$ under the chiral symmetry transformation. In the hidden local symmetry approach it is given by $U = \xi_L^\dagger \xi_R$, where $\xi_{L,R} = e^{i\sigma/f_\sigma} e^{\mp i\pi/f_\pi}$ and $\xi_{L,R}(x) \rightarrow h(x)\xi_{L,R}(x)$ ($\mathcal{L}^\dagger, \mathcal{R}^\dagger$). Here, $h(x)$ constitutes the hidden local symmetry. We can introduce vector mesons as gauge bosons associated with $h(x)$.

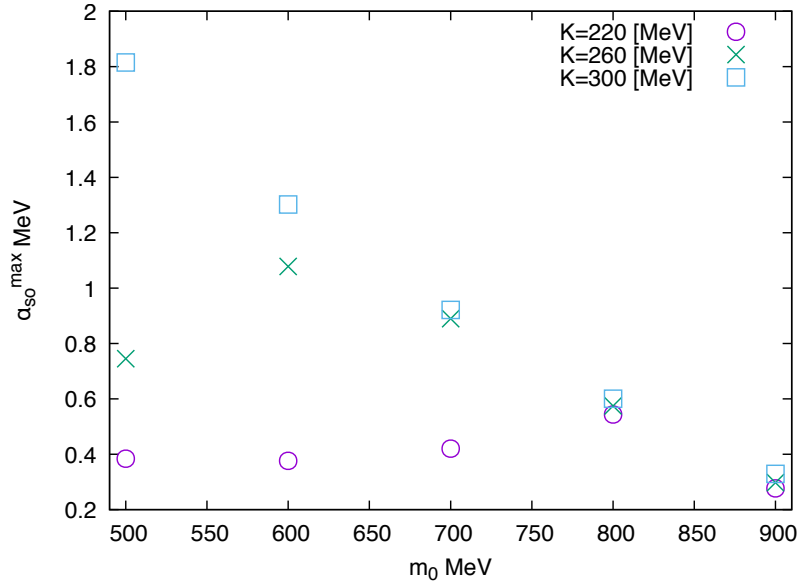


Figure 1: The maximum value of the spin-orbit interaction as a function of m_0 with various values of the incompressibility K .

3 Summary

Though it is out of questions that *ab initio* approaches in nuclear physics will reveal some aspects of the origin of nucleon mass in connection with rare isotopes, in this article we discussed how such a question can be addressed in nuclei based on the chiral effective approach of QCD. We first summarized two distinctive pictures on the origin of the nucleon mass in QCD effective approaches, the linear sigma model and the parity doublet model. We then introduced an extended parity doublet model and investigated possibility to tell the different pictures in nuclei. We found that the spin-orbit interaction is sensitive to the chiral invariant nucleon mass and can be used as litmus paper to study the origin of the nucleon mass in nuclei.

Acknowledgments

The author is grateful to Y. Motohiro and M. Harada for collaborations on parity doublet model in nuclear matter and in nuclei. This work was supported by the Rare Isotope Science Project of Institute for Basic Science funded by the Ministry of Science, ICT and Future Planning and the National Research Foundation of Korea (2013M7A1A1075764).

References

- [1] C. E. Detar and T. Kunihiro, Phys. Rev. D **39**, 2805 (1989).
- [2] D. Zschesche, L. Tolos, J. Schaffner-Bielich and R. D. Pisarski, Phys. Rev. C **75**, 055202 (2007).

-
- [3] Y. Motohiro, Y. Kim and M. Harada, Phys. Rev. C **92**, 025201 (2015).
 - [4] O. Hen, G. A. Miller, E. Piasezky and L. B. Weinstein, arXiv:1611.09748 [nucl-ex] (2016).
 - [5] K. K. Kim, Y. Kim and Y. Ko, JHEP **1010**, 039 (2010).
 - [6] Y. Kim, *Extended parity doublet model for asymmetric matter and finite nuclei*, talk given at 6th International Symposium on Nuclear Symmetry Energy (June 13–17, 2016, Tsinghua University, Beijing, China); Y. Motohiro, *A study of asymmetric nuclear matter with a parity doublet model* (doctoral thesis). Nagoya University, Nagoya, Japan (*unpublished*); Y. Motohiro, Y. Kim and M. Harada, *Spin-orbit interactions in finite nuclei with a parity doublet model (in preparation)*.
 - [7] F. E. Serr and J. D. Walecka, Phys. Lett. B **79**, 10 (1978); Erratum: Phys. Lett. B **84**, 529 (1979).

Nuclear Tetrahedral Shapes from Multidimensionally-Constrained Covariant Density Functional Theories

Jie Zhao^{a,b}, Bing-Nan Lu^{a,c}, En-Guang Zhao^{a,d}
and Shan-Gui Zhou^{a,d,e,f,*}

^a CAS Key Laboratory of Frontiers in Theoretical Physics, Institute of Theoretical Physics,
Chinese Academy of Sciences, Beijing 100190, China

^b Physics Department, Faculty of Science, University of Zagreb, Bijenicka 32, Zagreb 10000,
Croatia

^c Institut für Kernphysik (IKP-3) and Jülich Center for Hadron Physics, Forschungszentrum
Jülich, D-52425 Jülich, Germany

^d Center of Theoretical Nuclear Physics, National Laboratory of Heavy Ion Accelerator,
Lanzhou 730000, China

^e School of Physics, University of Chinese Academy of Sciences, Beijing 100049, China

^f Synergetic Innovation Center for Quantum Effects and Application, Hunan Normal
University, Changsha, 410081, China

* Email: sgzhou@itp.ac.cn

Abstract

Many different shape degrees of freedom play crucial roles in determining the nuclear ground state and saddle point properties and the fission path. By breaking both the axial and the spatial reflection symmetries simultaneously, we have developed multidimensionally-constrained covariant density functional theories (MDC-CDFTs) in which all shape degrees of freedom $\beta_{\lambda\mu}$ with even μ , such as β_{20} , β_{22} , β_{30} , β_{32} , β_{40} , etc., are included self-consistently. The MDC-CDFT's have been applied to the study of fission barriers and potential energy surfaces of actinide nuclei, third minima in potential energy surfaces of light actinides, shapes and potential energy surfaces of superheavy nuclei, the Y_{32} correlations in $N = 150$ isotones and Zr isotopes, and shapes of hypernuclei. In this contribution we introduce MDC-CDFT's and focus on applications to tetrahedral nuclear shapes. With functionals DD-PC1 and PC-PK1, the ground state shape of ^{110}Zr is predicted to be tetrahedral so is that of ^{112}Zr with DD-PC1. The tetrahedral shape originates from large energy gaps around $Z = 40$ and $N = 70$ when the β_{32} distortion is allowed. With the functional DD-PC1, $\beta_{32} > 0.03$ and the energy gain due to the β_{32} distortion is larger than 300 keV for the ground states of ^{248}Cf and ^{250}Fm with $N = 150$.

Keywords: Covariant density functional theory; tetrahedral shape; zirconium nuclei; transfermium nuclei

Proceedings of the International Conference 'Nuclear Theory in the Supercomputing Era — 2016' (NTSE-2016), Khabarovsk, Russia, September 19–23, 2016. Eds. A. M. Shirokov and A. I. Mazur. Pacific National University, Khabarovsk, Russia, 2018, p. 159.

<http://www.ntse-2016.khb.ru/Proc/Zhou.pdf>.

1 Introduction

Most of known atomic nuclei have intrinsic shapes deviating from a sphere; in other words, they are deformed [1–3]. Nuclear deformations not only manifest themselves in collective states but also play important roles in determining nuclear potential energy surfaces (PES's) and fission barriers [4–6]. One way to describe nuclear deformations is by parameterizing the nuclear surface with a multipole expansion

$$R(\theta, \varphi) = R_0 \left[1 + \sum_{\lambda=1}^{\infty} \sum_{\mu=-\lambda}^{\lambda} \beta_{\lambda\mu}^* Y_{\lambda\mu}(\theta, \varphi) \right], \quad (1)$$

where $\beta_{\lambda\mu}$'s are deformation parameters. β_{20} , describing axial and quadrupole shapes, is the most important nuclear deformation. Beyond β_{20} , one can either go to higher order multipole with $\lambda > 2$, in particular $\beta_{\lambda 0}$ with odd λ corresponding to reflection-asymmetric nuclear shapes [7–9], or consider triaxial deformations $\beta_{\lambda\mu}$ with $\mu \neq 0$. Several interesting nuclear phenomena are related to triaxial or reflection asymmetric shapes such as the wobbling motion [2, 10], chiral doublet bands [11–15], the termination of rotational bands [16], parity doublet bands [17–19], and the low-spin signature inversion [20–24]. Putting together β_{30} and β_{22} , it was revealed that the triaxial and octupole distortions both lower the second fission barrier of actinide nuclei considerably [25]. Furthermore, chirality-parity quartet bands are predicted in a nucleus with both a static triaxial deformation (β_{22}) and an octupole deformation (β_{30}) [26]. The triaxiality and reflection asymmetry are combined in deformations characterized by $\beta_{\lambda\mu}$ with odd λ and nonzero μ . Among such deformations, the β_{32} deformation is of particular interest and has been investigated extensively [27–36]. A nucleus with a pure β_{32} deformation, i. e., $\beta_{\lambda\mu} = 0$ if $\lambda \neq 3$ and $\mu \neq 2$, has a tetrahedral shape with the symmetry group T_d^P . The study of single-particle structure of nuclei with tetrahedral symmetry predicted large energy gaps at $Z(N) = 16, 20, 32, 40, 56\text{--}58, 70$, and $90\text{--}94$ and $N = 112$ and $136/142$ [29, 32, 37–46]. These shell gaps may be comparable to or even stronger than those at spherical shapes. Thus, a nucleus with proton and/or neutron numbers equal to these numbers may have a static tetrahedral shape or strong tetrahedral correlations.

For the study of nuclear ground states, shape isomers and PES's, it is desirable to have microscopic and self-consistent models which incorporate all known important shape degrees of freedom. We have developed such a model, the so-called multidimensionally-constrained covariant density functional theories (MDC-CDFT's), by breaking the reflection and axial symmetries simultaneously. Within the MDC-CDFT's, the nuclear shape is assumed to be invariant under the reversion of x and y axes, i. e., the intrinsic symmetry group is V_4 and all shape degrees of freedom $\beta_{\lambda\mu}$ with even μ ($\beta_{20}, \beta_{22}, \beta_{30}, \beta_{32}, \beta_{40}, \dots$) are included self-consistently. The MDC-CDFT's consist of two types of models: the multidimensionally-constrained relativistic mean field (MDC-RMF) model and the multidimensionally-constrained relativistic Hartree–Bogoliubov (MDC-RHB) model. In the MDC-RMF model, the BCS approach has been implemented for the particle-particle (pp) channel. This model has been used to study potential energy surfaces and fission barriers of actinides [25, 47–51], the spontaneous fission of several fermium isotopes [52], the Y_{32} correlations in $N = 150$ isotones [53], and shapes of hypernuclei [54, 55], see Refs. [6, 56, 57] for recent reviews. The Bogoliubov transformation generalizes the BCS quasi-particle concept and provides a unified description of particle-hole (ph) and pp correlations on the mean-field

level. In the MDC-RHB model, pairing correlations are treated by making the Bogoliubov transformation and a separable pairing force of a finite range [58–62] is adopted. The MDC-RHB model has been used to study the spontaneous fission of fermium isotopes [63] and neutron-rich Zr nuclei [64].

In this contribution, we present briefly the formalism of the MDC-RHB model and some results of neutron-rich Zr nuclei and $N = 150$ isotones. The formulae of the MDC-RHB model are given in Section 2. The results and discussions are presented in Section 3. A summary is given in Section 4.

2 Formalism

In the CDFT [65–74], there are four types of covariant density functionals: the meson exchange or point-coupling nucleon interactions combined with nonlinear or density dependent couplings [75–81] (see Ref. [82] for recent reviews). All these four types of functionals have been implemented in the MDC-RHB model. In this Section, we mainly present the formalism of the RHB model with density dependent point-couplings. The starting point of the RHB model with the density dependent point-couplings is the following Lagrangian,

$$\begin{aligned} \mathcal{L} = & \bar{\psi}(i\gamma_\mu\partial^\mu - M)\psi - \frac{1}{2}\alpha_S(\hat{\rho})\rho_S^2 - \frac{1}{2}\alpha_V(\hat{\rho})j_V^2 - \frac{1}{2}\alpha_{TV}(\hat{\rho})\vec{j}_{TV}^2 \\ & - \frac{1}{2}\delta_S(\partial_\nu\rho_S)(\partial^\nu\rho_S) - e\frac{1-\tau_3}{2}A_\mu j_V^\mu - \frac{1}{4}F^{\mu\nu}F_{\mu\nu}, \quad (2) \end{aligned}$$

where M is the nucleon mass, $\alpha_S(\hat{\rho})$, $\alpha_V(\hat{\rho})$, and $\alpha_{TV}(\hat{\rho})$ are density-dependent couplings for different channels, δ_S is the coupling constant of the derivative term, and e is the electric charge. ρ_S , j_V , and \vec{j}_{TV} are the iso-scalar density, the iso-scalar current, and the iso-vector current, respectively.

With the Green's function technique, one can derive the Dirac–Hartree–Bogoliubov equation [67, 83],

$$\int d^3\mathbf{r}' \begin{pmatrix} h - \lambda & \Delta \\ -\Delta^* & -h + \lambda \end{pmatrix} \begin{pmatrix} U_k \\ V_k \end{pmatrix} = E_k \begin{pmatrix} U_k \\ V_k \end{pmatrix}, \quad (3)$$

where E_k is the quasiparticle energy, λ is the chemical potential, and \hat{h} is the single-particle Hamiltonian,

$$\hat{h} = \boldsymbol{\alpha} \cdot [\mathbf{p} - \mathbf{V}(\mathbf{r})] + \beta[M + S(\mathbf{r})] + V_0(\mathbf{r}) + \Sigma_R(\mathbf{r}), \quad (4)$$

S , V^μ , and Σ_R are the scalar potential, the vector potential, and the rearrangement terms. The pairing potential reads

$$\Delta_{ff}(\mathbf{r}_1\sigma_1, \mathbf{r}_2\sigma_2) = \int d^3\mathbf{r}'_1 d^3\mathbf{r}'_2 \sum_{\sigma'_1\sigma'_2} V_{ff,ff}^{\text{PP}}(\mathbf{r}_1\sigma_1, \mathbf{r}_2\sigma_2, \mathbf{r}'_1\sigma'_1, \mathbf{r}'_2\sigma'_2) \kappa_{ff}(\mathbf{r}'_1\sigma'_1, \mathbf{r}'_2\sigma'_2), \quad (5)$$

where f and g are used to represent the large and small components of the Dirac spinor, V^{PP} is the effective pairing interaction and $\kappa(\mathbf{r}_1\sigma_1, \mathbf{r}_2\sigma_2)$ is the pairing tensor.

The RHB equation (3) is solved by expanding the large and small components of the spinors $U_k(\mathbf{r}\sigma)$ and $V_k(\mathbf{r}\sigma)$ in an axially-deformed harmonic oscillator (ADHO)

basis [84],

$$U_k(\mathbf{r}\sigma) = \left(\frac{\sum_{\alpha} f_U^{k\alpha} \Phi_{\alpha}(\mathbf{r}\sigma)}{\sum_{\alpha} g_U^{k\alpha} \Phi_{\alpha}(\mathbf{r}\sigma)} \right), \quad V_k(\mathbf{r}\sigma) = \left(\frac{\sum_{\alpha} f_V^{k\alpha} \Phi_{\alpha}(\mathbf{r}\sigma)}{\sum_{\alpha} g_V^{k\alpha} \Phi_{\alpha}(\mathbf{r}\sigma)} \right), \quad (6)$$

where $\Phi_{\alpha}(\mathbf{r}\sigma)$ are eigensolutions of the Schrödinger equation with the ADHO potential,

$$\left[-\frac{\hbar^2}{2M} \nabla^2 + V_B(\rho, z) \right] \Phi_{\alpha}(\mathbf{r}\sigma) = E_{\alpha} \Phi_{\alpha}(\mathbf{r}\sigma), \quad (7)$$

and

$$V_B(\rho, z) = \frac{1}{2} M (\omega_{\rho}^2 \rho^2 + \omega_z^2 z^2). \quad (8)$$

In Eq. (6), $\alpha = \{n_z, n_r, m_l, m_s\}$ is the collection of quantum numbers, and ω_z and ω_{ρ} are the oscillator frequencies along and perpendicular to the symmetry (z) axis, respectively. The V_4 symmetry is imposed in the MDC-CDFT [6]. Thus we expand the potentials and the densities in terms of the Fourier series,

$$f(\rho, \varphi, z) = f_0(\rho, z) \frac{1}{\sqrt{2\pi}} + \sum_{n=1}^{\infty} f_n(\rho, z) \frac{1}{\sqrt{\pi}} \cos(2n\varphi), \quad (9)$$

In the pp channel, we use a separable pairing force of a finite range [58–62]. The matrix element $\bar{V}_{12,1'2'}^{pp} = V_{12,1'2'}^{pp} - V_{12,2'1'}^{pp}$ in the center of mass frame reads

$$V_{12,1'2'} = -2\sqrt{2}G \sum_{N_z N_p M_p} \left(W_{12}^{N_z N_p M_p} \right)^* W_{1'2'}^{N_z N_p M_p}, \quad (10)$$

where

$$W_{12}^{N_z N_p M_p} = \delta_{K_1+K_2, M_p} \delta_{\pi_1 \pi_2, (-1)^{N_z+|M_p|}} \tau_1 \frac{1}{\sqrt{2}} C_1 C_2 \times \left(\sum_{n_z} M_{N_z n_z}^{n_{z1} n_{z2}} V_{n_z} \right) \left(\sum_{n_p} M_{N_p M_p n_p 0}^{n_{r1} m_1 n_{r2} m_2} U_{n_p} \right), \quad (11)$$

and

$$V_{n_z} = \frac{1}{(4\pi a^2)^{1/2}} \int_{-\infty}^{\infty} dz e^{-\frac{z^2}{2a^2}} \phi_{n_z}(z), \quad (12)$$

$$U_{n_p} = \frac{\sqrt{2\pi}}{4\pi a^2} \int_0^{\infty} d\rho \rho e^{-\frac{\rho^2}{2a^2}} R_{n_p}^0(\rho).$$

$M_{N_z n_z}^{n_{z1} n_{z2}}$ and $M_{N_p M_p n_p 0}^{n_{r1} m_1 n_{r2} m_2}$ are the Talmi–Moshinski brackets. The pairing field and pairing energy can be also written in a separable form as

$$\Delta_{12} = \sum_{1'2'} V_{12,1'2'} \kappa_{1'2'} = -2\sqrt{2}G \sum_{N_z} \sum_{N_p M_p} \left(W_{12}^{N_z N_p M_p} \right)^* P^{N_z N_p M_p}, \quad (13)$$

$$E_{\text{pair}} = \frac{1}{2} \sum_{12,1'2'} V_{12,1'2'} \kappa_{12}^* \kappa_{1'2'} = -\sqrt{2}G \sum_{N_z} \sum_{N_p M_p} |P^{N_z N_p M_p}|^2, \quad (14)$$

where

$$P^{N_z N_p M_p} = \sum_{12} W_{12}^{N_z N_p M_p} \kappa_{12}. \quad (15)$$

The details of the derivation are given in Appendices of Refs. [48, 64].

The total energy of the nucleus reads

$$\begin{aligned} E_{\text{total}} = \int d^3 \mathbf{r} \left\{ \sum_k v_k^2 \psi_k^\dagger (\boldsymbol{\alpha} \cdot \mathbf{p} + \beta M_B) \psi_k \right. \\ + \frac{1}{2} \alpha_S \rho_S^2 + \frac{1}{2} \alpha_V \rho_V^2 + \frac{1}{2} \alpha_{TS} \rho_{TS}^2 + \frac{1}{2} \alpha_{TV} \rho_{TV}^2 \\ + \frac{1}{3} \beta_S \rho_S^3 + \frac{1}{4} \gamma_S \rho_S^4 + \frac{1}{4} \gamma_V \rho_V^4 \\ + \frac{1}{2} \delta_S \rho_S \Delta \rho_S + \frac{1}{2} \delta_V \rho_V \Delta \rho_V \\ + \frac{1}{2} \delta_{TS} \rho_{TS} \Delta \rho_{TS} + \frac{1}{2} \delta_{TV} \rho_{TV} \Delta \rho_{TV} + \frac{1}{2} e \rho_C A \left. \right\} \\ + E_{\text{pair}} + E_{\text{c.m.}}, \quad (16) \end{aligned}$$

where the center of mass correction $E_{\text{c.m.}}$ can be calculated either phenomenologically or microscopically. The intrinsic multipole moments are calculated as

$$Q_{\lambda\mu}^\tau = \int d^3 \mathbf{r} \rho_V^\tau(\mathbf{r}) r^\lambda Y_{\lambda\mu}(\Omega), \quad (17)$$

where $Y_{\lambda\mu}(\Omega)$ are the spherical harmonics and τ refers to the proton, neutron, or the whole nucleus. The deformation parameter $\beta_{\lambda\mu}$ is obtained from the corresponding multipole moment by

$$\beta_{\lambda\mu}^\tau = \frac{4\pi}{3N_\tau R^\lambda} Q_{\lambda\mu}^\tau, \quad (18)$$

where $R = 1.2 \times A^{1/3}$ fm and N_τ is the number of proton, neutron, or nucleons.

3 Results and discussions

3.1 Tetrahedral shapes of neutron-rich Zr isotopes

In Ref. [64], one-dimensional potential energy curves ($E \sim \beta_{20}$) for even-even Zr nuclei with $100 \leq A \leq 114$ were calculated with functionals DD-PC1 [61] and PC-PK1 [85]. To investigate different roles played by the nonaxiality and reflection asymmetry, calculations are performed with different symmetries imposed: i) axial and reflection symmetry, ii) axial symmetry and reflection asymmetry, and iii) nonaxial and reflection asymmetry; the results are shown in Figs. 1 and 2 by dotted, dash-dotted, and solid lines respectively.

In Fig. 1, we present the results obtained with the functional DD-PC1. We can see that if nuclei are allowed to be reflection asymmetric but axial symmetric, the energy of the minimum with $\beta_{20} \approx 0$ for $^{106-114}\text{Zr}$ is lowered substantially by the β_{30} distortion. Due to this lowering effect, the energy of the minimum with the pear-like shape ($\beta_{20} \approx 0$, $\beta_{30} \neq 0$) is lower than the minimum with oblate or prolate shape for ^{110}Zr , ^{112}Zr , and ^{114}Zr . When the β_{32} deformation is allowed in the calculations,

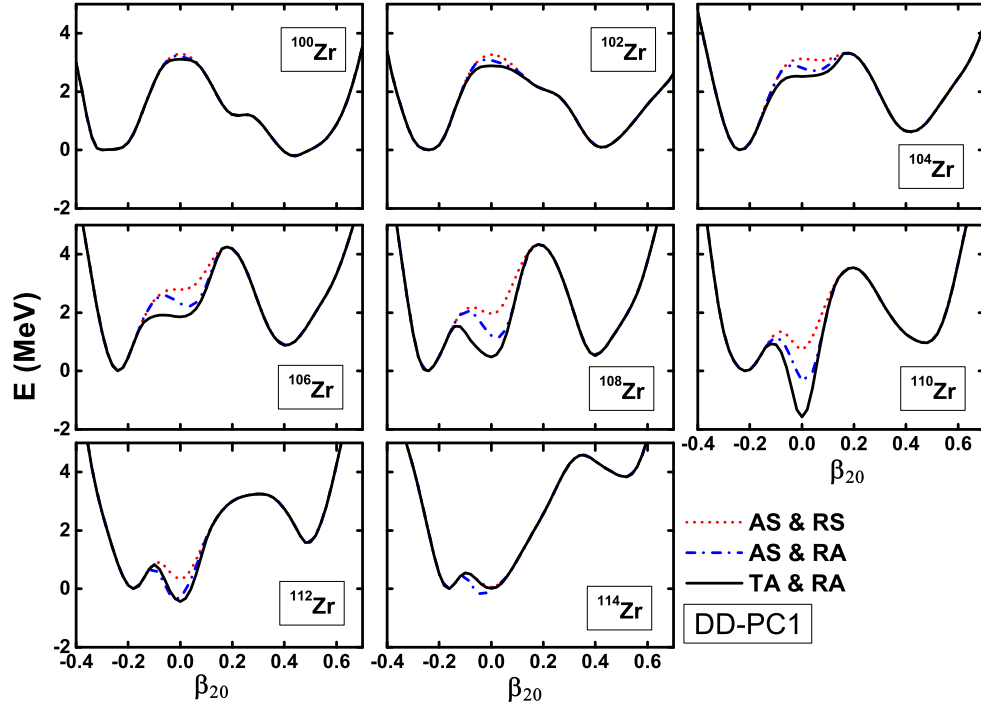


Figure 1: Potential energy curves for Zr isotopes with the functional DD-PC1. The energy is normalized with respect to the oblate minimum for each nucleus. Various symmetries are imposed in the calculations: axial symmetry (AS), triaxial (TA), reflection symmetry (RS) and reflection asymmetry (RA). Taken from Ref. [64].

both axial and reflection symmetries are broken. The β_{32} distortion effect is more pronounced than that of the β_{30} deformation for most of these nuclei. The energy of the minimum with $\beta_{20} \approx 0$ for $^{106-112}\text{Zr}$ is lowered much. A tetrahedral ground state is predicted for $^{110,112}\text{Zr}$. For ^{114}Zr , the predicted pear-like shape is lower in energy than the tetrahedral shape. From Fig. 1, we conclude that the β_{32} distortion effect is the most pronounced for ^{110}Zr where the inclusion of the β_{32} deformation lowers the energy of the minimum around $\beta_{20} = 0$ by about 2 MeV.

In Fig. 2, the results obtained with the functional PC-PK1 are presented. The β_{30} and β_{32} distortion effects are observed around $\beta_{20} = 0$ for $^{108,110}\text{Zr}$. The most pronounced distortion effects are predicted for ^{110}Zr which is consistent with the results obtained from DD-PC1. As a result, the ground states of $^{108,110}\text{Zr}$ are predicted to have tetrahedral shapes and there also exist pear-like isomeric states. Neither β_{30} nor β_{32} distortions have influences on the PEC's of $^{112,114}\text{Zr}$.

In Ref. [64], we also examined the origin of the strong β_{32} effect around ^{110}Zr . We found that the formation of the tetrahedral ground state around ^{110}Zr can be traced back to the large energy gaps at $Z = 40$ and $N = 70$ in the single-particle levels when the β_{32} deformation is included. In Fig. 3, we show the single-particle levels of ^{110}Zr near the Fermi surface as functions of β_{32} with β_{20} fixed at zero. Due to the tetrahedral symmetry, the single-particle levels are split into multiplets with

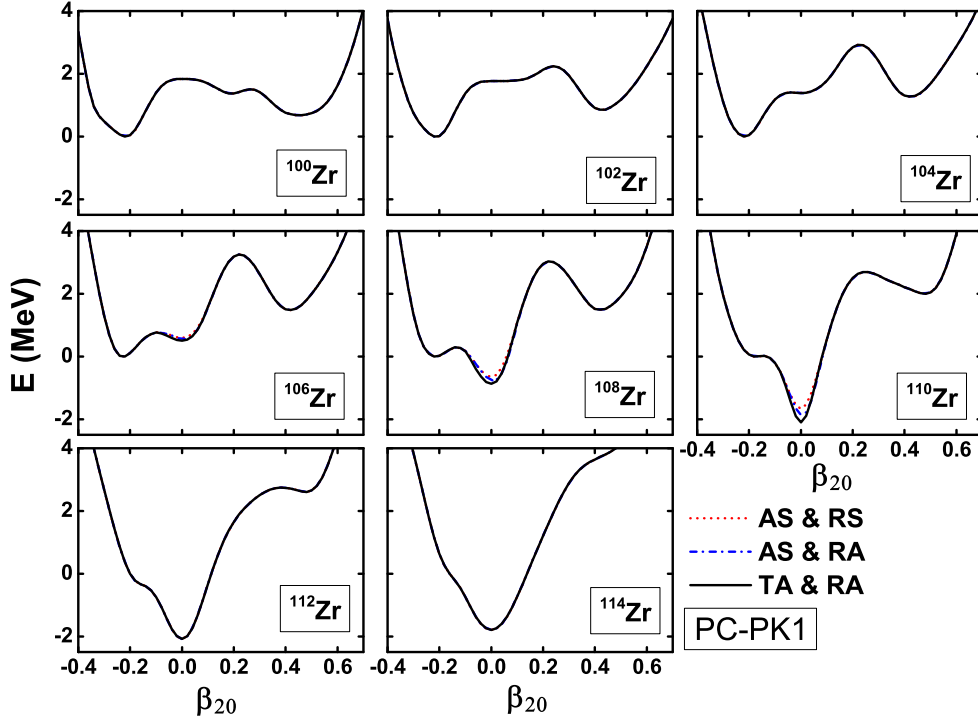


Figure 2: Potential energy curves for Zr isotopes with the functional PC-PK1. The energy is normalized with respect to the oblate minimum for each nucleus. Various symmetries are imposed in the calculations: axial symmetry (AS), triaxial (TA), reflection symmetry (RS) and reflection asymmetry (RA).

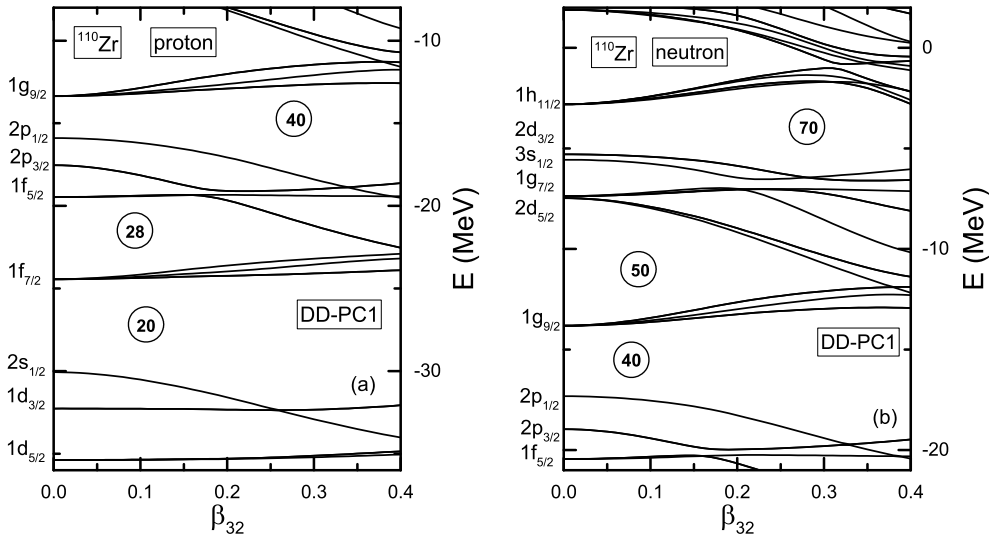


Figure 3: Single-particle levels near the Fermi surface for protons (a) and neutrons (b) of ^{110}Zr as functions of β_{32} with β_{20} fixed at zero. Taken from Ref. [64].

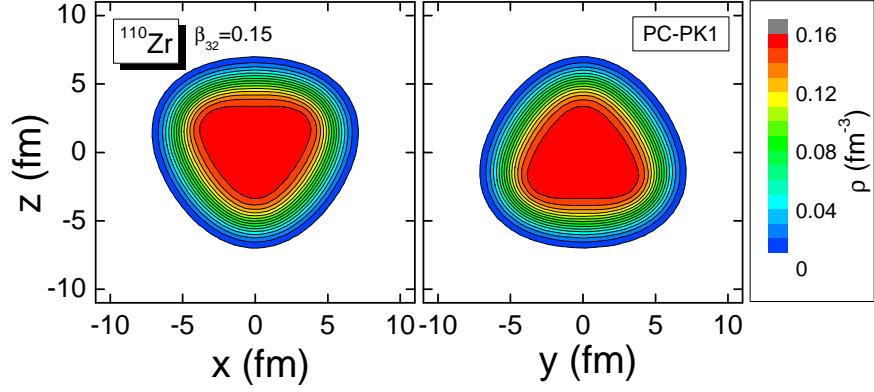


Figure 4: Ground state density profile of ^{110}Zr in the (x, z) and (y, z) planes obtained for the functional PC-PK1.

degeneracies equal to the irreducible representations of the T_d^D group. For protons, as shown in Fig. 3(a), the magic gap $Z = 20$ is enhanced while the gap at $Z = 28$ is suppressed as β_{32} increases. At $Z = 40$ a large energy gap shows up as β_{32} increases. From Fig. 3(b) we can see that large energy gaps appear at $N = 40$ and 70 while a spherical magic gap at $N = 50$ is suppressed as β_{32} increases. Due to the large energy gaps at $Z = 40$ and $N = 70$, a strong β_{32} effect is expected for ^{110}Zr and nearby nuclei. The ground state density profile of ^{110}Zr obtained from PC-PK1 is shown in Fig. 4.

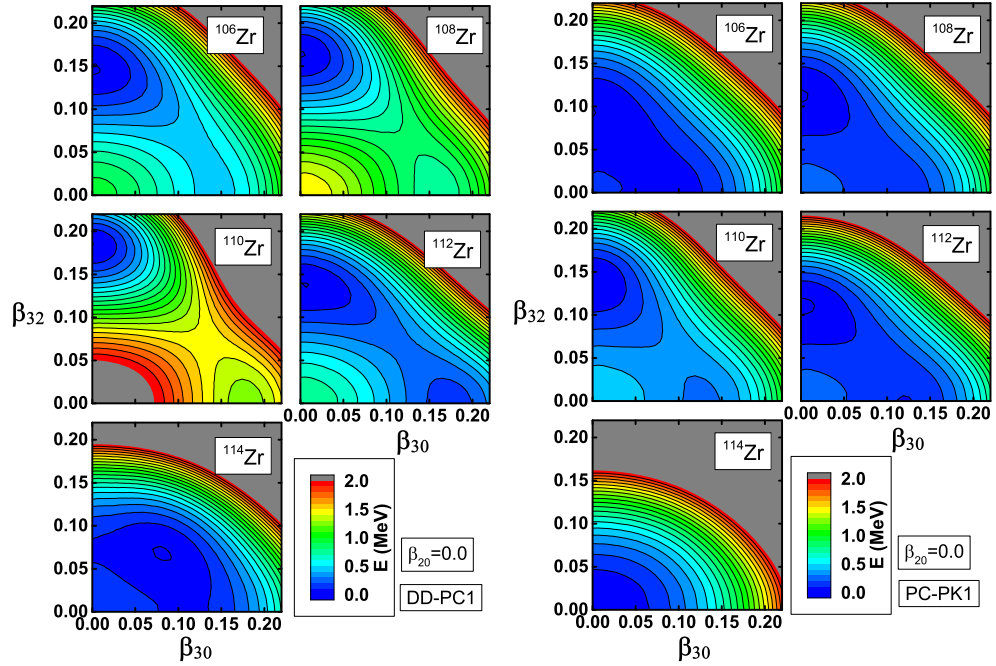


Figure 5: Potential energy surfaces of $^{106-114}\text{Zr}$ in the (β_{30}, β_{32}) plane with β_{20} fixed at zero. The contour interval is 0.1 MeV. Taken from Ref. [64].

The potential energy surfaces (PES) of $^{106-114}\text{Zr}$ in the (β_{30}, β_{32}) plane with β_{20} fixed at zero are shown in Fig. 5. It is clearly seen that the minima with tetrahedral shapes are deeper than that of pear-like shapes for $^{106-112}\text{Zr}$ with both functionals. The barriers separating the pear-like and tetrahedral minima are very low. For ^{106}Zr , the barrier is almost invisible with both functionals. For ^{108}Zr and ^{112}Zr , the barriers predicted by DD-PC1 are less than 0.2 MeV while the barriers predicted by PC-PK1 are around 0.1 MeV. For ^{110}Zr , the barrier predicted by DD-PC1 is higher but still less than 0.3 MeV, while the barrier height from the calculations with PC-PK1 is less than 0.2 MeV. In this sense, the pear-like isomeric states are rather unstable.

3.2 Non-axial octupole shapes in $N = 150$ isotones

In Ref. [53], the non-axial reflection-asymmetric β_{32} shape in some transfermium nuclei with $N = 150$, namely, in ^{246}Cm , ^{248}Cf , ^{250}Fm and ^{252}No , were investigated within the MDC-RMF model. The parameter set DD-PC1 was used [61]. One-dimensional potential energy curves (E vs β_{32}) are shown in Fig. 6. For the ground states of ^{248}Cf and ^{250}Fm , the non-axial octupole deformation parameter $\beta_{32} > 0.03$ and the energy gain due to the β_{32} distortion is larger than 300 keV. In ^{246}Cm and ^{252}No , shallow β_{32} minima are found.

The triaxial octupole Y_{32} effects stem from the coupling between pairs of single-particle orbits with $\Delta j = \Delta l = 3$ and $\Delta K = 2$ where j and l are respectively the single-particle total and orbital angular momenta and K is the projection of j on the symmetry axis. In Fig. 7, we show the proton and neutron single-particle levels near the Fermi surface for ^{248}Cf as a function of β_{32} with β_{20} fixed at 0.3. It has been shown that the spherical proton orbitals $\pi 2f_{7/2}$ and $\pi 1i_{13/2}$ are very close to each other. This near degeneracy results in octupole correlations. As seen in the left panel of Fig. 7, two proton levels, $[521]3/2$ originating from $2f_{7/2}$ and $[633]7/2$ originating from $1i_{13/2}$, satisfying the $\Delta j = \Delta l = 3$ and $\Delta K = 2$ condition, are very close to each other at $\beta_{20} = 0.3$. Therefore the non-axial octupole Y_{32} develops, and an energy gap appears at $Z = 98$ as β_{32} increases from zero. Similarly, the spherical neutron orbitals $\nu 2g_{9/2}$ and $\nu 1j_{15/2}$ are very close to each other. The neutron levels $[734]9/2$ originating from $1j_{15/2}$ and $[622]5/2$ originating from $2g_{9/2}$ are also close lying just above and below the Fermi surface. This leads to the development of a gap

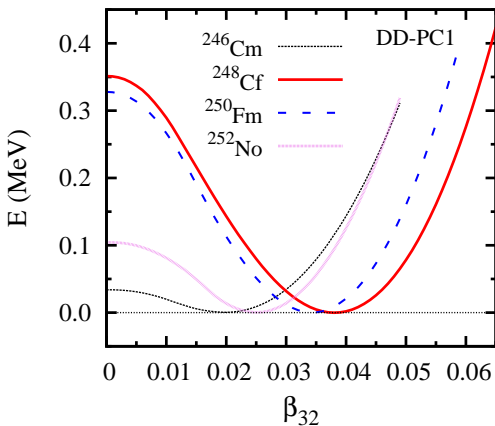


Figure 6: Binding energy E (relative to the ground state) for $N = 150$ isotones ^{246}Cm , ^{248}Cf , ^{250}Fm , and ^{252}No as functions of the non-axial octupole deformation parameter β_{32} . Taken from Ref. [53].

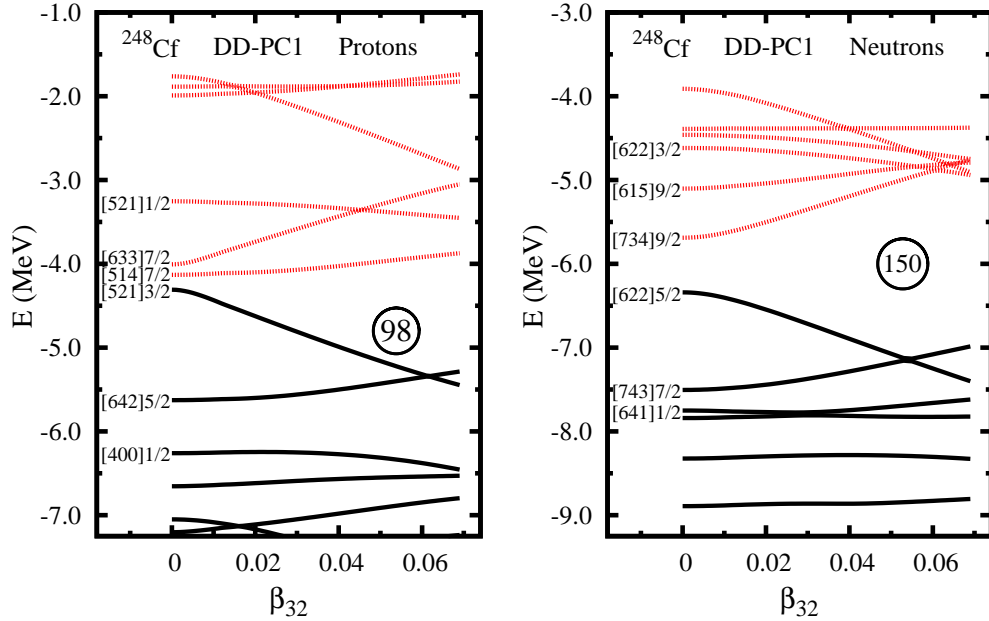


Figure 7: Single-particle levels near the Fermi surface for protons and neutrons of ^{248}Cf as functions of β_{32} with β_{20} fixed at 0.3.

at $N = 150$ with β_{32} increasing. The Y_{32} correlation in $N = 150$ isotones is caused by both protons and neutrons, and the correlation in ^{248}Cf is the most pronounced.

4 Summary

In this contribution we present briefly the formalism and some applications of the multidimensionally-constrained covariant density functional theories (MDC-CDFT) in which all shape degrees of freedom like $\beta_{\lambda\mu}$ deformations with even μ are allowed. We have calculated the potential energy curves (E vs β_{32}) of neutron-rich even-even Zr isotopes within the MDC-RHB model. It is found that the β_{32} deformation plays a very important role in the isomeric or ground states of these nuclei, especially for nuclei around $N = 70$. The ground state shape of ^{110}Zr is predicted to be tetrahedral with both functionals, DD-PC1 and PC-PK1. ^{108}Zr is also predicted to have the tetrahedral ground state with the functional PC-PK1 and ^{112}Zr is predicted to have the tetrahedral ground state with the functional DD-PC1. The strong β_{32} distortion effect is caused by the large energy gaps at $Z = 40$ and $N = 70$. The non-axial reflection-asymmetric β_{32} shape in some transfermium nuclei with $N = 150$, namely, in ^{246}Cm , ^{248}Cf , ^{250}Fm and ^{252}No , are studied. Due to the interaction between a pair of neutron orbitals, [734]9/2 originating from $\nu j_{15/2}$ and [622]5/2 originating from $\nu g_{9/2}$, and that of a pair of proton orbitals, [521]3/2 originating from $\pi f_{7/2}$ and [633]7/2 originating from $\pi i_{13/2}$, rather strong non-axial octupole Y_{32} effects have been found in ^{248}Cf and ^{250}Fm which are both well-deformed with large axial-quadrupole deformations, $\beta_{20} \approx 0.3$.

Acknowledgments

This work has been supported by the National Key Basic Research Program of China (Grant No. 2013CB834400), the National Natural Science Foundation of China (Grant Nos. 11120101005, 11275248, 11475115, 11525524 and 11621131001), and the Knowledge Innovation Project of the Chinese Academy of Sciences (Grant No. KJCX2-EW-N01). The computational results presented in this work have been obtained using the High-performance Computing Cluster of KLTP/ITP-CAS and the ScGrid of the Supercomputing Center, Computer Network Information Center of the Chinese Academy of Sciences.

References

- [1] A. Bohr and B. Mottelson, *Nuclear structure. Vol I.* World Scientific, Singapore, 1998.
- [2] A. Bohr and B. Mottelson, *Nuclear structure. Vol II.* World Scientific, Singapore, 1998.
- [3] P. Ring and P. Schuck, *The nuclear many-body problem.* Springer-Verlag, Berlin, Heidelberg, 1980.
- [4] S. Frauendorf, *Rev. Mod. Phys.* **73**, 463 (2001).
- [5] W. Nazarewicz, in *An advanced course in modern nuclear physics*, eds. J. Arias and M. Lozano, *Lecture Notes Phys.* **581**, 102. Springer, Berlin, Heidelberg, 2001.
- [6] S.-G. Zhou, *Phys. Scripta* **91**, 063008 (2016).
- [7] P. A. Butler and W. Nazarewicz, *Rev. Mod. Phys.* **68**, 349 (1996).
- [8] P. Möller, R. Bengtsson, B. G. Carlsson, P. Olivius, T. Ichikawa, H. Sagawa and A. Iwamoto, *At. Data Nucl. Data Tables* **94**, 758 (2008).
- [9] S. E. Agbemava, A. V. Afanasjev and P. Ring, *Phys. Rev. C* **93**, 044304 (2016).
- [10] S. W. Odegard, G. B. Hagemann, D. R. Jensen, M. Bergstroem, B. Herskind, G. Sletten, S. Toermaenen, J. N. Wilson, P. O. Tjom, I. Hamamoto, K. Spohr, H. Huebel, A. Goergen, G. Schoenwasser, A. Bracco, S. Leoni, A. Maj, C. M. Petrache, P. Bednarczyk and D. Curien, *Phys. Rev. Lett.* **86**, 5866 (2001).
- [11] S. Frauendorf and J. Meng, *Nucl. Phys. A* **617**, 131 (1997).
- [12] K. Starosta, T. Koike, C. J. Chiara, D. B. Fossan, D. R. LaFosse, A. A. Hecht, C. W. Beausang, M. A. Caprio, J. R. Cooper, R. Krucken, J. R. Novak, N. V. Zamfir, K. E. Zyromski, D. J. Hartley, D. L. Balabanski, Jing-ye Zhang, S. Frauendorf and V. I. Dimitrov, *Phys. Rev. Lett.* **86**, 971 (2001).
- [13] J. Meng, J. Peng, S. Q. Zhang and S.-G. Zhou, *Phys. Rev. C* **73**, 037303 (2006).
- [14] J. Meng and S. Q. Zhang, *J. Phys. G* **37**, 064025 (2010).

- [15] J. Meng, S.-Q. Zhang and P. Zhao, *Novel rotational excitations*, in *Relativistic mean field description of exotic nuclei, chap. 9*, Int. Rev. Nucl. Phys. **10**, 355. World Scientific, 2016.
- [16] A. V. Afanasjev, D. B. Fossan, G. J. Lane and I. Ragnarsson, Phys. Rep. **322**, 1 (1999).
- [17] L. P. Gaffney, P. A. Butler, M. Scheck, A. B. Hayes, F. Wenander, M. Albers, B. Bastin, C. Bauer, A. Blazhev, S. Bonig, N. Bree, J. Cederkall, T. Chupp, D. Cline, T. E. Cocolios, T. Davinson, H. De Witte, J. Diriken, T. Grahn, A. Herzan, M. Huysse, D. G. Jenkins, D. T. Joss, N. Kesteloot, J. Konki, M. Kowalczyk, T. Kroll, E. Kwan, R. Lutter, K. Moschner, P. Napiorkowski, J. Pakarinen, M. Pfeiffer, D. Radeck, P. Reiter, K. Reynders, S. V. Rigby, L. M. Robledo, M. Rudigier, S. Sambi, M. Seidlitz, B. Siebeck, T. Stora, P. Thoele, P. Van Duppen, M. J. Vermeulen, M. von Schmid, D. Voulot, N. Warr, K. Wimmer, K. Wrzosek-Lipska, C. Y. Wu and M. Zielinska, Nature **497**, 199 (2013).
- [18] B. Bucher, S. Zhu, C. Y. Wu, R. V. F. Janssens, D. Cline, A. B. Hayes, M. Albers, A. D. Ayangeakaa, P. A. Butler, C. M. Campbell, M. P. Carpenter, C. J. Chiara, J. A. Clark, H. L. Crawford, M. Cromaz, H. M. David, C. Dickerson, E. T. Gregor, J. Harker, C. R. Hoffman, B. P. Kay, F. G. Kondev, A. Korichi, T. Lauritsen, A. O. Macchiavelli, R. C. Pardo, A. Richard, M. A. Riley, G. Savard, M. Scheck, D. Seweryniak, M. K. Smith, R. Vondrasek and A. Wiens, Phys. Rev. Lett. **116**, 112503 (2016).
- [19] X. C. Chen, J. Zhao, C. Xu, H. Hua, T. M. Shneidman, S. G. Zhou, X. G. Wu, X. Q. Li, S. Q. Zhang, Z. H. Li, W. Y. Liang, J. Meng, F. R. Xu, B. Qi, Y. L. Ye, D. X. Jiang, Y. Y. Cheng, C. He, J. J. Sun, R. Han, C. Y. Niu, C. G. Li, P. J. Li, C. G. Wang, H. Y. Wu, Z. H. Li, H. Zhou, S. P. Hu, H. Q. Zhang, G. S. Li, C. Y. He, Y. Zheng, C. B. Li, H. W. Li, Y. H. Wu, P. W. Luo and J. Zhong, Phys. Rev. C **94**, 021301(R) (2016).
- [20] Y. Liu, Y. Ma, H. Yang, and S. Zhou, Phys. Rev. C **52**, 2514 (1995).
- [21] Y. Liu, J. Lu, Y. Ma, S. Zhou and H. Zheng, Phys. Rev. C **54**, 719 (1996).
- [22] S. G. Zhou, Y. Z. Liu, Y. J. Ma and C. X. Yang, J. Phys. G **22**, 415 (1996).
- [23] L. L. Riedinger, H. Q. Jin, W. Reviol, J.-Y. Zhang, R. A. Bark, G. B. Hagemann and P. B. Semmes, Prog. Part. Nucl. Phys. **38**, 251 (1997).
- [24] Y. Liu, J. Lu, Y. Ma, G. Zhao, H. Zheng and S. Zhou, Phys. Rev. C **58**, 1849 (1998).
- [25] B.-N. Lu, E.-G. Zhao and S.-G. Zhou, Phys. Rev. C **85**, 011301(R) (2012).
- [26] C. Liu, S. Y. Wang, R. A. Bark, S. Q. Zhang, J. Meng, B. Qi, P. Jones, S. M. Wyngaardt, J. Zhao, C. Xu, S.-G. Zhou, S. Wang, D. P. Sun, L. Liu, Z. Q. Li, N. B. Zhang, H. Jia, X. Q. Li, H. Hua, Q. B. Chen, Z. G. Xiao, H. J. Li, L. H. Zhu, T. D. Bucher, T. Dinoko, J. Easton, K. Juhász, A. Kamlawe, E. Khaleel, N. Khumalo, E. A. Lawrie, J. J. Lawrie, S. N. T. Majola, S. M. Mullins, S. Murray, J. Ndayishimye, D. Negi, S. P. Noncolela,

- S. S. Ntshangase, B. M. Nyakó, J. N. Orce, P. Papka, J. F. Sharpey-Schafer, O. Shirinda, P. Sithole, M. A. Stankiewicz and M. Wiedeking, *Phys. Rev. Lett.* **116**, 112501 (2016).
- [27] I. Hamamoto, B. Mottelson, H. Xie and X. Z. Zhang, *Z. Phys. D* **21**, 163 (1991).
- [28] J. Skalski, *Phys. Rev. C* **43**, 140 (1991).
- [29] X. Li and J. Dudek, *Phys. Rev. C* **49**, R1250 (1994).
- [30] S. Takami, K. Yabana and M. Matsuo, *Phys. Lett. B* **431**, 242 (1998).
- [31] M. Yamagami, K. Matsuyanagi and M. Matsuo, *Nucl. Phys. A* **693**, 579 (2001).
- [32] J. Dudek, A. Gozdz, N. Schunck and M. Miskiewicz, *Phys. Rev. Lett.* **88**, 252502 (2002).
- [33] J. Dudek, D. Curien, N. Dubray, J. Dobaczewski, V. Pangon, P. Olbratowski and N. Schunck, *Phys. Rev. Lett.* **97**, 072501 (2006).
- [34] P. Olbratowski, J. Dobaczewski, P. Powalowski, M. Sadziak and K. Zberecki, *Int. J. Mod. Phys. E* **15**, 333 (2006).
- [35] K. Zberecki, P. Magierski, P.-H. Heenen and N. Schunck, *Phys. Rev. C* **74**, 051302(R) (2006).
- [36] J. Dudek, A. Gozdz, K. Mazurek and H. Moliq, *J. Phys. G* **37**, 064032 (2010).
- [37] J. Dudek, J. Dobaczewski, N. Dubray, A. Gozdz, V. Pangon and N. Schunck, *Int. J. Mod. Phys. E* **16**, 516 (2007).
- [38] J. Dudek, A. Gozdz and N. Schunck, *Acta Phys. Pol. B* **34**, 2491 (2003).
- [39] W. D. Heiss, R. A. Lynch and R. G. Nazmitdinov, *Phys. Rev. C* **60**, 034303 (1999).
- [40] K. Arita and Y. Mukumoto, *Phys. Rev. C* **89**, 054308 (2014).
- [41] N. Schunck, J. Dudek, A. Gozdz and P. H. Regan, *Phys. Rev. C* **69**, 061305(R) (2004).
- [42] J. Dudek, D. Curien, D. Rouvel, K. Mazurek, Y. R. Shimizu and S. Tagami, *Phys. Scripta* **89**, 054007 (2014).
- [43] K. Zberecki, P.-H. Heenen and P. Magierski, *Phys. Rev. C* **79**, 014319 (2009).
- [44] R. Bijker and F. Iachello, *Phys. Rev. Lett.* **112**, 152501 (2014).
- [45] Y. Chen and Z. Gao, *Nucl. Phys. Rev.* **30**, 278 (2013).
- [46] Y. S. Chen and Z.-C. Gao, *Nucl. Phys. A* **834**, 378c (2010).
- [47] B.-N. Lu, J. Zhao, E.-G. Zhao and S.-G. Zhou, *J. Phys. Conf. Ser.* **492**, 012014 (2014).
- [48] B.-N. Lu, J. Zhao, E.-G. Zhao and S.-G. Zhou, *Phys. Rev. C* **89**, 014323 (2014).

- [49] B.-N. Lu, J. Zhao, E.-G. Zhao and S.-G. Zhou, *Phys. Scripta* **89**, 054028 (2014).
- [50] B.-N. Lu, J. Zhao, E.-G. Zhao and S.-G. Zhou, *EPJ Web Conf.* **38**, 05003 (2012).
- [51] J. Zhao, B.-N. Lu, D. Vretenar, E.-G. Zhao and S.-G. Zhou, *Phys. Rev. C* **91**, 014321 (2015).
- [52] J. Zhao, B.-N. Lu, T. Nikšić, D. Vretenar and S.-G. Zhou, *Phys. Rev. C* **93**, 044315 (2016).
- [53] J. Zhao, B.-N. Lu, E.-G. Zhao and S.-G. Zhou, *Phys. Rev. C* **86**, 057304 (2012).
- [54] B.-N. Lu, E.-G. Zhao and S.-G. Zhou, *Phys. Rev. C* **84**, 014328 (2011).
- [55] B.-N. Lu, E. Hiyama, H. Sagawa and S.-G. Zhou, *Phys. Rev. C* **89**, 044307 (2014).
- [56] L.-L. Li, B.-N. Lu, N. Wang, K. Wen, C.-J. Xia, Z.-H. Zhang, J. Zhao, E.-G. Zhao and S.-G. Zhou, *Nucl. Phys. Rev.* **31**, 253 (2014) (*in Chinese*).
- [57] B.-N. Lu, J. Zhao, E.-G. Zhao and S.-G. Zhou, *Superheavy nuclei and fission barriers*, in *Relativistic density functional for nuclear structure, chap. 5*, ed. J. Meng, *Int. Rev. Nucl. Phys.* **10**, 171. World Scientific, 2016.
- [58] Y. Tian and Z.-Y. Ma, *Chin. Phys. Lett.* **23**, 3226 (2006).
- [59] Y. Tian, Z. Y. Ma and P. Ring, *Phys. Lett. B* **676**, 44 (2009).
- [60] Y. Tian, Z.-Y. Ma and P. Ring, *Phys. Rev. C* **80**, 024313 (2009).
- [61] T. Nikšić, D. Vretenar and P. Ring, *Phys. Rev. C* **78**, 034318 (2008).
- [62] T. Nikšić, P. Ring, D. Vretenar, Y. Tian and Z.-Y. Ma, *Phys. Rev. C* **81**, 054318 (2010).
- [63] J. Zhao, B.-N. Lu, T. Nikšić and D. Vretenar, *Phys. Rev. C* **92**, 064315 (2015).
- [64] J. Zhao, B.-N. Lu, E.-G. Zhao and S.-G. Zhou, *Phys. Rev. C* **95**, 014320 (2017), arXiv:1606.08994 [nucl-th] (2016).
- [65] B. D. Serot and J. D. Walecka, *Adv. Nucl. Phys.* **16**, 1 (1986).
- [66] P. G. Reinhard, *Rep. Prog. Phys.* **52**, 439 (1989).
- [67] P. Ring, *Prog. Part. Nucl. Phys.* **37**, 193 (1996).
- [68] M. Bender, P.-H. Heenen and P.-G. Reinhard, *Rev. Mod. Phys.* **75**, 121 (2003).
- [69] D. Vretenar, A. V. Afanasjev, G. A. Lalazissis and P. Ring, *Phys. Rep.* **409**, 101 (2005).
- [70] J. Meng, H. Toki, S. G. Zhou, S. Q. Zhang, W. H. Long and L. S. Geng, *Prog. Part. Nucl. Phys.* **57**, 470 (2006).
- [71] N. Paar, D. Vretenar and G. Colo, *Rep. Prog. Phys.* **70**, 691 (2007).
- [72] T. Nikšić, D. Vretenar and P. Ring, *Prog. Part. Nucl. Phys.* **66**, 519 (2011).

- [73] H. Liang, J. Meng and S.-G. Zhou, Phys. Rep. **570**, 1 (2015).
- [74] J. Meng and S. G. Zhou, J. Phys. G **42**, 093101 (2015).
- [75] J. Boguta and A. R. Bodmer, Nucl. Phys. A **292**, 413 (1977).
- [76] R. Brockmann and H. Toki, Phys. Rev. Lett. **68**, 3408 (1992).
- [77] Y. Sugahara and H. Toki, Nucl. Phys. A **579**, 557 (1994).
- [78] B. A. Nikolaus, T. Hoch and D. G. Madland, Phys. Rev. C **46**, 1757 (1992).
- [79] T. Burvenich, D. G. Madland, J. A. Maruhn and P.-G. Reinhard, Phys. Rev. C **65**, 044308 (2002).
- [80] C. Fuchs, H. Lenske and H. H. Wolter, Phys. Rev. C **52**, 3043 (1995).
- [81] T. Nikšić, D. Vretenar, P. Finelli and P. Ring, Phys. Rev. C **66**, 024306 (2002).
- [82] J. Meng (ed.) *Relativistic density functional for nuclear structure*, Int. Rev. Nucl. Phys. **10**. World Scientific, 2016.
- [83] H. Kucharek and P. Ring, Z. Phys. A **339**, 23 (1991).
- [84] Y. K. Gambhir, P. Ring and A. Thimet, Ann. Phys. (NY) **198**, 132 (1990).
- [85] P. W. Zhao, Z. P. Li, J. M. Yao and J. Meng, Phys. Rev. C **82**, 054319 (2010).

Pygmy Dipole Modes in Shape-Coexisting ^{40}Mg

Kai Wang and Junchen Pei

State Key Laboratory of Nuclear Physics and Technology, School of Physics, Peking University, Beijing 100871, China

Abstract

Weakly bound nuclei have exotic collective excitations associated with halo structures and continuum effects. Our study of isovector dipole modes in the shape-coexisting ^{40}Mg is based on the fully self-consistent continuum FAM-QRPA in deformed large coordinate spaces. The K -splitting in low-lying pygmy resonances clearly deviates from the proportionality in terms of static deformations which is inherent for giant resonances.

Keywords: *Collective excitation; FAM-QRPA; shape-coexistence*

1 Introduction

Quantum many-body systems have emergent amazing macroscopic phenomena that can not be easily derived from their constituent parts [1]. Nuclei are in an evolution from few-body to many-body systems, and can possess deformed shapes and superfluidity which can enhance essentially the nuclear collective behavior [2]. Thus, an accurate treatment of continuum in large coordinate spaces is essential for the description of collective excitation modes in weakly bound nuclei.

A traditional way to implement the QRPA is the matrix diagonalization scheme (MQRPA). However, huge dimensions of the QRPA matrix, especially when the spherical symmetry is broken and continuum configurations are included, result in expensive computational costs, which become a major numerical challenge.

To this end, the finite amplitude method (FAM), which allows us to compute all induced fields using a finite difference method employing a subroutine of the static mean-field Hamiltonian, is introduced to calculate strength functions [3]. The FAM-QRPA for monopole modes has been implemented based on several well-known DFT-solvers, such as the spherical coordinate-space program HFBRAD, the deformed harmonic oscillator basis space program HFBTHO, and the deformed relativistic Hartree–Bogoliubov method [3, 4]. Previously, we also developed the FAM-QRPA based on our DFT-solver HFB-AX which provides very precise ground-state HFB solutions in the deformed coordinate space [5]. Recently M. Kortelainen *et al.* extended the FAM to a deformed multipole case, allowing the evaluation of QRPA modes for operators of arbitrary multipolarity LK with simplex- y basis [6]. Now we also extend our FAM-QRPA to multipole excitation modes based on the HFB-AX, which provides a good resolution of quasiparticle resonances and continuum spectra due to

Proceedings of the International Conference ‘Nuclear Theory in the Supercomputing Era — 2016’ (NTSE-2016), Khabarovsk, Russia, September 19–23, 2016. Eds. A. M. Shirokov and A. I. Mazur. Pacific National University, Khabarovsk, Russia, 2018, p. 174.

<http://www.ntse-2016.khb.ru/Proc/Pei.pdf>.

large box sizes and dense lattices [7]. This is an ideal tool for describing the collective excitations of weakly bound deformed nuclei.

^{40}Mg is the last experimentally observed magnesium isotope [8] with an $N = 28$ magic neutron number, but with a well-established prolate-oblate shape-coexistence [9, 10]. Such a shape-coexistence is ideal for a comparative analysis of deformation-related isovector dipole (IVD) modes, which are a natural probe of surface oscillations and are directly related to the photoabsorption cross section.

2 Theoretical models

As mentioned above, the HFB equation is solved by HFB-AX [11] within a large two-dimensional coordinate space based on B-spline techniques with an assumed axial symmetry. The mesh distance is 0.6 fm and the order of B-spline is 12. A hybrid MPI + OpenMP parallel scheme was utilized to get converged results within a reasonable time.

For the particle-hole interaction channel, a recently adjusted extended SLy4 force for light nuclei is adopted [12] including an additional density-dependent term. For the particle-particle channel, a density dependent delta interaction (DDDI) [13], $V_0[1 - \eta(\rho(\mathbf{r})/\rho_0)^\gamma]$, is used. With a pairing window of 60 MeV, the pairing force parameters are taken as $V_0 = -448.3 \text{ MeV fm}^3$, $\eta=0.8$ and $\gamma=0.7$, so that pairing gaps in both stable and very neutron-rich nuclei can be properly described. The resulted pairing gaps are between those from mixed and surface types of pairing in very neutron-rich nuclei, while the surface pairing interaction may overestimate pairing correlations in nuclei far from stability [14].

The next step is to calculate a strength function within the framework of FAM-QRPA utilizing the wave functions obtained by HFB-AX. The same parameters in the particle-hole and particle-particle channels are used in the DFT-solver and FAM for self-consistency. To study the fine structures of pygmy resonances, the smoothing parameter is taken to be 0.25 MeV (cf. with the usually adopted value of 0.5 MeV). For each frequency point ω , the calculation employs the OpenMP shared memory parallel scheme. For different frequencies, the MPI distributed parallel scheme is adopted. All computations are performed on the Tianhe-1A supercomputer located in Tianjin and Tianhe-2 supercomputer located in Guangzhou.

3 Results

As is seen from Table 1, the oblate shape is 1.9 MeV above the prolate shape reflecting the fact that ^{40}Mg has a soft potential energy surface. The shape competition is also reflected in the superfluidity difference: the prolate shape only has a neutron pairing gap while the oblate shape only has a proton pairing gap.

The neutron density and neutron pairing density distributions in ^{40}Mg in different shape are shown in Fig. 1. The densities are displayed along the cylindrical coordinates z (symmetrical axis) and $r = \sqrt{x^2 + y^2}$ (perpendicular to the symmetrical axis), respectively. The difference between two profiles reflects the surface deformation. The absolute value of pairing densities in oblate ^{40}Mg is small which is responsible for the almost vanishing neutron pairing gap. We see a significant neutron pairing density

Table 1: Some bulk properties of prolate and oblate ^{40}Mg obtained by HFB-AX within the box-size of 27.6 fm. β_2 is the quadruple deformation parameter, E_{tot} is the total energy, λ is the Fermi energy, and Δ is the pairing gap. Subscripts n and p denote neutron and proton, respectively. All energies are in MeV.

shape	β_2	E_{tot}	λ_n	Δ_n	Δ_p
prolate	0.39	-264.14	-0.33	1.23	0
oblate	-0.32	-262.27	-0.79	0	0.98

halo as compared to the neutron normal density. In addition, we do not see an evident core-halo shape decoupling.

In Fig. 2, the transition strengths of $K = 0$ and $|K| = 1$ (the sum of $K = 1$ and $K = -1$) are shown. To see the role of accurate treatment of continuum and surface extensions, the transition strengths of prolate ^{40}Mg are calculated with box size of 12, 21 and 27.6 fm. We see that, within a small box, the continuum discretization is not sufficient, which result in some false peaks. For instance, a false peak at 13 MeV is still present even with the box size of 21 fm. Moreover, the low-lying resonances are fragmented and less coherent without accurate continuum.

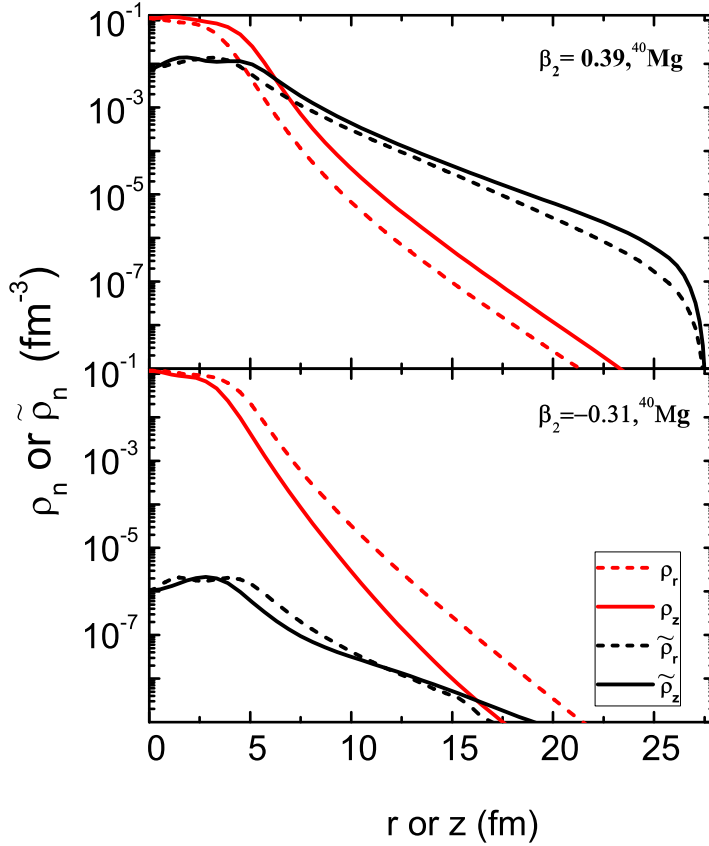


Figure 1: Neutron density ρ_n and neutron pairing density $\tilde{\rho}_n$ distributions in ^{40}Mg in prolate (upper panel) and oblate (lower panel) shapes displayed along the cylindrical coordinates z (solid curve) and r (dashed curve).

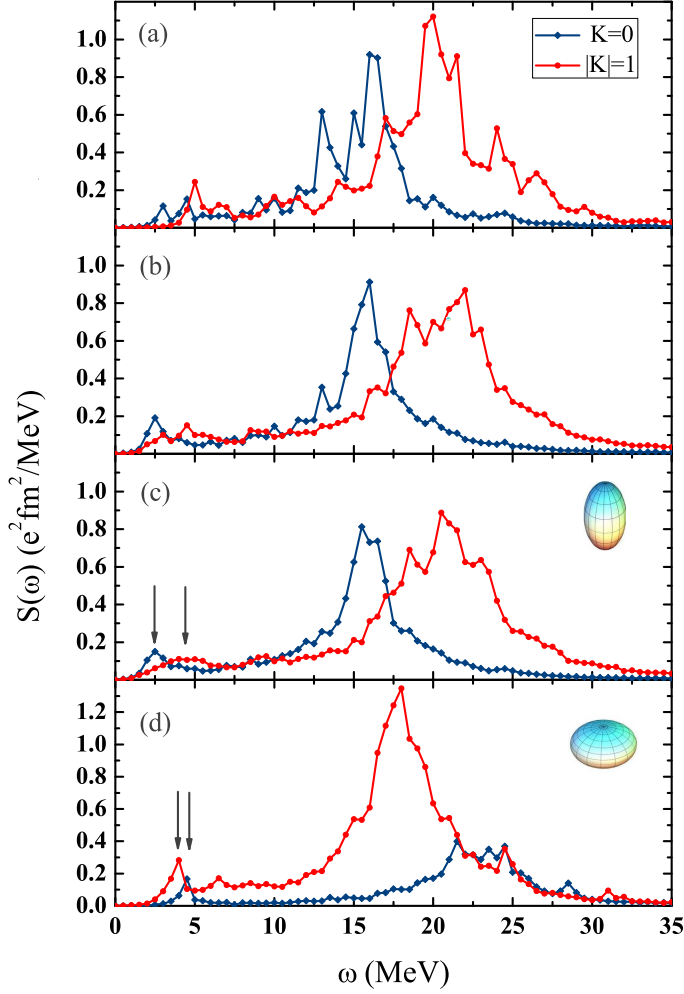


Figure 2: Calculated transition strengths of isovector dipole resonances in shape-coexisting ^{40}Mg as functions of excitation energy. Results for (a) prolate shape with box size of 12 fm; (b) prolate shape with box size of 21 fm; (c) prolate shape with box size of 27.6 fm; (d) oblate shape with box size of 27.6 fm.

In calculations with a large coordinate space of 27.6 fm, the obtained transition strengths clearly demonstrate pygmy resonances and deformation splitting, as shown in Fig. 2 (c,d). It is known from the hydrodynamic liquid-drop model [15] that the anisotropic splitting of the dipole transition strength is approximately proportional to centroid excitation energy and deformation. It is reasonable that both cases have similar giant resonance splitting ($\delta_E \sim 5$ MeV) considering different centroid energies and deformations. Then the estimated pygmy splitting should be around 0.95 MeV for the prolate shape and 1.05 MeV for the oblate case since ^{40}Mg actually has no evident core-halo shape decoupling [16]. However, we see the pygmy splitting of the prolate shape ($\delta_E \sim 1.4$ MeV) is significantly larger than expected while the oblate case ($\delta_E \sim 0.45$ MeV) is smaller. Obviously the hydrodynamic anisotropic splitting is not valid anymore for pygmy resonances. According to our tests, the pygmy splittings are not sensitive to pairing strengths. We speculate that the pygmy splitting is related not only with static shapes and but also with significant dynamical deformation surface effects. It will be very helpful to study the pygmy dipole resonance deformation splitting in deformed neutron-rich nuclei in high-resolution experiments.

Besides, the $|K| = 1$ dominates in the oblate case where the deformation splitting in the total cross section is not distinguishable in contrast to the prolate case.

References

- [1] P. W. Anderson, *Science* **177**, 393 (1972).
- [2] P. Ring and P. Schuck, *The nuclear many-body problem*. Springer-Verlag, Berlin, Heidelberg, 1980.
- [3] P. Avogadro and T. Nakatsukasa, *Phys. Rev. C* **84**, 014314 (2011).
- [4] M. Stoitsov, M. Kortelainen, T. Nakatsukasa, C. Losa and W. Nazarewicz, *Phys. Rev. C* **84**, 041305(R) (2011); T. Nikšić, N. Kralj, T. Tutiš, D. Vretenar and P. Ring, *ibid.* **88**, 044327(2013); H. Liang, T. Nakatsukasa, Z. Niu and J. Meng, *ibid.* **87**, 054310 (2013).
- [5] J. C. Pei, M. Kortelainen, Y. N. Zhang and F. R. Xu, *Phys. Rev. C* **90**, 051304(R) (2014).
- [6] M. Kortelainen, N. Hinohara and W. Nazarewicz, *Phys. Rev. C* **92**, 051302(R) (2015).
- [7] K. Wang, M. Kortelainen and J. C. Pei, arXiv:1612.06019 [nucl-th] (2016).
- [8] T. Baumann *et al.*, *Nature* **449**, 1022 (2007).
- [9] J. Terasaki, H. Flocard, P-H. Heenen and P. Bonche, *Nucl. Phys. A* **621**, 706 (1997).
- [10] R. Rodríguez-Guzmán, J. L. Egido and L. M. Robledo, *Phys. Rev. C* **65**, 024304 (2002).
- [11] J. C. Pei, M. V. Stoitsov, G. I. Fann, W. Nazarewicz, N. Schunck and F. R. Xu, *Phys. Rev. C* **78**, 064306 (2008).
- [12] X. Y. Xiong, J. C. Pei and W. J. Chen, *Phys. Rev. C* **93**, 024311 (2016).
- [13] A. Pastore, F. Barranco, R. A. Broglia and E. Vigezzi, *Phys. Rev. C* **78**, 024315 (2008).
- [14] S. A. Changizi and C. Qi, *Phys. Rev. C* **91**, 024305 (2015).
- [15] G. F. Bertsch and R. A. Broglia, *Oscillations in finite quantum systems*. Cambridge University Press, 1994.
- [16] J. C. Pei, Y. N. Zhang and F. R. Xu, *Phys. Rev. C* **87**, 051302(R) (2013); Y. N. Zhang, J. C. Pei and F. R. Xu, *ibid.* **88**, 054305 (2013).

Large-scale shell-model studies of exotic nuclei and nuclear level densities

Noritaka Shimizu

Center for Nuclear Study, the University of Tokyo, 7-3-1 Hongo, Tokyo, 113-0033, Japan

Abstract

An applicability of large-scale shell-model calculations grows rapidly owing to the developments of both the methodology and high-performance computing. We briefly describe two methods to go beyond the standard Lanczos method in the large-scale shell model calculations: the Monte Carlo shell model and the stochastic estimation of nuclear level density. For the latter one, we adopt an eigenvalue-density estimation based on a shifted Krylov-subspace method. It enables us to describe both a low-lying spectroscopy and the nuclear level density microscopically in a unified manner.

Keywords: *Nuclear shell model, Monte Carlo shell model, nuclear level density*

1 Introduction

Large-scale shell-model calculations is one of the powerful methods to study exotic structure of neutron-rich nuclei, which has been intensively investigated due to a recent growth of the high-performance computing enhancing a feasibility of the large-scale shell-model calculations in medium-heavy nuclei. The recent limit of the large-scale shell-model calculation with the conventional Lanczos diagonalization reaches $O(10^{11})$ M -scheme dimension [1, 2].

Tokyo nuclear theory group in the University of Tokyo has been continuing to promote the utilization of the high performance computing for the large-scale shell model calculations under the HPCI Strategic Program field 5 and priority issue 9 to be tackled by using post-K computer [3]. Conventionally the large-scale shell-model calculations are performed by solving an eigenvalue problem for a huge Hamiltonian matrix utilizing the Lanczos algorithm [1]. We developed a shell-model code “KSHELL” for the Lanczos calculations on a massively parallel computer and showed its capability up to $O(10^{11})$ M -scheme dimensions [4].

2 Monte Carlo shell model

In order to overcome the limitation of the standard Lanczos method, M. Honma, T. Mizusaki and T. Otsuka have suggested the Monte Carlo shell model (MCSM) [5],

Proceedings of the International Conference ‘Nuclear Theory in the Supercomputing Era — 2016’ (NTSE-2016), Khabarovsk, Russia, September 19–23, 2016. Eds. A. M. Shirokov and A. I. Mazur. Pacific National University, Khabarovsk, Russia, 2018, p. 179.

<http://www.ntse-2016.khb.ru/Proc/Shimizu.pdf>.

and the Tokyo group extended it by introducing a sophisticated variational method [6] and an extrapolation utilizing an expectation value of the energy variance [7]. The MCSM framework with these new features is called an “advanced MCSM”. It enables us to obtain the low-lying spectra with large model spaces. It is applied to no-core shell-model calculations in p -shell nuclei and large-scale shell-model calculations in medium-heavy nuclei.

In the application of the MCSM to the no-core shell-model calculations called no-core MCSM, we adopted the JISP16 interaction [8] and demonstrated that a cluster structure emerges in the intrinsic states of Be isotopes [9]. It also enables us to extrapolate the binding energies of the p -shell nuclei to those corresponding to the infinite size of the model space [10].

In the applications of the MCSM to medium-heavy nuclei, we investigated an exotic structure of neutron-rich nuclei such as neutron-rich Ni isotopes [11]. Recently we successfully reproduced a sudden drop of the 2^+ excitation energies in Zr isotopes around $N = 60$, and revealed that it is caused by the first-order quantum phase transition from spherical shape to prolate deformation [12, 13].

3 Stochastic estimation of level density

For understanding a neutron-capture process, a nuclear level density is an important input in the Hauser–Feshbach theory. Nuclear shell-model calculations are considered to be one of ideal methods to evaluate the level density. In the shell-model calculations, the level density is obtained as an eigenvalue density of the Hamiltonian matrix. However, there is a difficulty in numerical computation: the conventional Lanczos method shows a slow convergence and a lot of memory usages.

Although the MCSM provides a good description of the ground states and a few low-lying excited states, it cannot provide the nuclear level density. It is difficult to compute the nuclear level density by a direct counting of the eigenvalues obtained by the Lanczos method, since the number of eigenvalues to be obtained reaches a few thousands and the convergence of highly-excited states is slow in the Lanczos method. Several methods to obtain the nuclear level density were proposed based on shell-model calculations [14–16]. In Ref. [17], we adopted a stochastic estimation of eigenvalue count based on a shifted Krylov-subspace method [18] and applied it to the nuclear shell-model calculations. This estimation works efficiently especially for sparse matrices.

Here we describe the framework of this estimation method. The shell-model wave function is written as a linear combination of many-body configurations which are called the M -scheme basis states [1]. Since the eigenenergy of the shell-model Hamiltonian is obtained as an eigenvalue of the M -scheme shell-model Hamiltonian matrix, H , the nuclear level density corresponds to the number of the eigenvalues in a certain eigenvalue region. We count the number of eigenvalues μ_k in the range $E^{(k-1)} < E < E^{(k)}$ by evaluating the residue of the contour integral Γ_k in Fig. 1.

We compute the contour integral along Γ_k by discretizing the contour line with mesh points $z_j^{(k)}$ (blue crosses in Fig. 1) and their weights w_j as

$$\mu_k = \frac{1}{2\pi i} \oint_{\Gamma_k} dz \operatorname{Tr} \left(\frac{1}{z - H} \right) = \sum_j w_j \operatorname{Tr} \left(\frac{1}{z_j^{(k)} - H} \right). \quad (1)$$

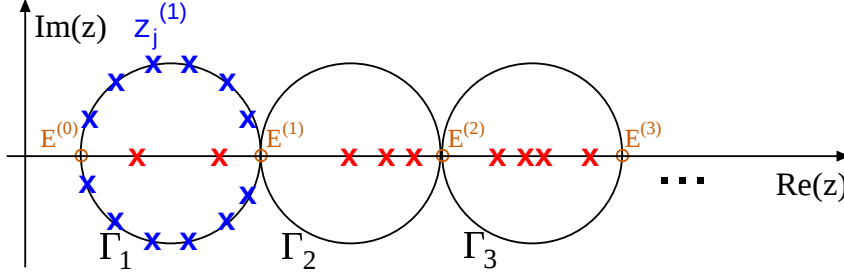


Figure 1: Schematic drawing of the contour line to count the eigenvalues between $E^{(k-1)}$ and $E^{(k)}$ in the complex plane of z . The red and blue crosses denote the eigenvalues and the discretized mesh points $z_j^{(1)}$ along the Γ_1 . The figure is taken from Ref. [17].

Since the trace of the inverse of matrix in Eq. (1) cannot be directly calculated, it is stochastically estimated by Hutchinson's estimator [19] as

$$\text{Tr}\left(\frac{1}{z-H}\right) \simeq \frac{1}{N_s} \sum_s^{N_s} \mathbf{v}_s^T \frac{1}{z-H} \mathbf{v}_s, \quad (2)$$

where \mathbf{v}_s are vectors whose components take values of 1 or -1 randomly with equal probability. N_s denotes the number of these random vectors. Typically, N_s is taken as 32 and its stochastic error is small enough.

In order to estimate the trace in Eq. (2), we have to compute $\mathbf{v}_s^T (z_j^{(k)} - H)^{-1} \mathbf{v}_s$. In the case of shell-model Hamiltonian matrix which is quite sparse, it is inefficient to compute the inverse matrix directly. Since the matrix H is quite sparse, we solve the linear equations $\mathbf{v}_s = (z - H)\mathbf{x}$ utilizing a Krylov-subspace method and obtain the $(z - H)^{-1}\mathbf{v}_s$. Among the Krylov-subspace methods, we adopt the block bilinear form of the blocked complex orthogonal conjugate gradient (BCOCG) method [20] for efficient computation. On top of that, we need to solve the equations $\mathbf{v}_s = (z - H)\mathbf{x}$ for any $z = z_j^{(k)}$. These equations are solved simultaneously based on the shifted algorithm [21].

As a benchmark for the validity of the estimation, Fig. 2 shows the level density obtained by the present estimation in comparison with the exact shell-model level density obtained by the Lanczos method. The model space is taken to be the sd shell and the USD interaction [22] is used. The result of the stochastic estimation shows a good agreement with the exact one with a certain stochastic error. The present method allows us to estimate the level density of a large system with the M -scheme dimension of up to 2×10^{10} [17]. This dimension is almost the current limit of the Lanczos method to obtain a few low-lying states.

This method enables us to estimate the level density in medium-heavy nuclei utilizing a realistic effective interaction successfully describing low-lying excited states and their spectroscopic information. In Ref. [17], using such a realistic effective interaction, we successfully reproduced an experimentally observed equilibration of $J^\pi = 2^+$ and 2^- states in ^{58}Ni .

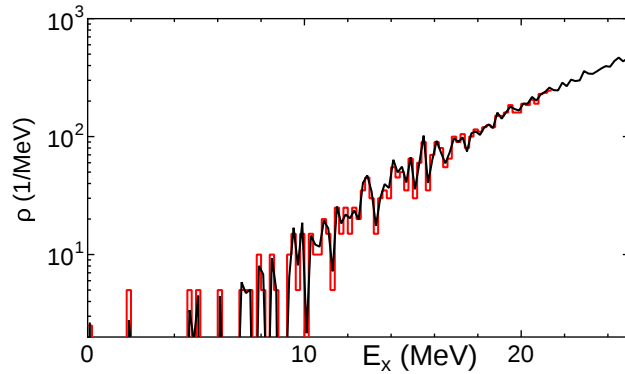


Figure 2: Benchmark test of the level density in ^{28}Si vs the excitation energy E_x . Red solid histogram — exact shell-model calculation by Lanczos method, black line — stochastic estimation. The figure is taken from Ref. [17].

4 Summary

In order to extend the limit of large-scale shell-model calculations, we developed the advanced MCSM for obtaining low-lying states and for the stochastic estimation of the nuclear level density. Further details and a review of the advanced MCSM can be found in Refs. [23,24]. A recent achievement of the MCSM calculations of Zr isotopes is available in Ref. [12]. Concerning the stochastic estimation of the level density, Refs. [17, 25] are referred.

Acknowledgments

I would like to thank Takashi Abe, Michio Honma, Takahiro Mizusaki, Takaharu Otsuka, Tomoaki Togashi, Yusuke Tsunoda, Yutaka Utsuno and Tooru Yoshida for our long-standing collaborations. I also thank Tetsuya Sakurai and Yasunori Futamura for the collaboration on methodological developments regarding the level density calculations.

This work has been supported by the HPCI Strategic Program from MEXT, CREST from JST, the CNS-RIKEN joint project for large-scale nuclear structure calculations, and KAKENHI grants (25870168, 23244049, 15K05094) from JSPS, Japan. The numerical calculations were performed on the K computer at RIKEN AICS (hp140210, hp150224, hp160211), FX10 supercomputer at the University of Tokyo, and COMA supercomputer at the University of Tsukuba.

References

- [1] E. Caurier, G. Martinez-Pinedo, F. Nowacki, A. Poves and A. P. Zuker, *Rev. Mod. Phys.* **77**, 427 (2005).
- [2] O. Legeza, L. Veis, A. Poves and J. Dukelsky, *Phys. Rev. C* **92**, 051303(R) (2015).
- [3] <http://www.jicfus.jp/en/>
- [4] N. Shimizu, arXiv:1310.5431 [nucl-th] (2013).
- [5] T. Otsuka, M. Honma, T. Mizusaki, N. Shimizu and Y. Utsuno *Prog. Part. Nucl. Phys.* **47**, 319 (2001).

- [6] N. Shimizu, Y. Utsuno, T. Mizusaki, M. Honma, Y. Tsunoda and T. Otsuka, *Phys. Rev. C* **85**, 054301 (2012).
- [7] N. Shimizu, Y. Utsuno, T. Mizusaki, T. Otsuka, T. Abe and M. Honma, *Phys. Rev. C* **82**, 061305(R) (2010).
- [8] A. M. Shirokov, J. P. Vary, A. I. Mazur and T. A. Weber, *Phys. Lett. B* **644** 33 (2007).
- [9] T. Yoshida, N. Shimizu, T. Abe and T. Otsuka *Few-Body Syst.* **54** 1465 (2013); *J. Phys. Conf. Ser.* **569** 012063 (2014).
- [10] T. Abe, P. Maris, T. Otsuka, N. Shimizu, Y. Utsuno and J. P. Vary, in *Proc. Int. Conf. Nucl. Theor. Supercomputing Era (NTSE-2014), Khabarovsk, Russia, June 23–27, 2014*, eds. A. M. Shirokov and A. I. Mazur. Pacific National University, Khabarovsk, 2016, p. 230, <http://www.ntse-2014.khb.ru/Proc/Abe.pdf>.
- [11] Y. Tsunoda, T. Otsuka, N. Shimizu, M. Honma and Y. Utsuno, *Phys. Rev. C* **89** 031301(R) (2014).
- [12] T. Togashi, Y. Tsunoda, T. Otsuka and N. Shimizu, *Phys. Rev. Lett.* **117**, 172502 (2016).
- [13] C. Kremer, S. Aslanidou, S. Bassauer, M. Hilcker, A. Krugmann, P. von Neumann-Cosel, T. Otsuka, N. Pietralla, V. Yu. Ponomarev, N. Shimizu, M. Singer, G. Steinhilber, T. Togashi, Y. Tsunoda, V. Werner and M. Zweidinger, *Phys. Rev. Lett.* **117**, 172503 (2016).
- [14] Y. Alhassid, G. F. Bertsch, S. Liu and H. Nakada, *Phys. Rev. Lett.* **84**, 4313 (2000); H. Nakada and Y. Alhassid, *ibid.* **79**, 2939 (1997).
- [15] R. A. Sen'kov and V. Zelevinsky, *Phys. Rev. C* **93**, 064304 (2016); R. A. Sen'kov and M. Horoi, *ibid.* **82**, 024304 (2010).
- [16] B. Strohmaier, S. M. Grimes and S. D. Bloom, *Phys. Rev. C* **32** 1397 (1985); S. M. Grimes, S. D. Bloom, R. F. Hausman, Jr. and B. J. Dalton, *ibid.* **19**, 2378 (1979).
- [17] N. Shimizu, Y. Utsuno, Y. Futamura, T. Sakurai, T. Mizusaki and T. Otsuka, *Phys. Lett. B* **753**, 13 (2016).
- [18] Y. Futamura, H. Tadano and T. Sakurai, *JSIAM Lett.* **2**, 127 (2010).
- [19] M. F. Hutchinson, *Commun. Stat. Simul. Comput.* **19**, 433 (1990).
- [20] L. Du, Y. Futamura and T. Sakurai, *Comput. Math. Appl.* **66**, 12 (2014).
- [21] S. Yamamoto, T. Sogabe, T. Hoshi, S.-L. Zhang and T. Fujiwara, *J. Phys. Soc. Jpn.* **77**, 114713 (2008).
- [22] B. A. Brown and B. H. Wildenthal, *Annu. Rev. Nucl. Part. Sci.* **38**, 29 (1988).
- [23] N. Shimizu, T. Abe, Y. Tsunoda, Y. Utsuno, T. Yoshida, T. Mizusaki, M. Honma and T. Otsuka, *Progr. Theor. Exp. Phys.* **2012**, 01A205 (2012).

- [24] N. Shimizu, T. Abe, M. Honma, T. Otsuka, T. Togashi, Y. Tsunoda, Y. Utsuno, and T. Yoshida, *to be submitted*.
- [25] N. Shimizu, Y. Utsuno, Y. Futamura, T. Sakurai and T. Otsuka, EPJ Web Conf. **122**, 02003 (2016).

Resonant States in ${}^5\text{He}$ and ${}^5\text{Li}$ and Nucleon- α Scattering

A. I. Mazur^a, A. M. Shirokov^{a,b,c}, I. A. Mazur^a, E. A. Mazur^a,
Y. Kim^d, I. J. Shin^d, L. D. Blokhintsev^{a,b} and J. P. Vary^c

^a*Department of Physics, Pacific National University, Khabarovsk 680035, Russia*

^b*Skobeltsyn Institute of Nuclear Physics, Lomonosov Moscow State University, Moscow 119991, Russia*

^c*Department of Physics and Astronomy, Iowa State University, Ames, IA 50011-3160, USA*

^d*Rare Isotope Science Project, Institute for Basic Science, Daejeon 305-811, Korea*

Abstract

The SS-HORSE approach to analysis of resonant states is generalized to the case of charged particle scattering utilizing analytical properties of partial scattering amplitudes and applied to the study of resonant states in the ${}^5\text{Li}$ nucleus and non-resonant s -wave proton- α scattering within the no-core shell model using the JISP16 and Daejeon16 NN interactions.

Keywords: *Charged particle scattering; resonances; scattering amplitude; effective range function; SS-HORSE approach; no-core shell model*

1 Introduction

There is considerable progress in developing *ab initio* methods for studying nuclear structure [1] based on a rapid development of supercomputer facilities and recent advances in the utilization of high-performance computing systems. In particular, modern *ab initio* approaches, such as the Green's Function Monte Carlo (GFMC) [2], the Hyperspherical expansion [1], the No-Core Shell Model (NCSM) [3], the Coupled-Cluster Theory [4, 5], and the Nuclear Lattice Effective Field Theory [6, 7] are able to reproduce properties of atomic nuclei with mass up to $A = 16$ and selected heavier nuclear systems around closed shells.

Within NCSM as well as within other shell model approaches, the calculation of nuclear ground states and other bound states starts conventionally from estimating the $\hbar\Omega$ dependence of the energy $E_\nu(\hbar\Omega)$ of the bound state ν in some model space. The minimum of $E_\nu(\hbar\Omega)$ is correlated with the energy of the state ν . The convergence of calculations and accuracy of the energy prediction is estimated by comparing with the results obtained in neighboring model spaces. To improve the accuracy of theoretical predictions, various extrapolation techniques have been suggested recently [8–19] which make it possible to estimate the binding energies in the complete infinite shell-model basis space. The studies of extrapolations to the infinite model spaces reveal general trends of convergence patterns of shell model calculations.

Proceedings of the International Conference 'Nuclear Theory in the Supercomputing Era — 2016' (NTSE-2016), Khabarovsk, Russia, September 19–23, 2016. Eds. A. M. Shirokov and A. I. Mazur. Pacific National University, Khabarovsk, Russia, 2018, p. 185.

<http://www.ntse-2016.khb.ru/Proc/AMazur.pdf>.

An extension of the *ab initio* methods to the studies of the continuum spectrum and nuclear reactions is one of the mainstreams of modern nuclear theory. A remarkable success in developing the *ab initio* reaction theory was achieved in few-body physics where exact Faddeev and Faddeev–Yakubovsky equations [20] or the AGS method [21] are nowadays routinely used for calculating various few-body reactions.

The most important breakthrough in developing *ab initio* theory of nuclear reactions in systems with total number of nucleons $A > 4$ was achieved by combining NCSM and Resonating Group Method (RGM); the resulting approach is conventionally referred to as NCSM/RGM or No-Core Shell Model with Continuum (NCSMC) [3, 22–24]. It is also worth noting the Lorentz integral transform approach to nuclear reactions with electromagnetic probes [1, 25] and the GFMC calculations of elastic $n\alpha$ scattering [26]. Nuclear resonance can be also studied within the No-core Gamow Shell Model (NCGSM) [27].

Both NCGSM and NCSM/RGM complicate essentially the shell model calculations. A conventional belief is that the energies of shell model states in the continuum should be associated with the resonance energies. It was shown however in Refs. [28, 29] that the energies of shell model states may appear well above the energies of resonant states, especially for broad resonances. Moreover, the analysis of Refs. [28, 29] clearly demonstrated that the shell model should also generate some states in a non-resonant nuclear continuum. In Refs. [30–34] we suggested an SS-HORSE approach which provides an interpretation of the shell model states in the continuum and makes it possible to deduce resonance energies and width or low-energy non-resonant phase shifts directly from shell-model results without introducing additional Berggren basis states as in NCGSM or additional RGM calculations as in the NCSM/RGM approach.

The SS-HORSE approach is based on a simple analysis of the $\hbar\Omega$ and basis-space dependencies of the results of standard variational shell-model calculations. We have successfully applied it to extracting resonance energies and widths in $n\alpha$ scattering as well as non-resonant $n\alpha$ elastic scattering phase shifts [30, 31] from the NCSM calculations of ${}^5\text{He}$ and ${}^4\text{He}$ nuclei with JISP16 NN interaction [35]. To describe democratic decays [36, 37] of few-nucleon systems, we developed a hyperspherical extension of the SS-HORSE method [38, 39]. An application of this extended SS-HORSE approach to the study of the four-neutron system (tetra-neutron) [38–40] make it possible to obtain for the first time a low-energy tetra-neutron resonance consistent with a recent experiment [41] with soft realistic NN interactions like JISP16 [35], Daejeon16 [42] and SRG-evolved chiral effective field theory (χEFT) NN interactions. On the other hand, the unperturbed χEFT Idaho N3LO interaction [43] does not support a tetra-neutron resonance narrow enough to be detected experimentally but instead provides a low-lying virtual tetra-neutron state [40]. This result provides a possible explanation why the tetra-neutron resonance has not been obtained before in numerous theoretical studies with various NN interactions with a repulsive core.

In this contribution, we discuss an extension of the SS-HORSE method to the case of charged particle scattering. The SS-HORSE technique provides the S -matrix or scattering phase shifts in some energy interval above the threshold where the shell model calculations generate eigenstates with various $\hbar\Omega$ values and various basis truncations. Next we parametrize the S -matrix to obtain it in a wider energy interval and to locate its poles associated with resonances. We have shown [30, 31] that this parametrization should provide a correct description of low-energy phase shifts. The

phase shift parametrization utilized in Refs. [30–32] was derived from the symmetry properties of the S -matrix. However, due to the long-range Coulomb interaction in the case of charged particle scattering, the analytical properties of the S -matrix become much more complicated and cannot be used for its low-energy parametrization. In Ref. [33] we suggested a version of the SS-HORSE approach which utilizes the phase shift parametrization based on analytical properties of the partial scattering amplitude. In the case of charged particle scattering, instead of the partial scattering amplitude one can use the so-called renormalized Coulomb-nuclear amplitude [44, 45] which has similar analytical properties. This opens a route to the generalization of the SS-HORSE method to the case of the charged particle scattering proposed in Ref. [34] where we have verified this approach using a model problem of scattering of particles interacting by the Coulomb and a short-range potential. To calculate the Coulomb-nuclear phase shifts, we make use of the version of the HORSE formalism suggested in Ref. [46] and utilized later in our studies of Refs. [28, 29].

In this contribution we present the results of SS-HORSE calculations of proton- α resonant and non-resonant scattering phase shifts based on the *ab initio* NCSM results for ${}^5\text{Li}$ and ${}^4\text{He}$ nuclei obtained with the JISP16 [35] and a newer Daejeon16 [42] NN interaction derived from a χEFT inter-nucleon potential and better fitted to the description of light nuclei than JISP16. We search for the S -matrix poles to evaluate the energies and widths of resonant states in ${}^5\text{Li}$ nucleus. The NCSM-SS-HORSE calculations of the ${}^5\text{He}$ resonant states have been performed with the JISP16 interaction in Refs. [30, 31]. We present here also the results of the NCSM-SS-HORSE ${}^5\text{He}$ resonant state calculations with the Daejeon16 to complete the studies of the nucleon- α resonances with the realistic JISP16 and Daejeon16 NN potentials. The previous *ab initio* analyses of nucleon- α resonances with various modern realistic inter-nucleon interactions were performed in Ref. [26] within the GFMC and in Refs. [22, 47–49] within the NCSM/RGM.

2 SS-HORSE method for channels with neutral and charged particles

2.1 General formulae

The SS-HORSE approach relies on the J -matrix formalism in quantum scattering theory.

Originally, the J -matrix formalism was developed in atomic physics [50] [4]; therefore, the so-called Laguerre basis was naturally used within this approach. A generalization of this formalism utilizing either the Laguerre or the harmonic oscillator bases was suggested in Ref. [51]. Later the harmonic-oscillator version of the J -matrix method was independently rediscovered by Kiev (G. F. Filippov and collaborators) [52] and Moscow (Yu. F. Smirnov and collaborators) [53] groups. The J -matrix with oscillator basis is sometimes also referred to as an *Algebraic Version of RGM* [52] or as a *Harmonic Oscillator Representation of Scattering Equations* (HORSE) [46]. We use here a generalization of the HORSE formalism to the case of charged particle scattering proposed in Ref. [46].

Within the HORSE approach, the basis function space is split into internal and external regions. In the internal region which includes the basis states with oscillator quanta $N \leq N$, the Hamiltonian completely accounts for the kinetic and potential

energies. The internal region can be naturally associated with the shell model basis space. In the external region, the Hamiltonian accounts for the relative kinetic energy of the colliding particles (and for their internal Hamiltonians if needed) only and its matrix takes a form of an infinite tridiagonal matrix of the kinetic-energy operator (plus the sum of eigenenergies of the colliding particles at the diagonal if they have an internal structure). The external region clearly represents the scattering channel under consideration. If the eigenenergies E_ν , $\nu = 0, 1, \dots$ and the respective eigenvectors of the Hamiltonian matrix in the internal region are known, one can easily calculate the S -matrix, phase shifts and other parameters characterizing the scattering process (see, e. g., Refs. [46, 51, 54, 55]).

An interesting feature peculiar to the J -matrix method was highlighted as far back as 1974 [50]. The point is that, at the energies coinciding with the eigenvalues E_ν of the Hamiltonian matrix in the internal region, the matching condition of the J -matrix method becomes substantially simpler while the accuracy of the S -matrix and phase shift description at these energies is much better than at the energies far enough from the eigenvalues E_ν [34, 56, 57]. Taking an advantage of this feature, H. Yamani [57] was able to construct an analytic continuation to the complex energy plane within the R -matrix method and to obtain accurate estimates for the energies and widths of resonant states.

The Single-State HORSE (SS-HORSE) method suggested in Refs. [30–32] also benefits from the improved accuracy of the HORSE approach at the eigenstates of the Hamiltonian matrix truncated to the internal region of the whole basis space. In the case of scattering of uncharged particles interacting by a short-range potential, the phase shifts $\delta_l(E_\nu)$ in the partial wave with the orbital momentum l at the eigenenergies E_ν of the internal Hamiltonian matrix are given by [30–32]

$$\tan \delta_l(E_\nu) = -\frac{S_{\mathbb{N}+2,l}(E_\nu)}{C_{\mathbb{N}+2,l}(E_\nu)}. \quad (1)$$

Here $S_{N,l}(E)$ and $C_{N,l}(E)$ are respectively regular and irregular solutions of the free Hamiltonian at energy E in the oscillator representation which analytical expressions can be found in Refs. [46, 51, 54, 55]. Varying the oscillator basis spacing $\hbar\Omega$ and the truncation boundary \mathbb{N} of the internal oscillator basis subspace, we obtain a variation of some eigenenergy E_ν of the truncated Hamiltonian matrix in some energy interval and obtain the phase shifts $\delta_l(E)$ in that energy interval by means of Eq. (1). Next we parametrize the phase shifts $\delta_l(E)$ as discussed in the next subsection to have the phase shifts and the S -matrix in a wider energy interval which makes it possible to locate the S -matrix poles.

In the case of scattering in the channels with two charged particles, we, following the ideas of Ref. [46], formally cut the Coulomb interaction at the distance $r = b$. As shown in Ref. [34], an optimal value of the Coulomb cutoff distance b is the so-called *natural channel radius* b_0 [46],

$$b = b_0 \equiv r_{\mathbb{N}+2,l}^{cl} = 2r_0 \sqrt{\mathbb{N}/2 + 7/4}, \quad (2)$$

i. e., b is equivalent to the classical turning point $r_{\mathbb{N}+2,l}^{cl}$ of the first oscillator function $R_{\mathbb{N}+2,l}(r)$ in the external region of the basis space. The parameter $r_0 = \sqrt{\hbar/(\mu\Omega)}$ entering Eq. (2) is the oscillator radius and μ is the reduced mass in the channel under consideration. With this choice of the Coulomb cutoff distance b , the elements of the

Hamiltonian matrix in the internal region are insensitive to the cut of the Coulomb interaction. Therefore the shell model Hamiltonian matrix elements in the internal region can be calculated without any modification of the Coulomb interaction between the nucleons. The scattering phase shifts δ_l^{aux} of the auxiliary Hamiltonian with the cutted Coulomb interaction can be calculated using the standard HORSE or SS-HORSE technique, e. g., with the help of Eq. (1). To deduce an expression for the Coulomb-nuclear phase shifts δ_l , one should match at the distance b the plane-wave asymptotics of the auxiliary Hamiltonian wave functions with Coulomb-distorted wave function asymptotics. As a result, we get the following SS-HORSE expression for the Coulomb-nuclear phase shifts $\delta_l(E_\nu)$ at the eigenenergies E_ν of the internal Hamiltonian matrix [34]:

$$\tan \delta_l(E_\nu) = - \frac{S_{\mathbb{N}+2,l}(E_\nu) W_b(n_l, F_l) + C_{\mathbb{N}+2,l}(E_\nu) W_b(j_l, F_l)}{S_{\mathbb{N}+2,l}(E_\nu) W_b(n_l, G_l) + C_{\mathbb{N}+2,l}(E_\nu) W_b(j_l, G_l)}. \quad (3)$$

Here $j_l \equiv j_l(kr)$ and $n_l \equiv n_l(kr)$ are respectively the spherical Bessel and Neumann functions [58] while $F_l \equiv F_l(\eta, kr)$ and $G_l \equiv G_l(\eta, kr)$ are respectively the regular and irregular Coulomb functions [58]; k is the relative motion momentum; $\eta = Z_1 Z_2 e^2 \mu / k$ is the Sommerfeld parameter; the quasi-Wronskian

$$W_b(\phi, \chi) = \left(\frac{d\phi}{dr} \chi - \phi \frac{d\chi}{dr} \right) \Big|_{r=b}. \quad (4)$$

As in the case of neutral particle scattering, we obtain the Coulomb-nuclear phase shifts $\delta_l(E)$ in some energy interval by varying the internal region boundary \mathbb{N} and the oscillator basis spacing $\hbar\Omega$ and next parametrize the phase shifts to have them in a wider energy interval. However the phase shift parametrization is more complicated for channels with charged colliding particles as discussed below.

An important scaling property of variational calculations with the harmonic oscillator basis was revealed in Refs. [9, 10]: the converging variational eigenenergies E_ν depend on $\hbar\Omega$ and \mathbb{N} not independently but only through a scaling variable

$$s = \frac{\hbar\Omega}{\mathbb{N} + 7/2}. \quad (5)$$

This scaling property was initially proposed in Refs. [9, 10] for the bound states. We have extended the scaling to the case of variational calculations with the harmonic oscillator basis of the unbound states [30, 31] within the SS-HORSE approach. The SS-HORSE extension to the case of charged particle scattering discussed here can be used to demonstrate that the long-range Coulomb interaction does not destroy the scaling property of the unbound states (see Ref. [34] for details).

2.2 Phase shift parametrization

The total partial-wave amplitude for scattering in the case of Coulomb and short-range interactions has the form of the sum of the purely Coulomb, $f_l^C(k)$, and Coulomb-nuclear, $f_l^{NC}(k)$, amplitudes [59],

$$f_l(k) = f_l^C(k) + f_l^{NC}(k), \quad (6)$$

which, in turn, are related to the purely Coulomb, $\sigma_l = \arg \Gamma(1+l+i\eta)$, and Coulomb-nuclear phase shifts, δ_l , as

$$f_l^C(k) = \frac{\exp(2i\sigma_l) - 1}{2ik}, \quad (7)$$

$$f_l^{NC}(k) = \exp(2i\sigma_l) \frac{\exp(2i\delta_l) - 1}{2ik}. \quad (8)$$

Analytic properties of the Coulomb-nuclear amplitude $f_l^{NC}(k)$ in the complex momentum plane differ from the analytic properties of the scattering amplitude for neutral particles. However, the *renormalized Coulomb-nuclear amplitude* [44,45],

$$\tilde{f}_l(E) = \frac{\exp(2i\delta_l) - 1}{2ik} \cdot \frac{\exp(2\pi\eta) - 1}{2\pi\eta} c_{l\eta}, \quad (9)$$

where

$$c_{l\eta} = \prod_{n=1}^l (1 + \eta^2/n^2)^{-1} \quad (l > 0), \quad c_{0\eta} = 1, \quad (10)$$

is identical in analytic properties on the real momentum axis with the scattering amplitude for neutral particles. In particular, the renormalized amplitude can be expressed [44,45]

$$\tilde{f}_l = \frac{k^{2l}}{\tilde{K}_l(E) - 2\eta k^{2l+1} H(\eta) (c_{l\eta})^{-1}} \quad (11)$$

in terms of the *Coulomb-modified effective-range function* [44,45]

$$\tilde{K}_l(E) = k^{2l+1} (c_{l\eta})^{-1} \left\{ \frac{2\pi\eta}{\exp(2\pi\eta) - 1} [\cot \delta_l(k) - i] + 2\eta H(\eta) \right\}, \quad (12)$$

where

$$H(\eta) = \Psi(i\eta) + (2i\eta)^{-1} - \ln(i\eta), \quad (13)$$

$\Psi(z)$ is the logarithmic derivative of the Γ function (digamma or Ψ function) [58]. In the absence of Coulomb interaction ($\eta = 0$), the Coulomb-modified effective-range function transforms into the standard effective-range function for neutral particle scattering,

$$\tilde{K}_l(E) = K_l(E) = k^{2l+1} \cot \delta_l, \quad (14)$$

while the renormalized amplitude becomes the conventional neutral particle scattering amplitude,

$$f_l(E) = \frac{k^{2l}}{K_l(E) - ik^{2l+1}}. \quad (15)$$

Due to their nice analytic properties, the renormalized Coulomb-nuclear amplitude, $\tilde{f}_l(E)$, and the neutral particle scattering amplitude, $f_l(E)$, can be used to parametrize respectively the Coulomb-nuclear and neutral particle scattering phase shifts ensuring their correct low-energy behavior. In Refs. [33,34], we introduced an auxiliary complex-valued function imbedding resonant pole parameters in the amplitude parametrization. These resonant pole parameters play a role of additional

fitting parameters in the phase-shift parametrization. Here we prefer to parametrize the Coulomb-modified effective-range function (12) or the standard effective-range function for neutral particle scattering (14) thus reducing the number of fit parameters. The resonant parameters are obtained by a numerical location of the amplitude pole as discussed below.

The Coulomb-modified effective-range function $\tilde{K}_l(E)$ as well as the effective-range function for neutral particle scattering $K_l(E)$ is real on the real axis of momentum k , is regular in the vicinity of zero, and admits an expansion in even powers of k , or, equivalently, in power series of the relative motion energy $E = \hbar^2 k^2 / 2\mu$ [44, 45],

$$\tilde{K}_l(E) = w_0 + w_1 E + w_2 E^2 + \dots \quad (16)$$

The expansion coefficients w_0 and w_1 are related to the so-called scattering length a_l and effective range r_l [59]:

$$w_0 = -\frac{1}{a_l}, \quad w_1 = \frac{r_l \mu}{\hbar^2}. \quad (17)$$

We use the expansion coefficients w_0 , w_1 and w_2 as fit parameters for the phase shift parametrization. Such a parametrization works well in the case of nucleon- α scattering but may fail in other problems. Note, as seen from Eq. (12) or Eq. (14), the energies at which the phase shift takes the values of $0, \pm\pi, \pm 2\pi, \dots$, are the singular points of the effective-range function. In the case of possible presence of such singular points in the range of energies of interest for a particular problem, one should use a more elaborate parametrization of the effective-range function, e. g., in the form of the Padé approximant.

2.3 Fitting process

In the case of neutral particle scattering, we combine Eqs. (1), (14) and (16) to obtain

$$w_0 + w_1 E + w_2 E^2 = k^{2l+1} \frac{C_{\mathbb{N}+2,l}(E)}{S_{\mathbb{N}+2,l}(E)}. \quad (18)$$

In the case of charged particle scattering, we derive a more complicated equation with the help of Eq. (3) and (12):

$$w_0 + w_1 E + w_2 E^2 = k^{2l+1} (c_{l\eta})^{-1} \times \left\{ -\frac{2\pi\eta}{\exp(2\pi\eta) - 1} \left[\frac{S_{\mathbb{N}+2,l}(E) W_b(n_l, G_l) + C_{\mathbb{N}+2,l}(E) W_b(j_l, G_l)}{S_{\mathbb{N}+2,l}(E) W_b(n_l, F_l) + C_{\mathbb{N}+2,l}(E) W_b(j_l, F_l)} + i \right] + 2\eta H(\eta) \right\}. \quad (19)$$

Let $E_\nu^{(i)}$, $i = 1, 2, \dots, D$, be a set of the lowest ($\nu = 0$) or some other particular eigenvalues ($\nu > 0$) of the Hamiltonian matrix truncated to the internal region of the basis space obtained with a set of parameters $(\mathbb{N}^{(i)}, \hbar\Omega^{(i)})$, $i = 1, 2, \dots, D$. We find energies $\mathcal{E}^{(i)}$ as solutions of Eq. (18) or Eq. (19) with some trial set of the effective-range function expansion coefficients w_0, w_1, w_2 for each combination of parameters $(\mathbb{N}^{(i)}, \hbar\Omega^{(i)})$ [note, the oscillator basis parameter $\hbar\Omega$ enters definitions of

functions $S_{N,l}(E)$ and $C_{N,l}(E)$]. The optimal set of the fit parameters w_0, w_1, w_2 parametrizing the phase shifts is obtained by minimizing the functional

$$\Xi = \sqrt{\frac{1}{D} \sum_{i=1}^D (E_\nu^{(i)} - \mathcal{E}^{(i)})^2}. \quad (20)$$

With the optimal set of the fit parameters w_0, w_1, w_2 we can use Eq. (18) or Eq. (19) to obtain the $\hbar\Omega$ dependences of the eigenenergies $E_\nu(\hbar\Omega)$ in any basis space N . Therefore Eqs. (18) and (19) provide extrapolation of the variational results for unbound states to larger basis spaces.

2.4 Resonance energy E_r and width Γ

We obtain resonance energies E_r and widths Γ by a numerical location of the S -matrix poles which coincide with the poles of scattering amplitude. If the amplitude has a resonant pole at a complex energy $E = E_p$, the resonance energy E_r and its width Γ are related to the real and imaginary part of E_p [59]:

$$E_p = E_r - i\frac{\Gamma}{2}. \quad (21)$$

It follows from Eqs. (11) and (15) that locating the pole of the scattering amplitude is equivalent to solving in the complex energy plane the equation

$$\mathcal{F}(E) \equiv \tilde{K}_l(E) - 2\eta k^{2l+1} H(\eta)(c_{l\eta})^{-1} = 0 \quad (22)$$

in the case of charged particle scattering or the equation

$$\mathcal{F}(E) \equiv K_l(E) - ik^{2l+1} = 0 \quad (23)$$

in the case of neutral particles. We can use the parametrization of functions $\tilde{K}_l(E)$ or $K_l(E)$ in Eqs. (22) and (23). To solve these equations, we calculate the integral

$$\Upsilon = \frac{1}{2\pi i} \oint_C \frac{\mathcal{F}'(E)}{\mathcal{F}(E)} dE \quad (24)$$

along some closed contour C in the complex energy plane, where $\mathcal{F}'(E) = \frac{d\mathcal{F}}{dE}$. The contour C should surround the area where we expect to have the pole of the amplitude. According to the theory of functions of a complex variable [60], the value of Υ is equal to the number of zeroes of the function $\mathcal{F}(E)$ in the area surrounded by the contour C . If needed, we modify the contour C to obtain

$$\Upsilon = 1. \quad (25)$$

The position of the pole in the energy plane is calculated as

$$E_p = \frac{1}{2\pi i} \oint_C E \frac{\mathcal{F}'(E)}{\mathcal{F}(E)} dE. \quad (26)$$

A numerical realization of the algorithm based on Eqs. (24)–(26) provides fast and stable locating of the poles of scattering amplitude.

3 Elastic scattering of nucleons by α particle in the NCSM-SS-HORSE approach

We present here an application of our SS-HORSE technique to nucleon- α scattering phase shifts and resonance parameters based on *ab initio* many-body calculations of ${}^5\text{He}$ and ${}^5\text{Li}$ nuclei within the NCSM with the realistic JISP16 and Daejeon16 NN interactions. The NCSM calculations are performed using the code MFDn [61,62] with basis spaces including all many-body oscillator states with excitation quanta N_{max} ranging from 2 up to 18 for both parities and with $\hbar\Omega$ values ranging from 10 to 40 MeV in steps of 2.5 MeV.

Note, for the NCSM-SS-HORSE analysis we need the ${}^5\text{He}$ and ${}^5\text{Li}$ energies relative respectively to the $n + \alpha$ and $p + \alpha$ thresholds. Therefore from each of the ${}^5\text{He}$ or ${}^5\text{Li}$ NCSM odd (even) parity eigenenergies we subtract the ${}^4\text{He}$ ground state energy obtained by the NCSM with the same $\hbar\Omega$ and the same N_{max} (with $N_{\text{max}} - 1$) excitation quanta, and in what follows these subtracted energies are referred to as the NCSM eigenenergies E_ν . Only these ${}^5\text{He}$ and ${}^5\text{Li}$ NCSM eigenenergies relative to the respective threshold are discussed below.

We note here that the NCSM utilizes the truncation based on the many-body oscillator quanta N_{max} while the SS-HORSE requires the oscillator quanta truncation of the interaction describing the relative motion of nucleon and α particle. A justification of using N_{max} for the SS-HORSE analysis is obvious if the α particle is described by the simplest four-nucleon oscillator function with excitation quanta $N_{\text{max}}^\alpha = 0$. Physically it is clear that the use of N_{max} within the SS-HORSE should work well also in a more general case when the α particle is presented by the wave function with $N_{\text{max}}^\alpha > 0$ due to the dominant role of the zero-quanta component in the α particle wave function. Instead of attempting to justify algebraically the use of N_{max} within the SS-HORSE, we suggested in Ref. [30,31] an *a posteriori* justification: we demonstrated in Ref. [30,31] that we obtained $n\alpha$ phase shift parametrizations consistent with the NCSM results obtained with very different N_{max} and $\hbar\Omega$ values; more, we were able to predict the NCSM results with large N_{max} using the phase shift parametrizations based on the NCSM calculations with much smaller model spaces. It was clearly impossible if the use of N_{max} truncation for the SS-HORSE analysis did not work properly. We perform the same *a posteriori* analysis of our results in this study of nucleon- α scattering to ensure the justification of our approach though do not present and discuss it below. Generally the fact that the phase shifts calculated using Eq. (1) or (3) at the NCSM eigenenergies obtained with different N_{max} truncations form a single curve as a function of energy serves as a confirmation of the consistency of the whole NCSM-SS-HORSE approach and of the use of the NCSM N_{max} for the SS-HORSE phase shift calculation in particular. The ranges of N_{max} and $\hbar\Omega$ values where this consistency is achieved differ for different NN interactions and different angular momenta and parities. Such a consistency which can be also interpreted as a convergence of the phase shift calculations is seen in the figures below to be achieved in all calculations at least at largest basis spaces in some range of $\hbar\Omega$ values.

3.1 Phase shifts of resonant $p\alpha$ scattering

The top left panel of Fig. 1 presents the results of the NCSM calculations of the ${}^5\text{Li } \frac{3}{2}^-$ ground state energies $E_0^{(i)}$ relative to the $p + \alpha$ threshold. The respective

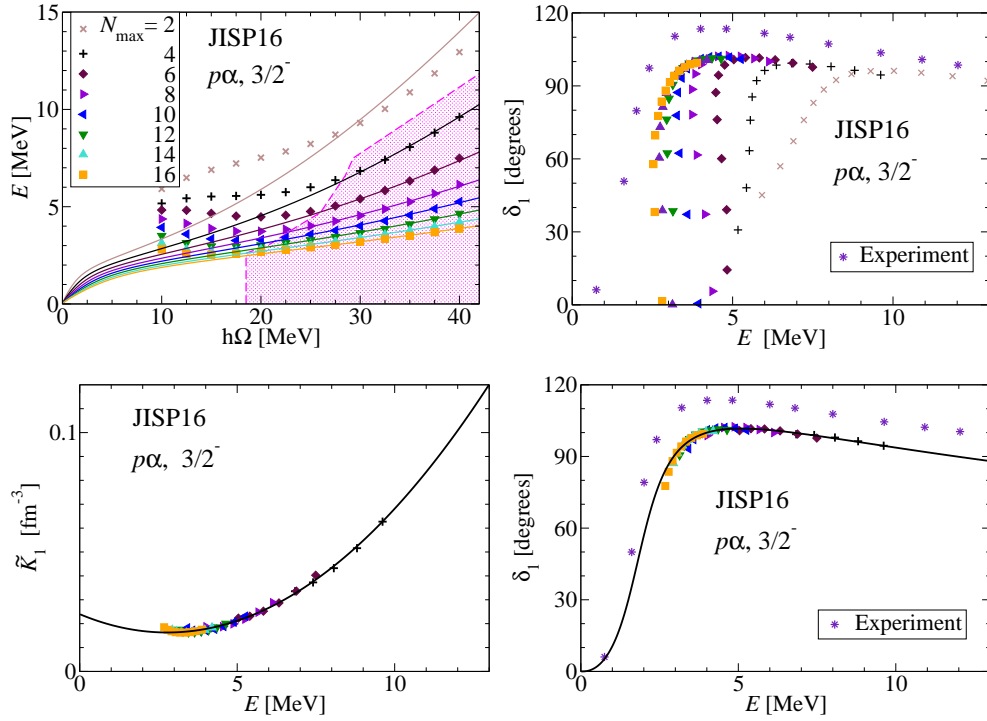


Figure 1: $p\alpha$ scattering in the $\frac{3}{2}^-$ state with JISP16 NN interaction. Top left: the lowest ${}^5\text{Li } \frac{3}{2}^-$ eigenenergies $E_0^{(i)}$ relative to the $p+\alpha$ threshold obtained by the NCSM with various N_{\max} (symbols) as functions of $\hbar\Omega$. The shaded area shows the energy values selected for the SS-HORSE analysis. Solid curves are solutions of Eq. (19) for energies E with parameters w_0 , w_1 and w_2 obtained by the fit. Top right: the $\frac{3}{2}^-$ $p\alpha$ phase shifts obtained directly for all calculated ${}^5\text{Li}$ eigenstates $E_0^{(i)}$ using Eq. (3). Bottom left: Coulomb-modified effective range function $\tilde{K}_l(E)$ calculated using Eq. (16) with parameters w_0 , w_1 and w_2 obtained by the fit (solid curve) and calculated using the r.h.s. of Eq. (19) at the selected eigenenergies $E_0^{(i)}$ (symbols). Bottom right: the fit of the $\frac{3}{2}^-$ $p\alpha$ phase shifts (solid curve) and the phase shifts obtained directly from the selected ${}^5\text{Li}$ eigenstates $E_0^{(i)}$ using Eq. (3) (symbols). Experimental data at the right panels (stars) are taken from Ref. [63].

phase shifts calculated using Eq. (3) for all ${}^5\text{Li}$ eigenstates $E_0^{(i)}$ are shown in the top right panel of Fig. 1.

For the SS-HORSE analysis we should select a set of consistent (converged) NCSM eigenstates $E_0^{(i)}$ which form a single curve of the phase shifts $\delta_l(E_0^{(i)})$ vs energy as discussed in detail in Refs. [30–34]. Alternatively one can use for the eigenstate selection the graph of $E_0^{(i)}$ vs the scaling parameter s or the graph of the Coulomb-modified effective range function points $\tilde{K}_l(E_0^{(i)})$ vs energy where the converged eigenstates should also form a single curve. Our selection of the eigenstates $E_0^{(i)}$ is illustrated by the shaded area in the top left panel of Fig. 1 while the method of the eigenstate

selection is seen from comparing the top right and bottom right panels in the same figure: the symbols in the top panel depict the phase shifts $\delta_1(E_0^{(i)})$ corresponding to all eigenstates $E_0^{(i)}$ while those in the bottom panel correspond to the selected eigenstates only. More details regarding the eigenstate selection can be found in Refs. [30,31] and we are not discussing the method of eigenstate selection in this paper in what follows.

A good quality of reproducing the Coulomb-modified effective range function points $\tilde{K}_l(E_0^{(i)})$ by the fit is illustrated by the bottom left panel in Fig. 1. We note the the quality of description by the fit of the functions $\tilde{K}_l(E)$ and $K_l(E)$ in cases of other states and interactions is approximately the same and we shall not present the graphs of these functions in what follows. A numerical estimate of the fit quality in our approach is the rms deviation Ξ of the eigenenergies $E_0^{(i)}$ presented in Table 1. It is seen that in all cases Ξ is of the order of few tens of keV.

The bottom right panel in Fig. 1 demonstrates a good quality of the fit of the phase shift points $\delta_1(E_0^{(i)})$. The fitted phase shifts are seen from this panel to be in a good correspondence with the results of the phase shift analysis of the experimental data of Ref. [63]. However the theoretical phase shift behavior indicates that the resonance has a slightly higher energy and a larger width than observed experimentally.

The results of the calculations of the same phase shifts with the Daejeon16 NN interaction are presented in Fig. 2. It is seen that in this case we reproduce the experimental phase shifts in the resonance region even better than with JISP16. However we can select for the SS-HORSE analysis much less NCSM results than in the case of JISP16: only the NCSM states obtained with Daejeon16 with $N_{\max} \geq 12$ are forming the same curve on the $\delta_1(E_0^{(i)})$ vs energy plot while in the JISP16 case we utilize for the SS-HORSE analysis the results with $N_{\max} \geq 4$. In other words, surprisingly, the convergence of continuum state calculations with the Daejeon16 NN interaction is much worse than with JISP16 while the Daejeon16 results in a much faster convergence of NCSM calculations for bound states of light nuclei [42]. The same trends in comparing convergence of Daejeon16 and JISP16 continuum calculations are seen in all the rest results presented here.

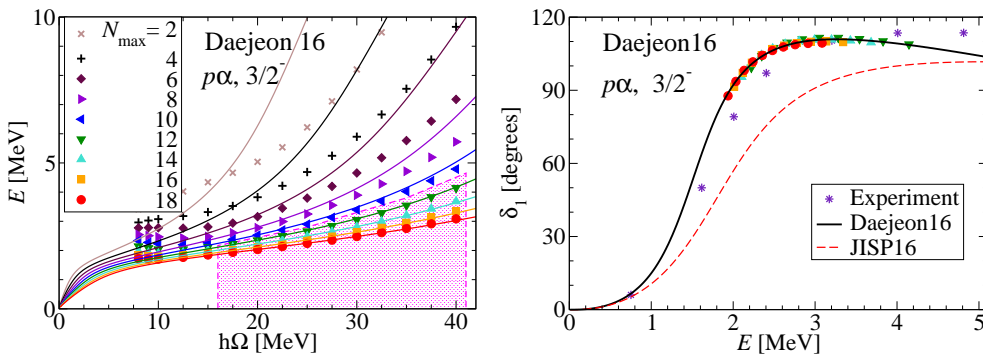


Figure 2: $p\alpha$ scattering in the $\frac{3}{2}^-$ state with Daejeon16 NN interaction. Dashed curve in the right panel presents phase shifts obtained with JISP16 for comparison. See Fig. 1 for other details.

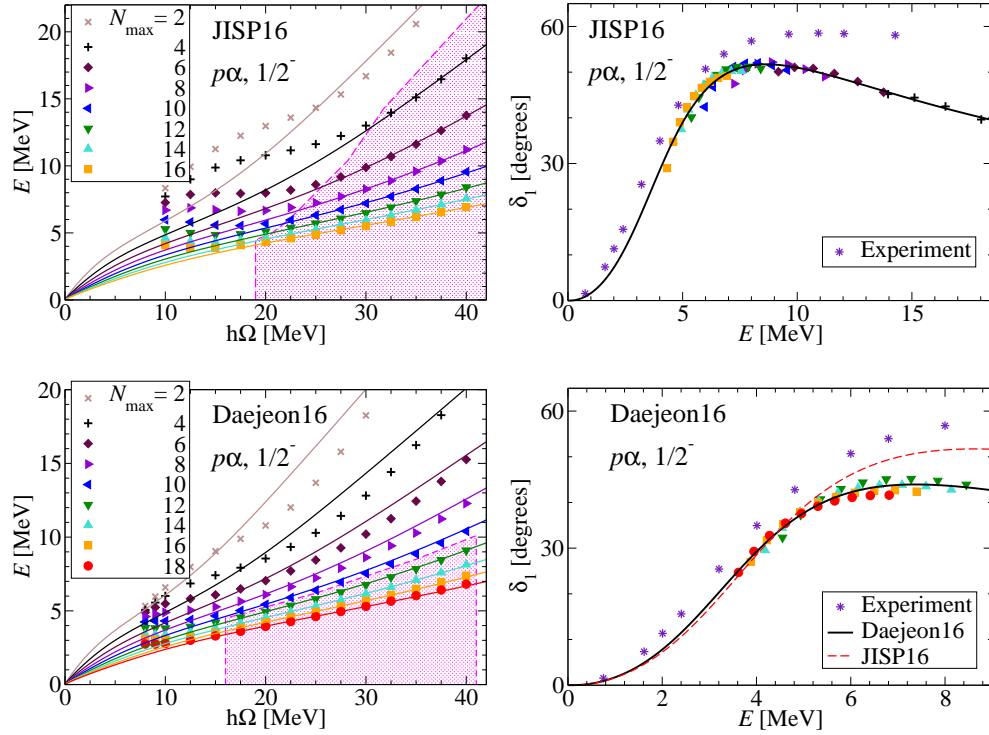


Figure 3: $p\alpha$ scattering in the $\frac{1}{2}^-$ state with JISP16 (top panels) and Daejeon16 (bottom panels) NN interactions. Dashed curve in the bottom right panel presents phase shifts obtained with JISP16 for comparison. See Fig. 1 for other details.

The results of calculations of the $p\alpha$ scattering in the $\frac{1}{2}^-$ state with JISP16 and Daejeon16 are presented in Fig. 3. Both interactions are reproducing well the experimental data in the resonance region while the JISP16 phase shifts are closer to the experiment at higher energies.

3.2 Phase shifts of resonant $n\alpha$ scattering

We have studied the $n\alpha$ scattering within the NCSM-SS-HORSE approach with the JISP16 NN interaction in Refs. [30,31]. We present for completeness the resonant $n\alpha$ phase shifts obtained with Daejeon16 in Fig. 4 in comparison with those from JISP16. As in the case of the $p\alpha$ scattering, the narrower $\frac{3}{2}^-$ resonance is better described by the Daejeon16 than by the JISP16 interaction while the description of the wider $\frac{1}{2}^-$ resonance region is nearly the same by both interaction but the $\frac{1}{2}^-$ phase shift behavior at energies above the resonant is reproduced better by JISP16. We note again a faster convergence of the JISP16 calculations of $n\alpha$ scattering phase shifts as compared with those with Daejeon16.

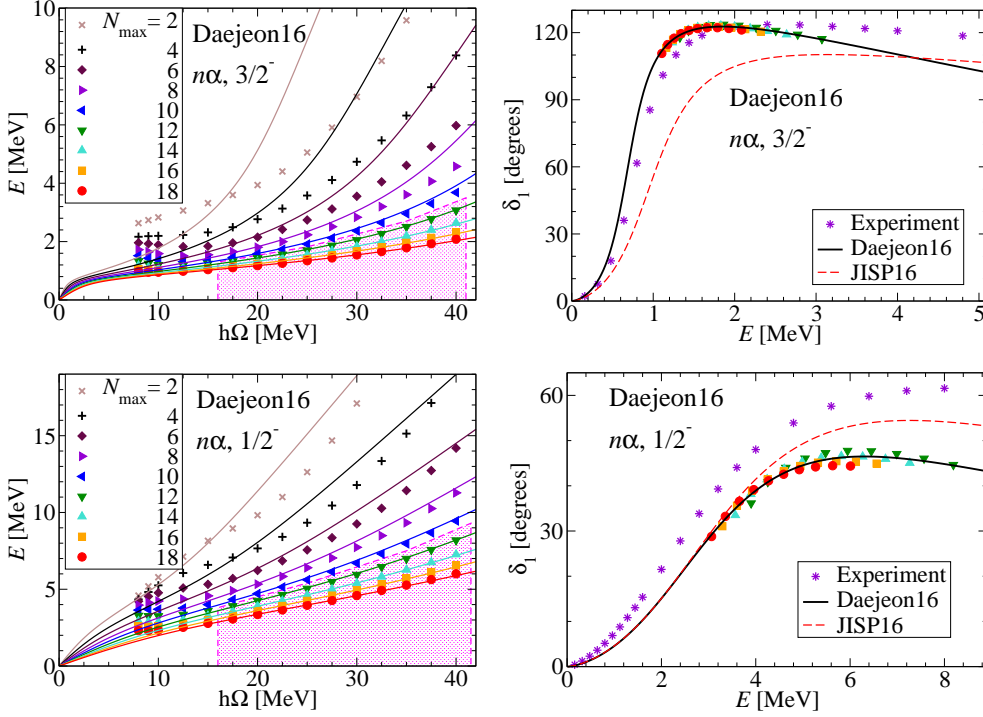


Figure 4: $n\alpha$ scattering in the $\frac{3}{2}^-$ (top panels) and $\frac{1}{2}^-$ (bottom panels) states with the Daejeon16 NN interaction. Dashed curves in the right panels present phase shifts obtained with JISP16 [30] for comparison. Experimental data (stars) are taken from Ref. [64]. See Fig. 1 for other details.

3.3 $\frac{3}{2}^-$ and $\frac{1}{2}^-$ resonances in ${}^5\text{Li}$ and ${}^5\text{He}$ nuclei

The results for energies and widths of the $\frac{3}{2}^-$ and $\frac{1}{2}^-$ resonances in ${}^5\text{Li}$ and ${}^5\text{He}$ nuclei with respect to the nucleon + α threshold obtained by the numerical location of the scattering amplitude poles as described in Subsection 2.4, are presented in Table 1. For comparison, we present in Table 1 also the results for the ${}^5\text{Li}$ resonances obtained with $\chi\text{EFT } NN$ and NNN interactions in the *ab initio* NCSM/RGM approach in Ref. [49]. We note that the energy of the resonance was calculated in Ref. [49] as a position of the maximum of the derivative $\frac{d\delta_l(E)}{dE}$ while the resonance width was evaluated as $\Gamma = 2/(d\delta_l/dE)|_{E=E_r}$. The phase shift $\delta_l(E)$ may have a contribution from a non-resonant background which can result in some shift of the resonance energy E_r and in a modification of its width Γ in such calculations as compared with a more theoretically substantiated method relating the resonance parameters to the S -matrix and/or scattering amplitude pole. The differences in energy and width from these different type calculations may be large for wide resonances.

We note that all *ab initio* calculations of resonance parameters in ${}^5\text{Li}$ and ${}^5\text{He}$ nuclei provide a good description of the experimental data of Ref. [65]. The difference in $\frac{3}{2}^-$ resonance energies in both nuclei obtained with different interactions is less than 300 keV, and the experimental resonance energies are within the respective

Table 1: Energies E_r and widths Γ of resonant states $\frac{3}{2}^-$ and $\frac{1}{2}^-$ in ${}^5\text{Li}$ and ${}^5\text{He}$ obtained in the NCSM-SS-HORSE approach with JISP16 and Daejeon16 NN interactions. Ξ presents the rms deviation of energies obtained in the fit. The NCSM/RGM results obtained with $\chi\text{EFT } NN$ and NNN interactions are from Ref. [49] and the experimental results are from Ref. [65].

	E_r (MeV)	Γ (MeV)	Ξ (keV)	E_r (MeV)	Γ (MeV)	Ξ (keV)	Δ (MeV)
	${}^5\text{Li}, 3/2^-$			${}^5\text{Li}, 1/2^-$			
Experiment	1.69	1.23		3.18	6.60		1.49
JISP16	1.80	1.79	45	3.57	6.09	65	1.77
Daejeon16	1.52	1.05	24	3.21	5.63	50	1.70
$\chi\text{EFT } NN + NNN$	1.77	1.70		3.11	7.90		1.34
	${}^5\text{He}, 3/2^-$			${}^5\text{He}, 1/2^-$			
Experiment	0.80	0.65		2.07	5.57		1.27
JISP16	0.94	1.02	40	2.63	5.31	62	1.69
Daejeon16	0.68	0.52	22	2.45	5.07	48	1.77

intervals of predictions obtained with different interactions. The theoretical predictions for the $\frac{3}{2}^-$ resonance widths also embrace the experimental values. However the spread of theoretical predictions for the $\frac{3}{2}^-$ resonance width is about 750 keV in the case of ${}^5\text{Li}$ and about 500 keV in the case of ${}^5\text{He}$ that are large numbers as compared with the width value.

In the case of the wider $\frac{1}{2}^-$ resonances in ${}^5\text{Li}$ and ${}^5\text{He}$ nuclei, the spreads of predictions for ${}^5\text{Li}$ also embrace the respective experimental energy and width values while our predictions for the ${}^5\text{He}$ resonance energy are slightly above and for the width are slightly below the experiment. However the spreads of the theoretical predictions for both energy and width of the $\frac{1}{2}^-$ resonances in ${}^5\text{Li}$ and ${}^5\text{He}$ do not exceed approximately 450 keV with an exception of the NCSM/RGM $\chi\text{EFT } NN + NNN$ prediction for the $\frac{1}{2}^-$ ${}^5\text{Li}$ resonance width. Even the 2.3 MeV difference between our Daejeon16 and $\chi\text{EFT } NN + NNN$ prediction of Ref. [49] for the $\frac{1}{2}^-$ ${}^5\text{Li}$ resonance width is much smaller than the experimental width. Therefore we can say that the relative accuracy of the *ab initio* predictions for the $\frac{1}{2}^-$ resonances in ${}^5\text{Li}$ and ${}^5\text{He}$ nuclei is much better than that for the $\frac{3}{2}^-$ resonances.

The difference $\Delta = (E_r^{1/2^-} - E_r^{3/2^-})$ between the energies of the $\frac{1}{2}^-$ and $\frac{3}{2}^-$ resonances in ${}^5\text{He}$ and ${}^5\text{Li}$ nuclei can be associated with the spin-orbit splitting of respectively neutrons and protons in the p shell. The Δ values are presented in Table 1. The $\chi\text{EFT } NN + NNN$ interaction slightly underestimates the proton spin-orbit splitting while JISP16 and Daejeon16 overestimate both proton and neutron spin-orbit splittings. It is interesting to note that the differences between our predictions with JISP16 and Daejeon16 for the resonance energies are of the order of 300 keV while the differences in Δ values are only about 75 keV. It is more important to note that the charge-independent JISP16 and Daejeon16 NN interactions support nearly

the same p -shell spin-orbit splittings for protons and neutrons while the experimental spin-orbit splitting for protons exceeds that for neutrons by approximately 200 keV.

3.4 Non-resonant $p\alpha$ scattering

We have used the NCSM-SS-HORSE approach in Ref. [30–32] for calculations of resonant as well as non-resonant $n\alpha$ scattering. The non-resonant phase shifts can be also calculated within the current extension of the NCSM-SS-HORSE to the case of channels with charged colliding particles. Contrary to the phase shifts parametrizations based on the S -matrix analytic properties utilized on Ref. [30–32], we use the same Coulomb-modified effective-range function parametrization of Eq. (16) for both resonant and non-resonant scattering.

The results of calculations of the non-resonant $p\alpha$ scattering phase shifts in the $\frac{1}{2}^+$ state with JISP16 and Daejeon16 NN interactions are presented in Fig. 5. It is seen that JISP16 provides a faster convergence of the phase shifts in this case too. The results obtained with JISP16 and Daejeon16 are close to each other and reproduce well the experimental phase shifts of Ref. [63].

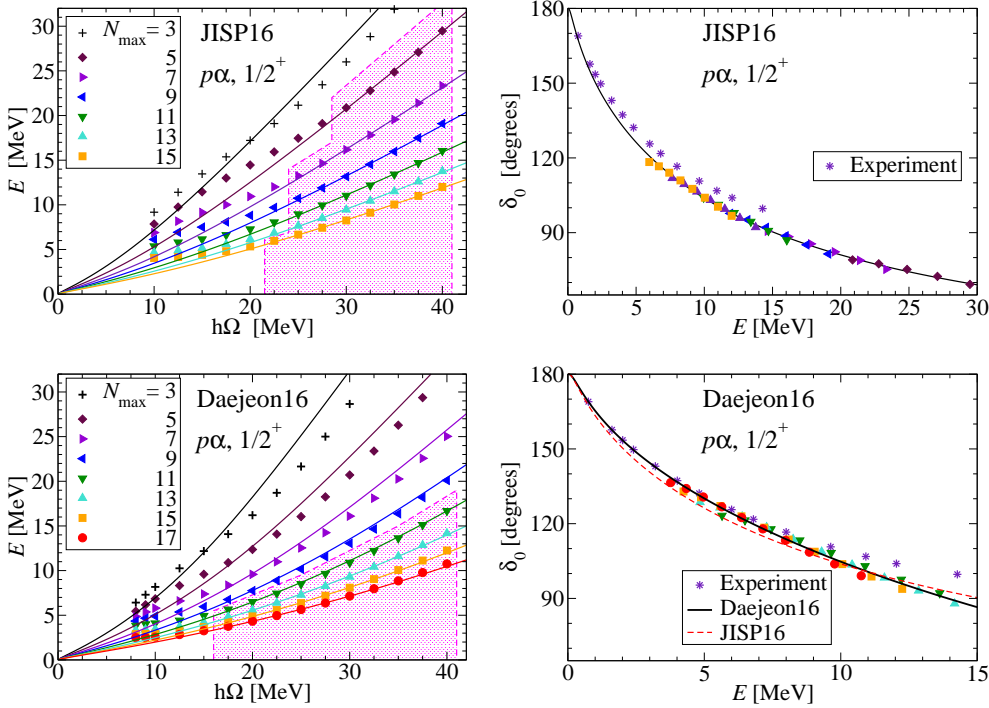


Figure 5: Non-resonant $p\alpha$ scattering in the $\frac{1}{2}^+$ state with JISP16 (top panels) and Daejeon16 (bottom panels) NN interactions. Dashed curve in the bottom right panel presents phase shifts obtained with JISP16 for comparison. See Fig. 1 for other details.

4 Summary

We present here an extension of the *ab initio* NCSM-SS-HORSE approach to the case of channels with charged colliding particles where the relative motion wave function asymptotics is distorted by the Coulomb interaction. The extended approach is applied to the study of $p\alpha$ scattering and resonances in ${}^5\text{Li}$ nucleus with realistic JISP16 and Daejeon16 NN interaction. The analysis of the $n\alpha$ scattering and resonances in ${}^5\text{He}$ nucleus with JISP16 NN interaction has been performed by us in Ref. [30–32]; we complete this analysis here by the corresponding calculations with Daejeon16.

We demonstrate that the extended NCSM-SS-HORSE approach works with approximately the same accuracy and convergence rate as its non-extended version applicable to the channels with neutral particles. Surprisingly, we obtain that the JISP16 interaction provides a faster convergence of the $n\alpha$ and $p\alpha$ phase shifts than the Daejeon16 while the convergence of bound states in light nuclei within NCSM is much faster with Daejeon16 than with JISP16 [42].

Both JISP16 and Daejeon16 provide a good description of the $\frac{3}{2}^-$ and $\frac{1}{2}^-$ resonances in ${}^5\text{Li}$ and ${}^5\text{He}$ nuclei as well as of the $\frac{1}{2}^+$ non-resonant $n\alpha$ and $p\alpha$ phase shifts. However the spin-orbit splitting of nucleons in the p shell is overestimated by these interactions; more, these charge-independent NN interactions provide nearly the same result for the spin-orbit splitting of neutrons and protons while experimentally the spin-orbit splittings for neutrons and protons differ by approximately 200 keV.

Acknowledgments

We are thankful to V. D. Efros and P. Maris for valuable discussions.

This work is supported in part by the Russian Foundation for Basic Research under Grant No. 15-02-06604-a and No. 16-02-00049-a, by the U.S. Department of Energy under Grants No. DESC00018223 (SciDAC/NUCLEI) and No. DE-FG02-87ER40371, by the US National Science Foundation under Grant No. 1516181, by the Rare Isotope Science Project of Institute for Basic Science funded by Ministry of Science and ICT and National Research Foundation of Korea (2013M7A1A1075764). Computational resources were provided by the National Energy Research Scientific Computing Center (NERSC), which is supported by the Office of Science of the U.S. Department of Energy under Contract No. DE-AC02-05CH11231, and by the Supercomputing Center/Korea Institute of Science and Technology Information including technical support (KSC-2015-C3-003).

References

- [1] W. Leidemann and G. Orlandini, *Prog. Part. Nucl. Phys.* **68**, 158 (2013).
- [2] S. C. Pieper and R. B. Wiringa, *Ann. Rev. Nucl. Part. Sci.* **51**, 53 (2001).
- [3] B. R. Barrett, P. Navrátil and J. P. Vary, *Prog. Part. Nucl. Phys.* **69**, 131 (2013).
- [4] H. Kümmela, K. H. Lührmann and J. Zabolitzky, *Phys. Rep.* **36**, 1 (1978).
- [5] G. Hagen, D. J. Dean, M. Hjorth-Jensen, T. Papenbrock and A. Schwenk, *Phys. Rev. C* **76**, 044305 (2007).

- [6] D. Lee, *Prog. Part. Nucl. Phys.* **63**, 117 (2009).
- [7] E. Epelbaum, H. Krebs, D. Lee and U. G. Meissner, *Phys. Rev. Lett.* **106**, 192501 (2011).
- [8] P. Maris, J. P. Vary and A. M. Shirokov, *Phys. Rev. C* **79**, 014308 (2009).
- [9] S. A. Coon, M. I. Avetian, M. K. G. Kruse, U. van Kolck, P. Maris and J. P. Vary, *Phys. Rev. C* **86**, 054002 (2012).
- [10] S. A. Coon, in *Proc. Int. Workshop Nucl. Theor. Supercomputing Era (NTSE-2012), Khabarovsk, Russia, June 18–22, 2012*, eds. A. M. Shirokov and A. I. Mazur. Pacific National University, Khabarovsk, 2013, p. 171, http://www.ntse-2012.khb.ru/Proc/S_Coon.pdf.
- [11] R. J. Furnstahl, G. Hagen and T. Papenbrock, *Phys. Rev. C* **86**, 031301(R) (2012).
- [12] S. N. More, A. Ekstrom, R. J. Furnstahl, G. Hagen and T. Papenbrock, *Phys. Rev. C* **87**, 044326 (2013).
- [13] M. K. G. Kruse, E. D. Jurgenson, P. Navrátil, B. R. Barrett and W. E. Ormand, *Phys. Rev. C* **87**, 044301 (2013).
- [14] D. Sääf and C. Forssén, *Phys. Rev. C* **89**, 011303 (2014).
- [15] R. J. Furnstahl, S. N. More and T. Papenbrock, *Phys. Rev. C* **89**, 044301 (2014).
- [16] S. König, S. K. Bogner, R. J. Furnstahl, S. N. More and T. Papenbrock, *Phys. Rev. C* **90**, 064007 (2014).
- [17] R. J. Furnstahl, G. Hagen, T. Papenbrock and K. A. Wendt, *J. Phys. G* **42**, 034032 (2015).
- [18] K. A. Wendt, C. Forssén, T. Papenbrock and D. Sääf, *Phys. Rev. C* **91**, 061301 (2015).
- [19] S. A. Coon and M. K. G. Kruse, *Int. J. Mod. Phys. E* **25**, 1641011 (2016).
- [20] L. D. Faddeev and S. P. Merkuriev, *Quantum scattering theory for several particle systems*. Kluwer, Dordrecht, 1993.
- [21] E. O. Alt, P. Grassberger and W. Sandhas, *Nucl. Phys. B* **2**, 167 (1967).
- [22] P. Navrátil, R. Roth and S. Quaglioni, *Phys. Rev. C* **82**, 034609 (2010).
- [23] P. Navrátil, S. Quaglioni, I. Stetcu, B. R. Barrett, *J. Phys. G* **36**, 083101 (2009).
- [24] P. Navrátil, S. Quaglioni, G. Hupin, C. Romero-Redondo and A. Calci, *Phys. Scr.* **91**, 053002 (2016).
- [25] V. D. Efros, W. Leidemann, G. Orlandini and N. Barnea, *J. Phys. G* **34**, R459 (2007).
- [26] K. M. Nollett, S. C. Pieper, R. B. Wiringa, J. Carlson and G. M. Hale, *Phys. Rev. Lett.* **99**, 022502 (2007).

- [27] G. Papadimitriou, J. Rotureau, N. Michel, M. Płoszajczak and B. R. Barrett, *Phys. Rev. C* **88**, 044318 (2013).
- [28] A. M. Shirokov, A. I. Mazur, J. P. Vary and E. A. Mazur, *Phys. Rev. C* **79**, 014610 (2009).
- [29] A. M. Shirokov, A. I. Mazur, E. A. Mazur and J. P. Vary, *Appl. Math. Inf. Sci.* **3**, 245 (2009).
- [30] A. M. Shirokov, A. I. Mazur, I. A. Mazur and J. P. Vary, *Phys. Rev. C* **94**, 064320 (2016).
- [31] A. I. Mazur, A. M. Shirokov, I. A. Mazur and J. P. Vary, in *Proc. Int. Conf. Nucl. Theor. Supercomputing Era (NTSE-2014), Khabarovsk, Russia, June 23–27, 2014*, eds. A. M. Shirokov and A. I. Mazur. Pacific National University, Khabarovsk, 2016, p. 183, <http://www.ntse-2014.khb.ru/Proc/A.Mazur.pdf>.
- [32] I. A. Mazur, A. M. Shirokov, A. I. Mazur and J. P. Vary, *Phys. Part. Nucl.* **48**, 84 (2017).
- [33] L. D. Blokhintsev, A. I. Mazur, I. A. Mazur, D. A. Savin and A. M. Shirokov, *Yad. Fiz.* **80**, 102 (2017) [*Phys. Atom. Nucl.* **80**, 226 (2017)].
- [34] L. D. Blokhintsev, A. I. Mazur, I. A. Mazur, D. A. Savin and A. M. Shirokov, *Yad. Fiz.* **80**, 619 (2017) [*Phys. Atom. Nucl.* **80**, 1093 (2017)].
- [35] A. M. Shirokov, J. P. Vary, A. I. Mazur and T. A. Weber, *Phys. Lett. B* **644**, 33 (2007); a Fortran code generating the JISP16 matrix elements is available at http://lib.dr.iastate.edu/energy_datasets/2/.
- [36] R. I. Jibuti and N. B. Krupennikova, *The method of hyperspherical functions in the quantum mechanics of few bodies*. Metsniereba, Tbilisi, 1984 (*in Russian*).
- [37] R. I. Jibuti, *Fiz. Elem. Chastits At. Yadra* **14**, 741 (1983).
- [38] A. M. Shirokov, G. Papadimitriou, A. I. Mazur, I. A. Mazur, R. Roth and J. P. Vary, in *Proc. Int. Conf. Nucl. Theor. Supercomputing Era (NTSE-2014), Khabarovsk, Russia, June 23–27, 2014*, eds. A. M. Shirokov and A. I. Mazur. Pacific National University, Khabarovsk, 2016, p. 174, <http://www.ntse-2014.khb.ru/Proc/Shirokov.pdf>.
- [39] A. M. Shirokov, G. Papadimitriou, A. I. Mazur, I. A. Mazur, R. Roth and J. P. Vary, *Phys. Rev. Lett.* **117**, 182502 (2016).
- [40] I. A. Mazur, A. M. Shirokov, A. I. Mazur, I. J. Shin, Y. Kim and J. P. Vary, *see these Proceedings*, p. 280, <http://www.ntse-2016.khb.ru/Proc/IMazur.pdf>.
- [41] K. Kisamori *et al.*, *Phys. Rev. Lett.* **116**, 052501 (2016).
- [42] A. M. Shirokov, I. J. Shin, Y. Kim, M. Sosonkina, P. Maris and J. P. Vary, *Phys. Lett. B* **761**, 87 (2016); a Fortran code generating the Daejeon16 matrix elements is available at http://lib.dr.iastate.edu/energy_datasets/1/.
- [43] D. R. Entem and R. Machleidt, *Phys. Lett. B* **524**, 93 (2002); *Phys. Rev. C* **68**, 041001(R) (2003).

- [44] J. Hamilton, I. Øverbö and B. Tromborg, Nucl. Phys. B **60**, 443 (1973).
- [45] H. van Haeringen, *Charged-particle interactions. Theory and formulas*. Coulomb Press Leyden, Leiden, 1985.
- [46] J. M. Bang, A. I. Mazur, A. M. Shirokov, Yu. F. Smirnov and S. A. Zaytsev, Ann. Phys. (NY) **280**, 299 (2000).
- [47] S. Quaglioni and P. Navrátil, Phys. Rev. C **79**, 044606 (2009).
- [48] G. Hupin, J. Langhammer, P. Navrátil, S. Quaglioni, A. Calci and R. Roth, Phys. Rev. C **88**, 054622 (2013).
- [49] G. Hupin, S. Quaglioni and P. Navrátil, Phys. Rev. C **90**, 061601(R) (2014).
- [50] E. J. Heller and H. A. Yamani, Phys. Rev. A **9**, 1201 (1974).
- [51] H. A. Yamani and L. J. Fishman, J. Math. Phys, **16**, 410 (1975).
- [52] G. F. Filippov and I. P. Okhrimenko, Yad. Fiz. **32**, 932 (1980) [Sov. J. Nucl. Phys. **32**, 480 (1980)]; G. F. Filippov, Yad. Fiz. **33**, 928 (1981) [Sov. J. Nucl. Phys. **33**, 488 (1981)].
- [53] Yu. F. Smirnov and Yu. I. Nechaev, Kinam **4**, 445 (1982); Yu. I. Nechaev and Yu. F. Smirnov, Yad. Fiz. **35**, 1385 (1982) [Sov. J. Nucl. Phys. **35**, 808 (1982)].
- [54] A. M. Shirokov, Yu. F. Smirnov and S. A. Zaytsev, in *Modern problems in quantum theory*, eds. V. I. Savrin and O. A. Khrustalev. Moscow State University, Moscow, 1998, p. 184.
- [55] S. A. Zaytsev, Yu. F. Smirnov and A. M. Shirokov, Teor. Mat. Fiz. **117**, 227 (1998) [Theor. Math. Phys. **117**, 1291 (1998)].
- [56] H. A. Yamani and M. S. Abdelmonem, J. Phys. A **26**, L1183 (1993).
- [57] H. A. Yamani, Eur. J. Phys. **34**, 1025 (2013).
- [58] M. Abramowitz and I. A. Stegun (eds.), *Handbook on mathematical functions*. Dover, New York, 1972; NIST digital library of mathematical functions, <http://dlmf.nist.gov/>.
- [59] R. G. Newton, *Scattering theory of waves and particles, 2nd. ed.* Springer-Verlag, New York, 1982.
- [60] A. G. Sveshnikov and A. N. Tikhonov, *The theory of functions of a complex variable, 2nd. ed.* Mir Publishers, Moscow, 1978.
- [61] P. Maris, M. Sosonkina, J. P. Vary, E. G. Ng and C. Yang, Proc. Comput. Sci. **1**, 97 (2010).
- [62] H. M. Aktulga, C. Yang, E. G. Ng, P. Maris and J. P. Vary, Concurrency Computat.: Pract. Exper. **26**, 2631 (2014).
- [63] D. C. Dodder, G. M. Hale, N. Jarmie, J. H. Jett, P. W. Keaton, Jr., R. A. Nisley and K. Witte, Phys. Rev. C **15**, 518 (1977).

- [64] R. A. Arndt, D. D. Long and L. D. Roper, Nucl. Phys. A **209**, 429 (1973).
- [65] A. Csótó and G. M. Hale, Phys. Rev. C **55**, 536 (1997).

Solving Few-Body Scattering Problems in a Discrete Representation by Using GPU

O. A. Rubtsova, V. N. Pomerantsev and V. I. Kukulin

*Skobeltsyn Institute of Nuclear Physics, Lomonosov Moscow State University, Moscow
119991, Russia*

Abstract

Different aspects of the Wave-Packet Continuum Discretization method are discussed in applications to few-body scattering problems. Scattering observables in multichannel two-body problems can be found by diagonalization of the total Hamiltonian in the free wave-packet basis without solving the scattering equations at all. In few-body case, wave functions and operators are projected into the discrete wave-packet representation which results in a matrix reduction of integral equations of the scattering theory. The necessary boundary conditions are taken into account by an employment of the finite-dimensional (matrix) representations for the free and channel resolvents. As a numerical illustration, we consider the nd scattering problem with realistic NN interaction, which is solved via the highly parallelized computational scheme on an ordinary PC within the GPU technique.

Keywords: *Scattering theory; discretization of continuum; graphics processing unit*

1 Introduction

A consistent solution for few-body scattering problems has been done, as is well known, many years ago by Faddeev and Yakubovsky [1] which gave rise to an extensive few-body activity worldwide both in theory and experiment. However, a practical solving of such problems still presents a difficult numerical task in spite of a great progress in computational facilities. Alternatively, the methods which use L_2 -normalized wave functions for continuum states in solving multi-channel and few-body scattering problems have been developed. Such methods are very useful nowadays in nuclear and atomic physics [2–5]. Some of them are adapted for treating the realistic interactions in few-nucleon systems (see the recent review [6]).

About a decade ago, our group in Moscow State University has developed an original approach [7–10] which allows to formulate problems in the continuum in terms of normalized analogs of initial scattering states, i. e., stationary wave packets (WPs) or eigendifferentials as they were introduced by Herman Weyl [11]. One of the central points of the approach is an analytical finite-dimensional representation for

Proceedings of the International Conference ‘Nuclear Theory in the Supercomputing Era — 2016’ (NTSE-2016), Khabarovsk, Russia, September 19–23, 2016. Eds. A. M. Shirokov and A. I. Mazur. Pacific National University, Khabarovsk, Russia, 2018, p. 205.

<http://www.ntse-2016.khb.ru/Proc/Rubtsova.pdf>.

the few-body free and channel resolvents. The solution scheme is realized in a discrete (on energy and momentum) representation allowing to replace few-body scattering integral equations by their matrix analogs. A detailed description of the entire wave-packet continuum discretization (WPCD) approach and its various applications can be found in our review paper [7].

The above WPCD method as well as a treatment of L_2 functions in the discretized continuum, have several important features [7]. First, according to the finite norms of states, one can take into account the long-range Coulomb interaction without any screening by using the Coulomb wave-packet formalism. Moreover, these normalized Coulomb WPs can be approximated in some appropriate L_2 basis and even in the basis of free WPs (the normalized analogs of the plane waves). Second, due to the matrix form of the resulting equations, there are no additional difficulties in treating non-local potentials (as well as complex-valued interaction operators). The numerical scheme remains the same. This fact is very important for the present direct nuclear reaction studies, where non-local interactions are employed instead of usual local energy-dependent potentials [12]. Another important feature is related to the fact that we use the integral equation formalism in the scattering theory with accurate approximations for the resolvents in the kernels which allows to avoid an explicit account of the boundary conditions. In particular, there are no difficulties to treat accurately closed channels in the coupled-channel problems [7].

In the present paper, we discuss mainly two issues of the general WPCD approach. A special attention is focused on the diagonalization technique, i. e., the discrete spectral shift (DSS) formalism, which allows to find scattering observables in a multichannel two-body problem by making use of spectral properties of the total and free Hamiltonians without solving scattering equations at all. The DSS method has a close relation to the Lüscher finite volume approach [13] which is well known in the lattice QCD applications [14]. Also our method has similar features with the SS-HORSE method which has been developed very recently [15, 16].

Another important theme studied here is a development of an efficient numerical scheme for a solution of few-body scattering problems in the Faddeev framework within the WPCD approach. Recently [9] we have performed a parallel optimization of our computational scheme for the nd elastic scattering problem and adapted it for a practical realization on a desk PC with the graphics processing unit (GPU). So, we describe the details of such an optimization in the present paper.

The paper is organized as follows. The definition of the stationary wave packets and their basic properties are given in Section 2. Section 3 is dedicated to the diagonalization technique which allows to find scattering observables as well as off-shell t matrix in a multichannel scattering problem without solving the scattering theory equations. A brief description of the closed WPCD formalism in solving few-body scattering problems via the matrix analogs of scattering equations is given in Section 4. The details of a practical solution of the discretized Faddeev equation for the three-nucleon system by using the GPU, are presented in Section 5. We summarize the main results in the last Section 6.

2 Stationary wave packets and their properties

2.1 Stationary wave packets

Let us consider some two-body Hamiltonian $h = h_0 + v$ where h_0 is a free Hamiltonian (kinetic energy operator) and v is an interaction potential, and divide the continuous spectrum of h into a set of non-overlapping intervals $\{[\mathcal{E}_{k-1}, \mathcal{E}_k]\}_{k=1}^N$. The stationary WPs are constructed as integrals of exact scattering wave functions $|\psi_p\rangle$ over corresponding momentum intervals $\mathfrak{D}_k \equiv [p_{k-1}, p_k]$ (with $p_k = \sqrt{2m\mathcal{E}_k}$):

$$|z_k\rangle = \frac{1}{\sqrt{B_k}} \int_{\mathfrak{D}_k} f(p) |\psi_p\rangle dp, \quad B_k \equiv \int_{\mathfrak{D}_k} |f(p)|^2 dp, \quad (1)$$

where m is the reduced mass of the system, B_k and $f(p)$ are normalization factors and weight functions respectively which are interrelated.

The states (1) are well known as the Weyl's eigendifferentials [11]. The integration over the energy (or momentum) intervals is just enough to make normalized wave-functions for the continuum. Then a complete system of eigenfunctions of the Hamiltonian h , according to Weyl, can be constructed from its bound states $\{|\psi_n\rangle\}_{n=1}^{N_b}$ and eigendifferentials (see the details in Ref. [7]). In such a representation, the Hamiltonian h as well as its resolvent $g(E) = [E + i0 - h]^{-1}$ have explicit diagonal forms (see below).

These properties are valid not only for short-range potentials. In fact, one can build similar wave packets for a Hamiltonian which includes the long-range repulsive¹ Coulomb interaction, i. e.,

$$h_C = h_0 + \frac{z_1 z_2 e^2}{r}, \quad (2)$$

where z_1 and z_2 are the particle charges, r is the distance between them. For this Hamiltonian, one can introduce the *Coulomb wave packets* $|x_k^C\rangle$ as the basis functions. These Coulomb WPs are built from the regular Coulomb wave functions $F_l(p, r)$ (for each partial wave l) by an integration over discretization intervals quite similarly to the general case [7]:

$$|x_k^C\rangle = \frac{1}{\sqrt{B_k}} \int_{\mathfrak{D}_k} dp f(p) |F_l(p)\rangle. \quad (3)$$

The states (3) are normalized, so that they can be practically constructed using pseudostates of the Coulomb Hamiltonian (2) on some L_2 basis.

2.2 Discrete representation for the total resolvent

The most useful property of the WP states of some Hamiltonian h is that one can construct a finite-dimensional representation for its resolvent $g(E) = [E + i0 - h]^{-1}$. For this purpose, the projector onto the WP space \mathfrak{p} should be defined:

$$\mathfrak{p} = \sum_{n=1}^{N_b} |\psi_n\rangle \langle \psi_n| + \sum_{k=1}^N |z_k\rangle \langle z_k|, \quad (4)$$

¹The Coulomb attraction can be also treated in the WP approach, however it requires a separate study.

where $|\psi_n\rangle$ are the bound-state wave functions. So that, one gets analytically the finite-dimensional representation for the projected resolvent [7],

$$\mathbf{g}(E) = \mathbf{p}g(E)\mathbf{p} = \sum_{n=1}^{N_b} \frac{|\psi_n\rangle\langle\psi_n|}{E - E_n} + \sum_{k=1}^N |z_k\rangle g_k(E) \langle z_k|, \quad (5)$$

where E_n are bound-state energies, and the eigenvalues $g_k(E)$ do not depend on interaction but depend on discretization parameters only. The free and a repulsive Coulomb Hamiltonians have the same representations (without the bound-state contribution) in the free and Coulomb WP bases respectively.

2.3 Free wave-packets as a basis

The most useful examples of WP states are free WPs corresponding to the kinetic energy operator h_0 since they have explicit forms.

Indeed, in the momentum representation, the free WP functions are simple step-like functions [7]: they do not vanish only on the given discretization interval, i. e., only in the on-shell region. In this area they are completely determined by the weight function $f(p)$:

$$x_k(p) = \frac{f(p) \theta(p \in \mathfrak{D}_k)}{\sqrt{B_k}}, \quad (6)$$

where θ is the Heaviside step-like function which is equal to unity if $p \in \mathfrak{D}_k$ while outside it is equal to zero [7]. When $f(p) = 1$ (and $B_k = d_k$ where $d_k = p_k - p_{k-1}$ is the width of the corresponding momentum interval) all the wave functions in the momentum WP representation take a histogram form. Being generalized onto a few-body case, the free few-body WP basis functions are built as a direct products of step-like functions for each independent momentum variable. Thus, the whole few-body momentum space is replaced by a finite momentum lattice. In this sense, we refer to the free WP basis as *the lattice basis*.

From the practical point of view, the lattice basis can be used in any scattering calculations on the same footing as a conventional discrete L_2 basis like the harmonic oscillator basis or the basis of Gaussians. Since the basis functions are step-like functions in momentum space, the momentum dependence of all functions expressed via such a basis has also a histogram-like form.

2.4 Construction of WP states for the total Hamiltonian

Free WPs can be used as a basis to construct scattering WPs for the total Hamiltonian h as its pseudostates. For this purpose, one applies a diagonalization procedure to the total Hamiltonian matrix in a free WP basis. As a result, one gets a discrete sets of eigenvalues E_k and respective eigenvectors $|\tilde{z}_k\rangle$.

By such a diagonalization procedure, one derives a very convenient discrete representation for the scattering WPs as a superposition of free WPs:

$$|z_k\rangle \approx |\tilde{z}_k\rangle = \sum_{i=1}^N O_{ki} |x_i\rangle. \quad (7)$$

As it has been mentioned above, there is no restriction that v should be a short-range potential. So that, this procedure can be applied even for the long-range Coulomb

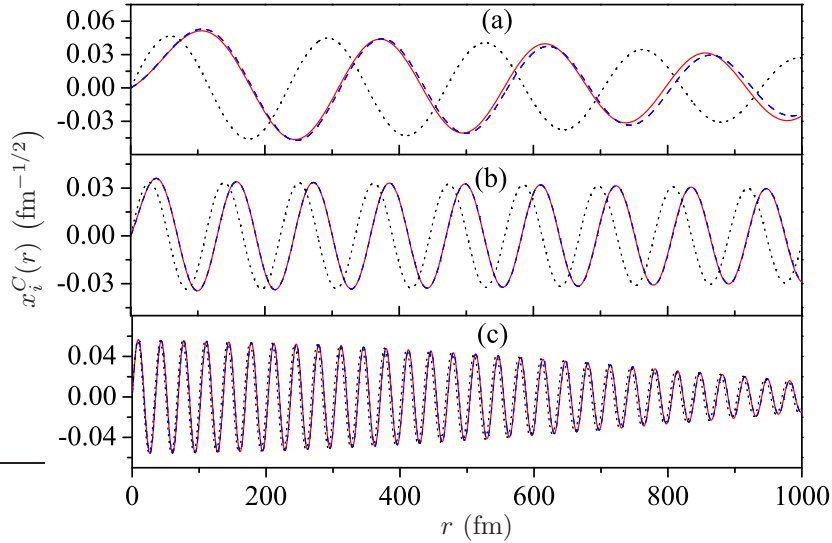


Figure 1: The exact S -wave Coulomb WPs (dashed curves), the pseudostates found via the free WP basis (solid curves) and the free WPs at the same energy (dotted curves) for pp system at three center of mass energies: $E_{c.m.} = 0.03$ MeV (a), $E_{c.m.} = 0.133$ MeV (b) and $E_{c.m.} = 1.474$ MeV (c). In the case (c) the Coulomb phase shift is rather small, hence the respective three curves are very close to each other.

interaction. This statement is illustrated in Fig. 1 where the exact Coulomb WPs for pp system are compared with the respective Coulomb pseudostates found by the diagonalization of the Coulomb Hamiltonian h_C on the free WP basis, and the free WPs themselves at the same energy. It is clearly seen from the Figure the Coulomb WP $|x_i^C\rangle$ can be very accurately approximated by free WPs.

The pseudostate approximation (7) for the scattering WPs is extremely useful for few-body scattering studies where one is able to build a few- and many-body WP basis not only for a free motion Hamiltonian but also for a few-body channel Hamiltonian.

3 Solving scattering problems without equations

3.1 Discrete spectral shift function formalism

The discrete representation for scattering theory objects opens new possibilities in practical solving scattering problems. Below we briefly report the method based on the spectral shift function formalism, which allows to find multichannel scattering matrix using spectral properties of the free and total Hamiltonian only [10].

The spectral shift function (SSF) $\xi(E) \equiv \xi(E; h, h_0)$ is an important object in the general spectral theory of perturbations which defines a spectral difference for two Hermitian operators h_0 and $h = h_0 + v$ (e. g., free and total Hamiltonians) in the discrete and continuous parts of the entire spectrum [17, 18]. This fact is known as the trace formula:

$$\text{Tr} [f(h) - f(h_0)] = \int dE f(E) \xi(E). \quad (8)$$

Here f is some function and ξ does not depend on f but depends on two operators h and h_0 only. Although v is called a *perturbation* there is no restriction that it should be small. It is only assumed that the operator v has a finite trace.

The most essential result of the SSF formalism for physical applications is the famous Birman–Krein formula [17], which relates the SSF with the determinant of the scattering operator S :

$$\det S(E) = \exp(-2\pi i \xi(E)). \quad (9)$$

In the single-channel scattering (e. g., at a fixed angular momentum), this formula implies that the SSF is equal up to a factor of $-\pi$ to a partial phase shift, $\delta(E) = -\pi \xi(E)$.

Let us add that, at negative energies, the SSF is a counting function which changes by one unit when crossing each bound state energy [10].

To define the SSF in a discretized representation, one has to use a concept of quasi-continuous spectrum introduced by I. M. Lifshitz [19] (see also details in ref. [10]). He considered a family of Hermitian operators $\{h_0^{(\alpha)}\}$ each depending on a small parameter α and having a purely discrete spectrum of eigenvalues (EVs) $\{E_j^0(\alpha)\}$ which can be approximated by a single continuous monotonic function $w(u)$:

$$\begin{aligned} E_j^0(\alpha) &= w(j\alpha) + O(\alpha), \\ D_j^{(\alpha)} &= E_{j+1}^0(\alpha) - E_j^0(\alpha) = \alpha \left[\frac{dw}{du} \Big|_{u=j\alpha} + O(\alpha) \right]. \end{aligned} \quad (10)$$

All differences $D_j^{(\alpha)}$ decrease as α decreases and the quasi-continuous spectrum becomes more and more dense. Thus, in the limit $\alpha \rightarrow 0$, one has the limiting operator h_0 with a continuous spectrum. By adding the perturbation v to $h_0^{(\alpha)}$ operators, one gets a family of total Hamiltonians $h^{(\alpha)}$ with shifted EVs $\{E_j(\alpha)\}$. One or several EVs of the perturbed spectrum may occur to be below the threshold and thus correspond to the bound states of h while the rest belong to the quasi-continuous spectrum of this operator. Lifshitz has shown that the following relation between perturbed and unperturbed EVs in quasi-continuous spectrum takes place [10, 19]:

$$E_j(\alpha) = E_j^0(\alpha) + D_j^{(\alpha)} \xi_j + o(\alpha), \quad (11)$$

where $D_j^{(\alpha)}$ is defined in Eq. (10) and $\xi_j = \xi(E_j(\alpha))$ is the spectral shift function defined at discrete energy values. The formula (11) is the basic for the Discrete Spectral Shift (DSS) method. It results in a very simple approximate expression for the partial phase shift:

$$\delta(E_j^0) = -\pi \xi(E_j^0) \approx -\pi \frac{E_j - E_j^0}{D_j}. \quad (12)$$

This method may be applied to any continuum discretization procedure, e. g., when one considers a particle scattering in a box and the box size R is increased to infinity ($\alpha \sim \frac{1}{R}$) [10]. Another useful case is the solution of the scattering problem in some finite L_2 basis when the parameter α is decreasing with increasing the basis dimension N [10].

It should be stressed that the above result is related to other methods which allow to find phase shifts without solving the scattering equations. It is worth to mention

here the Lüscher approach which is widely used in low energy EFT applications [14]. Recently the SS-HORSE method has been developed [15,16] which can be treated as a SSF formalism in the Harmonic Oscillator representation.

3.2 New treatment of multichannel pseudostates

In a multichannel case, the total Hamiltonian can be written in a matrix form as

$$h_{\nu\nu'} = h_0^\nu \delta_{\nu\nu'} + v_{\nu\nu'}, \quad \nu, \nu' = 1, \dots, d, \quad (13)$$

where ν is a channel index, h_0^ν are the channel unperturbed Hamiltonians and $v_{\nu\nu'}$ are coupling potentials.

The trace (8) and Birman–Krein (9) formulas are valid in the multichannel case as well. However they correspond to the total spectral density of the matrix Hamiltonian \mathbf{h} from Eq. (13) and cannot be used for separate calculations of elastic and inelastic amplitudes in different channels. In particular, the spectral shift function at each energy is just a sum of all *eigenphases* [10].

Nevertheless, we have shown that Eq. (12) can be generalized to evaluate separate eigenphases from the differences of free and total Hamiltonian eigenvalues [10] similarly to the single-channel case. Here each EV of the discretized spectrum $\{E_j^0\}$ of the multichannel free Hamiltonian \mathbf{h}_0 should be degenerate with the multiplicity d equal to the number of open channels at the given energy. An inclusion of a channel-coupling interaction leads to the splitting of the above multiple energy levels. Finally, the spectrum of the total multichannel Hamiltonian \mathbf{h} consists of serieses of eigenvalues $\{E_j^\varkappa\}_{\varkappa=1}^d$ for each j (here \varkappa is the eigenchannel index) arising from the initial unperturbed eigenvalues E_j^0 (see Ref. [10] for the details). This effect is illustrated in Fig. 2 for a two-channel problem.

Thus a diagonalization of the total Hamiltonian (13) matrix in the coupled-channel free WP basis $\{|x_i^\nu\rangle\}_{\nu=1}^d$ results in a set of pseudostates $|z_k^\varkappa\rangle$ with EVs E_k^\varkappa expanded in a series of free WP states:

$$|z_k^\varkappa\rangle = \sum_{\nu,i} O_{ki}^{\varkappa\nu} |x_i^\nu\rangle. \quad (14)$$

These pseudostates can be treated as approximations for the multichannel WPs of the total Hamiltonian \mathbf{h} [7].

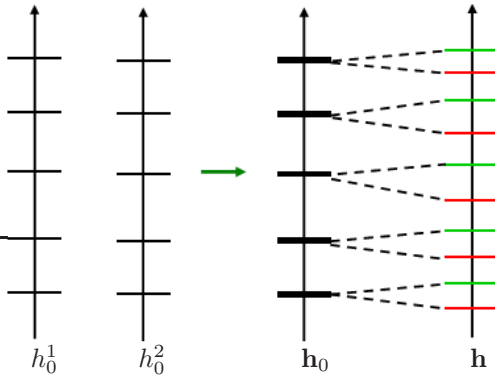


Figure 2: The splitting effect caused by the inclusion of the coupled-channel interaction \mathbf{v} : the similar eigenvalues of free Hamiltonians h_0^1 and h_0^2 form discretized spectrum of the matrix free Hamiltonian \mathbf{h}_0 with degenerated energy levels each splitted into a pair of levels (shown with different colors) of the total Hamiltonian \mathbf{h} .

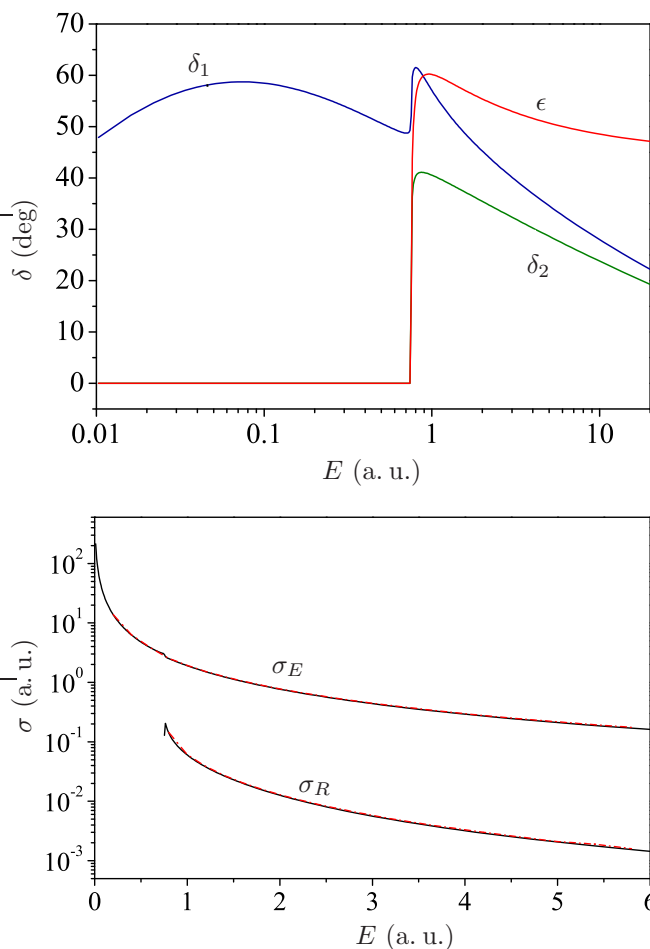


Figure 3: Eigenphases $\delta_{1,2}$ and mixing angle ϵ (top) together with elastic and reaction cross sections (bottom) found via the DSS method for the two-channel e -H scattering (solid curves). The dash-dotted curves (almost indistinguishable from the solid ones) in the bottom panel present the results of Ref. [20].

Then one can define different spectral shift functions in the eigenchannel representation (each for a separate eigenchannel) and relate them to the eigenphases of the multichannel problem. Finally, these eigenphases are defined again through the discrete spectral shifts:

$$\delta_{\kappa}(E_j^0) \approx -\pi \frac{E_j^{\kappa} - E_j^0}{D_j}, \quad \kappa = 1, \dots, d, \quad (15)$$

where E_j^0 is the eigenvalue of the free Hamiltonian \mathbf{h}_0 with the multiplicity d , E_j^{κ} is the eigenvalue of the total Hamiltonian \mathbf{h} , and D_j is the energy width of the corresponding discretization interval of \mathbf{h}_0 .

Our results for the model two-channel e -H scattering problem obtained in the DSS approach are shown in Fig. 3 in comparison with the results of Ref. [20]. A coupled-channel potential including $1S$ - $2S$ excitation of the hydrogen atom has been used in these calculations. The parameters of the model interaction has been taken from Ref. [20]. It is seen that the DSS technique reproduces the reaction cross section very well in a wide energy region except only for one or two energy points just near the threshold of the second channel.

A detailed description of the DSS approach and various numerical examples of single- and multi-channel scattering applications, including those with non-local and complex-valued potentials, can be found in Refs. [10].

3.3 Off-shell multichannel t -matrix from the diagonalization

With the treatment of the multichannel pseudostates as shown above, a finite-dimensional representation for the total resolvent takes a diagonal form in the multichannel case [7]:

$$g(E) \approx \sum_{n=1}^{N_b} \frac{|\psi_n\rangle\langle\psi_n|}{E - E_n} + \sum_{\varkappa=1}^d \sum_{k=1}^{N_{\varkappa}} |z_k^{\varkappa}\rangle g_k^{\varkappa}(E) \langle z_k^{\varkappa}|, \quad (16)$$

which is similar to the single-channel total resolvent (5). It should be stressed that the above expansion does not represent the pole-like pseudostate approximation for the total resolvent but it corresponds to the diagonalization of the coupled-channel continuous spectrum of the total Hamiltonian within the scattering wave-packet formalism.

Next, substituting the total resolvent by its representation (16) in the explicit formula for the transition operator,

$$t(E) = v + v g(E) v, \quad (17)$$

one obtains the off-shell multichannel t -matrix as the following matrix element in the channel free WP basis:

$$t_{\nu\nu'}(E; p, p') \sim \langle x_i^{\nu} | t(E) | x_{i'}^{\nu'} \rangle, \quad p \in \mathfrak{D}_i, \quad p' \in \mathfrak{D}_{i'}. \quad (18)$$

Thus this technique makes it possible to find the off-shell t -matrix for a multi-channel scattering problem by a one-fold diagonalization of the total Hamiltonian matrix in free WP basis for any energy E . Here, at all required energy points, the same set of pseudostates $|z_k^{\varkappa}\rangle$ should be used and only the eigenvalues $g_k^{\varkappa}(E)$ must be recalculated which is very simple.

As an example of an application of the diagonalization procedure to the calculation of the NN scattering amplitudes, we present in Fig. 4 the partial phase shifts for the coupled 3S_1 – 3D_1 spin-triplet channels supported by the CD-Bonn NN potential [21]. To check the accuracy of the approach, we compare in this figure the results of the direct numerical solution for the integral Lippmann–Schwinger equation with the results of a single diagonalization for the respective NN coupled-channel Hamiltonian in a very broad interval of laboratory energies E_{lab} from zero up to 800 MeV. The dimensionality of the free WP bases for these calculations is $N = 100$ in each partial wave. As the discretization mesh, we used here the Chebyshev grid (see details in Ref. [7]). It is clearly seen that the results for the direct and diagonalization solutions are nearly indistinguishable in the whole energy region studied.

It should be mentioned that the proposed diagonalization technique is useful for solving scattering problems in medium as well. Very recently [22], we have generalized this approach to solving the Bethe–Goldstone equation for the reaction matrix in infinite nuclear matter.

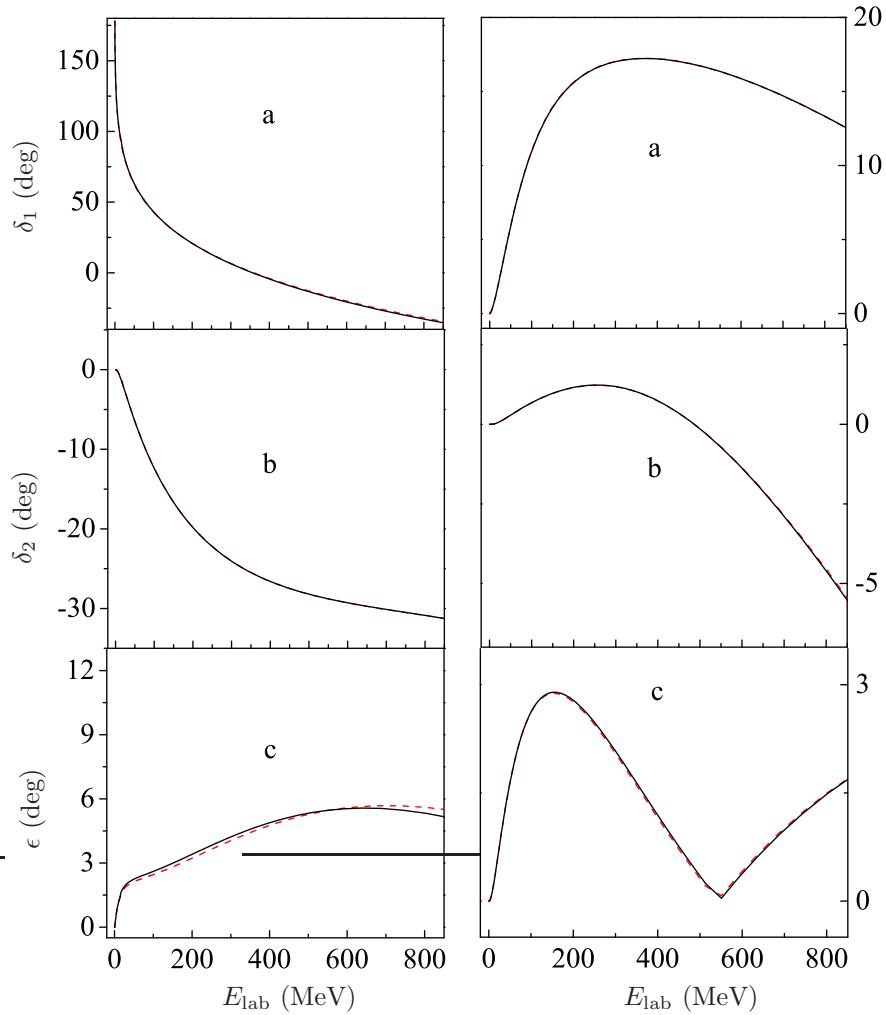


Figure 4: Partial phase shifts δ_1 (a), δ_2 (b) and mixing angle ϵ (c) for the coupled spin-triplet 3S_1 - 3D_1 (left) and 3P_2 - 3F_2 (right) channels of NN scattering calculated using the CD-Bonn NN potential (solid curves) in comparison with the results of a direct numerical solution of the respective Lippmann-Schwinger equation (dashed curves).

4 Few-body scattering problem in the momentum lattice basis

It has been shown above that the diagonalization procedure for the total Hamiltonian in the free WP basis allows to find on-shell or off-shell quantities for problems in continuum in a wide energy region without solving scattering equations. However a generalization of this approach to the three- and few-body cases is not straightforward due to a complexity of the few-body continuum and corresponding boundary conditions.

For the studies of the few-body scattering, we have developed a closed formalism based on the free WP basis (the momentum lattice basis) which allows to find matrix analogs of the integral scattering theory equations and to solve them efficiently. We start below from a general description of this formalism in the two-body case.

4.1 Discrete version of scattering theory

Within the WP lattice formalism, a three-step discretization procedure is introduced:

- (i) Division of continuous spectrum of the free Hamiltonian into non-overlapping intervals and introduction of the free WPs.
- (ii) Projection of the scattering (as well as bound-state) wave functions and operators onto the above WP space.
- (iii) Additional energy averaging of energy-dependent operators.

The last item means that one should apply the energy-averaging procedure, e. g., to the finite-dimensional representation (5) of the free resolvent $g_0(E) = [E + i0 - h_0]^{-1}$,

$$\mathfrak{g}(E) \rightarrow \mathfrak{g}_0^k = \frac{1}{D_k} \int_{\mathfrak{D}_k} \mathfrak{g}_0(E) dE, \quad (19)$$

where $D_k = \mathcal{E}_k - \mathcal{E}_{k-1}$ is an energy width of the interval \mathfrak{D}_k . This averaging makes it possible to avoid logarithmic singularities at the end-points of the energy intervals which are inherent in the matrix elements $g_k(E)$ in Eq. (5) and allows also to accomplish a complete discretization of the solution scheme [7].

It would be useful to demonstrate how the above discretization procedure works in practical applications by solving the Lippmann–Schwinger equation for the transition operator $t(E)$:

$$t(E) = v + v g_0(E) t(E). \quad (20)$$

Applying the above three steps (i)–(iii), one gets a discrete set of operators \mathfrak{t}^k at $E \in \mathfrak{D}_k$ (instead of the operator $t(E)$ continuously dependent on energy). The matrix elements of \mathfrak{t}^k in the WP basis are related directly to the off-shell elements of the t -matrix:

$$t(p, p', E) \approx \frac{[\mathfrak{t}^k]_{ij}}{\sqrt{D_i D_j}}, \quad \begin{pmatrix} p \in \mathfrak{D}_i \\ p' \in \mathfrak{D}_j \\ E \in \mathfrak{D}_k \end{pmatrix}. \quad (21)$$

These operators \mathfrak{t}^k satisfy simple matrix equations

$$\mathfrak{t}^k = \mathfrak{v} + \mathfrak{v} \mathfrak{g}_0^k \mathfrak{t}^k, \quad E \in \mathfrak{D}_k, \quad (22)$$

where the gothic letters denote the WP projections of the respective operators. Using Eq. (22), one can obtain any of on- and off-shell t -matrix elements whose energy and momentum dependencies are represented by histograms. It should be emphasized that the t -matrix constructed in the WP representation satisfies exactly the unitarity relation [7].

Finally, the S -matrix (and the partial phase shifts) can be found by means of the relation

$$S(E) \approx 1 - 2\pi i \frac{[\mathfrak{t}^k]_{kk}}{D_k}, \quad E \in \mathfrak{D}_k. \quad (23)$$

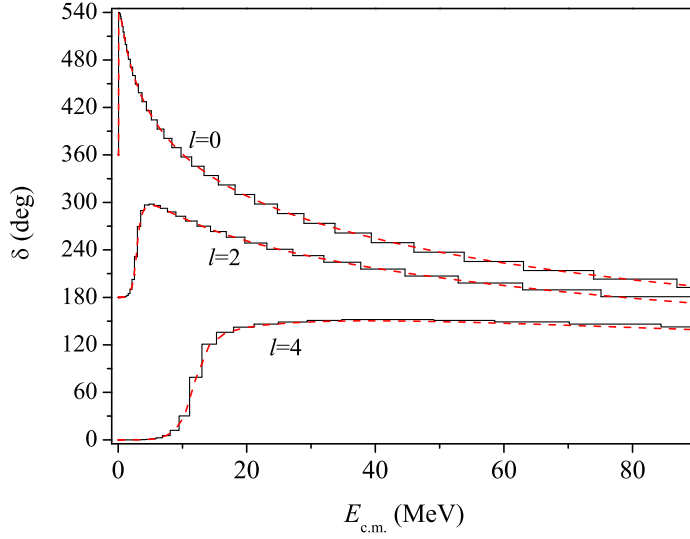


Figure 5: S , D and G partial phase shifts of α - α scattering obtained via the WP approach (solid curves) and by a direct numerical integration of the Schrödinger equation using the Numerov method (dashed curves).

As an illustration of accuracy of this fully-discretized technique for calculating the transition operator, we present here the solution of the α - α scattering problem with interaction including both nuclear and Coulomb potentials [7]. The basic S , D and G partial α - α phase shifts obtained using the above WP technique with the additional energy averaging are displayed in Fig. 5. Here the Coulomb WPs are used as a basis.

4.2 Wave-packet basis in few-body case

If a few-body Hamiltonian can be written in the form of a direct sum of two-body ones,

$$H_M = h_1 \oplus h_2 \oplus \dots \oplus h_M, \quad (24)$$

the WP basis states for H_M can be constructed straightforwardly as direct products of the two-body ones:

$$|Z_{i_1 i_2 \dots i_M}\rangle = |z_{i_1}\rangle \otimes |\bar{z}_{i_2}\rangle \otimes \dots \otimes |\bar{\bar{z}}_{i_M}\rangle, \quad (25)$$

where we use bars above the z -functions to distinguish states corresponding to different subsystems. In the basis (25), the matrix of the Hamiltonian H_M is diagonal and the matrix of the resolvent $G_M(E) = [E + i0 - H_M]^{-1}$ has also an explicit diagonal form.

In the studies of scattering in a system of three identical particles, 1, 2 and 3, useful examples of Hamiltonians of the type (24) are the free Hamiltonian,

$$H_0 = h_{0p} \oplus h_{0q}, \quad (26)$$

and the channel Hamiltonian,

$$H_1 = (h_{0p} + v_1) \oplus h_{0q}, \quad (27)$$

defined for a given Jacobi partition (e. g., $\{23\}1$) with momenta (p, q) , where h_{0p} and h_{0q} are the kinetic energy operators and v_1 is the interaction between the particles 2 and 3. One can introduce the free WP states $|X_{ij}^\gamma\rangle$ and the channel WP

states $|Z_{kj}^\gamma\rangle$ using the two-body ones (with an account of the necessary spin-angular parts labeled by quantum numbers γ) and relate the latter to the former by a simple rotation [7] (all necessary quantum numbers should be taken into account):

$$|Z_{kj}^\gamma\rangle = \sum_{\gamma',i} O_{ki}^{\gamma\gamma'} |X_{ij}^{\gamma'}\rangle. \quad (28)$$

This channel basis construction scheme can be also generalized to the charged particle case [7].

4.3 Solution of Faddeev equation for nd problem in the discrete representation

Here we discuss briefly the solving of Faddeev equations for a scattering of three identical particles 1, 2 and 3 with mass m (nucleons). In this case, elastic scattering observables can be obtained from a single Faddeev equation for the transition operator \bar{U} (the so-called AGS equation), e. g., in the following form [23]:

$$\bar{U} = PG_0^{-1} + PtG_0\bar{U}, \quad (29)$$

where t is the two-body off-shell t -matrix in three-body space, $G_0 = (E + i0 - H_0)^{-1}$ is the free three-body resolvent and P is the permutation operator which changes the momentum variables from one Jacobi set to another. In the case of three identical particles, the operator P is defined as a sum of two cyclic permutations:

$$P = P_{12}P_{23} + P_{13}P_{23}. \quad (30)$$

It should be emphasized that a similar permutation operator is included in the kernels of Faddeev equations in the case of non-identical particles.

We have shown [7] that one can rewrite Eq. (29) in the equivalent half-shell form,

$$U = Pv_1 + Pv_1G_1U, \quad (31)$$

where v_1 is the two-body interaction and $G_1(E) = [E + i0 - H_1]^{-1}$ is the resolvent of the channel Hamiltonian (27).

By projecting the integral equation (31) onto the channel WP basis (28), one derives the matrix equation

$$\mathbb{U} = \mathbb{P}\mathbb{V}_1 + \mathbb{P}\mathbb{V}_1\mathbb{G}_1\mathbb{U}. \quad (32)$$

Here \mathbb{V}_1 and \mathbb{G}_1 are the matrices of the pairwise interaction and of the channel resolvent, respectively, which matrix elements can be found in an explicit form.

Thus, to obtain the elastic scattering amplitude, it is required 1) to calculate the matrix elements of matrices \mathbb{P} , \mathbb{V}_1 , \mathbb{G}_1 and 2) to solve the system of algebraic equations (32).

The matrix \mathbb{V}_1 of the potential v_1 is diagonal in the indices of the wave-packet basis corresponding to the Jacobi coordinate q and thus has a block form. Its matrix in the channel WP basis is defined with the help of interaction matrix \mathbb{V}_1^0 in the free WP basis and the rotation matrix \mathbb{O} .

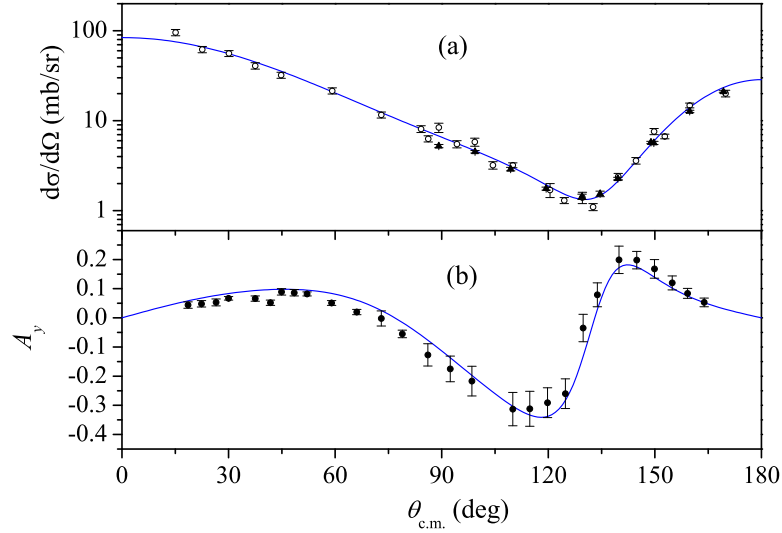


Figure 6: Elastic nd scattering differential cross section (a) and neutron vector analyzing power A_y (b) at 35 MeV obtained within the WP approach (solid curves). Experiment: pd data at 35 MeV [25] (filled circles), nd data at 36 MeV [26] (empty circles), nd data 35 MeV [27] (triangles).

The matrix of the operator P in the three-body lattice basis corresponds to the overlap of basis functions defined in different Jacobi sets:

$$[\mathbb{P}^0]_{ij,i'j'}^{\gamma,\gamma'} \equiv \langle X_{ij}^\gamma | P | X_{i'j'}^{\gamma'} \rangle. \quad (33)$$

Such matrix elements are calculated by integration over the basis functions in momentum space (see details in Refs. [8,9]). Thus, we have rather simple formulas and respective numerical algorithms to determine all quantities entering the kernel of the matrix Faddeev equation (32).

The elastic on-shell amplitude in the wave-packet representation is calculated as a diagonal (on-shell) matrix element of the \mathbb{U} -matrix [7] while the breakup amplitudes can be found from off-diagonal elements of the same matrix.

The differential cross sections of the nd elastic scattering and the neutron vector analyzing power A_y calculated using the realistic Nijmegen I NN potential [24] in the WP approach at 35 MeV are presented in Fig. 6 in comparison with the experimental data. It is evident from the figure that the agreement with the data is rather well. Here the WP basis of the dimensionality over the discretized p and q momenta of $N \times \bar{N} = 100 \times 100$ has been used and the partial waves with the total angular momentum up to $J \leq 17/2$ have been taken into account.

5 Solving by GPU

5.1 Details of numerical scheme for solving Faddeev equation in the discrete representation

As shown above, we have reduced the integral Faddeev equation (31) to the matrix equation (32). As a result, the conventional difficulties of solving the integral equa-

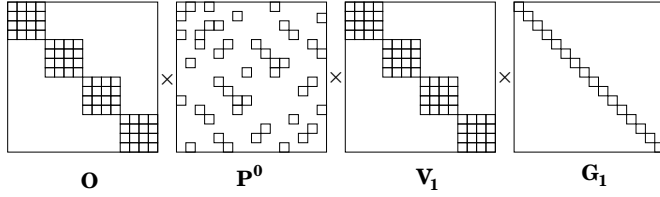


Figure 7: The structure of matrix kernel (34) of the Faddeev equation (32): nonzero elements are marked by squares.

tion (29) are avoided, however the price to be paid is a high dimensionality of the resulting system of algebraic equations.

In fact, we have found [7] that quite satisfactory results can be obtained with a basis size for each Jacobi momentum $N \sim \tilde{N} \sim 100\text{--}150$. This means that even in the simplest single-channel case when all quantum numbers in the set γ are conserved (e. g., for spin-quartet S -wave three-fermion scattering or S -wave three-boson scattering), one gets a kernel matrix of the dimensionality $M = N \times \tilde{N} \sim 10000\text{--}20000$. In the case of a realistic three-body scattering, it is necessary to include many spin-angular channels (up to 62 channels in the case of three-nucleon system) and therefore the dimensionality of the kernel matrix increases up to $5 \cdot 10^5\text{--}10^6$. It is clear that the kernel matrix of this size cannot be stored in the RAM of an ordinary PC.

However a specific matrix structure of the kernel of Eq. (32) makes it possible to overcome this difficulty and to eliminate completely the need for the external memory. Indeed, the matrix kernel \mathbb{K} in Eq. (32) can be written as a product of four matrices,

$$\mathbb{K} = \mathbb{P}\mathbb{V}_1\mathbb{G}_1 \equiv \mathbb{O}\mathbb{P}^0\tilde{\mathbb{V}}_1\mathbb{G}_1, \quad (34)$$

where $\tilde{\mathbb{V}}_1 = \mathbb{O}^T\mathbb{V}_1$. Here \mathbb{G}_1 is a diagonal matrix, \mathbb{P}^0 is the permutation matrix of a high sparsity, while $\tilde{\mathbb{V}}_1$ and \mathbb{O} are block matrices comprising identical blocks of the dimensionality N (see Fig. 7).

The problem of the high dimensionality is resolved by storing only the individual multipliers of the matrix kernel \mathbb{K} in RAM. Moreover, one can store the highly sparse matrix \mathbb{P}^0 in a compressed form (i. e., only its nonzero elements), then the complete set of data required for the iteration process can be placed in RAM. Although three extra matrix multiplication is added at each iteration step in this case, the computer time spent on iterations is reduced more than 10 times as compared to the procedure employing the external memory.

Thus our overall numerical scheme includes the following main steps:

1. Processing of the input data.
2. Calculation of nonzero elements of the permutation matrix \mathbb{P}^0 .
3. Calculation of the channel resolvent matrix \mathbb{G}_1 .
4. Iterations of the matrix equation (32) and finding its solution using the Padé approximant technique.

The runtimes for the steps 1 and 3 are practically negligible in comparison with the total running time, while the execution of the step 4 — finding the solution of the matrix system by iterations — takes about 20% of the total time needed for a single-thread computing of the whole problem. Hence we shall discuss below an optimization

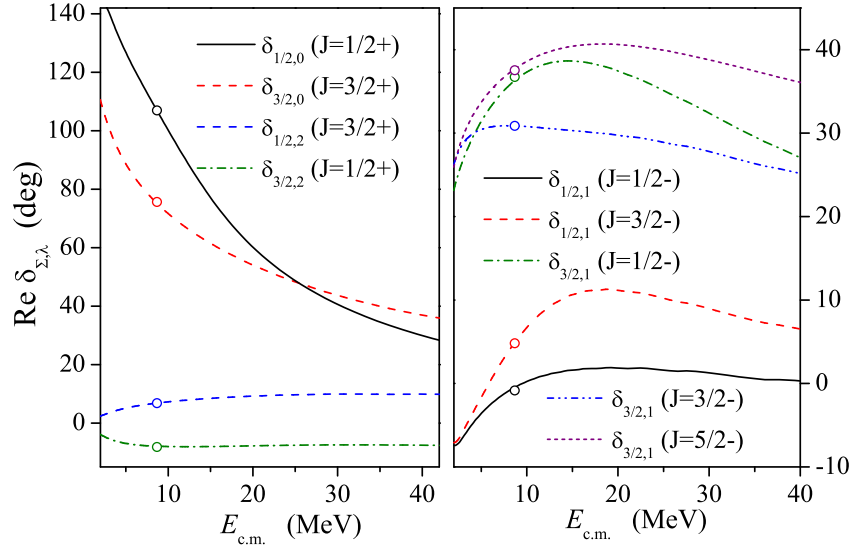


Figure 8: Some of S , D and P partial phase shifts of the elastic nd scattering obtained within the WP approach (solid curves) and within the standard Faddeev calculations (circles) [23].

of the step 2 only, viz. the calculation of the matrix \mathbb{P}^0 elements. Since all these elements are calculated using the same code and are completely independent from each other, the algorithm seems to be suitable for a parallelization and implementation on multiprocessor systems like GPU. However, since the matrix \mathbb{P}^0 is of a high sparsity, we have developed a special technique in order to get an essential acceleration due to the GPU realization. In particular, we apply an additional *pre-selection* of the nonzero \mathbb{P}^0 matrix elements.

It should be emphasized that the steps 1 and 2 do not depend on the incident energy. The current energy is taken into account only at steps 3 and 4 when one calculates the channel resolvent matrix elements and solves the matrix equation for the scattering amplitude. Therefore, if one needs to calculate the scattering observables in a wide energy region, the whole computing time is not increasing essentially because the most time-consuming part of the code (step 2) is carried out only once for many energy points.

Various even- and odd-parity partial phase shifts of the elastic nd scattering calculated with the Nijmegen I NN potential via the proposed WP approach are presented in a wide energy region in Fig. 8. The same permutation matrix has been used to derive all these results.

5.2 GPU acceleration for the nd scattering problem with s -wave NN potential

There is a number of issues associated with the organization of the data transfer between the RAM and GPU and also with the GPU computation itself which makes highly nontrivial the GPU realization in this case. These issues impose severe restrictions on the acceleration due to the GPU realization. One can define the GPU

acceleration η as a ratio of the single-thread CPU computation runtime to the multithread GPU computation runtime:

$$\eta = t_{\text{CPU}}/t_{\text{GPU}}. \quad (35)$$

This acceleration depends on the ratio of the actual time for the calculation of a single matrix element t_0 to the time of transmitting the result from the GPU back to the RAM T , on the number of GPU cores N_c and their speed r_{GPU} compared to the speed of the CPU core r_{CPU} , and also on the dimension of the matrix M :

$$\eta = f\left(\frac{t_0}{T}, N_c, r_{\text{GPU}}, r_{\text{CPU}}, M\right). \quad (36)$$

Figure 9 shows the dependence of the CPU and GPU computing times as well as the GPU acceleration η in calculation of the permutation matrix on its total dimensionality $M = N \times \bar{N}$ (for $N = \bar{N}$) in the case of the s -wave NN interaction MT III. In this calculation, the GPU code was executed with 65 536 threads. For the comparison, we display in this figure also the CPU and GPU times needed for the pre-selection of nonzero matrix elements. It is clear from the figure that one needs to use the GPU not only for the calculation of nonzero elements which takes most of the time in the single-thread CPU computing, but also for the pre-selection of nonzero matrix elements to achieve an essential acceleration.

It is seen that the runtime for the calculation of the \mathbb{P}^0 nonzero elements which takes the main fraction of the CPU computing time, is reduced by more than 100 times. The total GPU acceleration in calculating the S -wave partial phase shifts reaches 50. As a result of all these innovations, the total three-body scattering calculation takes only 7 sec on an ordinary PC with GPU.

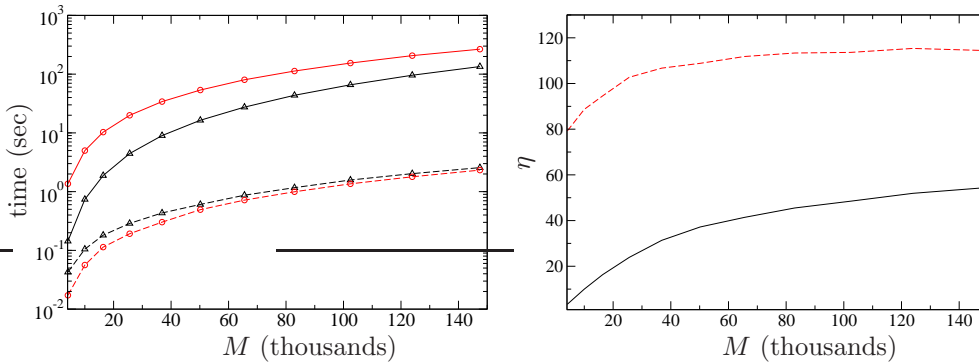


Figure 9: Left: the CPU (solid curves) and GPU (dashed curves) computing times for the pre-selection (triangles) and calculation of the \mathbb{P}^0 nonzero elements (circles) in the case of s -wave NN interaction. Right: the GPU acceleration η for calculation of the permutation matrix (dashed curve) and for the complete solution of the S -wave nd scattering problem (solid curve). Here M is the total basis dimensionality.

5.3 GPU acceleration in the nd scattering problem with realistic NN potential

Unlike the simplest single-channel nd scattering discussed above, in the case of realistic NN interactions, we have many coupled spin-angular channels (up to 62 channels if the total angular momentum in NN pairs is restricted to $j \leq 3$). In this case, the calculation of each element of the permutation matrix \mathbb{P}^0 comprises numerical calculations of several tens of double numerical integrals containing Legendre polynomials.

Figure 10 demonstrates the GPU acceleration η versus the total basis dimensionality M in the solution of 18-channel Faddeev equation for the partial three-body elastic amplitude with the total angular momentum $J = \frac{1}{2}^+$ in the case of realistic Nijmegen I NN interaction. The dashed and dash-dotted curves present the GPU acceleration at the stages of the pre-selection of nonzero elements of the permutation matrix \mathbb{P}^0 and of calculation of these elements, respectively.

From these results, it is evident that the acceleration for calculating the large coupled-channel permutation matrix is about 15 times that is considerably smaller than in the above single-channel case. Nevertheless, switching from the CPU to the GPU realization *on the same PC* makes it possible to obtain a quite impressive acceleration of about 10 times in the solution of the 18-channel scattering problem.

In realistic calculations of the observables of elastic three-body scattering, it is necessary to include up to 62 spin-orbital channels. For the current numerical scheme, the efficiency of the GPU optimization decreases with increasing the number of channels. As is shown in Ref. [9], the time of calculations of the permutation matrix elements is decreased by 8.7 times only due to the GPU optimization. Moreover, in this case,

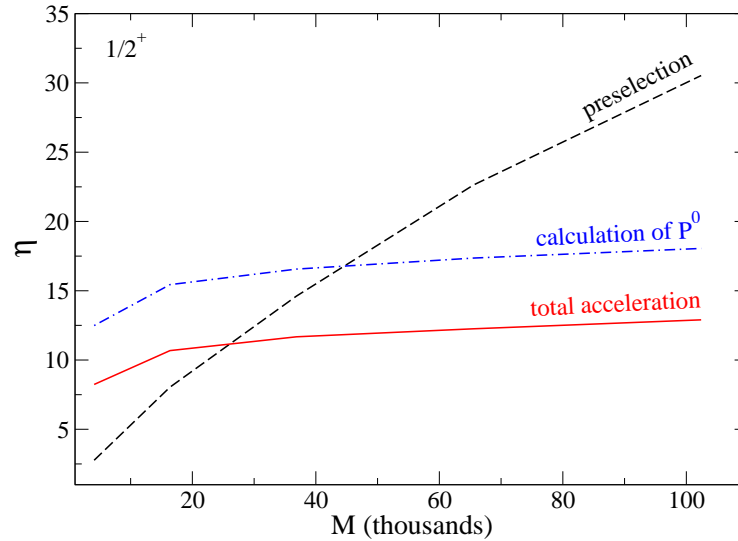


Figure 10: Dependence of the GPU acceleration η on the dimensionality of the basis M for the nd scattering problem with Nijmegen I NN potential at $J = \frac{1}{2}^+$: dashed curve — acceleration for the pre-selection of nonzero elements in the permutation matrix \mathbb{P}^0 , dash-dotted curve — acceleration for the calculation of these nonzero elements, solid curve — acceleration of the complete solution.

the major fraction of the computational time is spent not on the permutation matrix but on the successive iterations of the very large matrix equation, i. e., on the final step 4. This step takes now about 69% of the total computational time; as a result, the total acceleration of the entire procedure is only 3.2. It should be stressed however that the current numerical scheme can be further optimized. We plan to parallelize the final step 4 in our next studies. It is also clear that the use of a more powerful specialized graphics processor like Tesla K80 would lead even to a considerably larger acceleration of the calculations.

6 Summary

We have described here a general technique for solving few-body scattering problems based on a complete continuum discretization and a projection of scattering operators and wave functions onto the basis of stationary wave packets. Due to the properties of the basis functions, the approach combines the advantages of the L_2 -type techniques associated with calculations with normalized wave functions and, on the other hand, with the rigorous integral equation formalism of the scattering theory. As a result, such a WP projection makes it possible to transform complicated singular multi-dimensional integral equations like the Lippmann–Schwinger or Faddeev–Yakubovsky equations to regular matrix equations which can be solved directly within computational procedures similar to those used in the bound-state type calculations.

Moreover, it has been shown that the above computational procedures can be rather easily adapted to a parallel realization, in particular, they are suitable for processing on a desktop PC supplied with a GPU. Although we have found out that the acceleration achieved due to the GPU realization depends strongly on the dimensionality of the basis and on the complexity of the problem, e. g., on the number of spin-angular channels involved, the results obtained for the elastic nd scattering problem with semi-realistic and realistic NN potentials appear to be very promising for further investigations.

Let us note that the developed GPU-accelerated discrete approach for quantum scattering problems can be implemented in other areas of quantum physics, as well as in a number of important areas of classical physics involving the need to solve multidimensional problems for continuous media studies.

Acknowledgments

The authors appreciate a partial financial support of the RFBR grants 16-02-00049, 16-02-00265 and joint RFBR-DFG grant 16-52-12005.

References

- [1] L. D. Faddeev, Sov. Phys. JETP **12**, 1014 (1961); O. A. Yakubovsky, Sov. J. Nucl. Phys. **5**, 937 (1967).
- [2] V. D. Efros, W. Leidemann, G. Orlandini and E. L. Tomusiak, Phys. Rev. C **81**, 034001 (2010).

- [3] E. Garrido, A. Kievsky, M. Viviani and Phys. Rev. C **90**, 014607 (2014).
- [4] I. B. Abdurakhmanov, A. S. Kadyrov and I. Bray, Phys. Rev. A **94**, 022703 (2016).
- [5] J. A. Lay, A. M. Moro, J. M. Arias and J. Gomez-Camacho, Phys. Rev. C **82**, 024605 (2010).
- [6] J. Carbonell, A. Deltuva, A.C. Fonseca and R. Lazauskas, Prog. Part. Nucl. Phys. **74**, 55 (2014).
- [7] O. A. Rubtsova, V. I. Kukulin and V. N. Pomerantsev, Ann. Phys. (NY) **360**, 613 (2015).
- [8] V. N. Pomerantsev, V. I. Kukulin and O. A. Rubtsova, Phys. Rev. C **89**, 064008 (2014).
- [9] V. N. Pomerantsev, V. I. Kukulin, O. A. Rubtsova and S. K. Sakhiev, Comput. Phys. Commun. **204**, 121 (2016).
- [10] O. A. Rubtsova, V. I. Kukulin, V. N. Pomerantsev and A. Faessler, Phys. Rev. C **81**, 064003 (2010); O.A. Rubtsova, V. I. Kukulin and V. N. Pomerantsev, Phys. At. Nucl. **77**, 486 (2014).
- [11] W. Greiner, *Quantum mechanics: An introduction, 4th ed.* Springer, 2001.
- [12] N. K. Timofeyuk and R. C. Johnson, Phys. Rev. C **87**, 064610 (2013).
- [13] M. Lüscher, Nucl. Phys. B **354**, 531 (1991).
- [14] P. Guo, J. J. Dudek, R. G. Edwards and A. P. Szczepaniak, Phys. Rev. D **88**, 014501 (2013).
- [15] A. M. Shirokov, A. I. Mazur, I. A. Mazur, J. P. Vary, Phys. Rev. C **94**, 064320 (2016).
- [16] A. M. Shirokov, G. Papadimitriou, A. I. Mazur, I. A. Mazur, R. Roth and J. P. Vary, Phys. Rev. Lett. **117**, 182502 (2016).
- [17] D. R. Yafaev, *Mathematical scattering theory: General theory.* Amer. Math. Soc., Providence, RI, 1992.
- [18] M. S. Birman and A. B. Pushnitsky, Integr. Equ. Oper. Theory **30**, 191 (1998).
- [19] I. M. Lifshitz, Zh. Eksp. Teor. Fiz. **17**, 1076 (1947) (*in Russian*).
- [20] B. H. Brandsen and A. T. Stelbovics, J. Phys. B **17**, 1874 (1984).
- [21] R. Machleidt, F. Sammarruca and Y. Song, Phys. Rev. C **53**, R1483 (1996).
- [22] H. Mütter, O. A. Rubtsova, V. I. Kukulin and V. N. Pomerantsev, Phys. Rev. C **94**, 024328 (2016).
- [23] W. Glöckle, H. Witała, D. Hüber, H. Kamada, J. Golack, Phys. Rep. **274**, 107 (1996).

- [24] V. G. J. Stoks, R. A. M. Klomp, C. P. F. Terheggen and J. J. de Swart, *Phys. Rev. C* **49**, 2950 (1994).
- [25] S. N. Bunker, J. M. Cameron, R. F. Carlson, J. R. Richardson, P. Tomáš, W. T. H. Van Oers and J. W. Verba, *Nucl. Phys. A* **113**, 461 (1968).
- [26] J. L. Romero, J. A. Jungerman, F. P. Brady, W. J. Knox and Y. Ishizaki, *Phys. Rev. C* **2**, 2134 (1970).
- [27] F. P. Brady, W. B. Broste and J. C. Wang, *Phys. Rev. C* **9**, 1784 (1974).

Large-Scale Shell-Model Challenges within the RIB Era

L. Coraggio^a, A. Gargano^a and N. Itaco^{a,b}

^a*Istituto Nazionale di Fisica Nucleare, Complesso Universitario di Monte S. Angelo,
Via Cintia, I-80126 Napoli, Italy*

^b*Dipartimento di Matematica e Fisica, Università degli studi della Campania “Luigi
Vanvitelli”, viale Abramo Lincoln 5, I-81100 Caserta, Italy*

Abstract

In this contribution, we present a procedure that aims to reduce the computational complexity of large-scale shell-model calculations by taking into account the rejected degrees of freedom in an effective approach. Starting from a general large-scale shell-model Hamiltonian, the study of the behavior of its effective single-particle energies as a function of the number of valence nucleons, allows to establish a reduced model space made up only by orbitals needed to describe a certain class of isotopes or isotones. Next, an unitary transformation of the original Hamiltonian is performed from its model space into the truncated one. By virtue of this transformation, a new shell-model Hamiltonian is obtained, which is defined in a smaller model space preserving effectively the role of the excluded single-particle orbitals. As an application of this procedure, we present the results obtained for Mo isotopes outside the ⁸⁸Sr core, starting from shell-model Hamiltonians derived by way of the many-body perturbation theory from a realistic nucleon-nucleon potential. We present also a study of the dependence of shell-model results upon different truncations of the original model spaces, in order to demonstrate the reliability of this truncation procedure.

Keywords: *Nuclear shell model; realistic nucleon-nucleon potentials; effective interactions*

1 Introduction

The nuclear many-body problem is far more computationally complex than other physical many-body problems because of the nature of the nuclear force. The latter is responsible for correlations between the constituent particles of the nuclei which are stronger than the corresponding ones in atomic and molecular systems, giving a hard life to nuclear microscopic models that take into account single-particle (SP) degrees of freedom of the nucleons.

Recent advances in computer technology have stimulated the development of *ab initio* nuclear structure models which have extended their range of application from light- to medium-mass nuclei.

Proceedings of the International Conference ‘Nuclear Theory in the Supercomputing Era — 2016’ (NTSE-2016), Khabarovsk, Russia, September 19–23, 2016. Eds. A. M. Shirokov and A. I. Mazur. Pacific National University, Khabarovsk, Russia, 2018, p. 226.

<http://www.ntse-2016.khb.ru/Proc/Coraggio.pdf>.

For heavier mass nuclei, the nuclear shell model (SM) is still the most profitable approach to the description of nuclei in terms of microscopic degrees of freedom of the valence nucleons with respect to the inert core.

As mentioned before, high-performance computing devices are widely accessible and the SM calculations with large model spaces and for nuclear systems with many valence nucleons are becoming more feasible. These large-scale shell-model (LSSM) calculations are at present a formidable tool to describe the collective properties of atomic nuclei within a microscopic approach and a sound support of experimental efforts aimed to improve the knowledge of the chart of the nuclides in the rare-ion-beam era.

In this regard, it is worth to mention, among many works, the study of the onset of collectivity at $N = 40$ [1], the revelation of a novel shape evolution in nickel isotopes [2], the merging of the islands of inversion at $N = 20$ and $N = 28$ [3], the description of shell evolution leading to the quenching of the $N = 82$ shell gap near ^{120}Sr [4].

However, there exists always an upper limit to the dimension of matrices that have to be diagonalized to solve the SM eigenvalue problem, in spite of the progress in the computer technology. Consequently, most of the LSSM calculations need to introduce some truncation of the SM basis in order to compute theoretical quantities.

In Ref. [1], in order to study the observed onset of collectivity at $N = 40$ in the chromium and iron isotopic chains, a LSSM calculation has been performed employing a model space spanned by the four fp proton orbitals and five fpd neutron ones, with 4 and 6 valence protons and up to 12 valence neutrons. In order to diagonalize the SM Hamiltonian using the NATHAN code [5], the authors have truncated the basis including up to $14p-14h$ excitations across the $Z = 28$ and $N = 40$.

The appearance of the shape coexistence in low-energy states of nickel isotopes [2] has been investigated in terms of the SM considering both proton and neutron model spaces spanned by six orbitals $0f_{7/2}, 1p_{3/2}, 1p_{1/2}, 0f_{5/2}, 0g_{9/2}, 1d_{5/2}$ outside the doubly-closed ^{40}Ca core. In the m -scheme the dimension of the basis is $\simeq 10^{24}$, so in Ref. [2] it has been resorted to the importance sampling of the SM states performed within the Monte Carlo Shell Model (MCSM) approach to reduce the matrix dimension to 50 [6].

The $N = 20$ and $N = 28$ islands of inversion have been described by the LSSM calculations within the full $sdpf$ model space [3], but the basis has been restricted so that only the neutron $N = 20$ cross-shell excitations have been taken into account. In such a case, the SM basis has a dimensionality of up to 10^{10} .

In Ref. [4], the authors aim to study the evolution of the neutron $N = 82$ shell gap along the isotonic chain by way of the LSSM calculations. They have employed a model space spanned by proton orbitals $0f_{5/2}, 1p_{3/2}, 1p_{1/2}, 0g_{9/2}, 0g_{7/2}, 1d_{5/2}$, and 7 neutron orbitals $0g_{7/2}, 1d_{5/2}, 1d_{3/2}, 2s_{1/2}, 0h_{11/2}, 1f_{7/2}, 2p_{3/2}$, which allow core excitations across both the $N = 82$ neutron and $Z = 50$ proton shell gaps. In such a case, the diagonalization of the SM Hamiltonian could be performed only by truncating the basis so to allow only one valence-neutron in the $1f_{7/2}, 2p_{3/2}$ neutron orbitals.

These examples show how the calculations for nuclei with many valence nucleons — within large model spaces — are very demanding from the computational point of view, and oblige the researchers in many situations to employ some truncation of the SM basis.

However, whenever the number of valence particle increases, we should consider

also an evolution of theoretical effective SP energies (ESPE) of the SM Hamiltonian.

This evolution of the behavior of the ESPE as a function of the number of valence protons or neutrons may be helpful to locate the relevant degrees of freedom to describe the spectroscopy of a class of isotopes or isotones, and consequently to provide a criterion to reduce the degrees of freedom of the model space.

In a recent work [7], we have proposed a method, already employed in Ref. [8], to perform a very effective truncation of the model space, based on the study of the ESPE of the SM Hamiltonian H as a function of Z_{val} and/or N_{val} . Next, a new SM Hamiltonian \tilde{H} defined in a reduced model space with a smaller number of orbitals, is built up through an unitary transformation of the “mother Hamiltonian” H .

Here, as an application of this method, we will report some results obtained for Mo isotopes outside the closed-shell nucleus ^{88}Sr .

The “mother Hamiltonian” H is derived from the CD-Bonn potential [9], whose high-momentum repulsive components are smoothed out using the $V_{\text{low-k}}$ approach [10], utilizing the time-dependent perturbation theory [11]. This will be done within a large model space that includes seven *psdgh* proton and five *sdgh* neutron orbitals.

At the following step, the behavior of the proton and neutron ESPE as a function of the number of valence neutrons and protons is analyzed. The study of the ESPE suggests how to reduce the number of proton and neutron orbitals. After this, we derive — by means of a unitary transformation of the starting SM Hamiltonian — new effective Hamiltonians defined in the reduced model spaces and tailored to study specific isotopic chains. Finally, the SM calculations with these effective Hamiltonians are performed and the theoretical results are compared.

In the following Section, we present some details about the derivation of our shell-model Hamiltonians and effective charges of the electric quadrupole operators, and how we derive the new effective Hamiltonians within the truncated model spaces. In Section 3, we report the results of our calculations for Mo isotopes starting from different model spaces. Finally, we summarize our results in the final Section.

2 Outline of calculations

The first step in our procedure is the derivation from the CD-Bonn NN potential [9] of a starting effective SM Hamiltonian in the framework of the many-body perturbation theory. More explicitly, we first renormalize high-momentum repulsive components of the bare NN potential using the so-called $V_{\text{low-k}}$ approach [10], which provides a smooth potential preserving exactly the on-shell properties of the original NN potential up to a cutoff momentum $\Lambda = 2.6 \text{ fm}^{-1}$. Next, the SM Hamiltonian is derived using the well-known \hat{Q} -box plus folded-diagram method, where the \hat{Q} -box is a collection of irreducible valence-linked Goldstone diagrams which we calculate through the third order in the $V_{\text{low-k}}$ [11].

The effective Hamiltonian H_{eff} can be written in an operator form as

$$H_{\text{eff}} = \hat{Q} - \hat{Q}' \int \hat{Q} + \hat{Q}' \int \hat{Q} \int \hat{Q} - \hat{Q}' \int \hat{Q} \int \hat{Q} \int \hat{Q} + \dots, \quad (1)$$

where the integral sign represents a generalized folding operation, and \hat{Q}' is obtained from \hat{Q} by removing the terms of the first order in $V_{\text{low-k}}$. The folded-diagram series is summed up to all orders using the Lee–Suzuki iteration method [12].

The effective Hamiltonian H_{eff} provides both the SP energies and two-body matrix elements of the residual interaction [11], and we can derive consistently, within the same perturbative approach, the effective operators \hat{O}_{eff} (e. g., electromagnetic operators, Gamow–Teller transition operator) whose effects we want to study.

Both H_{eff} and \hat{O}_{eff} are defined in a large model space labelled $[N_p, N_n]$, where N_p and N_n are the numbers of proton and neutron orbitals spanning the model space, respectively. Therefore, for the sake of clarity, we dub the effective Hamiltonian and the effective operators as $H^{N_p N_n}$ and $\hat{O}^{N_p N_n}$.

As mentioned in the Introduction, in the case of large model spaces, the major computational difficulties arise when evolving the number of the valence protons Z_{val} (isotonic chains) and/or of the valence neutrons N_{val} (isotopic chains) makes the calculation unfeasible with up-to-date SM codes. It is then mandatory to reduce the complexity of the SM problem to be solved.

In the following we describe an approach that we have adopted with success in Refs. [7, 8], which leads to new effective Hamiltonians defined in truncated model spaces by way of a unitary transformation of $H^{N_p N_n}$. The choice of the truncated model space, $[n_p, n_n]$, is driven by the analysis of the behavior, as a function of Z_{val} and N_{val} , of the proton and neutron ESPE of the original Hamiltonian $H^{N_p N_n}$ so as to find out what are the most relevant degrees of freedom to describe the physics of nuclear systems of interest.

Here we describe the derivation of the new SM effective Hamiltonian $H^{n_p n_n}$ starting from the “mother Hamiltonian” $H^{N_p N_n}$.

The eigenvalue problem for $H^{N_p N_n}$ can be written in terms of its eigenvalues E_i and eigenfunctions ψ_i ,

$$H^{N_p N_n} |\psi_i\rangle = E_i |\psi_i\rangle, \quad (2)$$

where $H^{N_p N_n}$ may be expressed as the sum of a SP Hamiltonian H_0 and a residual two-body potential V :

$$H^{N_p N_n} = H_0 + V. \quad (3)$$

As it has been mentioned before, the analysis of the behavior of the ESPE induces a possible reduction of the number SP orbitals that span the model space. The original model space $[N_p N_n]$ is then split up into two subspaces defined by the projectors $P \equiv P^{n_p n_n}$ and $Q \equiv Q^{N_p - n_p, N_n - n_n}$, with the projector P expressed in terms of the H_0 eigenvectors

$$P = \sum_{i=1, d} |i\rangle \langle i|, \quad H_0 |i\rangle = E_i^0 |i\rangle. \quad (4)$$

The P -space effective Hamiltonian $H^{n_p n_n}$ is defined by the equation

$$H^{n_p n_n} |\phi_k\rangle = (PH_0P + V^{n_p n_n}) |\phi_k\rangle = E_k |\phi_k\rangle, \quad (5)$$

where we require that the eigenfunctions ϕ_k are the projections of the eigenfunctions ψ_k of the “mother Hamiltonian”,

$$|\phi_k\rangle = P |\psi_k\rangle.$$

Formally, we can express $H^{n_p n_n}$ as

$$H^{n_p n_n} = \sum_{k=1}^d E_k |\phi_k\rangle \langle \tilde{\phi}_k|, \quad (6)$$

where $|\tilde{\phi}_k\rangle$ are the $|\phi_k\rangle$ biorthogonal states satisfying $|\tilde{\phi}_k\rangle\langle\phi_{k'}| = \delta_{kk'}$ and obtained using the Schmidt biorthonormalization procedure.

The effective residual interaction $V^{n_p n_n}$ can therefore be expressed as

$$V^{n_p n_n} = \sum_{k=1}^d E_k |\phi_k\rangle\langle\tilde{\phi}_k| - PH_0P. \quad (7)$$

The knowledge of the eigenvalues and eigenfunctions of $H^{N_p N_n}$ is therefore essential to derive explicitly the effective Hamiltonian $H^{n_p n_n}$.

Let us now briefly describe the derivation of the P -space effective operator $\hat{O}^{n_p n_n}$. By definition, $\hat{O}^{n_p n_n}$ has to satisfy the following condition

$$\langle\Psi_k|\hat{O}^{N_p N_n}|\Psi_{k'}\rangle = \langle\tilde{\phi}_k|\hat{O}^{n_p n_n}|\phi_{k'}\rangle, \quad (8)$$

where $\hat{O}^{N_p N_n}$ is the operator defined in the starting large model space. By analogy with what we have done for the Hamiltonian, we can express $\hat{O}^{n_p n_n}$ formally as

$$\hat{O}^{n_p n_n} = \sum_{\alpha,\beta=1}^d \langle\Psi_\alpha|\hat{O}^{N_p N_n}|\Psi_\beta\rangle |\phi_\alpha\rangle\langle\tilde{\phi}_\beta|. \quad (9)$$

It can be easily shown that the above expression satisfies Eq. (8). The knowledge of the $\langle\Psi_k|\hat{O}^{N_p N_n}|\Psi_{k'}\rangle$ matrix elements is therefore essential for the explicit derivation of the effective operator $\hat{O}^{n_p n_n}$.

It is worth to point out that when solving the $H^{N_p N_n}$ eigenvalue problem for a A_{val} valence-nucleon system, the corresponding effective Hamiltonian $H^{n_p n_n}$ and effective operator $\hat{O}^{n_p n_n}$ contain 1-body, 2-body, ..., A_{val} -body contributions. To our knowledge, however, there are no public SM codes able to handle either these n -body forces with $n \geq 3$ or the effective operator n -body contributions with $n \geq 2$. Therefore, we have applied the above transformation only to the two valence-nucleon systems, thus obtaining only two-body matrix elements of $H^{n_p n_n}$, while we have taken into account only the one-body component of $\hat{O}^{n_p n_n}$.

3 Results of SM calculations

As already mentioned in the Introduction, we considered for calculations outside the ^{88}Sr core the model space spanned by seven proton $1p_{1/2}$, $0g_{9/2}$, $0g_{7/2}$, $1d_{5/2}$, $1d_{3/2}$, $2s_{1/2}$, $0h_{11/2}$ and five neutron $0g_{7/2}$, $1d_{5/2}$, $1d_{3/2}$, $2s_{1/2}$, $0h_{11/2}$ orbitals. Hereafter this model space will be labelled [75]. In accord with notations introduced in the previous Section, the respective SM effective Hamiltonian is dubbed H^{75} , the superscript referring to the number of proton (seven) and neutron (five) model-space orbitals. This large model space is able to take explicitly into account the $Z = 50$ cross-shell excitations of protons jumping from the $1p_{1/2}$, $0g_{9/2}$ orbitals to the *sdgh* ones.

We report in Table 1 the calculated SP energies and in Table 2 the theoretical proton and neutron effective charges, the latter being close to the usual empirical values ($e_p^{\text{emp}} = 1.5e$, $e_n^{\text{emp}} = 0.5-0.8e$).

The trouble with the SM Hamiltonian H^{75} is the computational complexity which arises when the atomic number Z of the isotopic chain under investigation is evolved.

Table 1: Theoretical SM SP energy spacings (in MeV) (see text for details).

nlj	proton SP energies	neutron SP energies
$1p_{1/2}$	0.0	
$0g_{9/2}$	1.5	
$0g_{7/2}$	5.7	1.5
$1d_{5/2}$	6.4	0.0
$1d_{3/2}$	8.8	3.4
$2s_{1/2}$	8.7	2.2
$0h_{11/2}$	10.2	5.1

Table 2: Proton and neutron effective charges of the electric quadrupole operator $E2$.

$n_a l_a j_a$	$n_b l_b j_b$	$\langle a e_p b \rangle$	$\langle a e_n b \rangle$
$0g_{9/2}$	$0g_{9/2}$	1.53	
$0g_{9/2}$	$0g_{7/2}$	1.58	
$0g_{9/2}$	$1d_{5/2}$	1.51	
$0g_{7/2}$	$0g_{9/2}$	1.77	
$0g_{7/2}$	$0g_{7/2}$	1.84	1.00
$0g_{7/2}$	$1d_{5/2}$	1.84	0.98
$0g_{7/2}$	$1d_{3/2}$	1.86	0.98
$1d_{5/2}$	$0g_{9/2}$	1.59	
$1d_{5/2}$	$0g_{5/2}$	1.73	0.92
$1d_{5/2}$	$1d_{5/2}$	1.73	0.87
$1d_{5/2}$	$1d_{3/2}$	1.71	0.90
$1d_{5/2}$	$2s_{1/2}$	1.76	0.73
$1d_{3/2}$	$0g_{7/2}$	1.83	0.94
$1d_{3/2}$	$1d_{5/2}$	1.79	0.93
$1d_{3/2}$	$1d_{3/2}$	1.81	0.92
$1d_{3/2}$	$2s_{1/2}$	1.83	0.75
$2s_{1/2}$	$1d_{5/2}$	1.73	0.73
$2s_{1/2}$	$1d_{3/2}$	1.73	0.73
$0h_{11/2}$	$0h_{11/2}$	1.89	0.87

For example, this Hamiltonian cannot be diagonalized for any tin isotope with up-to-date SM codes.

In order to apply the procedure reported in Section 2, we study the evolution of both proton and neutron ESPE as a function of Z_{val} which are reported in Figs. 1 and 2.

In Fig. 1, it can be observed that a well-defined separation between the proton subspaces $[1p_{1/2}, 0g_{9/2}, 1d_{5/2}, 0g_{7/2}]$ and $[2s_{1/2}, 1d_{3/2}, 0h_{11/2}]$ is provided by an almost

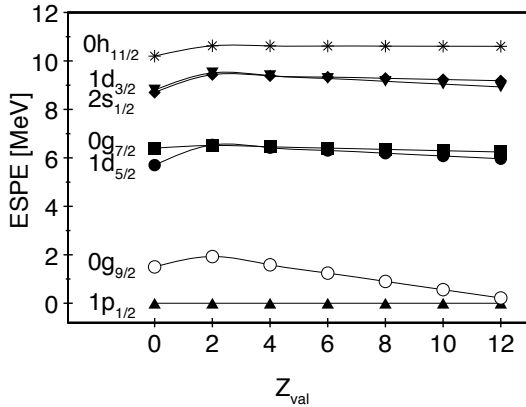


Figure 1: Calculated proton ESPE of H^{75} as a function of the number of valence protons Z_{val} .

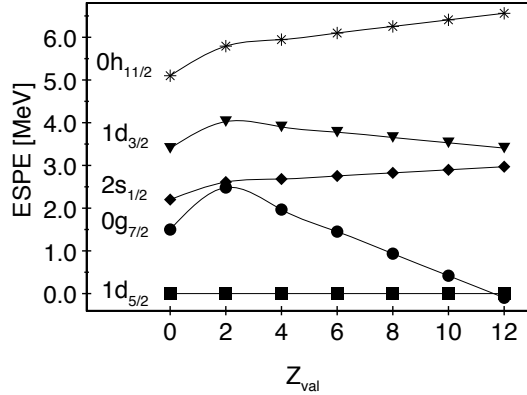


Figure 2: Calculated neutron ESPE of H^{75} as a function of the number of valence protons Z_{val} .

constant energy gap, leading to the conclusion that we can truncate the proton model space to the lowest four orbitals only.

On the neutron side, Fig. 2 evidences that the filling of the proton $0g_{9/2}$ orbital induces a relevant energy gap at $Z = 50$ between the $[1d_{5/2}, 0g_{7/2}]$ subspace and the $[2s_{1/2}, 1d_{3/2}, 0h_{11/2}]$ one. On the above grounds, it looks reasonable to investigate the neutron model space spanned only by the $1d_{5/2}$ and $0g_{7/2}$ orbitals.

Following the procedure reported in Section 2, we have derived two new effective Hamiltonians H_{eff}^{45} and H_{eff}^{42} defined within two model spaces [45] and [42] consisting of the proton $1p_{1/2}$, $0g_{9/2}$, $1d_{5/2}$, $0g_{7/2}$ and of the neutron $0g_{7/2}$, $1d_{5/2}$, $1d_{3/2}$, $2s_{1/2}$, $0h_{11/2}$ and $0g_{7/2}$, $1d_{5/2}$ orbitals, respectively. To verify the reliability of our truncation scheme, we consider the Mo isotopes, more precisely $^{92,94,96}\text{Mo}$, whose Hamiltonians may be diagonalized within the $[7, 5]$ model space.

In Fig. 3 we compare the absolute energies of yrast $J = 0^+$, 2^+ , 4^+ states in $^{92,94,96}\text{Mo}$ obtained by means of the above mentioned effective SM Hamiltonians. It can be noted that both H_{eff}^{45} and H_{eff}^{42} are able to reproduce quite well the absolute energies of the “mother Hamiltonian” H^{75} .

It should be also pointed out that, for ^{96}Mo , H_{eff}^{42} reproduces nicely the 2^+ excitation energy but underestimates the collectivity predicted by the “mother Hamiltonian”. In fact, the $R_{4/2}$ ratio between the calculated excitation energies of the 4^+ versus 2^+ states equal to 2.0 with H^{75} and H_{eff}^{45} , drops to 1.6 when evaluated with H_{eff}^{42} . As a matter of fact, from the inspection of Fig. 2, we should not expect the H_{eff}^{42} results to be in a good agreement with those from H^{75} since there is no a clear separation of the model space P from its complement Q for $Z_{val} = 4$ (Mo isotopes).

The above results evidence the adequacy of our truncation scheme when it is grounded on a neat separation of the model space P from its complement Q as depicted by the ESPE behavior (see Figs. 1 and 2).

As regards the calculation of the $E2$ transition rates using the effective charges derived consistently from the theory, we obtain, for ^{92}Mo , $B(E2; 2_1^+ \rightarrow 0_1^+) = 148 \text{ e}^2\text{fm}^4$ with H_{eff}^{75} and $160 \text{ e}^2\text{fm}^4$ with $H_{\text{eff}}^{45,42}$. For ^{94}Mo , the calculated result with H_{eff}^{75} is $B(E2; 2_1^+ \rightarrow 0_1^+) = 381 \text{ e}^2\text{fm}^4$, $323 \text{ e}^2\text{fm}^4$ with H_{eff}^{45} , and $231 \text{ e}^2\text{fm}^4$ with H_{eff}^{42} . Finally, in the case of ^{96}Mo , $B(E2; 2_1^+ \rightarrow 0_1^+) = 487 \text{ e}^2\text{fm}^4$ with H_{eff}^{75} , $451 \text{ e}^2\text{fm}^4$ with H_{eff}^{45} , and $244 \text{ e}^2\text{fm}^4$ with H_{eff}^{42} . It is evident that a faster degradation of the original $E2$ transition rate reproduction occurs when employing the $[4, 2]$ model space as compared to

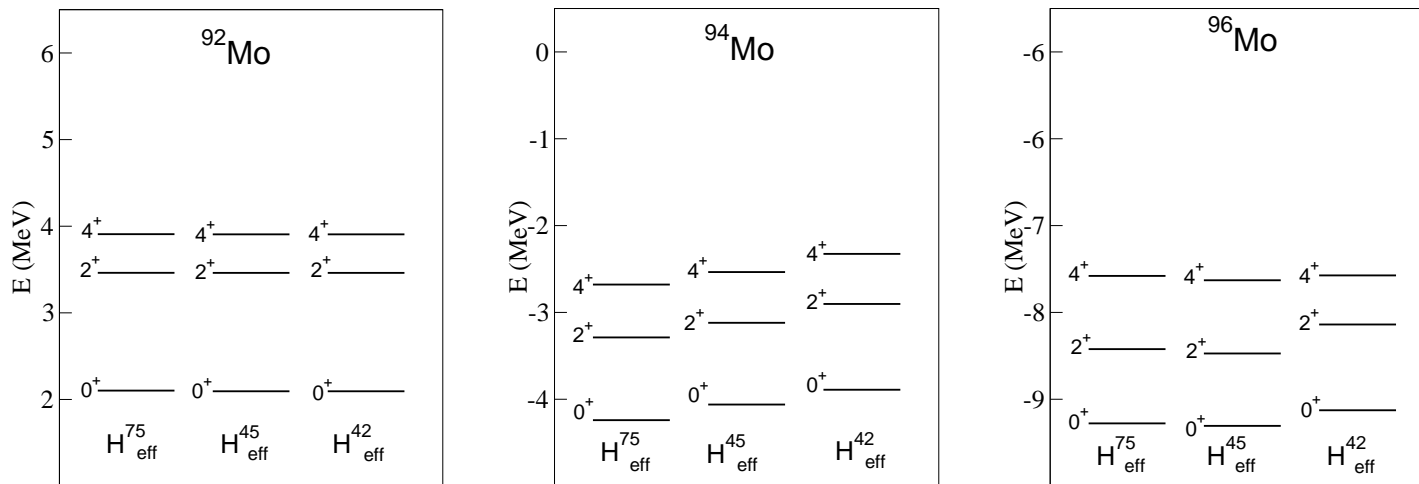


Figure 3: Yrast $J = 0^+, 2^+, 4^+$ states of $^{92,94,96}\text{Mo}$ isotopes calculated within model spaces $[7, 5]$, $[4, 5]$, and $[4, 2]$ (see text for details).

that calculated within the $[7, 5]$ model space.

As pointed out at the end of Section 2, in order to preserve exactly also the calculated transition rates for the two-valence nucleon systems when dealing with the effective Hamiltonians H^{pn} , the effective $E2$ operator should be further renormalized to take into account the neglected degrees of freedom. In this way, one would obtain an effective two-body $E2$ operator to be employed to calculate the electric quadrupole properties of the systems with a number of valence nucleons larger than two. As a consequence, the eventual observed discrepancy between the $E2$ properties calculated with H^{75} and those with the effective Hamiltonians H_{eff}^{42} is a signature of the fact that the corresponding H^{75} wave functions have relevant components outside the truncated $[42]$ model space.

4 Summary

In this paper we have reported on a double-step approach to simplify the computational problem of large-scale SM calculations. The method is based on the study of the ESPE of the large-scale Hamiltonian to identify the most relevant degrees of freedom to be taken into account in the construction of a truncated SM Hamiltonian. To this end, a unitary transformation is employed to derive new effective SM Hamiltonians defined within a reduced set of SP orbitals, accordingly to the ESPE analysis.

This procedure has been applied to a realistic SM Hamiltonian within a model space designed to describe the $Z = 50$ cross-shell excitations for nuclei outside ^{88}Sr by employing seven proton and five neutron orbitals. The behavior of the proton and neutron ESPE allows to identify two truncated model spaces made up by four proton orbitals and five or two neutron ones, and we have transformed our original Hamiltonian in these subsets.

As a test case, we have performed the calculations for Mo isotopes to check the reliability of our procedure. The results obtained with the effectively truncated Hamiltonians testifies the ability to reproduce the eigenvalues and electromagnetic transition rates of the original SM Hamiltonian when the ESPE provide a neat separation in energy between the new model subspaces and their complement.

We are confident that this double-step approach may provide a reliable truncation procedure in any large-scale SM calculation and a theoretical tool that may be applied in other regions where large model spaces lead to critical situations due to the computational complexity, especially when increasing the number of valence nucleons.

References

- [1] H. L. Crawford *et al.*, Phys. Rev. Lett. **110**, 242701 (2013).
- [2] Y. Tsunoda, T. Otsuka, N. Shimizu, M. Honma and Y. Utsuno, Phys. Rev. C **89**, 031301 (2014).
- [3] E. Caurier, F. Nowacki and A. Poves, Phys. Rev. C **90**, 014302 (2014).
- [4] H.-K. Wang, K. Kaneko and Y. Sun, Phys. Rev. C **90**, 014302 (2014).
- [5] E. Caurier and G. Martinez-Pinedo, Nucl. Phys. A **704**, 60c (2002).

-
- [6] N. Shimizu, T. Abe, Y. Tsunoda, Y. Utsuno, T. Yoshida, T. Mizusaki, M. Honma and T. Otsuka, *Progr. Theor. Exp. Phys.* **2012**, 01A205 (2012).
 - [7] L. Coraggio, N. Itaco and A. Gargano, *Phys. Rev. C* **93**, 064328 (2016).
 - [8] L. Coraggio, A. Covello, N. Itaco, A. Gargano and T. T. S. Kuo, *Phys. Rev. C* **91**, 041301 (2015).
 - [9] R. Machleidt, *Phys. Rev. C* **63**, 024001 (2001).
 - [10] S. Bogner, T. T. S. Kuo, L. Coraggio, A. Covello and N. Itaco, *Phys. Rev. C* **65**, 051301 (2001).
 - [11] L. Coraggio, A. Covello, N. Itaco, A. Gargano and T. T. S. Kuo, *Ann. Phys. (NY)* **327**, 2125 (2012).
 - [12] K. Suzuki and S. Y. Lee, *Progr. Theor. Phys.* **64**, 2091 (1980).

Electron Correlations in the Framework of the Quasi Sturmian Approach

A. S. Zaytsev^a, M. S. Aleshin^a, L. U. Ancarani^b
and S. A. Zaytsev^a

^a*Pacific National University, Khabarovsk, 680035, Russia*

^b*Equipe TMS, SRSMC, UMR CNRS 7565, Université de Lorraine, 57078 Metz, France*

Abstract

In the asymptotic region Ω_0 (large hyperradius), the two-electron continuum wave function presents formally a logarithmic phase term corresponding to the electron-electron interaction. The idea of this contribution is to include this phase into a Convolutioned Quasi Sturmian (CQS) basis whose elements already behave asymptotically as an outgoing (incoming) six-dimensional spherical wave. With an appropriately introduced phase factor, the new CQS possess an asymptotic form very close to the formal one, and hopefully constitute a suitable set of basis functions for the three-body Coulomb continuum wave function representation in the entire space. As demonstrated numerically by solving a first order ($e, 3e$) non-homogeneous Schrödinger equation in a two-channel case, a considerable improvement of the convergence rate is observed with a simple two-parameter form of the introduced phase factor.

Keywords: *Ionization of atoms; three-body Coulomb continuum; three-body wave function asymptotic behavior*

1 Introduction

The continuum spectrum of three charged particles is notoriously difficult to describe. In atomic or molecular ionization problems imposing cumbersome boundary conditions, the wave function should obey constituents of these conditions of primary mathematical and numerical difficulties. Besides, the long range nature of the Coulomb interaction implies solving Schrödinger equation on relatively large spatial domains and hence requires to use large basis sets and a high computational cost. Ideally, such a domain should be extended up to the boundary of the asymptotic region where all three particles are well separated. In real calculations, however, the domain size is not known in advance, even though the general boundary condition form has been obtained in Ref. [1]. As a general rule, the convergence rate of basis function expansion reflects its capacity in building up adequately the intricate asymptotic behavior.

Proceedings of the International Conference ‘Nuclear Theory in the Supercomputing Era — 2016’ (NTSE-2016), Khabarovsk, Russia, September 19–23, 2016. Eds. A. M. Shirokov and A. I. Mazur. Pacific National University, Khabarovsk, Russia, 2018, p. 236.

<http://www.ntse-2016.khb.ru/Proc/Zaytsev.pdf>.

For the sake of simplicity, hereafter we consider the two-electron continuum associated with the problem of two electrons with coordinates r_1 and r_2 escaping in the field of a nucleus of charge Z . Such a state may arise as a result of a single or double ionization of atoms or molecules by a charged projectile or by a photon.

A few *ab initio* methods (see, e. g., the review [2] and Introduction of Ref. [3]) have been and are being developed for constructing numerically three-body continuum wave functions. Two of them convert the ionization problem into an inhomogeneous differential equation with a spatially confined driven term, equation that is solved within a finite size box. The exterior complex scaling (ECS) method [4] makes it possible to solve the problem without explicit use of the asymptotic form of the wave function by recasting the original problem into a boundary problem with zero boundary conditions. An interesting extension of ECS to the case of long-range Coulomb interaction has been proposed in Refs. [5–7]. The generalized Sturmian approach [8,9] makes use of an expansion in terms of products of two single-particle generalized Sturmian functions with Coulomb outgoing-wave boundary conditions set at the box border; the angular coupling builds up a three-body scattering solution with a hyperspherical wave front in the Ω_0 region where all inter-particle distances are large. On the other hand, within the convergent close coupling method [10–12], the ionization problem is treated using a finite set of square integrable single-particle functions; in this case, accurate boundary conditions need not be imposed. Alternative approaches are provided by the Coulomb–Sturmian separable expansion [13,14] and the J -matrix [15,16] methods which deal with the wave function in the entire space using the Laguerre basis representation; the two-electron continuum problem is transformed in this case into a Lippmann–Schwinger equation with a kernel which is generally non-compact, and thus the validity of these approaches may be questionable.

In this contribution, we would like to put forward an alternative approach to the two-electron continuum representation in the entire space. The key idea is to use a basis set of functions with asymptotic behavior as close as possible to the formal one in the Ω_0 region [1,17]. Our principal goal is to show that the adequate asymptotic property leads to an acceptable convergence rate for expansions in such a basis.

The proposed basis set contains two ingredients. First, it uses two-particle functions named Convolved Quasi Sturmians (CQS) in Ref. [3] behaving asymptotically as a six-dimensional outgoing (incoming) spherical wave. This means that, contrary to pure products of single-particle functions, the basis functions already possess intrinsically some three-body features. However truncated expansions in CQS functions fail to converge satisfactorily. The reason behind that is the lack of an important term in the large hyperradius ($\rho = \sqrt{r_1^2 + r_2^2}$) domain, the Coulomb logarithmic phase corresponding to the inter-electronic interaction. This brings us to the second ingredient, which is the introducing — from the outset — of an appropriate phase factor into the basis set. The modified CQS functions possess an asymptotic behavior closer to the formal one, and lead to a considerable convergence improvement in numerical results. We have already mentioned that, when dealing with the Coulomb three-body scattering problem, we do not know *a priori* the size of the finite domain in which one needs to solve the corresponding driven Schrödinger equation. With the modified CQS basis, we know however that the functions satisfy the equation in the asymptotic region Ω_0 , and thus the size of this domain is determined by the range of the ‘perturbation’ operator (at least of its basis-independent part) induced by the phase factor.

As we focus on the region Ω_0 , we consider as a numerical test case the double ionization channel of helium atom in kinematical conditions measured experimentally [18]. In our previous paper [3] we analyzed the feasibility of the proposed approach within the Temkin–Poet framework. Here we extend the study by including higher partial waves. We first investigate the compatibility of introducing the phase factor when using truncated expansions to solve the Schrödinger driven equation in the entire space. Then, we use a simple two-parameters form of the introduced phase factor to demonstrate that a satisfactory convergence rate can be achieved indeed.

Atomic units ($\hbar = e = m_e = 1$) are used throughout unless otherwise stated.

2 Problem statement

The first order treatment of ionization of atoms can be recast into a driven differential equation with a square integrable inhomogeneity. For example, in the case of the double ionization of helium by photon impact or by impact of a fast charged projectile, the inhomogeneous Schrödinger equation takes the form

$$\left[E - \hat{H} \right] \Phi^{(+)}(\mathbf{r}_1, \mathbf{r}_2) = \hat{W}_{fi}(\mathbf{r}_1, \mathbf{r}_2) \Phi^{(0)}(\mathbf{r}_1, \mathbf{r}_2), \quad (1)$$

where $E = \frac{k_1^2}{2} + \frac{k_2^2}{2}$ is the energy of the two ejected electrons with coordinates \mathbf{r}_1 and \mathbf{r}_2 , $\Phi^{(0)}(\mathbf{r}_1, \mathbf{r}_2)$ represents the ground state of the helium atom, and the three-body helium Hamiltonian is given by

$$\hat{H} = \hat{H}_1 + \hat{H}_2 + \frac{1}{r_{12}}, \quad (2)$$

$$\hat{H}_j = -\frac{1}{2}\Delta_{r_j} - \frac{2}{r_j}, \quad j = 1, 2; \quad (3)$$

$r_{12} = |\mathbf{r}_1 - \mathbf{r}_2|$ denotes the relative inter-electronic distance. In the case of high incident electron impact energy, the perturbation operator is given by [9,19]

$$\hat{W}_{fi}(\mathbf{r}_1, \mathbf{r}_2) = \frac{1}{(2\pi)^3} \frac{4\pi}{q^2} (-2 + e^{i\mathbf{q}\cdot\mathbf{r}_1} + e^{i\mathbf{q}\cdot\mathbf{r}_2}), \quad (4)$$

where \mathbf{k}_i and \mathbf{k}_f are the momenta of the incident and scattered electrons, and $\mathbf{q} = \mathbf{k}_i - \mathbf{k}_f$ is the transferred momentum. The solution $\Phi^{(+)}$ with outgoing wave boundary condition, contains all information on the scattering dynamics.

In this section we examine the solution of Eq. (1) for given quantum numbers (L, M) in the space of CQS functions $Q_{n_1 n_2}^{\ell_1 \ell_2 (+)}$ [3],

$$|n_1 \ell_1 n_2 \ell_2; LM\rangle_Q \equiv \frac{Q_{n_1 n_2}^{\ell_1 \ell_2 (+)}(E; r_1, r_2)}{r_1 r_2} \mathcal{Y}_{LM}^{\ell_1 \ell_2}(\hat{\mathbf{r}}_1, \hat{\mathbf{r}}_2), \quad (5)$$

where the bispherical harmonics are given by

$$\mathcal{Y}_{LM}^{\ell_1 \ell_2}(\hat{\mathbf{r}}_1, \hat{\mathbf{r}}_2) = \sum_{m_1+m_2=M} (\ell_1 m_1 \ell_2 m_2 | LM) Y_{\ell_1 m_1}(\hat{\mathbf{r}}_1) Y_{\ell_2 m_2}(\hat{\mathbf{r}}_2). \quad (6)$$

The radial CQS functions $Q_{n_1 n_2}^{\ell_1 \ell_2 (\pm)}$ satisfy the inhomogeneous equation

$$\left[E - \hat{h}_1^{\ell_1} - \hat{h}_2^{\ell_2} \right] Q_{n_1 n_2}^{\ell_1 \ell_2 (\pm)}(E; r_1, r_2) = \frac{\psi_{n_1}^{\ell_1}(r_1) \psi_{n_2}^{\ell_2}(r_2)}{r_1 r_2}, \quad (7)$$

where

$$\hat{h}^\ell = -\frac{1}{2} \frac{\partial^2}{\partial r^2} + \frac{1}{2} \frac{\ell(\ell+1)}{r^2} - \frac{2}{r}, \quad (8)$$

and

$$\psi_n^\ell(r) = [(n+1)_{2\ell+1}]^{-\frac{1}{2}} (2br)^{\ell+1} e^{-br} L_n^{2\ell+1}(2br) \quad (9)$$

are square integrable Laguerre basis functions with a scaling parameter b . A number of properties of these CQS functions have been obtained in Ref. [3]. For example, they can be expressed as a convolution integral of two single-particle Quasi Sturmian functions [20]; using Green's function, the radial CQS can be expressed through a contour integral which is useful for deducing the leading asymptotic behavior at large hyperradius ρ :

$$Q_{n_1 n_2}^{\ell_1 \ell_2 (+)}(E; r_1, r_2) \simeq \sqrt{\frac{8}{\pi}} e^{\frac{i\pi}{4}} S_{n_1 \ell_1}(p_1) S_{n_2 \ell_2}(p_2) \frac{1}{\sqrt{k\rho}} \\ \times \exp \left\{ i \left[k\rho - \beta_1 \ln(2p_1 r_1) - \beta_2 \ln(2p_2 r_2) + \sigma_{\ell_1}(p_1) + \sigma_{\ell_2}(p_2) - \frac{\pi(\ell_1 + \ell_2)}{2} \right] \right\}, \quad (10)$$

where α is the hyperangle, $\tan(\alpha) = r_2/r_1$; $k = \sqrt{2E}$, $p_1 = k \cos(\alpha)$, $p_2 = k \sin(\alpha)$, $\beta_1 = \frac{-2}{p_1}$, $\beta_2 = \frac{-2}{p_2}$, and $\sigma_\ell(p) = \text{Arg}[\Gamma(\ell+1+i\beta)]$ is the Coulomb phase shift. $S_{n\ell}(p)$ is the sine-like J -matrix solution [21] [an explicit expression can be found, e. g., in Ref. [3], Eq. (14a)].

Assuming that the outgoing solution of Eq. (1) can be expanded as

$$\Phi^{(+)}(\mathbf{r}_1, \mathbf{r}_2) = \sum_{\ell_1, \ell_2=0}^{\infty} \sum_{n_1, n_2=0}^{\infty} C_{n_1 n_2}^{L(\ell_1 \ell_2)} |n_1 \ell_1 n_2 \ell_2; LM\rangle_Q, \quad (11)$$

we find the formal asymptotic expression

$$\Phi^{(+)}(\mathbf{r}_1, \mathbf{r}_2) \simeq A(\hat{\mathbf{r}}_1, \hat{\mathbf{r}}_2) \frac{1}{\rho^{5/2}} \exp \{ i [k\rho - \beta_1 \ln(2p_1 r_1) - \beta_2 \ln(2p_2 r_2)] \}, \quad (12)$$

$$A(\hat{\mathbf{r}}_1, \hat{\mathbf{r}}_2) = \frac{2}{E \sin(2\alpha)} \sqrt{\frac{2}{\pi}} (2E)^{3/4} e^{\frac{i\pi}{4}} \\ \times \sum_{\ell_1 \ell_2=0}^{\infty} \mathcal{Y}_{LM}^{\ell_1 \ell_2}(\hat{\mathbf{r}}_1, \hat{\mathbf{r}}_2) \exp \left\{ i \left[\sigma_{\ell_1}(p_1) + \sigma_{\ell_2}(p_2) - \frac{\pi(\ell_1 + \ell_2)}{2} \right] \right\} \\ \times \sum_{n_1, n_2=0}^{\infty} C_{n_1 n_2}^{L(\ell_1 \ell_2)} S_{n_1 \ell_1}(p_1) S_{n_2 \ell_2}(p_2). \quad (13)$$

The leading asymptotic behavior of the two-electron continuum wave function is known [1, 17] to include the Coulomb phase corresponding to the inter-electronic interaction $1/r_{12}$,

$$W_3(\mathbf{r}_1, \mathbf{r}_2) = -\frac{\rho}{k} \frac{1}{r_{12}} \ln(2k\rho). \quad (14)$$

Expression (12) clearly does not contain such a phase. As observed within a Temkin–Poet framework [3], this failure leads to a lack of convergence for the proposed CQS basis. The remedy proposed in Ref. [3] for the S -wave case is extended here to higher partial waves.

3 Two-electron continuum representation

In order to describe better the two-electron correlation in the continuum, in particular, in the Ω_0 region, we propose a solution of the form

$$\Phi^{(+)}(\mathbf{r}_1, \mathbf{r}_2) = e^{i\mathcal{W}(\mathbf{r}_1, \mathbf{r}_2)} \tilde{\Phi}^{(+)}(\mathbf{r}_1, \mathbf{r}_2), \quad (15)$$

where the leading asymptotic form of the phase \mathcal{W} is given by Eq. (14). Assuming $\tilde{\Phi}^{(+)}$ to be properly expandable in terms of the CQS functions (5),

$$\tilde{\Phi}^{(+)}(\mathbf{r}_1, \mathbf{r}_2) = \sum_{\ell_1, \ell_2=0}^{\infty} \sum_{n_1, n_2=0}^{\infty} \tilde{C}_{n_1 n_2}^{L(\ell_1 \ell_2)} |n_1 \ell_1 n_2 \ell_2; LM\rangle_Q, \quad (16)$$

the expression (15) is hereafter referred to as a *two-electron continuum* (TEC) representation of the solution.

Substituting $\Phi^{(+)}(\mathbf{r}_1, \mathbf{r}_2)$ in Eq. (1) by Eq. (15), we obtain

$$\left[E - \hat{H}_1 - \hat{H}_2 + \hat{\mathcal{L}} \right] \tilde{\Phi}^{(+)}(\mathbf{r}_1, \mathbf{r}_2) = e^{-i\mathcal{W}(\mathbf{r}_1, \mathbf{r}_2)} \hat{W}_{fi} \Phi^{(0)}(\mathbf{r}_1, \mathbf{r}_2), \quad (17)$$

where the operator

$$\begin{aligned} \hat{\mathcal{L}} = \frac{i}{2} [\Delta_{r_1} \mathcal{W} + \Delta_{r_2} \mathcal{W}] - \frac{1}{2} [(\nabla_{r_1} \mathcal{W})^2 + (\nabla_{r_2} \mathcal{W})^2] \\ + i [(\nabla_{r_1} \mathcal{W}) \cdot \nabla_{r_1} + (\nabla_{r_2} \mathcal{W}) \cdot \nabla_{r_2}] - \frac{1}{r_{12}}, \end{aligned} \quad (18)$$

can be eventually treated as a perturbation. Using the gradient operator expression [22],

$$\nabla_r = \frac{\mathbf{r}}{r} \frac{\partial}{\partial r} + \frac{1}{r} \nabla_{\Omega}, \quad (19)$$

we present the operator (18) as

$$\hat{\mathcal{L}} = \hat{\mathcal{U}} + \hat{\mathcal{V}}, \quad (20)$$

where

$$\begin{aligned} \hat{\mathcal{U}} = \frac{i}{2} [\Delta_{r_1} \mathcal{W} + \Delta_{r_2} \mathcal{W}] - \frac{1}{2} [(\nabla_{r_1} \mathcal{W})^2 + (\nabla_{r_2} \mathcal{W})^2] \\ + i \left[\frac{1}{r_1} (\nabla_{r_1} \mathcal{W}) \cdot \nabla_{\Omega_1} + \frac{1}{r_2} (\nabla_{r_2} \mathcal{W}) \cdot \nabla_{\Omega_2} \right], \end{aligned} \quad (21)$$

$$\hat{\mathcal{V}} = i \left[(\nabla_{r_1} \mathcal{W}) \cdot \frac{\mathbf{r}_1}{r_1} \frac{\partial}{\partial r_1} + (\nabla_{r_2} \mathcal{W}) \cdot \frac{\mathbf{r}_2}{r_2} \frac{\partial}{\partial r_2} \right] - \frac{1}{r_{12}}. \quad (22)$$

The operator $\hat{\mathcal{U}}$ acts only on the bispherical harmonics, and it can be easily verified that it is a short-range potential. Concerning the operator $\hat{\mathcal{V}}$, the phase \mathcal{W} in the asymptotic region is given by Eq. (14), and hence at large ρ

$$\nabla_{r_1} \mathcal{W} \simeq -\frac{1}{k} \left\{ \frac{\mathbf{r}_1}{r_{12}\rho} [1 + \ln(2k\rho)] - \frac{\mathbf{r}_{12}}{r_{12}^3} \rho \ln(2k\rho) \right\}, \quad (23)$$

$$\nabla_{r_2} \mathcal{W} \simeq -\frac{1}{k} \left\{ \frac{\mathbf{r}_2}{r_{12}\rho} [1 + \ln(2k\rho)] + \frac{\mathbf{r}_{12}}{r_{12}^3} \rho \ln(2k\rho) \right\}. \quad (24)$$

Moreover, using the asymptotics of the radial CQS functions (10), we obtain ($j = 1, 2$):

$$\frac{\partial}{\partial r_j} |n_1 \ell_1 n_2 \ell_2; LM\rangle_Q \simeq ik \frac{r_j}{\rho} |n_1 \ell_1 n_2 \ell_2; LM\rangle_Q. \quad (25)$$

Finally, by applying the operator (22) to Eq. (5) and taking into account Eqs. (23) and (25), we conclude that $\widehat{\mathcal{V}}$ acts upon these basis functions as a short-range potential that vanishes faster than ρ^{-1} in the limit $\rho \rightarrow \infty$. Thus the operator (18) may be treated as a perturbation and therefore the expansion (16) of the solution in our TEC representation is expected to converge.

The following issue has to be taken into account. Although the use of the phase factor allows one to take care of the Coulomb potential $1/r_{12}$, we cannot employ Eq. (14) directly because singular terms $1/r_{12}^3$ and $1/r_{12}^4$ appear in Eq. (21). However, this difficulty can be easily circumvented by using in both the Hamiltonian and the phase factor a truncated multipole expansion,

$$V_{12} = \sum_{\lambda=0}^{\lambda_{max}} \left(\frac{r_{<}^\lambda}{r_{>^{\lambda+1}}} \right) P_\lambda(x), \quad (26)$$

$$x = \frac{r_1^2 + r_2^2 - r_{12}^2}{2r_1 r_2}, \quad (27)$$

instead of $1/r_{12}$. In Ref. [3] we considered only the $\lambda = 0$ case (Temkin–Poet model).

4 Two-channel case

As an illustration, we compare below the functions $\Phi^{(+)}$ and $\widetilde{\Phi}^{(+)}$ by solving the inhomogeneous Eq. (1). More precisely, we consider the truncated expansions of $\Phi_N^{(+)}$ and $\widetilde{\Phi}_N^{(+)}$ containing $N \times N$ terms and compare their convergence rate as N increases. For test purposes, we consider the case of zero total angular momentum, $L = M = 0$, and, for simplicity, we retain in the partial-wave expansions in Eqs. (11) and (16) only two bispherical terms \mathcal{Y}_{00}^{00} and \mathcal{Y}_{00}^{11} . Hence it is sufficient to retain the first three multipole terms in Eq. (26).

We solve Eq. (1) with the initial helium ground state wave function in the driven term given by the product of hydrogen functions (with $Z_e = 2 - 5/16$), and we set $E = 0.791$ (i. e., 20 eV) and $q = 0.24$, as in one of the Orsay experiments [18] (see also Ref. [19]). The scale parameter of the CQS basis is chosen to be $b = 0.6$.

Consider first the expansion

$$\Phi_N^{(+)}(\mathbf{r}_1, \mathbf{r}_2) = \sum_{\ell=0,1} \sum_{n_1, n_2=0}^{N-1} C_{n_1 n_2}^\ell |n_1 \ell n_2 \ell; 00\rangle_Q. \quad (28)$$

With the help of Eq. (7) we rewrite Eq. (1) as

$$\sum_{\ell=0,1} \sum_{n_1, n_2=0}^{N-1} C_{n_1 n_2}^\ell \left[\frac{1}{r_1 r_2} |n_1 \ell n_2 \ell; 00\rangle_L - \frac{1}{r_{12}} |n_1 \ell n_2 \ell; 00\rangle_Q \right] = \widehat{W}_{fi} \Phi^{(0)}(\mathbf{r}_1, \mathbf{r}_2), \quad (29)$$

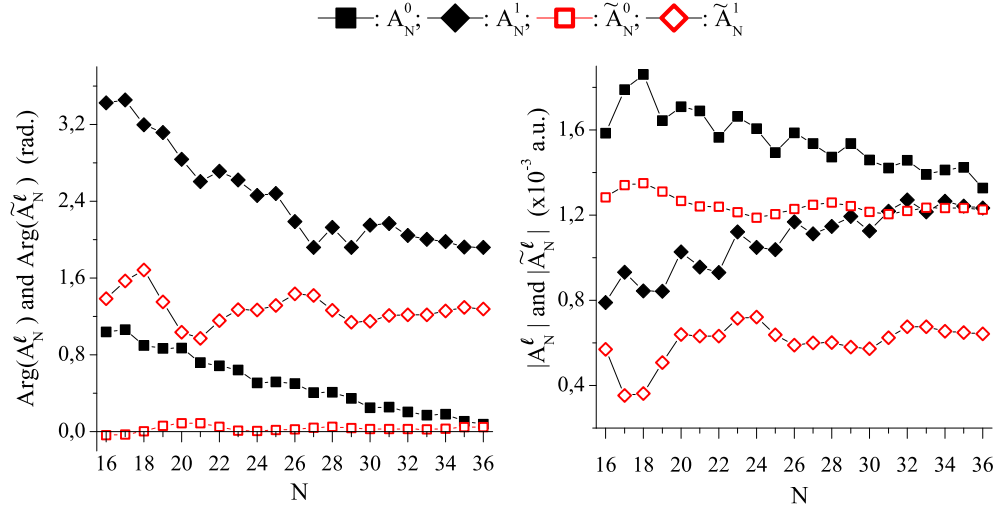


Figure 1: Convergence of the amplitudes A_N^ℓ (filled symbols) and \tilde{A}_N^ℓ (open symbols) for $\alpha = \frac{\pi}{4}$ and $\ell = 0, 1$. We present separately the results for the arguments $\text{Arg}(A_N^\ell)$ and $\text{Arg}(\tilde{A}_N^\ell)$ (left panel) and absolute values $|A_N^\ell|$ and $|\tilde{A}_N^\ell|$ (right panel).

where the coupled Laguerre basis functions

$$|n_1 \ell_1 n_2 \ell_2; LM\rangle_L \equiv \frac{\psi_{n_1}^{\ell_1}(r_1) \psi_{n_2}^{\ell_2}(r_2)}{r_1 r_2} \mathcal{Y}_{LM}^{\ell_1 \ell_2}(\hat{\mathbf{r}}_1, \hat{\mathbf{r}}_2). \quad (30)$$

We obtain a matrix equation for the coefficients $C_{n_1 n_2}^\ell$ (see, e. g., Ref. [23]) by projecting Eq. (29) onto the basis set (30) and making use of the orthogonality relation

$${}_L \langle n'_1 \ell'_1 n'_2 \ell'_2; LM | \frac{1}{r_1 r_2} | n_1 \ell_1 n_2 \ell_2; LM \rangle_L = \delta_{n'_1 n_1} \delta_{n'_2 n_2} \delta_{\ell'_1 \ell_1} \delta_{\ell'_2 \ell_2}. \quad (31)$$

The asymptotic behavior of the proposed solution is given by Eq. (12) where the amplitude

$$A(\hat{\mathbf{r}}_1, \hat{\mathbf{r}}_2) = \sum_{\ell=0,1} A_N^\ell \mathcal{Y}_{00}^{\ell\ell}(\hat{\mathbf{r}}_1, \hat{\mathbf{r}}_2) \quad (32)$$

is expressed in terms of partial amplitudes

$$A_N^\ell = \frac{2}{\sin(2\alpha)} \sqrt{\frac{8}{\pi}} e^{i\frac{\pi}{4}} k^{-1/2} \exp\{i[\sigma_\ell(p_1) + \sigma_\ell(p_2) - \pi\ell]\} \times \sum_{n_1, n_2=0}^{N-1} C_{n_1 n_2}^\ell S_{n_1 \ell}(p_1) S_{n_2 \ell}(p_2). \quad (33)$$

The amplitudes A_N^ℓ for $\alpha = \frac{\pi}{4}$ and $\ell = 0, 1$ are shown in Fig. 1 as functions of N (filled symbols). A poor convergence of both the argument $\text{Arg}(A_N^\ell)$ and the absolute value $|A_N^\ell|$ clearly demonstrates a limited practical usefulness of the expansion (28).

Consider now the solution $\tilde{\Phi}^{(+)}$ in the TEC representation given by the truncated expansion

$$\tilde{\Phi}_N^{(+)}(\mathbf{r}_1, \mathbf{r}_2) = \sum_{\ell=0,1} \sum_{n_1, n_2=0}^{N-1} \tilde{C}_{n_1 n_2}^{\ell} |n_1 \ell n_2 \ell; 00\rangle_Q. \quad (34)$$

Upon substitution into Eq. (17) we find

$$\begin{aligned} \sum_{\ell=0,1} \sum_{n_1, n_2=0}^{N-1} \left[\frac{1}{r_1 r_2} |n_1 \ell n_2 \ell; 00\rangle_L + \hat{\mathcal{L}} |n_1 \ell n_2 \ell; 00\rangle_Q \right] \tilde{C}_{n_1 n_2}^{\ell} \\ = e^{-i\mathcal{W}(\mathbf{r}_1, \mathbf{r}_2)} \hat{W}_{fi} \Phi^{(0)}(\mathbf{r}_1, \mathbf{r}_2). \end{aligned} \quad (35)$$

This equation should be solved in the same manner as Eq. (29) to obtain the expansion coefficients $\tilde{C}_{n_1 n_2}^{\ell}$.

We have seen how the leading asymptotic form of the phase \mathcal{W} given by Eq. (14) determines the features of the operator (18) acting on the CQS basis functions in the region Ω_0 . There is no need to reproduce precisely the r.h.s of Eq. (14) since it is asymptotical. On the other hand, we have to ensure the regularity at the origin of the $\hat{\mathcal{L}}$ operator representation. Apart from this constraint, we are free to modify properties of $\hat{\mathcal{L}}$ at moderate distances by including higher order terms in \mathcal{W} with the aim to optimize the basis set. We use the following phase parametrization (note, various other parametrizations can be also explored):

$$\mathcal{W}(\mathbf{r}_1, \mathbf{r}_2) = -\frac{s}{k} [\ln(2ks) + d] \left(\frac{1}{u} + \frac{r_1 r_2}{u^3} P_1(x) + \frac{(r_1 r_2)^2}{u^5} P_2(x) \right), \quad (36)$$

$$u = \sqrt{a^2 + r_>^2}, \quad s = \sqrt{c^2 + \rho^2}, \quad (37)$$

where real positive parameters a and c are introduced to avoid singularities at the origin (for simplicity we set $c^2 = a$). We have also introduced a real parameter d that allows one to improve the convergence rate of expansion (34). The results presented below are obtained with $a = 5$ and $d = -4.75$.

Let us now come back to the proposed truncated expansion (34). The asymptotic behavior of $\tilde{\Phi}_N^{(+)}$ is still given by Eq. (12) with the amplitude $A(\hat{\mathbf{r}}_1, \hat{\mathbf{r}}_2)$ which should be calculated using Eq. (32) where the partial amplitudes A_N^{ℓ} should be replaced by

$$\begin{aligned} \tilde{A}_N^{\ell} = \frac{2}{\sin(2\alpha)} \sqrt{\frac{8}{\pi}} e^{\frac{i\pi}{4}} k^{-1/2} \exp \{i [\sigma_{\ell}(p_1) + \sigma_{\ell}(p_2) - \pi\ell]\} \\ \times \sum_{n_1, n_2=0}^{N-1} \tilde{C}_{n_1 n_2}^{\ell} S_{n_1 \ell}(p_1) S_{n_2 \ell}(p_2). \end{aligned} \quad (38)$$

The convergence behavior of \tilde{A}_N^{ℓ} is shown in Fig. 1 (open symbols). As expected, the rate and smoothness of convergence are considerably improved by the TEC representation. This result demonstrates numerically that the inclusion of an appropriate phase factor into the basis functions is able to adequately absorb the leading asymptotic effect of the electron-electron interaction.

5 Summary

In our previous publication [3], we have proposed the phase factor method as a new approach to double ionization problems represented by the three-body driven equation with a square integrable inhomogeneity. Specifically, we tried to solve the S -model equation describing the fast electron impact double ionization of helium by expanding the solution in terms of the so-called Convolved Quasi Sturmian functions. Since the asymptotic behavior of these functions is inconsistent with that of formal Coulomb three-body continuum states, the CQS basis cannot represent the solution in the entire space. Even worse, we have found out that our solution diverges as the basis size increases. In order to circumvent this failure, and thus to improve the convergence rate, we have suggested equipping the basis CQS functions with the phase factor corresponding to the inter-electronic interaction. Within the S -wave framework, this strategy has been demonstrated to be successful.

In this paper an extension of the phase factor approach of Ref. [3] to arbitrary angular momenta is proposed. Since the phase factor is intended to account for the inter-electronic Coulomb interaction, it is natural to use the same truncated multipole expansion of $1/r_{12}$ in the generalized phase as employed to approximate this potential in the Hamiltonian. We examine the validity of our modified CQS approach in a two-channel case by constructing a suitable formula for the phase. The inclusion of higher order terms in $1/\rho$ in the leading asymptotic behavior, results in a significant convergence acceleration of the calculated amplitudes. We also demonstrate the convergence rate of the solution expansion to be rather sensitive to the phase behavior at moderate distances; optimized parameters (only two in our case) can therefore improve the efficiency of the basis. We expect the CQS basis combined with the proposed phase method to provide an efficient tool for the studies of full $(e, 3e)$ processes as well.

Acknowledgments

We are thankful to the Computer Center, Far Eastern Branch of the Russian Academy of Sciences (Khabarovsk, Russia), and Moscow State University (supercomputer Lomonosov) for providing the computer resources. The work was supported by the Russian Science Foundation under the project No. 16-12-10048.

References

- [1] L. D. Faddeev and S. P. Merkuriev, *Quantum scattering theory for several particle systems*. Kluwer, Dordrecht, 1993.
- [2] I. Bray, D. I. Fursa, A. S. Kadyrov, A. T. Stelbovics, A. Kheifets and A. M. Mukhamedzhanov, *Phys. Rep.* **520**, 135 (2012).
- [3] A. S. Zaytsev, L. U. Ancarani and S. A. Zaytsev, *Eur. Phys. J. Plus* **131**, 48 (2016).
- [4] C. W. McCurdy, M. Baertschy and T. N. Rescigno, *J. Phys. B* **37**, R137 (2004).
- [5] M. V. Volkov, N. Elander, E. Yarevsky and S. L. Yakovlev, *Europhys. Lett.* **85**, 30001 (2009)

- [6] N. Elander, M. Volkov, Å. Larson, M. Stenrup, J. Z. Mezei, E. Yarevsky and S. Yakovlev, *Few-Body Syst.* **45**, 197 (2009).
- [7] E. Yarevsky, S. L. Yakovlev, Å. Larson and N. Elander, *J. Phys. B* **48**, 115002 (2015).
- [8] G. Gasaneo, L. U. Ancarani, D. M. Mitnik, J. M. Randazzo, A. L. Frapiccini and F. D. Colavecchia, *Adv. Quant. Chem.* **67**, 153 (2013).
- [9] M. J. Ambrosio, F. D. Colavecchia, G. Gasaneo, D. M. Mitnik and L. U. Ancarani, *J. Phys. B* **48**, 055204 (2015).
- [10] I. Bray and A. T. Stelbovics, *Phys. Rev. Lett.* **69**, 53 (1992).
- [11] I. Bray, D. V. Fursa, A. Kheifets and A. T. Stelbovics, *J. Phys. B* **35**, R117 (2002).
- [12] A. S. Kadyrov, A. M. Mukhamedzhanov, A. T. Stelbovics and I. Bray, *Phys. Rev. A* **70**, 062703 (2004).
- [13] Z. Papp, C.-Y. Hu, Z. T. Hlousek, B. Kónya and S. L. Yakovlev, *Phys. Rev. A* **63**, 062721 (2001).
- [14] Z. Papp, J. Darai, C.-Y. Hu, Z. T. Hlousek, B. Kónya and S. L. Yakovlev, *Phys. Rev. A* **65**, 032725 (2002).
- [15] S. A. Zaytsev, V. A. Knyr, Yu. V. Popov and A. Lahmam-Bennani, *Phys. Rev. A* **75**, 022718 (2007).
- [16] M. S. Mengoue, M. G. Kwato Njock, B. Piraux, Yu. V. Popov and S. A. Zaytsev, *Phys. Rev. A* **83**, 052708 (2011).
- [17] M. R. H. Rudge, *Rev. Mod. Phys.* **40**, 564 (1968).
- [18] A. Lahmam-Bennani, I. Taouil, A. Duguet, M. Lecas, L. Avaldi and J. Berakdar, *Phys. Rev. A* **59**, 3548 (1999).
- [19] G. Gasaneo, D. M. Mitnik, J. M. Randazzo, L. U. Ancarani and F. D. Colavecchia, *Phys. Rev. A* **87**, 042707 (2013).
- [20] J. A. Del Punta, M. J. Ambrosio, G. Gasaneo, S. A. Zaytsev and L. U. Ancarani, *J. Math. Phys.* **55**, 052101 (2014).
- [21] A. D. Alhaidari, E. J. Heller, H. A. Yamani and M. S. Abdelmonem (eds.), *The J-matrix method. Developments and applications*. Springer, 2008.
- [22] D. A. Varshalovich, A. N. Moskalev and V. K. Khersonskii, *Quantum theory of angular momentum*. World Scientific, Singapore, 1988.
- [23] M. S. Aleshin, S. A. Zaitsev, G. Gasaneo and L. U. Ancarani, *Izv. Vyssh. Uchebn. Zaved. Fiz.* **58**, No 7, 62 (2015) [*Russ. Phys. J.* **58**, 941 (2015)].

Highlights from the 17-Year Heavy Ion Program at the PHENIX Experiment at RHIC

John C. Hill
for the PHENIX Collaboration

Department of Physics and Astronomy, Iowa State University, Ames, IA 50011, USA

Abstract

A review is given of evidence from particle yields, elliptic flow and temperature measurements that a Quark Gluon Plasma (QGP) has been formed in relativistic collisions of heavy Au + Au nuclei. PHENIX studies of $d + \text{Au}$ and $^3\text{He} + \text{Au}$ collisions at 200 GeV/A were carried out to see if such correlations persist at lower energies compared to those at the LHC. Data from Au + Au collisions collected during the beam energy scan (BES) were used to determine both quark and nucleon number scaling. The HBT method was used to determine radii of the nuclear fireball at kinetic freeze out. Implications for the nuclear Equation of State (EoS) are discussed. After taking data starting in the year 2000 PHENIX was shut down in 2016. Plans for its successor named sPHENIX will be briefly discussed.

Keywords: *RHIC; PHENIX; nuclear modification factor R_{AA} ; elliptic flow; QGP temperature; $d + \text{Au}$; $^3\text{He} + \text{Au}$; HBT; sPHENIX*

1 Introduction

The Relativistic Heavy Ion Collider (RHIC) was built at Brookhaven National Laboratory (BNL) and collisions of beams of 130 GeV/A Au nuclei were observed in June 2000. PHENIX and STAR are two large detector systems built to study these collisions. In the summer of 2001 experiments with collisions of Au beams at the full RHIC energy of 200 GeV/A were studied. After extensive analysis of the results of runs from the years 2000 to 2004 a white paper [1] was published where evidence was given for the production of a Quark Gluon Plasma (QGP). The plasma was designated sQGP in illusion to the strong coupling observed. In addition the sQGP behaved not as a gas as many expected but like a liquid with almost zero viscosity, the so called “perfect liquid”. In 2010 the collisions of Pb nuclei were observed at the Large Hadron Collider (LHC) at a much higher energy density than at RHIC. This talk first discusses the suppression of particles in the hot dense nuclear medium created at RHIC which gives evidence that the QGP is strongly coupled. Next evident for flow of the QGP indicates that the plasma acts like a liquid rather than a

Proceedings of the International Conference ‘Nuclear Theory in the Supercomputing Era — 2016’ (NTSE-2016), Khabarovsk, Russia, September 19–23, 2016. Eds. A. M. Shirokov and A. I. Mazur. Pacific National University, Khabarovsk, Russia, 2018, p. 246.

<http://www.ntse-2016.khb.ru/Proc/Hill.pdf>

gas. A description of recent measurements at PHENIX to measure the temperature of the QGP are presented. Results of measurements made at RHIC on $d + \text{Au}$ and $^3\text{He} + \text{Au}$ systems to determine if long-range correlations exist in small systems will be presented. Results of the low energy scan of $\text{Au} + \text{Au}$ collisions and HBT measurements of the radius of the nuclear fireball at freeze out will be given. Finally a short discussion of future experiments possible with the upgrade of PHENIX entitled sPHENIX will be presented followed by the conclusions.

2 Particle suppression in the QGP

In order to produce a QGP you need not only high energies but large volumes (times of the order of magnitude of 10 fm/c and 3–10 times normal nuclear density). This is necessary to sustain high energy densities and temperatures for an adequately long period of time. In the initial collision products of hard scattering are created followed by the creation of large numbers of quarks and gluons out of the vacuum resulting in a dense partonic medium. This medium can initially be the QGP but as it cools and expands it evolves into a hadronic gas. For 200 GeV/A Au collisions of the order of 10^4 particles are created. In order to study the properties of the QGP, particles that traverse the hot dense medium serve as a probe of its properties. For these studies of the properties of the medium we introduce a Nuclear Modification Factor R_{AA} .

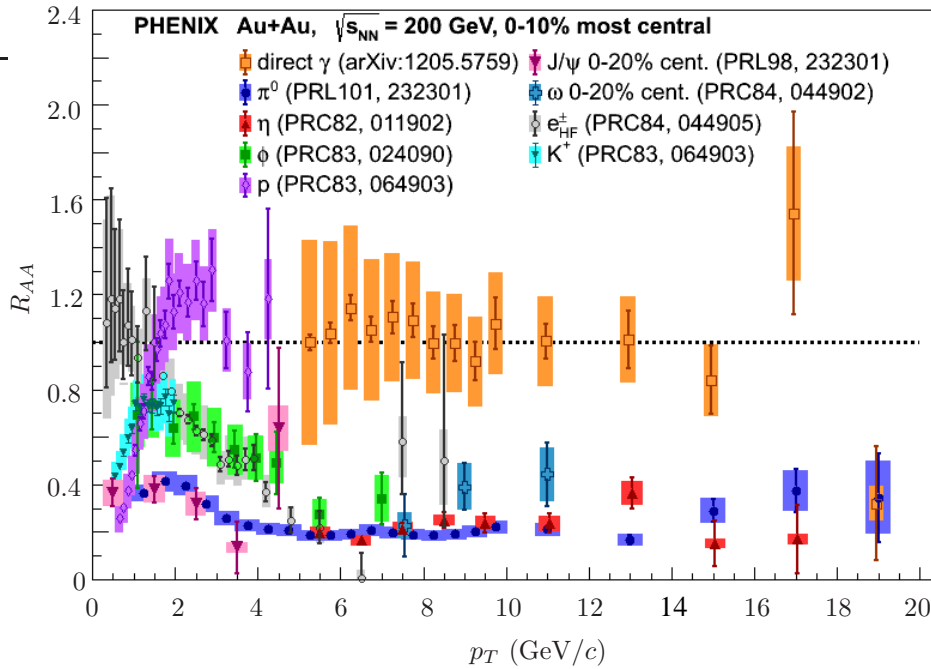


Figure 1: Plots showing R_{AA} for the 0 to 10 percent most central 200 GeV/A $\text{Au} + \text{Au}$ collisions for a wide variety of mesons, protons and direct photons at particle transverse momenta up to 19 GeV/c. Note the large suppression of hadrons but not direct photons.

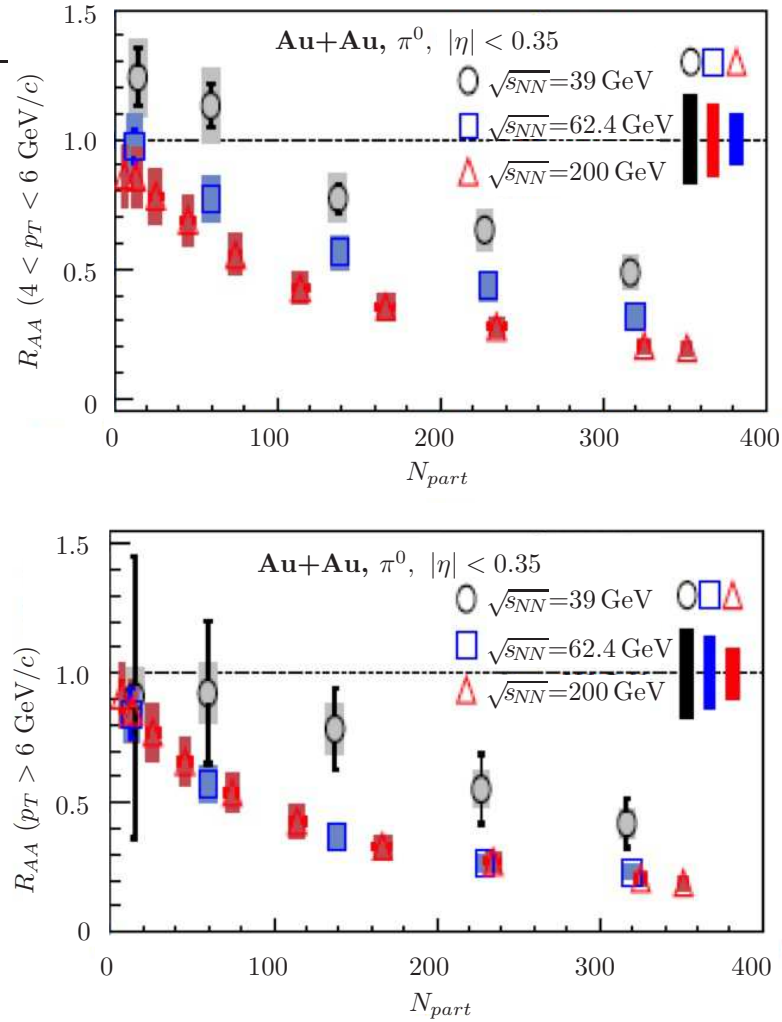


Figure 2: R_{AA} results for π^0 mesons for collision energies of 62.4 and 39 GeV/A. Particle numbers from 0 to 400 indicate a range from the most central to the most peripheral collisions.

In this factor the yield in nucleus-nucleus collisions is divided by the yield in $p + p$ collisions but scaled by the appropriate number of binary collisions N_{coll} which is calculated using the Glauber model. We do not expect to produce the QGP in $p + p$ collisions. Thus if the particles are not suppressed by the medium we expect $R_{AA} = 1.0$. A large number of measurements have been carried out at PHENIX to measure the response of various particles to passage through the hot dense medium created in Au + Au collisions. Using both Au + Au and $p + p$ data measured at PHENIX, R_{AA} for a number of different particles has been measured and the results are shown in Fig. 1 from the 2005 white paper [1]. Particularly striking is the large suppression of π^0 mesons [2] all the way out to 19 GeV/c. In addition large suppression of η [3] and ω mesons [4] was observed. This is an evidence for a strong suppression of mesons

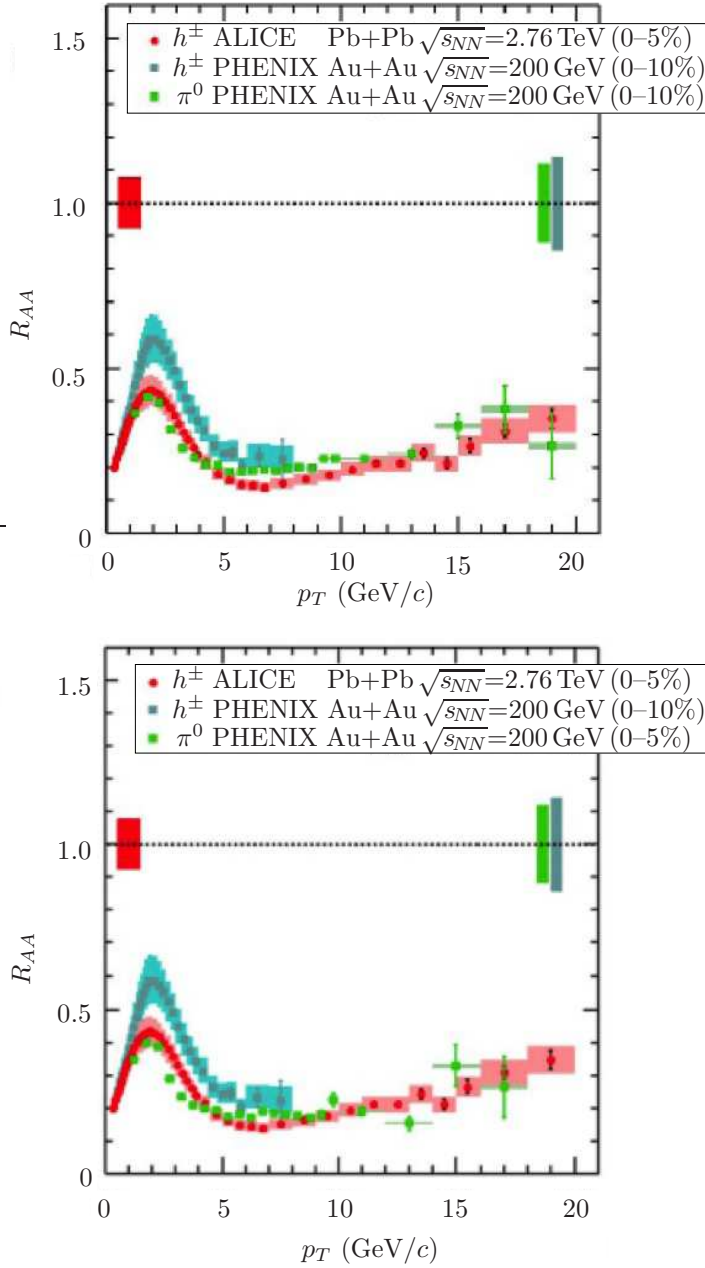


Figure 3: Plot showing R_{AA} for 200 GeV/A Au + Au collisions at PHENIX and 2.76 TeV/A Pb + Pb collisions at ALICE.

composed of the light u and d quarks in the sQGP.

The suppression of ϕ and K^+ mesons that contain a heavy s quark was measured. The suppression was less but still [5] significantly below an R_{AA} of 1.0 [5]. It might be expected that photons produced in direct interactions with the colliding quarks and gluons would not be suppressed by the sQGP since they only interact electromagnetically with the hot dense medium. This can be seen in the results in Fig. 1 for direct photons [6] where their R_{AA} is 1.0 within the error. We conclude that the sQGP

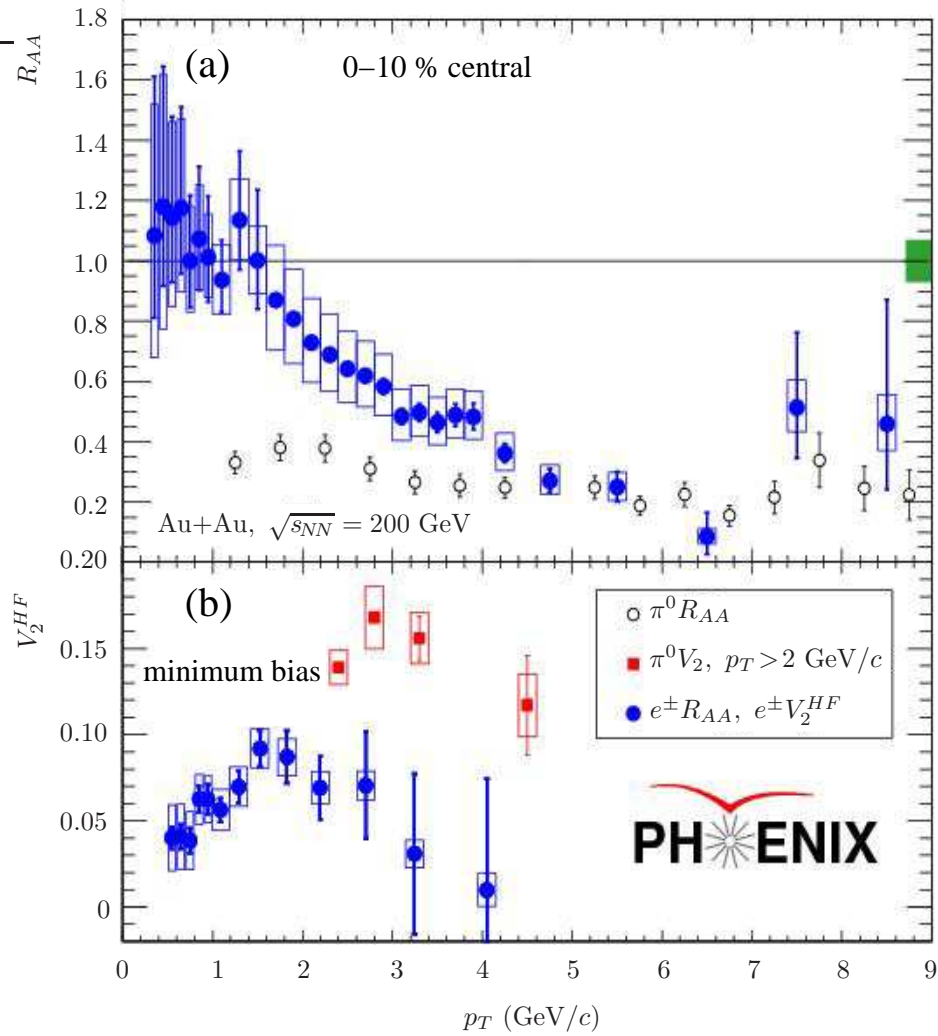


Figure 4: Plots of R_{AA} and v_2 in parts (a) and (b), respectively, for electrons from the decay of open charm and beauty. The data is for Au + Au collisions at 200 GeV and the 10 percent most central collisions.

strongly suppresses mesons made up of light u and d quarks but also significantly suppresses mesons composed of a heavier s quark. As expected direct photons are not significantly suppressed by the sQGP.

An important question is how does suppression in the sQGP change if we reduce the collision energy or the centrality of the collision. We would thus expect less suppression both for lower collision energy and more peripheral collisions. The Au + Au collisions were studied at 39 and 62.4 GeV/A and the results are compared with those at 200 GeV/A in Fig. 2. The suppression for a collision energy of 62.4 GeV/A is very similar to that for 200 GeV/A except that the suppression is slightly lower at 62.4 GeV/A for π^0 momenta below 6 GeV/c. By contrast when the collision energy is lowered to 39 GeV/A the π^0 is still suppressed but to a lesser extent than

at 62.4 GeV/A. It would be of interest to determine how far can we go down in collision energy and still see suppression. The data in Fig. 2 also shows that π^0 suppression is still large at all three collision energies [7] down to peripheral collisions where of the order of 50 particles are emitted.

The LHC has produced Pb + Pb collisions with an energy of 2.76 TeV/A. R_{AA} for the production of charged hadrons was measured with the ALICE detector. These results for R_{AA} are compared with those from Au + Au collisions at PHENIX [8] at a collision energy of 200 GeV/A in Fig. 3. From the figure it is observed that there is very little change in the suppression of the charged hadrons even though the collision energies at ALICE are much greater. One might expect a higher suppression due to the greater energy densities at ALICE but many more particles are produced so the recombination must be taken into account.

The suppression of u , d and s quarks in the sQGP is significant so it is interesting to test to what extent the much heavier c and b quarks are suppressed. To study this the R_{AA} for Au + Au collisions at 200 GeV/A was measured for electrons and positrons from decay of open charm and beauty. The R_{AA} for these particles is shown in the top part of Fig. 4 and compared [9] with results from π^0 . For the most central collisions electrons with p_T greater than 2.0 GeV/c are significantly suppressed.

From the study of the hot dense medium produced in Au + Au collisions at RHIC we can conclude the following:

1. In Au + Au collisions we have created a color opaque medium called the sQGP. The evidence is an observation of nuclear modification factors $R_{AA} < 1.0$.
2. Suppression of particles in the medium is prominent for collision energies down to 39 GeV/A.
3. The level of suppression at the higher energy densities at the LHC is similar to that at RHIC.
4. The level of suppression is still very significant for the heavy c and b quarks.

3 Evidence for flow in the QGP

A critical aspect of the establishment of the nature of the QGP has been the observation that the hot dense matter created in relativistic heavy ion collisions flows. The geometry of flow is illustrated in Fig. 5.

In studying the flow the following points are relevant.

1. The reaction geometry produces an almond shaped interaction region.
2. The compression of mass in the center produces an anisotropic p_T distribution.
3. The resulting p_T distribution is described in terms of $[1 + \sum_{n=1}^{\infty} 2v_n \cos[n(\phi - \Psi_R)]]$.
4. A finite v_2 is termed the elliptic flow. Ψ is in the plane of the beam and the impact parameter.

Flow data [8] for v_2 for collisions of Au + Au from PHENIX along with data from the much higher Pb + Pb collisions at the LHC is shown in Fig. 6. The values of v_2

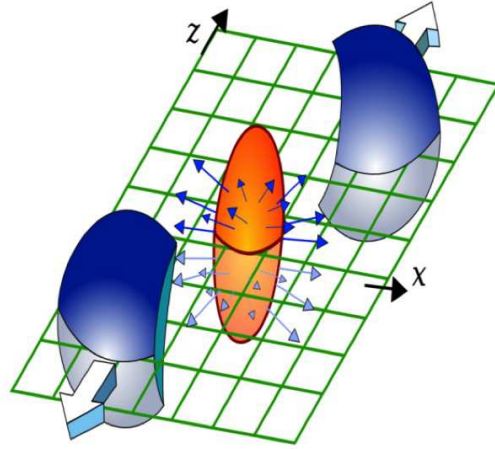


Figure 5: Diagram showing the geometry of flow for collisions of heavy nuclei.

show that flow is a prominent feature of Au+Au collisions. Relativistic hydrodynamic calculations [9] are a good fit to the data for $p_T < 2.0$ GeV/ c . A saturation of v_2 occurs as the energy reaches the RHIC regime. At saturation the QGP reaches the maximum achievable collective flow predicted by ideal hydrodynamics and the medium behaves as a nearly perfect fluid with very low viscosity. The ratio of shear viscosity to entropy density is very near the quantum lower bound. The data in Fig. 6 indicates that the fluid produced at LHC energies is very similar to that at RHIC. Evidently a much higher energy density is needed to create the QGP as a gas.

The quark scaling is an important signal indicating that a QGP has been formed. In Fig. 7 v_2 vs $m_T - m_0$ is plotted on the upper panel for a number of mesons ($n_q = 2$)

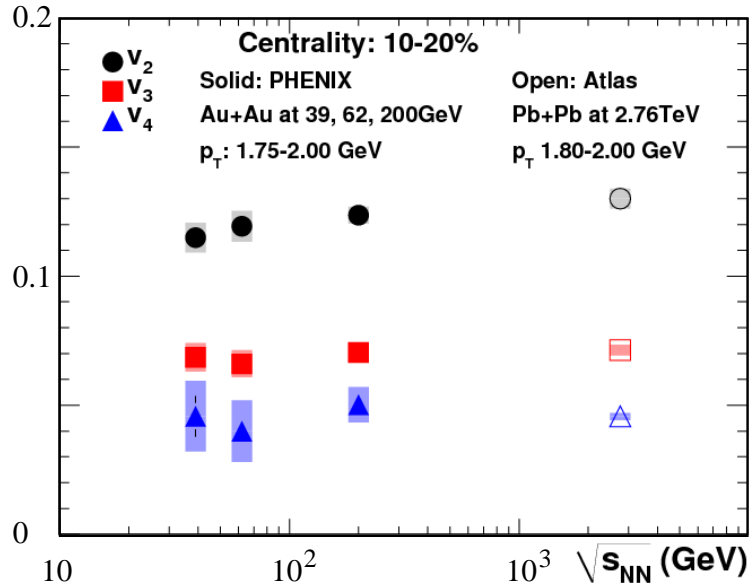


Figure 6: Data for v_{2-4} for collisions of $A + A$ at RHIC and LHC energies.

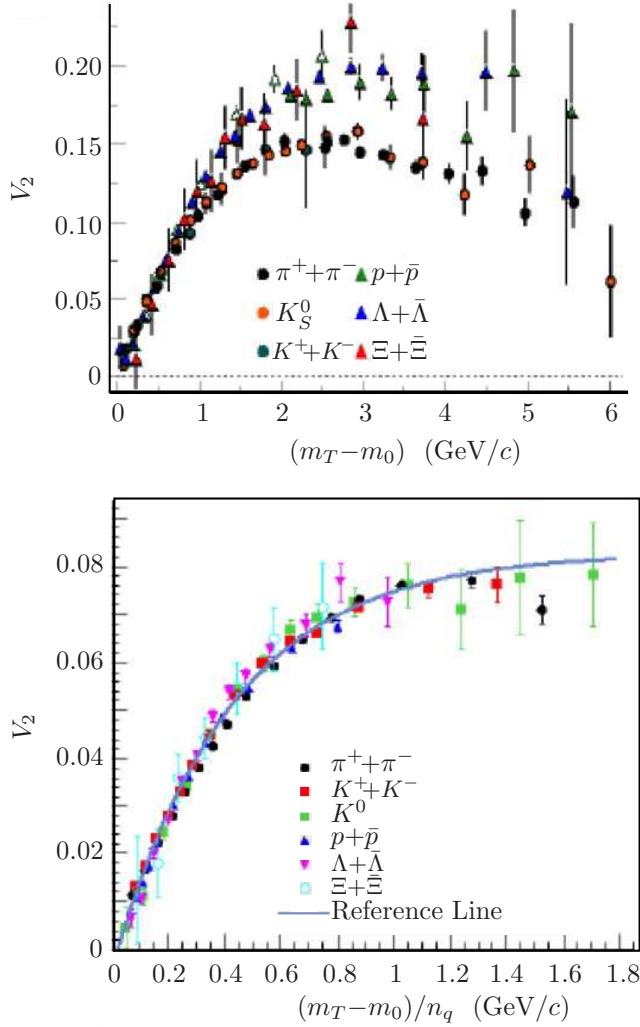


Figure 7: Data for v_2 for baryons and mesons indicating scaling by quark number.

Fluid \rightarrow QuasiParticles \rightarrow Hadrons

and baryons ($n_q = 3$) for 200 GeV/A Au+Au collisions. Note that on the average the v_2 for baryons is higher than for mesons. On the bottom panel we have plotted the same parameters but with each divided by the appropriate quark number n_q . Note that the meson and baryon points come together in a common curve thus scaling according to the valence quark count. The scaling identifies collective behavior as established during the partonic phase of evolution of the system indicating that the degrees of freedom are partonic. This is a direct signature of deconfinement and production of the QGP.

Although the flow has been established for particles containing u , d and s quarks, it is of interest to determine if the much heavier c and b quarks produced in 200 GeV/A Au + Au collisions exhibit flow. In the bottom part of Fig. 4 v_2 is plotted in blue for electrons and positrons from decays of particles with open c and b quarks. For comparison v_2 for π^0 is shown in red. The flow for particles with c and b quarks is

less than for π^0 but is still significant.

The results from the studies of flow at RHIC and LHC can be summarized as follows:

1. The elliptic flow is observed for Au and Pb collisions.
2. The flow at higher energy densities at the LHC is very similar to that at RHIC indicating the saturation.
3. The flow is significant for heavy c and b quarks.
4. The quark scaling of v_2 supports the formation of the QGP.

4 Temperature of the QGP

A primary goal of studies of the sQGP is to measure its temperature through observation of prompt gamma rays emitted as the nuclear fireball expands. The gamma ray spectrum is complex since the photons are emitted in all phases of the expansion. A diagram illustrating this process is shown in Fig. 8. In the initial phase hard scattering of the incident quarks produces jets that emit bremsstrahlung and thermalize producing the sQGP. The plasma next expands into a mixed phase eventually hadronizing into a hadron gas. The phases from sQGP to the hadron gas can be described by relativistic hydrodynamics.

In order to estimate the temperature of hot hadronic matter produced at RHIC, PHENIX measured dilepton production for 200 GeV/A Au and p collisions. These data were used to deduce the direct photon spectra shown in Fig. 9. The figure also shows estimated yields of photons from various stages of the collision. As can be seen from the figure the photon yield becomes softer but more intense as the reaction progresses from the initial hard scattering to the final stages of hadronization.

The data from the PHENIX measured dilepton production for 200 GeV/A Au and p collisions are also shown in Fig. 10. The data are compared with a number of theoretical calculations that assume a system with an initial temperature between 300 and 600 MeV and formation times between 0.6 and 0.15 fm/ c . The PHENIX data are in good agreement with calculations [9] that assume initial temperatures above 300 MeV which is well above the predicted formation temperature for the QGP of 170 MeV.

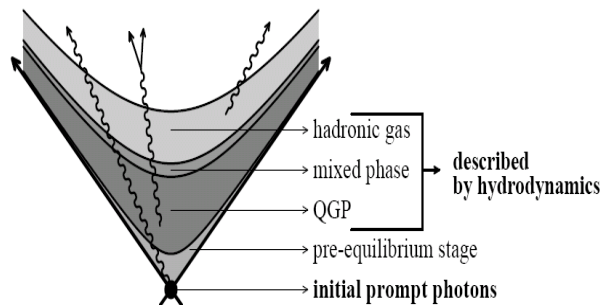


Figure 8: Diagram showing the phases in formation and expansion of the sQGP.

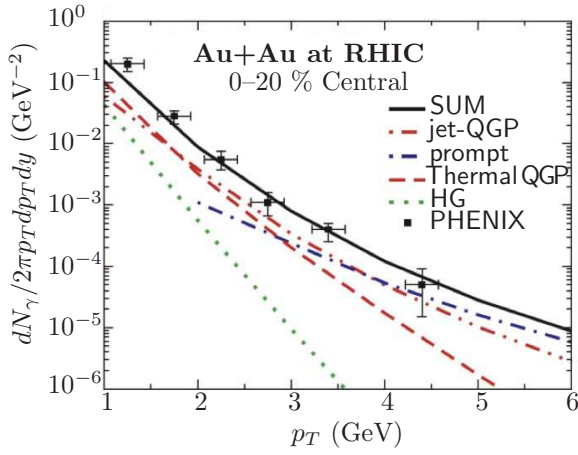


Figure 9: Photon yields from Au + Au collisions compared with calculated yields from various stages of the collision.

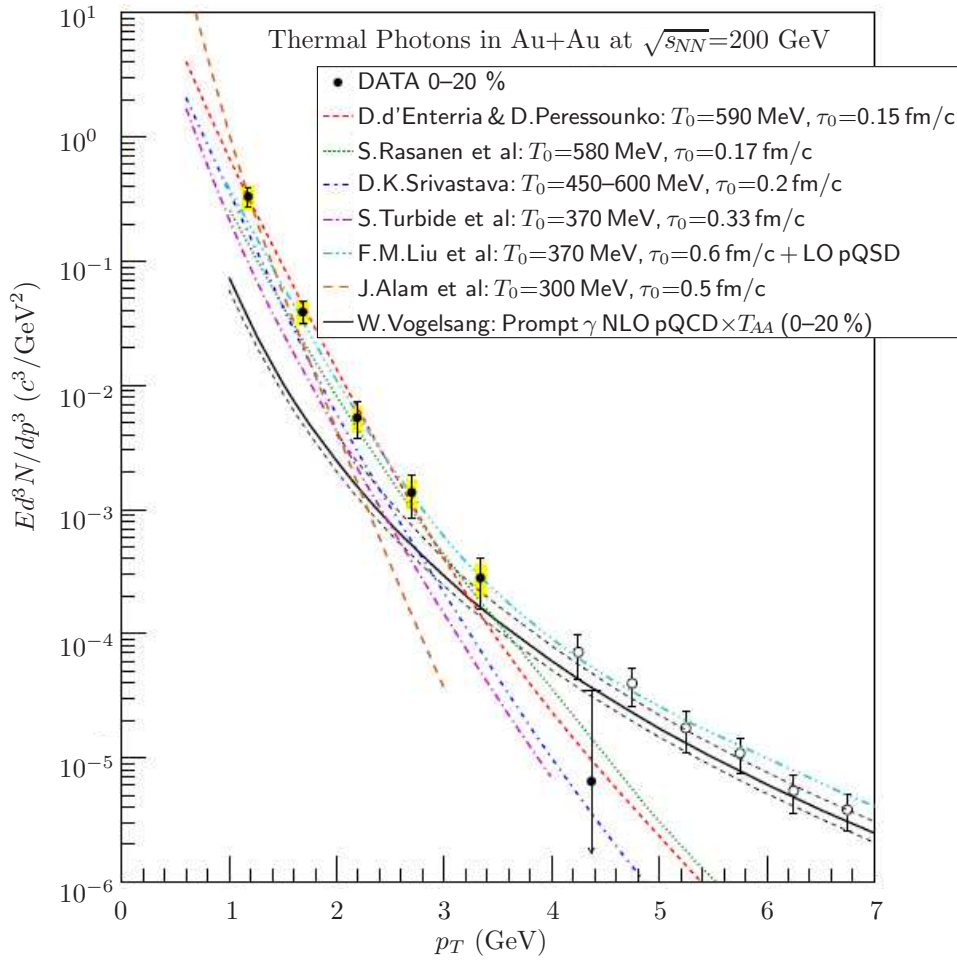


Figure 10: Spectrum of thermal photons from Au + Au collisions at 200 GeV/A compared with calculations assuming various values for formation energies and times.

5 The QGP and long-range correlations in low mass systems

In relativistic $A + A$ collisions a sQGP medium is formed which signals its presence through the long range correlations and a finite flow v_2 . It was thought that $p + p$ and $p + A$ collisions could not form such a medium because of the small system size. Recently results from ALICE [10] and CMS [11] for 5.02 TeV $p + \text{Pb}$ collisions at the LHC indicate the presence of long range correlations. A small v_2 and ridge were observed indicating the long range correlations and a significant flow. One might argue that for the lower beam energies at RHIC such correlations would be absent or much smaller. It is thus of interest to explore whether v_2 and a ridge would be observed with $d + \text{Au}$ collisions at RHIC at 200 GeV/A. In Fig. 11 results for v_2 for 200 GeV $d + \text{Au}$ for the 0 to 5% most central collisions are shown [12] and compared with the results of similar centrality for 5.02 TeV $p + \text{Pb}$ collisions at the LHC [10]. The following observations can be made.

1. A mass splitting of v_2 is seen for both $d + \text{Au}$ and $p + \text{Pb}$ reactions with v_2 generally larger for pions.
2. The viscous hydrodynamics [6] describes $d + \text{Au}$ below $p_T = 2.0 \text{ GeV}/c$.
3. Note a larger mass splitting for $p + \text{Pb}$ below $p_T = 2.0 \text{ GeV}/c$ that may indicate a stronger radial flow for $p + \text{Pb}$.

It is clear from Fig. 11 that a non-zero v_2 and flow are observed for both relativistic $d + \text{Au}$ collisions at RHIC and $p + \text{Pb}$ collisions at the LHC. It is thus of interest to determine if a ridge is observed in $d + \text{Au}$ collisions at RHIC. Therefore a correlation function $C(\Delta\phi, p_T)$ is constructed in the following steps.

1. Correlate one track in the central arm with one in the forward muon piston calorimeter.

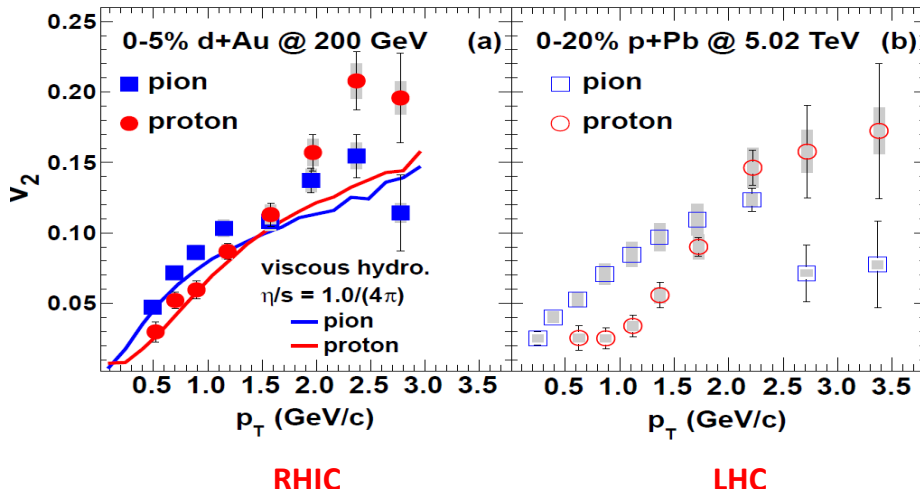


Figure 11: v_2 observed for 200 GeV $d + \text{Au}$ collisions.

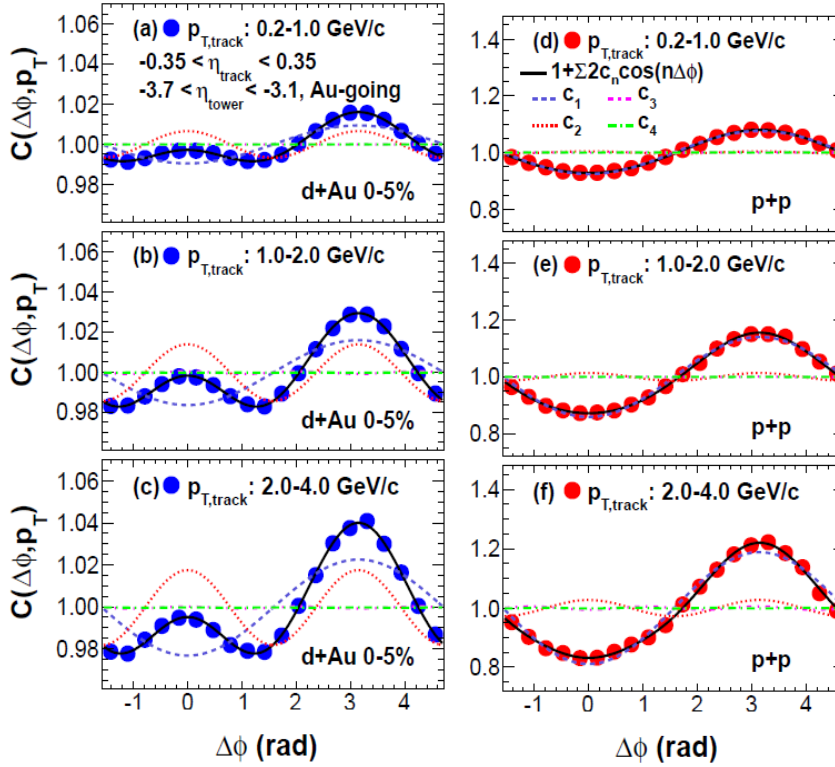


Figure 12: Correlation functions for Au + Au and $p + p$ collisions at RHIC.

2. Construct a signal distribution $S(\Delta\phi, p_T)$ where $\phi = \phi_{track} - \phi_{tower}$.
3. Construct mixed-event distribution $M(\Delta\phi, p_T)$ from different events.
4. Construct a normalized correlation function $C(\Delta\phi, p_T)$.

Correlation functions for central $d + Au$ collisions and mid-bias $p + p$ collisions for several p_T ranges [12] are shown in Fig. 12. Fits from c_1 to c_4 in $\cos(n\Delta\phi)$ are shown. The following conclusions can be drawn.

1. The $p + p$ reactions are dominated by the dipole term (no ridge).
2. The $d + Au$ reactions show a near side peak (ridge) that increases with p_T .

Since the $d + Au$ reactions show a ridge it is of interest to study in more detail the separate correlation functions from the d going and the Au going sides of the reaction. The result of this comparison is shown in Fig. 13. Note that a ridge is clearly visible for the Au but not for the d going side. Also the c_2 component for the d going side is not zero but is much reduced compared to c_2 for the Au going side. Studies of the correlation functions have also been made for the d and Au going sides as a function of centrality. For the Au going side there is a clear ridge that emerges as the centrality is increased. The peripheral collision pattern is similar for the d and Au sides showing essentially no ridge. For the d side no ridge is observed but the c_2 correlation increases with centrality [7].

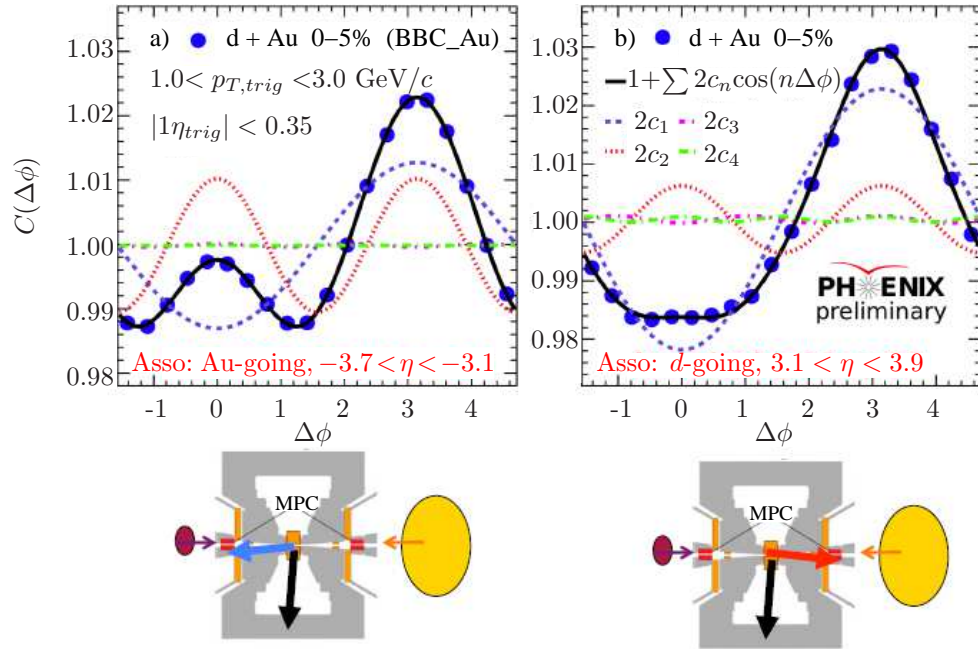


Figure 13: Comparison of correlation functions for the d going and Au going sides of $d + Au$ collisions.

Since long range correlations were observed in $d + Au$ collisions it was of interest to observe if such correlations were present in $^3\text{He} + Au$ collisions. Data was collected

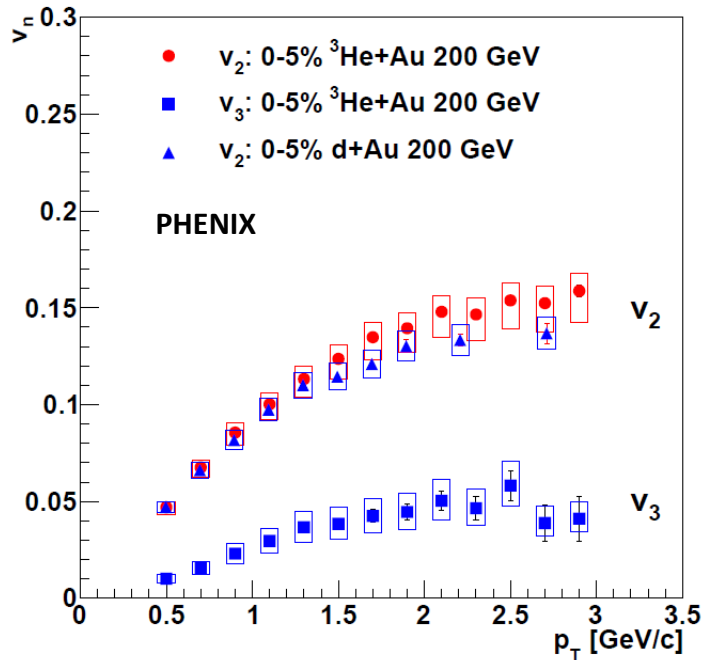


Figure 14: Measured v_2 and v_3 for 0-5% $^3\text{He} + Au$ collisions.

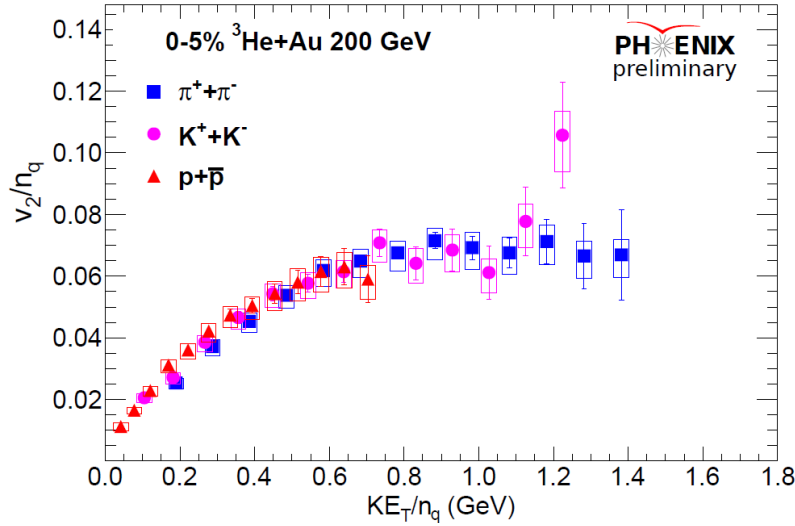


Figure 15: Quark scaling observed in central $^3\text{He} + \text{Au}$ collisions.

for $^3\text{He} + \text{Au}$ collisions for two weeks at 200 GeV/A at RHIC. A sample of 2.2 billion events at MB was collected. These collisions can be thought of as producing three hot spots that should result in a significant n_3 as well as a n_2 component of flow. A ridge was observed in high multiplicity (0–5%) $^3\text{He} + \text{Au}$ collisions. In the reference $p + p$ collisions, the correlation was dominated by momentum conservation (including dijets). A sizable v_2 and v_3 were observed in 0–5% $^3\text{He} + \text{Au}$ collisions [13], extracted by the event plane method as is shown in Fig. 14. The v_2 in 0–5% $^3\text{He} + \text{Au}$ and 0–5% $d + \text{Au}$ collisions is very similar [12]. Also a significant v_3 component is observed for the $^3\text{He} + \text{Au}$ collisions.

For identified charged particles v_2 was determined for the 0–5% $^3\text{He} + \text{Au}$ collisions at 200 GeV/A. Differences in the values for nucleons and mesons was observed at high p_T . This behavior is very similar to that in Au + Au collisions. As can be seen in Fig. 15 mesons and nucleons fall on a smooth curve when each particle v_2 is divided by its n_q . Thus the conclusion is that the quark scaling observed in Au + Au collisions has now been seen in the small $^3\text{He} + \text{Au}$ system. Flow and the ridge have been observed for collisions of Au on p , d and ^3He at RHIC and $p + \text{Pb}$ at the LHC. This suggests that in some cases QGP droplets have been formed in high energy collisions of large with small nuclei.

6 Results from low energy scans of Au + Au systems

Since the first collisions of Au + Au in the summer of 2000, RHIC has run a number of energy projectile combinations including Au + Au, U + U, Cu + Au, Cu + Cu, $^3\text{He} + \text{Au}$, $d + \text{Au}$ and $p + p$. The results from Au + Au collisions can be used to test the beam energy scaling. RHIC has provided Au + Au collision energies of 7.7, 15, 19.6, 27, 39, 62.4, 130 and 200 GeV/A providing a wide range of energies to test the energy scaling. To test the quark scaling, the yields of Au + Au collisions from 7.7 to 200 GeV/A were determined as a function of centrality [14]. The results are

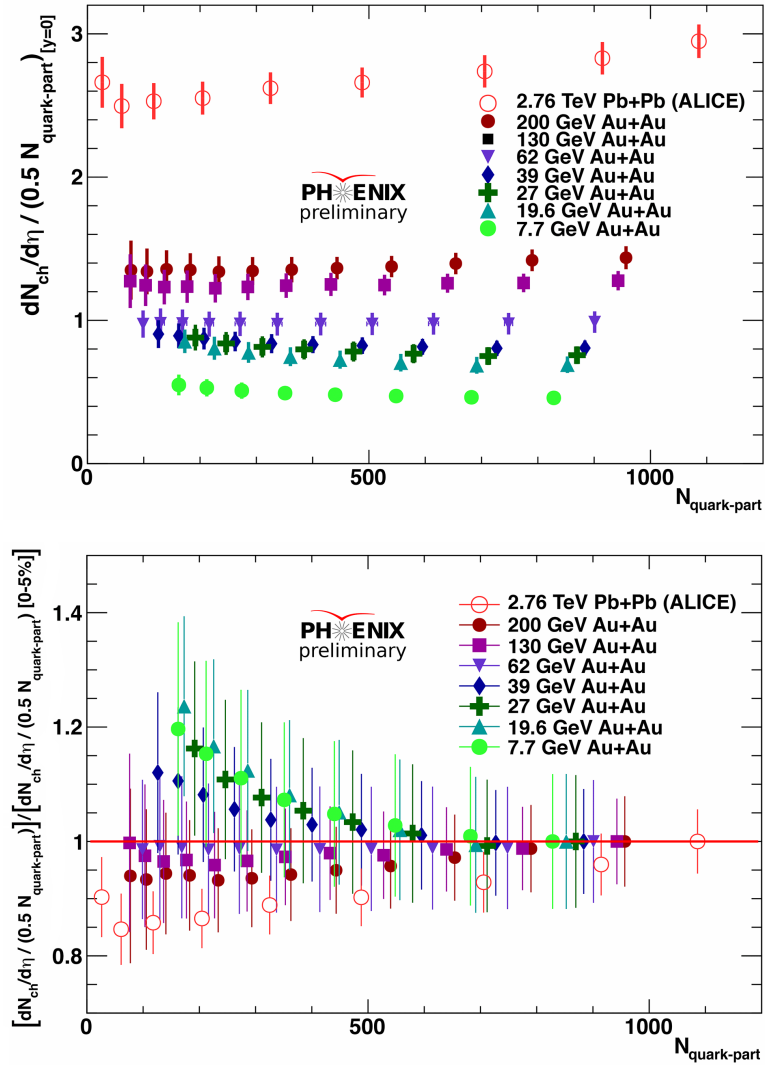


Figure 16: Beam energy scan quark scaling results for Au + Au collisions.

shown in Fig. 16. The plot on the upper panel in the figure shows the yield of Au+Au collisions from 7.7 to 200 GeV/A as a function of centrality but divided by the number of valence quarks. The plot on the lower panel shows the same data but with the highest centrality points for each beam energy normalized to 1.0 to show the trends.

As can be seen from Fig. 16, the quark scaling works well from 200 to 62 GeV but breaks down at lower energies. A plot can also be made (not shown) [14] where the yield is divided by the number of nucleons rather than the number of quarks. That plot shows that the nucleon scaling works well for energies below 40 GeV.

7 Studies of the nuclear fireball radii using the HBT method

In 1956 Hanbury Brown and Twiss (HBT) measured the angular diameter of Sirius from light by observing correlations of light from different parts of the planet's surface [15]. In 1960 Goldhaber *et al.* [16] measured correlation functions between pions in $p+\bar{p}$ reactions. It is thus possible to use HBT to determine correlation functions for the QGP fireball at kinetic freeze out. In order to do this, the 2-particle pion correlation functions of the form $C_2(q) = A(q)/B(q)$ were constructed using the following steps.

1. $A(q)$ is the measured distribution momentum difference $q = p_2 - p_1$.
2. $B(q)$ is the pair uncorrelated distribution from different events.
3. $C_2(q) = N[(\lambda(1 + G(q)))F_c + (\lambda - l)]$.
4. $G(q) = \exp(-R_{side}^2 q_{side}^2 - R_{out}^2 q_{out}^2 - R_{long}^2 q_{long}^2)$.

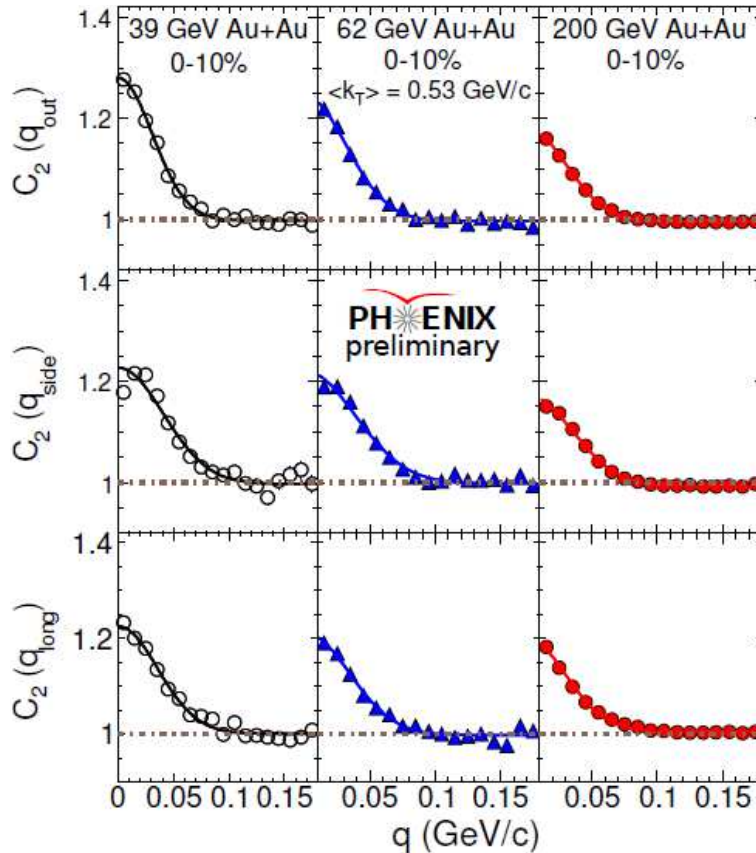


Figure 17: C_2 for 39, 62 and 200 GeV Au + Au central collisions.

In the equations above N is a normalization factor, λ is the correlation strength, F_c is the Coulomb correction factor and the R 's are the measured Gaussian HBT radii. The parameterization of Bertsch [17] and Pratt [18] was used for R where R_{long} is measured in the $q_{long} = 0$ frame. The parameter q_{long} is along the beam direction, q_{out} is parallel to k_T of the pair and q_{side} is perpendicular to the beam and k_T of the pair. The measured $C_2(q)$ can be used to determine R .

The C_2 correlation functions for 39, 62 and 200 GeV collisions of Au + Au [19] are shown in Fig. 17. From the correlation functions $C_2(q_{out})$, $C_2(q_{side})$ and $C_2(q_{long})$ the corresponding HBT pion radii R_{out} , R_{side} and R_{long} were calculated [14]. The radii have interesting scaling properties. Results for radii determined by both STAR [20] and PHENIX [21] are consistent with radii scaling linearly with $m_T^{-1/2}$. In addition it is found that the HBT pion radii scale linearly with the initial radius [19]. These results are consistent with calculations [21] which associate a larger expansion time with a larger size. In Fig. 18 the measured HBT pion radii are plotted as a function of Au + Au collision energy [19]. The results include data from PHENIX, STAR and ALICE. All the data is interpolated to $m_T = 0.26$ GeV. This is valid due to the m_T scaling. For all three radii an increase of kinetic freeze out radius with collision energy is observed.

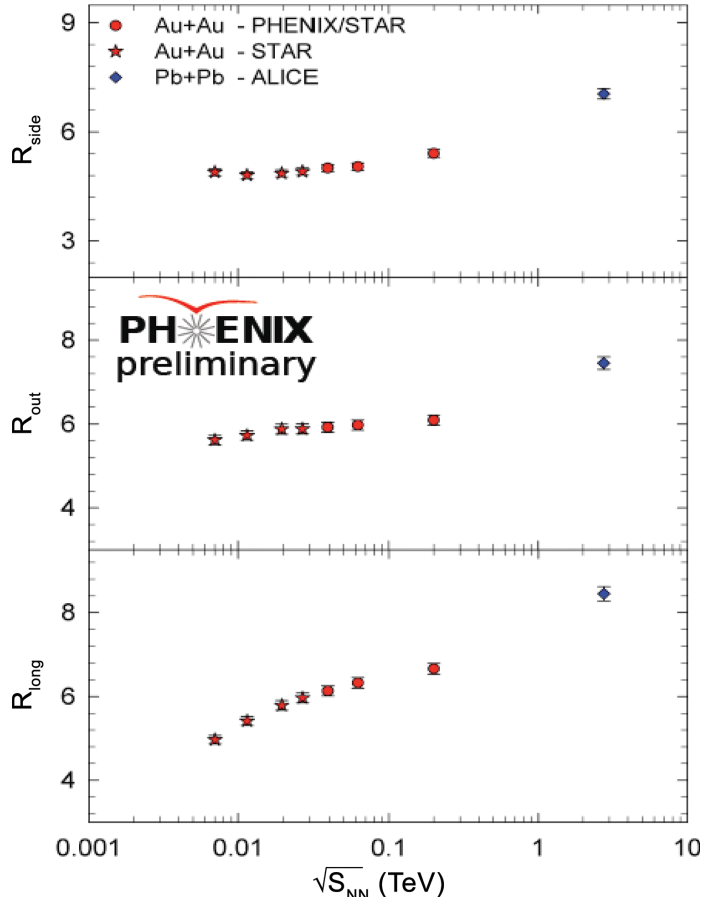


Figure 18: Results for HBT radii vs collision energy.

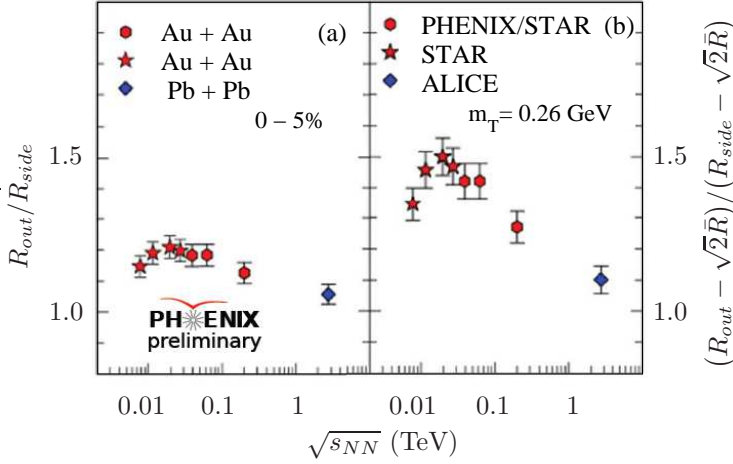


Figure 19: Trends of radii results with energy.

Ratios and differences of various HBT radii give information on both the kinetic freeze out time τ and the duration of kinetic freeze out $\Delta\tau$. $R_{out}^2 - R_{side}^2$ is a proxy for emission duration $\Delta\tau$ and R_{side}/R_{long} is a proxy for expansion speed and the speed of sound c_s in the medium [22]. The results for these parameters as a function of Au + Au collision energy are shown in Fig. 19. The results are not linear with energy. The curve for $R_{out}^2 - R_{side}^2$ shows a maximum in the vicinity of 30 GeV collision energy. The curve for R_{side}/R_{long} shows a minimum in the vicinity of 30 GeV [19]. These non-monotonic patterns are consistent with the minimum observed as a function of collision energy for the viscous coefficients [22] and could be a further indication of trajectories passing through the softest region in the Equation of State (EoS).

8 The future and sPHENIX

The next generation of PHENIX is designated sPHENIX. A primary goal of the sPHENIX program is to complete the picture for the sQGP of its evolution and coupling strength from the initial high temperature through expansion and cooling to the transition scale and below. A fragmentation of partons will be studied by measuring jets and the melting of the three Υ states, namely $1s$, $2s$ and $3s$. The direct photons and high p_T hadrons will be measured with higher statistics than in the past due to high rates and large acceptance expected with sPHENIX. It will be possible to study the R_{AA} of photons, jets, charged mesons and baryons and π^0 s at higher p_T . For example it should be possible to measure direct γ and charged hadrons up to 50 GeV/ c . The detector will be optimized to study jets. It should thus be possible to study jets up to 75 GeV/ c and b jets up to 40 GeV/ c .

An artists view of sPHENIX is shown in Fig. 20. A critical component of the detector was the solenoid magnet acquired from the Babar experiment. The sPHENIX detector is basically cylindrically symmetric. Starting from the interaction point at the center of the detector there is an electromagnetic calorimeter followed by an inner hadronic calorimeter. Next comes the Babar solenoid magnet and finally the outer hadronic calorimeter. Tracking detectors will be located near the beam interaction point.

A major goal for the sPHENIX program will be to study melting of the three Υ

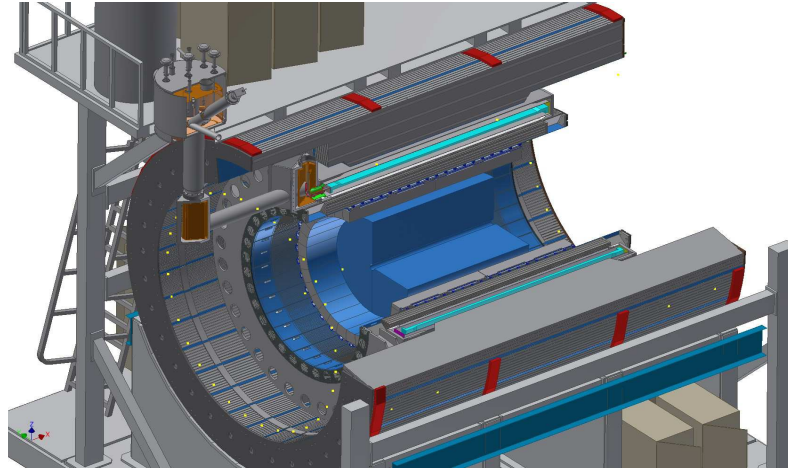
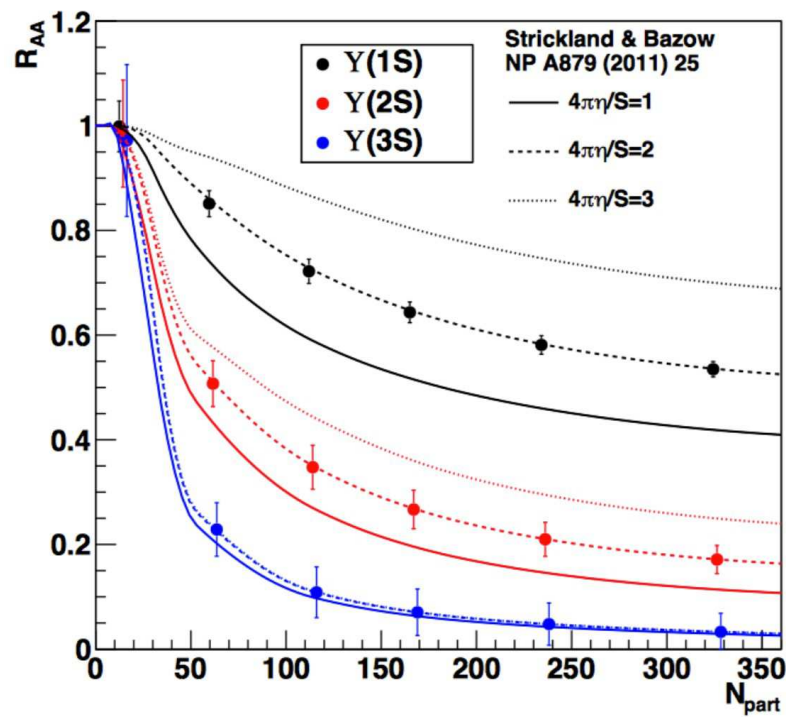


Figure 20: An artist's view of sPHENIX.

states in the sQGP. Figure 21 shows a simulation of R_{AA} data for the three Υ states that could be obtained after 22 weeks of Au + Au and 10 weeks of $p + p$ running. Calculations [16] indicate the relative suppression of the three states. This should give information on the temperature of the sQGP at the point where the melting of the Υ states occurs.

Figure 21: Nuclear modification projections for Υ .

The present status of sPHENIX is as follows. A Department of Energy panel accepted the science case for sPHENIX at a review completed May 2015. Brookhaven National Laboratory (BNL) has made sPHENIX an integral part of its plan for the future now that the PHENIX experiment has been completed in 2016. Design, simulation, R&D, and prototyping for sPHENIX are all moving forward. BNL convened a workshop to form a new sPHENIX collaboration in June 2015 and the first collaboration meeting was held on December 10–12, 2015 at Rutgers University. The planning calls for the sPHENIX detector to begin operation in 2022.

9 Conclusions

The main conclusions from the above paper are listed below:

1. A hot dense medium has been created in Au + Au collisions. The evidence is a nuclear modification factor $R_{AA} < 1.0$.
2. The hot dense medium flows. The sQGP acts as a high temperature low viscosity liquid. The evidence is $v_2 > 0$.
3. The sQGP is actually created. The evidence is the quark scaling of v_2 for mesons ($q = 2$) and baryons ($q = 3$).
4. No phase transition is observed implying the crossover from the sQGP to a hadron gas.
5. The evidence for QGP droplets is observed in p , d and ^3He collisions with heavy nuclei.
6. HBT studies measured radii at freeze out and point to a possible softening of the nuclear EoS around 30 GeV.
7. The predicted first order phase transition and critical point yet to be observed.
8. The PHENIX program ended in 2016 and now the collaboration is transitioning to sPHENIX.

References

- [1] K. Adcox *et al.*, Nucl. Phys. A **757**, 184 (2005).
- [2] A. Adare *et al.*, Phys. Rev. Lett. **101**, 232301 (2008).
- [3] A. Adare *et al.*, Phys. Rev. C **82**, 011902 (2010).
- [4] A. Adare *et al.*, Phys. Rev. C **84**, 044902 (2011).
- [5] A. Adare *et al.*, Phys. Rev. C **83**, 024909 (2011).
- [6] S. Afanasiev *et al.*, Phys. Rev. Lett. **109**, 152302 (2012).
- [7] A. Adare *et al.*, Phys. Rev. Lett. **109**, 152301 (2012).
- [8] J. Adams *et al.*, Phys. Rev. C **72**, 014904 (2005).

- [9] P. Huovinen, private communication (2004).
- [10] B. Abelev *et al.* (ALICE Collaboration), Phys. Lett. **B726**, 164 (2013).
- [11] D. Abbaneo *et al.* (CMS Collaboration), Phys. Lett. **B718**, 795 (2013).
- [12] A. Adare *et al.* (PHENIX Collaboration), Phys. Rev. Lett. **114**, 192301 (2015).
- [13] A. Adare *et al.* (PHENIX Collaboration), Phys. Rev. Lett. **115**, 142301 (2015).
- [14] R. Soltz (for the PHENIX Collaboration), Nucl. Phys. A **931**, 780 (2014).
- [15] R. H. Brown and R. Q. Twiss, Nature **178**, 1046 (1956).
- [16] G. Goldhaber, S. Goldhaber, W. Lee and A. Pais, Phys. Rev. **120**, 300 (1960).
- [17] G. Bertsch, Nucl. Phys. A **498**, 173 (1989).
- [18] S. Pratt, Phys. Rev. D **33**, 1314 (1986).
- [19] A. Adare *et al.* (PHENIX Collaboration), arXiv:1410.2559 (2014).
- [20] L. Adamczyk *et al.* (STAR Collaboration), Phys. Rev. C **92**, 014904 (2015).
- [21] E. Shuryak and I. Zahed, Phys. Rev. C **88**, 044915 (2013).
- [22] R. A. Lacey, A. Taranenko, J. Jia, D. Reynolds, N. N. Ajitanand, J. M. Alexander, Y. Gu and A. Mwai, Phys. Rev. Lett. **112**, 082302 (2014).

Algebraic Versions of Resonating Group and Orthogonality Condition Models as Fundamentals of Theoretical Approaches to the Description of Radiative Capture

A. S. Solovyev^{a,b}, S. Yu. Igashov^a and Yu. M. Tchuvil'sky^{a,b,c}

^a*Dukhov Research Institute of Automatics (VNIIA), Moscow 127055, Russia*

^b*Pacific National University, Khabarovsk 680035, Russia*

^c*Skobeltsyn Institute of Nuclear Physics, Lomonosov Moscow State University, Moscow 119991, Russia*

Abstract

Radiative capture reactions being an important class of nuclear fusion processes attract a significant interest, in particular, for nuclear astrophysics. Their cross sections at low energies are strongly suppressed by the Coulomb barrier and therefore are not available for reliable experimental measurements. As a result, there is a strong need in theoretical approaches to the studies of the radiative capture reactions cross sections.

In this work, the basic ideas of the algebraic versions of the resonating group and orthogonality condition models are presented. Microscopic approaches to the radiative capture reactions based on the algebraic version of resonating group model and semimicroscopic one combining the algebraic versions of resonating group and orthogonality condition models, are reviewed. An applicability of these approaches is demonstrated. Perspectives of their further applications are discussed.

Keywords: *Algebraic version of resonating group model; algebraic version of orthogonality condition model; microscopic approach; radiative capture reactions; low energies; cross section; astrophysical S-factor; nuclear astrophysics*

1 Introduction

Cross sections of a number of nuclear reactions at low sub-Coulomb energies are desired for numerous fundamental studies and advanced applications. For example, radiative capture cross sections at low energies are required for the studies of stellar processes, nucleosynthesis in the Universe, etc. [1–5]. These cross sections are strongly suppressed by the Coulomb barrier and therefore are not available for reliable experimental measurements. As a rule, cross section extrapolations to low energies also

Proceedings of the International Conference ‘Nuclear Theory in the Supercomputing Era — 2016’ (NTSE-2016), Khabarovsk, Russia, September 19–23, 2016. Eds. A. M. Shirokov and A. I. Mazur. Pacific National University, Khabarovsk, Russia, 2018, p. 267.

<http://www.ntse-2016.khb.ru/Proc/Solovyev.pdf>.

turn out to be unreliable. As a result, theoretical predictions based on microscopic approaches are expected to be the most justified and promising way to obtain the cross sections in the energy region inaccessible for experiment. These microscopic approaches should be able to describe a dynamics of all nucleons of a nuclear system considered with a complete account of the Pauli exclusion principle and a rigorous treatment of the center-of-mass motion. From the mathematical viewpoint, it means that the wave functions should be fully antisymmetrized and translationally invariant and have an explicit dependence on space and spin-isospin coordinates of all the nucleons of the system.

At the present moment, there is a number of approaches to the description of radiative capture reactions. In particular, there are various two-body approaches utilizing either the direct capture model [6, 7] or the potential cluster model [8–12]. There are also hybrid approaches which use either the variational Monte Carlo method [13, 14] or the no-core shell model [15–17] for bound states and the potential cluster model for continuum. Finally, there are fully microscopic approaches based either on the resonating group model (RGM) [18–21] or on the fermionic molecular dynamics [22], as well as on the no-core shell model with continuum [23].

In the present work, two microscopic approaches and a semimicroscopic approach to the radiative capture reactions [24–32] are briefly reviewed. One of these microscopic approaches [24–29] is based on the single-scale algebraic version of RGM (AVRGM) [33, 34] while the other [32] relies on the multiscale AVRGM. The semimicroscopic approach [30, 31] combines the single-scale AVRGM with the algebraic version of the orthogonality condition model (AVOCM) [35–39]. An applicability to the radiative capture processes and capabilities of these approaches have been demonstrated in the studies of mirror ${}^3\text{H}(\alpha, \gamma){}^7\text{Li}$ and ${}^3\text{He}(\alpha, \gamma){}^7\text{Be}$ reactions important for nuclear astrophysics. Both these reactions are responsible for the ${}^7\text{Li}$ production during the Big Bang nucleosynthesis. Their cross sections at low energies are necessary for calculating the ${}^7\text{Li}$ abundance required to resolve a number of problems concerning the Big Bang nucleosynthesis and to get a general understanding the primordial nucleosynthesis. Moreover, the latter reaction is a starting point of the second and the third chains of the pp cycle of hydrogen burning in stars. The cross section of this reaction at low energies is necessary for the studies of processes in the solar core and for the solar model verification.

2 Brief description of AVRGM and AVOCM. Generating functions method

In the framework of the single-channel RGM, the total wave function of a two-cluster nuclear system is expressed as an antisymmetrized product of internal wave functions $\phi^{(1)}$, $\phi^{(2)}$ of the clusters and the wave function f of their relative motion [40, 41]:

$$\Psi = \hat{A}\{\phi^{(1)}\phi^{(2)}f\}. \quad (1)$$

The translationally-invariant oscillator shell-model wave functions of the lowest states compatible with the Pauli principle are conventionally adopted as the internal wave functions of the clusters. The relative motion wave function is unknown and should be found by solving the integro-differential equation of RGM.

The main idea of AVRGM is to expand the relative motion wave function in series of the oscillator basis functions:

$$f_{\nu lm}(\vec{q}) = N_{\nu l} \bar{q}^l L_{(\nu-l)/2}^{(l+1/2)}(\bar{q}^2) \exp(-\bar{q}^2/2) Y_{lm}(\vec{n}_{\vec{q}}), \quad (2)$$

$$\bar{q} = q/r_0, \quad N_{\nu l} = (-1)^{(\nu-l)/2} \sqrt{\frac{2\Gamma((\nu-l+2)/2)}{r_0^3 \Gamma((\nu+l+3)/2)}},$$

where \vec{q} is the Jacobi vector characterizing the relative distance between the clusters; r_0 is the oscillator radius; ν is the oscillator quanta; l and m are the orbital momentum and its projection respectively; Γ is the gamma-function; $L_n^{(\beta)}$ is the generalized Laguerre polynomial; Y_{lm} is the spherical harmonic. As a result, the total wave function can be written as an expansion,

$$\Psi = \sum_{J^\pi M l s \nu} C_{J^\pi M l s \nu} \Psi_{J^\pi M l s \nu}, \quad (3)$$

over the so-called AVRGM basis,

$$\Psi_{J^\pi M l s \nu} = N_{J^\pi l s \nu} \hat{A} \left\{ \sum_{m+\sigma=M} C_{lm s \sigma}^{JM} [\phi_{s_1}^{(1)} \phi_{s_2}^{(2)}]_{s \sigma} f_{\nu lm}(\vec{q}) \right\}. \quad (4)$$

Here J and M are the total angular momentum and its projection respectively; π is the parity of the system; s_1 and s_2 are the cluster spins coupled to the channel spin s with projection σ ; $C_{lm s \sigma}^{JM}$ is the Clebsch–Gordan coefficient; $N_{J^\pi l s \nu}$ is the normalization factor; $C_{J^\pi M l s \nu}$ are unknown expansion coefficients satisfying an infinite set of homogeneous linear algebraic equations [33, 42],

$$\left\{ \begin{array}{l} \sum_{s=|s_1-s_2|}^{s_1+s_2} \sum_{l=|J-s|}^{J+s} \sum_{\nu=\nu_0}^{\infty} \left(\langle J^\pi M \tilde{l} \tilde{s} \tilde{\nu} | \hat{H} | J^\pi M l s \nu \rangle - E \delta_{\tilde{s}s} \delta_{\tilde{l}l} \delta_{\tilde{\nu}\nu} \right) C_{J^\pi M l s \nu} = 0, \\ \tilde{s} = |s_1 - s_2|, \dots, s_1 + s_2, \quad \tilde{l} = |J - \tilde{s}|, \dots, J + \tilde{s}, \quad \tilde{\nu} = \nu_0, \nu_0 + 2, \dots \end{array} \right. \quad (5)$$

Here \hat{H} and E are the Hamiltonian and the total energy of the system respectively, ν_0 is the minimal oscillator quanta compatible with the Pauli principle. It should be noted that the summations over ν in Eqs. (3) and (4) as well as in other expressions below are performed with a step of 2 since $\nu = 2n_r + l$, where $n_r = 0, 1, 2, \dots$ is the radial quantum number.

In the case of the discrete spectrum, we can use instead of Eq. (5) a reduced finite set of algebraic equations,

$$\left\{ \begin{array}{l} \sum_{s=|s_1-s_2|}^{s_1+s_2} \sum_{l=|J-s|}^{J+s} \sum_{\nu=\nu_0}^{\nu_{\max}} \left(\langle J^\pi M \tilde{l} \tilde{s} \tilde{\nu} | \hat{H} | J^\pi M l s \nu \rangle - E \delta_{\tilde{s}s} \delta_{\tilde{l}l} \delta_{\tilde{\nu}\nu} \right) C_{J^\pi M l s \nu}^{(D)} = 0, \\ \tilde{s} = |s_1 - s_2|, \dots, s_1 + s_2, \quad \tilde{l} = |J - \tilde{s}|, \dots, J + \tilde{s}, \quad \tilde{\nu} = \nu_0, \nu_0 + 2, \dots, \nu_{\max}, \end{array} \right. \quad (6)$$

where ν_{\max} should be sufficiently large depending on a desired accuracy. In the case of the continuum, the AVRGM equations (5) should be rewritten as a set of inhomogeneous linear algebraic equations,

$$\left\{ \begin{array}{l} \sum_s \sum_l \sum_{\nu=\nu_0}^{\nu_{\text{as}}-2} \left(\langle J^\pi M \tilde{l} \tilde{s} \tilde{\nu} | \hat{H} | J^\pi M l s \nu \rangle - E \delta_{\tilde{s}s} \delta_{\tilde{l}l} \delta_{\tilde{\nu}\nu} \right) C_{J^\pi M l s \nu}^{(C)} = F_{J^\pi M \tilde{l} \tilde{s} \tilde{\nu}}, \\ \tilde{s} = |s_1 - s_2|, \dots, s_1 + s_2, \quad \tilde{l} = |J - \tilde{s}|, \dots, J + \tilde{s}, \quad \tilde{\nu} = \nu_0, \nu_0 + 2, \dots, \nu_{\text{as}}. \end{array} \right. \quad (7)$$

The expansion coefficients $C_{J^\pi M l s \nu}^{(C)}$ are replaced starting from $\nu = \nu_{\text{as}}$ by their asymptotic expressions $C_{J^\pi M l s \nu}^{(\text{as})}$ [34, 43] entering the right-hand side (inhomogeneity) of Eq. (7):

$$F_{J^\pi M \tilde{l} \tilde{s} \tilde{\nu}} = - \sum_s \sum_l \sum_{\nu=\nu_{\text{as}}}^{\nu'_{\text{max}}} \langle J^\pi M \tilde{l} \tilde{s} \tilde{\nu} | \hat{H} | J^\pi M l s \nu \rangle C_{J^\pi M l s \nu}^{(\text{as})}. \quad (8)$$

Although the AVRGM and the RGM are similar from the physical viewpoint, their numerical realizations differ essentially: the AVRGM requires to find solutions of linear algebraic equations while within the conventional single-channel RGM one has to solve a more complicated integro-differential equation. In the case of the multichannel RGM, one faces a problem of solving a set of integro-differential equations [40, 41].

One of the main problems of the AVRGM realization is a calculation of the Hamiltonian matrix elements between the antisymmetrized AVRGM basis functions (4). This problem can be resolved using an elegant technique of the generating functions method [33, 42, 44, 45]. The basic idea of this method is to utilize the generating function of the harmonic oscillator functions:

$$f_{\nu l m}(\vec{q}) = A_{\nu l} \frac{\partial^\nu}{\partial R^\nu} \int \exp(-q^2/2r_0^2 + \vec{q}\vec{R}/r_0 - R^2/4) Y_{lm}(\vec{n}_{\vec{R}}) d\vec{n}_{\vec{R}} \Big|_{R=0}, \quad (9)$$

$$A_{\nu l} = \frac{2^{\nu-1/2}}{(\pi r_0)^{3/2} \nu!} \sqrt{\Gamma((\nu-l+2)/2) \Gamma((\nu+l+3)/2)}.$$

With the help of Eq. (9) one can easily derive the generating functions for the AVRGM basis. The calculations are essentially simplified by constructing Slater determinants of the generating functions for the initial and final states,

$$|\vec{R}\rangle = \frac{1}{\sqrt{A!}} \sum_{\{j_1, j_2, \dots, j_A\}} (-1)^{P(\{j_1, j_2, \dots, j_A\})} \varphi_{j_1}(1) \varphi_{j_2}(2) \dots \varphi_{j_A}(A), \quad (10)$$

$$|\vec{Q}\rangle = \frac{1}{\sqrt{A!}} \sum_{\{j_1, j_2, \dots, j_A\}} (-1)^{P(\{j_1, j_2, \dots, j_A\})} \phi_{j_1}(1) \phi_{j_2}(2) \dots \phi_{j_A}(A),$$

or sums of these Slater determinants. In Eq. (10), $P(\{j_1, j_2, \dots, j_A\})$ is the parity of the permutation $\{j_1, j_2, \dots, j_A\}$ of indices $\{1, 2, \dots, A\}$. Moreover, expressing matrix elements $\langle J_f^{\pi_f} M_f l_f s_f \nu_f | V | J_i^{\pi_i} M_i l_i s_i \nu_i \rangle$ of some operator V in the AVRGM basis through its generating matrix elements $\langle \vec{Q}, s_f \sigma_f | V | \vec{R}, s_i \sigma_i \rangle$,

$$\langle J_f^{\pi_f} M_f l_f s_f \nu_f | V | J_i^{\pi_i} M_i l_i s_i \nu_i \rangle = \frac{1}{\kappa_{\nu_f l_f s_f} \kappa_{\nu_i l_i s_i} \nu_f! \nu_i!} \frac{\partial^{\nu_f}}{\partial Q^{\nu_f}} \frac{\partial^{\nu_i}}{\partial R^{\nu_i}} I_{i \rightarrow f}(Q, R) \Big|_{Q=R=0}, \quad (11a)$$

$$I_{i \rightarrow f}(Q, R) = \sum_{m_f \sigma_f m_i \sigma_i} C_{l_f m_f s_f \sigma_f}^{J_f M_f} C_{l_i m_i s_i \sigma_i}^{J_i M_i} \times \iint Y_{l_f m_f}^*(\vec{n}_{\vec{Q}}) \langle \vec{Q}, s_f \sigma_f | V | \vec{R}, s_i \sigma_i \rangle Y_{l_i m_i}(\vec{n}_{\vec{R}}) d\vec{n}_{\vec{Q}} d\vec{n}_{\vec{R}}, \quad (11b)$$

$$\kappa_{\nu l s}^2 = \frac{1}{(\nu l)^2} \frac{\partial^\nu}{\partial Q^\nu} \frac{\partial^\nu}{\partial R^\nu} \iint Y_{lm}^*(\vec{n}_{\vec{Q}}) \langle \vec{Q}, s\sigma | \vec{R}, s\sigma \rangle Y_{lm}(\vec{n}_{\vec{R}}) d\vec{n}_{\vec{Q}} d\vec{n}_{\vec{R}} \Big|_{Q=R=0}, \quad (11c)$$

one can additionally simplify the calculations by making use of the so-called recurrence technique [42] suitable for numerical realization.

If the single-particle states φ_j and ϕ_k entering the Slater determinants in Eq. (10) satisfy the orthogonality condition

$$\langle \phi_k | \varphi_j \rangle \sim \delta_{kj}, \quad (12)$$

matrix elements in the basis of Slater determinants of an operator V which is a sum of two-particle operators V_{kj} , $V = \sum_{k>j}^A V_{kj}$, can be written as

$$\begin{aligned} \langle \vec{Q} | V | \vec{R} \rangle &= \sum_{k>j}^A \left(\langle \phi_k(1) | \langle \phi_j(2) | V_{12} | \varphi_j(2) \rangle | \varphi_k(1) \rangle \right. \\ &\quad \left. - \langle \phi_k(1) | \langle \phi_j(2) | V_{12} | \varphi_k(2) \rangle | \varphi_j(1) \rangle \right) \prod_{n \neq k, j} \langle \phi_n | \varphi_n \rangle. \end{aligned} \quad (13)$$

In this expression, the terms of the type

$$\langle \phi_k(1) | \langle \phi_j(2) | V_{12} | \varphi_j(2) \rangle | \varphi_k(1) \rangle \prod_{n \neq k, j} \langle \phi_n | \varphi_n \rangle \quad (14)$$

are referred to as direct ones while the terms of the type

$$\langle \phi_k(1) | \langle \phi_j(2) | V_{12} | \varphi_k(2) \rangle | \varphi_j(1) \rangle \prod_{n \neq k, j} \langle \phi_n | \varphi_n \rangle \quad (15)$$

are referred to as exchange ones. If the operator V is an operator describing the interaction in the system, the terms (15) with the indices k and j corresponding to single-nucleon states belonging to different clusters are responsible for the exchange effects in the cluster-cluster interaction. The neglect of these exchange terms in the interaction matrix elements simplifies significantly the calculations and leads to the AVOCM [35–39].

It should be emphasized that the potential cluster model widely used in literature neglects all exchange terms in the matrix elements of the Hamiltonian and all other operators describing the reactions. From this point of view, the AVOCM is a better approximation since within this model the exchange terms associated with permutations of indexes related to nucleons belonging to different clusters are only neglected in the matrix elements of the interaction operator. Matrix elements of the kinetic energy and electromagnetic operators as well as the overlaps are calculated precisely.

3 Approaches to description of radiative capture. The ${}^3\text{H}(\alpha, \gamma){}^7\text{Li}$ and ${}^3\text{He}(\alpha, \gamma){}^7\text{Be}$ reactions

At low energies, the mirror ${}^3\text{H}(\alpha, \gamma){}^7\text{Li}$ and ${}^3\text{He}(\alpha, \gamma){}^7\text{Be}$ reactions proceed mainly via the electric dipole ($E1$) transitions with formation of ${}^7\text{Li}$ and ${}^7\text{Be}$ nuclei in their

ground and first excited states. The respective cross sections are denoted σ_0 and σ_1 and the total cross section is their sum, $\sigma = \sigma_0 + \sigma_1$. Similarly, σ_0 and σ_1 are the sums of respectively three and two partial cross sections. An expression for these partial cross sections was derived [25, 27, 29] using the Fermi golden rule, the long-wavelength limit [46], and an expansion of the initial and final state wave functions in the series of the AVRGM basis functions (4):

$$\sigma_{i \rightarrow f}(E_{c.m.}) = \frac{8\pi}{9\hbar(2l_i + 1)} \left(\frac{E_\gamma}{\hbar c} \right)^3 \times \left| \sum_{\nu_i, \nu_f} C_{J_f^{\pi_f} l_f s \nu_f}^{(D)} \langle J_f^{\pi_f} l_f s \nu_f || M_1^E || J_i^{\pi_i} l_i s \nu_i \rangle C_{J_i^{\pi_i} l_i s \nu_i}^{(C)} \right|^2. \quad (16)$$

Here $E_{c.m.}$ is the relative motion energy of the colliding clusters (nuclei) in the center-of-mass system, E_γ is the energy of the emitted photon, and M_1^E is the electric dipole operator. For the considered $E1$ transitions, a pair of the initial quantum numbers (J_i, l_i) in Eq. (16) can take the values of $(1/2, 0)$, $(3/2, 2)$ and $(5/2, 2)$ for the capture to the ground state $[(J_f, l_f) = (3/2, 1)]$, and the values of $(1/2, 0)$ and $(3/2, 2)$ for the capture to the first excited state $[(J_f, l_f) = (1/2, 1)]$.

We use three approaches in the present work to calculate the discrete $C_{J_f^{\pi_f} l_f s \nu_f}^{(D)}$ and continuous $C_{J_i^{\pi_i} l_i s \nu_i}^{(C)}$ spectrum wave function expansion coefficients in the AVRGM basis and hence the partial cross sections of the considered reactions. The first approach [24–29] hereafter referred to as a conventional AVRGM, is based on the single-scale AVRGM. In the framework of this microscopic approach, we utilize an unified AVRGM basis with a single oscillator radius playing a role of scale parameter. The second approach [30, 31] combining the single-scale AVRGM and AVOCM, is hereafter referred to as a combined AVRGM + AVOCM. The AVOCM is utilized in this semimicroscopic approach to simplify the calculation of the expansion coefficients for the continuum wave functions, all the rest calculations are performed using the single-scale AVRGM. The third approach [32] is based on the multiscale AVRGM. This is a more advanced approach utilizing the AVRGM bases with different oscillator radii to expand the discrete and continuous spectrum wave functions. It is the principle feature of this microscopic approach which we refer to as a multiscale or generalized AVRGM.

The radiative capture cross section drops down exponentially with the energy decrease at low sub-Coulomb energies. As a result, this cross section is conventionally expressed through the astrophysical S -factor $S(E_{c.m.})$,

$$\sigma(E_{c.m.}) = \frac{1}{E_{c.m.}} \exp(-\sqrt{E_G/E_{c.m.}}) S(E_{c.m.}), \quad (17)$$

where E_G is the Gamow energy. The astrophysical S -factor has a smoother behavior than the cross section and therefore is more suitable for analysis at low energies.

The astrophysical S -factors for the considered reactions calculated within the conventional AVRGM are presented in Figs. 1 and 2 by solid curves. The dashed curves in these figures are the results obtained within the combined AVRGM + AVOCM. All calculations are performed with the oscillator radius $r_0 = 1.22$ fm and the adjustable intensity of the central Majorana force $g_c = 1.035$ which is a parameter of

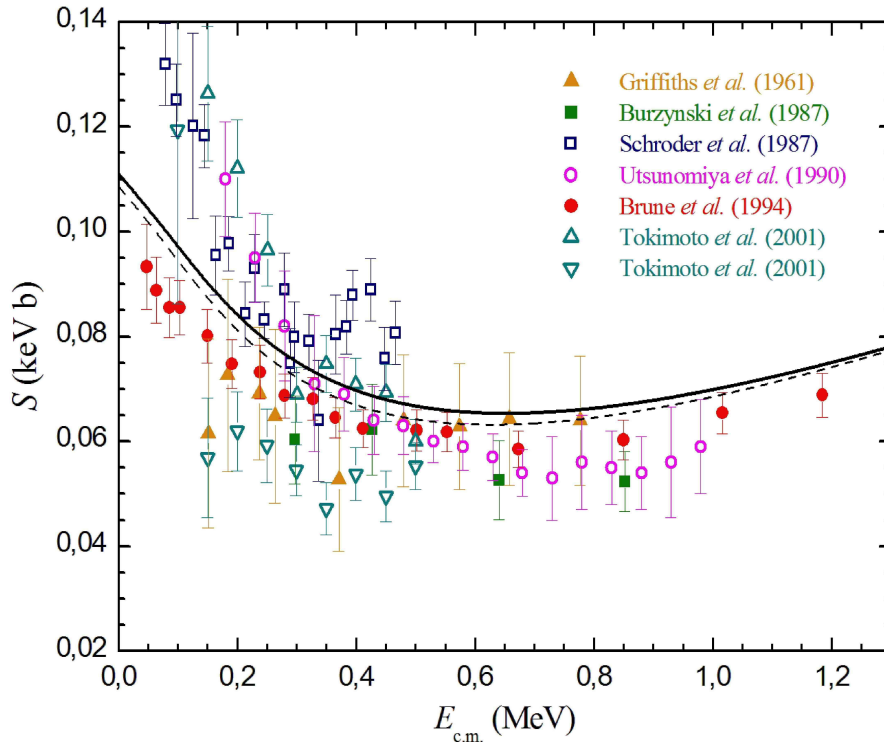


Figure 1: Astrophysical S -factor for the ${}^3\text{H}(\alpha, \gamma){}^7\text{Li}$ reaction. Solid curve — conventional AVRGM; dashed curve — combined AVRGM + AVOCM; symbols — experimental data from Refs. [48–53].

the effective modified Hasegawa–Nagata NN potential [47] used to describe the inter-nucleon interaction. The obtained cross sections are seen to be in an agreement with experimental data of Refs. [48–53] and [54–64] for the ${}^3\text{H}(\alpha, \gamma){}^7\text{Li}$ and ${}^3\text{He}(\alpha, \gamma){}^7\text{Be}$ reactions respectively. The results for the phase shifts in the entrance channels of these reactions also agree with experimental findings of Refs. [65–71].

It should be noted that the conventional AVRGM generates observables that differ only slightly from those obtained in the framework of the combined AVRGM+AVOCM (see Figs. 1 and 2). Therefore the exchange effects do not affect essentially these reactions in the low energy region. This fact can be used to develop approximate approaches to the description of reactions in heavier systems where the neglect of the exchange terms becomes necessary due to an avalanche-like growth of the calculation complexity with the number of nucleons.

We present in Figs. 3 and 4 the astrophysical S -factors for the ${}^3\text{H}(\alpha, \gamma){}^7\text{Li}$ and ${}^3\text{He}(\alpha, \gamma){}^7\text{Be}$ reactions calculated within the generalized AVRGM. The results are seen to agree well with the experimental data of Refs. [48–64]. The continuum wave functions for the ${}^4\text{He} + {}^3\text{H}$ and ${}^4\text{He} + {}^3\text{He}$ systems are expanded over the AVRGM basis with the oscillator radius $r_{01} = 1.386$ fm which results in the α particle binding energy of $E_\alpha = 28.296$ MeV consistent with experiment [72]. The wave functions of the ground and first excited states of ${}^7\text{Li}$ are expanded over the AVRGM bases with the oscillator radii $r_{020} = 1.303$ fm and $r_{021} = 1.282$ fm respectively; in the case

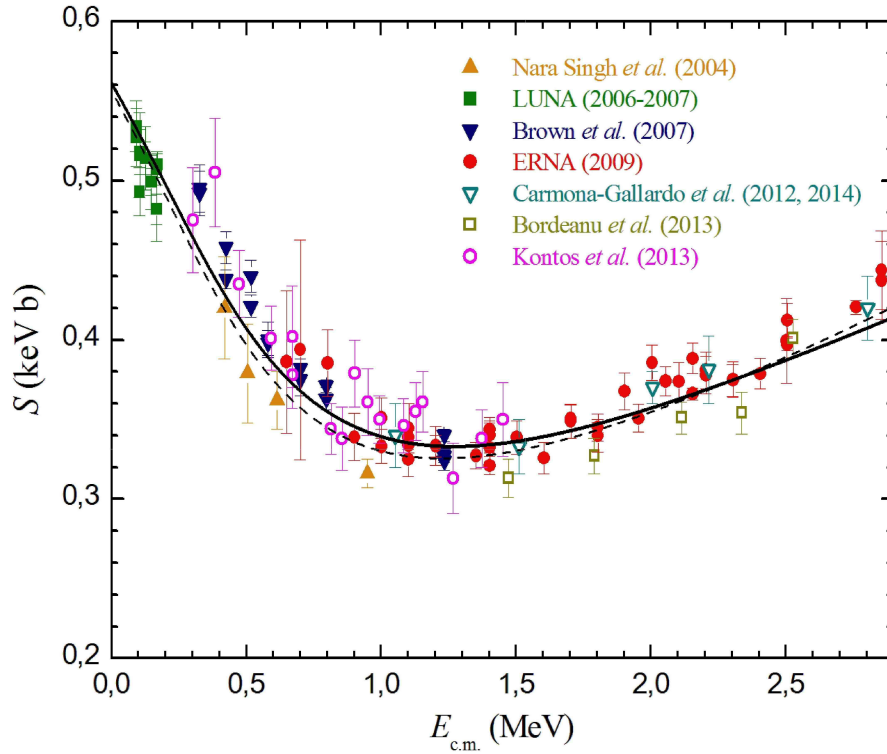


Figure 2: Astrophysical S -factor for the ${}^3\text{He}(\alpha, \gamma){}^7\text{Be}$ reaction. Symbols — experimental data from Refs. [54–64]; see Fig. 1 for other details.

of ${}^7\text{Be}$ the respective oscillator radii are $r_{020} = 1.3068$ fm and $r_{021} = 1.4205$ fm — these values are tuned to reproduce the experimental breakup thresholds [73] of the ground ($\varepsilon_0 = 2.467$ MeV) and the first excited ($\varepsilon_1 = 1.989$ MeV) states of ${}^7\text{Li}$ with respect to the ${}^4\text{He} + {}^3\text{H}$ channel and the ${}^7\text{Be}$ thresholds ($\varepsilon_0 = 1.586$ MeV, $\varepsilon_1 = 1.157$ MeV) with respect to the ${}^4\text{He} + {}^3\text{He}$ channel. The intensity of the central Majorana force $g_c = 0.977$ is set to describe the ${}^4\text{He} + {}^3\text{H}$ and ${}^4\text{He} + {}^3\text{He}$ phase shifts extracted from the experiments in Refs. [65–71].

Thus the generalized AVRGM provides reasonable energy dependences of the astrophysical S -factors of the ${}^3\text{H}(\alpha, \gamma){}^7\text{Li}$ and ${}^3\text{He}(\alpha, \gamma){}^7\text{Be}$ reactions as well as of the scattering phase shifts in the entrance channels of these reactions together with the description of the α -particle binding energy and of the breakup thresholds in ${}^7\text{Li}$ and ${}^7\text{Be}$ nuclei. This is a significant advantage of the generalized AVRGM as compared to the conventional AVRGM and combined AVRGM + AVOCM which underestimate [25, 27–29] the α -particle binding energy and the ${}^7\text{Li}$ and ${}^7\text{Be}$ breakup thresholds.

4 Conclusions

The main points of the present work are the following:

1. Theoretical approaches to the description of radiative capture reactions based

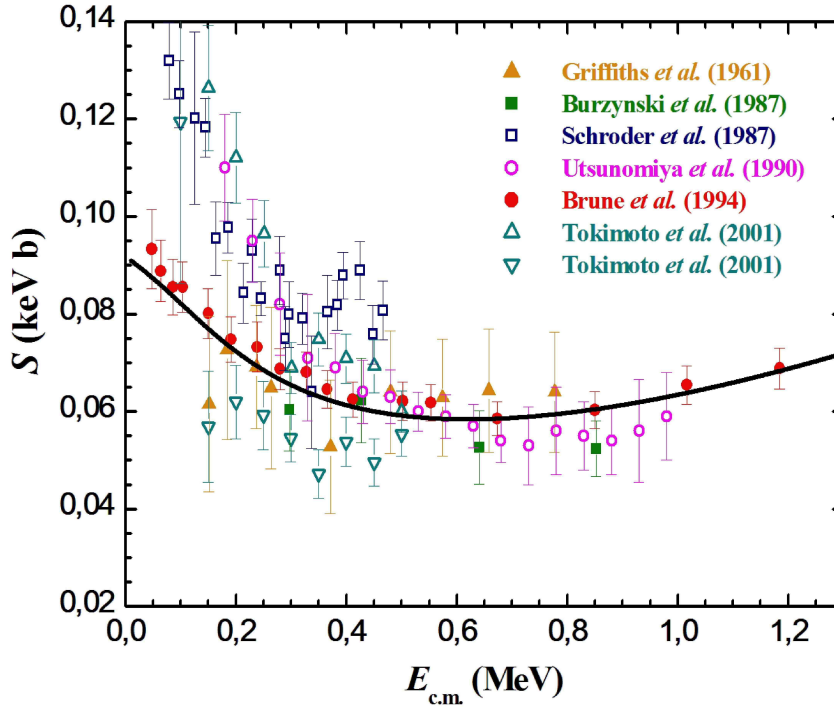


Figure 3: Astrophysical S -factor for the ${}^3\text{H}(\alpha, \gamma){}^7\text{Li}$ reaction. Solid curve — generalized AVRGM.

on AVRGM and AVOCM have been reviewed.

2. The results of the mirror ${}^3\text{H}(\alpha, \gamma){}^7\text{Li}$ and ${}^3\text{He}(\alpha, \gamma){}^7\text{Be}$ reaction studies within these approaches have been discussed.

3. Abilities of these approaches to describe simultaneously the astrophysical S -factors and scattering phase shifts in the entrance channels of the radiative capture reactions have been demonstrated.

4. We revealed an advantage of the generalized AVRGM over other reviewed approaches that is a capability of an unified description of the astrophysical S -factors of the mirror ${}^3\text{H}(\alpha, \gamma){}^7\text{Li}$ and ${}^3\text{He}(\alpha, \gamma){}^7\text{Be}$ reactions and of the scattering phase shifts in the ${}^4\text{He} + {}^3\text{H}$ and ${}^4\text{He} + {}^3\text{He}$ systems along with the breakup thresholds in the ${}^7\text{Li}$ and ${}^7\text{Be}$ nuclei.

5. An insignificance of the exchange terms in the matrix elements of interaction operator in the entrance channels of the reactions at the considered energies has been shown. This feature is useful for realization of approximate approaches to the description of reactions with heavier nuclei.

Acknowledgments

The work was supported by the Russian Science Foundation, grant No. 16-12-10048.

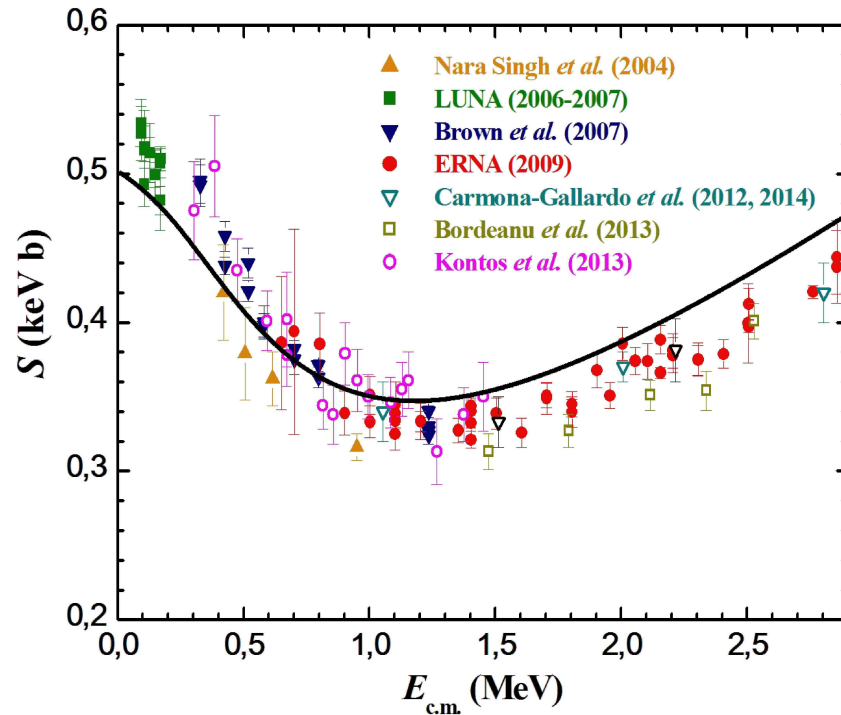


Figure 4: Astrophysical S -factor for the ${}^3\text{He}(\alpha, \gamma){}^7\text{Be}$ reaction. Solid curve — generalized AVRGM.

References

- [1] R. H. Cyburt and B. Davids, *Phys. Rev. C* **78**, 064614 (2008).
- [2] F. Iocco, G. Mangano, G. Miele *et al.*, *Phys. Rep.* **472**, 1 (2009).
- [3] B. D. Fields, *Ann. Rev. Nucl. Part. Sci.* **61**, 47 (2011).
- [4] E. G. Adelberger, A. Garcia, R. G. H. Robertson *et al.*, *Rev. Mod. Phys.* **83**, 195 (2011).
- [5] Y. Xu, K. Takahashi, S. Goriely *et al.*, *Nucl. Phys. A* **918**, 61 (2013).
- [6] P. Mohr, H. Abele, R. Zwiebel *et al.*, *Phys. Rev. C* **48**, 1420 (1993).
- [7] P. Mohr, *Phys. Rev. C* **79**, 065804 (2009).
- [8] B. Buck and A. C. Merchant, *J. Phys. G* **14**, L211 (1988).
- [9] S. B. Igamov and R. Yarmukhamedov, *Nucl. Phys. A* **781**, 247 (2007).
- [10] Q. I. Tursunmahatov and R. Yarmukhamedov, *Phys. Rev. C* **85**, 045807 (2012).
- [11] L. Canton and L. G. Levchuk, *Nucl. Phys. A* **808**, 192 (2008).

- [12] A. Mason, R. Chatterjee, L. Fortunato and A. Vitturi, *Eur. Phys. J. A* **39**, 107 (2009).
- [13] K. M. Nollett, *Phys. Rev. C* **63**, 054002 (2001).
- [14] L. E. Marcucci, K. M. Nollett, R. Schiavilla and R. B. Wiringa, *Nucl. Phys. A* **777**, 111 (2006).
- [15] P. Navrátil, C. A. Bertulani and E. Caurier, *Phys. Rev. C* **73**, 065801 (2006).
- [16] P. Navrátil, C. A. Bertulani and E. Caurier, *Nucl. Phys. A* **787**, 539c (2007).
- [17] P. Navrátil, S. Quaglioni, I. Stetcu and B. R. Barrett, *J. Phys. G* **36**, 083101 (2009).
- [18] T. Kajino, *Nucl. Phys. A* **460**, 559 (1986).
- [19] T. Altmeyer, E. Kolbe, T. Warmann *et al.*, *Z. Phys. A* **330**, 277 (1988).
- [20] A. Csóttó and K. Langanke, *Few-Body Syst.* **29**, 121 (2000).
- [21] K. Arai, D. Baye and P. Descouvemont, *Nucl. Phys. A* **699**, 963 (2002).
- [22] T. Neff, *Phys. Rev. Lett.* **106**, 042502 (2011).
- [23] J. Dohet-Eraly, P. Navrátil, S. Quaglioni *et al.*, *Phys. Lett. B* **757**, 430 (2016).
- [24] A. S. Solov'yev and S. Yu. Igashov, *Yad. Fiz. Inzh.* **4**, 989 (2013) (*in Russian*).
- [25] A. S. Solov'yev, S. Yu. Igashov and Yu. M. Tchuvil'sky, *Bull. Russ. Acad. Sci. Phys.* **78**, 433 (2014).
- [26] A. S. Solov'yev, S. Yu. Igashov and Yu. M. Tchuvil'sky, *Phys. Atom. Nucl.* **77**, 1453 (2014).
- [27] A. S. Solov'yev, S. Yu. Igashov and Yu. M. Tchuvil'sky, *J. Phys. Conf. Ser.* **569**, 012020 (2014).
- [28] A. S. Solov'yev, S. Yu. Igashov and Yu. M. Tchuvil'sky, *EPJ Web Conf.* **86**, 00054 (2015).
- [29] A. S. Solov'yev, S. Yu. Igashov and Yu. M. Tchuvil'sky, *Bull. Russ. Acad. Sci. Phys.* **79**, 499 (2015).
- [30] A. S. Solov'yev, S. Yu. Igashov and Yu. M. Tchuvil'sky, *EPJ Web Conf.* **117**, 09017 (2016).
- [31] A. S. Solov'yev, S. Yu. Igashov and Yu. M. Tchuvil'sky, *Bull. Russ. Acad. Sci. Phys.* **80**, 290 (2016).
- [32] A. S. Solov'yev, S. Yu. Igashov and Yu. M. Tchuvil'sky, *J. Phys. Conf. Ser.* **863**, 012015 (2017).
- [33] G. F. Filippov and I. P. Okhrimenko, *Sov. J. Nucl. Phys.* **32**, 480 (1980).
- [34] G. F. Filippov, *Sov. J. Nucl. Phys.* **33**, 488 (1981).

- [35] S. Yu. Igashov, Yu. F. Smirnov and Yu. M. Tchuvil'sky, *Bull. Russ. Acad. Sci. Phys.* **73**, 756 (2009).
- [36] S. Yu. Igashov, A. V. Sinyakov and Yu. M. Tchuvil'sky, *Bull. Russ. Acad. Sci. Phys.* **74**, 1608 (2010).
- [37] S. Yu. Igashov, A. V. Sinyakov and Yu. M. Tchuvil'sky, *Bull. Russ. Acad. Sci. Phys.* **74**, 1612 (2010).
- [38] S. Yu. Igashov and Yu. M. Tchuvil'sky, *Phys. Atom. Nucl.* **74**, 1588 (2011).
- [39] S. Yu. Igashov and Yu. M. Tchuvil'sky, *EPJ Web Conf.* **38**, 16002 (2012).
- [40] K. Wildermuth and Y. C. Tang, *A unified theory of the nucleus*. Vieweg, Braunschweig, 1977.
- [41] Y. C. Tang, M. Lemere and D. R. Thompson, *Phys. Rep.* **47**, 167 (1978).
- [42] I. P. Okhrimenko, *Nucl. Phys. A* **424**, 121 (1984).
- [43] S. Yu. Igashov, in *The J-matrix method. Developments and applications*, eds. A. D. Alhaidari, E. J. Heller, H. A. Yamani and M. S. Abdelmonem. Springer, New York, 2008, p. 49.
- [44] G. F. Filippov, V. S. Vasilevsky and L. L. Chopovsky, *Phys. Part. Nucl.* **15**, 600 (1984).
- [45] G. F. Filippov, V. S. Vasilevsky and L. L. Chopovsky, *Phys. Part. Nucl.* **16**, 153 (1985).
- [46] J. M. Blatt and V. F. Weisskopf, *Theoretical nuclear physics*. Springer, New York, 1979.
- [47] H. Kanada, T. Kaneko, S. Nagata and M. Nomoto, *Progr. Theor. Phys.* **61**, 1327 (1979).
- [48] G. M. Griffiths, R. A. Morrow, P. J. Riley and J. B. Warren, *Can. J. Phys.* **39**, 1397 (1961).
- [49] S. Burzyński, K. Czerski, A. Marcinkowski and P. Zupranski, *Nucl. Phys. A* **473**, 179 (1987).
- [50] U. Schröder, A. Redder, C. Rolfs *et al.*, *Phys. Lett. B* **192**, 55 (1987).
- [51] H. Utsunomiya, Y.-W. Lui, D. R. Haenni *et al.*, *Phys. Rev. Lett.* **65**, 847 (1990); *Phys. Rev. Lett.* **69**, 863(E) (1990).
- [52] C. R. Brune, R. W. Kavanagh and C. Rolfs, *Phys. Rev. C* **50**, 2205 (1994).
- [53] Y. Tokimoto, H. Utsunomiya, T. Yamagata *et al.*, *Phys. Rev. C* **63**, 035801 (2001).
- [54] B. S. Nara Singh, M. Hass, Y. Nir-El and G. Haquin, *Phys. Rev. Lett.* **93**, 262503 (2004).

- [55] D. Bemmerer, F. Confortola, H. Costantini *et al.*, Phys. Rev. Lett. **97**, 122502 (2006).
- [56] Gy. Gyürky, F. Confortola, H. Costantini *et al.*, Phys. Rev. C **75**, 035805 (2007).
- [57] F. Confortola, D. Bemmerer, H. Costantini *et al.*, Phys. Rev. C **75**, 065803 (2007).
- [58] H. Costantini, D. Bemmerer, F. Confortola *et al.*, Nucl. Phys. A **814**, 144 (2008).
- [59] T. A. D. Brown, C. Bordeanu, K. A. Snover *et al.*, Phys. Rev. C **76**, 055801 (2007).
- [60] A. Di Leva, L. Gialanella, R. Kunz *et al.*, Phys. Rev. Lett. **102**, 232502 (2009); Phys. Rev. Lett. **103**, 159903(E) (2009).
- [61] C. Bordeanu, Gy. Gyürky, Z. Halász *et al.*, Nucl. Phys. A **908**, 1 (2013).
- [62] A. Kontos, E. Uberseder, R. deBoer *et al.*, Phys. Rev. C **87**, 065804 (2013).
- [63] M. Carmona-Gallardo, B. S. Nara Singh, M. J. G. Borge *et al.*, Phys. Rev. C **86**, 032801(R) (2012).
- [64] M. Carmona-Gallardo, A. Rojas, M. J. G. Borge *et al.*, EPJ Web Conf. **66**, 07003 (2014).
- [65] M. Ivanovich, P. G. Young and G. G. Ohlsen, Nucl. Phys. A **110**, 441 (1968).
- [66] R. J. Spiger and T. A. Tombrello, Phys. Rev. **163**, 964 (1967).
- [67] P. D. Miller and G. C. Phillips, Phys. Rev. **112**, 2048 (1958).
- [68] T. A. Tombrello and P. D. Parker, Phys. Rev. **130**, 1112 (1963).
- [69] D. M. Hardy, R. J. Spiger, S. D. Baker *et al.*, Nucl. Phys. A **195**, 250 (1972).
- [70] A. C. L. Barnard, C. M. Jones and G. C. Phillips, Nucl. Phys. **50**, 629 (1964).
- [71] W. R. Boykin, S. D. Baker and D. M. Hardy, Nucl. Phys. A **195**, 241 (1972).
- [72] G. Audi, A. H. Wapstra and C. Thibault, Nucl. Phys. A **729**, 337 (2003).
- [73] D. R. Tilley, C. M. Cheves, J. L. Godwin *et al.*, Nucl. Phys. A **708**, 3 (2002).

Ab Initio Description of the Tetraneutron with Realistic NN Interactions within the NCSM-SS-HORSE Approach

I. A. Mazur^a, A. M. Shirokov^{a,b,c}, A. I. Mazur^a, I. J. Shin^d,
Y. Kim^d and J. P. Vary^c

^a*Pacific National University, Tikhookeanskaya 136, Khabarovsk 680035, Russia*

^b*Skobeltsyn Institute of Nuclear Physics, Lomonosov Moscow State University, Moscow 119991, Russia*

^c*Department of Physics and Astronomy, Iowa State University, Ames, IA 50011-3160, USA*

^d*Rare Isotope Science Project, Institute for Basic Science, Daejeon 34047, Korea*

Abstract

We continue the study of the tetraneutron resonance within the democratic SS-HORSE extension of the *ab initio* No-Core Shell Model [16] using modern NN interactions. With Daejeon16 and SRG-evolved chiral Idaho N3LO NN interactions we obtain the S -matrix pole corresponding to the tetraneutron resonance with energy between 0.7 and 1.0 MeV and width between 1.1 and 1.7 MeV. However we do not obtain a low-lying narrow resonance with the original Idaho N3LO but, instead, we obtain a very low-lying virtual state with the energy of 15 keV.

Keywords: *Tetraneutron; resonant states; realistic NN -interactions; No-Core Shell Model; SS-HORSE method; democratic decay*

1 Introduction

Interest in the tetraneutron was revived by a recent experiment [1] where a few events were detected which were interpreted as a resonant state in the four-neutron system with an energy of 0.83 ± 0.65 (stat.) ± 1.25 (syst.) MeV and a width not exceeding 2 MeV. As indicated in a historical review of the studies of few-neutron systems of Ref. [2], this is the first observation of the tetraneutron resonance which has been sought for more than fifty years [3]. The possibility of a bound tetraneutron state was proposed 15 year ago in Ref. [4] in the ^{14}Be breakup reaction $^{14}\text{Be} \rightarrow ^{10}\text{Be} + 4n$. This experimental result, however, has not been confirmed.

The state-of-the-art theoretical studies conclude [5–14] that the tetraneutron cannot be bound without a significant altering of modern nuclear forces that will spoil a description of other nuclei. There are some indications on the existence of a low-lying tetraneutron resonance based on an artificial binding of the tetraneutron by

Proceedings of the International Conference ‘Nuclear Theory in the Supercomputing Era — 2016’ (NTSE-2016), Khabarovsk, Russia, September 19–23, 2016. Eds. A. M. Shirokov and A. I. Mazur. Pacific National University, Khabarovsk, Russia, 2018, p. 280.

<http://www.ntse-2016.khb.ru/Proc/IMazur.pdf>.

strengthening the NN interaction [5] or by putting the four-neutron system in a trap [15] and by extrapolating these bound states to the case when the strengthening parameter is continuously reduced or the trap is continuously removed. Such extrapolations cannot predict the width of the resonance and should not be regarded as a firm proof of the resonant state. Existing calculations that explicitly account for the continuum [6, 9–14] using various approaches [hyperspherical harmonics (HH), Faddeev–Yakubovsky equations, no-core Gamow shell model, complex scaling, etc.] with various realistic inter-nucleon forces resulted in the absence of a low-lying tetra-neutron resonance narrow enough to be detected experimentally.

However, in our recent theoretical study [16], we obtained the tetra-neutron resonance with the energy $E_r = 0.8$ MeV and the width $\Gamma = 1.4$ MeV. To the best of our knowledge, this is an only theoretical prediction consistent with the experimental finding of Ref. [1]. These calculations utilized the NN interaction JISP16 [17] and were performed within the so-called SS-HORSE (single state harmonic oscillator representation of scattering equations) extension [18–22] of the no-core shell model (NCSM) [23] adapted in Ref. [16] to the description of democratic decays (also known as a true four-body scattering or $4 \rightarrow 4$ scattering) [24, 25]. So, it is important to understand whether this low-lying resonance should be associated with the JISP16 NN interaction which was used in the tetra-neutron studies only in Ref. [16] or with the new democratic NCSM-SS-HORSE approach able to describe correctly some specific features of the four-particle decay which are likely beyond the scope of other methods.

To this end, we perform here the NCSM-SS-HORSE calculations of the tetra-neutron resonance with additional contemporary NN interactions. In particular, we adopt a new NN interaction Daejeon16 [26] which is better fitted to observables in light nuclei than JISP16. We also adopt the chiral NN interaction Idaho N3LO [27], both unperturbed (‘bare’) and softened by the methods of the Similarity Renormalization Group (SRG) [28, 29] with flow parameters $\Lambda = 1.5 \text{ fm}^{-1}$ and 2.0 fm^{-1} . We note that the Daejeon16 interaction was obtained by applying phase-equivalent transformations to the SRG-evolved with $\Lambda = 1.5 \text{ fm}^{-1}$ Idaho N3LO which adjust the interaction to describe light nuclei without referring to three-nucleon forces.

The next Section presents a brief description of the SS-HORSE method and its application to calculating democratic four-body decays within the NCSM. The tetra-neutron calculation results with the Daejeon16, SRG-evolved and ‘bare’ Idaho N3LO interactions are given in Sections 3, 4, and 5 respectively. The last Section summarizes these studies.

2 SS-HORSE method for the $4 \rightarrow 4$ scattering

We use here the same theoretical approach as in our previous paper [16]. That is, we utilize the democratic decay approximation [24, 25] to describe the four-neutron decay channel within the NCSM-SS-HORSE approach. A decay of a system into A particles is called ‘*democratic*’ if none of subsystems built of these A particles has a bound state. In particular, the tetra-neutron presents a nice example of nuclear system decaying through a four-body democratic channel only, and the study of the tetra-neutron of Ref. [30] is one of the first applications of the democratic decay approximation.

It is natural to study democratic decays within the HH method, which introduces a ‘democratic’ collective coordinate, the hyperradius $\rho = \sqrt{\sum_{i=1}^A (\mathbf{r}_i - \mathbf{R})^2}$ (\mathbf{r}_i are the coordinates of individual nucleons and \mathbf{R} is the center-of-mass coordinate), and describes the dynamics of a system in terms of this coordinate. Formally, the democratic decay channel involves a superposition of an infinite number of HH with hypermomenta $K = K_{\min}, K_{\min} + 2, \dots$, where K_{\min} is the minimal hypermomentum consistent with the Pauli principle for a given nucleus; however, in practical applications, one usually uses a restricted set of HH adequate for the description of the decay channel. We use here the minimal approximation for the tetra-neutron decay mode, i. e., we retain only the HH with hypermomentum $K = K_{\min} = 2$. This approximation relies on the fact that the decay in the hyperspherical states with $K > K_{\min}$ is strongly suppressed by a large hyperspherical centrifugal barrier $\mathcal{L}(\mathcal{L} + 1)/\rho^2$, where the effective angular momentum

$$\mathcal{L} = K + \frac{3A - 6}{2} = K + 3. \quad (1)$$

Note, the minimal approximation is used for the description of the decay channel only, i. e., for the description of the wave function asymptotics, while all possible HH are retained in the NCSM basis. The accuracy of this approximation was confirmed in studies of democratic decays in cluster models [31–34].

The NCSM utilizes the harmonic oscillator basis, and a natural extension of the NCSM to the continuum can be achieved within the J -matrix [35] (also known as the HORSE [36]) formalism in scattering theory, in particular, in an efficient SS-HORSE version [18–22] of this formalism. The general theory of the democratic decay within the HORSE formalism was proposed in Refs. [37, 38]; a derivation of the democratic SS-HORSE version along the lines suggested in Refs. [18, 19] is straightforward [16].

Within the minimal approximation, the S -matrix of the four-body decay is expressed through the hyperspherical phase shift δ as

$$S = e^{2i\delta}. \quad (2)$$

The SS-HORSE formalism provides the following expression for the phase shifts at the eigenenergies E_ν of the NCSM Hamiltonian [16, 18, 19]:

$$\tan \delta(E_\nu) = -\frac{S_{\mathbb{N}+2, \mathcal{L}}(E_\nu/\hbar\Omega)}{C_{\mathbb{N}+2, \mathcal{L}}(E_\nu/\hbar\Omega)}. \quad (3)$$

Here, $S_{N\mathcal{L}}$ and $C_{N\mathcal{L}}$ are linearly-independent solutions of the infinite tridiagonal free Hamiltonian matrix in the hyperspherical harmonic oscillator basis for which analytical expressions can be found in Refs. [37, 38], and \mathbb{N} is the maximal total quanta of many-body oscillator states included in the NCSM basis,

$$\mathbb{N} = N_{\max} + N_{\min}, \quad (4)$$

$N_{\min} = 2$ is the quanta of the lowest possible oscillator state of the $4n$ system, and N_{\max} is the maximal excitation quanta in the NCSM basis.

Varying N_{\max} and $\hbar\Omega$ in the NCSM calculations, we obtain the phase shifts and S -matrix in some energy interval. Parametrizing the S -matrix in this energy interval, we obtain information about its nearby poles and hence resonances in the system.

Note, the phase shifts used for the parametrization should form some curve as a function of energy. However some phase shifts calculated by Eq. (3), especially those corresponding to the NCSM results obtained in small enough model spaces, deviate from the common curve signaling that convergence is not achieved. Therefore, before parametrizing the phase shifts, one needs to preselect the NCSM results retaining only those that are sufficiently converged so as to lie on the common curve.

Due to S -matrix symmetry properties [39,40], the hyperspherical phase shift $\delta(E)$ should be an odd function of momentum $k \sim \sqrt{E}$,

$$\delta(E) = v_1\sqrt{E} + v_3(\sqrt{E})^3 + \dots + v_9(\sqrt{E})^9 + v_{11}(\sqrt{E})^{11} + \dots \quad (5)$$

On the other hand, at low energies, i. e., in the limit $k \rightarrow 0$, the phase shifts should behave as $\delta \sim k^{2\mathcal{L}+1}$ [39,40]. In the case of $4 \rightarrow 4$ scattering, $\mathcal{L} = K_{\min} + 3 = 5$ and therefore the expansion (5) starts at the eleventh power, i. e.,

$$v_1 = v_3 = \dots = v_9 = 0. \quad (6)$$

To parametrize the phase shifts, we use the equation

$$-\arctan \frac{S_{N_{\max}+4,5}(E/\hbar\Omega)}{C_{N_{\max}+4,5}(E/\hbar\Omega)} = \sum_p \delta_p(E) + \phi(E), \quad (7)$$

which is obtained by rewriting Eq. (3) with the help of Eq. (4). Here $\phi(E)$ is a background phase, which is expected to be a smooth function parametrized as a Padé approximant,

$$\phi(E) = -\frac{w_1\sqrt{E} + w_3(\sqrt{E})^3 + c(\sqrt{E})^5}{1 + w_2E + w_4E^2 + w_6E^3 + dE^4}. \quad (8)$$

The sum in the rhs of Eq. (7) presents rapidly changing with E contributions from pole terms associated with the S -matrix poles located close to the origin of the complex momentum plane, in particular, resonant poles ($p = r$), false (redundant) poles at a positive imaginary momentum ($p = f$) which does not correspond to a bound state [39,40], or virtual state poles at a negative imaginary momentum ($p = v$) [39,40]. The respective phase shifts are

$$\delta_r(E) = -\arctan \frac{a\sqrt{E}}{E - b^2}, \quad (9a)$$

$$\delta_f(E) = -\arctan \sqrt{\frac{E}{|E_f|}}, \quad (9b)$$

$$\delta_v(E) = \arctan \sqrt{\frac{E}{|E_v|}}. \quad (9c)$$

The resonance energy E_r and width Γ are expressed through parameters a and b as

$$E_r = b^2 - a^2/2, \quad \Gamma = a\sqrt{4b^2 - a^2}. \quad (10)$$

We attempted various fits including one, two, or three pole terms in Eq. (7) aimed to obtain a smooth background phase $\phi(E)$. The parameters w_1 , w_2 , w_3 , w_4 , and w_6

should guarantee that Eq. (6) is satisfied [note, the pole terms contribute to the low-order expansion terms in Eq. (5)]. The parameters c and d entering Eq. (8) together with the parameters a , b , E_f , and E_v of the included pole terms are used as fit parameters.

For each set of parameters, we solve Eq. (7) to find the energies $\mathcal{E}^{(i)} = \mathcal{E}(N_{\max}^i, \hbar\Omega^i)$ for each combination of N_{\max}^i and $\hbar\Omega^i$ values and search for the parameter set minimizing the rms deviation

$$\Xi = \sqrt{\frac{1}{D} \sum_{i=1}^D (E_0^{(i)} - \mathcal{E}^{(i)})^2} \quad (11)$$

of $\mathcal{E}^{(i)}$ from the selected set of the lowest NCSM eigenenergies E_0^i obtained with the same N_{\max}^i and $\hbar\Omega^i$.

3 Results with Daejeon16

We performed the NCSM calculations using the code MFDn [41,42] for the tetraneutron with N_{\max} values ranging from 2 to 20 and $\hbar\Omega$ values ranging from 1 to 50 MeV. As in Refs. [16,18–22], we select for the phase shift parametrization the NCSM results generating the phase shifts according to Eq. (3) that form approximately a common curve as a function of energy E . Additionally, we do not include in the analysis the NCSM eigenenergies above 7 MeV thus improving the description of the resonance region. The eigenenergy selection is shown by the shaded area in left panel of Fig. 1. The right panel of Fig. 1 shows the phase shifts obtained directly from the selected NCSM results using Eq. (3).

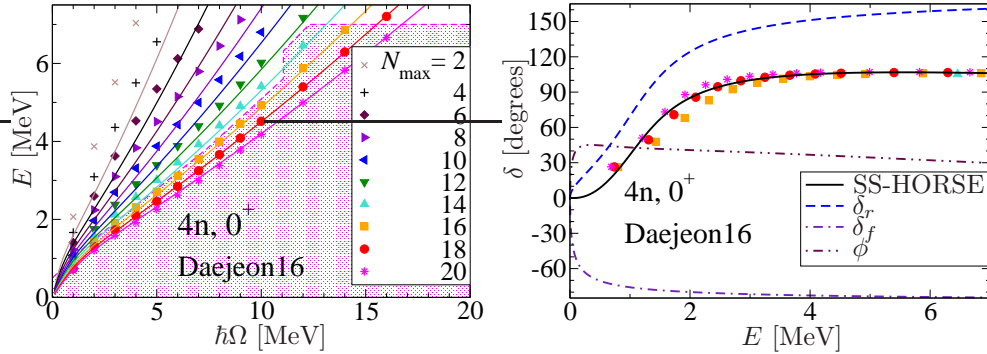


Figure 1: Left panel: the lowest 0^+ tetraneutron states obtained in the NCSM with the Daejeon16 NN interaction (symbols) with various N_{\max} as functions of $\hbar\Omega$ and the energies $\mathcal{E}^{(i)}$ (solid curves) obtained from the phase shifts parametrization; the shaded area shows the NCSM result selection for the phase shift parametrization. Right panel: the $4 \rightarrow 4$ phase shift parametrization (solid curve) and phase shifts obtained directly from the selected NCSM results using Eq. (3) (symbols); contributions to the phase shifts of the resonant pole, the false pole and the background phase are shown by dashed, dashed-dotted and dashed-double-dotted curves respectively.

Table 1: Tetra-neutron resonance energy E_r and width Γ and other fit parameters including the energy of the false pole E_f and of the virtual state $|E_v|$ as well as the rms deviation of energies Ξ characterizing the quality of the fit, obtained with JISP16 [16], Daejeon16, SRG-evolved with flow parameters $\Lambda = 1.5$ and 2.0 fm^{-1} Idaho N3LO, and ‘bare’ Idaho N3LO NN interactions.

Interaction	JISP16,	Daejeon16	Idaho N3LO, SRG		Idaho N3LO
	Ref. [16]		$\Lambda = 1.5 \text{ fm}^{-1}$	$\Lambda = 2.0 \text{ fm}^{-1}$	
$a \text{ (MeV}^{\frac{1}{2}}\text{)}$	0.701	0.749	0.613	0.662	—
$b^2 \text{ (MeV)}$	1.09	1.28	0.970	1.07	—
$c \text{ (MeV}^{-\frac{5}{2}}\text{)}$	-27.0	-16.2	-31.6	-28.1	4960
$d \text{ (MeV}^{-4}\text{)}$	0.281	0.717	0.720	0.776	2330
$E_r \text{ (MeV)}$	0.844	0.997	0.783	0.846	—
$\Gamma \text{ (MeV)}$	1.38	1.60	1.15	1.29	—
$E_f \text{ (keV)}$	-54.9	-63.4	-52.1	-54.5	—
$ E_v \text{ (keV)}$	—	—	—	—	15.2
$\Xi \text{ (keV)}$	43.8	47.9	29.0	31.7	19.4

We can accurately describe the NCSM results using only one resonant pole term. However this parametrization, as in the case of JISP16 [16], results in a very rapid changes of the background phase signaling the presence of another S -matrix pole in the vicinity of zero energy. A description of the selected NCSM eigenenergies approximately with the same rms deviation is achieved also by a parametrization with two pole terms associated with a resonant state and a false state. This parametrization essentially decreases the variation of the background phase and appears to be acceptable from the physical viewpoint. The resulting phase shifts are presented in the right panel of Fig. 1 while the fit parameters including the resonance energy and width and the energy of the false pole are given in Table 1. It is seen that the Daejeon16 NN interaction suggests a low-lying resonance in the system of four neutrons with energy about 1 MeV and width about 1.6 MeV consistent with the experimental observations of Ref. [1].

For comparison, we present in Table 1 also the results of Ref. [16] obtained with the JISP16 interaction with the same two-pole parametrization. It is seen that JISP16 and Daejeon16 interactions provide very similar predictions not only for the tetra-neutron resonance energy and width but also for other fit parameters.

4 Results with SRG-evolved Idaho N3LO

As it was already noted, the Daejeon16 interaction was fitted to the observables in light nuclei by applying phase-equivalent transformations to the SRG-evolved Idaho N3LO NN interaction with flow parameter $\Lambda = 1.5 \text{ fm}^{-1}$. Therefore it is interesting to investigate the effect of this adjustment of the NN interaction, which makes it possible to calculate nuclei without an explicit use of three-nucleon forces, on the tetra-neutron resonance. We perform the tetra-neutron calculations with the SRG-evolved Idaho N3LO NN interaction with flow parameters $\Lambda = 1.5 \text{ fm}^{-1}$ and $\Lambda = 2.0 \text{ fm}^{-1}$ to examine also the dependence of the tetra-neutron resonance energy and width on the

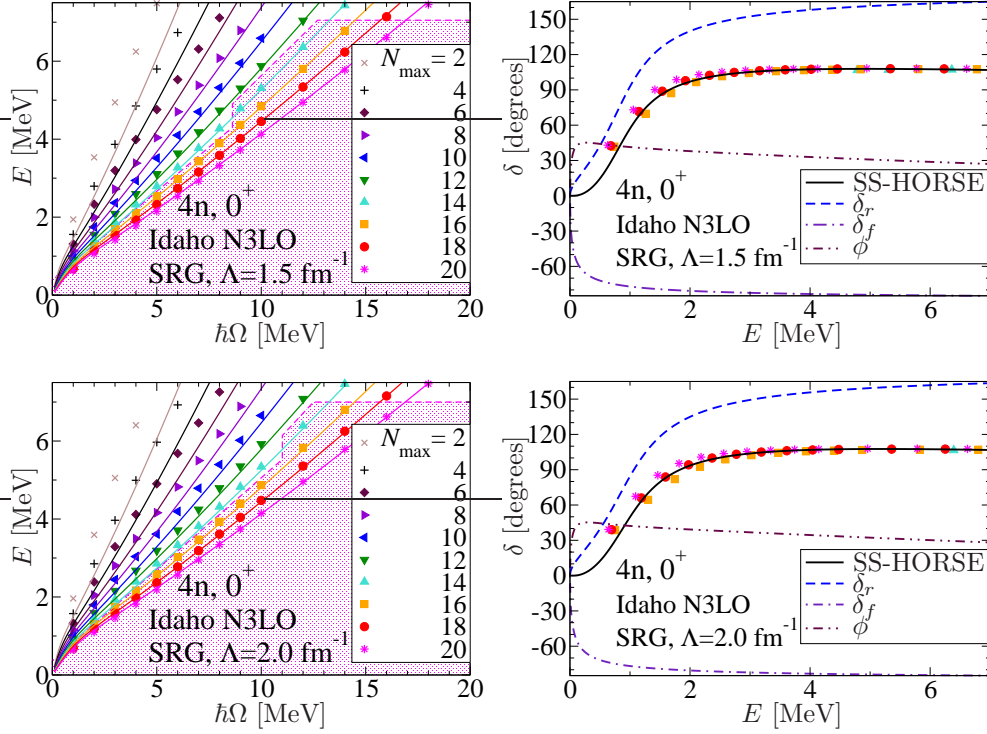


Figure 2: NCSM results for the lowest 0^+ tetra-neutron states and the $4 \rightarrow 4$ phase shifts obtained with SRG-evolved Idaho N3LO NN interactions with flow parameters $\Lambda = 1.5 \text{ fm}^{-1}$ (upper panel) and $\Lambda = 2.0 \text{ fm}^{-1}$ (lower panel). See Fig. 1 for details.

flow parameters Λ .

It is interesting to note here that the SRG-evolved chiral Idaho N3LO with these values of flow parameters Λ , as well as the JISP16 and Daejeon16 interactions, provide without three-nucleon forces ground states of the bound $A = 3$ and $A = 4$ systems close to experiment while the original Idaho N3LO significantly underbinds these systems (see, e. g., Ref. [23,43]). For example, the SRG-evolved chiral Idaho N3LO with our adopted flow parameters Λ , as well as the JISP16 and Daejeon16 interactions, all provide ground state energies of $A = 3$ nuclei and ${}^4\text{He}$ within 100 keV of experiment. On the other hand, the original Idaho N3LO underbinds ${}^3\text{H}$ by 620 keV and underbinds ${}^4\text{He}$ by 2.9 MeV.

We perform the calculations similar to those presented in the previous Section. In particular, we use the same set of N_{max} and $\hbar\Omega$ values in the NCSM calculations and make similar though not identical selections of the NCSM results for the phase shift parametrizations. We again come to a conclusion that physically reasonable parametrizations should include pole terms corresponding to resonant and false states, which suggest low-energy tetra-neutron resonances. The results are presented in Fig. 2 and Table 1.

It is seen that we obtain the results similar to those obtained with JISP16 and Daejeon16 interactions. It is interesting that the interaction with $\Lambda = 2.0 \text{ fm}^{-1}$

results in the values of the resonance energy and width as well as in the energy of the false state nearly identical to those obtained with JISP16. Decreasing Λ to 1.5 fm^{-1} causes small decreases of the resonant energy and width which become nearly 30% smaller than the width obtained with Daejeon16 while the difference in resonance energies is about 20%. These differences between the Daejeon16 and SRG-evolved with $\Lambda = 1.5 \text{ fm}^{-1}$ interactions may serve as a rough estimate of the three-body force effects in the tetra-neutron since the Daejeon16, being fitted to light nuclei, mimics three-body force effects by off-shell properties of this two-nucleon only interaction.

A close look at the phase shift parametrizations in Figs. 1 and 2 reveals that the discrete energies, E_0^i , in the region of the extracted resonance are not as well converged as those outside this region. This slower convergence is reasonable in light of the low energy of the resonance which results from the delicate cancelation of small kinetic and small potential contributions to the values of E_0^i .

Generally, the results obtained with the SRG-evolved Idaho N3LO interactions are consistent with those from JISP16 and Daejeon16 interactions and with the experiment [1].

5 Results with original Idaho N3LO

Although the original Idaho N3LO interaction significantly underbinds the bound light nuclei with $A > 2$, we include results with this interaction since it does produce an excellent description the two-nucleon data. That is, normally, one includes a three-nucleon interaction with the original Idaho N3LO interaction to produce good binding results for the bound light nuclei with $A > 2$. It is also interesting to compare our results for this interaction with numerous studies of other authors that employed NN interactions with a strong short-range repulsion and did not obtain a narrow low-lying resonance in the tetra-neutron.

We find that the same calculations with the ‘bare’ Idaho N3LO NN interaction alone, without a three-nucleon interaction, bring us to a very different conclusion about the tetra-neutron resonance.

The NCSM calculations are performed in the same range of N_{max} , $2 \leq N_{\text{max}} \leq 20$, and $\hbar\Omega$, $1 \text{ MeV} \leq \hbar\Omega \leq 20 \text{ MeV}$; Fig. 3 shows the low-energy fraction (below 6 MeV) of the obtained NCSM results for the tetra-neutron ground state together with the selection of eigenstates for the further SS-HORSE analysis. The phase shifts obtained directly from all NCSM results using Eq. (3) are shown in the left panel of Fig. 4. Contrary to other interactions discussed above, we have a convergence with the ‘bare’ N3LO only at low enough energies, below approximately 6 MeV, where the phase shifts with increasing N_{max} tend to a common curve formed by the phase shifts from the largest available model spaces. Therefore we select for the phase shift parametrization only the NCSM results with $N_{\text{max}} = 16, 18, \text{ and } 20$ lying below 6 MeV. Starting from the energies of 6 MeV, the convergence is clearly not achieved. One can speculate that the tendency of the phase shifts in this energy region suggests that the converged phase shift will form an additional smooth increase between 6 and 15 MeV that may indicate a presence of a wide resonant state with energy around 10 MeV, which, most probably, will be not possible to detect experimentally. There is also an indication that the convergence is achieved at energies around 20 MeV and higher which are of no interest for our analysis.

The behavior of the converged phase shifts in the right panel of Fig. 4 which

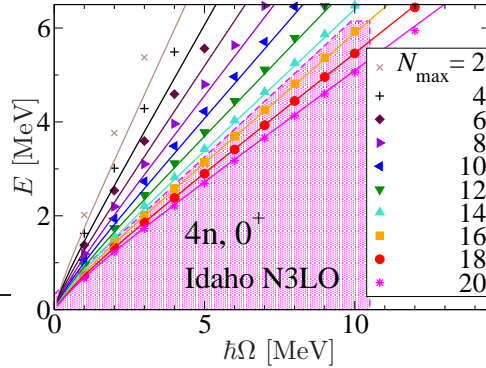


Figure 3: Low-energy fraction of the NCSM results obtained with ‘bare’ Idaho N3LO NN interaction. See Fig. 1 for details.

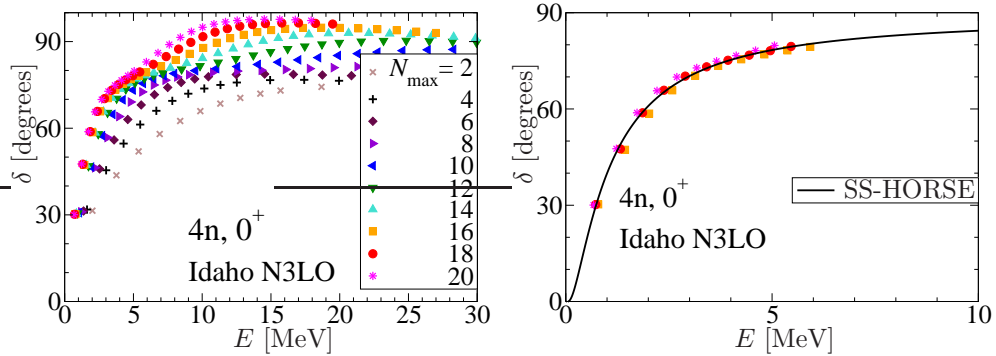


Figure 4: $4 \rightarrow 4$ phase shifts obtained directly from all available (left panel) and from the selected (right panel) NCSM results using Eq. (3) (symbols) together with the $4 \rightarrow 4$ phase shift parametrization (solid curve).

are increasing smoothly up to approximately 80° in a wide enough energy interval, suggests an absence of a narrow resonance; however, this phase shift increase may be caused by a wide resonance or by a low-lying virtual state as well as by some combination of S -matrix poles of different types. We have studied various possibilities and have come to the conclusion that the only way to describe the NCSM results with the unperturbed Idaho N3LO NN interaction is to introduce a single pole term associated with a virtual state with a very small energy of 15.2 keV. The fit parameters are listed in Table 1, the fitted hyperspherical phase shifts are depicted in the right panel of Fig. 4.

6 Summary and conclusions

We have studied in a democratic NCSM-SS-HORSE approach with various NN interactions a low-lying resonance in a system of four neutrons, which was recently observed in a RIKEN experiment [1]. We found that a narrow resonance consistent with experimental data is supported by soft NN interactions, in particular, by JISP16 and Daejeon16 interactions accurately describing the two-nucleon data and fitted to properties of light nuclei without making use of three-nucleon forces as well as by the SRG-evolved chiral Idaho N3LO NN interactions with flow parameters $\Lambda = 1.5 \text{ fm}^{-1}$

and 2.0 fm^{-1} . All these interactions provide similar results indicating a resonance with energy between 0.7 and 1.0 MeV and width between 1.1 and 1.7 MeV. On the other hand, the original Idaho N3LO, which underbinds light nuclei in the absence of a three-body interaction, does not support a tetra-neutron resonance but predicts a very low-lying tetra-neutron virtual state with the energy of 15 keV. This is consistent with results of other theoretical studies of various authors who did not obtain a narrow low-lying tetra-neutron resonance within various approaches with NN interactions with a strong short-distance repulsion. However, it appears that nobody before was searching for a virtual state in the four-neutron system.

Regarding the comparison with the experiment [1], we note that the experimentalists are not studying the S -matrix poles in the system of four neutrons but are studying cross sections of a complicated reaction ${}^4\text{He}({}^8\text{He}, {}^8\text{Be})$, where the reaction mechanism plays a very important role. This reaction mechanism can reveal the tetra-neutron resonance but, probably, at a somewhat shifted energy, or just mimic a resonance behavior in a system that has no low-lying resonance but a broad continuum structure as discussed in Ref. [9]. It is also possible that the virtual tetra-neutron state can manifest itself as a resonant structure of the cross section due to some features of the reaction mechanism. Therefore it would be very interesting to study the reaction ${}^4\text{He}({}^8\text{He}, {}^8\text{Be})$ in a realistic reaction-theory approach which will account for the pole structure of the tetra-neutron.

It would also be interesting to study the tetra-neutron with a combination of modern NN and three-nucleon forces. We experience technical difficulties in allowing for three-nucleon forces in our approach. In particular, we need matrix elements of a three-nucleon force in oscillator bases with large N_{max} and very small $\hbar\Omega$ values which presents a real challenge. This need arises since the NCSM results with large N_{max} and small $\hbar\Omega$ are of special importance for calculating low-energy behavior of the S -matrix and for locating its poles. We, however, hope to overcome this difficulty in future studies. The effects of the three-nucleon force on the tetra-neutron resonance properties are roughly estimated to be around 20–30% by comparing the results obtained with Daejeon16 and SRG-evolved N3LO interactions.

Acknowledgments

We are thankful to V. D. Efros, L. D. Blokhintsev, J. Carbonell, R. Lazauskas, L. V. Grigorenko, P. Maris, G. Papadimitriou and R. Roth for valuable discussions.

This work is supported in part by the Russian Foundation for Basic Research under Grant No. 15-02-06604-a, by the U.S. Department of Energy under Grants No. DESC00018223 (SciDAC/NUCLEI) and No. DE-FG02-87ER40371, by the US National Science Foundation under Grant No. 1516181, by the Rare Isotope Science Project of Institute for Basic Science funded by Ministry of Science and ICT and National Research Foundation of Korea (2013M7A1A1075764). Computational resources were provided by the National Energy Research Scientific Computing Center (NERSC), which is supported by the Office of Science of the U.S. Department of Energy under Contract No. DE-AC02-05CH11231, and by the Supercomputing Center/Korea Institute of Science and Technology Information including technical support (KSC-2015-C3-003).

References

- [1] K. Kisamori *et al.*, Phys. Rev. Lett. **116**, 052501 (2016).
- [2] R. Ya. Kezerashvili, arXiv:1608.00169 [nucl-th] (2016).
- [3] C. A. Bertulani and V. Zelevinsky, Nature **532**, 448 (2016).
- [4] F. M. Marqués *et al.*, Phys. Rev. C **65**, 044006 (2002).
- [5] S. C. Pieper, Phys. Rev. Lett. **90**, 252501 (2003).
- [6] S. A. Sofianos, S. A. Rakityansky and G. P. Vermaak, J. Phys. G **23**, 1619 (1997).
- [7] C. A. Bertulani and V. Zelevinsky, J. Phys. G **29**, 2431 (2003).
- [8] N. K. Timofeyuk, J. Phys. G **29**, L9 (2003).
- [9] L. V. Grigorenko, N. K. Timofeyuk and M. V. Zhukov, Eur. Phys. J. A **19**, 187 (2004).
- [10] Yu. A. Lashko and G. F. Filippov, Phys. At. Nucl. **71**, 209 (2008).
- [11] R. Lazauskas and J. Carbonell, Phys. Rev. C **72**, 034003 (2005).
- [12] E. Hiyama, R. Lazauskas, J. Carbonell and M. Kamimura, Phys. Rev. C **93**, 044004 (2016).
- [13] R. Lazauskas, E. Hiyama and J. Carbonell, arXiv:1705.07927 [nucl-th] (2017).
- [14] K. Fosse, J. Rotureau, N. Michel and M. Płoszajczak, Phys. Rev. Lett. **119**, 032501 (2017).
- [15] S. Gandolfi, H.-W. Hammer, P. Klos, J. E. Lynn and A. Schwenk, Phys. Rev. Lett. **118**, 232501 (2017).
- [16] A. M. Shirokov, G. Papadimitriou, A. I. Mazur, I. A. Mazur, R. Roth and J. P. Vary, Phys. Rev. Lett. **117**, 182502 (2016).
- [17] A. M. Shirokov, J. P. Vary, A. I. Mazur and T. A. Weber, Phys. Lett. B **644**, 33 (2007); a Fortran code generating the JISP16 matrix elements is available at http://lib.dr.iastate.edu/energy_datasets/2/.
- [18] A. M. Shirokov, A. I. Mazur, I. A. Mazur and J. P. Vary, Phys. Rev. C **94**, 064320 (2016).
- [19] A. I. Mazur, A. M. Shirokov, I. A. Mazur and J. P. Vary, in *Proc. Int. Conf. Nucl. Theor. Supercomputing Era (NTSE-2014), Khabarovsk, Russia, June 23–27, 2014*, eds. A. M. Shirokov and A. I. Mazur. Pacific National University, Khabarovsk, 2016, p. 183, <http://www.ntse-2014.khb.ru/Proc/A.Mazur.pdf>.
- [20] I. A. Mazur, A. M. Shirokov, A. I. Mazur and J. P. Vary, Phys. Part. Nucl. **48**, 84 (2017).

- [21] L. D. Blokhintsev, A. I. Mazur, I. A. Mazur, D. A. Savin and A. M. Shirokov, *Yad. Fiz.* **80**, 102 (2017) [*Phys. At. Nucl.* **80**, 226 (2017)].
- [22] L. D. Blokhintsev, A. I. Mazur, I. A. Mazur, D. A. Savin and A. M. Shirokov, *Yad. Fiz.* **80**, 619 (2017) [*Phys. At. Nucl.* **80**, 1093 (2017)].
- [23] B. R. Barrett, P. Navrátil and J. P. Vary, *Prog. Part. Nucl. Phys.* **69**, **131** (2013).
- [24] R. I. Jibuti and N. B. Krupennikova, *The method of hyperspherical functions in the quantum mechanics of few bodies*. Metsniereba, Tbilisi, 1984 (*in Russian*).
- [25] R. I. Jibuti, *Fiz. Elem. Chastits At. Yadra* **14**, 741 (1983).
- [26] A. M. Shirokov, I. J. Shin, Y. Kim, M. Sosonkina, P. Maris and J. P. Vary, *Phys. Lett. B* **761**, 87 (2016); a Fortran code generating the Daejeon16 matrix elements is available at http://lib.dr.iastate.edu/energy_datasets/1/.
- [27] R. Machleidt and D. R. Entem, *Phys. Rep.* **503**, 1 (2011).
- [28] S. D. Glazek and K. G. Wilson, *Phys. Rev. D* **48**, 5863 (1993).
- [29] F. Wegner, *Ann. Phys. (NY)* **506**, 77 (1994).
- [30] R. I. Jibuti, R. Ya. Kezerashvili and K. I. Sigua, *Phys. Lett. B* **102**, 381 (1981).
- [31] Yu. A. Lurie, Yu. F. Smirnov and A. M. Shirokov, *Izv. Ross. Akad. Nauk, Ser. Fiz.* **57**, 193 (1993) [*Bull. Russ. Acad. Sci., Phys. Ser.* **57**, 943 (1993)].
- [32] Yu. A. Lurie and A. M. Shirokov, *Izv. Ross. Akad. Nauk, Ser. Fiz.* **61**, 2121 (1997) [*Bull. Russ. Acad. Sci., Phys. Ser.* **61**, 1665 (1997)].
- [33] Yu. A. Lurie and A. M. Shirokov, *Ann. Phys. (NY)* **312**, 284 (2004).
- [34] Yu. A. Lurie and A. M. Shirokov, in *The J-matrix method. Developments and applications*, eds. A. D. Alhaidari, E. J. Heller, H. A. Yamani and M. S. Abdelmonem. Springer, 2008, p. 183.
- [35] H. A. Yamani and L. J. Fishman, *J. Math. Phys.* **16**, 410 (1975).
- [36] J. M. Bang, A. I. Mazur, A. M. Shirokov, Yu. F. Smirnov and S. A. Zaytsev, *Ann. Phys. (NY)* **280**, 299 (2000).
- [37] A. M. Shirokov, Yu. F. Smirnov and S. A. Zaytsev, in *Modern problems in quantum theory*, eds. V. I. Savrin and O. A. Khrustalev. Moscow State University, Moscow, 1998, p. 184.
- [38] S. A. Zaytsev, Yu. F. Smirnov and A. M. Shirokov, *Teor. Mat. Fiz.* **117**, 227 (1998) [*Theor. Math. Phys.* **117**, 1291 (1998)].
- [39] A. I. Baz', Ya. B. Zel'dovich and A. M. Perelomov, *Scattering, reactions and decay in non-relativistic quantum mechanics*. Israel Program for Scientific Translation, Jerusalem, 1969.
- [40] R. G. Newton, *Scattering theory of waves and particles, 2nd ed.* Springer-Verlag, New York, 1982.

- [41] P. Maris, M. Sosonkina, J. P. Vary, E. G. Ng and C. Yang, *Proc. Comput. Sci.* **1**, 97 (2010).
- [42] H. M. Aktulga, C. Yang, E. G. Ng, P. Maris and J. P. Vary, *Concurrency Computat.: Pract. Exper.* **26**, 2631 (2014).
- [43] E. D. Jurgenson, P. Maris, R. J. Furnstahl, P. Navratil, W. E. Ormand and J. P. Vary, *Phys. Rev. C* **87**, 054312 (2013).

Alphabetic list of the NTSE-2016 speakers

- **Carlo Barbieri**, University of Surrey, UK 36
- **Sergey Burkov**, Pacific National University, Russia —
- **Luigi Coraggio**, Istituto Nazionale di Fisica Nucleare, Italy 226
- **Victor Efros**, National Research Center “Kurchatov Institute”, Russia ... 66
- **Charlotte Elster**, Ohio University, USA 76
- **John Hill**, Iowa State University, USA 246
- **Nikolay Khokhlov**, Komsomolsk-on-Amur State Technical University,
Russia 124
- **Youngman Kim**, Institute for Basic Science, South Korea 154
- **Vasily Kulikov**, Moscow State University, Russia —
- **Joel Lynn**, Technische Universität Darmstadt, Germany 140
- **Alexander Mazur**, Pacific National University, Russia 185
- **Igor Mazur**, Pacific National University, Russia 280
- **Alexander Motovilov**, Joint Institute for Nuclear Research, Russia —
- **Myeong-Hwan Mun**, Korea Atomic Energy Research Institute, South
Korea —
- **Junchen Pei**, Peking University, China 174
- **Olga Rubtsova**, Moscow State University, Russia 205
- **Kimiko Sekiguchi**, Tohoku University, Japan 60
- **Noritaka Shimizu**, The University of Tokio, Japan 179
- **Andrey Shirokov**, Moscow State University, Russia —
- **Roman Skibiński**, Jagiellonian University, Poland 90
- **Alexander Soloviev**, Dukhov Research Institute of Automatics (VNIIA),
Russia 267
- **Yurii Tchuvil’sky**, Moscow State University, Russia —

- **James Vary**, Iowa State University, USA 15
- **Kai Wen**, University of Tsukuba, Japan 115
- **Furong Xu**, Peking University, China 52
- **Sergey Yakovlev**, Saint Petersburg State University, Russia —
- **Sergey Zaytsev**, Pacific National University, Russia 236
- **Xingbo Zhao**, Institute of Modern Physics, China 102
- **Shan-Gui Zhou**, Institute of Theoretical Physics, China 159

**NUCLEAR THEORY
IN THE SUPERCOMPUTING ERA – 2016
(NTSE-2016)**

International Conference Proceedings

Khabarovsk, Russia
September 19–23, 2016

Printing date: 10.01.18. Format 70x108 1/16.
Writing paper. “Computer modern” font. Digital printing.
Quire 25,9. Number of copies 100. Order number 33.

Publisher: Pacific National University,
136 Tikhookeanskaya street, Khabarovsk 680035, Russia.